UILU-ENG-95-2019

CIVIL ENGINEERING STUDIES
Hydraulic Engineering Series No. 47

ISSN: 0442-1744

PARTICLE-TURBULENCE INTERACTION IN AN OPEN-CHANNEL FLOW: IMPLICATIONS FOR BEDLOAD TRANSPORT AND SEDIMENT ENTRAINMENT INTO SUSPENSION

By

Yarko Niño

Fabián López

and

Marcelo García

Sponsored by:

National Science Foundation (CTS-9210211)
American Chemical Society (PRF 24328-G2)

HYDROSYSTEMS LABORATORY
DEPARTMENT OF CIVIL ENGINEERING
UNIVERSITY OF ILLINOIS AT URBANA-CHAMPAIGN
URBANA, ILLINOIS

December 1995

ABSTRACT

The research reported herein has been aimed at improving the present level of understanding of the physical processes involved in the transport of individual sediment particles in the near bed region of a turbulent open channel flow. Two different aspects of this phenomenon are examined, namely the mode of transport denoted as saltation, and the process of particle entrainment into suspension. The main approach followed is experimental, using visualizations of flow and particles, as well as particle tracking techniques to study particle motion and its interaction with near wall turbulence. A high-speed video system is used extensively which yields a good temporal resolution of particle motion. The experimental information is used to develop conceptual and quantitative models of the phenomena analyzed. A Lagrangian approach is used to model both saltation and particle entrainment into suspension. In the former case, the interaction between saltating particles and the bed is modelled stochastically, and the effect of turbulence on saltation is investigated separately by means of a random walk model. To model particle entrainment into suspension it is assumed that particles interact with near bed coherent flow structures which are characterized using a heuristic model. Results of the study on particle saltation provide new insights as well as unprecedented data on the characteristics of particle trajectories and velocities, particle collision with the bed, particle rotation, particle re-entrainment, and transverse particle motion. These results are used to validate the stochastic model for saltation, which appears to be a useful tool to simulate statistics of this process. Modelling bedload transport using the results of the saltation model and a Bagnoldean formulation reveals a few problems with such formulation, particularly regarding the continuum hypothesis for the bedload layer. Results of the random walk model for particle saltation indicate that turbulence tends to decrease the length and height of saltation trajectories, and also to induce a variability in the process which seems to affect primarily the length of the jumps. Nevertheless, such effects tend to decrease as the particle size increases. Shear layers typically observed in the near wall region of the open channel flow analyzed interact with sediment particles lying in the channel bottom, which eventually results in the particles being entrained into suspension. Although there has been some speculation that this process would not be effective in entraining particles totally immersed in the viscous sublayer, the results obtained demonstrate the opposite. The experiments in flows with a rough bed indicate that hiding effects tend to preclude the entrainment of particles with sizes finer than that of the roughness elements. Those experiments also indicate that the presence of roughness elements does not affect the mechanism that generates flow ejections, which would be ultimately responsible for particle entrainment. The heuristic model for particle entrainment into suspension seems to reproduce the basic characteristics of this process relatively well, however improving the predictions of the model would require a better characterization of the coherent flow structures.

ACKNOWLEDGMENTS

This report is based on the research dissertation submitted by Yarko Niño in partial fulfillment of the requirements for the degree of Doctor of Philosophy in Civil Engineering in the Graduate College of the University of Illinois at Urbana-Champaign in 1995.

Most of the experiments on the characterization of turbulence in open channels (chapters 3 and 4) and part of the experiments on particle entrainment into suspension (chapters 7 and 8) were conducted in close collaboration with the second author, Fabián López, who also used such observations to complete his M.S. Thesis in Civil Engineering at the University of Illinois in 1994.

This research was made possible thanks to grants awarded to Professor Marcelo García by the Fluid, Hydraulic, and Particulate Systems Program (Dr. M. Rocco, Program Director) of the National Science Foundation (Research Initiation Award CTS-9210211), the Donors of the Petroleum Research Fund of the American Chemical Society (grant PRF 24328-G2), and the Research Board of the University of Illinois. All the support is very gratefully acknowledged.

The acquisition of the high-speed video camera used in this study would not have been possible without the support of the above-mentioned agencies and the financial help provided by Professor Neil Hawkins, Head of the Civil Engineering Department at the University of Illinois.

Thanks are also due to Jeff Freeman who as an undergraduate research assistant, helped with some of the experiments and did the analysis of most of the video images.

Yarko Niño would also like to acknowledge the support of the Civil Engineering Department of the University of Chile and of MIDEPLAN for the fellowship granted during his studies at the University of Illinois. Fabián López would like to thank the leaves of absence granted by INCyTH, Argentina, and the Civil Engineering Department of the National University of Córdoba, Argentina.

TABLE OF CONTENTS

1. INTRODUCTION

The understanding and formulation of models of motion and transport of solid granular particles in and by liquid flows are important issues within the fields of hydraulics, fluvial geomorphology, environmental engineering, and others. The inherent complexity of the problem, which typically involves aspects related to two-phase flow as well as to interface phenomena, makes a general theoretical approach difficult, and basic research in such aspects necessary.

The study of water flow in a movable bed channel represents an interface problem. There is the water flow that adjusts itself to the loose boundary. There is loose, granular solid material upon which the flow acts deforming and changing its boundaries. The direct interaction between the fluid and solid particles is complex and involve aspects of fluid mechanics which are yet poorly understood.

In particular, the turbulence structure of the flow, which plays a major role on any transport process taking place in the system, influences the motion of granular material from and towards the boundary as well as within the flow field, and at the same time is modulated by the boundary as well as by the presence of solid particles in the flow. These processes are far from being totally understood and constitute subjects of ongoing research.

Because of the intrinsic difficulties in formulating analytical models to describe fluid-particle interactions, sediment transport problems have often remained subject to semiempirical or empirical treatment. A typical example of this is the existence of many different empirical formulae to estimate the rate of bedload transport in open channel flows. In general this approach has the disadvantage that it does not provide adequate insight on the physical processes involved, nor it permits the application of the empirical formulae to conditions different from those for which they were originally developed.

An alternative approach, which is the one followed in the present research, is to use experimental observations to try to understand the physical processes involved in sediment transport phenomena and to use such understanding to develop physically based analytical models. Understanding the physics of the problem considered gives also the possibility of adapting the models to non-canonical situations, or to conditions that differ from those for which the model was originally conceived.

The research reported herein has been aimed at improving the present level of understanding of the physical processes involved in the transport of individual sediment particles in the near bed region of a turbulent open channel flow. Two different aspects of this phenomenon are examined, namely the mode of transport denoted as saltation, and the process of particle entrainment into suspension.

Particle saltation constitutes the dominant mode of bedload transport and is characterized by the unsuspended motion of particles over a granular bed in the form of consecutive hops. This mode of transport occurs for conditions of rather low transport capacity of the flow relative to the particle inertia, and for that reason the process appears to be controlled mainly by the interactions between the saltating particles and the mean flow as well as the bed, the turbulence of the flow playing a rather secondary role in the phenomenon.

As the transport capacity of the flow increases, the turbulence starts playing a more fundamental role on the transport of sediment particles. Eventually particles are picked up by the flow from the bed and are entrained into suspension. In this mode of transport the particles are carried into the outer region of the flow and remain suspended for relatively long distances. The study of the process of particle entrainment into suspension requires analyzing the details of the interaction between turbulence and particles occurring near the bed. It is apparent that the existence of coherent flow structures in the near wall region might have a great importance on the interactions between sediment and turbulence that lead to particle entrainment.

The main approach followed in the research reported herein is experimental, using visualizations of flow and particles to elucidate the physical processes involved in particle motion and particle-flow interactions. A high-speed video system is used extensively which yields an adequate temporal resolution of particle motion. The digitization and analysis of acquired images generates highly resolved particle trajectories from which data characterizing particle velocities and other kinematic properties are obtained. This information is complemented with measurements of time series of the flow streamwise velocity component made with the help of hot-film anemometry.

The experimental information is used to develop conceptual and quantitative models of the phenomena analyzed. With respect to the latter, a Lagrangian approach is used throughout to describe particle motion as a function of time. This approach is used to model particle saltation as well as particle entrainment into suspension. In the former case, the interaction between the saltating particle and the bed is modelled stochastically. Also, the effect of turbulence on particle saltation is investigated by means of a random walk model.

Results of the study on particle saltation generate sufficient insight on the physics of bedload transport which can be applied to model this phenomenon. In fact, different alternative approaches are used in the present investigation to formulate such model, which are based on the details of the saltation process. Results of the simulation of particle saltation prove to be useful to evaluate characteristic properties of this mode of particle motion which are used in the bedload model.

Traditional models for estimating suspended sediment concentrations in turbulent channel flow consider turbulent diffusion as the basic physical process responsible for the transport of particles in suspension. Identification of the particle diffusion coefficient with the eddy diffusivity

of the flow, however, has proved not to generate accurate results. Besides, these models usually require a boundary condition for their integration, which corresponds to a near bed sediment concentration. The estimation of this reference concentration is a yet unsolved problem.

It is plausible that the understanding of the process of particle entrainment into suspension obtained in the present investigation could help to develop models for the reference concentration, which would be based in the mechanics of particle interactions with coherent flow structures. The introduction of convection processes associated with coherent flow structures may help, as well, to improve the performance of diffusion models by incorporating a more realistic representation of the turbulence of the flow.

Relationships for estimating bedload transport rates or the reference sediment concentration near the bed usually constitute closure relationships in models developed to analyze different problems related to river mechanics and environmental hydraulics. The application of concepts of particle saltation to model bedload transport in non-canonical situations, or the incorporation of transport mechanisms associated with the presence of flow coherent structures to the modelling of suspended sediment transport might help developing more physically sound closures for models addressing such problems.

The organization of the present report is as follows. In Chapter 2 a literature review on the main topics covered by this research is presented. In Chapter 3 general characteristics of the turbulence of the open channel flow used in the sediment transport experiments, measured using hot-film anemometry, are analyzed and compared with predictions given by existing models. Characteristics of coherent flow structures are also presented in this chapter, obtained from the analysis of velocity time series acquired with the hot-film equipment. In Chapter 4 a more thorough analysis of coherent flow structures in the near bed region of the open channel flow in study, obtained from simultaneous flow visualization and hot-film measurements, is presented. In Chapter 5 results of experimental studies on particle saltation, covering particle sizes ranging from gravel to fine sand, are reported and discussed. In Chapter 6 the formulation and numerical results of a stochastic model for particle saltation are reported and analyzed, including comparison with the experimental results reported in Chapter 5. In Chapter 7 results of the experiments on the threshold conditions for particle entrainment into suspension are presented and discussed. In Chapter 8 results of the experimental study on particle entrainment into suspension are reported and analyzed. In Chapter 9 models of different aspects of particle-turbulence interactions in the near bed region of an open channel flow are formulated. These include a heuristic model for particle entrainment into suspension, a simple model to account for turbulent effects on the mean saltation trajectories based on an ensemble averaged equation of particle motion, and a random walk model for sediment particle motion in turbulent open channel flow that includes the crossing-trajectories effect, which is applied to the case

of particle saltation to elucidate the effect of turbulence on this phenomenon. Finally, in Chapter 10 a few closure remarks including recommendations for future research are presented.

2. LITERATURE REVIEW

2.1 Particle saltation and bedload transport

Particle saltation

Gilbert (1914) seems to have been the first to use the term saltation, derived from the Latin *saltare*, which means to leap or dance, to describe the motion of sand particles in water. Saltation can be described according to Bagnold (1973) as the unsuspended transport of particles over a gravity bed by a fluid flow, in the form of consecutive hops, and in which no upward impulses are imparted to the particles other than those attributable to successive contacts between them and the bed. This definition rules out the effect of turbulence as the mechanism that sustains saltation, in this way distinguishing this process from that of transport in suspension. Nevertheless it also implies that hydrodynamic lift is not important to the saltation process, which, as discussed by Leeder (1979), does not seem to be accurate, at least for the case of saltation of relatively coarse sediment.

Perhaps the most complete experimental studies on particle saltation in water are those of Francis (1973), and Abbott and Francis (1977). Using photographic techniques, these researchers observed the motion of isolated particles saltating over a fixed bed of similar material, making detailed observations of different aspects of the saltation process. Particles used in such studies ranged from natural sediment to more light, artificial materials, with uniform particle sizes in the range from about 5 to about 10 mm. Experimental conditions covered a fairly wide range of shear stresses, with values of the ratio u_*/u_{*_c}, where u_* denotes flow shear velocity and u_{*_c} denotes the threshold value of u_* for incipient particle motion, up to about 3, and flow depth to particle size ratios of 5.8 and 8.6. Experimental results included mean values of saltation height, length and streamwise particle velocity, as well as mean values of the dynamic friction coefficient associated with particle motion. The schematic shown in Fig. 2.1 defines some of this variables.

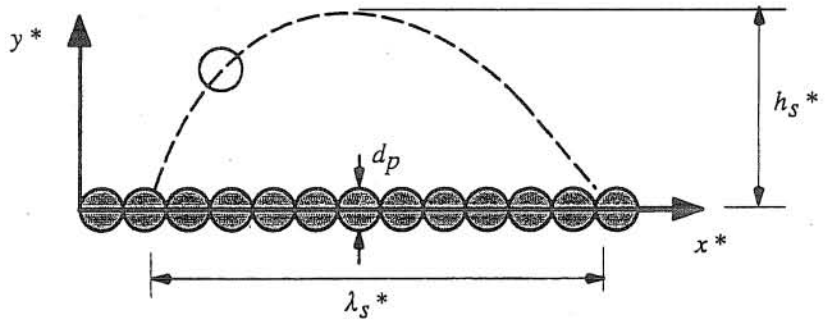

Fig. 2.1 Definition sketch for particle saltation.

Experiments conducted by Gordon et al. (1972) also addressed the saltation phenomenon in water, giving a description of the saltation of plastic balls in a very narrow flume, with a channel width to particle size ratio of about 1.2. Even though such results have a rather qualitative value,

their conclusions are relevant to the study proposed herein, particularly those regarding the process of particle collision with the bed. Those experimental results, suggest that the particle velocity component along the line of centers of striking and bed particles at initial contact is lost on impact, and that the tangential component of such velocity is completely retained. This have relevance to a model for particle collision with the bed such as that used by García and Niño (1992), as is discussed below.

Another experimental study related to particle saltation corresponds to that of Fernadez-Luque and van Beek (1976). In this case, the analysis of filmed sequences of saltating particles in a movable bed channel allowed for the estimation of mean streamwise particle velocities of such particles. The experiments considered natural sediment, as well as other lighter and heavier materials, with uniform particle sizes in the range from about 1 to about 3 mm. Experimental conditions covered flow depth to particles size ratios ranging from 25 to 120. The results concerning particle velocities were also used to develop a semiempirical bedload formula. Among other observations, these researchers point out that hydrodynamic lift plays an important role on particle saltation.

Drake et al. (1988) used motion-picture photography to analyze bedload motion in a natural stream, obtaining interesting descriptions about the transport of natural gravel particles in a movable bed. Their results however, did not include any quantitative characterization of the saltation process itself.

Meland and Norrman (1969), in an interesting experimental study, measured streamwise particle velocities of individual size fractions in heterogeneous bedload transport. Particles corresponded to glass beads and natural sediment, with sizes ranging from 0.85 to 7 mm. Nevertheless, experimental conditions allowed for the formation of bed forms, which introduces an additional complexity to the analysis of the already complex problem of bed sorting in heterogeneous sediment. Because of this, not very conclusive information was obtained.

Saltation of sediment mixtures has also been studied experimentally by Arbulieva et al. (1987) and Sutsepin (1987). These researchers used photographic techniques to measure velocities of particles in a mixture with sizes ranging from 2 to 7 mm. Their experiments consider a fixed bed, and therefore did not allow for the analysis of armoring and hiding effects on the bedload transport.

More recently, Lee and Hsu (1994) analyzed the characteristics of the saltation of sand particles, 1.4 and 2.5 mm in diameter, over a fixed bed formed by the 1.4 mm particles, using standard video recording. Due to the relatively low recording rate of standard video, they could not track the motion of individual particles, however they developed a technique which allowed them to obtain average trajectories of the saltating particles for different hydraulic conditions.

Several experimental and analytical studies have addressed the problem of particle saltation in air (e.g., Bagnold, 1936; Owen, 1964; White and Schulz, 1977; Anderson and Haff, 1988;

Ciccone et al., 1990; Nalpanis et al., 1993). Saltation in air, though, is essentially different from the saltation in water, due to the large difference in densities of both fluids, which have incidence primarily on the characteristics of the process of particle collision with the bed. Indeed, according to experimental observations (e.g., Gordon et al. 1992; Abbott and Francis, 1977), dislodging of bed particles due to the collision with saltating particles seldom occurs in a water environment, as opposed to the case of saltation in air, where such phenomenon constitutes the main mechanism for particle entrainment (Bagnold, 1936).

The numerical description of trajectories followed by saltating particles in water has attracted several researchers (e.g., Tsuchiya, 1969; Reizes, 1978; Hayashi and Ozaki, 1980; Murphy and Hooshiari, 1982; van Rijn, 1984; Wiberg and Smith, 1985; Debolsky and Shon, 1991; Sekine and Kikkawa, 1992; García and Niño, 1992). Basically all such models consist of a Lagrangian equation governing particle motion, coupled with some assumptions regarding the boundary conditions for the integration of saltating particles trajectories. The crucial point, however, is to evaluate those boundary conditions adequately, taking into account the stochastic nature of the process of particle collision with the bed, which, of the models mentioned above, only those of Wiberg and Smith (1985), Sekine and Kikkawa (1992), and García and Niño (1992) consider explicitly.

Wiberg and Smith (1985) introduce an equation for particle motion that takes into account hydrodynamic lift forces. They model the bed as formed by uniformly packed spheres, assigning a uniform probability for bed particles to be located anywhere in the path of saltating particles, as they approach the bed at collision. They assume that friction and restitution coefficients for particle collision are equal, even though their value is taken to depend on particle momentum. This is explained by pointing out that it seems likely that a sediment bed will undergo progressively greater deformation as the momentum of grain impacts increases, which would cause the bed to take progressively more of the energy of the impact, thus reducing the restitution coefficient.

Sekine and Kikkawa (1992), on the other hand, neglect hydrodynamic lift, in their equation for particle motion. The bed is also modeled as formed by uniformly packed spheres, however, the bed elevation (i.e. the relative position of bed particles in the vertical) is assumed to have a Gaussian distribution. This configuration allow these researchers to introduce a condition for stopping particle saltation, namely when a particle falls into a "hole" in the bed. They also assume that friction and restitution coefficients are equal, and give them a constant value of 0.65. Although, the computed saltations compare favorably with experimental evidence, their model predicts a value for the dynamic friction coefficient of 0.8, which appears to be too high when compared to the value 0.4 found experimentally by Abbott and Francis (1977), or the value 0.63 proposed by Bagnold (1973).

García and Niño (1992) use an stochastic model for particle collision with the bed which is akin with that of Wiberg and Smith (1985). The main difference with such model is that friction and restitution coefficients are taken to be different. This appears to be in better agreement with the observations of Gordon et al. (1972) and Abbott and Francis (1977), although the value of the restitution coefficient is not assumed to vanish, as proposed in such studies.

It is important to point out that none of the above studies have considered the effect of flow turbulence on particle saltation explicitly. A typical argument is that of Sekine and Kikkawa (1992), which affirms that turbulence effects on particle motion are negligible if $u_*/v_s << 1$, where v_s denotes particle fall velocity. Bedload transport of natural sediment usually satisfies such criterion, which, according to Sekine and Kikkawa, indicates that turbulence is important only regarding suspended sediment transport. However, no attempt to verify this argument from the equations of motion is made.

Bedload transport

The main motivation to study particle saltation in water flows is that kinematic and geometric characteristics of this process can be used in developing conceptual models of bedload transport (Yalin, 1958). Saltation is the dominant mode of bedload transport, with other modes, rolling and sliding, occurring to a lesser extent, mainly near the threshold of motion and in between individual saltation events (Bridge and Dominic, 1984).

Empirical and semiempirical approaches have been traditionally used to develop bedload equations. A clear example of a totally empirical formula is the well-known equation of Meyer-Peter and Muller (1948). More involved approaches usually consist on developing semiempirical relationships for the mean velocity of saltating particles, as well as for other parameters characterizing mean properties of the saltation process, which are then used in an analytical model for bedload transport (e.g., Ashida and Michiue, 1972; Bagnold, 1973; Engelund and Fredsøe, 1976; Fernadez-Luque and van Beek, 1976; Bridge and Dominic, 1984, Bridge and Bennett, 1992). It was not until recently that numerical models for particle saltation in water have also been used to evaluate sediment transport rates (e.g., Wiberg and Smith, 1989; Sekkine and Kikkawa, 1992; Sekine and Parker, 1992; García and Niño, 1992). The procedure in these numerical cases consists of estimating mean values of the calculated saltation variables, which are then introduced into analytical expressions for bedload transport.

A typical route followed to obtain bedload estimates based on saltation properties, is that explained by Bridge and Dominic (1984). The bedload transport rate, taken as immersed weight per unit width, is expressed as the product of the mean velocity of bedload grains, u_b*, and the immersed weight of the bedload layer per unit bed area, W_b. Invoking Bagnold's (1973) hypothesis, called herein his first hypothesis, that the immersed weight of bedload particles is balanced only by

upward forces arising from the process of particle collision with the bed, that is; neglecting lift forces exerted by the fluid during the saltation of bedload particles, then by definition of the dynamic friction coefficient, μ_d, W_b can be estimated as the ratio between the grain shear stress τ_g, defined as the force per unit area exerted by the moving grains on the bed , and μ_d. In order to evaluate τ_g, it is necessary to use Bagnold's (1956) hypothesis, called herein his second hypothesis), proposing the existence of a bedload layer within which the fluid shear stress decreases towards the bed due to the presence of moving particles. It is assumed that at the bed the fluid shear stress takes the value τ_c, associated with the critical condition for incipient motion of bed particles, which involves an equilibrium state of bedload transport. From this, τ_g is estimated as the difference between the total shear stress available at the bed and τ_c.

The problem with the above approach is that it relies heavily on Bagnold's hypotheses, which may not be totally applicable, at least in certain particular cases. In fact, Leeder (1979) found that Abbott and Francis (1977) data, obtained with relatively coarse particles, would indicate that lift forces other than those attributable to the process of particle collision with the bed are present in the saltation process. The same is pointed out by Fernandez-Luque and van Beek (1976), whose data was obtained with finer material. On the other hand, even though Bagnold's second hypothesis has been reasonably confirmed by experimental data (Leeder, 1984), the existence of a constant stress bedload layer in the case of saltation of coarse material does not seem to be very plausible, specially because those cases are usually associated with high values of the saltation height to flow depth ratio.

Wiberg and Smith (1989) follow a slightly different approach to compute bedload. Instead of estimating the weight of the bedload layer via using μ_d, these researchers introduce a mean concentration distribution of particles in the vertical, which is deduced from geometrical properties of the saltation trajectories. Nevertheless, Bagnold's second hypothesis is still used implicitly to estimate the grain shear stress at the boundary, which is related with the near bed sediment concentration by estimating the drag force acting on the bed.

An interesting application of a numerical simulation of particle saltation to the non-canonical case of bedload transport in a transverse slope is that of Sekine and Parker (1992). Basically, they used a stochastic simulation of particle saltation in a plane which is inclined in the transverse direction. Because of gravity effects, particles tend to move down the transverse slope as they saltate in the streamwise direction. The ratio between transverse and streamwise bedload transport is obtained simply by calculating the mean value of the tangent of the angle between the projection of the particle trajectory in a horizontal plane and the streamwise direction. Results are observed to compare favorably with experimental observations (e.g., Ikeda, 1982).

Parker's (1990) model for bedload transport of gravel mixtures represents one of the most recent attempts to understand the physical mechanisms involved in such phenomenon. This model uses the idea of the existence of a surface layer that is coarser than the substrate, which develops due to differential transport under equilibrium or near-equilibrium conditions of bedload transport (Parker and Klingeman, 1982). At low rates of transport (low-flow conditions), only finer material contained in the surface layer moves, which results on a coarse surface layer termed "static armor". As the rate of transport increases, progressively coarser fractions of the surface layer material are entrained into bedload motion. Such a coarse surface layer is termed "mobile armor". At high transport rates, the degree of surface coarsening would decline, up to a point at which the surface layer would be completely swept away, for very high flow conditions.

The possibility of extending saltation-based bedload models to analyze the bedload transport of mixtures has not been explored yet. As pointed out by Parker (1991), a major difficulty would appear to be the generalization of Bagnold's second hypothesis. Indeed, the value that the fluid shear stress at the bed would take for equilibrium bedload conditions, when the size distribution of bed material is not uniform, remains, to say the least, uncertain.

2.2 Coherent structures in wall turbulence

A mechanistic description of the process of particle entrainment into suspension in open channel flows, requires an adequate understanding of the interactions between individual particles and the turbulence of the flow. In particular, the process of particle entrainment into suspension appears to be closely related to the coherent structure of near-wall turbulence (Grass, 1982).

Let consider the case of a smooth wall boundary layer, with a two-dimensional mean flow (e.g., a flat plate or channel flow), in the absence of pressure gradient. According to Robinson (1991), the streamwise velocity field in the viscous sublayer and buffer region is organized into alternating narrow streaks of high- and low-speed fluid, having a mean spacing of about 100 wall units, which are quite persistent in time. The majority of the turbulence production in the entire boundary layer occurs in the buffer region during intermittent, violent outward ejections of low-speed fluid and during inrushes of high speed fluid toward the wall. This near-wall turbulence-production process is considered to be an intermittent, quasi-cyclic sequence, usually referred to as "bursting".

The intermittent nature of the wall region is associated with the presence of coherent flow structures, however, it is apparent that several different structural elements may arise, and eventually coexist in such region. Diverse vortical structures are known to exist, embedded in the wall region, being inclined horseshoes or hairpins typical shapes proposed for such vortices, although recent numerical simulations seem to indicate that vortices in the shape of complete loops are indeed rare

(Moin and Spalart, 1987; Robinson, 1990). Shear layers are also common in the near wall region, and instability arguments are usually invoked to explain the generation of vortices (Jiménez, 1987).

Flow visualizations have played a major role in the study of turbulent coherent motions. According to Landahl and Mollo-Chriestensen (1986), it was probably Kline et al. (1967) who first demonstrated the crucial role played by the near wall activity on the turbulence dynamics of channel flows. These researchers used hydrogen bubbles to visualize flow structures in the wall region, which clearly reveal the streaky nature of the wall layer, and the associated instabilities of the streaks that lead to the so called bursting phenomenon. After Kline et al.'s flow visualization experiments, several other experimental observations using the hydrogen bubble visualization technique or some other techniques, such as dye injection, particle tracking, and more recently, PIV (particle image velocimetry), have been conducted to elucidate the structural features of wall turbulence (e.g., Grass, 1971; Kim et al., 1971; Nychas et al., 1973; Offen and Kline, 1974; Praturi and Brodkey, 1978; Perry et al., 1981; Head and Bandyopadhyay, 1981; Smith and Paxon, 1983; Utami and Ueno, 1987; Liu et al., 1991). In general, flow visualization methods offer much higher information density than single probes, however, because of the rapid dispersion of marker patterns at high flow velocities, they are limited to relatively low Reynolds numbers. This, added to the fact that three-dimensional vortices are extremely difficult to characterize in the laboratory, make the conclusions obtained from visual studies partially ambiguous (Robinson, 1991). Of the aforementioned techniques, only particle (or sometimes bubble) tracking and PIV yield quantitative data, even though they have been mostly applied to the analysis of two-dimensional planes of turbulent flows (Adrian, 1986; Robinson and Rockwell, 1993).

An alternative, but also empirical approach to the study of coherent structures in bounded turbulence, is the use of statistical analysis techniques in order to detect and characterize the structure of organized turbulent motion from time series of measured turbulent quantities, and to quantify contributions of the structures to the gross statistical properties of the flow (e.g., Blackwelder and Kaplan, 1976; Wallace et al., 1977; Nakawaga and Nezu, 1981; Johansson and Alfredsson, 1982 and 1983; Blackwelder and Haritonidis, 1983; Lu and Smith, 1985; Bogard and Tiederman, 1986; Luchik and Tiederman, 1987; Lu and Smith, 1991; Morrison et al., 1992). A number of conditional-sampling techniques oriented to detect coherent structures from single probe measurements (e.g., hot wire anemometry, LDV) have been developed, being the variable-interval time average (VITA) method (e.g., Blackwelder and Kaplan, 1976), and the $u'v'$ quadrant method (e.g., Wallace et al., 1972) among the most popular. According to Wallace et al. (1977), the difficulty in using a single probe to detect coherent structures is in the fact that a flow structure passing a probe will only occasionally be intersected directly through its center, and in addition, structures will pass the probe at different stages of their lifetimes. Because of this, wide distributions of both frequencies

and magnitudes of the structures usually result from this kind of analysis. Nevertheless, Wallace et al. conclude that coherent structures can definitely be detected using conditional sampling, and furthermore, that their predominant features are better observed in the streamwise velocity signal. Bogard and Tiederman (1986), on the other hand, point out that the quadrant technique, which involves streamwise and vertical components of the velocity, is more accurate than the VITA and other techniques in detecting bursting activity.

Numerically simulated data bases using large eddy simulations (LES) or direct numerical simulations (DNS) of wall turbulence represent an alternative to experimental data bases, from which characteristics of coherent structures can be inferred (e.g., Kim and Spalart, 1987; Brooke, 1991; Johansson et al., 1991; Jiménez and Moin, 1991; Kasagi and Ohtsubo, 1993). Even though numerical data bases are associated with low Reynolds numbers, they would have advantage over physical experiments, because of the possibility of obtaining a complete space-time mapping in three dimensions of flow properties (Johansson et al., 1991), which is not achievable using current experimental methods.

Since Kline et al.'s (1967) first attempt to elucidate the three-dimensional features of the coherent structures observed in their experiments, different conceptual models have been put forward with the aim of giving an idealized description of the physical processes underlying the observed behavior of turbulent boundary layers. Kline et al. (1967) describe the near wall streaks of high and low flow speed as formed by streamwise vorticity, which would be related to alternating vortex compression and stretching due to inrushes and ejections of fluid, towards and from the wall, respectively. Another important structural feature observed by Kline et al. is the streak breakup and ejection from the wall, which they also relate to the existence of streamwise vorticity. The associated secondary motions would collect low-speed fluid into streaks and then lift the streaks gradually away from the wall until a point is reached where some sort of sudden instability appears to occur, at a distance of about 10 to 30 wall units from the wall, which leads to the amplifying rapid oscillation termed "breakup". The occurrence of intermittent local shear layers generated by vortex stretching is proposed, whose instability would lead to the breakup or bursting process.

Offen and Kline (1974) point out that the oscillatory motion of lifted streaks would be explained as due to the passage of a horseshoe vortex. Hinze (1975) suggests that fluid lifted between the legs of a horseshoe or hairpin shaped vortex loop give rise to a locally unstable shear layer, which then breaks down into a fairly violent motion, a burst, apparently destroying the parent vortex structure in the process. This event would be followed by an inrush or sweep, involving the inflow of high-speed fluid towards the wall. Following these ideas, the streaky pattern of the wall-layer would result from the existence of counter-rotating streamwise vortex pairs (the legs of

the hairpin vortex) embedded in the sublayer (Grass, 1982). An schematic of the above model for the bursting process, taken from Allen (1985), is shown in Fig. 2.2.

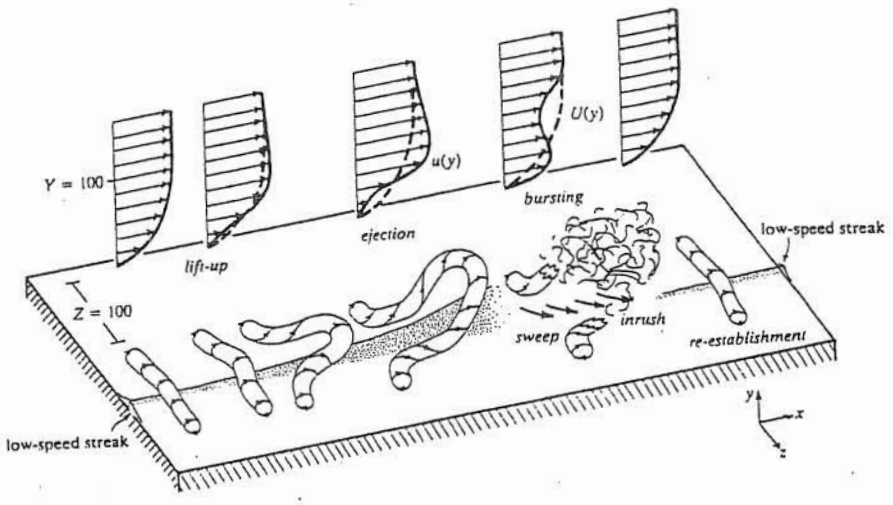

Fig. 2.2 Model of the streak-bursting cycle. The developing hairpin vortex is shown as it might be seen by an observer travelling with it. (From Allen, 1985).

Falco (1991), presents a model that integrates and inter-relates coherent motions in outer and wall regions of a bounded turbulent boundary layer. In the outer region Falco proposes the existence of two families of motions, which he calls typical eddies (TES), having distorted vortex ring-like configurations and behavior, and large-scale motions (LSMS). The TES would be phased to the upstream boundaries of the LSMS, apparently because the TES, on average, move slower than the LSMS, which causes the former to continually reform and redefine the boundaries of the latter, where they reside. The interaction with the LSMS would cause the TES to move towards the wall, where they would induce near wall region motions, such as the onset of hairpin vortices, and the formation of so called pockets, or regions in between streak pairs. Falco speculates that the initiation of the wall bursting process (in the sense of Kline et al., 1967) is phased to the upstream boundary of the LSMS , where the large scale wallward sweeps would bring the TES towards the wall. An schematic of this model, taken from Falco (1991), is shown in Fig. 2.3.

Falco's ideas exposed above are similar to those of Grass (1982), who suggests that the interactions between the large scale structures associated with the outer flow, which appears to take the form of large slowly rotating vortex-type motion, and the wall region would trigger the bursting process. Grass also speculates that the large scale motion would be formed by the coalescence of

a large number of the tips of the stretched hairpin vortices lifted up from the wall into the outer zone by the bursting process.

Robinson (1990), based on the analysis of DNS results concludes that "quasi-streamwise" vortices are the predominant structure in the wall region. According to him, the bursting process would be the result of a relatively long-lived, single, quasi-streamwise vortex which ejects low-speed fluid away from the wall by vortex induction. Robinson argues that convected pieces of principally streamwise vorticity act as "pumps" which produce ejections on one side of the vortex core and sweeps on the other, as they move along (see Fig. 2.4).

Smith et al. (1991) propose a model for the dynamical physical process occurring in the near wall region of a turbulent flow, pointing out that although the symmetric hairpin vortex is the simplest conceptual model which can account for the essential features of turbulent dynamics near the wall, it is likely that due to the large number of competing vortices and background disturbances, the majority of the vortices in a turbulent boundary layer would be asymmetric or "one-legged" hairpins. This is also in agreement with the results of DNS (e.g., Robinson, 1990). According to Smith et al., hairpin vortices (symmetric or asymmetric) can form both within the vorticity field above the wall and by viscous-inviscid interactions with the flow near the wall. Once a hairpin vortex forms, side-lobe subsidiary vortices can then develop, which retain the basic hairpin shape and act to promote lateral growth of the overall flow structure. The legs of a hairpin vortex would move rapidly towards the wall, with the spacing between legs decreasing as the vortex penetrates into regions of increasing shear near the wall. Behind the head and inboard of the legs of a convected hairpin vortex, an adverse local pressure gradient is induced near the wall, which leads to a concentration of vorticity in that region, followed by an ejection, or separation, of spires of low momentum fluid from the wall. This process represents a local breakdown of the wall layer that culminates with the eruptive spires rolling up into secondary hairpin vortices. During the initial generation process, the secondary hairpin vortices would be almost symmetric, however, due to the highly sheared surroundings, those vortices would evolve into asymmetric or "one-legged" hairpins. The characteristic low-speed streaks observed in the wall region would be the traces of a vortex interaction with the wall-layer fluid. The majority of a given streak is relatively inactive, except that portion immediately adjacent to the causative hairpin vortex. In this active region, the adverse pressure gradient associated with the hairpin vortex would eventually provoke the development of a wall layer eruption, with a subsequent roll-over into a new hairpin vortex. A schematic of Smith et al.'s model, is shown in Fig. 2.5.

More recently, PIV studies have revealed the existence of inclined, thin filaments of concentrated spanwise vorticity in the near wall region, which have been called shear layers (e.g., Liu et al., 1991; Urushihara et al., 1993). These structures, which appear to be the interface between

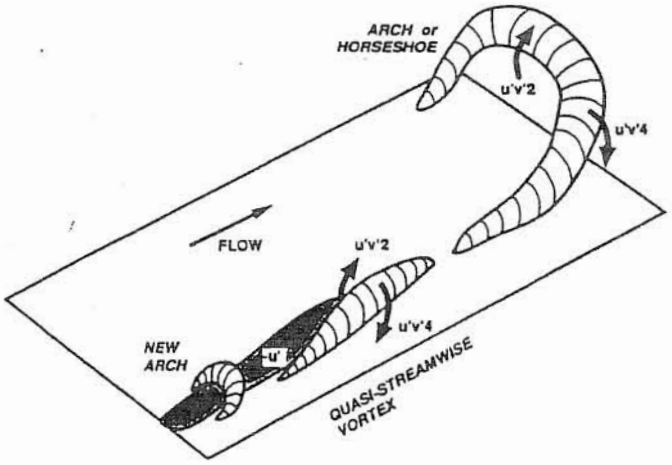

Fig. 2.3 Conceptual model of the kinematical relationships between 1) ejection/sweep motions and quasi-streamwise vortices in the near wall region and 2) ejection/sweep motions and arch-shaped vortical structures in the outer region. Model proposed for low Reynolds number boundary layers. (From Robinson, 1990).

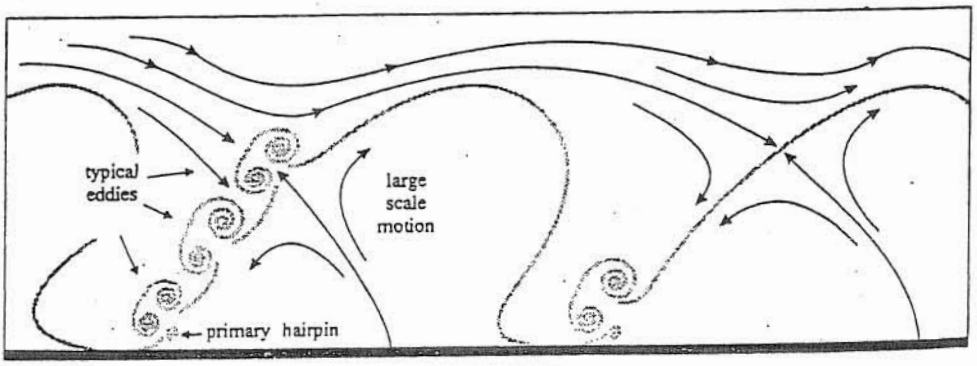

Fig. 2.4 The outer region. This includes the TES phased to the upstream boundaries of the LSMS, and the flow of high speed fluid around and within the LSMS as seen by an observer moving with the upstream boundary of the LSMS. (From Falco, 1991).

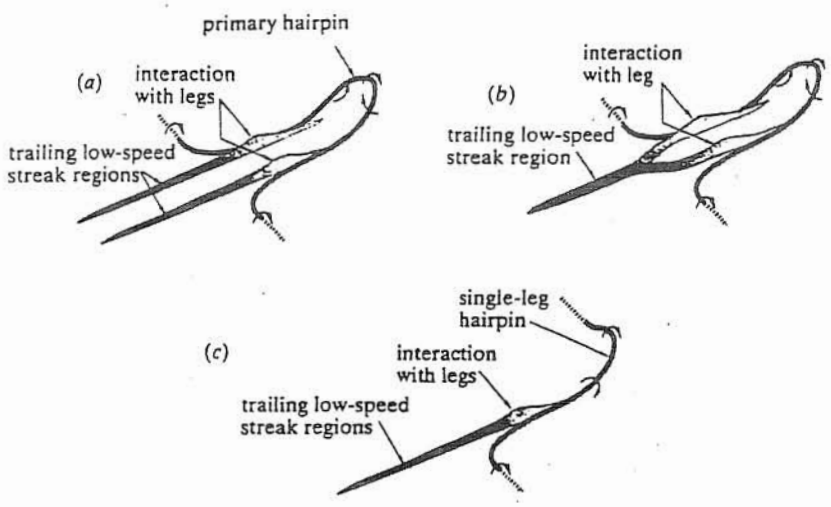

Fig. 2.5i) Schematic diagram of the processes whereby moving hairpin vortices induce low-speed streaks. a) Symmetric case with wide separation of legs. b) Symmetric case with legs closer together; the two streaks merge. c) Asymmetric case. (From Smith et al., 1991).

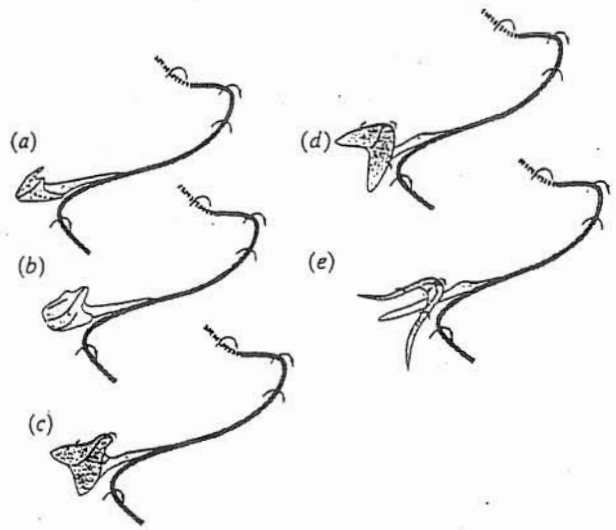

Fig. 2.5ii) The generation of secondary vortex via surface interaction for an asymmetric hairpin vortex. a) The onset of interaction; sharp, crescent-shaped ridge develops in the surface flow where the induced pressure gradient near the surface is adverse. b) Rapid outward movement of the erupting ridge which contains concentrated vorticity. c) The erupting sheet starts to roll over. d) Partial roll-over reached. e) Complete generation of secondary hairpin vortex. (From Smith et al., 1991).

regions of low momentum fluid ejected away from the wall and regions of high momentum fluid moving toward the wall, have an inclination to the channel bottom of less than 45°. Structures resembling closely the shear layers observed in the PIV studies cited above, have been obtained from direct numerical simulations of turbulent channel flow (e.g., Guezennec et al., 1987; Jiménez et al., 1988; Brooke, 1991). According to Jiménez et al. (1988) the inclined shear layers woud constitute the dominant structure in the near wall region of turbulent channel flow, and their generation mechanism appears to be similar to that of two-dimensional Tollmien-Schlichting waves.

2.3 Particle entrainment into suspension

According to Grass (1982), his earlier, 1974, flow visualization experiments of the bursting phenomenon using fine sand, provided conclusive proof that the mechanism for the entrainment and suspension of particles in a turbulent boundary layer indeed corresponds to ejections associated with coherent structures, as described in the preceding section. This idea was previously put forward by Sutherland (1967), who speculated that a mechanism to entrain sediment grains into suspension would correspond to turbulent eddies disrupting the viscous sublayer and impinging directly onto the sediment bed, such that the swirling motion of the fluid within the eddy would increase the local shear stress acting over individual grains, causing their acceleration, and eventually, due to the induced rolling motion and depending on their relative exposition over the mean bed level, such grains would leave the bed. Although Sutherland's idea of eddies coming from above and impinging on the bed may not be totally correct in the light of the antecedents presented in the previous section, it delineates the basic turbulence-particle interaction that results in particle entrainment, which constitutes the main hypothesis for such mechanism used in more recent studies.

From a Chemical Engineering point of view, Cleaver and Yates (1976) analyzed the problem of particle deposition and re-entrainment in a bounded turbulent flow, taking into account the structure of the wall layer. According to them, particles are convected into the wall layer by a coherent downsweep and are either deposited in that downsweep (or subsequent downsweeps), or are transported back into the flow by an outward burst, which may also cause the re-suspension of previously deposited particles. Even though Cleaver and Yates concentrate on small, neutrally buoyant or otherwise very light particles, their analysis is interesting because they introduce a stochastic description for the occurrence of bursting events, and make use of reported values of bursting temporal and spatial characteristic scales to develop a simple model for particle re-suspension.

Even though after Grass (1974) experiments several laboratory and field studies have been carried out with the purpose of relating bursting and particle transport process, the most detailed observations have been made for light particles in water flows, and possibly only field studies have

explored the response of natural sediment to the bursting phenomenon (e.g Jackson, 1976; Heathershaw and Thorne, 1985; Lapointe, 1992).

Jackson (1976) generalized the bursting model shown in Fig. 2.2 to alluvial channels, concluding that although the intensity of the bursting can be modified by the roughness of the bed, the presence of sediment waves, and even by the sediment transport processes occurring in the boundary layer, these features would not alter the basic characteristics of the bursting cycle. As an indirect prove of the above assertion, Jackson points out that the typical boils observed on the water surface of rivers seem to correspond to highly energetic bursts, which are able to eject throughout the whole thickness of the boundary layer. Based on his observations of high sediment concentration in kolks and boils in rivers, he concludes that bursts would be the primary mechanism for the suspension of sediment and also for the entrainment of much coarser particles than the mean flow tractive forces alone could accomplish. Jackson also argues that the strong upward flow in a burst event, would provide the vertical anisotropy in the turbulence needed to maintain sediment in suspension. Although Jackson's arguments seem reasonable, it is apparent that they somehow stretch the concept of the bursting process, which according to the discussion of the previous section would refer to phenomena localized in the wall layer, to explain the turbulence structure of the whole boundary layer.

More detailed observations of the motion of almost neutrally buoyant particles in a smooth boundary open channel flow were made by Sumer and Oguz (1978), using values of particle relative density in the range 1.003 to 1.008. They conclude that, in general, ejected particles are initially located in low-speed wall streaks, protruding over the viscous sublayer. The particle lift-up would be the result of temporary local adverse pressure gradients related to ejections occurring in the wall layer. The rise of lifted particles seems to be strongly controlled by the ejected flow structure until it breaks up. From then on, the particle would stop rising and begin to go down until it either reaches the channel bottom, or eventually finds another ejection which would keep the particle in suspension. Another observed feature is that measured velocities of ejected particles coincide fairly well with flow velocities, which is also reported by Grass (1971). Sumer and Oguz also point out that small particles, totally immersed in the viscous sublayer, were not entrained by bursting activity.

Sumer and Deigaard (1981) extended the experiments with light particles of Sumer and Oguz, so as to cover rough boundary conditions. Their findings would indicate that the burst cycle and the mechanism for particle entrainment are essentially the same as those corresponding to a smooth boundary. The particles in the rough boundary experiments, however, were ejected to larger heights than in the case of a smooth boundary, apparently due to more violent bursting activity, which is in agreement with the observations of Grass (1971). Sumer and Deigaard also analyzed the response of slightly heavier particles, having a relative density of the order of 1.03. They concluded that

although the ejection of the latter particles does not differ appreciably from that of lighter ones, it seems that they would not completely follow the lifted fluid, but leave the main body of it, due to gravity, before the bursting breakup occurs, thus reaching lesser heights than in the case of lighter particles. This description appears to coincide with the so called "crossing-trajectories effect", i.e., a particle falls out of an eddy before the eddy losses its identity (Wells and Stock, 1983; Zhuang et al., 1989).

As it was already mentioned, Grass (1974) measured streamwise and vertical components of sand particles suspended by ejection events in a flat plate boundary layer. His measurements show that the mean streamwise particle velocities tend to be lower than the local mean flow velocity, which is in agreement with the idea of the particle being suspended by an ejection event, corresponding to flow velocity fluctuations $u' < 0$, $v' > 0$ (i.e., events of quadrant 2). Mean vertical particle velocities, on the other hand, tend to have values of the order of 1.0 to 1.5 times the shear velocity, u_*, in the region up to 100 wall units from the plate. Sumer and Deigaard (1981) also measured mean velocities of suspended light particles in the wall region, obtaining results that are similar to those of Grass (1974). Nevertheless, none of the above researchers gives values of instantaneous velocities of ejected particles, nor they measured instantaneous flow velocities simultaneously.

Van Rijn (1984) discusses the conditions for the initiation of suspension of sediment particles. A classical criterion for this problem is that of Bagnold (1966), who based on the assumption that particles remain in suspension as long as the turbulent eddies have dominant vertical velocity components, which would scale with u_*, that exceed the particle settling velocity, v_s. Accordingly, the critical value of the flow shear velocity for the initiation of suspension would satisfy: $u_*/v_s = 1$. Experimental results by van Rijn, though, show that such criterion is too restrictive, the entrainment of sediment into suspension being observed for much smaller values of the flow wall shear stress. Moreover, those experiments also show that small particles immersed in the viscous sublayer are indeed entrained into suspension, which appears to be in contradiction with the results of Sumer and Oguz (1978).

Conventional sediment transport experiments frequently utilize turbulent channel flow above a bed of erodible material. Among the difficulties of making detailed observations of the entrainment of particles in such experimental set-up is the fact that many entrainment events are occurring simultaneously. Browand and Plocher (1985) simplify the problem by analyzing the effect of a single turbulent spot on the entrainment of particles. These researchers point out that even though the nose of the turbulent spot is not active in the entrainment process, particles are observed to be lifted during the lift-up of the vortex loops conforming the main body of the turbulent spot. Such particles would attain heights comparable to the height of the vortex loops, but lag the fluid motion and are left behind. Subsequently, the falling particles may again be boosted as they are

overtaken by larger vortex structures travelling in the outer region of the turbulent spot. An average of three or four of those boosts were observed in each case, corresponding roughly to the number of vortex structures comprising the active portion of the turbulent spot. Browand and Plocher also point out that there is a difference between entrainment (the actual lift-up of bed material) and what might be called "suspendability" (the propensity of particles to remain suspended in a turbulent flow). Small particles lying on the bed, which were never observed to be lifted by the turbulent spot, remained suspended with no difficulty when they were injected in the spot above the wall.

Another experimental study on sediment suspension is that of Ashida and Fujita (1986). These researchers used a high-speed video system to record trajectories of polystyrene particles entrained from a rough bed formed by similar particles. The results obtained are used to estimate the probability density function of lift forces during particle entrainment, which is then introduced in a stochastic model of particle suspension. Observations suggest that a particle on a rough bed is entrained into the flow by lift forces due to accelerated upward flows which occur during an ejection event of bursting. Although the lift force decreases to about zero in a short period after the entrainment, the particle further rises up by effect of drag forces due to the same upward flow.

Yung et al. (1989) analyzed the role of turbulent bursting in particle re-entrainment in aqueous systems. They conducted a series of experiments for flow and particle visualization using a high-speed cine camera, which provided information on bursting characteristics, such as frequency, spatial dimensions, ability to re-suspend particles (cleaning efficiency), etc. The most prominent feature observed was that most of the particles tend to roll downstream along the surface, arranged in a streaky pattern, such that they would remain stationary for a short time before resuming motion. This erratic motion is attributed to the unsteady nature of the wall layer. Yung et al. report that for the experiments with small particles, immersed in the viscous sublayer, most particles did not respond to any upward movement when flow structures were observed to eject from the surface. Only occasionally, individual particles were observed to be rolling at a slight angle, and gradually moved up and carried downstream by the main flow. For the experiments with particles protruding from the viscous sublayer, the majority of the particles began movement by rolling, but were soon lifted up without travelling more than two particle diameters. Thereafter, particles were transported in small jumps. At high flow rates the particles were ejected at angles between 15° and 30°. Yung et al. conclude that the bursting phenomenon appears to have a stronger interaction with large-sized particles and at higher fluid velocities. The ability of turbulent bursts to create a sufficient lift force to re-entrain particles immersed in the viscous sublayer would seem to be doubtful.

More recently, Rashidi et al. (1990) made particle motion observations with simultaneous flow visualization of turbulent flow over a smooth boundary. Besides analyzing the particle response to wall turbulence, they also studied the modulation of the bursting phenomenon due to

the presence of particles. Their results show that both the frequency of the bursting activity and the intensity of the ejection events tend to increase as the size and/or concentration of the particles immersed in the flow increases. On the other hand they found that the variation of particle density has no apparent effect on the modulation of the turbulence. Rashidi et al. also conclude that it appears that particle transport is controlled mainly by the ejections originating from lift-up and breakdown of the low-speed streaks in the wall region. As particles are introduced in the flow, they mostly accumulate in the low-speed streaks of the wall structures. These particles are then lifted-up by the flow structures (depending on their size, density and flow Reynolds number), and ejected into the bulk flow. The ejected particles later return towards the wall, some of them finding wall ejections already in progress which may cause such particles to be re-entrained into suspension.

The motion of near-bed suspended sediment has been analyzed by Christoforou et al. (1991), who introduce the modelling of bursting events associated with near wall turbulence in a Lagrangian model for particle motion, in a way akin to the modelling of particle saltation reviewed in previous sections.

Not many studies applying data bases generated using large eddy simulations or direct numerical simulations to the analysis of particle response to wall turbulence have been reported in the literature, even though some analyses have been made of the case of particles in homogeneous turbulence, and in decaying isotropic turbulence (e.g., Deutsch and Simonin, 1991; Elghobashi and Truesdell, 1992). Browand et al. (1991) present some preliminary results of a DNS applied to the case of transport in suspension of heavy particles immersed in a bounded flow. This simulation, however, put more attention to the motion of particles in the outer region than in the transport processes occurring near the wall, not even introducing into the model the possibility of particle entrainment. The latter mainly because of the uncertainties in the equation of particle motion in the vicinity of a wall, which makes the modeling of such processes not an easy task. More recently, Brooke (1993) has also applied DNS data bases to the analysis of aerosol particles in a bounded turbulent flow. Again, the analysis concentrates in the outer flow rather than in the near wall processes.

Pedinotti et al. (1992) performed a direct numerical simulation of particle behavior in the wall region of a turbulent channel flow. They found that particles with very low specific density, $R = 0.03$, tend to be grouped along low-speed streaks, however the degree of sorting appears to depend on the particle time constant (a measure of the particle inertia). Pedinotti et al. point out that the sorting mechanism would be due to the presence of a rotation motion in the high-speed regions which pushes the particles out of them. They speculate that this mechanism would be effective on grouping particles along the viscous sublayer as long as their time constant is small enough as to follow the streak motion, but not so small as to be sensitive to high-frequency fluctuations, which would tend

to distribute the particles uniformly. Also, Pedinotti et al.'s simulations have shown that particles are lifted from the bed by the action of upflows caused by quasi-streamwise vortices which detach low-speed fluid from the wall.

Wells (1992) studied the problem of particle pick-up by an impinging vortex ring. He argues that the resulting particle-vortex interaction would resemble the processes occurring in the wall region of a boundary layer flow. According to Wells, the dominant coherent structures in such region would include concentrated streamwise vortices inclined at a shallow angle to the boundary in the streamwise direction, and thin shear layers on the upstream face of fluid being lifted by the vortices. He argues that the mechanism of entrainment would be essentially that proposed by Sutherland (1967), replacing his concept of "eddy impact" by "eddy convection", which comes from the idea that a quasi-steady streamwise vortex structure being convected past an observer at the wall should appear much as an "impinging" vortex. In this sense Wells' proposed entrainment mechanism (or Sutherland's for that effect) is intrinsically different from that proposed by Sumer and Oguz (1981), who suggest that particle lift-up would be the result of temporary local adverse pressure gradients related to ejections occurring in the wall layer, as it was already commented. Wells points out that particle erosion and lift-up are essentially different processes, occurring one after the other, and which may in fact occur at separated times for a given particle. Erosion would occur in the high-speed streaks of the wall layer, where shear stress is highest, on the side of the vortex where the flow is directed towards the bed. Following erosion, the particle would be swept under the streamwise vortex towards the longitudinal streaks of slower fluid, where the particle may immediately be swept upwards. This, according to Wells, would be the only way for particles with a high fall velocity to be suspended; their weight would result in them being re-deposited in any but the strongest updrafts.

2.4 References

Abbott, J. E., and Francis, J. R. D. (1977). "Saltation and suspension trajectories of solid grains in a water stream". *Philos. Trans., Royal Soc. of London.* A, 284, pp 225–254.

Adrian, R. J. (1986). "Multi-point optical measurements of simultaneous vectors in unsteady flow-a review". *Int. J. Heat and Fluid Flow*, Vol 7, No 2, pp 127–145.

Allen, J. R. L. (1985). Principles of physical sedimentology. *George Allen & Unwin (publishers).*

Anderson, R. S., and Haff, P. K. (1988). "Simulation of eolian saltation". *Science*, 241, pp 820-823.

Arbulieva, K. M., Olevinskaya, S. K., and Pivovarov, A. A. (1987). "Some findings of experimental studies conducted on the intermittent movement of gravel in a turbulent current". *Dynamics and Thermal Regimes of Rivers.* Ed K. I. Rossinskii. Russian Translations Series 52.

Ashida, K., and Fujita, M. (1986). "Stochastic model for particle suspension in open channels". *J. Hydroscience and Hydraulic Engrg.*, vol 4, No 2, pp 21–46.

Ashida, K., and Michiue, M. (1972). "Study on hydraulic resistance and bedload transport rate in alluvial streams". *Proc. Japan Soc. Civ. Engrg.*, 206, pp 59–69.

Bagnold, R. A. (1973). "The nature of saltation and of 'bed-load' transport in water". *Proc. Royal Soc. of London.* A, 332, pp 473–504.

Bagnold, R. A. (1966). "An approach to the sediment transport problem for general physics". *Geological Survey Professional Paper* 422-I, Washington, D. C.

Bagnold, R. A. (1956). "The flow of cohesionless grains in fluids". *Philos. Trans., Royal Soc. of London.* A, 249, pp 235–297.

Bagnold, R. A. (1936). "The movement of desert sand". *Proc. Royal Soc. of London.* A, 157, pp 594–620.

Blackwelder, R. F., and Haritonidis, J. H. (1983). "Scaling of the bursting frequency in turbulent boundary layers". *J. Fluid Mech.*, vol 132, pp 87–103.

Blackwelder, R. F., and Kaplan, R. E. (1976). "On the wall structure of the turbulent boundary layer". *J. Fluid Mech.*, vol 76, pp 389–413.

Bogard, D. G., and Tiederman, W. G. (1986). "Burst detection with a single-point velocity measurements". *J. Fluid Mech.*, vol 162, part 1, pp 389–413.

Bridge, J. S., and Bennett, S. J. (1992). "A model for the entrainment and transport of sediment grain of mixed sizes, shapes and densities". *Water Resour. Res.*, 28 (2), pp 337–363.

Bridge, J. S., and Dominic, D. F. (1984). "Bedload grain velocities and sediment transport rates". *Water Resour. Res.*, 20 (4), pp 476–490.

Brooke, J. W. (1993). "Transport processes in a direct numerical simulation of turbulent channel flow". *Ph.D. Thesis, Univ. of Illinois at Urbana-Champaign.* Urbana, Illinois.

Brooke, J. W. (1991). "A study of coherent eddy structure in turbulent channel flow". *Masters Thesis, Univ. of Illinois at Urbana-Champaign.* Urbana, Illinois.

Browand, F. K., Nassef, H., and Spalart, P. R. (1991). "The motion of heavy particles in a turbulent boundary layer: problem formulation and preliminary statistical results". *Dept. Aerospace Engrg., Univ. of Southern California*, Report USCAE 148.

Browand, F. K., and Plocher, D. A. (1985). "Image processing for sediment transport". *Proceedings, 21st Congress* I.A.H.R., Melbourne. pp 8–14.

Christoforou, V., Prinos, P., and Goulas, A. (1991). "Lagrangian modelling of near-bed suspended sediments". *Int. Symp. Transport of Suspended Sediments and its Mathematical Modelling*. Florence, Italy.

Ciccone, A. D., Kawall, J. G., and Keffer, J. F. (1990). "Flow visualization/digital image analysis of saltating particle motions". *Experiments in Fluids* 9, pp 65–73.

Cleaver, J. W., and Yates, B. (1976). "The effect of re-entrainment on particle deposition". *Chemical Engrg. Science.*, vol 31, pp 147–151.

Debolsky, V. K., and Shon, N. M. (1991). "A mathematical model of sediment particles saltation near the bed of an alluvial stream". *Int. Symp. Transport of Suspended Sediments and its Mathematical Modelling*. Florence, Italy.

Deutsch, E., and Simonin, O. (1991). "Large eddy simulation applied to the motion of particles in stationary homogeneous fluid turbulence". *Turbulence Modification in Multiphase Flows*, ASME. FED–Vol 110, pp 35–42.

Drake, T. G., Shreve, R. L., Dietrich, W. E., Whiting, P. J., and Leopold, L. B. (1988). "Bedload transport of fine gravel observed by motion-picture photography". *J. Fluid Mech.*, vol. 192, pp 193–217.

Elghobashi, S., and Truesdell, G. C. (1992). "Direct simulation of particle dispersion in a decaying isotropic turbulence". *J. Fluid Mech.*, vol 242, pp 665–700.

Engelund, F., and Fredsøe, J. (1976). "A sediment transport model for straight alluvial channels". *Nordic Hydrol.*, 7, pp 293–306.

Falco, R.E. (1991). "A coherent structure model of the turbulent boundary layer and its ability to predict Reynolds number dependence". *Philos. Trans., Royal Soc. of London*. A, 336, pp 103–129.

Fernandez-Luque, R., and van Beek, R. (1976). "Erosion and transport of bed sediment". *J. Hydr. Res.*, 14 (2), pp 127–144.

Francis, J. R. D. (1973). "Experiments on the motion of solitary grains along the bed of water stream". *Proc. Royal Soc. of London*. A, 332, pp 443–471.

García, M., and Niño, Y., (1992). "Lagrangian description of bedload transport by saltating particles". *Proc. VI I.A.H.R. Int. Symp. on Stochastic Hydr.*, Taipei, Taiwan. pp 259–266.

Gilbert, G. K. (1914). "The transportation of debris by running water". *Prof. Paper 86, US Geological Survey*, Reston, Va.

Gordon, R., Charmichael J. B., and Isackson, F. J. (1972). "Saltation of plastic balls in a 'one-dimensional' flume". *Water Resour. Res.*, 8 (2), pp 444–459.

Grass, A. J. (1982). "The influence of boundary layer turbulence on the mechanism of sediment transport". *Euromech 156: Mechanics of sediment transport.* Istanbul. pp 3–17.

Grass, A. J. (1974). "Transport of fine sand on a flat bed: turbulence and suspension mechanics". *Euromech 48.* Inst. Hydrodynamic and Hydraulic Engrg., Tech. Univ. Denmark, pp 33–34.

Grass, A. J. (1971). "Structural features of turbulent flow over smooth and rough boundaries". *J. Fluid Mech.*, vol 50, pp 233–255.

Guezennec, Y. G., Piomelli, U., and Kim, J. (1989). "On the shape and dynamics of wall structures in turbulent channel flow". *Phys. of Fluids* A 1 (4), pp 764–766

Hayashi, T., and Ozaki, S. (1980). "On the unit step length of saltation of sediment particles in the bedload layer". *Third Int. Symp. on Stochastic Hydr.*, Tokyo, Japan.

Head, M. R., and Bandyopadhyay, P. (1981). "New aspects of turbulent boundary-layer structure". *J. Fluid Mech.*, vol 107, pp 297–338.

Heathershaw, A. D., and Thorne, P. D. (1985). "Sea-bed noises reveal role of turbulent bursting phenomenon in sediment transport by tidal currents". *Nature, v*ol 316, pp 339–342.

Hinze, J. O. (1975). "Turbulence". *McGraw-Hill Series in Mechanical Engrg.*

Ikeda, S. (1982). "Incipient motion of sand particles on side slopes". *J. Hydraulic Div.*, ASCE, 108 (HY1), pp 95–114.

Jackson, R. G. (1976). "Sedimentological and fluid dynamics implications of the turbulent bursting phenomenon in geophysical flows". *J. Fluid Mech.*, vol 77, pp 531–560.

Jiménez, J., and Moin, P. (1991). "The minimal flow unit in near-wall turbulence". *J. Fluid Mech.*, vol 225, pp 213–240.

Jiménez, J., Moin, P., Moser, R., and Keefe, L. (1988). "Ejection mechanism in the sublayer of a turbulent channel". *Phys. Fluids.* 31 (6), pp 1311–1313.

Jiménez, J. (1987). "Bifurcations and bursting in two-dimensional Poiseuille flow". *Phys. Fluids.* 30 (12), pp 3644–3646.

Johansson, A. V., Alfredsson, P. H., and Kim J. (1991). "Evolution and dynamics of shear-layer structures in near wall turbulence". *J. Fluid Mech.*, vol 224, pp 579–599.

Johansson, A. V., and Alfredsson, P. H. (1983). "Effects of imperfect spatial resolution on measurements of wall-bounded turbulent shear flows". *J. Fluid Mech.*, vol 137, pp 409–421.

Johansson, A. V., and Alfredsson, P. H. (1982). "On the structure of turbulent channel flow". *J. Fluid Mech.*, vol 122, pp 295–314.

Kasagi, N., and Ohtsubo, Y. (1993). "Direct numerical simulation of low Prandtl number thermal field in a turbulent channel flow". Turbulent Shear Flows 8: selected papers form the Eigth

International Symposium on Turbulent Shear Flows, Munich, 1991. F. Durst et al., eds. Springer-Verlag.

Kim, J., and Spalart, P. R. (1987). "Scaling of the bursting frequency in turbulent boundary layers at low Reynolds numbers". *Phys. Fluids*, 30 (11), pp 3326–3328.

Kim, H. T., Kline, S. J., and Reynolds, W. C. (1971). "The production of turbulence near a smooth wall in a turbulent boundary layer". *J. Fluid Mech.*, vol 50, part 1, pp 133–160.

Kline, S. J., Reynolds, W. C., Schraub, F. A., and Runstadler, P. E. (1967). "The structure of turbulent boundary layers". *J. Fluid Mech.*, vol 30, part 4, pp 741–773.

Landahl, M. T., and Mollo–Chriestensen, E. (1986). "Turbulence and random processes in fluid mechanics". *Cambridge University Press.*

Lapointe, M. (1992). "Burst–like sediment suspension events in a sand bed river". *Earth Surface Processes and Landforms*, vol 17, pp 253–270.

Lee, H., and Hsu, I. (1994). "Investigation of saltating particle motions". *J. Hydr. Engrg.*, ASCE, 120 (7), pp 831–845.

Leeder, M. R. (1984). "Bedload stresses and sediment transport theory-a correction". *Sedimentology* 31, pp 277–278.

Leeder, M. R. (1979). "Bedload dynamics: grain impacts, momentum transfer and derivation of a grain Froude number". *Earth Surface Processes*, vol 4, pp 291–295.

Liu, Z. C., Landreth, C. C., Adrian, R. J., and Hanratty T. J. (1991). "High resolution measurement of turbulent structure in a channel with particle image velocimetry". *Experiments in Fluids* 10, pp 310–312.

Lu, L. J., and Smith, C. R. (1991). "Use of flow visualization data to examine spatial–temporal velocity and burst-type characteristics in a turbulent boundary layer". *J. Fluid Mech.*, vol 232, pp 303–340.

Lu, L. J., and Smith, C. R. (1985). "Image processing of hydrogen bubble flow visualization for determination of turbulence statistics and bursting characteristics". *Experiments in Fluids,* 3, pp 349–356.

Luchik, T. S., and Tiederman, W. G. (1987). "Time-scale and structure of ejections and bursts in turbulent channel flows". *J. Fluid Mech.*, vol 174, pp 529–552.

Meland, N., and Norrman, J. O. (1969). "Transport velocities of individual size fractions in heterogeneous bedload". *Geografiska Annaler* 51, A, 3, pp 127–144.

Meyer-Peter, E., and Muller, R. (1948). "Formulas for bedload transport". *Proceedings, 2nd Congress* I.A.H.R., Stockholm.

Moin, P., and Spalart, P. (1987). "Contributions of numerical simulation data bases to the physics, modeling and measurement of turbulence". *Advances in Turbulence*. Eds. W .K. George and R. Arndt. pp 11–38.

Morrison, J. F., Subramanian, C. S., and Bradshaw, P. (1992). "Bursts and the law of the wall in turbulent boundary layers". *J. Fluid Mech.*, vol 241, pp 75–108.

Murphy, P. J., and Hooshiari, H. (1982). "Saltation in water dynamics". *J. Hydraulic Div.*, ASCE, 108 (HY11), pp 1251–1267.

Nakawaga, H., and Nezu, I. (1981). "Structure of space-time correlations of bursting phenomena in an open channel flow". *J. Fluid Mech.*, vol 104, pp 1–43.

Nalpanis, P., Hunt, J. C. R., and Barret, C. F. (1993). "Saltating particles over flat beds". *J. Fluid Mech.*, vol 251, pp 661–685.

Nychas, S. G., Hershey, H. C., and Brodkey R. S. (1973). "A visual study of turbulent shear flow". *J. Fluid Mech., v*ol 61, part 3, pp 513–540.

Offen, G. R., and Kline, S. J. (1974). "Combined dye-streak and hydrogen–bubble visual observations of a turbulent boundary layer". *J. Fluid Mech.*, vol 62, part 2, pp 223–239.

Owen, P. R. (1964). "Saltation of uniform grains in air". *J. Fluid Mech.*, vol 20, part 2, pp 225-242

Parker, G. (1991). "Some random notes on grain sorting". *Proc. Int. Grain Sorting Seminar.* Ascona, Switzerland.

Parker, G. (1990). "Surface-based bedload transport relation for gravel bed rivers". *J. Hydr. Res.*, vol 28, No 4, pp 417–436.

Parker, G. and Klingeman, P. C. (1982). "On why gravel bed streams are paved". *Water Resour. Res.*, vol 18, No 5, pp 1409–1423.

Pedinotti, S., Mariotti, G. and Banerjee, S. (1992). "Direct numerical simulation of particle behavior in the wall region of turbulent flows in horizontal channels". *Int J. Multiphase Flow*, vol 18, No 6, pp 927-941.

Perry, A. E., Lim, T. T., and Teh, E. W. (1981). "A visual study of turbulent spots". *J. Fluid Mech.*, vol 104, pp 387–405.

Praturi, A. K., and Brodkey, R. S. (1978). "A stereoscopic visual study of coherent structures in turbulent shear flow". *J. Fluid Mech.*, vol 89, part 2, pp 251–272.

Rashidi, M., Hetsroni, G., and Banerjee, S. (1990). "Particle-turbulence interaction in a boundary layer". *Int. J. Multiphase Flow*, vol 16, No 6, pp 935–949.

Reizes, J. A. (1978). "Numerical study of continuous saltation". *J. Hydraulic Div.*, ASCE, 104 (HY9), pp 1303–1321.

Robinson, O., and Rockwell, D. (1993). "Construction of three-dimensional images of flow structure via particle tracking techniques". *Experiments in Fluids*, 14, pp 257–270.

Robinson, S. K. (1991). "Coherent motions in the turbulent boundary layer". *Annu. Rev. Fluid Mech.*, 23, pp 601–639.

Robinson, S. K. (1990). "Kinematics of turbulent boundary layer structure". *Ph.D. dissertation, Stanford Univ.* Stanford, California.

Sekine, M., and Kikkawa, H. (1992). "Mechanics of saltating grains II". *J. Hydr. Engrg.*, ASCE, 118 (4), pp 536–558.

Sekine, M., and Parker, G. (1992). "Mechanics of saltating grains I". *J. Hydr. Engrg.*, ASCE, 118 (4), pp 513–535.

Smith, C. R., Walker, J.D.A., Haidari, A. H., and Sobrun, U. (1991). "On the dynamics of near-wall turbulence". *Philos. Trans., Royal Soc. of London.* A, 336, pp 131–175.

Smith, C. R., and Paxon, R. D. (1983). "A technique for evaluation of three-dimensional behavior in turbulent boundary layers using computer augmented hydrogen bubble-wire flow visualization". *Experiments in Fluids*, 1, pp 43–49.

Sumer, B. M., and Deigaard. R. (1981). "Particle motions near the bottom in turbulent flow in an open channel. Part 2. *J. Fluid Mech.*, vol 109, pp 311–337.

Sumer, B. M., and Oguz, B. (1978). "Particle motions near the bottom in turbulent flow in an open channel. *J. Fluid Mech.*, vol 86, pp 109–127.

Sutherland, A. J. (1967). "Proposed mechanism for sediment entrainment by turbulent flows". *J. Geophysical Res.*, vol 72, No 24, pp 6183–6194.

Sutsepin, V. A. (1987). "Vertical distribution of bedload materials when the current flowing over a rough bed is stable and weak". *Dynamics and Thermal Regimes of Rivers.* Ed K. I. Rossinskii. Russian Translations Series 52.

Tsuchiya, Y. (1969). "On the mechanics of saltation of a spherical sand particle in a turbulent stream". *Proc. 13th Congr.* I.A.H.R., 2, pp 191–198.

Urushihara, T., Meinhart, C. D., and Adrian, R. J. (1993). "Investigation of the logarithmic layer in pipe flowusing Particle Image Velocimetry". *Near-wall turbulent flows.* R. M. C. So, C. G. Speziale and B. E. Launder (Eds.). Elsevier Science Publishers B. V.

Utami, T., and Ueno, T. (1987). "Experimental study on the coherent structure of turbulent open–channel flow using visualization and picture processing". *J. Fluid Mech.*, vol 174, pp 399–440.

Van Rijn, L. C. (1984). "Sediment transport, Part I: Bedload transport". *J. Hydr. Engrg.*, ASCE, 110 (10), pp 1431–1456.

Van Rijn, L. C. (1984). "Sediment transport, Part II: Suspended load transport". *J. Hydr. Engrg.*, ASCE, 110 (11), pp 1613–1641.

Wallace, J. M., Brodkey, R. S., and Eckelmann, H. (1977). "Pattern-recognized structures in bounded turbulent shear flows". *J. Fluid Mech.*, vol 83, part 4, pp 673–693.

Wallace, J. M., Eckelmann, H., and Brodkey, R. S. (1972). "The wall region in turbulent shear flow". *J. Fluid Mech.*, vol 54, pp 39–48.

Wells, J. (1992). "Expériences sur les impacts liquide-solide et le soulèvement de particules par un tourbillon annulaire: applications à l'érosion des sols et du transport des sédiments". *Ph.D. Thesis, l'Universite Joseph Fourier–Grenoble I.* France.

Wells, M. R., and Stock, D. E. (1983). "The effect of crossing trajectories on the dispersion of particles in a turbulent flow". *J. Fluid Mech.*, vol 136, pp 31–62.

White, B. R., and Schulz, J. C. (1977). "Magnus effect in saltation". *J. Fluid Mech.*, vol 81, part 3, pp 497–512.

Wiberg, P. L., and Smith, J. D. (1989). "Model for calculating bedload transport of sediment". *J. Hydr. Engrg.*, ASCE, 115 (1), pp 101–123.

Wiberg, P. L., and Smith, J. D. (1985). "A theoretical model for saltating grains in water". *J. Geophysical Res.*, 90 (C4), pp 7341–7354.

Yalin, S. (1958). "Sur la mécanique du mouvement des matériaux solides". *La Houile Blanche*, No. 6, pp 607–618.

Yung, B. P. K., Merry, H., and Bott, T. R. (1988). "The role of turbulent bursts in particle re–entrainment in aqueous systems". *Chemical Engrg. Science.*, vol 44, No 4, pp 873–882.

Zhuang, Y., Wilson, J. D., and Lozowski, E. P. (1989). "A trajectory-simulation model for heavy particle motion in turbulent flow". *J. Fluids Engrg.*, vol 111, pp 492–494.

3. CHARACTERIZATION OF TURBULENCE IN OPEN CHANNEL FLOW

3.1 Introduction

As indicated in Chapter 1 most of the research reported in this thesis is related to the study of phenomena involving interactions between sediment particles and turbulence in an open channel flow. The main approach followed in the study is empirical, based on experiments conducted in a laboratory flume. The present chapter aims at characterizing the turbulence of the open channel flow corresponding to those experiments.

Herein a general characterization of the open channel flow under consideration is attempted, which involves the analysis of the main statistics of the flow streamwise velocity component, measured in the present experiments with the help of a hot-film probe. These statistics include various moments of the velocity as well as related length and time scales and power spectra. The characterization of coherent structures of the flow in the near bed region is also attempted, for which the VITA pattern recognition algorithm is used. A more thorough analysis of coherent structures of the flow in the near bed region is presented in next chapter, which includes the simultaneous acquisition of hot-film measurements and images of flow visualization.

The results obtained herein are supposed to verify the generality of the open channel flow used in the present study, as well as to provide a data base to validate different models for the turbulence characteristics of the flow under consideration that are used in later chapters.

3.2 Experiments

3.2.1 Facilities

The experiments were carried out in an open channel, 18.6 m long, 0.297 m wide, and 0.279 m high. The slope of the channel was set to a value of about 0.0009. The test section was located about 12 m downstream from the entrance. In this zone, of about 0.9 m long, a sidewall made of plexiglass allowed for visualization studies. Water flow was provided by a constant head tank. The flow discharge was controlled with a valve located immediately upstream from the inlet to the channel. The flume discharged into a rectangular tank which was used for measuring volumetric discharges.

Flow velocities were measured with a hot-film probe. A 1050 TSI Series Constant Temperature Anemometer was used together with a Model 1239 W ruggedized hemisphere probe. Due to the presence of impurities in the water flow used in the experiments, which tend to cover the sensing elements of the probes thus affecting the measurements, it was not possible to use regular hot-film or hot-wire probes which are too delicate to allow for frequent cleaning, as opposed to the hemisphere probe used herein. The sensing element of the latter is a quartz coated platinum film band located at the end of the hemisphere, which is 0.12 mm wide and has a diameter of about 0.35

mm. For the range of Reynolds numbers covered in the experimental work reported herein, the dimensions of the probe correspond to about 6 to 8 viscous units.

The signal from the hot-film sensors was digitized into a personal computer using an A/D board, a digital oscilloscope and appropriate software. Further processing and analysis of the data was carried out on workstations of the Civil Engineering Research Network.

3.2.2 Experimental method

The velocity measurements required the calibration of the hot-film probe every time it was used. The calibration was made by towing the probe in still water at different speeds using a variable speed motor. The towing speed was measured independently, from the analysis of video recordings of the probe motion along the flume.

The experiments were conducted under uniform flow conditions. The volumetric discharge was measured with the help of the tank located at the downstream end of the channel. Water levels were measured with a point gage. Velocity measurements were made at no less than 5 different stations along a vertical line located in the center of the channel. The first station was always located at a height of 2 mm from the bottom, which corresponded to the minimum possible distance given the dimensions of the supporting structure for the probe. Because of this no velocity measurements were made within the viscous sublayer. In each station at least one data series of 15000 or 30000 points was acquired and digitized into the computer.

A typical overheat ratio (operation resistance over cold resistance) of about 1.05 was used for the hot-film sensor. Given a maximum significant frequency of about 200 Hz for the turbulent flow typically observed in the present experiments, a sampling frequency of 500 Hz with a low-pass filter set at 200 Hz were used for the data acquisition in order to satisfy Nyquist criterion and to avoid aliasing problems.

3.2.3 Experimental conditions

Two different series of experiments (S and T) were conducted, corresponding to two different surface roughness. The first series of experiments (Series S) corresponded to a channel with smooth walls. The second series (Series T) corresponded to a channel with a bottom roughness in the smooth-rough transition regime. The bottom roughness was created by glueing sand particles with a mean size of about 0.5 mm to the originally smooth surface of the channel bottom.

Flow depths in both series of experiments were in the range from 25 to 55 mm, which gives values of the width to depth ratio greater than about 6, thus minimizing side wall effects. Flow conditions corresponded to values of the Reynolds number ($Re = Uh/\nu$, where U denotes the mean flow velocity, h denotes flow depth, and ν denotes kinematic viscosity) in the range from about 5000 to 24000. The Froude numbers of the flows were in the range from 0.45 to 0.65, corresponding to

subcritical flows. A more detailed summary of experimental conditions is presented in the next section.

3.3 Results

3.3.1 Calibration

According to Goldstein (1983) the relationship between voltages and velocities for hot-film measurements is given by:

$$V^n = A\,E^2 + B \tag{3.1}$$

where E denotes voltage and V denotes velocity. The constants A, B and n in (3.1) must be determined through a best fit to the calibration data. Typically the exponent n has a value of about 0.5. Equation (3.1) is valid for turbulent intensities lower than about 20%, which is the case in the present experiments.

The values of A, B and n resulting from the calibrations are presented in Table 3.1. Fig. 3.1 shows as an example one of the fits obtained corresponding to the calibration for series T3.

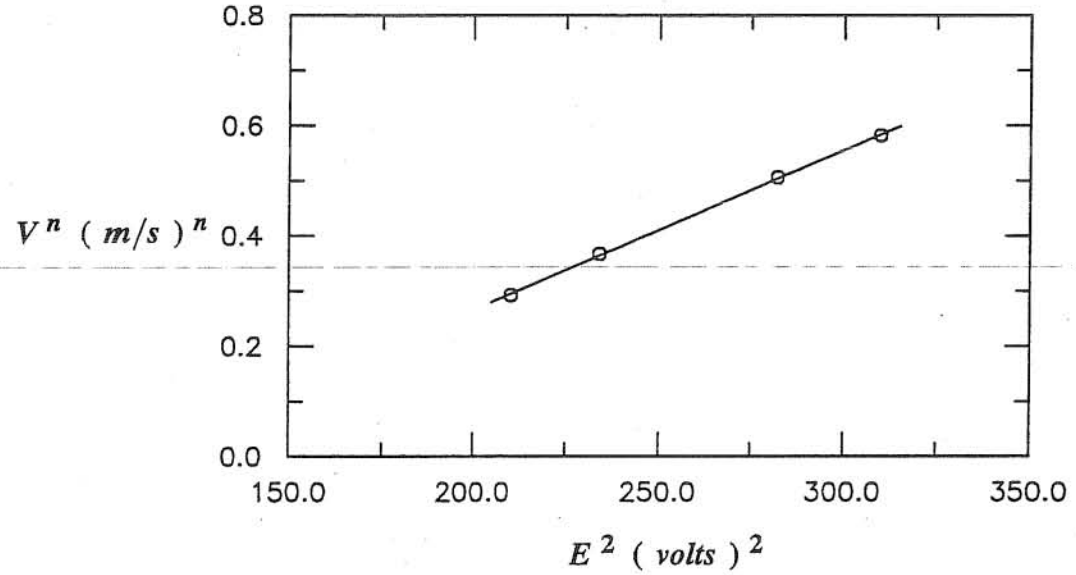

Fig. 3.1 Example of calibration curve (Series T3, n=0.50).

Table 3.1 Results of calibration

Series	Surface	A	B	n
S1	smooth	0.00354	–0.2126	0.47
S2	smooth	0.00329	–0.2030	0.49
T1	transition	0.00260	–0.3115	0.50
T2	transition	0.00311	–0.3671	0.50
T3	transition	0.00291	–0.3155	0.50

3.3.2 Rating curves

Experimental values of the volumetric discharge, Q, are plotted in Fig. 3.2 as a function of the flow depth, h, for both series of experiments, S and T. The following relationships between Q and h result from a least square fit to each data series:

Series S $$Q = 1.353\ h^{1.773} \tag{3.2}$$

Series T $$Q = 1.198\ h^{1.758} \tag{3.3}$$

where Q is in (m^3/s) and h in (m). As observed in Fig. 3.2 the same discharge results in less flow depth in the case of the channel with a smooth bottom than in the case of the channel with a rough bottom, which indicates a higher hydraulic resistance associated with the latter.

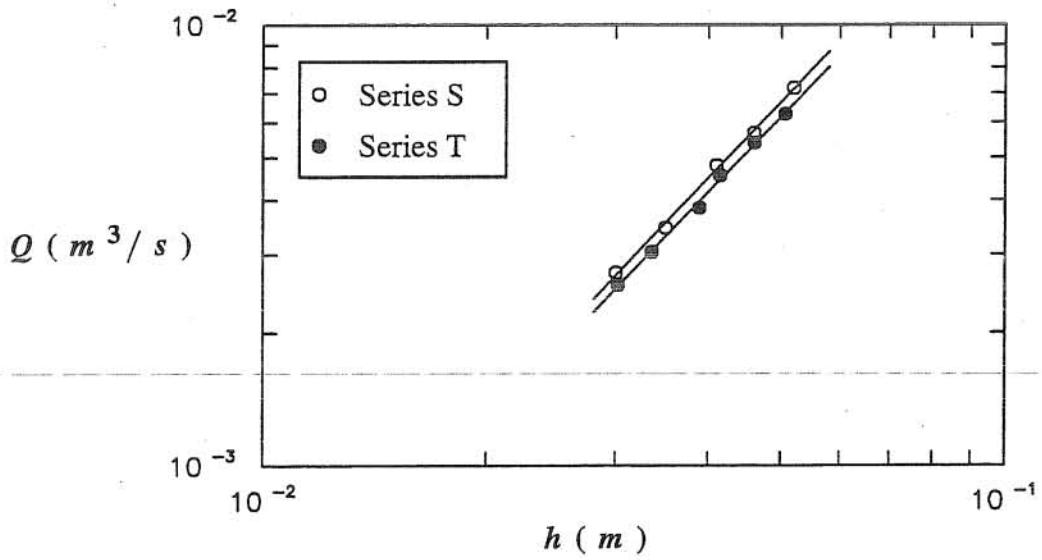

Fig. 3.2 Rating curves for Series S and T.

3.3.3 Shear velocity

To estimate the local value of the flow shear velocity at the channel centerline, u_*, the procedure described by Nezu (1977) is followed, in which u_* is computed by adjusting the semi-logarithmic law for the mean velocity distribution in turbulent open channel flows to the experimental data.

The following equation for the mean velocity distribution was used:

$$u_+ = \frac{u}{u_*} = \frac{1}{\varkappa}\ Ln\ (\ \frac{y}{k_s}\ ) + B \tag{3.4a}$$

$$B = f\ (\ k_{s+}\ ) \quad , \quad k_{s+} = \frac{k_s\ u_*}{\nu} \tag{3.4b, c}$$

where u denotes the local mean flow velocity, $\varkappa$ is the von Karman's constant (taken to be equal to 0.4), y denotes the vertical coordinate measured from the channel bottom, k_s denotes the height of the roughness elements, and B is a function that depends on the roughness characteristics of the flow. The flow regime is considered hydraulically smooth if $k_{s+} < 5$, and in such case B is given by the relationship (Clauser, 1956):

$$B = 4.9 + \frac{1}{\varkappa} Ln (k_{s+}) \qquad (3.5a)$$

If $k_{s+} > 70$, the flow regime is considered fully rough and in such case B is a constant equal to 8.5 (Schlichting, 1968). In the range $5 < k_{s+} < 70$ the flow is transitionally rough, and B is given by the function of k_{s+} plotted in Fig. 3.3 (Schlichting, 1968), which can be approximated using (Yalin, 1992):

$$B = 8.5 + (2.5 \, Ln (k_{s+}) - 3) \exp (- 0.127 (Ln (k_{s+}))^2) \qquad (3.5b)$$

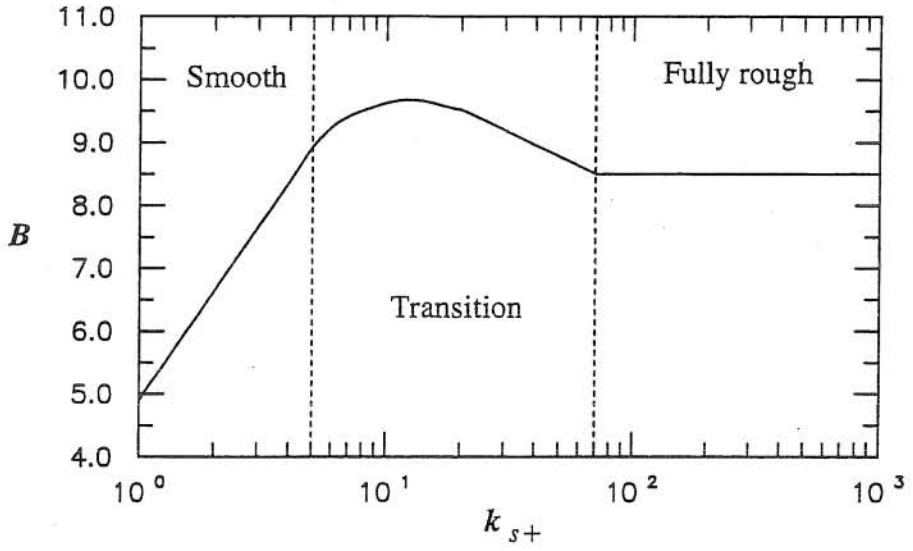

Fig. 3.3 Function B for the mean velocity distribution of open channel flow.

The series of experiments S corresponded to smooth flows and therefore the corresponding velocity distribution was estimated using (3.4) together with (3.5). In this case the theoretical law was fitted to the experimental points only by adjusting the parameter u_*. The Series T corresponded to flows in the transitionally rough regime in all cases, thus the velocity distribution was evaluated using (3.4) together with the values of B given by Fig. 3.3. In this case the theoretical law was fitted to the experimental points by adjusting both u_* and k_s. Only one value of the latter parameter was adjusted to all the experiments of the Series T, which was selected in order to get a global best fit to all such experimental data.

The adjusted values of u_* and k_s for each experiment of series S and T are presented in Table 3.2. In that table, the subseries S1 and S2, and T1, T2, and T3, correspond to groups of experiments

having the same hot-film calibration curve as given in Table 3.1. The experimental values of u_* are plotted in Fig. 3.4 as a function of h, together with least square fits to the data, which resulted in the following relationships:

Series S $$u_* = 0.1028\ h^{0.495} \tag{3.6a}$$

Series T $$u_* = 0.3097\ h^{0.761} \tag{3.6b}$$

where u_* is in (m/s) and h in (m). As observed in Fig. 3.4, the values of u_* for the transitionally rough flows are larger than those for the smooth flows. Given a channel of infinite width having a bottom slope S, the value of u_* can be estimated based on force balance considerations as:

$$u_* = (g\ h\ S)^{0.5} \tag{3.7}$$

where g denotes gravitational acceleration. Equation (3.7) indicates that for the infinitely wide channel, u_* does not depend on the bottom roughness. The dependence of the local, centerline values of u_* on the roughness regime of the flow can be explained as an effect of the finite width of the experimental channel. Clearly, in the experiments of Series T the shear stress taken by the smooth side walls differs from that taken by the rough bottom which necessarily differs also from the shear stress taken by the smooth bottom in the experiments of Series S.

Table 3.2 Values of u_* and k_s adjusted to the experimental data

Series	Experiment	h (m)	u_* (m/s)	k_s (mm)
S1	S11	0.0250	0.0165	0.0
	S12	0.0350	0.0200	0.0
S2	S21	0.0300	0.0181	0.0
	S22	0.0410	0.0210	0.0
	S23	0.0460	0.0221	0.0
	S24	0.0520	0.0238	0.0
T1	T11	0.0271	0.0199	1.0
	T12	0.0298	0.0209	1.0
	T13	0.0329	0.0223	1.0
T2	T21	0.0335	0.0239	1.0
	T22	0.0415	0.0288	1.0
	T23	0.0460	0.0293	1.0
	T24	0.0506	0.0320	1.0
T3	T31	0.0389	0.0267	1.0

As an example of the results obtained from the estimation of u_*, theoretical and experimental velocity distributions corresponding to Series S are plotted in Fig. 3.5 in dimensionless terms, where $y_+ = y\, u_*/\nu$.

3.3.4 Basic statistics of turbulence

Given the results obtained in previous sections, a summary of dimensionless parameters characterizing experimental conditions of Series S and T is shown in Table 3.3. Therein, $U = Q/Bh$ denotes the mean flow velocity with B=0.297 m denoting the channel width, $Fr = U/\sqrt{gh}$ denotes Froude number, and $Re_* = u_* h/\nu$ denotes the Reynolds number based on the shear velocity. All other parameters have been already defined.

For each experiment of series S and T, basic statistics of the turbulence measurements were computed. The streamwise instantaneous velocity $\tilde{u}$ is decomposed in a mean u and a fluctuation u'. The vertical distribution of the turbulent intensities, defined as the ratio between the root mean square value of the velocity fluctuations, u_{rms}, and the mean velocity, u, corresponding to the experiments of series S and T, is plotted in Figs. 3.6 and 3.7, respectively. The vertical distribution of the values $u_{rms+} = u_{rms}/u_*$, corresponding to the experiments of series S and T, is plotted in Figs. 3.8 and 3.9, respectively.

Table 3.3 Experimental conditions

Series	Experiment	h (m)	U (m/s)	Re	Fr	Re_*	k_{s+}
S1	S11	0.0250	0.227	5675	0.459	413	0.0
	S12	0.0350	0.324	11340	0.553	700	0.0
S2	S21	0.0300	0.299	8972	0.551	543	0.0
	S22	0.0410	0.384	15750	0.606	861	0.0
	S23	0.0460	0.406	18651	0.605	1017	0.0
	S24	0.0520	0.454	23625	0.636	1237	0.0
T1	T11	0.0271	0.290	8459	0.563	580	21.4
	T12	0.0298	0.312	10008	0.577	670	22.5
	T13	0.0329	0.331	11695	0.583	788	23.9
T2	T21	0.0335	0.306	10742	0.534	839	25.0
	T22	0.0415	0.370	15944	0.581	1241	29.9
	T23	0.0460	0.395	18898	0.588	1402	30.5
	T24	0.0506	0.418	21938	0.594	1679	33.2
T3	T31	0.0389	0.333	13265	0.540	1064	27.4

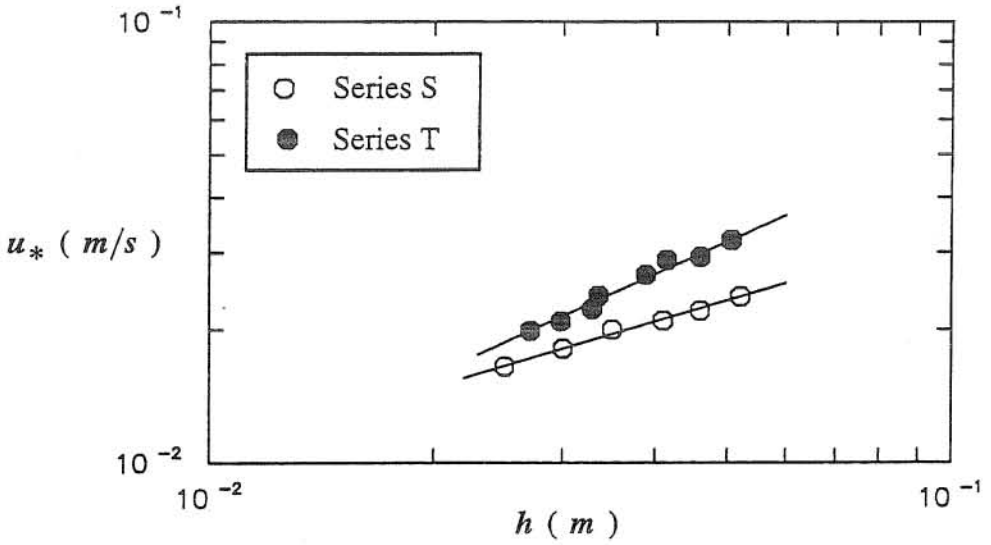

Fig. 3.4 Values of the shear velocity adjusted to the experimental data.

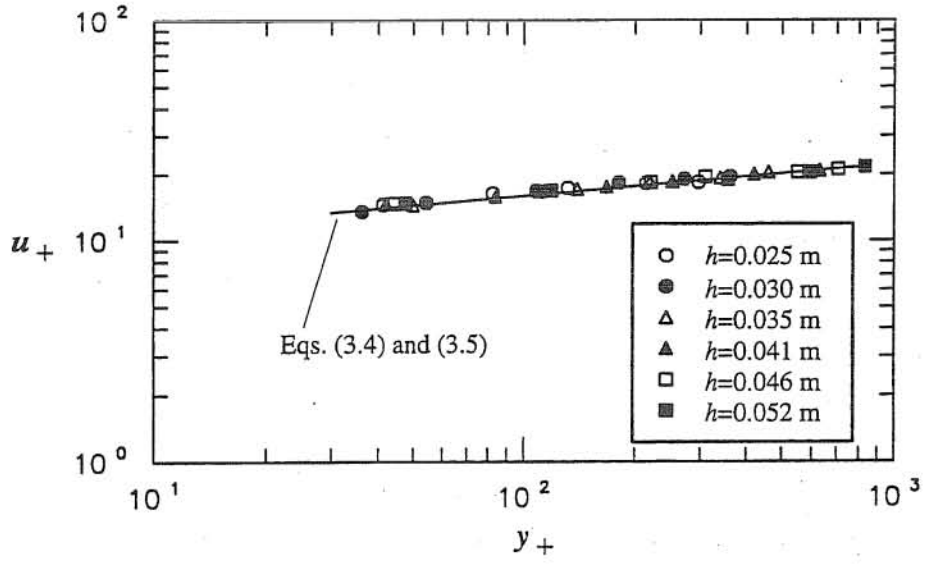

Fig. 3.5 Theoretical and experimental dimensionless mean velocity distribution. Experiments of Series S.

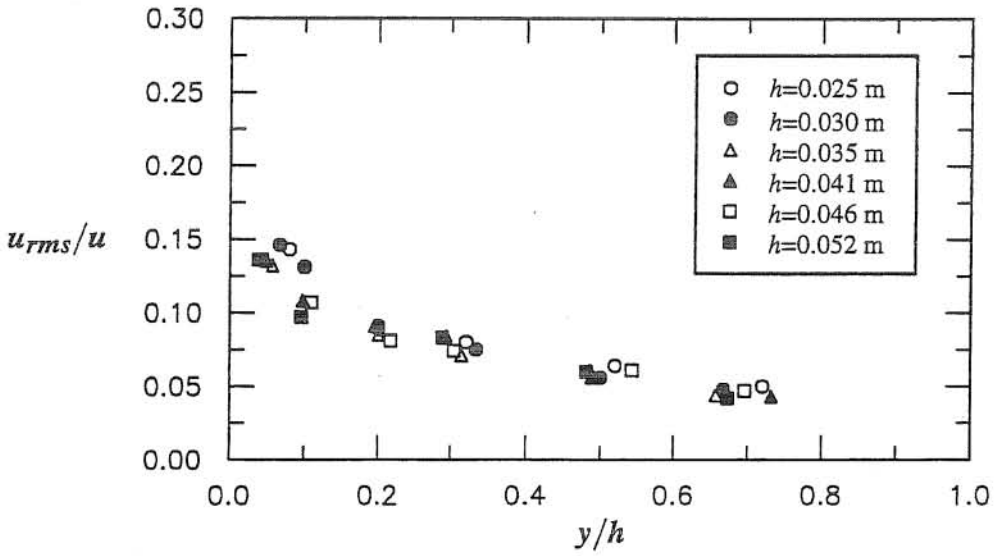

Fig. 3.6 Vertical distribution of turbulence intensities. Experiments of Series S.

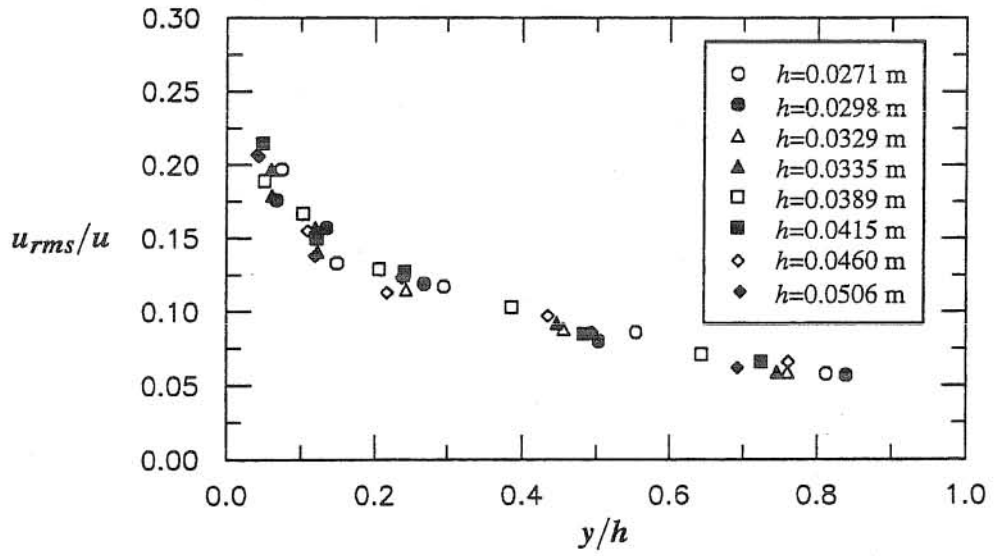

Fig. 3.7 Vertical distribution of turbulence intensities. Experiments of Series T.

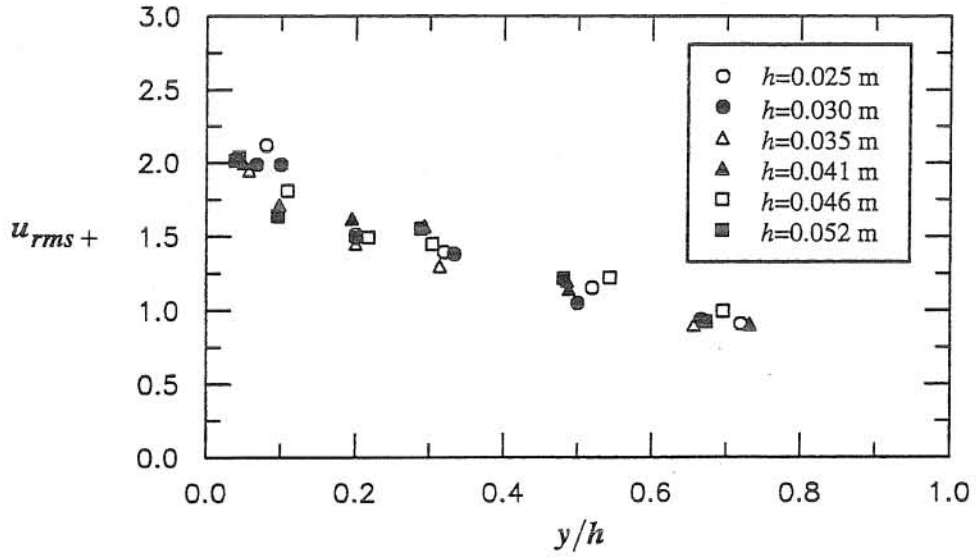

Fig. 3.8 Vertical distribution of dimensionless rms value of fluctuating velocities. Experiments of Series S.

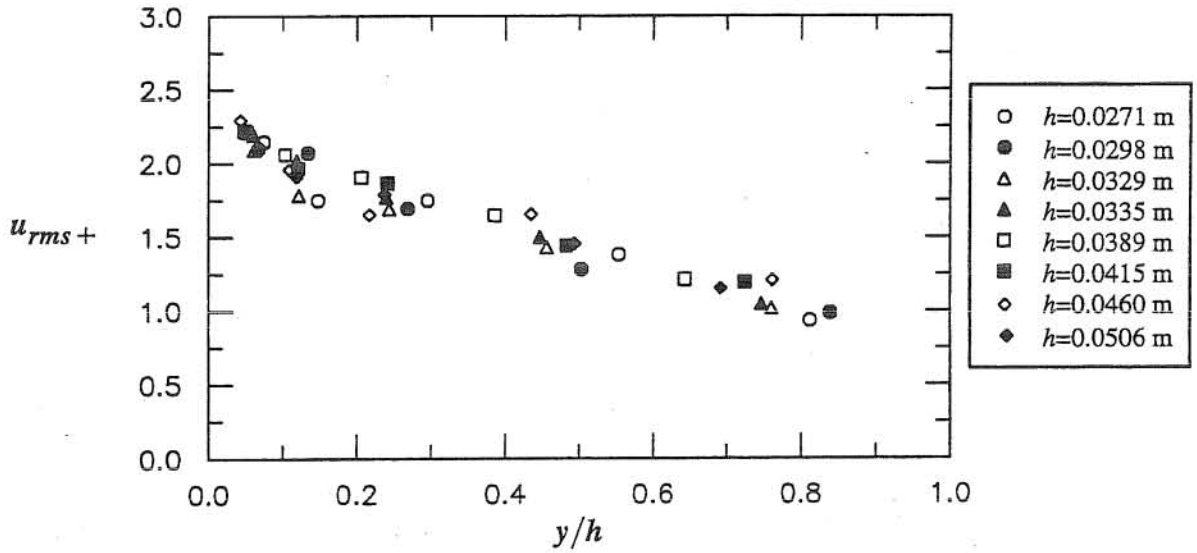

Fig. 3.9 Vertical distribution of dimensionless rms value of fluctuating velocities. Experiments of Series T.

The values of the skewness of the velocity fluctuations, S_u, corresponding to the experiments of series S and T are plotted in Figs. 3.10 and 3.11, respectively, as a function of y/h. As a reference, the value $S_u = 0$ associated with a Gaussian probability distribution for u' is also plotted in those figures. Similarly, values of the kurtosis or flatness of the velocity fluctuations , F_u, corresponding to the experiments of series S and T are plotted in Figs. 3.12 and 3.13, respectively, as a function of y/h. As a reference, the value $F_u = 3$ corresponding to a Gaussian probability distribution for u' is also plotted in those figures.

3.4 Analysis

3.4.1 Basic statistics

As observed in Figs. 3.6 and 3.7 there is a good collapse of the vertical distributions of turbulent intensities u_{rms}/u, plotted as a function of y/h, for different flow depths (or equivalently for different values of Re) in both series S and T. For comparison purposes, the vertical distributions of u_{rms}/u corresponding to the experiments of series S and T are plotted together in Fig. 3.14. Therein, the following theoretical relationship for turbulent intensities valid for hydraulically smooth flows is also plotted. Writing the turbulence intensity as:

$$\frac{u_{rms}}{u} = \frac{u_{rms+}}{u_+} \tag{3.8}$$

where u_{rms+} can be evaluated using the relationship proposed by Nezu and nakagawa (1993):

$$u_{rms+} = 2.3 \exp\left(-y/h \right) \tag{3.9}$$

and taking u_+ as given by equations (3.4) and (3.5), then (3.8) can be expressed as:

$$\frac{u_{rms}}{u} = \frac{2.3 \exp\left(-y/h \right)}{\varkappa^{-1}\left(Ln\left(y/h \right) + Ln\left(\mathrm{Re}_* \right) \right) + 4.9} \tag{3.10}$$

which is a function of Re_*. This relationship is evaluated in Fig. 3.14 for the values of Re_* of 413 and 1237, which correspond to the extremes of the range of values of this parameter for the experiments of the Series S.

From Fig. 3.14 is clear that the turbulent intensities for the transitionally rough flows are larger than those for the smooth ones, although the differences are somewhat greater near the bottom (about 70%) than near the free surface (about 30%). This is in complete agreement with findings by Nezu and Nakagawa (1993) who indicate that as the roughness of the bottom surface increases, the values of u_{rms}/u also increases considerably near the wall. In fact, by analyzing Fig. 3.7 there is a clear tendency for u_{rms}/u to increase with k_{s+} near the wall, at values of $y/h < 0.1$. On the other hand, it is apparent from Fig. 3.14 that the experimental results for the smooth flows tend to locate below the theoretical predictions given by (3.10).

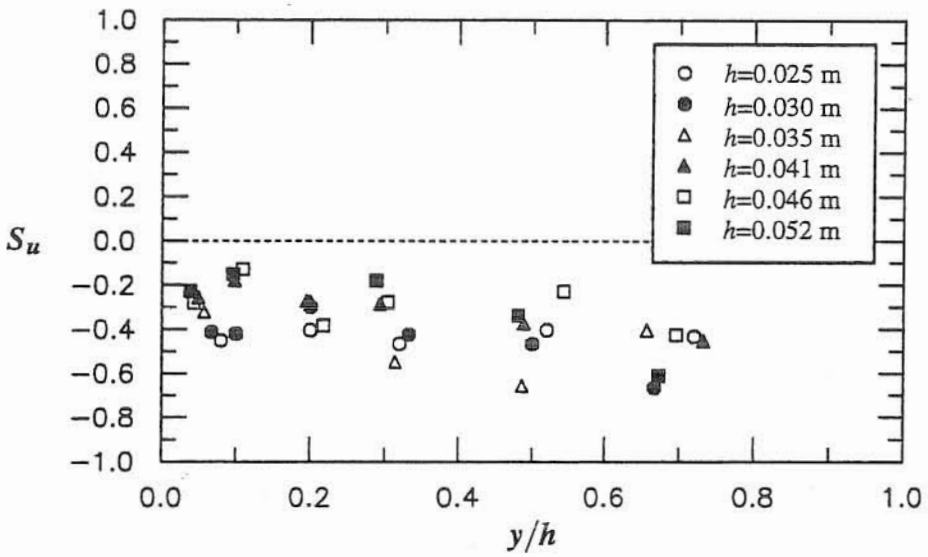

Fig. 3.10 Vertical distribution of skewness of velocity fluctuations. Experiments of Series S.

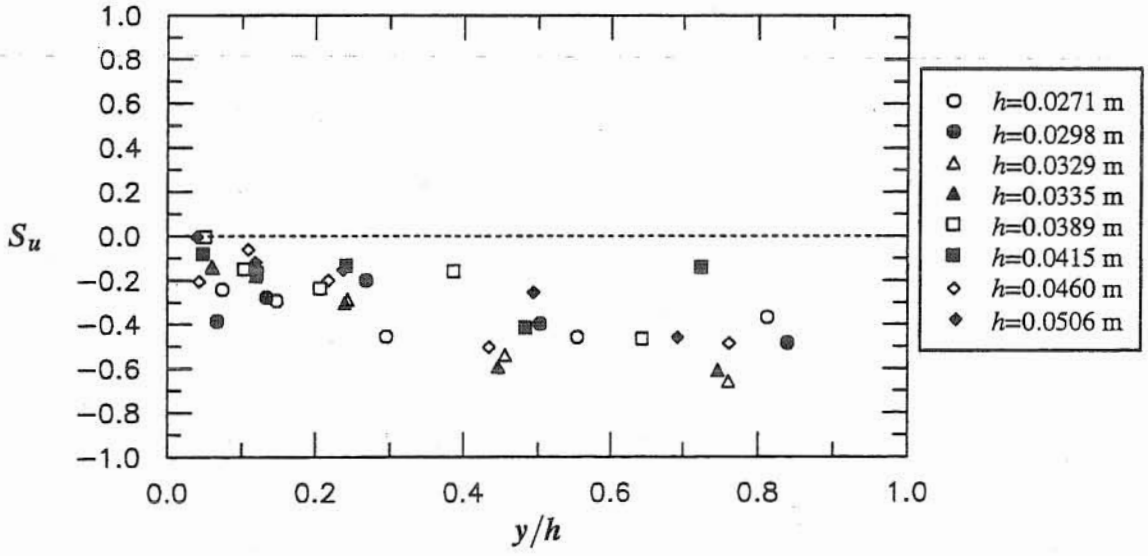

Fig. 3.11 Vertical distribution of skewness of velocity fluctuations. Experiments of Series T.

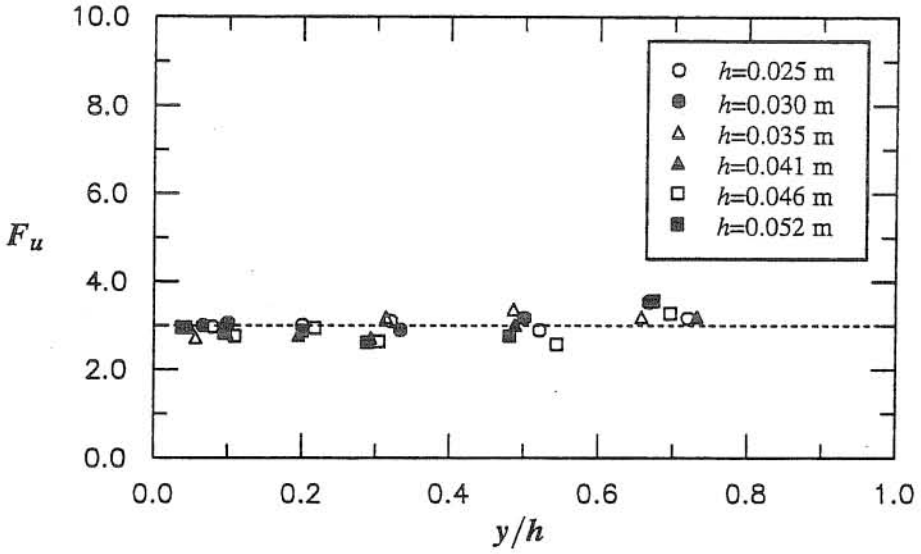

Fig. 3.12 Vertical distribution of flatness of velocity fluctuations. Experiments of Series S.

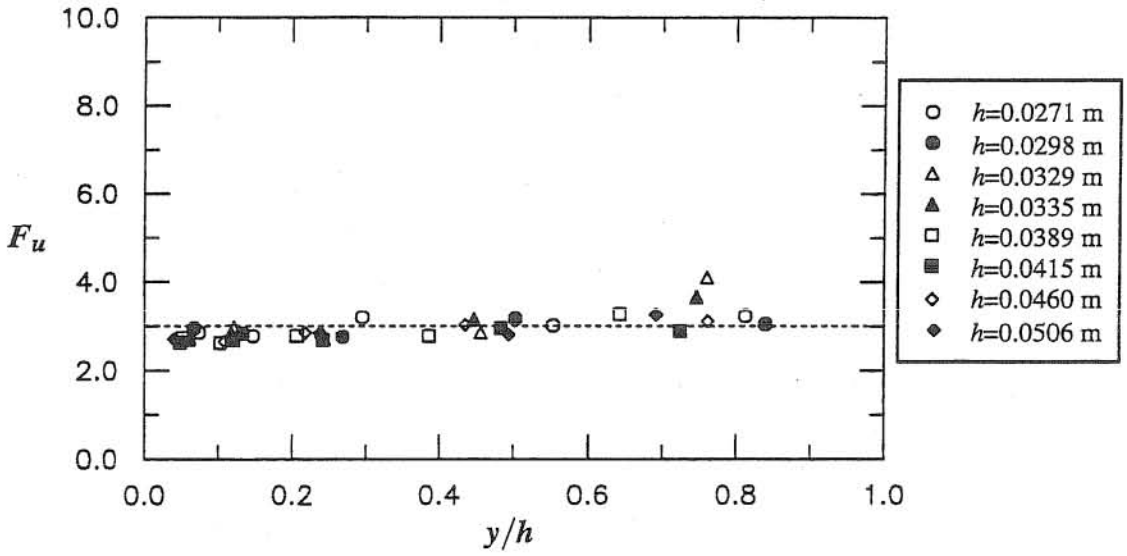

Fig. 3.13 Vertical distribution of flatness of velocity fluctuations. Experiments of Series T.

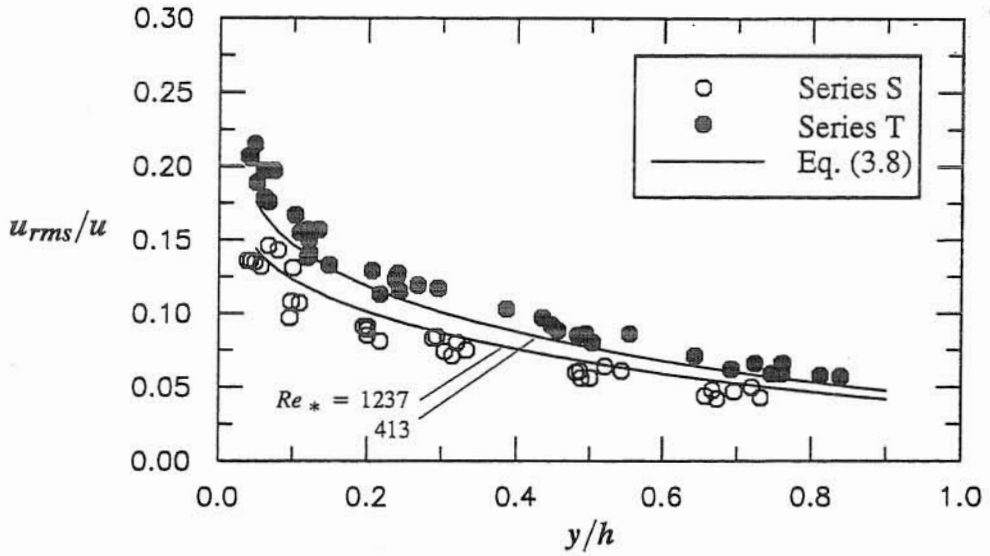

Fig. 3.14 Vertical distribution of turbulent intensity (Series S and T). Comparison with theoretical prediction.

From Figs. 3.8 and 3.9 it can be concluded that there is also a good collapse of the vertical distributions of the rms values of the velocity fluctuations made dimensionless with the shear velocity, u_{rms+}, plotted as a function of y/h, for different flow depths (or equivalently for different values of Re) in both series S and T. For comparison purposes, the vertical distributions of u_{rms+} corresponding to the experiments of series S and T are plotted together in Fig. 3.15, where the theoretical relationship (3.9) valid for hydraulically smooth flows is also plotted.

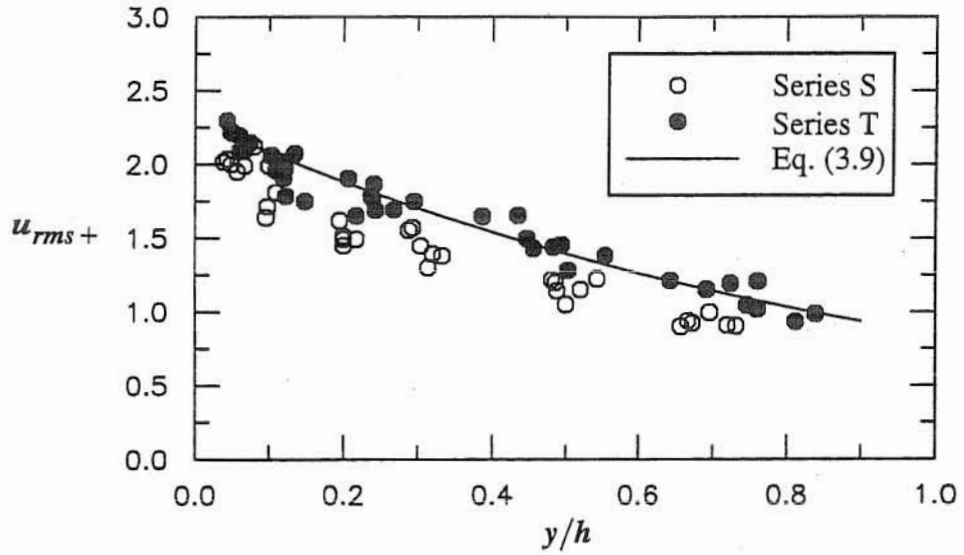

Fig. 3.15 Vertical distribution of dimensionless rms value of velocity fluctuations (Series S and T). Comparison with theoretical prediction.

As observed in Fig. 3.15, the values of u_{rms+} of the transitionally rough flows are somewhat larger than those of the smooth flows along the whole depth, although there is a tendency for this

difference to be slightly smaller near the bottom wall. This is because the values of u_{rms+} of the smooth flows tend to increase comparatively more near the wall than those corresponding to the transitionally rough flows. According to Nezu and Nakagawa (1993), the values of u_{rms+} for both the rough and smooth flows are of similar magnitude all along the flow depth except near the wall where the values of u_{rms+} for the smooth flows tend to increase comparatively more, thus reaching higher values than those corresponding to the rough flows. This tendency is indeed observed in the present experimental results in spite of the general low values exhibited by u_{rms+} corresponding to the smooth flows, as it is evident when compared with the predictions of (3.9). This is also observed in the values of the turbulent intensities when compared with (3.8), which would indicate that apparently it is the rms values of the velocity fluctuations in the smooth flows that are low, so that the low values of u_{rms+} are not due to an overestimation of u_* in those experiments. On the other hand, the values of u_{rms+} corresponding to the transitionally rough flows agree fairly well with the theoretical prediction (3.9), valid for the smooth flows, which is expected according to Nezu and Nakagawa (1993) as discussed above.

In order to facilitate the analysis of the values of S_u and F_u obtained in the present experiments, the values of those variables corresponding to the smooth and transitionally rough flows, are plotted together in Figs. 3.16 and 3.17, respectively.

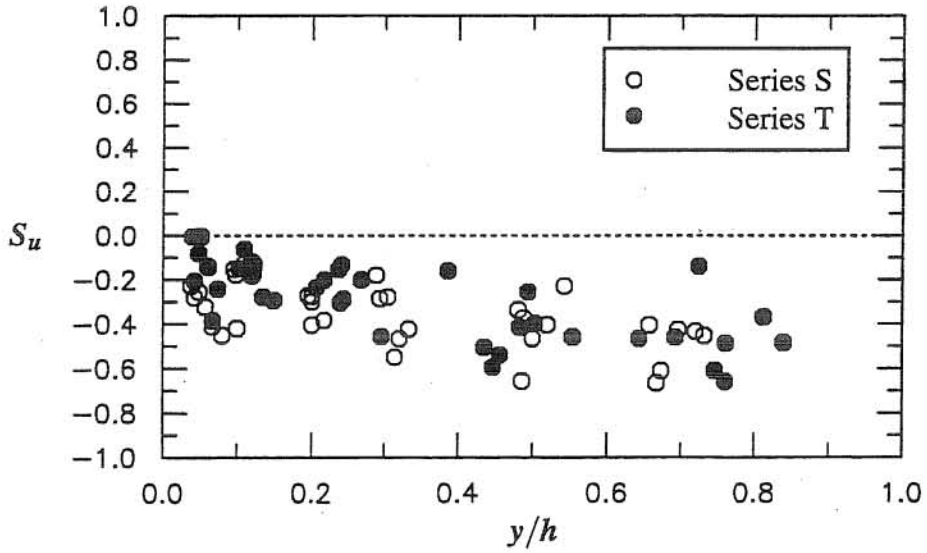

Fig. 3.16 Vertical distribution of skewness of velocity fluctuations (Series S and T).

As seen in Fig. 3.16, the values of the skewness of the streamwise velocity fluctuations are negative with values no smaller than about –0.7, for experiments of both series S and T. The negative skewness indicates that large positive values of u' are not as frequent as negative ones. Although the scatter of the experimental points is relatively large, and there is no clear dependence on Re as seen in Figs. 3.10 and 3.11, there is a tendency for S_u to increase toward the positive quadrant as the

bottom wall is approached and this tendency is stronger in the case of the transitionally rough flows. Comparing the values of S_u corresponding to the smooth and transitionally rough flows it is evident that in the latter case those values tend to be closer to zero near the wall than in the former. Away from the wall there is no clear distinction in the values of S_u between the experiments of both series S and T. These results are in good agreement with the results of Nakagawa and Nezu (1977) and Raupach (1981).

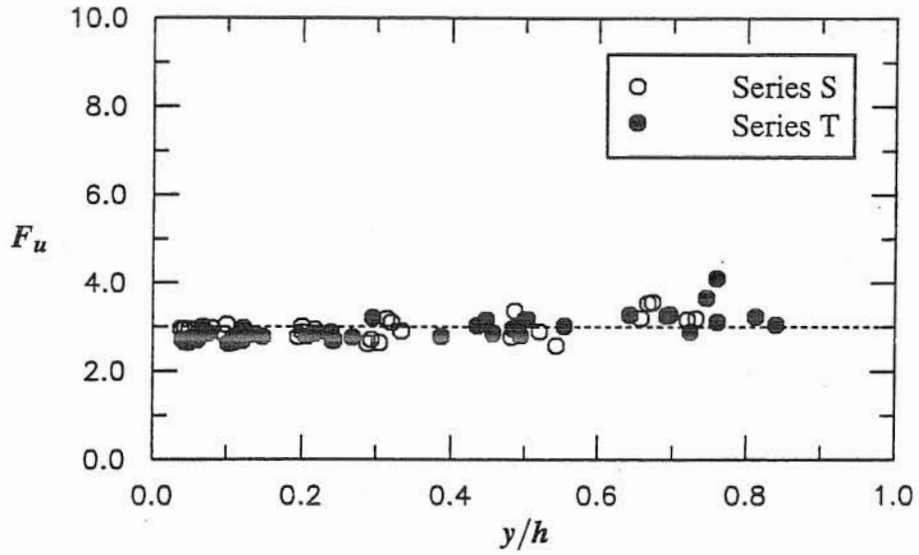

Fig. 3.17 Vertical distribution of flatness of velocity fluctuations (Series S and T).

Raupach (1981) proposed the following relationship:

$$\Delta S = S_4 - S_2 = 0.37\ S_u \tag{3.11}$$

where S_i denotes the fractional contribution of the Reynolds shear stress due to events of quadrant i with respect to the total Reynolds shear stress, such that:

$$S_i = < u'v' >_i / \overline{u'v'} \tag{3.12}$$

where $< u'v' >_i$ denotes the conditional average of Reynolds shear stress due to events of quadrant i, $\overline{u'v'}$ denotes the total Reynolds shear stress, and v' denotes the vertical component of the velocity fluctuation. Events of quadrant $i = 4$ correspond to values $u' > 0$, $v' < 0$, and are usually called sweeps, while events of quadrant $i = 2$ correspond to values $u' < 0$, $v' > 0$, and are usually called ejections. According to (3.11) a negative value of S_u indicates a higher contribution of the events of quadrant 2 to the total shear stress than that of the events of quadrant 4. Now the experimental fact that the value of S_u increases toward the wall means that events of quadrant 4 tend to contribute relatively more to the total shear stress in the near wall region than in regions away from the wall. Experimental results by Nakagawa and Nezu (1977) and Raupach et al. (1991) confirm this observation. Moreover, Raupach et al. (1991) conclude that in the case of rough flows the values

of S_u very close to the wall become positive which indicates a greater contribution of events of quadrant 4 to the total Reynolds shear stress than those of quadrant 2 in this region. The present results tend to confirm this observation, in that the values of S_u near the wall in the case of the transitionally rough flows tend to be closer to zero than in the case of smooth flows, however the measurements did not reach zones closer to the wall than about 5% of the flow depth, so no positive values of S_u were measured.

As observed in Fig. 3.17 values of the flatness F_u do not depart much from the Gaussian value 3.0, except for regions near the free surface. This departure is stronger in the case of the transitionally rough flows than in the case of smooth flows. Since the flatness is a measure of the intermittency of the time series, we conclude that the streamwise velocity fluctuations tend to be more intermittent near the free surface, which is in agreement with the results reported by Nakagawa and Nezu (1977) who showed that this is apparently true for the vertical component of the velocity fluctuations also.

3.4.2 Power spectra and characteristic scales

In order to further analyze the present experimental results the power spectrum of the streamwise velocity fluctuations is estimated herein, which is used afterwards for estimating several characteristic scales of the turbulence as is described below.

Power Spectra

Consider the normalized autocorrelation function $R_{xx}\ (\ r\ )$ between two streamwise velocity fluctuations, $u'(\ x\ )$ and $u'(\ x + r\ )$, with a streamwise lag distance r, defined as:

$$R_{xx}\ (\ r\ ) = \frac{\overline{u'(\ x\ )\ u'(\ x + r\ )}}{u^2_{rms}} \tag{3.13}$$

where the overbar denotes ensemble average. The normalized one-dimensional wavenumber spectral function of the streamwise velocity fluctuations is defined in terms of R_{xx} as:

$$S_w\ (\ k\ ) = \frac{2}{\pi} \int_0^\infty R_{xx}\ (\ r\ )\ \exp\ (-\ i\ k\ r\ )\ dr \tag{3.14}$$

where k denotes wavenumber. Since R_{xx} is in general very difficult to measure S_w is estimated in practice from the frequency spectrum $G_{uu}\ (\ f\ )$ using Taylor's frozen turbulence hypothesis.

Defining the normalized autocorrelation function $R_{uu}\ (\ \tau\ )$ as:

$$R_{uu}\ (\ \tau\ ) = \frac{\overline{u'(\ t\ )\ u'(\ t + \tau\ )}}{u^2_{rms}} \tag{3.15}$$

where u' is measured at a fixed location (x,y) and τ is a time lag, then the normalized frequency spectrum is given by:

$$G_{uu}(f) = \frac{2}{\pi} \int_0^{\infty} R_{uu}(\tau) \exp(-i f \tau)\, d\tau \tag{3.16}$$

where f denotes frequency.

Taylor's frozen turbulence hypothesis states that if A is a transferable quantity, then:

$$\frac{\partial A}{\partial t} = -u \frac{\partial A}{\partial x} \tag{3.17}$$

where u is the streamwise local mean velocity. Using (3.17) it is possible to prove that S_w and G_{uu} are related by the following transformation (Nezu and Nakagawa, 1993):

$$S_w(k) = \frac{u}{2\pi} G_{uu}(f) \quad , \quad k = \frac{2\pi f}{u} \tag{3.18a, b}$$

which according to Monin and Yaglom (1975) can be applied with acceptable accuracy except within the productive subrange associated with low values of the wavenumber k.

The normalized frequency spectrum is estimated herein by using the following relationships (Bendat and Piersol, 1986):

$$G_{uu}(f) = \frac{1}{u_{rms}^2} \frac{1}{N T} \sum_{i=1}^{N} |X_i(f, T)|^2 \tag{3.19}$$

$$X_i(f, T) = \int_0^T u'(t) \exp(-i\, 2\pi f t)\, dt \tag{3.20}$$

where N denotes the number of data series used in the computation, T denotes the total time-length of the time series u', and X_i represents the Fourier transform of u' which is estimated numerically through a Fast Fourier Transform algorithm.

Examples of the results obtained from the computations of G_{uu} are presented in Figs. 3.18 to 3.20. A general very good agreement of the present results with other reported results in open channel flows is apparent (e.g., Nezu, 1977; Lyn, 1992). Three distinct regions can be distinguished rather clearly, which seem to follow –1, –5/3, and –3 power laws, respectively. Maximum values of the frequencies observed are about 250 Hz, which corresponds to half the sampling frequency (Nyquist criterion). The existence of an inertial subrange, where the –5/3 law holds, is also apparent in all cases, which corresponds to values of f in the range from about 5 to about 40 Hz, and which seems to get wider as the Reynolds number increases. This range of frequencies for the inertial subrange coincides very well with that of previous results in water flows (McQuivey et al., 1969; Raichlen, 1967).

A comparison of the frequency spectra obtained for the experiment T22 of the series of transitionally rough flows at different locations y/h is shown in Fig. 3.18. As observed therein a good

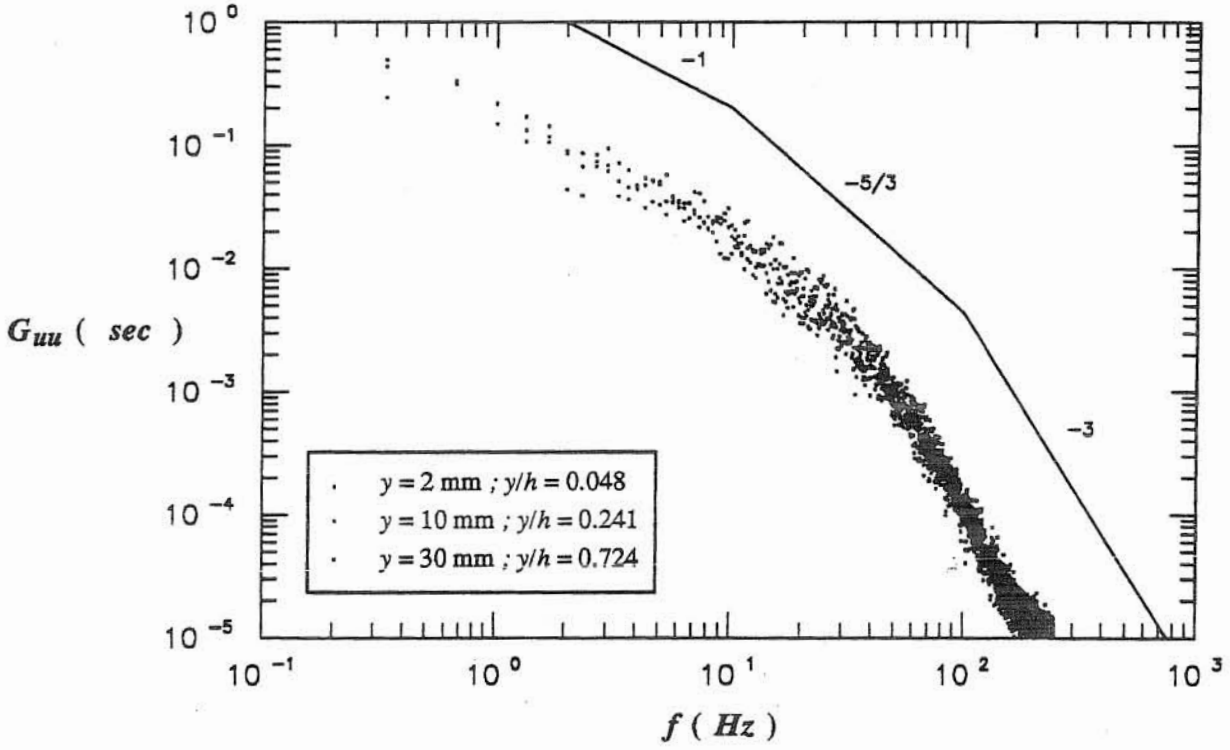

Fig. 3.18 Normalized frequency spectrum at different locations y/h. Experiment T22, h=0.0415 m.

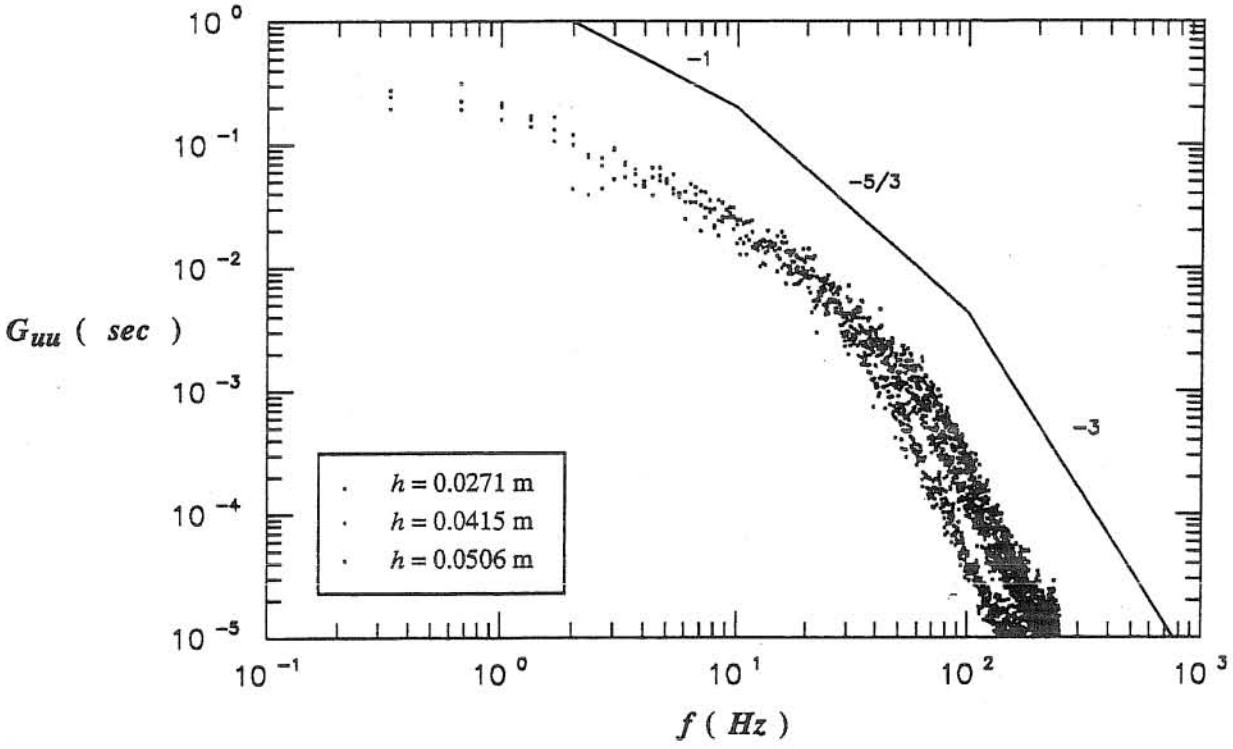

Fig. 3.19 Normalized frequency spectrum for different flow depths. Experiments of Series T, $y = 2$ mm, $y/h = 0.040$–0.074.

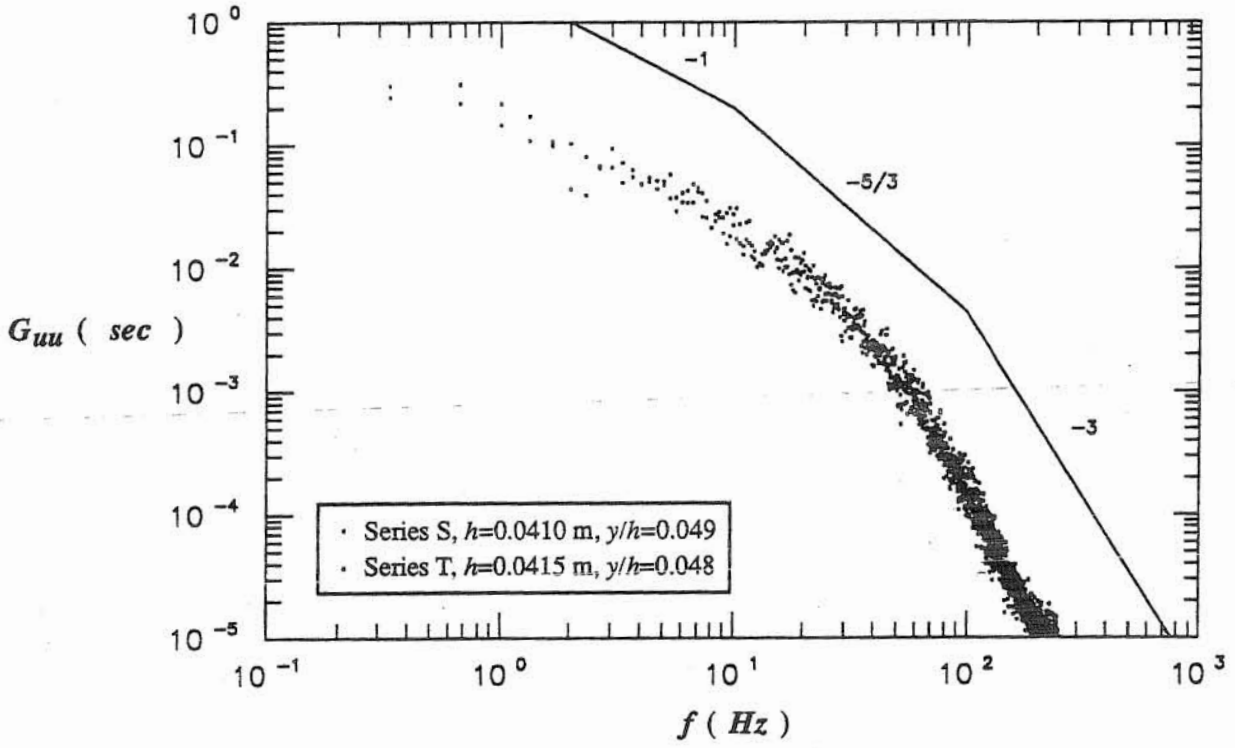

Fig. 3.20 Normalized frequency spectrum for similar experiments of Series S and T.

collapse of the normalized data at different locations is observed, although there is a tendency for the normalized energy in the inertial subrange to increase as the bottom wall is approached. A comparison of the frequency spectra obtained at the closest location to the bottom wall available for three different experiments of the Series T corresponding to the transitionally rough flows is shown in Fig. 3.19. Such data correspond to a range of Reynolds numbers from about 8460 to 22000. From Fig. 3.19 it is clear that even though there is a good collapse of the data for different Reynolds numbers in the production and inertial subranges, the normalized energy density associated with higher frequencies tends to increase with the Reynolds number. This is a well known phenomenon which is a consequence of the reduction of the length scales of the fine structure of the turbulence as the Reynolds number increases. In order to demonstrate that the results presented so far only for the transitionally rough flows are completely analogous to those for the smooth flows, a comparison of the power spectra obtained in experiments of Series S and T at almost identical Reynolds number is presented in Fig. 3.20. As observed therein there exists a good collapse of both data series in the whole range of frequencies, including the production and inertial subranges, and also at higher frequencies.

Characteristic scales

In this section, characteristic length scales of the present turbulent flows are estimated and analyzed. Although there are several methods that can be used for estimating such scales, herein those making use of the power spectrum of the velocity fluctuations are adopted, which proved to yield results of better quality than those given by alternative methods, like those based on the autocorrelation of the velocity fluctuations. This argument is in total agreement with conclusions by Nezu and Nakagawa (1993).

The streamwise integral macroscale of the turbulence, L_x, is defined as:

$$L_x = \int_0^\infty R_{xx}\,(\,r\,)\,dr \tag{3.21}$$

or evaluating (3.14) and (3.18) at $k = 0$:

$$L_x = \frac{\pi}{2}\,S_w\,(\,0\,) = \frac{u}{4}\,G_{uu}\,(\,0\,) \tag{3.22}$$

According to (3.22) a simple way to evaluate L_x would be to extrapolate the frequency spectrum to estimate the normalized energy density at $f = 0$. However, this procedure introduces an important error in the estimation of L_x due to the fact that Taylor's frozen turbulence hypothesis breaks down for low values of f. Monin and Yaglom (1975) suggest that Taylor's frozen turbulent hypothesis cannot be applied in the productive subrange of the wavenumber spectrum, which corresponds to values of the wavenumber that satisfy $k\,L_x < 1$. This limit, in the case of the present experiments, corresponds to values of the frequency less than about 2 Hz. Therefore, it can be

expected that the estimation of G_{uu} is in error for low values of f, hence, the evaluation of L_x through (3.22) would be also in error. Nezu and Nakagawa (1993) propose a method to correct the values of L_x estimated through (3.22), which is based on the universality of Kolmogorov's –5/3 power law in the inertial subrange. Herein an alternative method is proposed, slightly different than that of Nezu and Nakagawa and also based on Kolmogorov's power law, which does not require to evaluate the frequency spectrum at low frequencies and that yields results very similar to those of Nezu and Nakagawa's method.

Following Nezu and Nakagawa (1993), von Karman's wavenumber spectrum valid in the production and inertial subranges can be written as:

$$S_w (k) = \frac{2}{\pi} L_x (1 + (\frac{k}{k_0})^2)^{-5/3} \tag{3.23}$$

where k_0 is a reference wavenumber which is related to L_x by:

$$k_0 = \frac{\alpha}{L_x} \tag{3.24}$$

and α is a dimensionless parameter of the order of unity, that is, k_0^{-1} is itself a macroscale of the turbulence. As k becomes sufficiently large, (3.23) approaches Kolmogorov's –5/3 power law such that:

$$S_w (k) = \frac{2}{\pi} L_x (\frac{k}{k_0})^{-5/3} = C (\frac{\varepsilon^{1/3}}{u_{rms}})^2 k^{-5/3} \tag{3.25}$$

where C is Kolmogorov's universal constant, which is approximately equal to 0.5, and ε denotes the dissipation rate of turbulent kinetic energy.

From (3.25) the following relationship results:

$$\varepsilon = K \frac{u_{rms}^3}{L_x} \quad , \quad K = (\frac{2}{\pi C})^{3/2} \alpha^{5/2} \tag{3.26a, b}$$

which allows to evaluate the parameter α as follows. According to Nezu and Nakagawa (1993) ε and L_x can be estimated using the relationships:

$$\frac{\varepsilon h}{u_*^3} = \frac{1}{\kappa} \frac{1 - y/h}{y/h} \tag{3.27}$$

$$\frac{L_x}{h} = B_1 (\frac{y}{h})^{1/2} \tag{3.28}$$

where B_1 is an empirical constant having a value of about unity. Using (3.9), (3.27), and (3.28), then K can be estimated as:

$$K = \frac{\varepsilon L_x}{u_{rms}^3} = \frac{1}{\kappa} \frac{1 - y/h}{\sqrt{y/h} \ (2.3 \exp (- y/h))^3} \tag{3.29}$$

which allows to estimate α through (3.26b) using a value $C = 0.5$. An evaluation of K and α as functions of y/h is presented in Fig. 3.21. Therein it is seen that the values of these parameters are almost constant all along the vertical of the flow with the exception of the near wall region and the region near the free surface for which (3.29) is no longer valid. For the constant region: $K = 0.647$ and $\alpha = 0.727$. Nezu and Nakagawa (1993) indicates that K is a function of the Reynolds number $R_L = u_{rms}\, L_x/\nu$, such that for values of R_L greater than about 200, K is a weak function of this parameter, and that for the limit $R_L \rightarrow \infty$ K tends to the value 0.69, which is slightly larger than the value of K obtained herein.

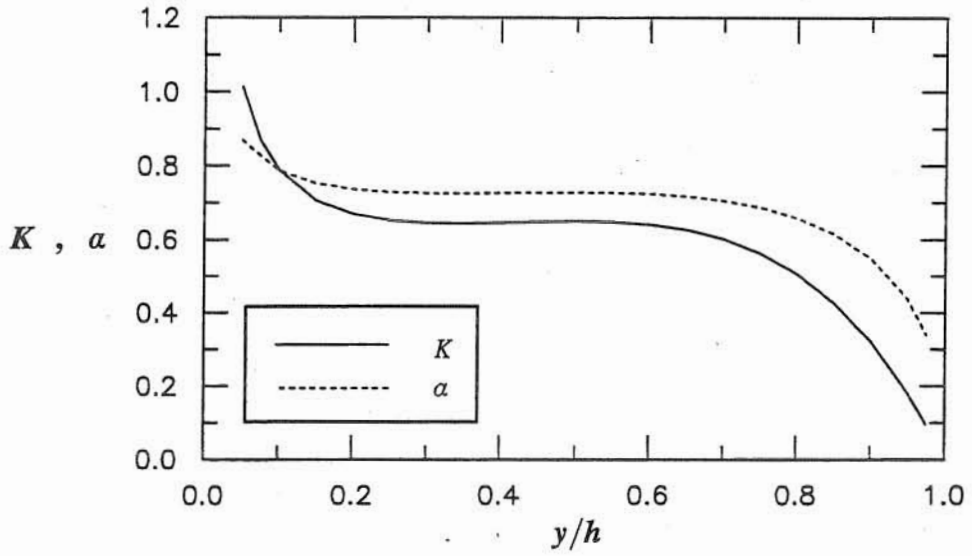

Fig. 3.21 Theoretical vertical distribution of parameters K and α.

Combining (3.23) with (3.24) and using the transformation (3.18), the resulting theoretical frequency spectrum is:

$$G_{uu}(f) = \frac{4}{u} L_x \left(1 + \left(\frac{2\pi f}{u}\frac{L_x}{\alpha}\right)^2\right)^{-5/6} \qquad (3.30)$$

The values of the integral length scale corresponding to the present experimental results are estimated herein by adjusting L_x in order to obtain a best fit of (3.30), using the value $\alpha = 0.727$, to the experimental frequency spectrum in the inertial subrange. As an example of the results obtained, a typical fit of the theoretical spectrum to the experimental data is shown in Fig. 3.22.

As seen in Fig. 3.22, a good agreement between the experimental frequency spectrum and the theoretical one given by (3.30) is obtained, for the appropriate value of $L_x = 0.008$ m, in the range of frequencies from about 3 Hz to about 40 Hz, which corresponds approximately to the inertial subrange. For frequencies lower than about 1.5 Hz a clear divergence of the theoretical spectrum from the experimental data is observed, which as was explained before, is due to the fact that in the

production subrange, corresponding in this case approximately to such region, the frozen turbulence hypothesis used to derive (3.30) from (3.23) does not apply.

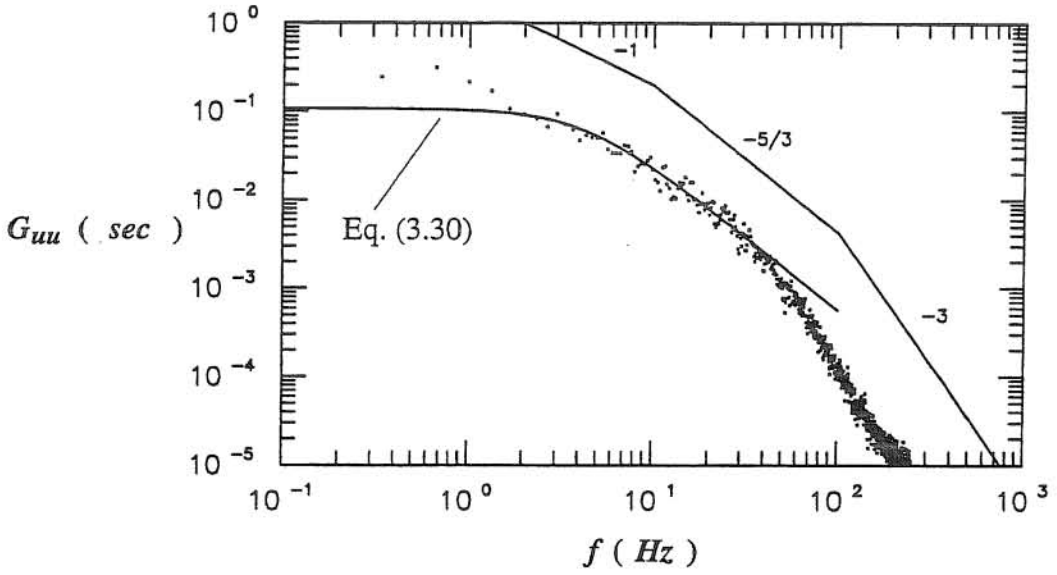

Fig. 3.22 Theoretical and experimental frequency spectra. Experiment T22, $h = 0.0415$ m, $y = 2$ mm, $y/h = 0.048$. Equation (3.30) was evaluated using the adjusted value $L_x = 0.008$ m.

The values of L_x estimated using the method explained above for the experiments of series S and T are plotted in Figs. 3.23 and 3.24, respectively, as a function of y/h and made dimensionless with the flow depth h. In those figures the semi-theoretical relationship proposed by Nezu and Nakagawa (1993) given by:

$$\frac{L_x}{h} = \begin{cases} \left(\frac{y}{h}\right)^{1/2} & y/h \leq 0.6 \\ 0.775 & y/h \geq 0.6 \end{cases} \tag{3.31}$$

is also plotted for comparison purposes. Also, to allow for an easier comparison between the results for the smooth and transitionally rough flows, L_x data from both series of experiments are plotted together in Fig. 3.25.

A relatively good collapse of the dimensionless experimental values of the integral macroscale of both series S and T with (3.31), independent of the Reynolds number, is apparent from Figs. 3.23 to 3.25. The data corresponding to the transitionally rough flows tend to locate slightly below the curve given by (3.31), and slightly below the data corresponding to the smooth flows in the region y/h lower than about 0.2. The latter is in agreement with the conclusions of Nezu and Nakagawa (1993), who state that near the bottom wall, the presence of roughness has the effect of decreasing the length scale L_x, although such effect is weaker in the outer region for $y/h > 0.2$. Near the free surface the ratio L_x/h tends to be constant, as predicted by (3.31). In this region the data corresponding to the transitionally rough flows tend to define a constant value of the ratio L_x/h of

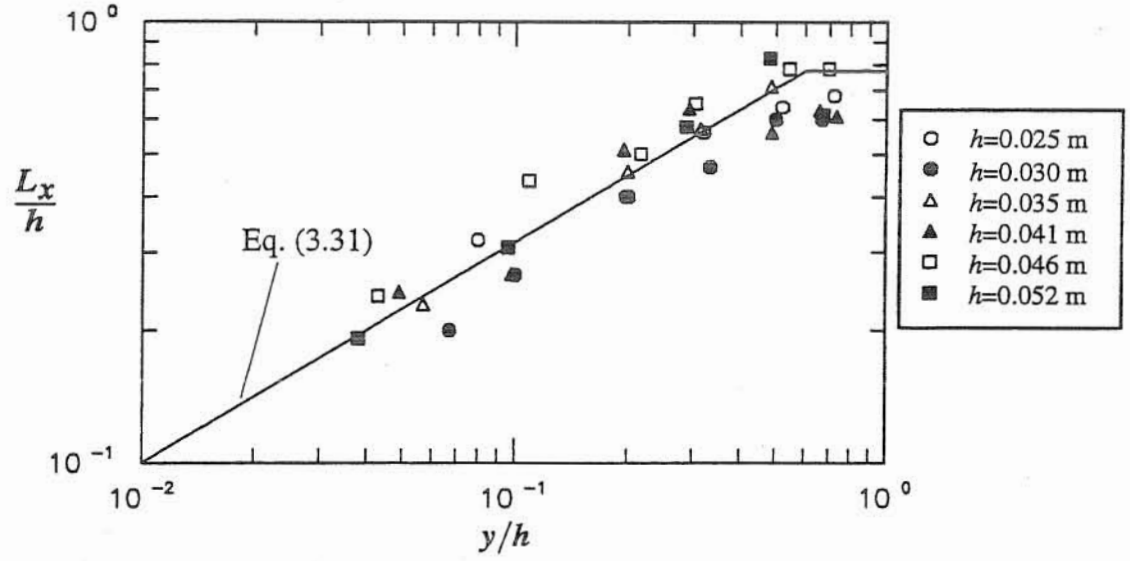

Fig. 3.23 Vertical distribution of dimensionless streamwise integral macroscale. Experiments of Series S.

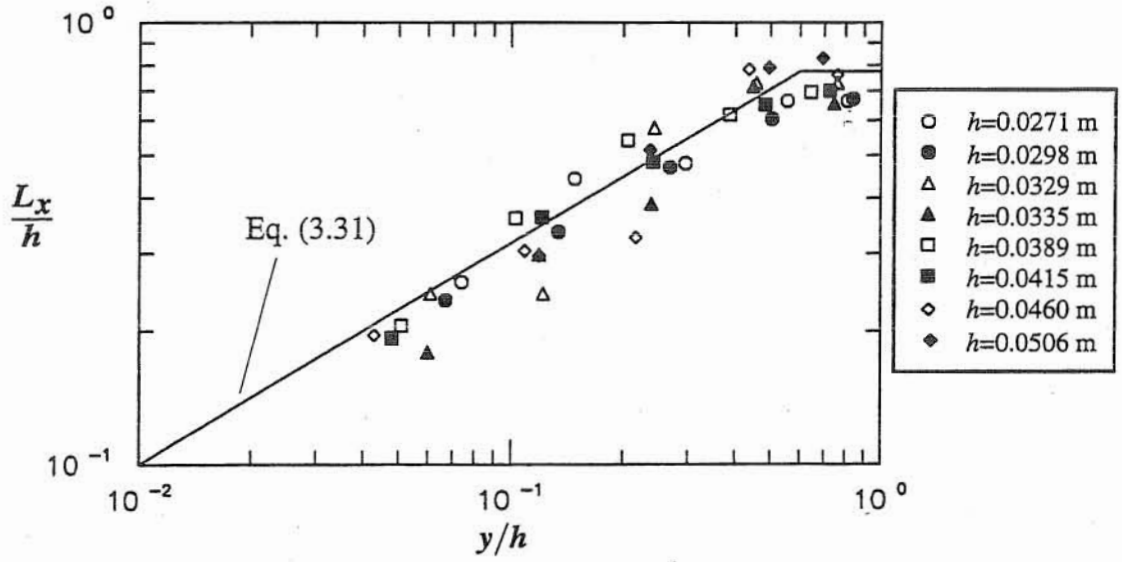

Fig. 3.24 Vertical distribution of dimensionless streamwise integral macroscale. Experiments of Series T.

about 0.75, in good agreement with (3.31), however the data corresponding to the smooth flows tend to define a slightly lower value for this constant, of about 0.7.

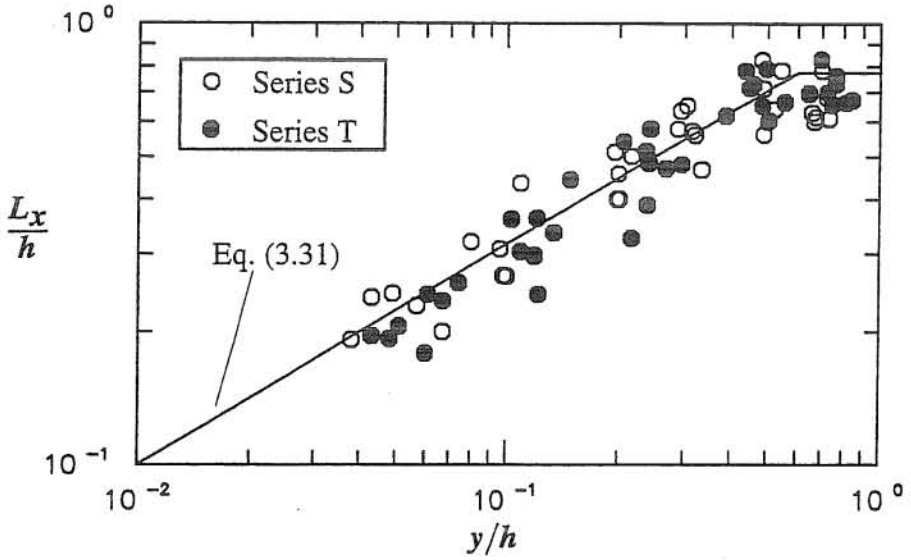

Fig. 3.25 Vertical distribution of dimensionless streamwise integral macroscale (Series S and T).

From (3.26), since the experimental values of u_{rms} and L_x are already known, the dissipation rate of turbulent kinetic energy, ε, can be evaluated. The results of this, using the value $K = 0.647$ obtained previously are plotted in the dimensionless form: $\varepsilon\ h/u_*^3$, as a function of y/h in Fig. 3.26. In this figure the results of both series S and T are plotted together, without any distinction for the Reynolds number of the different data points, which responds to the fact that the data in each series of experiments did not show any relevant dependence on this parameter. For comparison purposes, the theoretical relationship (3.27) proposed by Nezu and Nakagawa (1993) is also plotted in Fig. 3.26.

As seen in Fig. 3.26 the experimental values of the dimensionless dissipation rate agree fairly well with the theoretical relationship (3.27), although there is a tendency for the experimental data to locate below the theoretical curve in the near wall region, y/h lower than about 0.2. This tendency is much more evident in the case of the smooth flows than for the transitionally rough flows. Since in the near wall region production and dissipation of turbulent kinetic energy nearly balance each other (Nezu, 1993), a higher dissipation rate associated with the transitionally rough flows indicates that such flows seem to exhibit a slightly higher production of turbulent kinetic energy near the wall than the smooth ones, which is in agreement with results by Nezu and Nakagawa (1993).

The streamwise Taylor's microscale, λ_x, is defined as:

$$\lambda_x = \frac{u_{rms}}{(\overline{(\partial u'/\partial x)^2})^{1/2}} \tag{3.32}$$

However, since for isotropic turbulence it can be shown that (Batchelor, 1953):

$$\lambda = \sqrt{\frac{15\ \nu\ u_{rms}^2}{\varepsilon}} \tag{3.33}$$

and assuming local isotropy for the small scales of the present open channel flow, λ_x can be approximated by λ given by (3.33). Based on this assumption Nezu and Nakagawa (1993) propose the following relationship:

$$\frac{\lambda}{h} = \left(\frac{15}{2.3\ K\ Re_*}\right)^{1/2} \left(\frac{y}{h}\right)^{1/4} \exp\left(\frac{y}{2\ h}\right) \tag{3.34}$$

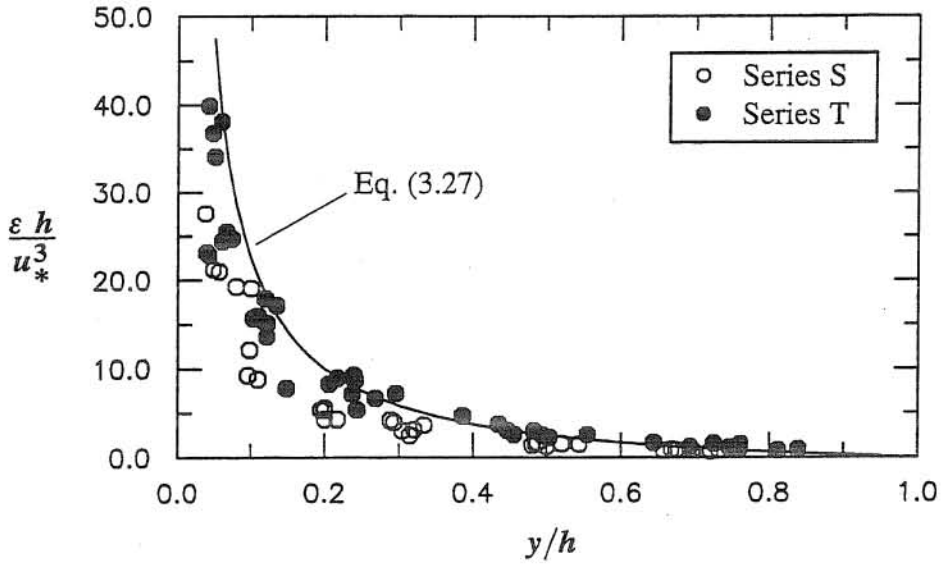

Fig. 3.26 Vertical distribution of dimensionless dissipation rate of turbulent kinetic energy (Series S and T).

Herein the values of λ associated with the present experiments are estimated using both (3.32) and (3.33). The results obtained for the dimensionless Taylor's microscale, λ/h, for the experiments of series S and T using (3.32) are shown in Figs. 3.27 and 3.28, respectively, together with the theoretical relationship (3.34) evaluated for two different values of Re_*, corresponding to the limits of the range of values of this parameter in those experiments. Corresponding results for λ/h estimated using (3.33) are shown in Figs. 3.29 and 3.30, also plotted together with (3.34).

As observed in Figs. 3.27 and 3.28, the experimental values of λ/h estimated using the strict definition of λ_x given by (3.32) show a good stratification with Re_*, increasing with decreasing values of this parameter, and also increasing with increasing values of y/h. The data corresponding to smooth flows (Fig. 3.27), seem to follow the isotropic relationship (3.34) very well outside the wall layer ($y/h > 0.2$), however closer to the wall the experimental values of λ/h tend to be larger than the theoretical ones. The experimental values of λ/h corresponding to the transitionally rough

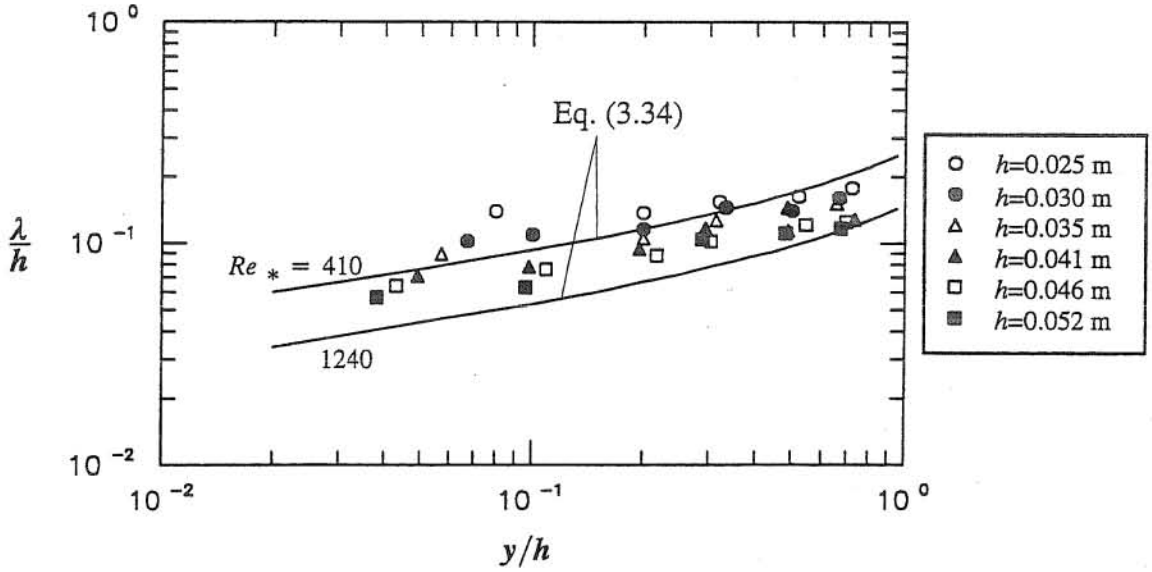

Fig. 3.27 Vertical distribution of dimensionless Taylor's microscale estimated using (3.32). Experiments of Series S.

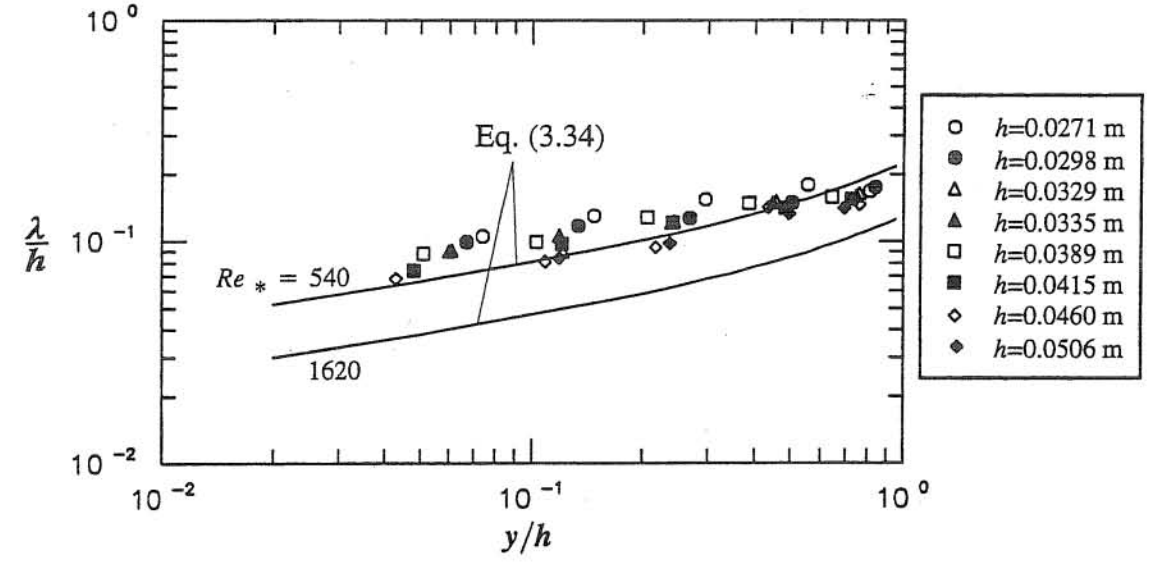

Fig. 3.28 Vertical distribution of dimensionless Taylor's microscale estimated using (3.32). Experiments of Series T.

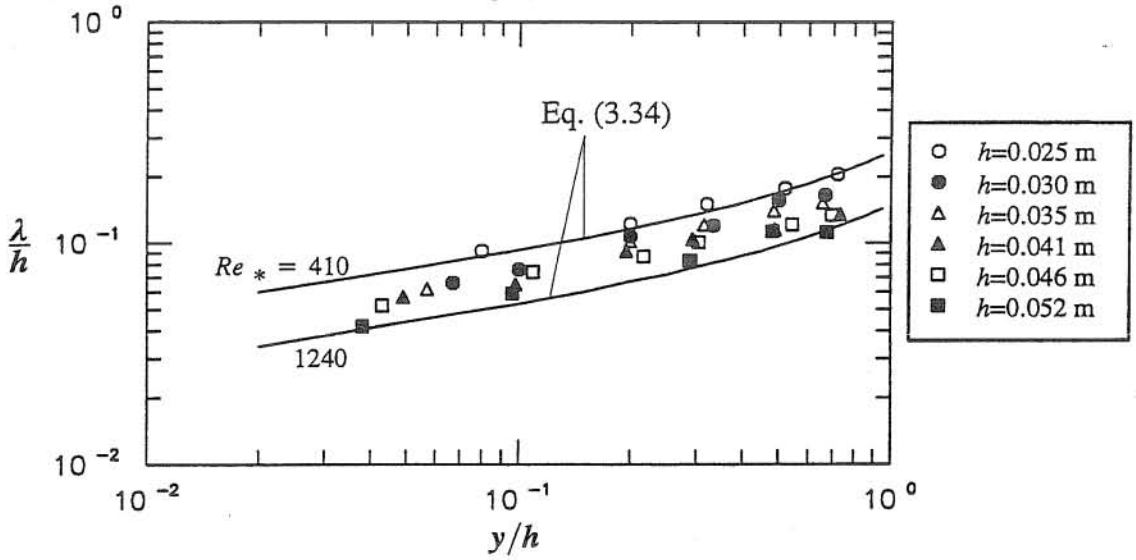

Fig. 3.29 Vertical distribution of dimensionless Taylor's microscale estimated using (3.33). Experiments of Series S.

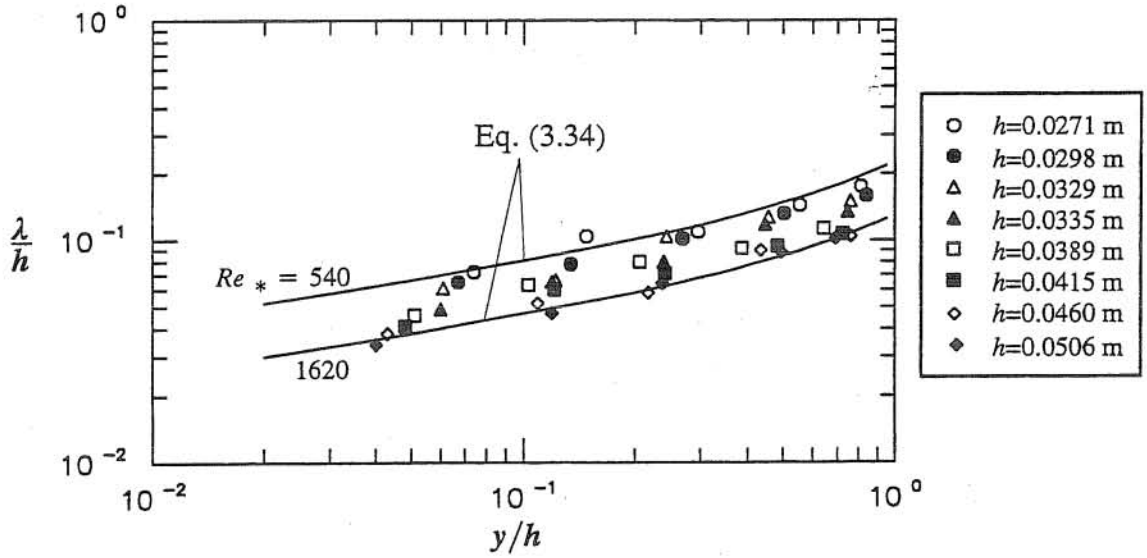

Fig. 3.30 Vertical distribution of dimensionless Taylor's microscale estimated using (3.33). Experiments of Series T.

flows (Fig. 3.28), on the other hand, appear to be larger than those predicted by the isotropic relationship (3.34) almost all along the vertical, except near the free surface.

Nevertheless, when λ/h is estimated using the isotropic relationship (3.33) a very good agreement between (3.34) and the experimental data is obtained, for both series of experiments S and T, as seen in Figs. 3.29 and 3.30. This is rather obvious, because (3.34) is based on a theoretical evaluation of (3.33) using expressions for u_{rms} and ε that represent the present experimental data very well, as has been previously discussed.

The results of Figs. 3.27 and 3.28 seem to indicate that for smooth flows, the small scales would be nearly isotropic outside the wall layer, however this would not be true closer to the wall. On the other hand, for the transitionally rough flows, the departure from isotropy appears to involve almost the whole depth of flow. It is necessary to point out that Nezu and Nakagawa (1993) also noticed that (3.34) underestimated their experimental values of λ/h near the wall, however their discussion is not conclusive with respect to what would be the cause of such departure.

One additional length scale that can be estimated for the present data is the Kolmogorov's microscale, which is defined as:

$$\eta = \left(\frac{\nu^3}{\varepsilon} \right)^{1/4} \tag{3.35}$$

For the present experiments this can be calculated from the already estimated values of ε. The values of η obtained for the series of experiments S and T are plotted in Figs. 3.31 and 3.32, respectively, made dimensionless with the flow depth, h.

Following Nezu and Nakagawa (1993), the ratio η/h can be estimated by the relationship:

$$\frac{\eta}{h} = K^{-1/4} R_L^{-3/4} \frac{L_x}{h} \tag{3.36}$$

however by using the definition $R_L = u_{rms} L_x/\nu$, and the relationships (3.9) and (3.31), (3.36) can be rewritten as:

$$\frac{\eta}{h} = \begin{cases} K^{-1/4} \left(y/h \right)^{1/2} \left[2.3 \; Re_* \left(y/h \right)^{1/2} \exp\left(-y/h \right) \right]^{-3/4} & y/h \leq 0.6 \\ 0.775 \; K^{-1/4} \left[2.3 \; Re_* \; 0.775 \exp\left(-y/h \right) \right]^{-3/4} & y/h \geq 0.6 \end{cases} \tag{3.37}$$

This equation is plotted together with the experimental data of series S and T in Figs. 3.31 and 3.32, respectively, for two different values of Re_*, corresponding to the limits of the range of values of this parameter in those experiments, and for the value $K = 0.647$ obtained previously.

As seen in Figs. 3.31 and 3.32, the experimental values of η/h show a clear stratification with Re_*, increasing with decreasing values of this parameter, and also increasing with increasing values of y/h. A good agreement between the experimental data and (3.37) is apparent from those figures,

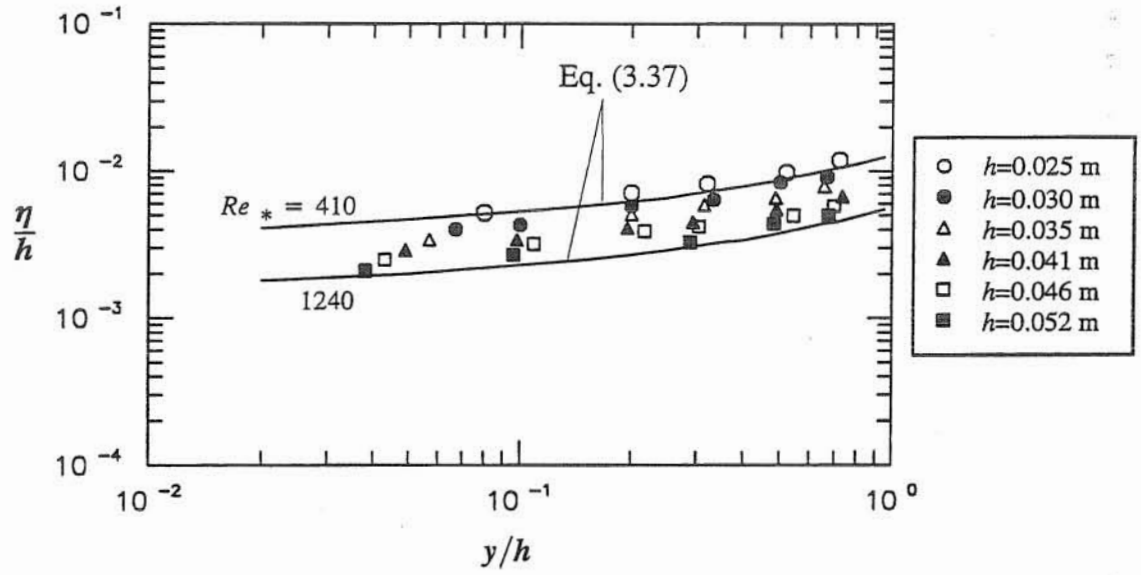

Fig. 3.31 Vertical distribution of dimensionless Kolmogorov's microscale. Experiments of Series S.

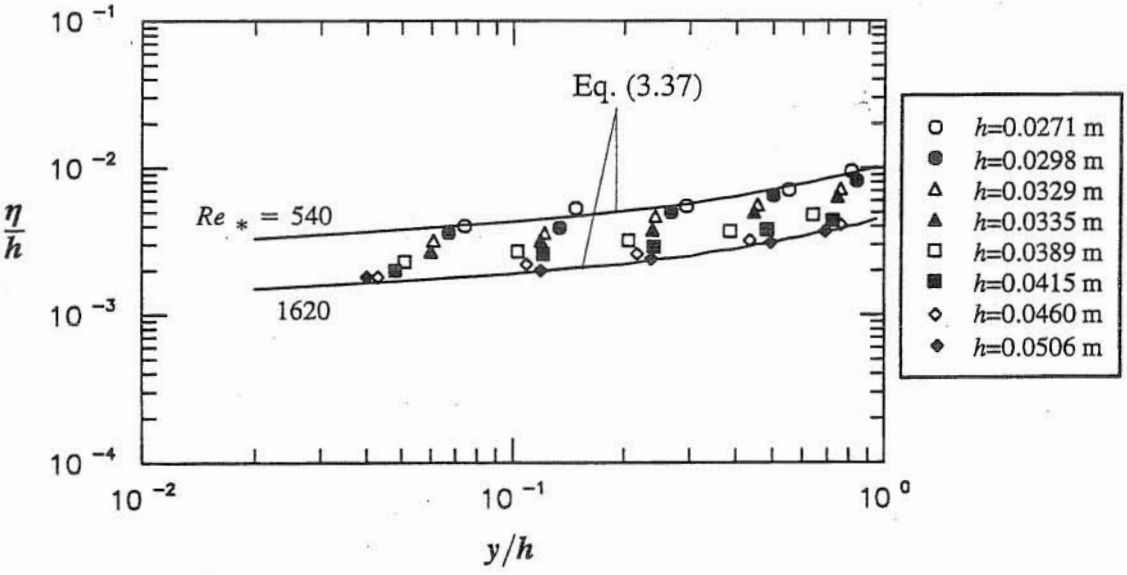

Fig. 3.32 Vertical distribution of dimensionless Kolmogorov's microscale. Experiments of Series T.

which is rather obvious because this equation is based on an evaluation of (3.35) using expressions for u_{rms} and L_x/h that represent the experimental data very well, as has been previously discussed.

From the analysis of the characteristic length scales in the present turbulent open channel flows it can be concluded that values of L_x/h are generally in the range from about 0.2 to about 0.8, values of λ/h are generally in the range from about 0.06 to about 0.2, and values of η/h are generally in the range from about 0.002 to about 0.01. This indicates that in the present experiments the ratio λ/L_x has a value of about 0.3, while the ratio η/L_x has a value of about 0.01. Given the flow depths in the present experiments these results indicate that near the bottom wall the integral macroscale has values of about 5 mm to 10 mm, the Taylor's microscale has values of about 1.5 mm to 3 mm, and the Kolmogorov's microscale has values of about 0.05 mm to 0.1 mm.

3.4.3 VITA analysis for coherent structures detection

Several pattern recognition algorithms have been developed in order to detect and characterize the structure of organized turbulent motion from time series of measured turbulent quantities. From these, a number of conditional-sampling techniques are oriented to detect such coherent structures from single probe measurements (e.g., hot-film anemometry, LDV), with the variable-interval time average (VITA) method (Blackwelder and Kaplan, 1976), and the $u'v'$ quadrant method (Wallace et al., 1972) being among the most popular. Although Wallace et al. (1977) point out that the difficulty in using a single probe to detect coherent structures is in the fact that a flow structure passing a probe would only occasionally be intersected directly through its center, and in addition, structures would pass the probe at different stages of their lifetimes, all of which would result in a wide distribution of frequencies and magnitudes of the structures, they also conclude that coherent structures can definitely be detected using conditional-sampling and furthermore their predominant features are better observed in the streamwise velocity signal.

Herein, the VITA algorithm is applied to the single-probe measured streamwise velocity signals in the present experiments of series S and T, in order to detect coherent structures developing in the near wall region of the flows. This method is based on the assumption that when a coherent structure passes through the probe it causes a violent change in the instantaneous streamwise velocity component which produces a high level of variance, that is, such event would be strongly correlated with peaks in the time series of the short-time, or localized, variance. Because of this such events are usually called turbulent bursts.

The variable-interval time-average of any fluctuating quantity $X(t)$ is defined as:

$$\hat{X}(t,\tau) = \frac{1}{\tau}\int_{t-\tau/2}^{t+\tau/2} X(s)\,ds \qquad (3.38)$$

where τ is the averaging time. It can be shown that $\hat{X}(t, \tau)$ is effectively a low-pass filter of $1/\tau$ cut-off frequency and zero phase shift applied to the original function. As τ becomes larger, $\hat{X}$ tends to the mean value of X.

A localized measure of the fluctuating turbulent energy associated with the streamwise velocity fluctuations is obtained by applying (3.38) to $u'(t)^2$ and subtracting the square of the localized mean value of $u'(t)$, such that:

$$\hat{var}(t, \tau) = \frac{1}{\tau} \int_{t-\tau/2}^{t+\tau/2} u'(s)^2 \, ds - \left(\frac{1}{\tau} \int_{t-\tau/2}^{t+\tau/2} u'(s) \, ds \right)^2 \tag{3.39}$$

When τ becomes large the second term of the right hand side of (3.39) tends to zero, and $\hat{var}$ tends to the variance of $u'(t)$. On the other hand, as τ tends to zero both terms of the right hand side of (3.39) become identical and therefore $\hat{var}$ vanishes.

For a given finite value of τ, large excursions of the localized turbulent energy, or $\hat{var}$ signal, from the long-time average of such energy, u_{rms}^2, are associated with the presence of bursting events. Accordingly, a detection function, $D(t)$, is defined as:

$$D(t) = \begin{cases} 1 & \text{if} \quad \hat{var}(t, \tau)/u_{rms}^2 > k_v \\ 0 & \text{otherwise} \end{cases} \tag{3.40}$$

where k_v denotes a threshold level.

According to Chen and Blackwelder (1978), bursting events are associated with high values of the local acceleration of the flow. Moreover, positive accelerations are associated with sweep events (events of quadrant 4), while negative accelerations are associated with ejection events (events of quadrant 2). Based on this, the following criterion is used to detect bursting events and discriminate between sweeps and ejections:

$$\begin{array}{llll} D(t) = 1 & \text{and} & du'(t)/dt > 0 & \Leftrightarrow \quad \text{Sweep} \\ D(t) = 1 & \text{and} & du'(t)/dt < 0 & \Leftrightarrow \quad \text{Ejection} \end{array} \tag{3.41}$$

Like all detection techniques, the VITA method requires the definition of adjustable parameters, namely the threshold level, k_v, and the averaging time, τ. It has been shown that the number of detected events decreases with increasing threshold levels (Johansson and Alfredsson, 1984), which implies some kind of arbitrariness in the results obtained. Nevertheless, Bogard and Tiederman (1986) have shown that the VITA method has a low probability of making a false detection when high threshold levels (values of k_v larger or equal than unity) are used. Herein, a value of $k_v = 1.0$ is used throughout the analysis. On the other hand, although Blackwelder and Kaplan (1976) recommend the use of a value of the integration time such that $\tau_+ = \tau \, u_*/\nu \approx 10$,

which corresponds roughly to the time scale of the bursting events, herein a method is developed in order to optimize the selection of this parameter as is explained below.

The detection criterion (3.41) was applied to the experimental data of series S and T. Since the present analysis aims at characterizing flow structures within the near wall region, only the velocity time series corresponding to the measuring station closer to the wall ($y = 2$ mm) was used for each experiment, which corresponded to values of y_+ in the range from about 30 to about 60, and for which the frequency of bursting events detected with the VITA method seems to be maximum (Blackwelder and Haritonidis, 1983). Different values of τ were used in the evaluation of (3.41), such that the dimensionless integration time, τ_+, was varied in the range from 5 to 30. It was found that the value of τ_+ has a strong influence on the number of detected events. Fig. 3.33 shows , as an example, the results obtained for experiment S22 in terms of the number of detected sweep and ejection events as a function of τ_+.

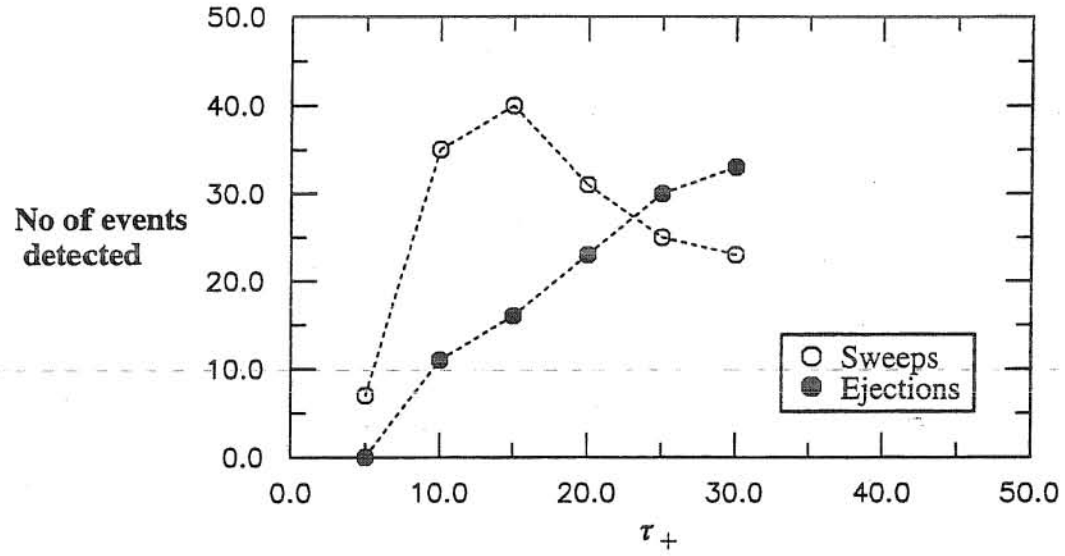

Fig. 3.33 Effect of the time of integration over the number of events detected by the VITA method. Experiment S22, $h = 0.041$ m.

As observed in Fig. 3.33, the number of sweeps detected reaches a peak for a value $\tau_+ = 15$, while the number of ejections detected increases monotonically with τ_+. In general, this pattern is common for all the experiments of series S and T, although the value of τ_+ that maximizes the number of sweeps detected varies from one experiment to another. Evidently, the best detection method is that one which can detect most of the events that occur. In this sense the optimum value of τ_+ to be used in (3.41) is the one that maximizes the number of events detected. In the case of sweeps this conclusion seems to be adequate, in that all the events detected using the optimum value of τ_+ appear to be well defined highly energetic events with a large positive acceleration. This can be clearly observed in Fig. 3.34, corresponding to the same experiment S22 and a value of $\tau_+ = 15$,

where streamwise velocity signals associated with the detected sweep events; made dimensionless with the local value of u_{rms}, are plotted as a function of the dimensionless time $t_+ = t\, u_*/\nu$, for a range of values of t_+ centered around the time of detection, which was arbitrarily reset to zero for the purpose of plotting them together. In the same figure, the corresponding ensemble averaged sweep event is also plotted.

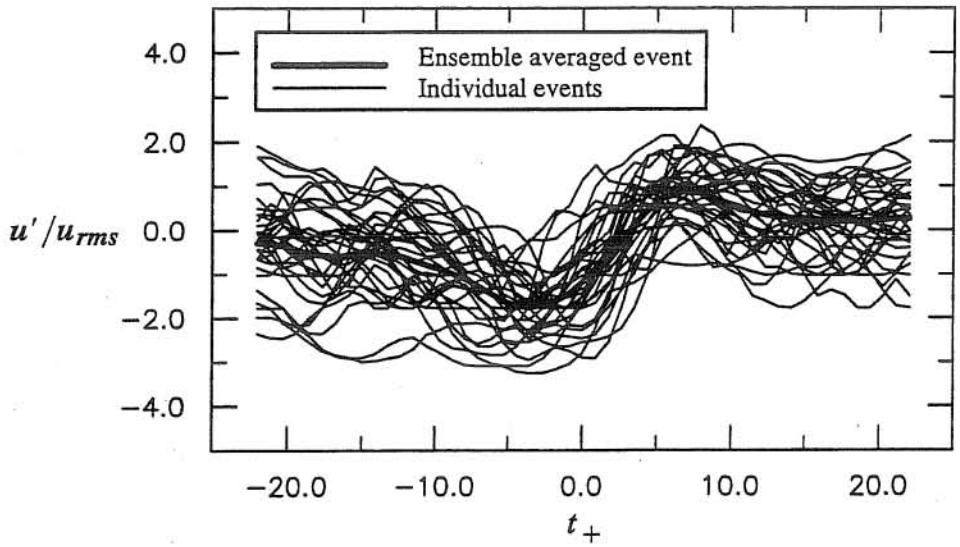

Fig. 3.34 Detected sweep events for $\tau_+ = 15$. Experiment S22, $h = 0.041$ m.

Unfortunately, the same behavior is not observed for the ejection events. As already discussed, the number of ejections detected increases monotonically with τ_+ in the range analyzed. Nevertheless, there appears to exist a maximum value of τ_+ for which the events detected correspond effectively to ejections. For larger values of τ_+ a number of events that do not show a large negative acceleration, and thus that do not correspond to ejections, are also detected, which contaminates the analysis. This is illustrated in Figs. 3.35 and 3.36.

Fig. 3.35, corresponding to the experiment S22, shows dimensionless streamwise velocity signals associated with the detected ejection events using a value $\tau_+ = 10$, plotted together with the corresponding ensemble averaged event. As observed therein, all the events detected exhibit a large negative acceleration at the time of detection. On the other hand, Fig. 3.36 show analogous results obtained with a value $\tau_+ = 15$. It is clear from this figure that a number of sweep events were also detected in this case, and therefore the latter value of τ_+ is less adequate for the analysis of this particular experiment than the value $\tau_+ = 10$ used for the results of Fig. 3.35. Consequently, although the number of events detected by the VITA method applied to the detection of ejections increases monotonically with τ_+, there appears to be a limit value of τ_+ that maximizes the number of ejections detected, such that for larger values of this parameter also sweeps events are, misleadingly, detected.

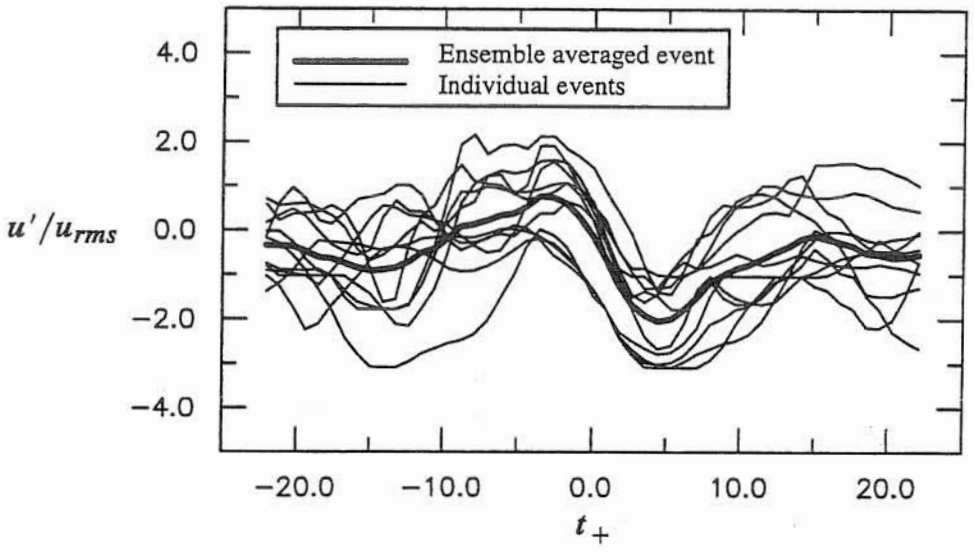

Fig. 3.35 Detected ejection events for $\tau_+ = 10$. Experiment S22, $h = 0.041$ m.

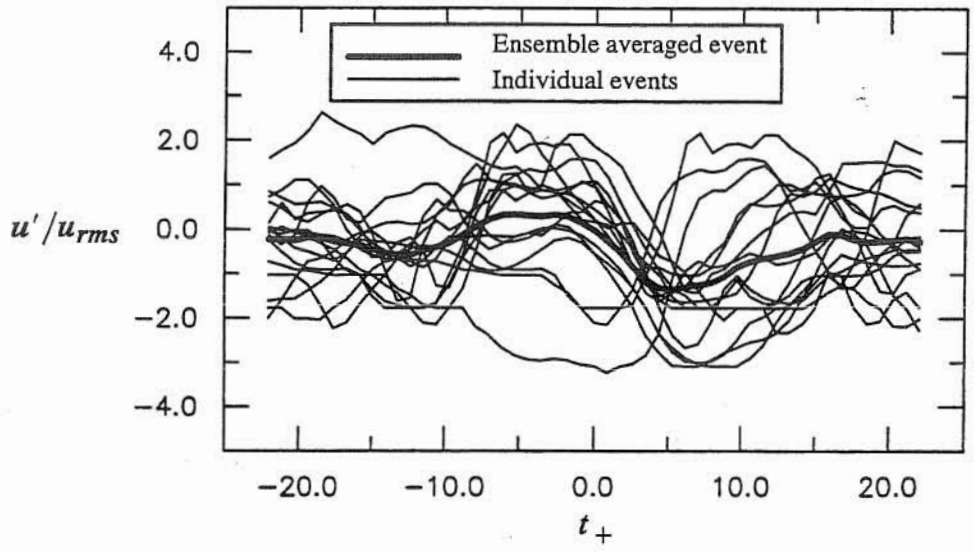

Fig. 3.36 Detected ejection events for $\tau_+ = 15$. Experiment S22, $h = 0.041$ m.

In conclusion, the criterion proposed herein to select the value of τ_+ is different for sweeps than for ejections. For sweeps, the optimum value of τ_+ corresponds to the one that maximizes the number of sweep events detected. For ejections, the optimum value of τ_+ corresponds to the maximum value of this parameter for which only ejections are detected. Nevertheless, the results obtained indicate that the optimum value of τ_+ for both sweeps and ejections are in general very similar in magnitude, and can vary in the range from about 10 to about 30.

The above criterion was applied to the analysis of the experiments of both series S and T. The results obtained in terms of the optimum values of τ_+ and the corresponding dimensionless frequency of detected events, $f_+ = f\,\nu/u_*^2$, where f denotes the number of events per unit time, are presented in Table 3.4, separately for sweeps and ejections. A plot of the resulting dimensionless frequency of sweeps and ejections as a function of the Reynolds number of the flow, for both series of experiments S and T is shown in Fig. 3.37. In order to compare this results with those of Blackwelder and Haritonidis (1983), which correspond to turbulent boundary layer flows in a wind tunnel, the same results shown in Fig. 3.37 are plotted in Fig. 3.38, this time as a function of the Reynolds number based on the momentum thickness of the boundary layer (defined as $Re_\theta = \theta\, U_{max}/\nu$, where θ denotes the momentum thickness, and U_{max} denotes the maximum streamwise mean velocity, which in the case of open channel flows occurs at the free surface).

Table 3.4 Results of VITA analysis

Experiment	h (m)	Re	Re_θ	τ_{+sweep}	f_{+sweep}	τ_{+eject}	f_{+eject}
S11	0.0250	5675	849	10.0	0.00405	10.0	0.00037
S12	0.0350	11340	1498	10.0	0.00292	12.5	0.00083
S21	0.0300	8972	1139	20.0	0.00326	10.0	0.00092
S22	0.0410	15750	1825	15.0	0.00303	10.0	0.00083
S23	0.0460	18651	2187	15.0	0.00260	10.0	0.00082
S24	0.0520	23625	2659	20.0	0.00265	15.0	0.00077
T11	0.0271	8459	891	15.0	0.00287	15.0	0.00084
T12	0.0298	10008	1032	20.0	0.00275	20.0	0.00145
T13	0.0329	11695	1243	20.0	0.00228	20.0	0.00074
T21	0.0335	10742	1360	25.0	0.00269	25.0	0.00064
T22	0.0415	15944	2075	25.0	0.00141	20.0	0.00036
T23	0.0460	18898	2368	30.0	0.00152	30.0	0.00035
T24	0.0506	21938	2884	20.0	0.00140	20.0	0.00029
T31	0.0389	13265	1794	20.0	0.00154	20.0	0.00033

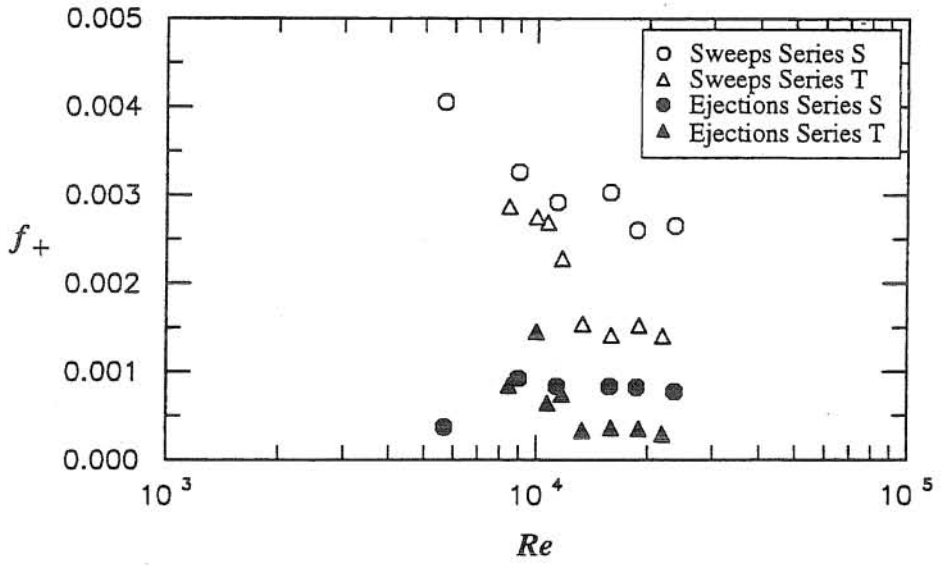

Fig. 3.37 Dimensionless frequency of bursting events as a function of Reynolds number (Series S and T).

As seen in Fig. 3.38, the present results for the dimensionless frequency of sweeps in the smooth flows compare very well with those of Blackwelder and Haritonidis (1983), which tend to define a more or less constant value for f_+, independent of the Reynolds number, of about 0.003 to 0.004. On the other hand, Fig. 3.37 shows that when plotted in linear scale a definite tendency for this variable to decrease with the Reynolds number is apparent. This is true also for the behavior of the dimensionless frequency of sweeps in the transitionally rough flows, and also of the dimensionless frequency of ejections in both smooth and transitionally rough flows, although in the latter case there is also a tendency for f_+ to decrease as Re decreases below 10^4. From Figs. 3.37 and 3.38 it is also clear that the values of the dimensionless frequency of sweeps are larger than corresponding values of the dimensionless frequency of ejections, by a factor of about 3 to 4. That is, for the same flow conditions there appears to be 3 to 4 times more sweeps than ejections. Finally, it seems that the frequency of both sweeps and ejections tends to be larger in the case of smooth flows than in the case of the transitionally rough flows, particularly at values of Re larger than about 10^4, for which the values of f_+ corresponding to the smooth flows tend to decrease faster than those of the transitionally rough flows.

Even though the value of the dimensionless integration time, τ_+, has an important effect over the frequency of detected events, it does not seem to have a major impact over the characteristics of the ensemble averaged events resulting from the VITA analysis. As an example to show this, the ensemble averaged sweep events obtained from the analysis of experiment S22 using three different values of τ_+, namely, 10, 15, and 20, are presented in Fig. 3.39, where the optimum value of τ_+ used in the determination of the frequency was 15. As observed therein, the main effect of τ_+ is

on the steepness of the signal during the accelerating part of the event, such that a higher acceleration is obtained for decreasing values of τ_+. On the other hand, the magnitude of the ensemble averaged event does not appear to be sensibly influenced by τ_+. These conclusions are generally valid for sweeps and ejections of both series S and T.

The characteristics of the ensemble averaged sweep and ejection events, resulting from the VITA analysis of the experiments of series S and T are discussed next. Fig. 3.40 shows the dimensionless ensemble averaged sweep events corresponding to both series S and T, while Fig. 3.41 presents the dimensionless ensemble averaged ejection events corresponding also to series S and T. Therein the events of series S are plotted in red and the events of series T are plotted in blue. Events corresponding to different Reynolds numbers within each series of experiments were not differentiated in those figures, mainly for the sake of the clarity of the plot, since no clear dependence on the Reynolds number was detected.

It is apparent from Fig. 3.40 that the dimensionless ensemble averaged sweeps tend to collapse in one characteristic shape. The total duration of the sweeps is about 40 to 50 wall units (that is, in terms of the time scale ν/u_*^2). The ensemble averaged events start with a mild deceleration of the streamwise velocity until reaching negative values of the fluctuating velocity of the order of 1.5 to 2.0 times the rms velocity, u_{rms}. A strong acceleration of the flow follows, in which the fluctuating velocity reaches a positive peak of about 1.0 to 1.5 times u_{rms} in a time interval of about 10 wall units, after which it decelerates mildly to nearly vanishing values at the end of the event. No major differences exist between the sweeps of the smooth flows and those of the transitionally rough flows, except for a tendency of the former to have slightly larger accelerations. This, however seems to be consequence of the larger values of τ_+ used in the VITA analysis of the experiments of Series T, as shown in Table 3.4.

From Fig. 3.41 it seems that the collapse of the dimensionless ensemble averaged ejection events in one curve is less clear than in the case of sweeps, although still all the events follow the same general trend. As in the case of sweeps, the total duration of the ejections is about 40 to 50 wall units. The ensemble averaged events start with a mild acceleration of the streamwise velocity until reaching positive values of the fluctuating velocity of the order of 0.5 to 1.0 times the rms velocity. A strong deceleration of the flow follows, in which the fluctuating velocity reaches a negative peak of about 1.5 to 2.0 times u_{rms} in a time interval of about 10 to 15 wall units, after which it accelerates mildly to nearly vanishing values at the end of the event. Some differences between the ensemble averaged ejections of the smooth flows and those of the transitionally rough flows are apparent. In the first place, there is a tendency for the deceleration of the former to be slightly larger than that of the latter, which as in the case of sweeps seems to be a consequence of the larger values of τ_+ used in the analysis of the experiments of Series T. A second major difference seems to be

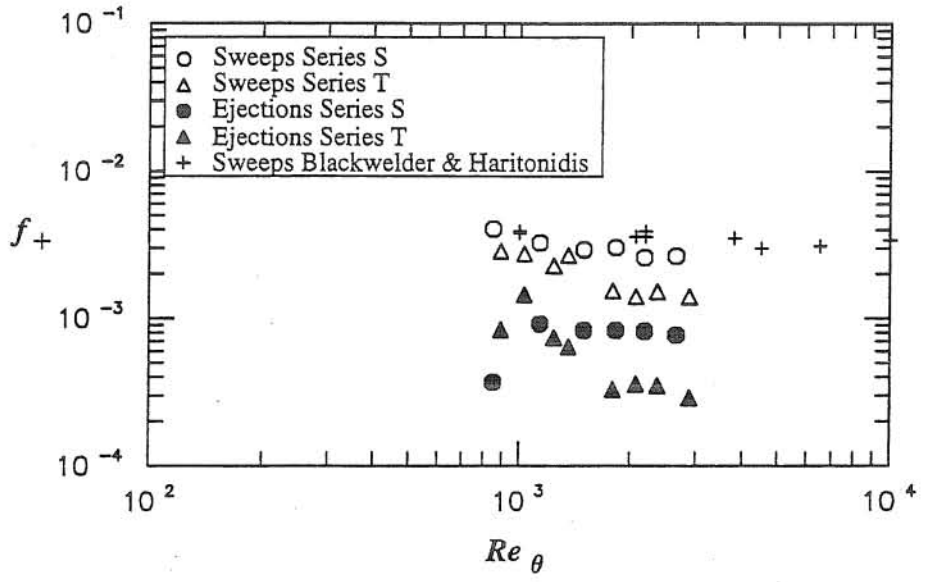

Fig. 3.38 Dimensionless frequency of bursting events as a function of Reynolds number based on momentum thickness (Series S and T, and Blackwelder and Haritonidis, 1983).

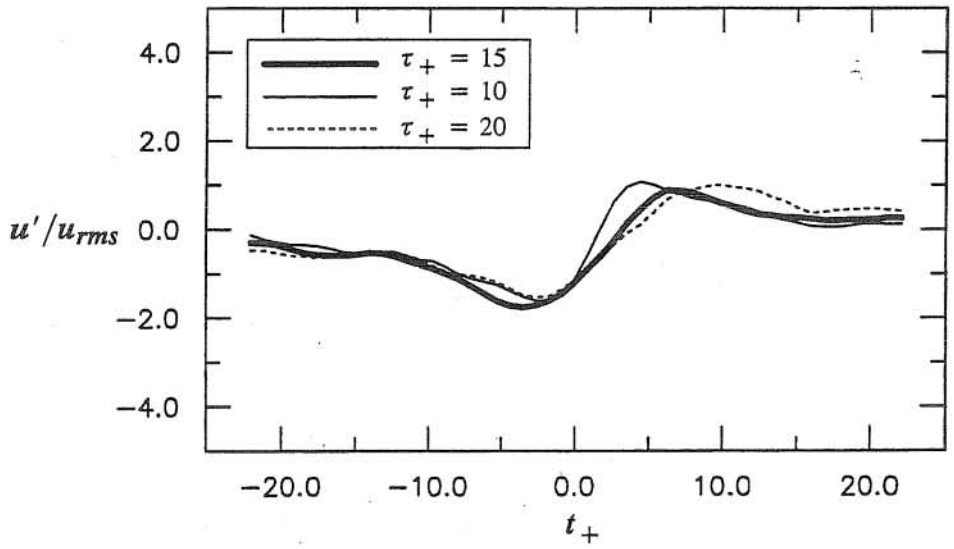

Fig. 3.39 Ensemble averaged sweep events as a function of τ_+. Experiment S22, h = 0.041 m.

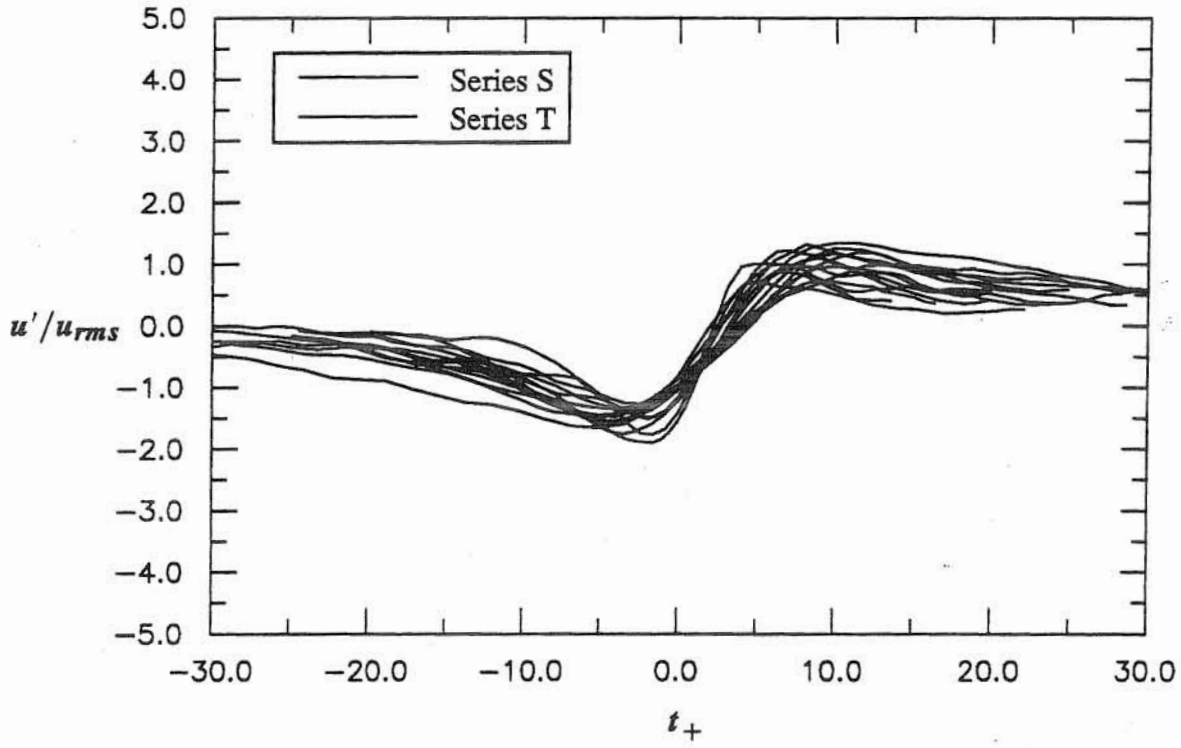

Fig. 3.40 Ensemble averaged sweep events (Series S and T).

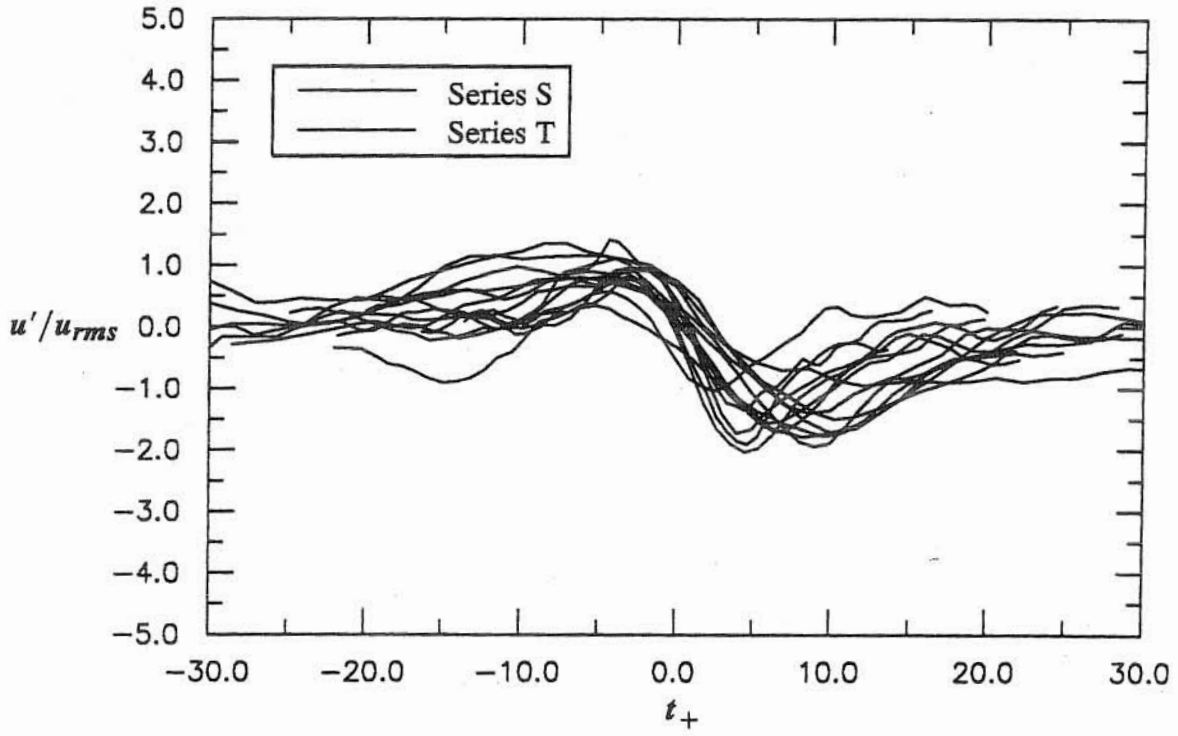

Fig. 3.41 Ensemble averaged ejection events (Series S and T).

the fact that the time interval between the time of detection ($t_+ = 0$) and the time corresponding to the negative peak of the velocity fluctuations is longer in the case of transitionally rough flows (about 10 wall units) than in the case of the smooth flows (about 5 wall units).

In order to improve the collapse of the curves describing the ensemble averaged ejection events, a different method of averaging was applied. The curves shown in Figs. 3.40 and 3.41 were obtained by ensemble averaging individual events which were centered about the time of detection (reset to $t_+ = 0$ in those figures). Fig. 3.42 shows the results obtained from the ensemble averaging of individual ejection events now centered about the time corresponding to the negative peak of the velocity fluctuations (which is reset to $t_+ = 0$ in that figure). As observed therein the collapse of the curves improved substantially, specially in the region of the negative peak. Now the ensemble averaged ejection events can be described as having a rather abrupt deceleration of the fluctuating velocity until reaching a negative peak of about 2.0 to 2.5 times the rms velocity, followed by an also rather abrupt acceleration of the flow towards vanishing values of the fluctuating velocity. On the other hand, the dimensionless ensemble averaged ejections corresponding to the smooth flows seem to have a narrower region of negative velocities than those corresponding to the transitionally rough flows.

From the analysis presented above a number of conclusions can be derived. First, it seems that sweeps and ejections are not two different stages of the same bursting event, as suggested by the classical conceptual models for bursting (e.g., Kline et al., 1967; Offen and Kline, 1974). These models conjecture that a flow ejection would be followed by a sweep, which would induce a new ejection, and so on, thus defining a self-sustained process. The evidence gathered herein seems to indicate that sweeps and ejections are, in general, disconnected processes, in that they have different frequency of occurrence, and detected sweep events do not usually occur right after detected ejection events in the velocity time series. Furthermore, the ensemble averaged ejection events do not show a positive peak of the streamwise velocity fluctuation after the accelerating phase as it would be necessary for a sweep event to occur. This type of behavior of the conditionally averaged velocity fluctuations has also been observed by Talmon et al. (1986), and by Luchik and Tiederman (1987). It is interesting to note, however, that during sweeps, positive peaks in the velocity fluctuations are always preceded by negative peaks of this variable, which have a magnitude generally larger that that of the positive peaks but characterized by a very mild deceleration of the streamwise velocity. In this sense it seems that the sweeps are indeed preceded by some kind of mild ejection, although different from the highly energetic events characterized by a strong deceleration of the flow which herein have been denoted ejections events.

Another conclusion that can be obtained from the present results is that, in general, negative peaks of the ensemble averaged velocity fluctuations during sweeps and ejections are of higher

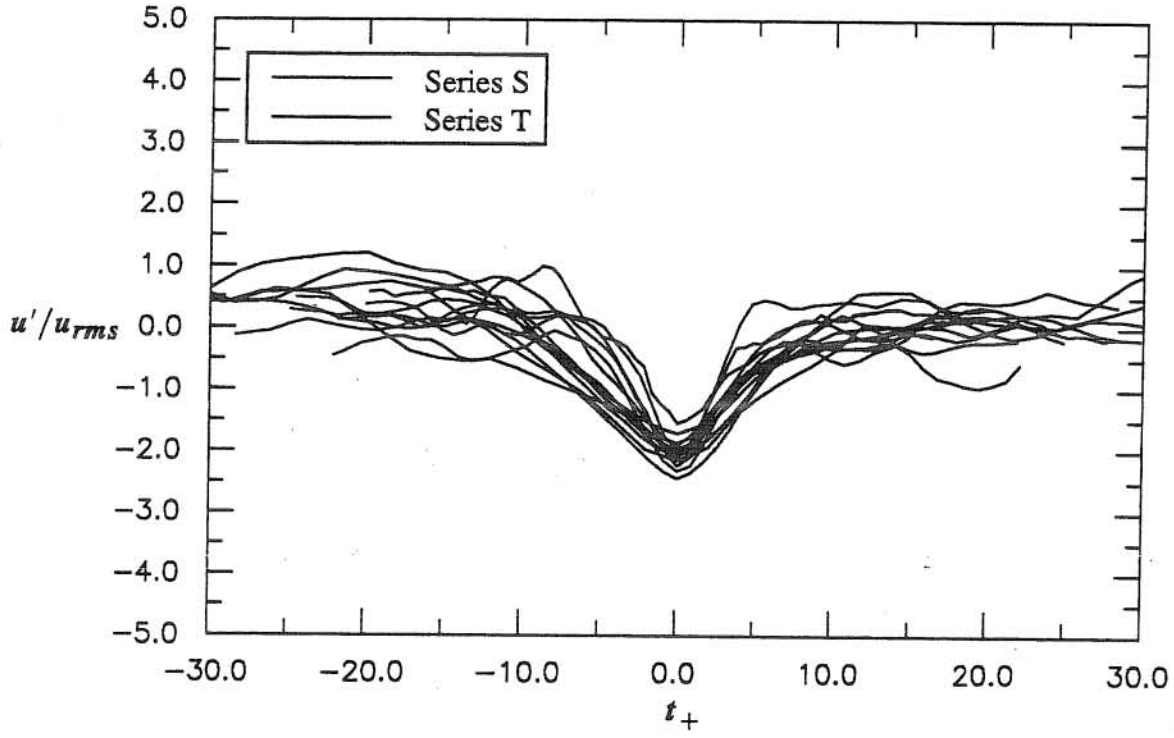

Fig. 3.42 Ensemble averaged ejection events centered around time to negative peak (Series S and T).

magnitude than positive peaks of this variable. In fact, the conditionally averaged velocity fluctuations during sweeps and ejections have negative peaks with a magnitude of about 2.0 times the rms velocity, while positive peaks of these velocities are rarely much larger than about 1.5 times the rms velocity. This seems to be related to the negative values of the skewness typically observed in the streamwise velocity time series of the flows analyzed herein (Figs. 3.10 and 3.11), which as was already discussed, implies that large positive values of the velocity fluctuations are not as frequent as as negative ones.

3.5 Conclusions

The turbulence characteristics of the open channel flows analyzed in the present experimental study are in a general very good agreement with observations and models reported by Nezu and Nakagawa (1993) in their monograph on turbulence in open channel flows, which are based in a fairly large amount of experimental data. This somehow supports the validity of the experimental work and the methods of analysis utilized herein. A few conclusions derived from the discussions presented in the preceding section are summarized in what follows.

The vertical distribution of turbulent intensities, u_{rms}/u, plotted as a function of y/h, show a good collapse for experiments of different values of Re, in both smooth and transitionally rough flows. The turbulent intensities of the transitionally rough flows are larger than those of the smooth ones, although the differences are somewhat greater near the bottom than near the free surface, in agreement with other experimental observations. There is also a good collapse of the vertical distribution of u_{rms+} for different values of Re, and the values of this variable corresponding to the transitionally rough flows are somewhat larger than those of the smooth flows all along the vertical. It seems that this occurs because the rms values of the velocity fluctuations corresponding to the smooth flows are slightly lower than expected. A comparison with (3.9) indicates that this equation represents the vertical distribution of u_{rms+} corresponding to the transitionally rough flows very well, although it slightly overestimates those values corresponding to the smooth flows because of the reasons already mentioned.

The values of the skewness of the streamwise velocity fluctuations are negative for the experiments of both series S and T, and there is a tendency for this variable to increase toward positive values as the bottom wall is approached, which appears to be stronger in the case of transitionally rough flows than in the case of smooth flows. The negative values of the skewness can be interpreted, following Raupach (1981), as a consequence of a higher contribution of the events of quadrant 2 to the total turbulent shear stress than that of the events of quadrant 4. The fact that the values of the skewness tends to increase toward the bottom wall would indicate that events of quadrant 4 contribute relatively more to the total shear stress in the near wall region than in regions away from the wall. The values of the flatness of the streamwise velocity fluctuations do not deviate

much from the Gaussian value 3.0, in both series of experiments S and T, except near the free surface, where larger values of the flatness were observed. This would be related with a higher intermittency of the turbulence in that region.

From the analysis of the frequency spectrum of the streamwise velocity fluctuations in both the smooth and transitionally rough flows, the existence of an inertial subrange where the –5/3 law holds is apparent, which corresponds to values of f in the range from about 5 to about 40 Hz, and which tends to get wider as Re increases. A good collapse of the normalized frequency spectra corresponding to different locations in the vertical for a constant value of Re, is observed for both series of experiments S and T. No major differences are observed between the normalized frequency spectra of the smooth and transitionally rough flows, at similar vertical locations and Reynolds numbers. Although there is a good collapse of the frequency spectra at a given location and different Reynolds numbers in the production and inertial subranges, the normalized energy density associated with higher frequencies tends to increase with Re, which is a consequence of the reduction of the length scales of the fine structure of the turbulence as Re increases.

An alternative method to that of Nezu and Nakagawa (1993) to estimate the integral length scale of the flows from the frequency spectrum was proposed, which consists on calibrating this length scale in order to adjust (3.30) to the inertial subrange of the experimental frequency spectrum. A very good agreement of the resulting values of L_x/h with (3.31) was obtained, although there is a tendency for the values corresponding to the transitionally rough flows to be slightly lower than those predicted by (3.31), and also slightly lower than those corresponding to the smooth flows, in the near wall region, which is in agreement with other experimental observations. In the near wall region, the present results indicate a magnitude of the integral length scale of about 5 to 10 mm.

A simple estimation of the rate of dissipation of turbulent kinetic energy, ε, using (3.26) gave results that are in good agreement with (3.27). The results corresponding to the transitionally rough flows tend to be somewhat larger than those of the smooth flows in the near wall region, which assuming that production nearly balance out dissipation in such region, would indicate that the transitionally rough flows exhibit a slightly higher production of turbulent kinetic energy near the wall than the smooth flows, which is also in agreement with other experimental observations.

Taylor's microscale of the streamwise velocity fluctuations was evaluated using the strict definition (3.32) and the isotropic relationship (3.33). It was found that the results obtained from using (3.32) did not agree well with the isotropic theoretical relationship (3.34) proposed by Nezu and Nakagawa (1993), specially in the near wall region, for both the experiments of series S and T, although the agreement was generally worst in the latter case. On the contrary, using (3.33) a very good agreement with (3.34) was observed which is rather obvious because (3.34) is based on a theoretical evaluation of (3.33) using expressions for u_{rms} and ε that represent the present

experimental data very well. These results seem to indicate a departure from isotropy on the small scales, involving mainly the wall region for the smooth flows, and almost the whole flow depth for the transitionally rough flows, at least for the present range of values of Re. In general, the results obtained indicate values of Taylor's microscale that are on the order of 30% of the values of the integral length scale, with magnitudes of this variable in the near wall region in the range from 1.5 to 3.0 mm.

Kolmogorov's microscale, η, of the turbulent open channel flows studied herein was estimated using the definition (3.35) and the already obtained values of ε. The vertical distribution of the experimental values of the ratio η/h are in very good agreement with the predictions of (3.37), for both series S and T. In general, the results obtained indicate values of the Kolmogorov's microscale that are on the order of 1% of the values of the integral length scale, with magnitudes of this variable in the near wall region of about 0.05 to 0.1 mm.

A method to estimate optimum values of the integration time required in the VITA algorithm for the detection of bursting-like events in the streamwise velocity fluctuations time series was developed. This parameter has special importance on the number of the events detected by the VITA method. For sweep events, the optimum value of τ_+ would be to the one that maximizes the number of events detected by the detection criterion (3.41). For ejection events, the optimum value of τ_+ would correspond to the maximum value of this parameter for which only ejections are detected. The results obtained indicate that optimum values of τ_+ are in the range from 10 to 30, and are in general very similar for both sweeps and ejections.

The dimensionless frequency of the detected sweep events for the smooth flows compares very well with analogous results by Blackwelder and Haritonidis (1983) in a wind tunnel, which define a more or less constant value of f_+, independent of the Reynolds number, of about 0.003 to 0.004. A comparison of the frequencies of detected sweeps and ejections for both series S and T, indicates that in general, there appears to be about 3 to 4 times more sweeps than ejections. Also, it seems that the frequency of both sweeps and ejections tends to be larger in the case of smooth flows than in the case of the transitionally rough flows, particularly at values of Re larger than about 10^4.

Even though the value of the dimensionless integration time, τ_+, has an important effect over the frequency of detected events, it does not seem to have a major impact over the characteristics of the ensemble averaged events resulting from the VITA analysis, the main effect being that at lower values of τ_+ slightly higher steepness of the accelerating (decelerating) portions of the sweeps (ejections) results.

The dimensionless ensemble averaged sweeps corresponding to different values of Re for the experiments of series S and T tend to collapse in one characteristic shape. This is less clear in the case of the dimensionless ensemble averaged ejections, although all the events follow the same

general trend. The total duration of the sweeps is similar to that of the ejections, about 40 to 50 wall units. The ensemble averaged sweeps are characterized by a very strong acceleration during which the velocity fluctuation increases from negative values of about 1.5 to 2.0 u_{rms} to a positive peak of about 1.0 to 1.5 u_{rms} in a time interval of about 10 wall units. No major differences exist between the sweeps of the smooth flows and those of the transitionally rough flows. The ensemble averaged ejections are characterized by a very strong deceleration during which the velocity fluctuation decreases from positive values of about 0.5 to 1.0 u_{rms} to a negative peak of about 1.5 to 2.0 u_{rms} in a time interval of about 10 to 15 wall units. Ensemble averaged ejections of the smooth flows and those of the transitionally rough flows seem to differ in the magnitude of the time interval between the time of detection and the time corresponding to the negative peak of the velocity fluctuations, such that it is longer in the case of transitionally rough flows than in the case of the smooth flows. A better collapse of the conditionally averaged curves corresponding to the ejection events was obtained by ensemble averaging individual events which were centered about the time corresponding to the negative peak of the velocity fluctuations, instead of about the time of detection.

It seems that sweep and ejection events detected using the VITA algorithm, and characterized by being highly energetic events with a strong acceleration or deceleration of the streamwise velocity, are independent events, and one does not appear to be the consequence of the other. For instance, the frequency of sweeps and ejections is different, being the former 3 to 4 times larger than the latter. On the other hand, although sweeps seem to be preceded by some kind of mild ejection of low energy, ejections do not appear to be followed by positive peaks of the velocity fluctuations, required for the existence of sweeps.

Finally, negative peaks of the conditionally averaged velocity fluctuations tend to be generally higher than corresponding positive peaks for both sweeps and ejections, which would be related to the negative values of the skewness typically observed in the streamwise velocity time series of the flows analyzed herein.

3.6 References

Batchelor, G. K. (1953). "The theory of homogeneous turbulence". *Cambridge University Press.*

Bendat, J. S., and Piersol, A. G. (1986). "Random data". *Wiley-Interscience.*

Blackwelder, R. F., and Haritonidis, J. H. (1983). "Scaling of the bursting frequency in turbulent boundary layers". *J. Fluid Mech.*, vol 132, pp 87-103.

Blackwelder, R. F., and Kaplan, R. E., (1976). "On the wall structure of the turbulent boundary layer". *J. Fluid Mech.*, vol 76, pp 89-112.

Bogard, D. G., and Tiederman, W. G. (1986). "Burst detection with single-point velocity measurements". *J. Fluid Mech.*, vol 162, pp 389-413.

Chen, C. P., and Blackwelder, R. F. (1978). "Large-scale motion in a turbulent boundary layer: a study using temperature contamination". *J. Fluid Mech.*, vol 89, pp 1-31.

Clauser, F. H. (1956). "The turbulent boundary layer". *Adv. Applied Mech.*, vol. 4, pp 1-31.

Goldstein, R. J. (1983). "Fluid mechanics measurements". *Hemisphere Publishing Corporation.*

Johansson, A. V., and Alfredsson, P. H. (1984). "On the structure of turbulent channel flow". *J. Fluid Mech.*, vol 122, pp 295-314.

Kline, S. J., Reynolds, W. C., Schraub, F. A., and Runstadler, P. W. (1967). "The structure of turbulent boundary layers". *J. Fluid Mech.*, vol 30, pp 741-773.

Luchik, T. S., and Tiederman, W. G. (1987). "Timescale and structure of ejections and bursts in turbulent channel flows". *J. Fluid Mech.*, vol 174, pp 529-552.

Lyn, D. A. (1992). "Turbulence characteristics of sediment-laden flows in open channels". *J. Hydr. Engrg.*, 118 (7), pp 971-988.

McQuivey R. S., and Richardson, E. V. (1969). "Some turbulence measurements in open-channel flow". *J. Hydr. Div. ASCE*, vol 95, No HY1, pp 209-223.

Monin, A. S., and Yaglom, A. M. (1975). "Statistical Fluid Mechanics, vol 1". *MIT Press.*

Nakagawa, H., and Nezu, I. (1977). "Prediction of the contributions to the Reynolds stress from bursting events in open-channel flows". *J. Fluid Mech.*, vol 80, pp 99-128.

Nezu, I., and Nakagawa, H. (1993). "Turbulence in open-channel flows". *IAHR Monograph.* A. A. Balkema, Rotterdam.

Nezu, I. (1977). "Turbulent structure in open-channel flows". *Translation of Doctoral dissertation in Japanese.* Kyoto University, Kyoto, Japan.

Offen, G. R., and Kline, S. J. (1974). "Combined dye-streak and hydrogen bubble visual observations of a turbulent boundary layer". *J. Fluid Mech.*, vol 62, part 2, pp 223-239.

Raichlen, F. (1967). "Some turbulence measurements in water". *J. Engrg. Mech. Div. ASCE*, vol 93, No EM2, pp 73-97.

Raupach, M. R., Antonia, R. A., and Rajagopalan, S. (1991). "Rough-wall turbulent boundary layers". *Appl. Mech. Rev.*, vol 44, no 1.

Raupach, M. R. (1981). "Conditional statistics of Reynolds stress in rough-wall and smooth-wall turbulent boundary layers". *J. Fluid Mech.*, vol 108, pp 363-382.

Schlichting, H. (1968). "Boundary-layer theory". *McGraw-Hill Book Company.*

Talmon, A. M., Kunen, J. M. G., and Ooms, G. (1986). "Simultaneous flow visualization and Reynolds-stress measurement in a turbulent boundary layer". *J. Fluid Mech.*, vol 163, pp 459-478.

Wallace, J. M., Brodkey, R. S., and Eckelmann, H. (1977). "Pattern-recognized structures in bounded turbulent shear flows". *J. Fluid Mech.*, vol 83, part 4, pp 673-693.

Wallace, J. M., Eckelmann, H., and Brodkey, R. S. (1972). "The wall region in turbulent shear flow". *J. Fluid Mech.*, vol 54, pp 39-48.

Yalin, M. S. (1992). "River Mechanics". *Pergamon Press.*

4. CHARACTERIZATION OF NEAR BED COHERENT STRUCTURES IN OPEN CHANNEL FLOW

4.1 Introduction

The landmark investigation of Kline et al. (1967) was probably the first showing the important role played by quasi-periodic repeating patterns of organized motions occurring in the near wall region of a turbulent boundary layer on the turbulence dynamics of the flow. These coherent flow structures appear to be involved in the mechanism by which kinetic energy from the mean flow is converted into turbulent fluctuations, and therefore their study constitutes one of the most important topics on turbulent boundary layer research (Robinson, 1991).

In wall bounded flows the majority of the turbulence production throughout the whole flow field occurs at values of $y_+ = u_* y/\nu$ (where u_* denotes the flow shear velocity, ν denotes the kinematic viscosity of the fluid and y denotes the upward vertical coordinate) less than about 100, a region known as the wall layer, through the so called bursting process, i.e. intermittent, violent ejections of low-speed streaks away from the wall and inrushes of high-speed fluid towards the boundary (Kim et al., 1971; Robinson, 1991). Flow visualizations show the structure of boundary layers being composed by a 'forest' of hairpin vortices (e.g., Head and Bandyopadhyay, 1981), while numerical data bases (e.g., Jimenez et al., 1988; Guezennec et al., 1989) as well as Particle Image Velocimetry (PIV) (e.g., Liu et al., 1991) reveal the existence of inclined, thin shear layers of concentrated spanwise vorticity. All these more or less organized features have been called *coherent structures*, meaning "a three-dimensional region of the flow over which at least one fundamental flow variable exhibits significant correlation with itself or with another variable over a range of space and/or time that is significantly larger than the smallest local scales of the flow" (Robinson, 1991).

One of the major motivations for investigating and characterizing turbulent coherent structures arises from the fact that they also play an important role in turbulent transport processes near boundaries (Nezu and Nakagawa, 1993). For example, near-wall turbulent organized motions would be responsible for the entrainment into suspension of fine sediment particles laying on the bed of an open channel flow as is shown in following Chapters. This entrainment process is related to the fact that such coherent motions strongly contribute to the vertical turbulent transport of momentum. Therefore, a good understanding of the associated flow field is needed in order to construct any sound model of transport processes near the bed, which truly accounts for the physics involved.

Different experimental as well as computational techniques have been developed to detect and characterize coherent events. Most of the earlier laboratory studies on coherent structures employed flow visualizations, however descriptions based on this technique alone are too qualitative to

provide a complete picture of all the processes involved. Consequently later works have employed simultaneous visualizations and hot-film anemometry or, more recently, laser Doppler velocimetry, hence providing a good combination of images and data-signals. Experiments involving simultaneous visualizations and measurements were carried out among others by Offen and Kline (1973), Falco (1977), and Talmon et al. (1986). Most of these studies employed film cameras, which have some disadvantages concerning film developing, digitalization of the results, etc. On the other hand, pattern-detection algorithms have been developed for detecting the occurrence of organized patterns from a turbulent signal. The most commonly used being the $u'v'$-quadrant-2 method (u' and v' denoting streamwise and vertical velocity fluctuations, respectively), the VITA technique and the u-level algorithm (Luchik and Tiederman, 1987). More recently the application of PIV has allowed to instantaneously measure the whole spatial structure of the flow field (e.g., Liu et al., 1991; Urushihara et al., 1993), thus giving a direct two-dimensional picture of the organized patterns associated with the occurrence of coherent structures.

To date the vast majority of experimental as well as numerical work has been concentrated on low-Reynolds number boundary layer and channel flows, with less attention directed towards free-surface water flows. The present work deals with the experimental study of near-bed coherent structures in a turbulent open-channel flow and the characterization of the associated coherent streamwise velocity and bed shear stress field. The original experimental set-up allowed for the acquisition at high sampling rates (500 Hz) of synchronized video images and hot-film signals from velocity and bed shear stress sensors.

4.2 Experiments

4.2.1 Experimental setup

The experiments were conducted in a rectangular open channel 18.6 m long, 0.297 m wide, and 0.280 m high, which has an observation window located a distance of about 12 m downstream of the entrance. The channel slope was set to a value of about 0.0009.

Two different hot-film probes were used, namely, a ruggedized hemisphere velocity probe (TSI 1239W) and a shear stress probe (TSI 1237W) mounted flush to the bottom surface of the channel. Data acquisition was made with an A/D card connected to a personal computer and appropriate software. The equipment used had the capability of digitizing two channels simultaneously with different triggering options.

A high-speed video system, Kodak Ektapro TR Motion Analyzer, was used to record simultaneously the signals from the hot-film sensors with images resulting from flow visualizations. The solid state sensor of this system has a pixel array structure of 240 columns and 192 rows. Blocks of 16 rows are read simultaneously by means of 16 channels, which gives the system the capability

to record up to 1000 frames per second in full frame mode, or up to 6000 frames per second in split screen mode.

The video system outputs a synchronization signal, which was employed to trigger the acquisition of data with the hot-film sensors simultaneously with the video recording. The synchronization level of the system was tested using a sine-function generator and an external data interface which allowed recording the generated signal levels into the video frames.

A strobe light with a flash-duration of 20 microseconds was synchronized with the high-speed video system to provide whole-field illumination. This type of illumination was preferred to a laser sheet, mainly because the extremely short pulse of the strobe light helped to reduce image blur. Also, since the light sensitivity of the high-speed video camera is rather poor it was found that the quality of the images obtained with the strobe light illumination was better than those obtained using an available, relatively low power, laser.

The video images acquired with the high-speed video system were downloaded from special high-speed Kodak tapes onto standard VHS tapes, from where were digitized into a personal computer using a frame grabber. The images were analyzed using the National Institute of Health's *Image* public domain software. A schematic view of the experimental setup is shown in Fig. 4.1.

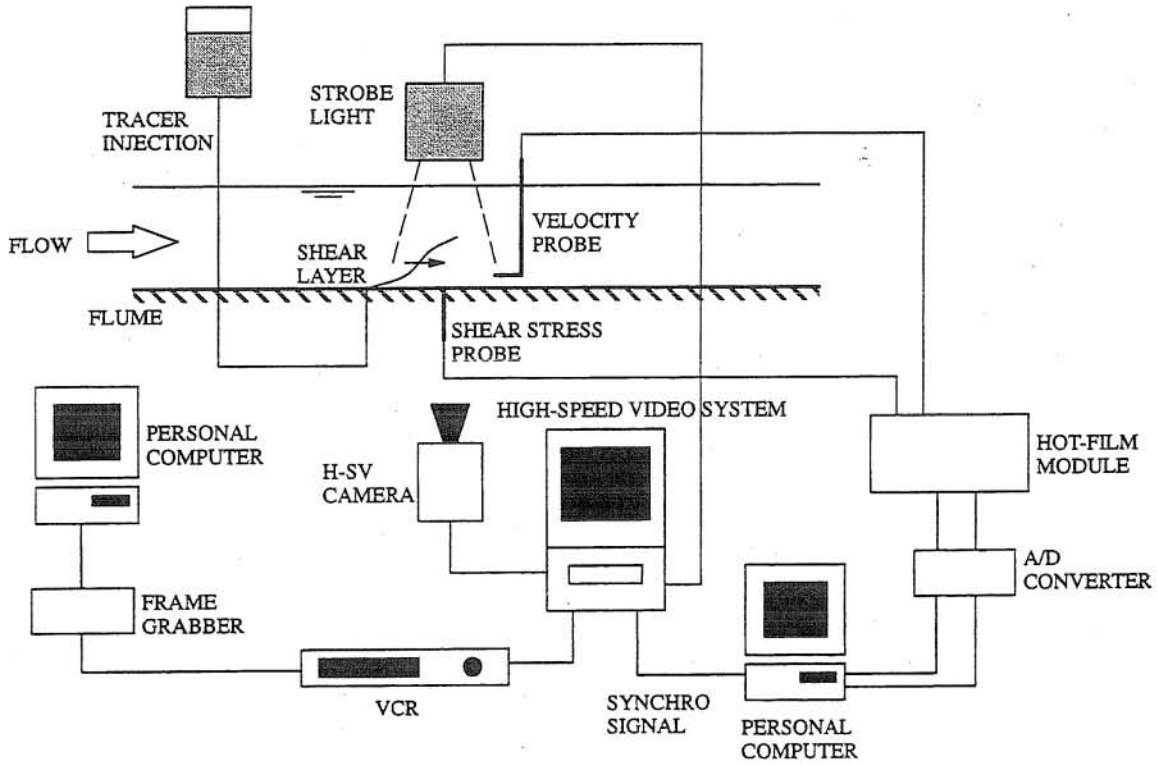

Fig. 4.1 Schematic view of experimental set-up.

4.2.2 Experimental method

Three different sets of experiments were carried out: experiments of Series ES1, which correspond to flow visualizations of coherent structures in the near wall region, experiments of Series ES2, where synchronized measurements of flow velocity and bed shear stress using the hot-film probes and recording of images of flow visualization using the high-speed video system were carried out, and experiments of Series ES3, which correspond to simultaneous measurements of flow velocity and bed shear stress using the hot-film probes, with no flow visualizations.

In what follows, x, y, and z denote coordinates in the streamwise, vertical and transverse directions, respectively. Also, wall units denote characteristic scales formed using u_* and ν as variables, such that for example, ν/u_* represents a length scale, u_* represents a velocity scale, and ν/u_*^2 represents a time scale. Variables with the subindex + have been made dimensionless with wall units.

Series ES1

Series ES1 considered two bed roughness conditions, which corresponded to smooth flows: Series ES1-S, and transitionally rough flows: Series ES1-T. In Series ES1-T the bed roughness was created by glueing sand particles with a mean size of about 0.53 mm to the originally smooth surface of the channel bottom.

In this series of experiments, plan and side view flow visualizations were recorded using the high-speed video system, with the aim of studying typical coherent structures and flow patterns occurring in the near wall region of open channel flows. For the side views a solution of white clay in water was injected through an orifice in the channel bottom located 30 mm upstream of the shear stress sensor to act as a marker for flow structures developing at the wall. It must be noted that the white clay solution was preferred to common fluorescein because it showed much better in the video images given the relatively low light sensitivity of the high-speed video camera used. The tracer discharge was controlled as to minimize disturbance of the flow, and to allow the tracer to displace attached to the bed before flow ejections lifted filaments away from the bottom. This technique allows to visualize flow ejections fairly well, however it does not provide visual information about the flow structure in the region above the ejection, nor is it efficient in marking sweeps events.

Plan view visualizations were also performed to study the structure of the viscous sublayer in the $x-z$ plane, using fine glass beads 94 μm in diameter (which corresponds to a dimensionless size, d_{p+}, of about 1 to 2 wall units), similarly to experiments conducted by Grass (1971).

In the case of side view visualizations, typical dimensions of the flow field registered by the camera were about 200 by 150 to about 850 by 700 wall units (streamwise/vertical), while in the

case of plan views, such dimensions were about 900 by 1000 to 1500 by 2000 wall units (streamwise/transverse).

Series ES2

In this series of experiments, side view flow visualizations of coherent structures in the near wall region of the present open channel flows were recorded using the high-speed video system and synchronized with hot-film measurements of flow velocity and bed shear stress. These experiments were conducted over a smooth surface only.

For the flow visualizations, the field of view of the camera corresponded to a window of about 850 by 750 wall units, hence having a longitudinal dimension close to the typical length of viscous sublayer streaks (McComb, 1990). Working with such a small viewing area requires a high temporal resolution in order to accurately measure the main characteristics of observed coherent structures. For example, given an estimated convection velocity of such structures, u_c, of about 10 wall units and considering a typical structure 300 wall units long, it takes a dimensionless time $t_+ = 70$ for the center of a complete visualized structure to travel from the left to the right end of the screen where the velocity sensor was located. For the average Reynolds number of the experiments reported herein this means that with a conventional video sampling frequency of 30 Hz only 4 to 5 frames could have been acquired, whereas the high-speed capability of the Kodak system allowed to store 80 to 90 frames at 500 frames per second. Since Taylor's frozen turbulence hypothesis is invoked herein, it was also important to accurately define the time at which the structures crossed the probes. This transformation allows using the local Eulerian time series measured with the hot-film probes to infer the spatial flow field in the downstream vicinity of the shear structure. With a conventional video camera the uncertainties would have been of the order of ± 40 pixels, whereas the high-speed system reduced them to the order of ± 2 pixels.

Velocity and bed shear stress measurements were synchronized with side view flow visualizations, with the velocity sensor located at different distances from the bed. Results corresponding to measurements taken at four different dimensionless locations are reported in the present paper, namely $y_+ = 38$ ($Re = 5300$), 52 ($Re = 12400$), 64 ($Re = 18100$) and 80 ($Re = 5300$) (or equivalently, $y/h = 0.10$, 0.07, 0.06 and 0.22, respectively), where $Re = Uh/\nu$ denotes the Reynolds number of the flow, with U denoting the mean flow velocity in the cross section, and h denoting the flow depth.

Hot-film data were acquired at a rate of 500 Hz, thus satisfying Nyquist's criteria, given the present maximum frequencies of about 200 Hz and 90 Hz of the velocity and shear stress signals, respectively. Each time series acquired had a total of 15000 data points. Video images were recorded at 500 frames per seconds, hence keeping a direct correspondence between data points and video

frames. Video recordings had a duration of about 20 sec, which gives a number of about 10000 images per experiment.

Series ES3

The clay solution employed as tracer in the present study to mark flow patterns seemed to affect the quality of the signal of the bed shear stress sensor. Because of this, the experiments of Series ES3 were conducted which involved no flow visualizations, thus eliminating the problem caused by the tracer on the shear-stress probe and providing reliable shear stress data.

These experiments consisted of simultaneous acquisition of the signals from both hot-film probes, where the velocity sensor was located at different heights from the channel bottom and at variable distances downstream from the shear stress probe. The data set ES3 was mainly employed for performing cross-correlation analysis between velocity and shear stress signals, and corresponded only to smooth flows. Hot-film data were acquired at the same rate of 500 Hz of Series ES2, thus satisfying Nyquist's criteria. Each time series acquired had a total of 30000 data points.

4.2.3 Experimental conditions

Experiments were carried out under uniform flow conditions. In Series ES1, two different roughness conditions were studied: hydraulically smooth walls (Series ES1-S) and transitionally rough walls (Series ES1-T). In Series ES2 and ES3 only smooth flows were considered.

In Series ES2 and ES3 data corresponding to three different Reynolds numbers are reported. The experimental conditions are shown in Table 4.1, where $Fr = U/\sqrt{gh}$ denotes the Froude number of the flow, with g denoting gravitational acceleration, and $Re_* = u_* h/\nu$ denotes the Reynolds number based on the shear velocity. As can be observed therein, all the flows were subcritical and thus characterized by Froude numbers smaller than one.

Table 4.1 Experimental conditions

h (m)	U (m/s)	u_* (m/s)	Re	Re_*	F_r
0.023	0.231	0.016	5300	370	0.485
0.036	0.344	0.020	12400	720	0.580
0.044	0.412	0.022	18100	970	0.626

In Series ES1-S, the results of the flow visualizations are representative of conditions with values of h in the range 0.023 to 0.055 m, of u_* in the range 0.016 to 0.024, of Re in the range 5300 to 24000, of Re_* in the range 370 to 1240, and of Fr in the range 0.49 to 0.64. Corresponding conditions in Series ES1-T were: h in the range 0.030 to 0.055 m, u_* in the range 0.021 to 0.035, Re in the range 10000 to 25000, Re_* in the range 370 to 1900, Fr in the range 0.58 to 0.61, and k_{s+} in the range 30 to 35, where k_{s+} denotes the dimensionless bed roughness height.

4.3 Method of analysis

Details about the procedures used for the calibration of, and measurement with the hot-film probes, and the general characteristics of the present turbulent flows have been presented in Chapter 3.

4.3.1 Series ES1

Analysis of the recorded video images of Series ES1 provided information about the shape, geometry, convective velocity, and general behavior of the flow structures observed. These structures consisted mainly of near-wall shear layers as described by Robinson (1991), resulting from low-speed fluid ejections away from the wall. Images of detected structures were grabbed into a computer, and their shape was digitized manually with the help of the *Image* software. Similarly, the convection velocity of the structures was estimated by tracking them in successive video frames.

4.3.2 Series ES2

Despite the well-known three-dimensional character of the near-wall structures, the observed events showed little meandering in the spanwise direction, so that it was assumed herein that the signals acquired by the sensors, before the structures passed through them, are representative of the nearly two-dimensional flow field associated with the occurrence of such organized turbulent motions.

Video images of the flow visualizations were analyzed in order to detect, by visual inspection, developing flow structures approaching the hot-film sensors. The range of video frames corresponding to images of each structure moving in the region from about 400-500 wall units upstream of the velocity sensor was registered, and subseries of the hot-film data corresponding to such a range of frames were extracted from the original series. These subseries were later used to perform conditional ensemble averages of the velocity and some shear stress signals. Taylor's frozen turbulence hypothesis together with measured mean convective velocities were used in order to transform temporal data into spatial information for each event, which allowed estimation of the spatial flow velocity field associated with the occurrence of observed shear layers.

4.3.3 Series ES3

This set of data had no associated flow visualization images, and hence was only used to estimate the cross-correlation between velocity and bed shear stress signals, $R_{u\tau}$, which was evaluated as:

$$R_{u\tau}(\Delta x, \Delta y, \Delta t) = \frac{< \tau'(0, 0, t)\, u'(\Delta x, \Delta y, t + \Delta t) >}{u_{rms}\, \tau_{rms}} \qquad (4.1)$$

where angular brackets stand for ensemble averages (assumed herein to be equivalent to time averages), u' denotes the streamwise velocity fluctuations, τ' denotes the shear stress fluctuations,

Δx and Δy denote the separation between both sensors in the streamwise and vertical directions, respectively (the velocity probe located always downstream from the bed shear stress sensor), t and Δt denote time and time lag, respectively, and u_{rms} and τ_{rms} denote the standard deviation of the velocity and bed shear stress time series, respectively.

4.4 Results

4.4.1 Series ES1

Analysis of the flow visualizations in the smooth flows of Series ES1-S show structures similar to the ones reported by previous visualization studies (e.g., Kline et al., 1967). Plan views reveal the main structure of the viscous sublayer, consisting of alternating, elongated regions of high- and low-speed streaks, where accumulation of glass beads occurs, with an average transverse wavelength of about 100 wall units. An example of such organized structure is shown in Fig. 4.2 for the experimental conditions: Re = 9000, and d_{p+} = 1.7.

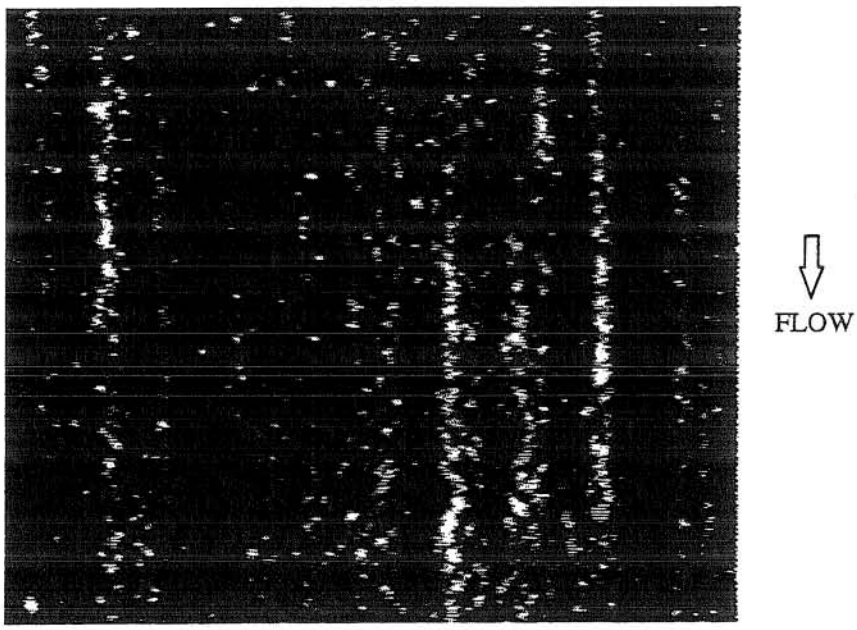

Fig. 4.2 Glass beads moving along low-speed streaks. Field of view is about 900 by 1000 wall units. Experimental conditions correspond to Re = 9000, d_p = 94 μm, d_{p+}= 1.7.

On the other hand, plan views in the transitionally rough flows of Series ES1-T show no particle accumulation along wall streaks. According to Grass et al. (1991), however, wall streaks would continue to exist in the transitionally rough and rough flow regimes, although they would be much less conspicuous, less coherent, less persistent and would have a much lower vertical extension than in the smooth flows. It must be pointed out that Grass used hydrogen bubbles to visualize the wall streaks, which appear to be a better tracer in the case of flow over a rough surface than the fine glass beads used herein, which were observed to move within the interstices of the roughness

elements of the bed without sorting along any preferential path. Nevertheless, flow visualizations using coarser particles, which moved over the bed roughness elements, did not show tendency for any such sorting either (see Chapter 8).

Side view visualization in both Series ES1-S and ES2-T show the lifting-up of the low-speed streaks as a consequence of quasi-periodic ejections of low-momentum fluid away from the channel bed. In such instances, shear layers developed which correspond to inclined, thin filaments of concentrated spanwise vorticity, similar to those revealed by the analysis of data bases generated through Direct Numerical Simulations (e.g., Jimenez et al., 1988; Guezennec et al., 1989), and those observed experimentally using PIV (e.g., Liu et al., 1991; Urushihara et al., 1993). These shear layers were observed to be lifted from the bottom surface and then stretched out as they rose away from the bed into the outer regions of the wall layer. In some cases the tips of the structures were observed to roll over in the form of quasi-transverse vortices (with diameters of the order of the Taylor's micro length-scale) which may be related to the cross-section of hairpin vortices, while in some other cases streamwise coalescence of lifted low-speed streaks was apparent as in the conceptual model by Smith (1984), although these phenomena had a rather low frequency of occurrence.

Figs. 4.3 and 4.4 show examples of the type of structures observed in the flow visualization experiments of Series ES1-S and ES1-T, respectively. Therein typical shear layers are shown at different stages of development. In some cases a quasi-transverse vortex can be observed in the tip of the structure. Clearly Figs. 4.3 and 4.4 show no noticeable difference in the geometry and general characteristics of the shear layers observed in the smooth and transitionally rough flows, which seems to imply that the same mechanism of formation and development of these structures would be operating in both such cases.

Another type of structure observed much less frequently than the shear layers shown in Figs. 4.3 and 4.4 corresponds to some kind of inclined hairpin shape, like that shown in Fig. 4.5 corresponding to one experiment of Series ES1-T, which develops very similarly as the shear layers, extends about 85 wall units over the bed and displaces in the streamwise direction with a convection velocity of about 10.5 wall units. It is interesting to note that although the hairpin shape in Fig. 4.5 is very conspicuous, no rolling motion (which would be associated with a transverse vortex) is observed in the tip of the structure. The structure shown therein is very similar in shape and dimensions to that obtained by Kim (1987) through Direct Numerical Simulation of channel flow.

Digitized shapes of the shear layers observed in the experiments of Series ES1-S and ES1-T are plotted in dimensionless form using wall units in Figs. 4.6 and 4.7, respectively, for different values of the Reynolds numbers. These shear layers have been centered around a point located at an elevation of 50 wall units which gives the best collapse of the structures. Clearly, the shear layers

in the smooth and transitionally rough flows appear to be very similar, and their dimensionless shape seems to be invariant with the Reynolds number. A common average shear layer shape was estimated from the data corresponding to both such flows, and is also plotted in Figs. 4.6 and 4.7. The angle to the bed of this mean shape varies with the distance from the wall, however its average value is about 14°.

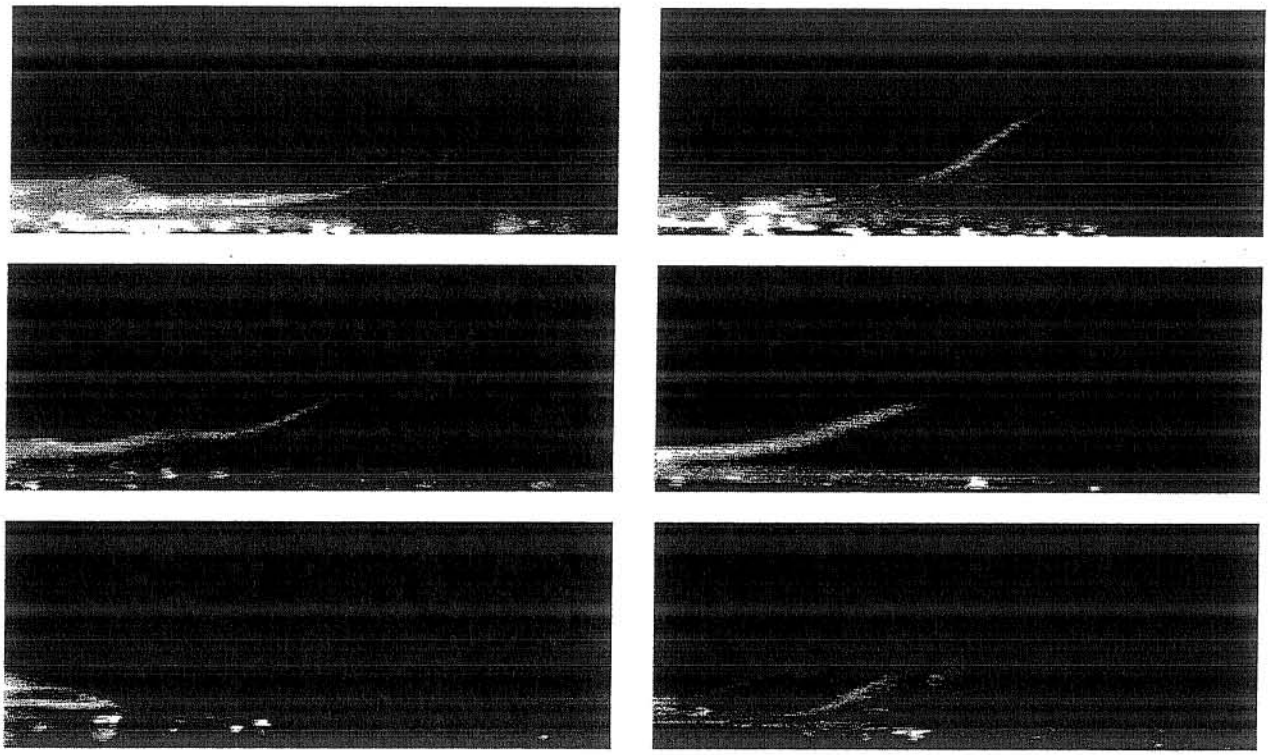

Fig. 4.3 Shear layers at different stages of development. Experiments of Series ES1-S, Re = 15750. Field of view of each image is about 328 by 125 wall units.

The frequency of occurrence of the shear layers was estimated by visual detection from the analysis of the acquired video images. Average values of the dimensionless frequency, f_{s+}, of about 0.003 and 0.001 wall units were obtained for the smooth flows and the transitionally rough flows, respectively, and they appear to be independent of the Reynolds number, at least within the present range of values of this variable.

The shear layers were observed to maintain their identity for a considerably long time span of the order of 60 to 80 wall time units, and it was similar in both the smooth and transitionally rough flows. The loss of coherence of the structure seems to occur through different mechanisms. Two different examples are shown in Fig. 4.8. One of them shows a shear layer undergoing an instability process in the form of a longitudinal oscillation of the stretched filament, similar to that obtained numerically by Jimenez et al. (1988) in their direct numerical simulations of channel flow. As the amplitude of the oscillation grows in time the shear layer eventually loses coherence and the tracer

finally diffuses into the turbulent flow and the marked structure disappears. The second example presented in Fig. 4.8 shows a shear layer evolving into a helical motion with longitudinal vorticity. The diameter of the longitudinal roll corresponds to about 45 wall units and has its centerline located at an elevation of about 40 wall units. In this case the shear layer is observed to lose coherence in a more dramatic way and to collapse into some kind of chaotic motion after the helical motion itself loses coherence.

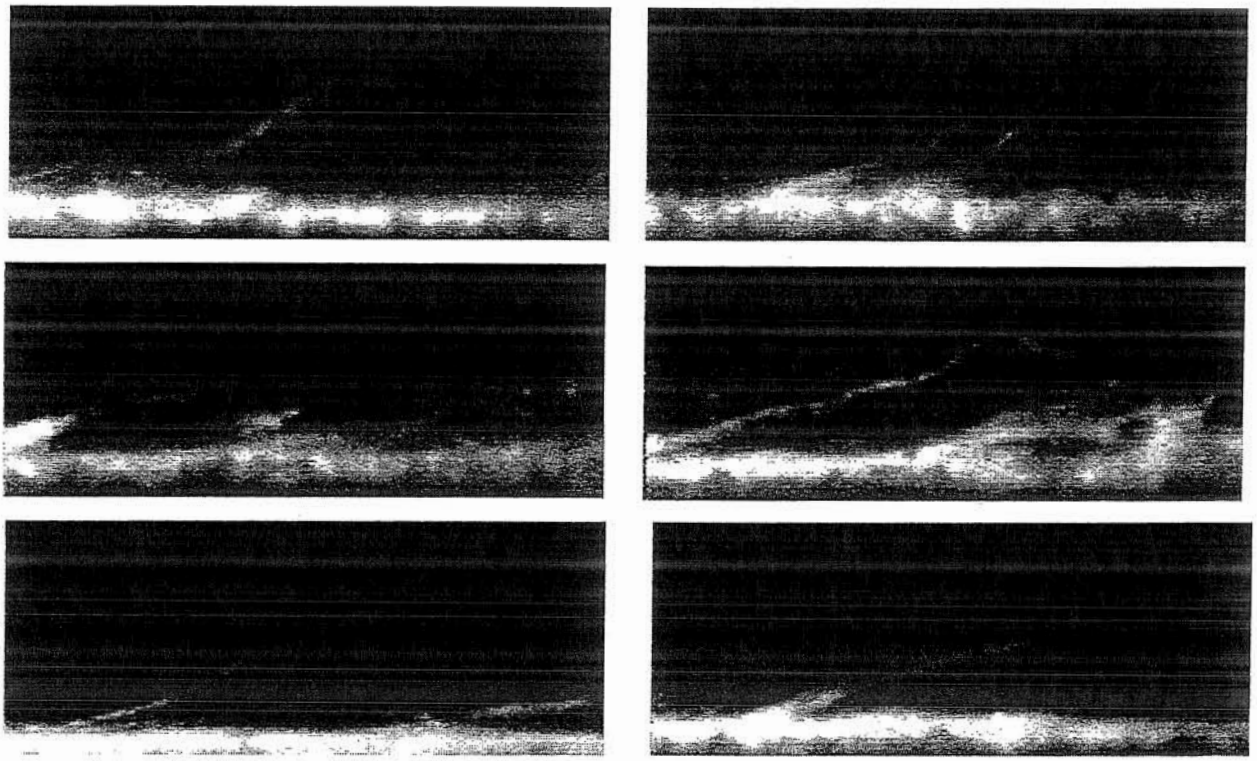

Fig. 4.4 Shear layers at different stages of development. Experiments of Series ES1-T, Re = 18840. Field of view of each image is about 380 by 149 wall units.

For different Reynolds numbers corresponding to experiments of Series ES1-S and ES1-T, mean values of the convective velocity of observed shear layers were estimated from the analysis of the video recordings, by tracking the structures along consecutive frames. The structures were tracked with respect to a reference point located on the structure at a certain location y_{R+} over the bed. The values of y_{R+} used herein correspond to those given by the location of the velocity probe at a distance of 2 mm above the bed, which yields values of y_{R+} in the range 38 to 64. The results obtained in terms of the dimensionless convection velocity, u_{c+}, made dimensionless with wall units, are presented in Fig. 4.9 plotted as a function of the Reynolds number. Therein estimations of the standard deviation of the convection velocity are also shown. The mean convection velocity results presented in Fig. 4.9 but this time expressed in dimensionless terms using the cross-sectional mean velocity, U, and the local mean velocity u, are plotted in Figs. 4.10 and 4.11, respectively. In

the latter case, the values of u utilized correspond to those given by the corresponding smooth or transitionally rough logarithmic velocity profile (see Chapter 3), evaluated at the position y_{R+}.

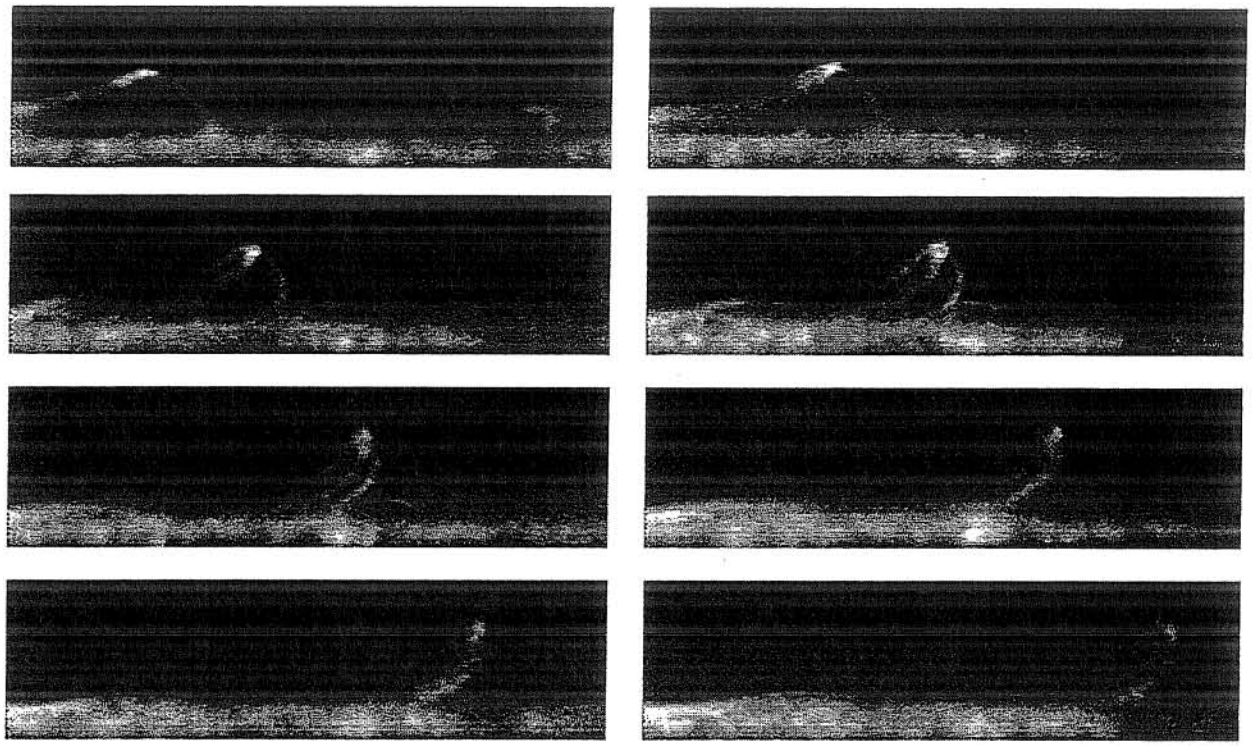

Fig. 4.5 Sequence of development and evolution of hairpin-shaped structure. Experiments of Series ES1-T, Re = 18840. Field of view of each image is about 410 by 110 wall units, and the time interval between images is 0.004 s.

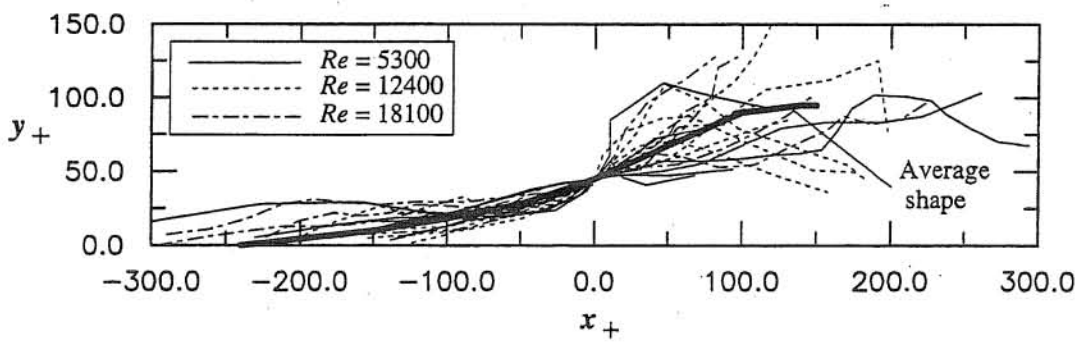

Fig. 4.6 Dimensionless shape of shear layers. Experiments of Series ES1-S.

4.4.2 Series ES2

For each Reynolds number several shear layers were followed, while keeping track of the associated probe signals. An example of the video images and corresponding data obtained by applying the synchronized technique reported herein is shown in Fig. 4.12, where flow direction is from left to right. Fig. 4.12a shows a partial sequence of three images of a shear layer, Re = 5300, being convected in the downstream direction while lifted up, away from the bed of the channel. The

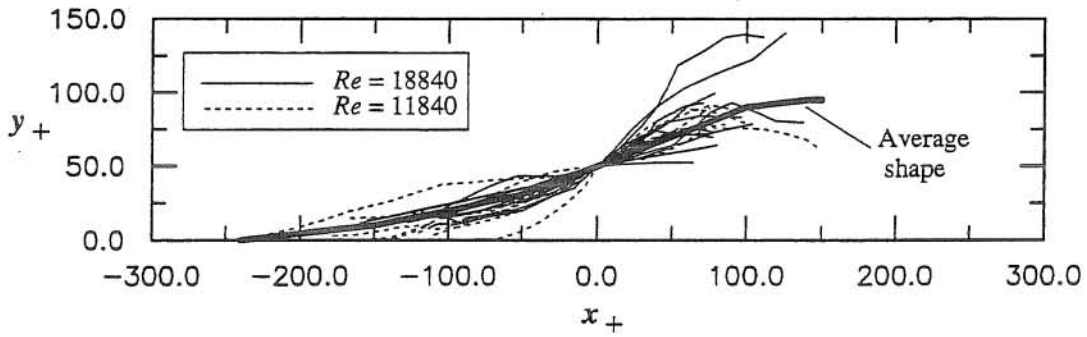

Fig. 4.7 Dimensionless shape of shear layers. Experiments of Series ES1-T.

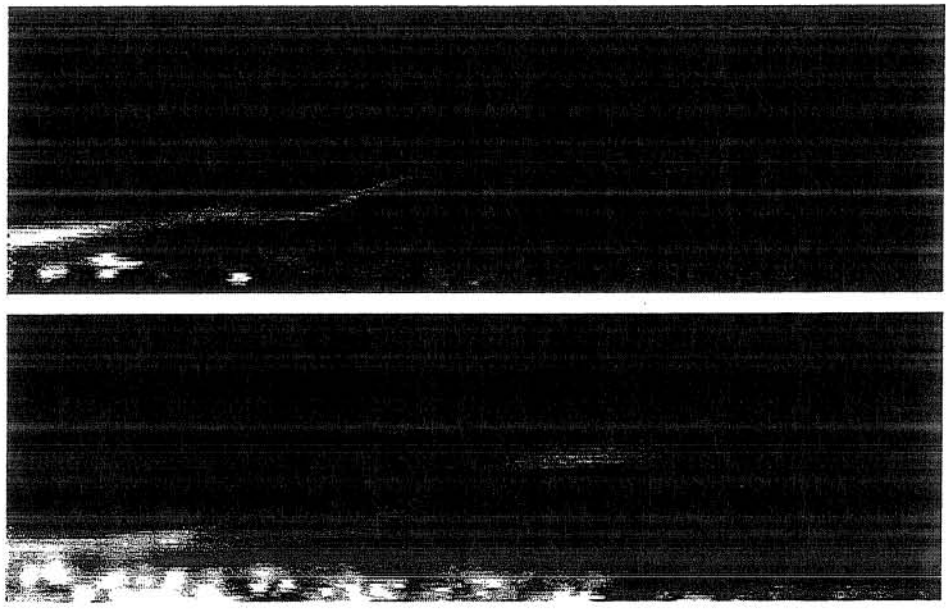

Fig. 4.8 Shear layers at late stages of evolution. Upper image shows a developing instability, lower image shows a developing helical motion. Experiments of Series ES1-S, $Re = 15750$. Field of view of each image is about 400 by 125 wall units.

images shown are 0.04 s apart, and for the same time span the complete series had a total of 40 frames. The velocity probe (marked as P1) can be easily seen at the right end of each image, on the other hand, the bed shear stress probe can not be distinguished, but its location has been marked as P2 in the upper frame. Fig. 4.12b shows the corresponding digitized shapes of the structure as it develops in time and space. The spatial dimensions are given in wall units, x_+ and y_+, with the velocity sensor located at $(x_+, y_+) = (417, 38)$ and the bed shear stress sensor at $(x_+, y_+) = (258, 0)$. Values of velocity and bed shear stress fluctuations (u', τ'), measured during the passage of the organized structure, made dimensionless with their corresponding standard deviations (u_{rms}, τ_{rms}), and plotted as a function of t_+, are also shown. In order to relate temporal and spatial scales, i.e. t_+ and x_+, Taylor's frozen turbulence hypothesis was assumed using the mean convective velocity

of the structure. Since the zeros of both scales coincide, the value of each signal at time t_+ corresponds to what the respective sensor detected when the structure was traveling at an upstream dimensionless streamwise distance equal to $417-x_+$, and $258-x_+$ from the velocity and bed shear stress sensors, respectively.

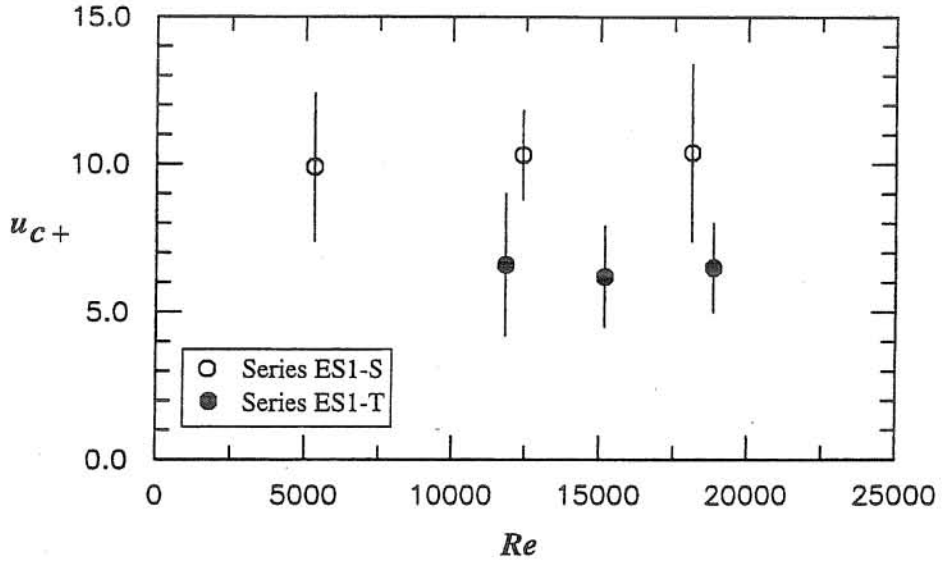

Fig. 4.9 Convective velocity of shear layers made dimensionless with wall units. Symbols represent mean values and vertical lines represent a total length of two standard deviations.

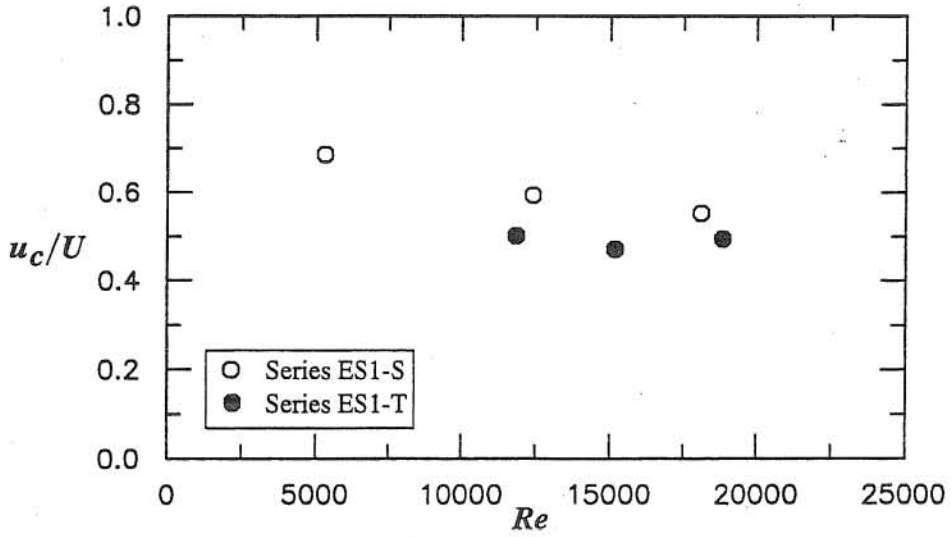

Fig. 4.10 Convective velocity of shear layers made dimensionless with cross-sectional mean velocity.

Through the analysis of several events similar to those shown in Fig. 4.12, conditional ensemble averaged values of dimensionless velocity fluctuations during the passage of the structures were computed for each Reynolds number. The results corresponding to the lowest and highest Reynolds number reported herein are shown in Figs. 4.13 and 4.14, where angular brackets denote

conditional averages computed over detected events. Upper and lower bounds of the conditionally sampled velocity signals are also shown, as well as some observed shear layer shapes. Again, temporal, local data were converted into spatial information by assuming Taylor's frozen turbulence hypothesis and using measured mean convective velocities of each structure.

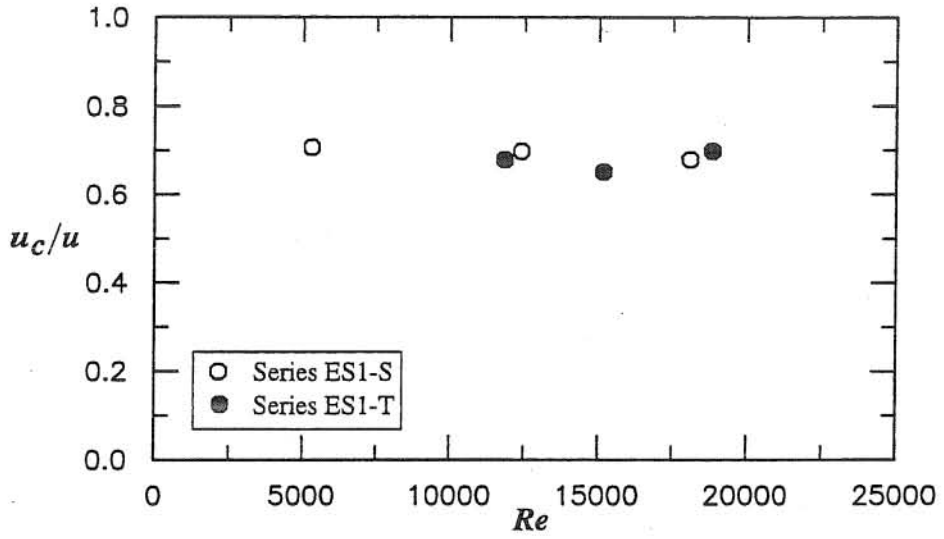

Fig. 4.11 Convective velocity of shear layers made dimensionless with local mean velocity.

From results of the conditional ensemble averages of dimensionless velocity fluctuations, the associated organized velocity structure could be inferred. Fig. 4.15 shows the average shear layer, presented in Figs. 4.6 and 4.7, plotted in dimensionless variables together with the ensemble averaged velocity distribution for the whole set of three Reynolds numbers, computed from series taken at four different distances from the bed, namely y_+= 38, 52, 64 and 80 (or y/h = 0.10, 0.07, 0.06 and 0.22, respectively). Black circles are intended to show the position of the minimum of the dimensionless velocity profile at each distance from the bed, whereas the line passing through them is a best fit regression, which shows the angle of inclination of the location of those minima. In Fig. 4.15, invariance of the velocity profiles with respect to Reynolds number when made dimensionless using the local value of u_{rms+} is assumed.

The absolute value of the minimum of each ensemble averaged velocity distribution of Fig. 4.15 is plotted as a function of y_+ in Fig. 4.16, made dimensionless with the standard deviation of each series, where vertical bars denote absolute value. Likewise, the same minima are plotted as a function of y_+ in Fig. 4.17, this time made dimensionless with the shear velocity. For comparison purposes, the vertical distribution of the dimensionless standard deviation u_{rms+} in the wall region is also shown in Fig. 4.17, estimated from a best fit of a model proposed by Nezu and Nakagawa (1993) to turbulence measurements made in the present flows, which is given by:

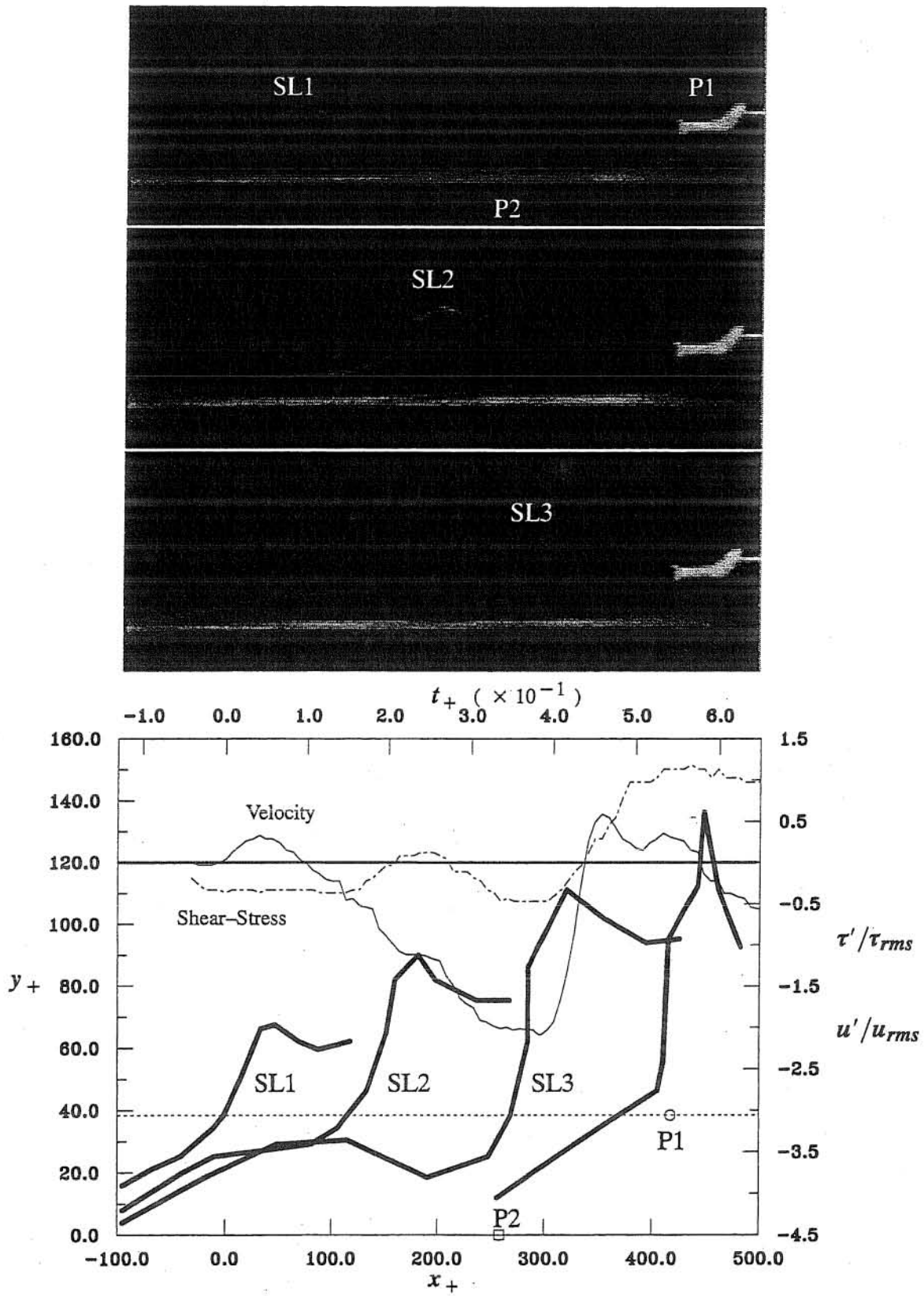

Fig. 4.12 (a) Video images of shear layers; (b) Digitized images and associated velocity and bed shear stress data. Experiments of Series ES2. Re = 5300.

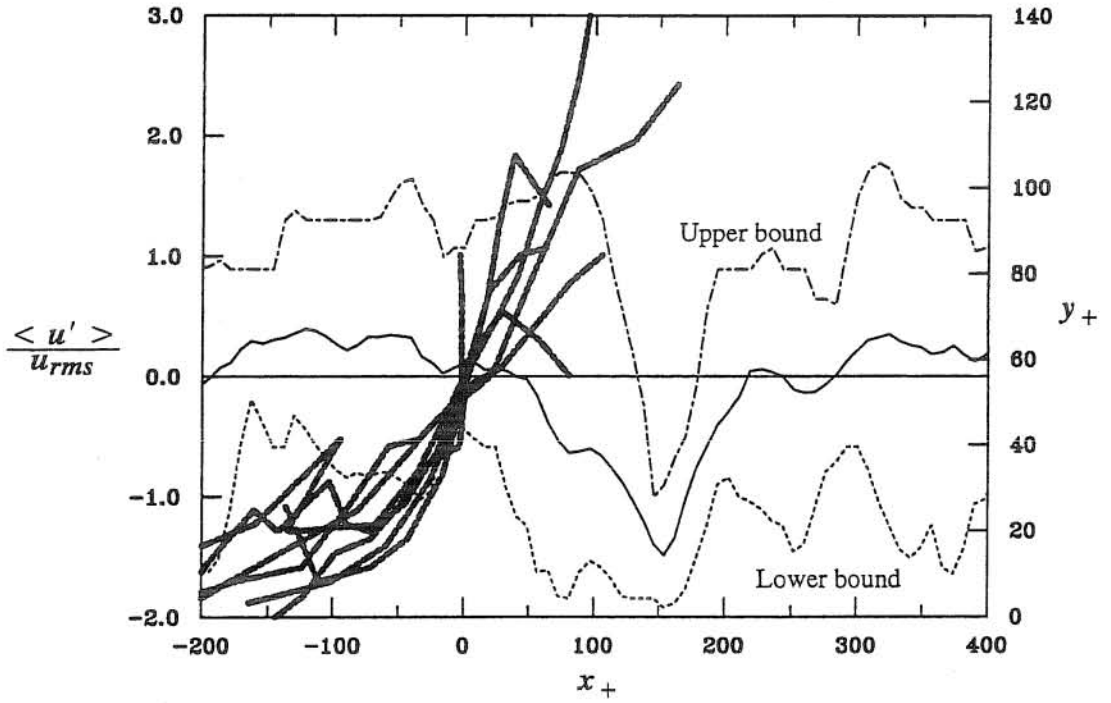

Fig. 4.13 Ensemble averages of velocity fluctuations and shape of coherent structures. Experiments of Series ES2, Re = 5300.

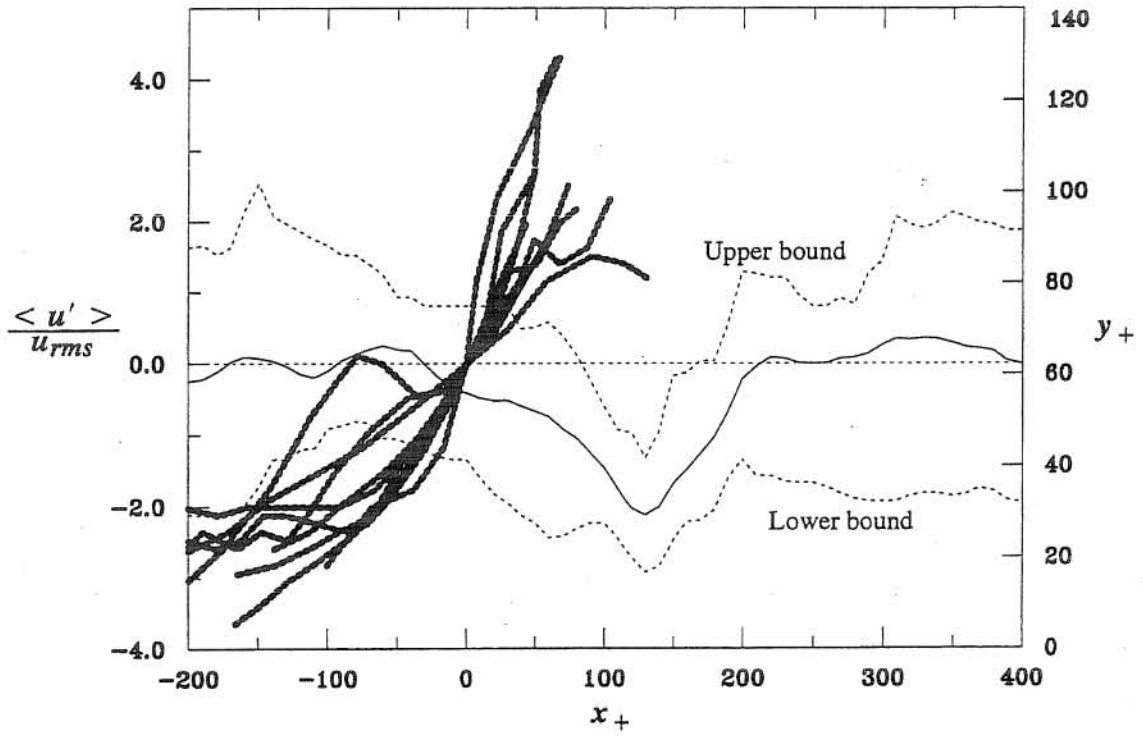

Fig. 4.14 Ensemble averages of velocity fluctuations and shape of coherent structures. Experiments of Series ES2, Re = 18100.

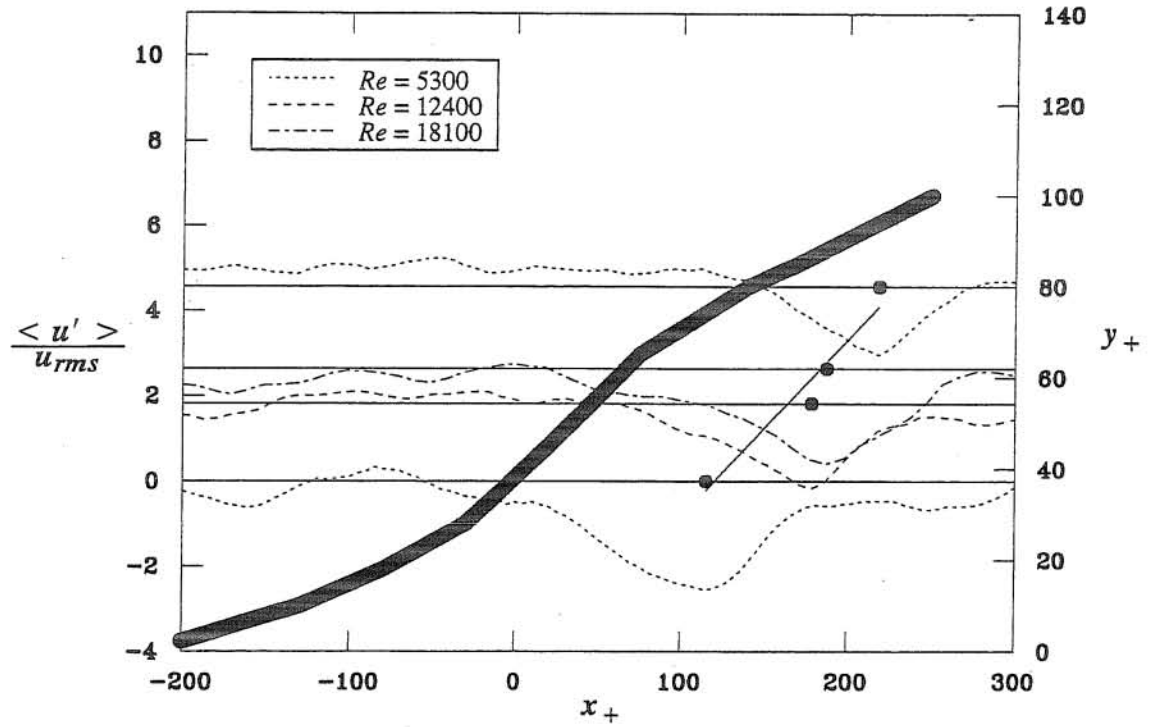

Fig. 4.15 Conditional ensemble averages of streamwise velocity fluctuations.
● indicates location of minima of ensemble averaged profile.

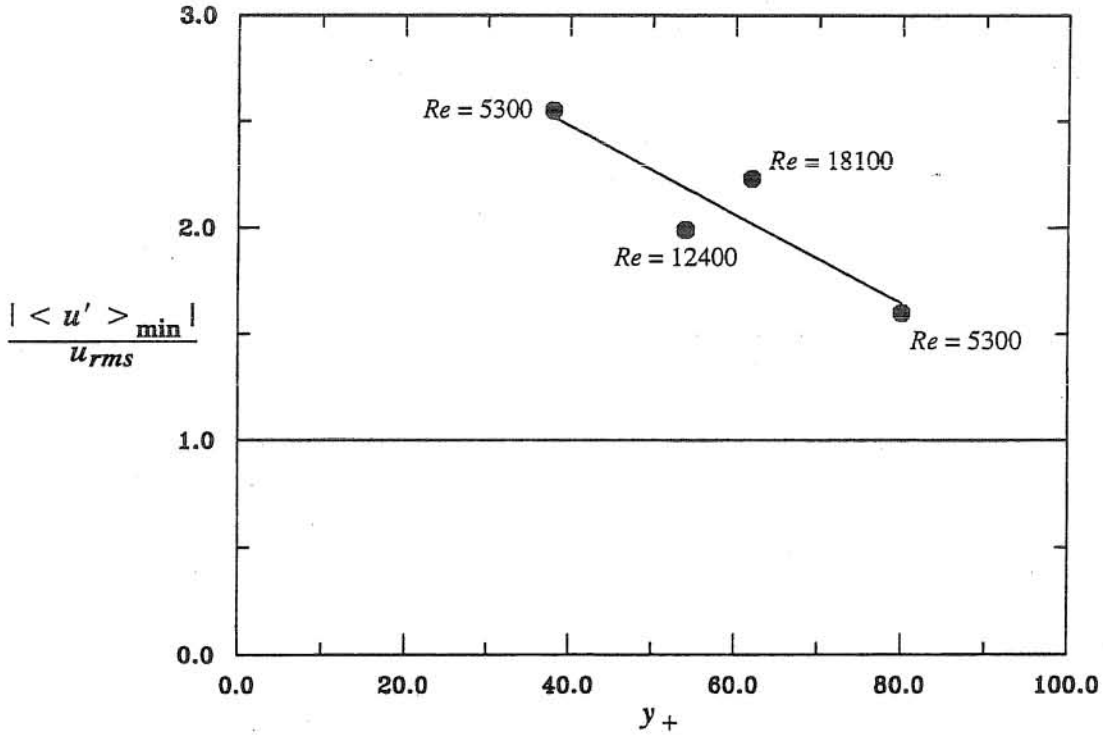

Fig. 4.16 Variation of dimensionless minima of ensemble averaged velocity distributions scaled using u_{rms}.

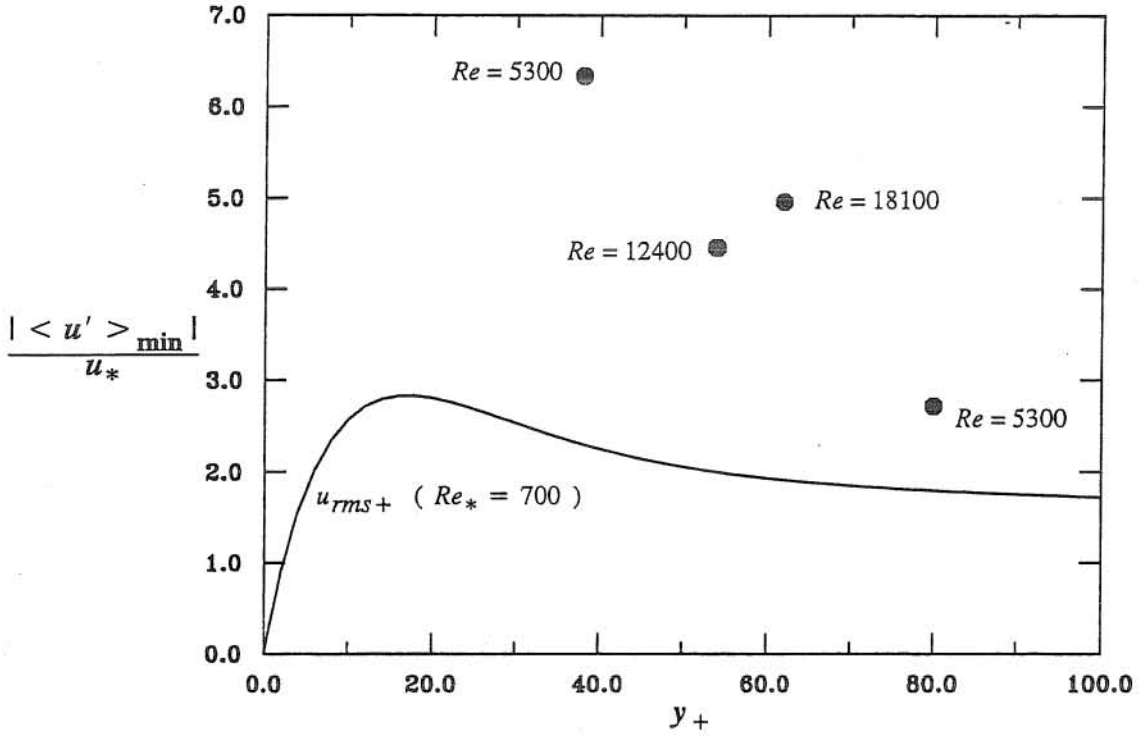

Fig. 4.17 Variation of dimensionless minima of ensemble averaged velocity distributions scaled using u_*.

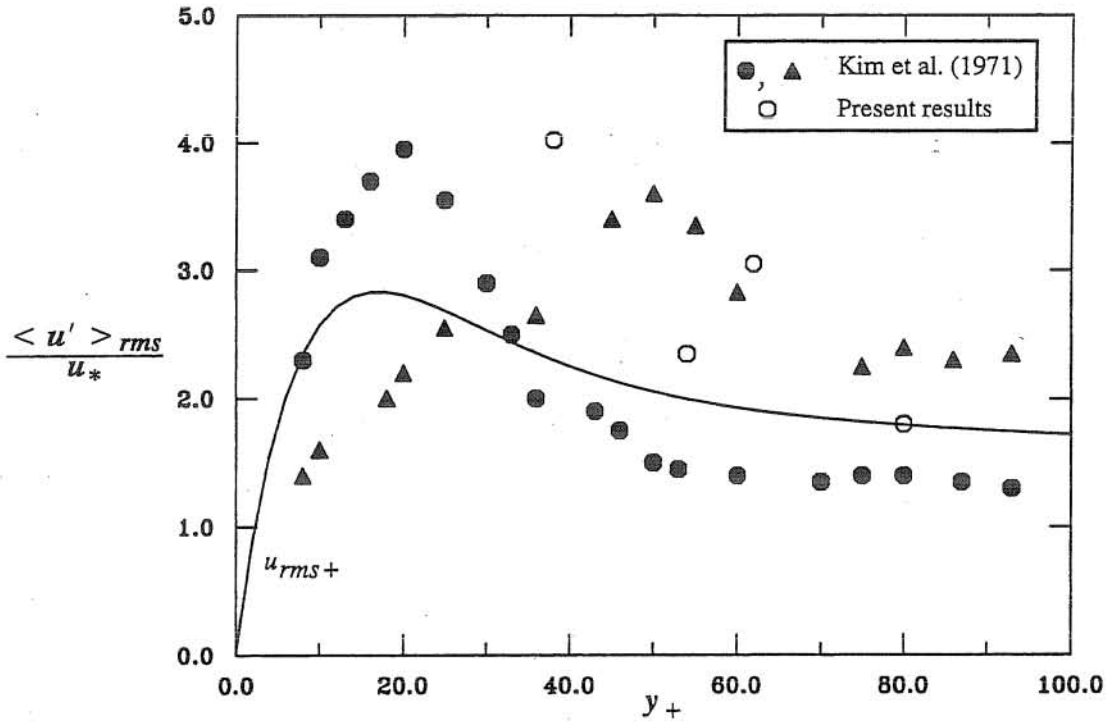

Fig. 4.18 Variation of conditional root-mean-squared values of the streamwise velocity fluctuations in the wall region.

$$u_{rms+} = 2.00 \exp\left(-1.08 \frac{y_+}{Re_*}\right)\left(1 - \exp\left(-\frac{y_+}{11.6}\right)\right) + 0.34\, y_+ \exp\left(-\frac{y_+}{11.6}\right) \qquad (4.2)$$

A value of $Re_* = 700$ was used to evaluate (4.2) in Fig. 4.17, which is representative of the range of values of this parameter for the experimental conditions of Series ES2.

The basis for some pattern detection algorithms, such as the VITA algorithm, is the presence of localized high values of turbulent energy represented by the variance of the streamwise velocity fluctuations. To check the existence of high local values of turbulent energy, dimensionless conditional root-mean-square values of the streamwise velocity fluctuations, $< u' >_{rms+}$, were computed from the conditionally averaged velocity distributions shown in Fig. 4.15. The results obtained are presented in Fig. 4.18, together with the values of u_{rms+} given by (4.2) using a value $Re_* = 700$, as well as with similar results reported by Kim et al. (1971).

In order to delineate a picture of the flow pattern, interpolated surface and contour plots of the associated streamwise velocity field were computed from the obtained information, and are shown in Figs. 4.19 and 4.20, respectively. Dashed lines below $y_+ = 38$ in Fig. 4.20 represent only an estimated extrapolation of the measured field based upon results of cross-correlations between velocity and bed shear stress signals presented in the following section. Likewise, the thick line in that figure represents the average shear layer as shown in Figs. 4.6 and 4.7.

4.4.3 Series ES3

As an example of the results of the cross-correlation computations between bed shear stress and velocity signals obtained from the analysis of the data set ES3, Fig. 4.21 illustrates the variation of the cross-correlation coefficient estimated using (4.1) with time-lag in wall units, for $Re = 12400$ and a separation of $(\Delta x, \Delta y) = (10 \text{ mm}, 2.5 \text{ mm})$, or $(\Delta x_+, \Delta y_+) = (198.4, 49.6)$. This figure was selected because the relative location of both sensors define a line at an angle of approximately 14° to the channel bed, i.e. similar to the mean inclination of the observed structures. For this relative location of the two sensors, the maximum value of the cross-correlation coefficient, $(R_{u\tau})_{max}$, reaches a peak as is shown in Fig. 4.22a, in which the variation of $(R_{u\tau})_{max}$ with $\alpha = tan^{-1}(\Delta y/\Delta x)$ is plotted. On the other hand, the variation of the time lag Δt corresponding to $(R_{u\tau})_{max}$ for each relative angle α is shown in Fig. 4.22b.

4.5 Analysis

4.5.1 Series ES1

Results of the digitized shear layers for different Reynolds numbers and roughness conditions shown in Figs. 4.6 and 4.7 clearly indicates a collapse of the geometry of the structures when plotted in wall units, with an almost constant mean inclination angle to the bed of the channel of 14°. The averaged shape of the structures shows a mild S-shaped profile, with a length of about 400 wall units

in the streamwise direction and extending vertically to elevations close to the limit of the wall region ($y_+ \approx 100$).

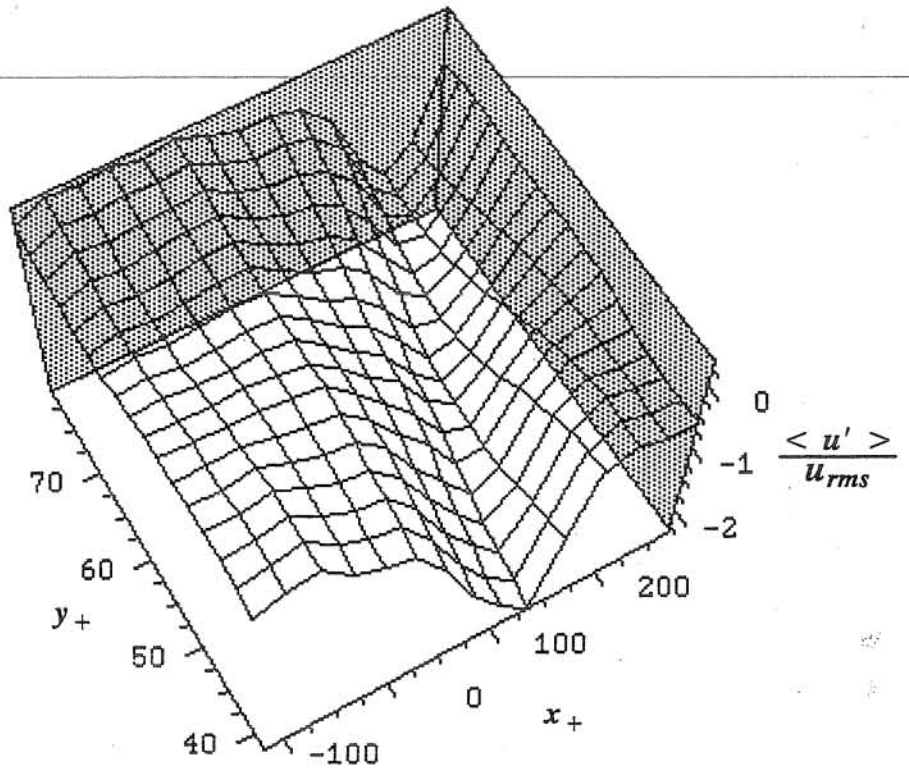

Fig. 4.19 Surface plot of conditional ensemble averaged streamwise velocity fluctuations.

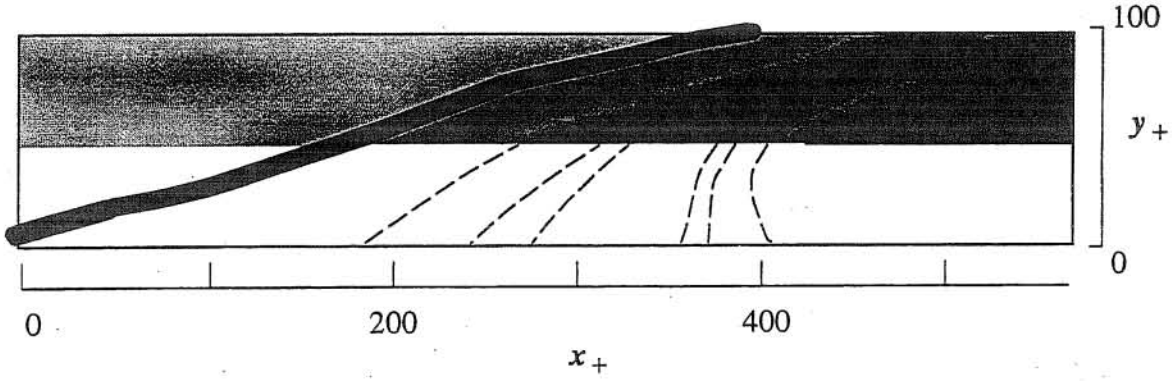

Fig. 4.20 Contour plot of conditional ensemble averaged streamwise velocity fluctuations.

These results, which correspond to open channel water flows, agree well with reported results of experiments conducted with different fluids and types of flows. For example, Liu et al. (1991) applied PIV to analyze turbulent water flow in a channel (Reynolds number of 2872, based on the half height and average fluid velocity) finding that the near-wall shear layers extend up to a distance

of 100 wall units from the bed and are inclined at an angle of less than 45°, with streamwise dimensions similar to the ones reported herein. On the other hand, Urushihara et al.'s (1993) computations of transverse vorticity from PIV data (air pipe flow at Reynolds number based on pipe diameter of 51000), show regions of high values of localized shear stress close to the wall inclined at angles between 15° and 30°.

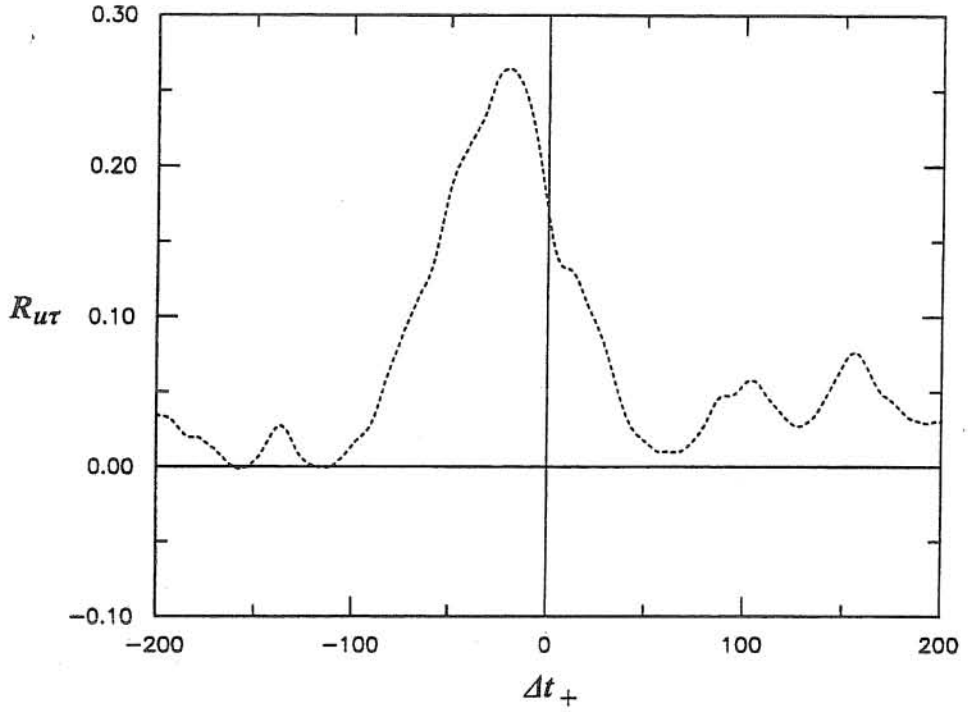

Fig. 4.21 Cross-correlation between streamwise velocity and bed shear stress fluctuations. Experiment of Series ES3, Re = 12400, Δx = 10 mm, Δy = 2.5 mm, α = 14°.

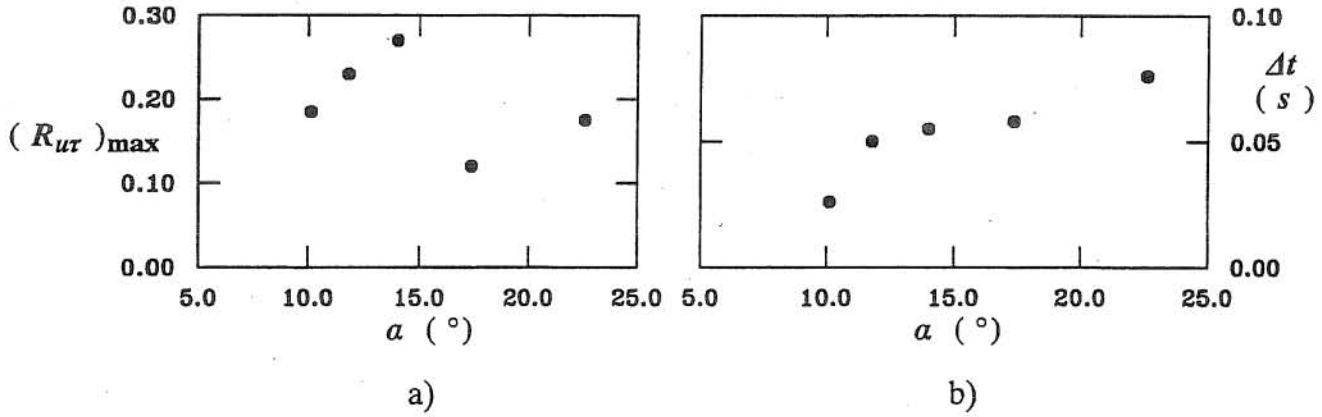

Fig. 4.22 a) Variation of cross-correlation peak with angle between sensors. b) Variation of time lag with angle between sensors. Experiments of Series ES3.

It is remarkable that the mean dimensionless shape of the shear layers is virtually the same for both smooth and transitionally rough flows, which seems to imply that the same mechanism of formation of these structures would be operating in both cases. This is in partial agreement with

observations by Grass (1971) who conclude that although flow ejections observed in smooth flows persist in transitionally rough and rough flows, with similar characteristics but with somewhat higher intensity for increasing roughness, different dominant modes of instability would prevail for different boundary roughness conditions. Bessen and Stevens (1984), based on their measurements of cross-correlations of bed shear stress and velocity fluctuations in a rough flow (similarly to those performed in Series ES3 herein), found the existence of structures with an inclination angle to the bed of about 16° which, they point out, is very similar to the angle of inclination of the structures found by Brown and Thomas (1977) using an analogous procedure. Bessen and Stevens conclude that the same type of structures would exist in both smooth and rough flows, which is in total agreement with the present results.

The frequency of the visually detected shear layers can be compared with those obtained through the VITA analysis of measured near bed streamwise velocity fluctuations of Chapter 3. A first interesting result obtained from such VITA analysis is that, in general, sweeps seem to be more frequent than ejections in both smooth and transitionally rough flows. Andreopoulos and Bradshaw (1981) and Raupach (1981) obtained the same conclusion from their analysis of rough flat plate boundary layer flows. Also the VITA analysis seem to indicate that the frequency of sweeps or ejections in the smooth flows tend to be larger than the frequency of those events in the transitionally rough flows, which is in agreement with the results obtained herein from the visual detection analysis, at least at a qualitative level. Quantitatively however, the VITA analysis gave values of the dimensionless frequency, f_{s+}, of ejections of about 0.0008 wall units in the smooth flows, and of about 0.0005 wall units in the transitionally rough flows. In the case of the smooth flows, these values are about 4 times smaller than the results obtained through the visual detection, while in the case of the transitionally rough flows they are about 2 times smaller. These results seem to indicate that the VITA algorithm is not very accurate in the detection of flow ejections. However, it is necessary to indicate that this algorithm requires the adjustment of two parameters, the threshold level of detection, k_v, and the averaging time, τ_v, (Blackwelder and Kaplan, 1976; see also Chapter 3). In Chapter 3 a method was developed to adjust τ_v, although a constant value $k_v = 1$ was used throughout the analysis. Obviously, decreasing the value of k_v would result in increasing the frequency of detected events, which implies that the resulting frequencies detected by the VITA algorithm in Chapter 3 do not necessarily have to agree with those detected visually herein, and which gives the VITA algorithm a rather subjective character. This, however, is common to most of the existing criteria for detecting organized, coherent structure in turbulent flows (Wallace et al.,1977).

Nevertheless, both the VITA algorithm and the visual detection criterion give larger values of f_{s+} in smooth flows than in transitionally rough flows. This, however, contradicts results by

Krogstad et al. (1992) who found the opposite to be true in their analysis of rough flat plate boundary layer flow in a wind tunnel, where the roughness was created by attaching a mesh screen to the plate. On the other hand, Hetsroni (1991) based on the experimental results of Rashidi et al. (1990) conclude that the presence of loose particles in the wall region of a channel flow can increase or decrease the frequency of flow ejections, depending on the size of the particles. Particles of sizes larger than the thickness of the viscous sublayer tend to increase the number of flow ejections, which Hetsroni explains as a distabilizing effect, such that the interaction of the particles with lifted vortex filaments would cause their premature detachment from the bed. Smaller particles tend to decrease the number of flow ejections, which would be related with a stabilizing effect that might be associated with extra dissipation of turbulent energy. It is possible that a stabilizing mechanism similar to that operating in the case of smaller particles causes the reduction of the frequency of ejections in the present transitionally rough flows. It is also plausible that in the case of fully rough flows this effect is reversed and an increase in the number of ejections with respect to that in a smooth flow would occur.

As seen in Fig. 4.9, the mean convective velocity of the observed structures appears to be rather invariant with the Reynolds number when made dimensionless in wall units, in both the smooth and transitionally rough flows, at least for the present range of values of this variable. The values of u_{c+} for the smooth flows of Series ES1-S are close to about 10.0, about 1.5 times larger than those observed in the transitionally rough flows of Series ES1-T, which are close to about 6.5. When the convective velocity of the flow structures is made dimensionless with the cross-sectional mean velocity, the results corresponding to the smooth flows appear to decrease with increasing Reynolds numbers, with values of u_c/U in the range 0.7 to 0.55. On the other hand, the results corresponding to the transitionally rough flows seem to be independent of Re, and to have values of u_c/U of about 0.5, smaller than those of the smooth flows (Fig. 4.10). Finally, when the observed convective velocities are made dimensionless with the local mean flow velocity, a good collapse is obtained for the results in both the smooth and transitionally rough flows, with values of u_c/u of about 0.7, independent of Re (Fig. 4.11). This results suggest that although an inner scaling (using wall variables) for u_c seems to be more appropriate than an outer scaling (using U) for the smooth flows, since independence of Re appear to be more evident in the former case than in the latter, this is not so clear for the transitionally rough flows, for which either scaling appears to give independence of Re, at least for the present range of values of this variable. Nevertheless, the better scaling appears to be given by the local variable u, for which independence of the roughness condition of the boundary and Re is obtained simultaneously. This result explain the reduction on u_{c+} in the transitionally rough flows with respect to that in the smooth flows, simply as a retardation of the

coherent structure of the flow induced by the presence of roughness elements, which is directly correlated to that experienced by the mean flow.

The present results also agree with results by Head and Bandyopadhyay (1981), who also observed the downstream traveling of hairpin vortices at almost constant uniform velocities, and with results from direct numerical simulations of turbulent flows in a smooth channel made by Guezennec et al. (1989). Using the quadrant technique (Wallace et al., 1972) to analyze the numerically generated data base, Guezennec et al. showed that second (as well as fourth) quadrant events propagate in the streamwise direction at an average speed close to 10 wall units, and maintain their identity for as long as 40-60 viscous time units. This persistence in time while maintaining an almost constant shape seems to indicate that the observed events do not generally go through a violent and rapid breakup, which is in agreement with the present observations. As already discussed, although the shear layers usually become unstable as seen in Fig. 4.8, this does not always lead to a catastrophic breakup of the structure, and they rather lose coherence through a process more related to turbulent diffusion (see also Guezennec et al., 1989).

By using the computed dimensionless frequency of occurrence, f_{s+}, and the mean life-time of the observed structures, t_{s+}, the average fraction of time, T_s, during which coherent patterns were observable can be estimated as:

$$T_s = f_+ \; t_{s+} \tag{4.3}$$

giving an average value of about 20% in the case of smooth flows of Series ES1-S and about 10% in the case of the transitionally rough flows of Series ES1-T. It is interesting to note, that because the dimensionless values in wall units of both frequency and life-time of the structures showed to be almost invariant with Reynolds number, our results indicate that the percent of the total time where structures were observable becomes also approximately constant and independent of Reynolds number. This latter result differs with values reported by others. For example Corino and Brodkey (1969) found that ejections disturbed the flow on a variable percentage of the total time between about 18% and 70% for Reynolds numbers varying from nearly 2×10^4 to 6×10^4.

4.5.2 Series ES2

Ensemble averaged distributions of streamwise velocity fluctuations associated with the occurrence of coherent events resulting from lifting up of low-speed streaks clearly show the existence of an organized pattern, with a minimum of the streamwise velocity downstream and at varying distances from the structures depending upon the distance from the bed. Coherence in the associated velocity field could not only be distinguished in the ensemble averaged profiles, but also in the lower and upper bounds (Figs. 4.13 and 4.14), which show the small variation in shape and in the location of the minimum for each of the individual profiles. The characteristics of the

associated dimensionless flow field indicate an invariance with Reynolds number in the range of the reported experiments. The existence of the detected minima implies an organized contribution to the Reynolds stress in the second quadrant, since vertical flow ejections correlate with streamwise velocity deficits. In fact, it has been found experimentally that almost every contribution (90%) in the second quadrant of magnitude $k \mid \overline{u'v'} \mid$ with $k \geq 2$ is caused by a low-speed streak (Talmon et al., 1986). PIV results also show neighboring regions of the near-wall shear layers as strong contributors to the Reynolds stresses (Liu et al., 1991).

It is interesting to note also that the ensemble averaged distributions of streamwise velocity fluctuations associated with the shear layers obtained herein coincide totally with the ensemble averaged velocity time series during ejection events detected by the VITA algorithm reported in Chapter 3. Given the strong similarity of the dimensionless ensemble averaged velocity distributions corresponding to the smooth and transitionally rough flows obtained in Chapter 3, it can be concluded that the analysis presented herein for smooth flows would be completely analogous in the case of the transitionally rough flows.

The minima of each of the ensemble averaged profiles shown in Figs. 4.13 and 4.14 is located on a line with an inclination to the bed similar to the observed angle of the coherent structures. On the other hand the absolute value of the dimensionless minimum ensemble averaged fluctuations decreases with increasing distance from the bed (Figs. 4.16 and 4.17), as does the streamwise extent where the coherent pattern is observable (Fig. 4.15). For $y_+ = 38$ coherence in streamwise velocity fluctuations is observed up to a downstream distance of 250-300 wall units from the structure, whereas for the largest distance from the bed, $y_+ = 80$, the organized motion is distinguishable only in a region of about 100 wall units downstream. This variation of the streamwise dimension (time span) of the coherent flow field with distance from the bed may serve as a basis for the selection of the time-of-averaging parameter in several pattern-detection algorithms based on localized high values of turbulent energy.

In order to check the validity of the definition of *coherent structures* given in the introduction, obtained dimensions of coherent patterns should be compared to characteristic turbulent length scales of the flow. According to Nezu and Nakagawa (1993) (see Chapter 3) the following expressions represent the vertical variation of the macro-length scale, L_x, and the Taylor micro-scale, λ, in the outer region of turbulent open channel flows:

$$\frac{L_x}{h} = \begin{cases} \left(\frac{y}{h}\right)^{1/2} & y/h \leq 0.6 \\ 0.775 & y/h \geq 0.6 \end{cases} \tag{4.4}$$

$$\frac{\lambda}{h} = \left(\frac{15}{2.3\ K\ Re_*}\right)^{1/2} \left(\frac{y}{h}\right)^{1/4} \exp\left(\frac{y}{2h}\right) \tag{4.5}$$

where $K = 0.647$, as estimated in Chapter 3. In Table 4.2 the dimensionless values of L_x and λ estimated using (4.4) and (4.5) are compared to the approximate streamwise dimensions of the observed organized patterns. As seen therein, the ensemble averaged profiles reveal the existence of coherence in scales well above the Taylor micro-length scale and of the order of the macro-length scale of the turbulent motion. Since this latter scale is associated with the average size of the energy containing eddies, it follows that the observed structures are a plausible mechanism by which energy is extracted from the mean flow and transferred to the turbulent fluctuations, thus maintaining the turbulent state against the dissipative action of viscosity.

Table 4.2 Turbulent length scales and dimensions of detected organized patterns

Re	$y+$	L_{x+}	λ_+	Δx_+
5300	38	118	36	250
12400	52	193	46	250
18100	64	249	52	220
5300	80	172	46	150

Fig. 4.16 shows that the absolute value of the minima of each ensemble averaged profile of u', made dimensionless with u_*, tend to the long-term averaged value of the relative turbulence intensity as the edge of the wall region is approached. On the other hand, dimensionless conditional root-mean-square computations of the ensemble averaged profiles of u', i.e. estimates of localized turbulent kinetic energy, show values ranging from 4.0 to 1.8 wall units for $y_+ = 38$ and 80 respectively, which are in agreement with values reported by others using different techniques, e.g., Kim et al., 1971 (Fig. 4.17). Those estimates tend to the long-term averaged values of streamwise velocity intensities as the border of the wall region is approached. This latter fact indicates, as others have already found (e.g., Kim et al., 1971), that the turbulent bursting seems to directly affect the structure of turbulence up to a distance from the wall of about 100 wall units, i.e. the so-called wall region.

Assuming that the detected structures, associated with large scales of turbulence, would pass the extracted energy from the mean flow down the cascade towards smaller eddies while losing their coherence, an estimate of the internal energy transfer rate from large to small scales can be obtained by dividing the computed localized value of turbulent energy $< u' >^2_{rms}$ by the mean observed life-time of the structures, t_s. Since in open channel flows for $y/h \lesssim 0.60$ the production of turbulent energy, P, becomes nearly equal to its dissipation, ε, (the turbulent diffusion term is approximately balanced by pressure diffusion, Nezu and Nakagawa, 1993) then P can be estimated as:

$$P = \varepsilon \approx \frac{< u' >^2_{rms}}{t_s} \tag{4.6}$$

The values of ε estimated using (4.6) and made dimensionless with u_* and h are plotted in Fig. 4.23 for the four different values of y/h reported herein, together with the following expression proposed by Nezu (1977):

$$\frac{\varepsilon\, h}{u_*^3} = E \left(\frac{y}{h} \right)^{-1/2} \exp \left(-3 \frac{y}{h} \right) \tag{4.7}$$

where E is a parameter assumed constant for Reynolds numbers between 10^4 and 10^5, with a value of about 9.8. As seen therein, the temporal-localized values of the dissipation evaluated from (4.6) are much higher than the predictions of (4.7). However, if the mean period of occurrence of the structures, t_s/T_s, is used instead of their life-time for averaging the localized energy, smaller values of ε are obtained as shown in Fig. 4.23, which fall closer to the estimates of (4.7). The observed agreement strongly suggests that the detected structures are indeed not only related to the mechanism that transfers mean flow energy to turbulent fluctuations, but that they lose coherence while transferring energy to smaller turbulent scales, where dissipation takes place. The intermittent nature of production and dissipation becomes also evident, where almost all the turbulent energy generation seems to take place, in average, in about 20% of the time.

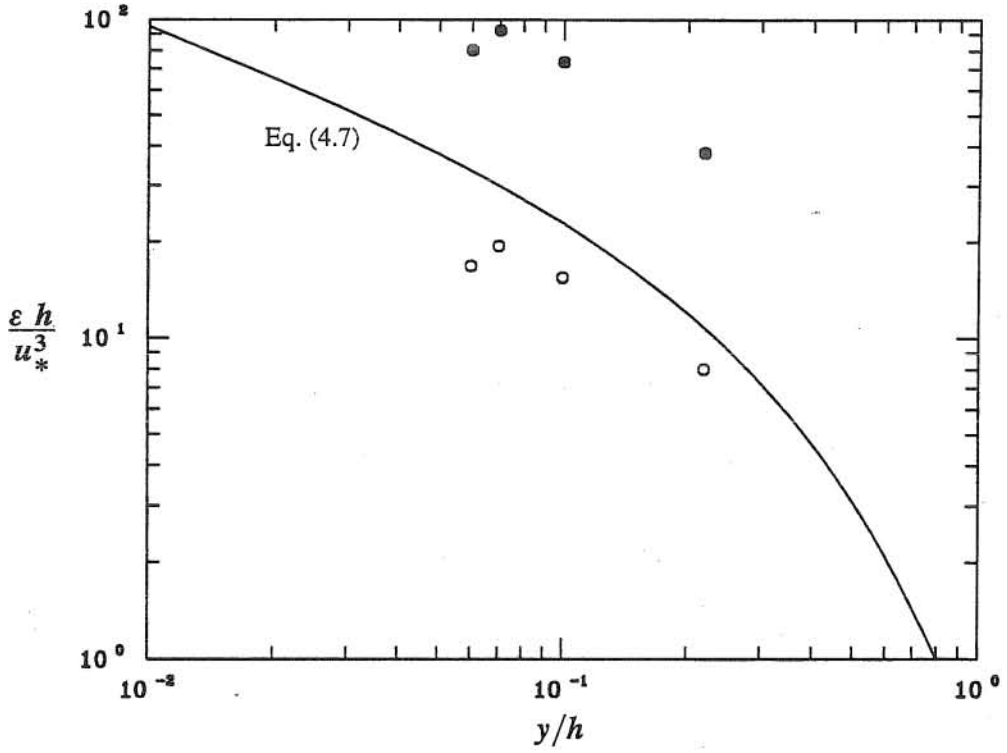

Fig. 4.23 Vertical distribution of dimensionless turbulent energy dissipation.
- Averaged over mean life-time of observed coherent structures.
- o Averaged over mean time span between structures.

Although the observed structures correspond to locations of change of sign of the velocity fluctuations, no strong positive peak of the ensemble averaged streamwise velocity fluctuations was observed downstream of the negative peak characteristic of such fluctuations as seen in Fig. 4.15. These kind of ensemble averaged profiles are reminiscent of similar results of conditionally averaged velocity signals obtained by Luchik and Tiederman (1987) at $y_+ = 15$ and $y_+ = 30$ (although their minimum values were higher than the ones obtained in the present work) and by Talmon et al. (1986) at $y_+ = 43$. It is worth noting that this behavior was also observed in the ensemble averaged velocity time series during ejection events detected using the VITA algorithm in Chapter 3, and that it differs from that of the ensemble averaged velocity time series during sweep events also detected using the VITA algorithm in Chapter 3, which do exhibit a momentum excess, a positive peak of the velocity fluctuations, as a consequence of a strong acceleration of the flow following an initial momentum defect. The latter is in agreement with equivalent results obtained by Blackwelder and Kaplan (1976). From the results showed in Fig. 4.15, the evolution of the vertical profile of coherent streamwise velocity was computed and is shown in Fig. 4.24, again illustrating that no clear, strong sweep events were observed during the passage of the traced organized motions. This indicates that during the occurrence of these ejection-related (second-quadrant) events a streamwise momentum deficit builds up, reaching a maximum after which the velocity profile returns again towards the mean values without passing through a fourth-quadrant event, i.e. without experiencing the sweep-phase of bursting, which is in agreement with the conclusions obtained from the VITA analysis in Chapter 3.

4.5.3 Series ES3

Results from Series ES2, which show the existence of inclined near-wall shear layers and also an inclination of the line connecting the minima of the ensemble averaged velocity profiles are confirmed by space-time cross-correlations between velocity and bed shear stress fluctuations obtained from the analysis of experiments of Series ES3. It was observed that when both sensors were located on a line inclined to the wall at about 14° ($\Delta y/\Delta x = 0.25$) the cross-correlation coefficient attained its maximum value of about 0.28. This peak value of the cross-correlation coefficient agrees with previously reported results in duct flows by Rajagopalan and Antonia (1979), while the inclination angle of 14° associated with this peak is similar to the value of 16° reported by Brown and Thomas (1977) for wind tunnel smooth flows and Bessen and Stevens (1984) for wind tunnel rough flows. On the other hand, the zero time lag is expected to occur for a relative separation of $\Delta x = 18$ mm at $\Delta y = 2.5$ mm, i.e. for an inclination angle of about 8°. Although the inclination angle corresponding to the peak value of the cross-correlation coefficient does not coincide with the one corresponding to the zero time lag, the differences are attributed to inherent computational and experimental errors. The fact that the organized structure responsible for the non-zero value of the

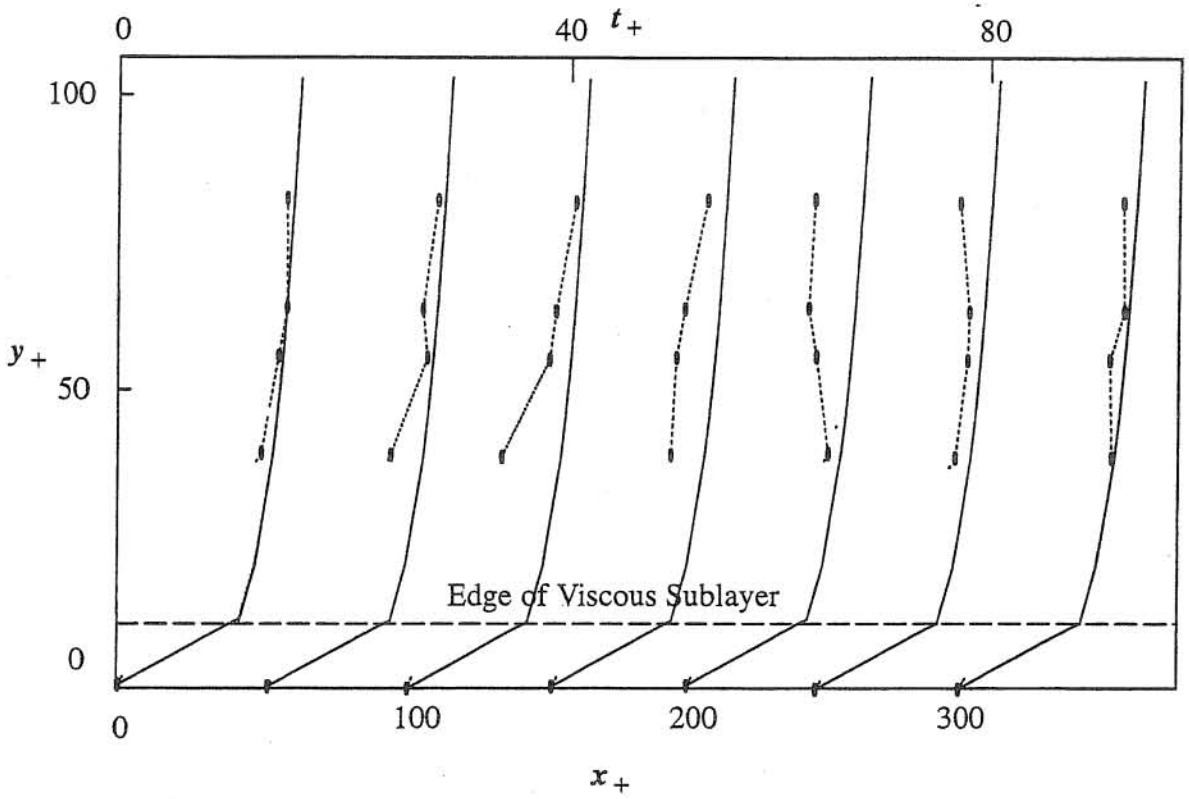

Fig. 4.24 Evolution of vertical profile of streamwise velocity during bursting compared to mean velocity profile estimated with the logarithmic law for smooth channel flows.

cross-correlation coefficient is in fact inclined to the bed of the channel is regarded here as the most relevant result. The dependence of the above mentioned values with Reynolds number was not explored herein.

4.6 Conclusions

Analysis of rather limited experimental information of synchronized high-speed video recordings and hot-film sensor signals in an open channel flow allowed for the characterization of observed coherent structures resulting from bursting and the associated, organized streamwise velocity field. Present results seem to indicate that the phenomena associated with the observed structures (shape, convective velocities, frequencies of occurrence, life-times, etc.) scale with wall units.

Observed shear layers showed a good collapse onto a constant shape when plotted in wall units, which appears to be invariant with both the Reynolds number and the boundary roughness condition, and which have a mean inclination angle to the bed of about 14°. The shear layers move with an almost constant convection velocity of about 10 wall units in the smooth flow case, and of about 6.5 wall units in the transitionally rough flow case, independent of the Reynolds number.

When scaled with the local mean flow velocity, the resulting dimensionless convective velocity appears to be also independent of the boundary roughness condition, having a value of about 0.7. The observed shear layers appear to extend vertically a distance of about 100 wall units, equivalent to the thickness of the wall layer, and to persist for about 60 to 80 wall time units.

The dimensionless flow field associated with the shear layers in the smooth flows, showed a characteristic coherent pattern, independent of the Reynolds number, with the existence of minima of streamwise velocities downstream from the traveling structures at variable distances depending upon the distance from the bed. No significant positive peak of streamwise velocity fluctuations was found in the conditional averaged profiles. The minima tend to locate along a line with an inclination to the bed similar to the angle of the visualized shear layers, and their absolute value decreases with increasing dimensionless distance from the bed. Coherent patterns of streamwise velocity fluctuations were observed to persist over variable space spans, which also decrease with increasing dimensionless distance from the bed, and are of the order of the macro-length scales of turbulence.

Conditional averaging suggests that the occurrence of these coherent patterns mainly affects the turbulence structure in the wall region, $y_+ \lesssim 100$, and that the observed events reveal a plausible mechanism by which energy is extracted from the mean flow to large scale turbulence fluctuations, and then further transferred toward smaller eddies, while the structures lose their coherence. The intermittent nature of production and dissipation of turbulent energy becomes noticeable, taking place in about 20% of the time.

Cross-correlation analyses between velocity and bed shear stress signals also show the existence of inclined structures, with an average angle of inclination to the bed between 15° and 18°.

Comparison of present results with other experiments conducted in different types of flows strongly confirms the universal structure of coherent events in wall bounded flows. Finally, it is believed that the main characteristics of the turbulent coherent structures reported herein could serve as a basis for a better understanding of transport processes occurring near the bed of open channel flows.

4.7 References

Andreopoulos, J., and Bradshaw, P. (1981). "Measurements of turbulence structure in the boundary layer of a rough surface". *Boundary-Layer Meteorology*, 20, pp 201-213.

Bessen, J. M., and Stevens, L. J. (1984). "Cross-correlation measurements in a turbulent boundary layer above a rough wall". *Phys. of Fluids*, 27(9), pp 2365-2366.

Blackwelder, R. F., and Kaplan, R. E. (1976). "On the wall structure of the turbulent boundary layer". *J. Fluid Mech.*, vol 76, pp 89-112.

Brown, G. L., and Thomas, A. S. W. (1977). "Large structure in a turbulent boundary layer". *Phys of Fluids*, 20, pp S243-S252.

Corino, E. R., and Brodkey, R. S. (1969). "The wall region in turbulent flow". *J. Fluid Mech.*, vol 37, pp 1-30.

Falco, E. (1977) "Coherent motions in the outer region of turbulent boundary layers". *Phys. of Fluids*, 20, S124, Pt II.

Grass, A. J., Stuart, R. J., and Mansour-Tehrani, M. (1991). "Vortical structures and coherent motion in turbulent flow over smooth and rough boundaries". *Phil. Trans. R. Soc. Lond.* A, vol 336, pp 35-65.

Grass, A. J. (1971). "Structural features of turbulent flow over smooth and rough boundaries". *J. Fluid Mech.*, vol 50, pp 233–255.

Guezennec, Y. G., Piomelli, U., and Kim, J. (1989). "On the shape and dynamics of wall structures in turbulent channel flow". *Phys. of Fluids* A 1 (4), pp 764-766.

Head, M. R., and Bandyopadhyay, P. (1981). "New aspects of turbulent boundary-layer structure". *J. Fluid Mech.*, vol 107, pp 297-337.

Hetsroni, G. (1991). "The effect of particles on the turbulence in a boundary layer". *Two Phase Flow*, Chap. 8. M. Rocco, Ed. Butterworth.

Jimenez, J., Moin, P., Moser, R., and Keefe, L. (1988). "Ejection mechanisms in the sublayer of a turbulent channel". *Phys. of Fluids*, 31, pp 1311-1313.

Kim, H. T., Kline, S. J., and Reynolds, W. C. (1971). "The production of turbulence near a smooth wall in a turbulent boundary layer". *J. Fluid Mech.*, vol 50, part 1, pp 133-160.

Kline, S. J., Reynolds, W. C., Schraub, F. A., and Runstadler, P. W. (1967). "The structure of turbulent boundary layers". *J. Fluid Mech.*, vol 30, pp 741-773.

Krogstad, P. A., Antonia, R. A., and Browne, L. W. B. (1992). "Comparison between rough- and smooth-wall turbulent boundary layers". *J. Fluid Mech.*, vol 245, pp 599-617.

Liu, Z., Landreth, C. C., Adrian, R. J., and Hanratty, T. J. (1991). "Measurements in turbulent channel flow by high resolution Particle Image Velocimetry". *Experiments in Fluids*, 10, pp 301-312.

Luchik, T. S., and Tiederman, W. G. (1987). "Timescale and structure of ejections and bursts in turbulent channel flows". *J. Fluid Mech.*, vol 174, pp 529-552.

McComb, W. D. (1990). "The physics of fluid turbulence". *Clarendon Press*. Oxford.

Nezu, I., and Nakagawa, H. (1993). "Turbulence in open-channel flows". *IAHR Monograph*. A. A. Balkema, Rotterdam.

Nezu, I. (1977). "Turbulent structure in open-channel flows". *Translation of doctoral Dissertation in Japanese*. Kyoto University, Kyoto, Japan.

Offen, G. R., and Kline, S. J. (1973). "Experiments on the velocity characteristics of 'burst' and on the interaction between the inner and outer regions of a turbulent boundary layer". *Rep. No. MD-31*, Stanford University, Stanford, California.

Rajagopalan, S., and Antonia, R. A. (1979). "Some properties of the large structure in a fully developed turbulent duct flow". *Phys. Fluids*, 22(4), pp 614-622.

Rashidi, M., Hetsroni, G., and Banerjee, S. (1990). "Particle-turbulence interaction in a boundary layer". *Int. J. Multiphase Flow*, vol 16, No 6, pp 935-949.

Raupach, M. R. (1981). "Conditional statistics of Reynolds stress in rough-wall and smooth-wall turbulent boundary layers". *J. Fluid Mech.*, vol 108, pp 363-382.

Robinson, S. K. (1991). "Coherent motions in the turbulent boundary layer". *Annu. Rev. Fluid Mech.*, 23, pp 601-639.

Smith, C. R. (1984). "A synthesized model of the near-wall behavior in turbulent boundary layers". *Proc. 8th Symp. Turbul.*, Missouri-Rolla, Missouri. pp 299-327.

Talmon, A. M., Kunen, J. M. G., and Ooms, G. (1986). "Simultaneous flow visualization and Reynolds-stress measurement in a turbulent boundary layer". *J. Fluid Mech.*, vol 163, pp 459-478.

Urushihara, T., Meinhart, C. D., and Adrian, R. J. (1993). "Investigation of the logarithmic layer in pipe flow using Particle Image Velocimetry". *Near-wall turbulent flows*. R. M. C. So, C. G. Speziale and B. E. Launder (Eds.). Elsevier Science Publishers B. V.

Wallace, J. M., Brodkey, R. S., and Eckelman, H. (1977). "Pattern-recognized structures in bounded turbulent shear flows". *J. Fluid Mech.*, vol 83, part 4, pp 673-693.

Wallace, J. M., Eckelmann, H., and Brodkey, R. S. (1972). "The wall region in turbulent shear flow". *J. Fluid Mech.*, vol 54, pp 39-48.

5. EXPERIMENTS ON SALTATION

5.1 Introduction

Gilbert (1914) seems to have been the first to use the term saltation, derived from the Latin verb *saltare,* which means to leap or dance, to describe the motion of sand particles in water. Bagnold (1973) described saltation as the unsuspended transport of particles over a granular bed by a fluid flow, in the form of consecutive hops, and in which no upward impulses are imparted to the particles other than those attributable to successive contacts between them and the bed. This definition rules out the effect of turbulence as the mechanism that sustains saltation, in this way distinguishing this process from that of transport in suspension. Nevertheless, it also implies that hydrodynamic lift is not important to the saltation process, which, as it has been discussed in previous studies (e.g., Leeder, 1979; Bridge and Bennett, 1992), and also as it is shown herein, does not seem to be correct.

Most of the knowledge on particle saltation in water comes from the studies of Francis (1973), and Abbott and Francis (1977). Using photographic techniques, these researchers observed the motion of isolated particles saltating over a fixed bed of similar material. Particles used in such studies ranged from natural sediment to lighter, artificial materials, with uniform sizes in the range of 5 to 10 mm. Their results include a description of particle trajectories in terms of mean values of the height and length of the jumps and the streamwise particle velocity, as well as of the particle collision with the bed. Several other experimental studies have provided information on particle saltation velocity (e.g., Meland and Norman, 1969; Fernandez-Luque and Van Beek, 1976), although in none of them other properties of the saltation phenomenon have been analyzed.

Gordon et al. (1972) also addressed the saltation phenomenon experimentally. They give a detailed description of the saltation of plastic balls in a very narrow flume, with a channel width to particle size ratio of about 1.2. Even though such results have a rather qualitative value, their conclusions regarding the process of particle collision with the bed provide empirical evidence that can be used for modelling purposes. For instance, they suggest that the particle velocity component normal to the surface of contact is lost on impact, and that the tangential component of such velocity does not change with the collision. This notion, which has also been somehow supported by Abbott and Francis' (1977) conclusions, is of relevance to the model for particle collision with the bed discussed herein.

Drake et al. (1988) used motion-picture photography to analyze bedload motion in a natural stream. They gave detailed descriptions about the transport of natural gravel particles in a movable bed, including different stages within the saltation motion such as the entrainment, subsequent impacts with the bed, and the distrainment of saltating particles. However, their results did not include a quantitative characterization of the saltation process itself.

More recently, Lee and Hsu (1994) analyzed the characteristics of the saltation of sand particles, 1.4 and 2.5 mm in diameter, over a fixed bed formed by the 1.4 mm particles, using standard video recording. Due to the relatively low recording rate of standard video, they could not track the motion of individual particles, however they developed a technique which allowed them to obtain average trajectories of the saltating particles for different hydraulic conditions.

Herein, experimental results concerning the saltation characteristics of natural gravel particles moving as bedload in a movable bed channel, and of natural sand particles moving over a bed of fixed particles are reported. The present experiments with gravel differ from those of Abbott and Francis (1977) and Lee and Hsu (1994) in that they involve much larger particle sizes, and in that bed particles were not fixed as in their experiments. The present experiments with sand particles differ from those of Abbott and Francis (1977) and Lee and Hsu (1994) in that they involve much smaller particle sizes, and in that a much higher temporal resolution of particle motion was obtained. Also, they differ from the experiments of Lee and Hsu (1994) in that herein the motion of individual particles is tracked, therefore individual saltation events can be analyzed including the details of the particle collision with the bed.

In the experiments with gravel, standard video techniques were used to record the motion of saltating particles, while in the experiments with sand, a high-speed video system was employed. From the acquired images of particle motion, geometric and kinematic properties of the saltation events as well as characteristics of particle collisions with the bed, including the dynamic friction coefficient associated with particle motion, were obtained. The laboratory observations provide new insight on the physical processes involved in the bedload transport of sediment under a wide range of particle sizes and hydraulic conditions.

5.2 Dimensional considerations

Before presenting and discussing experimental results, it is important to introduce fluid flow and particle characteristics involved in the saltation process. Consider a particle of mean diameter d_p, and density ϱ_s, immersed in a moving fluid of density ϱ, kinematic viscosity ν, and flow depth h, saltating over a bed formed by similar particles as illustrated in Fig. 5.1. It is easy to show by dimensional analysis, using particle diameter and flow shear velocity as length and velocity scales respectively, that the following is a valid functional relationship:

$$\underline{X} = \underline{f}\,(\tau_* ,\ h/d_p ,\ R_p ,\ R) \tag{5.1}$$

where

$$\tau_* = u_*^2/(\ g\ R\ d_p\ ) \quad , \quad R_p = \sqrt{R\ g\ d_p^3}\ /\nu \quad , \quad R = (\ \varrho_s - \varrho\ )/\varrho \tag{5.2a–c}$$

and u_* denotes flow shear velocity, and g denotes gravitational acceleration.

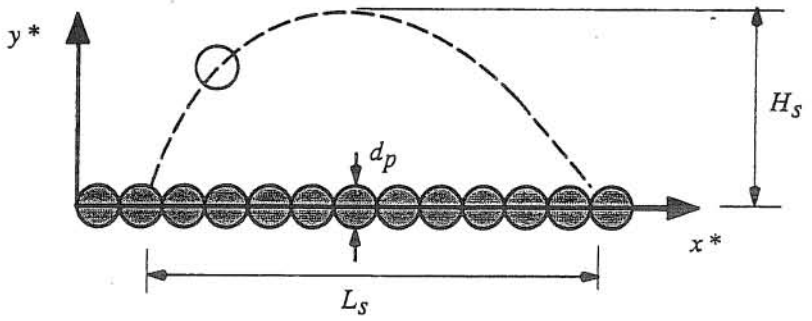

Fig. 5.1 Definition sketch for particle saltation.

In (5.1), $\underline{X}$ represents a vector whose components are dimensionless variables characterizing the saltation phenomenon. For instance, the following can be considered: the dimensionless saltation height and length, h_s and λ_s, respectively, made dimensionless with d_p, the dimensionless mean streamwise particle velocity and streamwise particle velocity change at collision, u_s and Δu_s, respectively, made dimensionless with u_*, and the dynamic friction coefficient, μ_d, which is evaluated as (Abbott and Francis, 1977; Sekine and Kikkawa, 1992):

$$\mu_d = (R + 1) \tau_* (\Delta u_s \, u_s) / \lambda_s \tag{5.3}$$

The dependence on τ_* shown in (5.1) has been replaced in other studies (e.g., Francis, 1973; Abbott and Francis, 1977) by a dependence on the transport stage, defined as τ_*/τ_{*c}, where τ_{*c} denotes the dimensionless critical shear stress for sediment motion. However, introducing τ_{*c} in (5.1) brings in the difficulty of estimating the proper value of this parameter, and furthermore, this is indeed not necessary since it can be shown that τ_{*c} is itself a function of R_p. On the other hand, τ_{*c} could be used in place of other dimensionless parameter such as R_p. For instance, Abbott and Francis (1977) obtained a good collapse of saltation characteristics for different particle conditions using the transport stage, τ_*/τ_{*c}, as independent variable instead of τ_*.

5.3 Experiments on gravel saltation

5.3.1 Experimental study

The experimental work was conducted at the Water Resources Center Laboratory of the University of Chile by Ayala and Valenzuela (1993). The experimental facility consisted of a tilting, movable-bed flume, having a length of 15 m, a width of 0.49 m and a height of 0.5 m. The flume allowed recirculation of coarse bed material, and its slope could be varied between 0 and 7.3 %. Two series of experiments, Series G1 and G2, involving two different natural sediments, $R = 1.65$, with mean diameters, d_p, of 0.015 m and 0.031 m, respectively, and geometric standard deviations of 1.33 and 1.25, respectively, were conducted. The associated experimental conditions are shown in Table 5.1, where S_0 denotes channel bottom slope and Fr denotes flow Froude number.

Supercritical flow conditions existed in all the experiments. Values of the flow shear velocity in Table 5.1 correspond to those associated with the effective shear stress acting on the bed, and were estimated as $u_* = \sqrt{g\, r_b\, S_f}$, where r_b denotes the hydraulic radius associated with bed resistance, obtained after subtracting the effect of the side walls, and S_f denotes the mean friction slope of the flow, which was found to be sufficiently close to S_0 in all cases.

Table 5.1 Experimental conditions Series G1 and G2

Exp	D (mm)	S_0	u_* (m/s)	τ_*	h/d_p	R_p	Fr
G11	15	0.03	0.14	0.09	4.7	7400	1.29
G12	15	0.05	0.17	0.12	4.1	7400	1.03
G13	15	0.07	0.18	0.14	3.3	7400	1.10
G21	31	0.03	0.20	0.08	4.8	21900	1.53
G22	31	0.05	0.22	0.09	3.2	21900	1.29
G23	31	0.07	0.23	0.10	2.6	21900	1.48

The experiments were carried out under uniform flow conditions, and equilibrium bedload transport. Equilibrium conditions were achieved by adjusting the sediment feeding rate at the headbox of the flume to match the rate of sediment leaving the downstream end. The resulting mean bed slope was found to be sufficiently close to that of the channel bottom in all cases.

A schematic representation of the experimental set-up is shown in Fig. 5.2. Images of bedload particles saltating over the movable bed were recorded from the side of the flume using standard video. The observation window had a length of about 0.5 m, and was framed by graduated scales. A collimated light source located above the observation zone allowed to illuminate only a central slice of the flow, having a width of about 0.1 m. The experimental conditions were designed to simulate gravel transport in steep channels under conditions typically found in mountain rivers of Chile. More details about the experimental study can be found elsewhere (Ayala et al., 1992; Ayala and Valenzuela, 1993).

5.3.2 Method of analysis

The analysis of the video-taped experiments was conducted at the Hydrosystems Laboratory of the University of Illinois. The standard video system used in the experimental study recorded images at a rate of 30 frames per second. Individual frames were selected for each experiment and digitized into a personal computer by means of a frame grabber connected to a video cassette recorder (Fig. 5.2). Coordinates of the saltating particles centroids were then obtained with the help of public domain software for the processing and analysis of digital images produced by the National Institute of Health. The calibration of the distances measured on the images was based on the graduated scales framing the observation window, and a correction for the paralax of the camera was

introduced to account for the fact that the scales were not located on the same plane where particle motion was observed. Since the number of particles moving through the observation zone at any given time was relatively small, individual particles could be tracked rather easily among successive frames. Through the analysis of successive frames, trajectories of bedload particles were determined, as seen projected onto a vertical plane parallel to the flow.

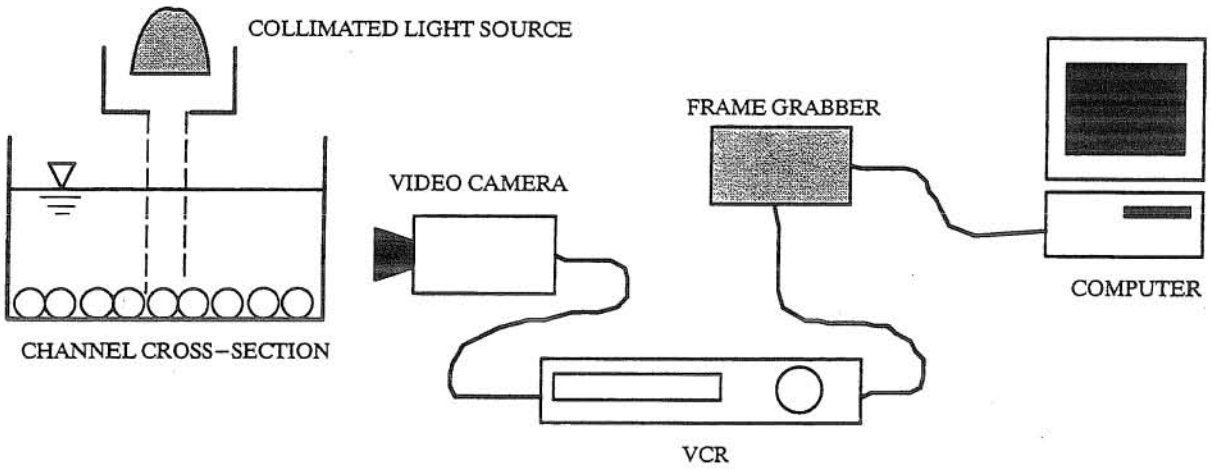

Fig. 5.2 Schematic representation of experimental set-up.

Two different sampling criteria were used in the analysis of the video recordings, depending on the rate of sediment transport. For the experiments of Series G1, with particles of $d_p = 0.015$ m, for which the transport rates were relatively high, a sampling time of 1 sec, a sampling interval of 5 sec (between successive samplings) and a total sampling period of about 1 min were chosen. Each individual sampling consisted of the analysis of all particles crossing the control window during the sampling time, resulting in about 5 to 15 particles depending on the value of τ_*. For the experiments of Series G2, with particles of $d_p = 0.031$ m, for which the transport rates were relatively low, a continuous sampling of particle trajectories was chosen, with a total sampling period of 2 to 3 min. With both sampling methods, a total of about 80 individual saltations were analyzed for each experiment. This was found to generate records long enough to obtain representative mean values and standard deviations of the variables of interest.

5.3.3 Experimental results

Statistics of saltation trajectories

From the recorded particle trajectories, geometric and kinematic properties of individual saltation events were determined. Knowing the duration of the saltation event, T_s, the mean streamwise velocity of an individual saltation event is obtained as $U_s = L_s/T_s$, where L_s denotes the

dimensioned saltation length. Then, ensemble averages and standard deviations of saltation height, length, and mean streamwise particle velocity are computed for each experiment and made dimensionless in the form:

$$h_s = H_s/d_p \quad , \quad \lambda_s = L_s/d_p \quad , \quad u_s = U_s/u_* \qquad (5.4a\text{-}c)$$

where H_s denotes the dimensioned saltation height. The results obtained in Series G1 and G2 are plotted in Figs. 5.3 and 5.4, as functions of the ratio τ_*/τ_{*c} (for comparison with the results of Abbott and Francis, 1977) and R_p, where the value of the dimensionless critical shear stress, τ_{*c}, has been estimated using Shields curve, to be consistent with Abbott and Francis (1977). This yields values of τ_{*c} of about 0.06 for the particles used in this study, which is very similar to the value $\tau_{*c} = 0.05$ found for those particles in a previous experimental study (Ayala et al., 1990).

Statistics of particle collision with the bed

From the analysis of recorded events of particle collision with the bed, particle velocity changes and incidence and takeoff angles at collision can be obtained. The evaluation of the particle streamwise velocity change at collision, Δu_s, allows estimation of the dynamic friction coefficient, μ_d, associated with particle motion. Mean values and standard deviations of this variable, computed using (5.3) for the experiments of Series G1 and G2 are plotted in Fig. 5.5, as functions of τ_*/τ_{*c} and R_p. Values of Δu_s were determined using three particle positions: the one closest to the instant of collision available from the recorded images, and those observed one frame immediately before and after. Given the recording rate of 30 frames per seconds, the exact moment of collision was not always captured by the video camera, which is likely to introduce some error in the estimation of Δu_s.

Angles of incidence, θ_{in}, and takeoff, θ_{out}, at collision, measured with respect to a line parallel to the channel bottom, were evaluated through the estimation of normal and streamwise particle velocities just before and after the collision with the bed particles. Individual values of these angles, obtained for each experiment are plotted in Fig. 5.6. Ensemble averages and standard deviations of these variables for the experiments of Series G1 and G2 are plotted in Fig. 5.7 as functions of τ_* and R_p.

5.3.4 Analysis of experimental results

Statistics of saltation trajectories

Results shown in Fig. 5.3 indicate that mean values of h_s are in the range 1.0 to 2.0, whereas mean values of λ_s are in the range 4.5 to 8.0. Both variables increase with τ_*/τ_{*c}. Corresponding standard deviations are about 30% to 40% of the mean values.

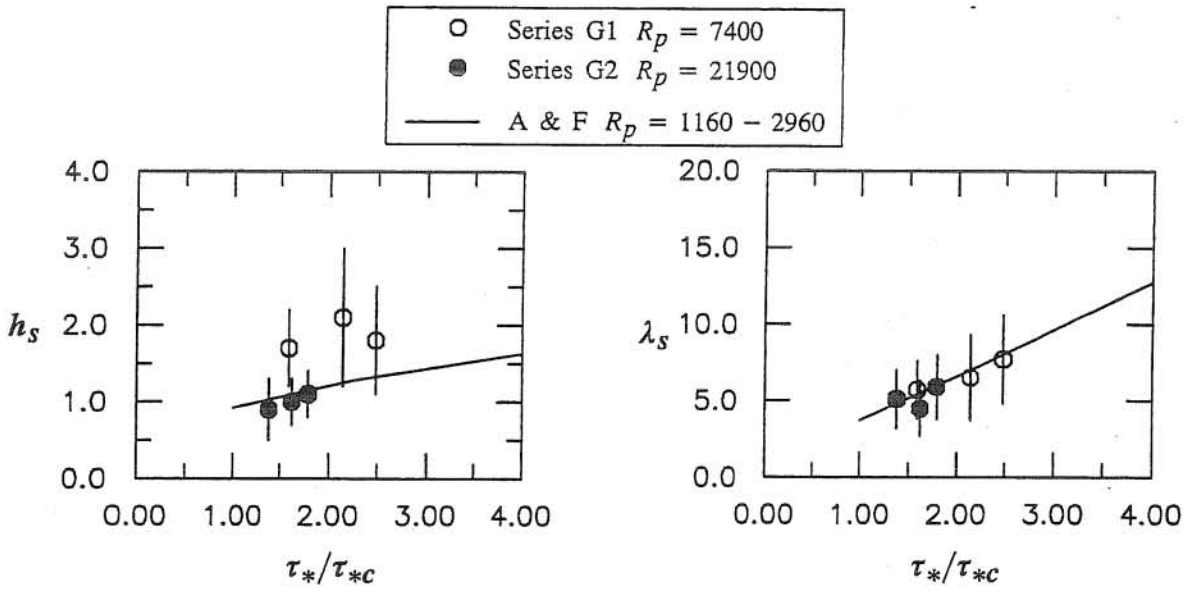

Fig. 5.3 Dimensionless saltation height and length. Symbols denote mean values and vertical lines represent a total length of two standard deviations. Solid lines are curves fitted by Abbott and Francis (1977) (A & F in the leyend) to their experimental data.

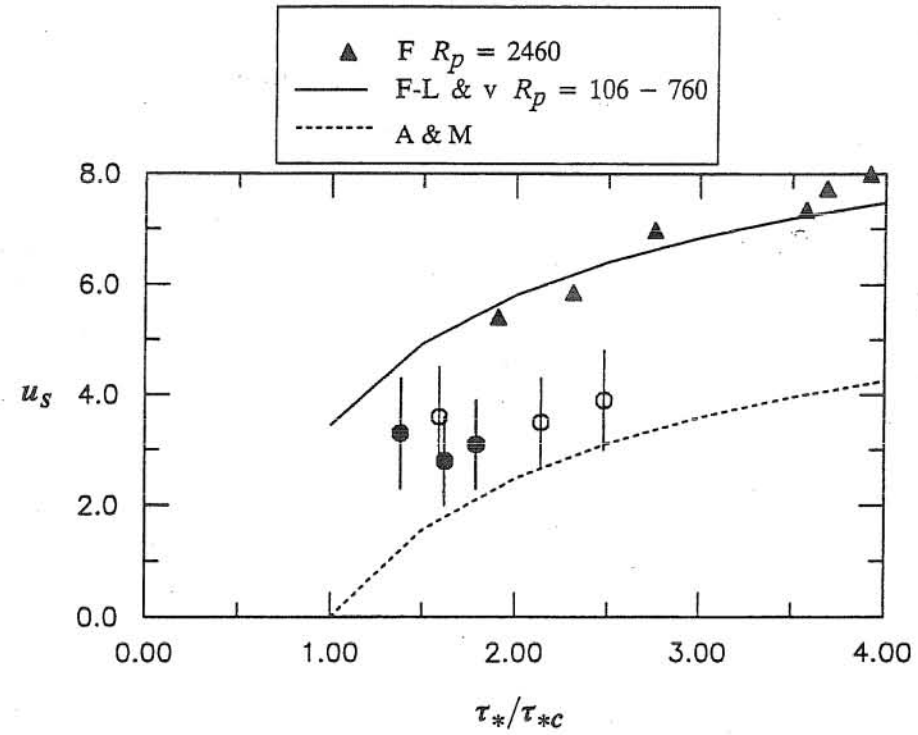

Fig. 5.4 Dimensionless saltation streamwise velocity. Symbols denote mean values and vertical lines represent a total length of two standard deviations. In the leyend, F denotes Francis (1973), F-L & v denotes Fernandez–Luque and van Beek (1976), and A & M denotes Ashida and Michiue (1972). All other symbols are as in Fig. 5.3

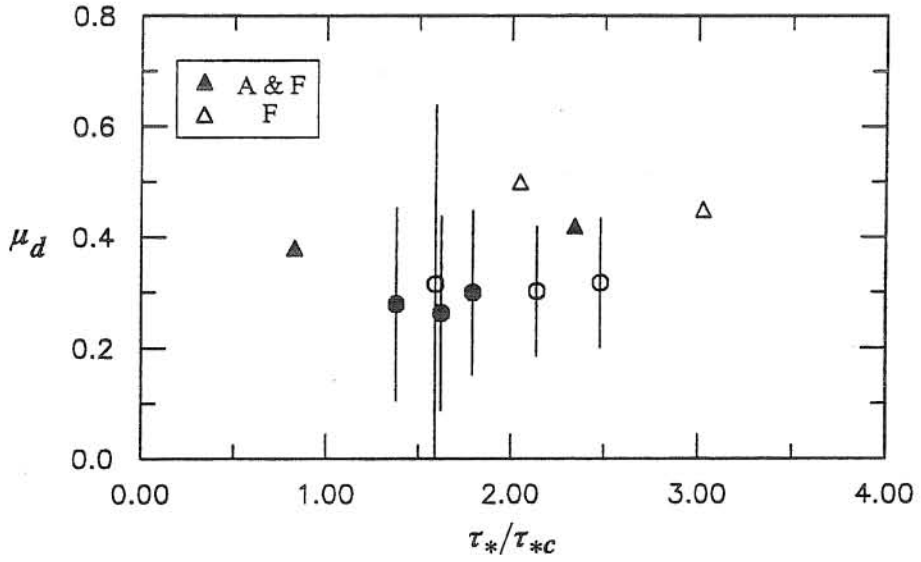

Fig. 5.5 Dynamic friction coefficient. Symbols represent mean values, vertical lines represent a total length of two standard deviations. In the legend, A & F denotes Abbott and Francis (1977), and F denotes Francis (1973). All other symbols are as in Fig. 5.3.

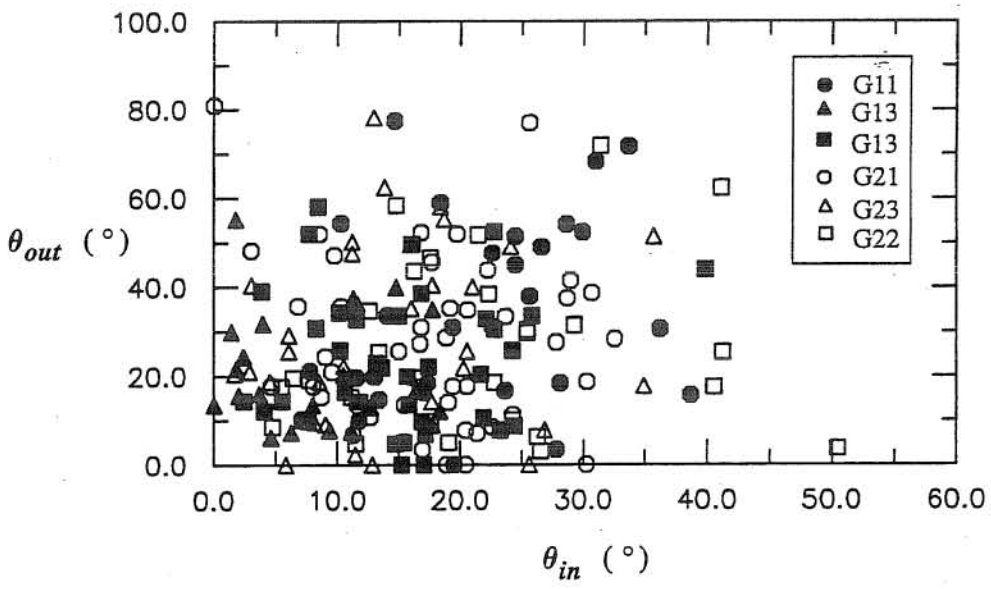

Fig. 5.6 Incidence and takeoff angles at collision. Experiments of Series G1 and G2.

Although saltation lengths agree with the data of Abbott and Francis (1977), saltation heights do not, particularly those of Series G1, associated with the lower R_p value. These differences in saltation height may be due to the fact that Abbott and Francis' experiments were conducted using a fixed bed. A fixed bed would have lower roughness than a movable bed and therefore lower probability for the particles to rebound from the bed with a relatively large takeoff angle.

Surface waves associated with high Froude numbers may also have influenced saltation characteristics. It is possible that the flow field associated with such waves caused fine grains to hop higher, which would also explain the discrepancies with Abbott and Francis results presented in Fig. 5.3. Similar Froude number effects have been suggested by Rickenmann (1990) when looking at bedload transport of slurries in steep channels.

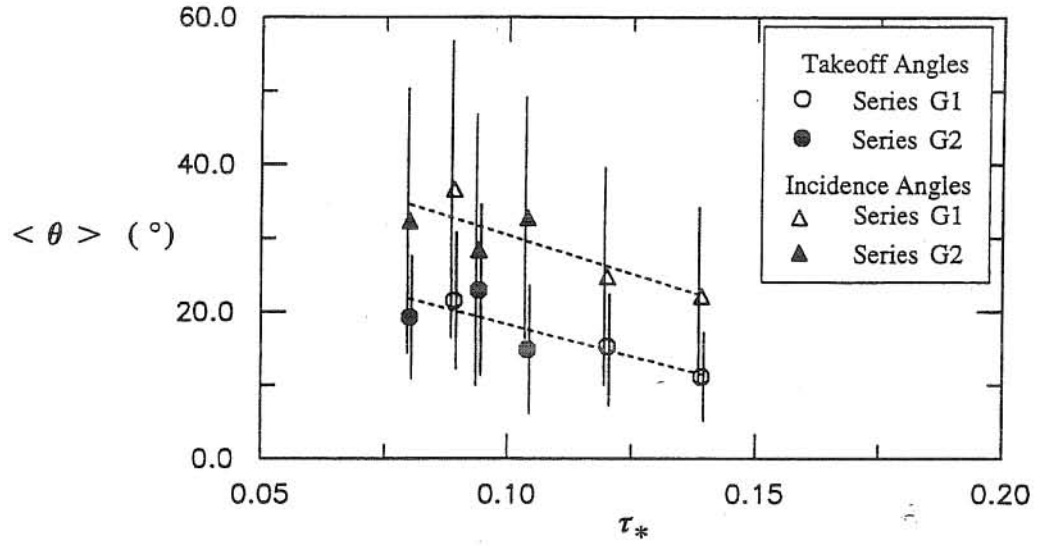

Fig. 5.7 Incidence and takeoff angles at collision. Symbols represent mean values, vertical lines represent a total length of two standard deviations. Experiments of Series S1.

Given the coarse material and steep slopes used in the present study, some influence of h/d_p over saltation characteristics is also expected. In fact, we observed some particles jumping up to the free surface, such that their trajectory was truncated with respect to that they would have had in a deeper flow. Abbott and Francis (1977) concluded from their experiments that flow depth changes do not affect mean values of saltation height, length, and velocity, for values of h/d_p of 5.8 and 8.6. The values of h/d_p in the present study are probably near the limit below which saltation trajectories would be influenced by flow depth.

Mean values of u_s are in the range 2.0 to 4.0 (Fig. 5.4), with standard deviations of about 20 to 30% of the mean values. The data fall between the experimental curve of Fernandez-Luque and Van Beek (1976), and the theoretical curve of Ashida and Michiue (1972). Data of Francis (1973) agree well with Fernandez-Luque and Van Beek's curve.

In Fig. 5.4, Fernandez-Luque and van Beek's (1976) experimental curve is given by:

$$u_s = 11.5 \left(1 - 0.7 \sqrt{\tau_{*c}/\tau_*} \right) \tag{5.5}$$

while Ashida and Michiue's (1972) theoretical curve is given by:

$$u_s = 8.5 \left(1 - \sqrt{\tau_{*c}/\tau_*} \right) \tag{5.6}$$

Bridge and Dominic (1984) proposed the following equation for the dimensionless mean streamwise velocity of saltating particles in hydraulically rough flows:

$$u_s = a \left(1 - \sqrt{\tau_{*c}/\tau_*} \right) \tag{5.7a}$$

$$a = 2.5 \ln \left[\left(h_n/h_s \right) \left(d_p/k_s \right) \left(2.53 \sqrt{\tau_* - \tau_{*c}} + 0.5 \right) \right] + 8.5 \tag{5.7b}$$

where h_n denotes the height of effective fluid thrust on saltating grains (Bagnold, 1973), and k_s denotes the bed roughness height. The form of (5.7a) is similar to equations proposed by Fernandez-Luque and Van Beek (1976), Ashida and Michiue (1972), Engelund and Fredsøe (1976), Sekine and Kikkawa (1992), and others. The evaluation of a through (5.7b), however, gives this parameter physical meaning, since it is related to variables characterizing particle saltation. Bridge and Bennett (1992) revised the expression for a given by (5.7b). For hydraulically rough flows they proposed:

$$a = (1/\varkappa) \ln \left(h_n/k_s \right) + 8.5 \tag{5.8}$$

where $\varkappa$ denotes the von Karman's constant, which is assumed to take values less than 0.4, even with only weak bedload transport. Values of h_n/k_s are expected to be in the range 0.5 to 1.0.

Values of τ_{*c} to be used in (5.7) must correspond to those associated with the threshold of motion of particles lying over the bed (Bridge and Dominic, 1984). Herein we choose the value of this parameter in order to let the curve given by (5.7) fit the present experimental results. The best fit is obtained for $\tau_{*c} = 0.036$, using the values $h_n/h_s = 0.84$ and $d_p/k_s = 1.0$ (Abbott and Francis, 1977; Bridge and Dominic, 1984), however the value of a is not very sensitive to reasonable variations of these parameters. The results obtained are presented in Fig. 5.8, together with Fernandez-Luque and Van Beek, and Ashida and Michiue curves. Interestingly, the renormalization of τ_*/τ_{*c} caused the theoretical curve of the latter to fit the experimental data fairly well.

According to Leeder (1979), Bagnold's premise that the immersed weight of moving bedload solids in saltation is supported only by an upward stress due to the normal reaction of the solids with the stationary bed leads to the equilibrium condition $F_g^2 = U_s^2/(g L_s) = 1$, where F_g represents a grain Froude number. However, using Abbott and Francis (1977) data, Leeder showed that F_g is,

in general, much less than unity, which implies that upward forces other than those arising from particle collision with the bed must be present in the saltation process. These upward forces may correspond to hydrodynamic lift and also to Magnus force due to particle rotation. Values of F_g^2 for the present experiments using the results presented in Figs. 5.3 and 5.4, are in the range 0.28–0.44, with a mean value of 0.33, which is in agreement with Leeder's argument.

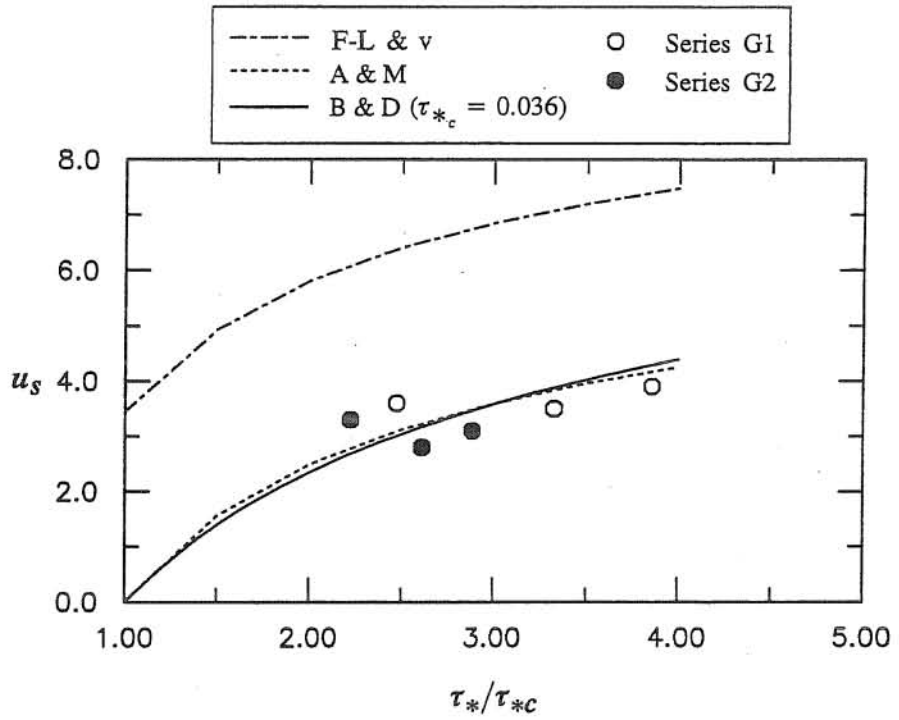

Fig. 5.8 Comparison of dimensionless saltation streamwise velocity with the experimental curve of Fernandez–Luque and van Beek (1976) (F-L & v), and the theoretical curves of Ashida and Michiue (1972) (A & M), and Bridge and Dominic (1984) (B & D), using a value $\tau_{*c} = 0.036$.

Statistics of particle collision with the bed

Results for the dynamic friction coefficient in Series G1 and G2 shown in Fig. 5.5 have an almost constant value of about 0.3, which is much lower than the value 0.8 predicted numerically by Sekine and Kikkawa (1992), and is in good agreement with the value 0.32 obtained experimentally by Bagnold (1956) for smooth spheres. Values obtained by Francis (1973) and Abbott and Francis (1977) have a mean value of about 0.4 (Fig. 5.5). According to Bagnold (1973), the value of μ_d should be very close to the static friction coefficient $\tan\phi$, which for natural sediment takes a value of about 0.63. The difference between this value and the observed values of μ_d is explained by Abbott and Francis (1977) as a bias introduced by the method of estimation of this variable from the experimental observations, caused by the inability to accurately determine particle velocities just before and after the collision with the bed. Although this is likely to affect the present

estimations of μ_d as well, we sustain that the value of μ_d may actually be lower than $tan\phi$, in agreement with Bagnold's earlier ideas.

Fig. 5.6 shows that incidence angles tend to concentrate in the range 5° to 30°, whereas takeoff angles spread out in the range 0° to 60°. Mean values of both, incidence and takeoff angles decrease with τ_*, with trends that are almost parallel to each other (Fig. 5.7).

Contradictory viewpoints regarding the process of particle collision with the bed appear in the literature. Some authors favor the concept of particle collision and rebound (e.g., Wiberg and Smith, 1985; Sekine and Kikkawa, 1992), whereas others put forward the idea that a particle does not actually rebound after the collision, but instead reestablishes the saltation after a transient rolling motion (e.g., Gordon et al., 1972; Abbott and Francis, 1977). The analysis of recorded collision events in the present experiments seems to indicate a coexistence of both modes of collision (collision-rolling and collision-rebound), their occurrence depending mainly on the local configuration of bed particles at the point of collision. Whenever a saltating particle collided directly with a bed particle, a collision–rebound mode was more frequently observed; whenever a particle fell in an interstitial zone, a collision-rolling mode was more frequently observed.

Determination of the splash function

In order to further analyze the present results regarding particle collisions with the bed, a collision-rolling model similar to those proposed by Gordon et al. (1972) and Wiberg and Smith (1985) was tested. The results obtained are not presented herein, however, takeoff velocities predicted by the model are much lower than those observed in the present experiments. A model of the collision-rebound type proposed by García and Niño (1992) was also tested. Such model considers the situation illustrated in Fig. 5.9, where a saltating particle approaching the bed at an angle θ_{in}, strikes a surface that faces upstream with an angle θ_b. The striking particle velocity is resolved into normal and tangential components with respect to the collision surface, $u_N\,|_{in}$ and $u_T\,|_{in}$, respectively, and it is assumed that these components are reduced after the collision, so that:.

$$u_T\,|_{out} = f\,u_T\,|_{in} \qquad , \qquad u_N\,|_{out} = -\,e\,u_N\,|_{in} \tag{5.9}$$

where e and f are restitution and friction coefficients, respectively. In such a case, the particle rebounds with an angle θ_r given by:

$$tan\ \theta_r = \frac{e}{f}\ tan\ (\ \theta_{in} + \theta_b\ ) \tag{5.10}$$

and the particle velocity components immediately after the collision, $u_p\,|_{out}$ and $v_p\,|_{out}$, can be expressed in terms of the particle velocity components immediately before the collision, $u_p\,|_{in}$ and $v_p\,|_{in}$, as follows:

$$u_p\,|_{out} = f\,(\,u_p^2\,|_{in} + v_p^2\,|_{in}\,)^{1/2}\cos\,(\,\theta_{in} + \theta_b\,)\,\frac{\cos\,(\,\theta_r + \theta_b\,)}{\cos\,(\,\theta_r\,)} \qquad (5.11a)$$

$$v_p\,|_{out} = f\,(\,u_p^2\,|_{in} + v_p^2\,|_{in}\,)^{1/2}\cos\,(\,\theta_{in} + \theta_b\,)\,\frac{\sin\,(\,\theta_r + \theta_b\,)}{\cos\,(\,\theta_r\,)} \qquad (5.11b)$$

where u_p and v_p denote particle velocity components in the streamwise and normal to the bed directions, respectively.

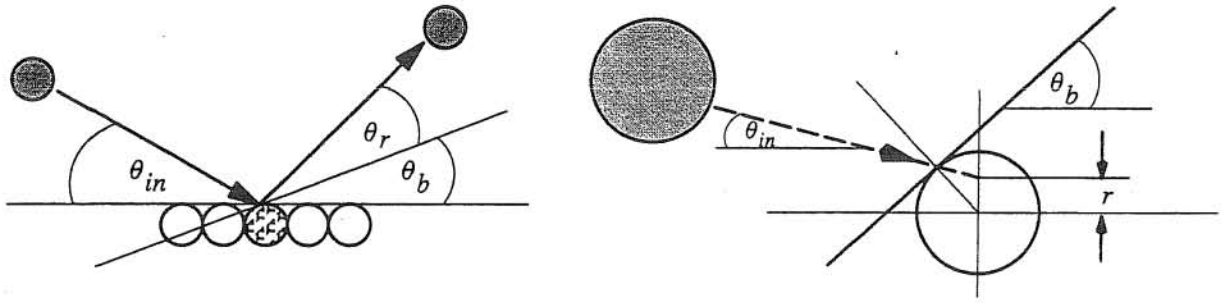

Fig. 5.9 Definition diagram for particle collision with the bed

From the analysis of the experimental results of Series G1 and G2, all variables required to estimate the coefficients e and f can be obtained, with the exception of the angle θ_b, which could not be measured directly from the recorded collision events because this would require an extremely high spatial resolution, which was not available with the video set-up used. To overcome this problem, a stochastic model proposed by García and Niño (1992) to determine the probability distribution of θ_b (named the splash function by Anderson and Haff, 1988), akin to those proposed by Wiberg and Smith (1985) and Tsujimoto and Nakagawa (1983), was used.

Assuming that the bed is formed by uniformly packed spheres as shown in Fig. 5.9, a conditional probability density function $p\,(\,\theta_b|\theta_{in}\,)$ (where the notation $A|B$ indicates that A depends on B, i.e., "A given B") of the angle θ_b for a given value of θ_{in} can be obtained by considering a bed particle. Geometrical considerations dictate that the angle θ_b can vary from a maximum value of 30° at the upstream side of the particle, to a minimum of –30° at the downstream side of the particle. The set of angles within that range is mapped onto a set of values r along a vertical line passing through the center of the particle. The probability density of the r values is assumed to be uniform, which is equivalent to assuming that the considered particle has a uniform probability of being located anywhere in the bed. Introducing geometrical transformations, the uniform probability density of r can be readily converted to $p\,(\,\theta_b|\theta_{in}\,)$. The results obtained are shown in Fig. 5.10, where expected, maximum, and minimum values of θ_b as functions of θ_{in}, are also presented.

By using the mean values of θ_{in} and θ_{out} shown in Fig. 5.7 and ensemble averages of particle velocity components just before and after collisions with the bed, the values of e and f corresponding

to the present experiments are computed with (5.10) and (5.11), and with the mean value of θ_r estimated as:

$$\theta_r = < \theta_{out} > - \mathrm{E} [\theta_b | < \theta_{in} >] \tag{5.12}$$

where angular brackets represent ensemble average and E denotes expected value, computed from the probability density function $p (\theta_b | \theta_{in})$. The results obtained for each experiment are plotted in Fig. 5.11, as functions of τ_* and R_p.

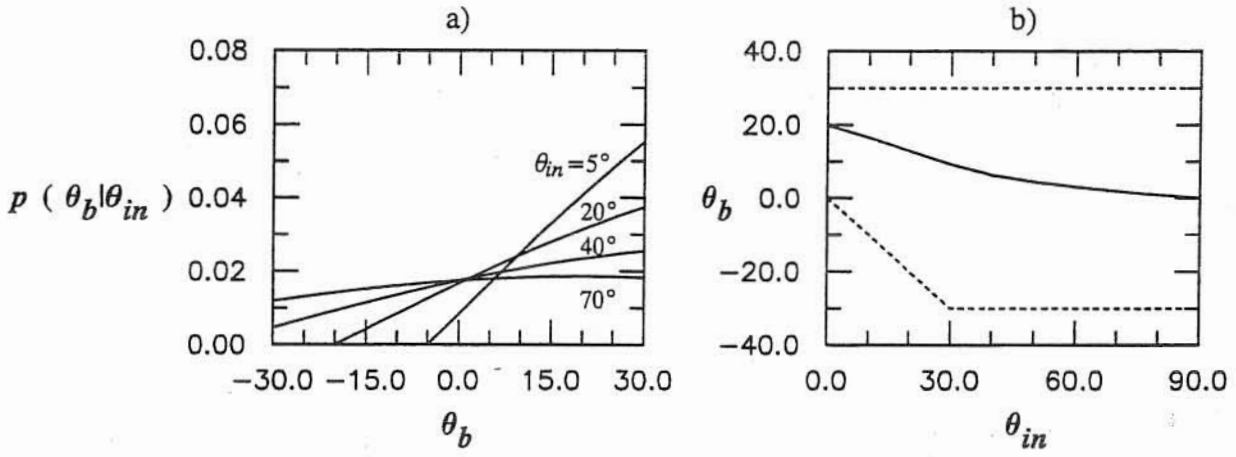

Fig. 5.10 a) Conditional probability density function of the collision angle θ_b, given the incidence angle θ_{in}. b) Expected, maximum, and minimum values of θ_b as functions of θ_{in}. Solid line represents the expected value while dashed lines represent maximum and minimum values.

The computed values of the coefficient f appear to be almost independent of τ_* and R_p, with a constant value of about 0.73. On the other hand, the computed values of the coefficient e appear to be linearly related with τ_*, approximately described by:

$$e = 0.84 - 4.84\ \tau_* \tag{5.13}$$

According to Gordon et al. (1972), their experimental results suggest that the particle velocity component normal to the surface of contact is lost on impact, and that the tangential component is completely retained. The first assumption is based on the fact that no backwards bounces were ever observed, which also agrees with Abbott and Francis' (1977) observations. This evidence indicates that e must vanish, and that f should be close to unity. The present experimental results seem to indicate, however, that only about 73% of the tangential velocity component of the striking particle is conserved at collision, so that the difference must be attributable to friction losses. With respect to the normal velocity component, it is apparent that at values of τ_* larger than about 0.15, this component is indeed completely lost at impact. However, for values of τ_* less than 0.15, a certain portion of this component is retained at collision with a maximum value of about 40% at values of

τ_* of about 0.08. In order to have a backwards bounce, the angle $\theta_{in} + \theta_b$ must be greater or equal to 90°. The results herein indicate that such an event has a very low probability of occurrence, which, added to the fact that the estimated values of e are in fact small, would explain why a backwards bounce was never observed during the experiments of Gordon et al. and Abbott and Francis, or in the present study.

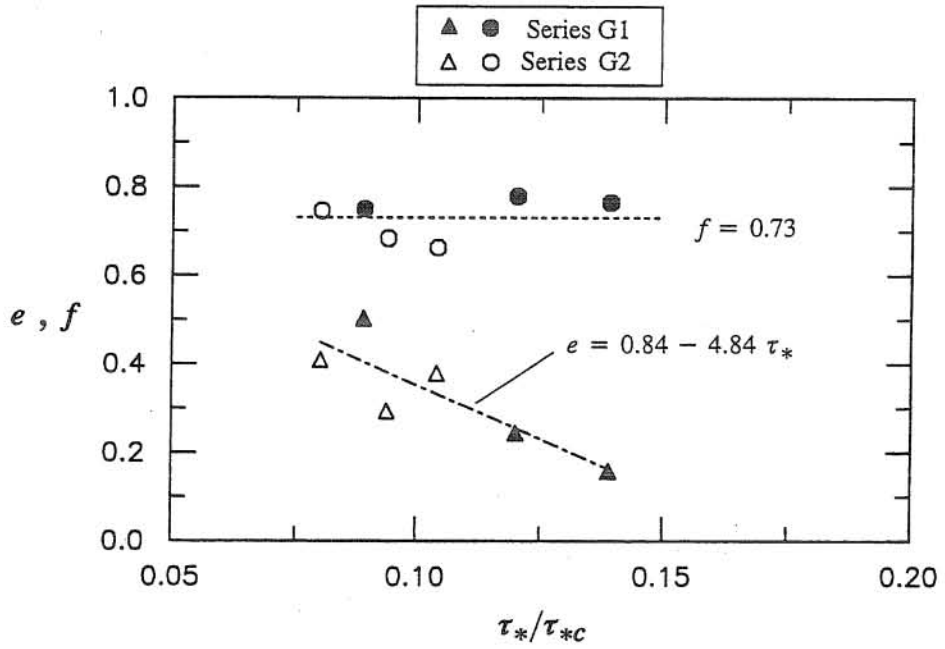

Fig. 5.11 Values of the tangential and normal velocity coefficients. Experiments of Series G1 and G2.

Finally, the dependence of the coefficient e on τ_* can be explained with the aid of a comment made by Wiberg and Smith (1985). According to them, it seems likely that a sediment bed will undergo progressively greater deformation as the momentum of grain impacts increases, which would justify the use of a restitution coefficient, e, that decreases as the particle momentum increases in association with increasing flow shear stress.

5.3.5 Conclusions

Video imaging techniques have been used successfully to analyze the characteristics of the saltation process of gravel particles in a movable bed channel. The resulting statistics of saltation trajectories, as well as of the process of particle collision with the bed, give new insights on the saltation phenomenon, extending and completing previous experimental observations.

Mean values of h_s are in the range 1.0 to 2.0, mean values of λ_s are in the range 5.0 to 10.0, and mean values of u_s are in the range 2.0 to 4.0, all these variables increasing with τ_*/τ_{*c}, for values of this parameter in the range 1.0 to 3.0. Standard deviations are in the range of 30% to 40% of the mean values for h_s and λ_s, and in the range of 20% to 30% of the mean values for u_s. Mean values

of the latter variable are estimated well by Bridge and Dominic (1984) equation, when the threshold shear stress corresponding to a particle lying over the bed is properly selected.

Small values of h/d_p can affect the saltation process mainly by truncating particle trajectories. Values of h/d_p in the present study are probably near the limit below which saltation trajectories would be influenced by flow depth. Surface waves associated with high Froude numbers may also influence particle saltation.

Experimental values of F_g^2 are in the range 0.28 to 0.44, which indicates that upward forces other than those arising from particle collisions with the bed must be present in the saltation process. The dynamic friction coefficient, μ_d, has a mean value of about 0.3, which is slightly smaller than the values obtained experimentally by Francis (1973) and Abbott and Francis (1977), about half of the value 0.63 proposed by Bagnold (1973), and almost one third of that estimated numerically by Sekine and Kikkawa (1992). Although some error is expected in the estimation of this variable, the experimental evidence indicates that values of μ_d would be actually lower than the value expected by Bagnold.

The coefficient f has a constant value of 0.73, whereas the coefficient e is in the range 0.0 to 0.5, and decreases linearly with τ_*. Vanishing values of e are expected for values of τ_* larger than about 0.17. The dependence of e on τ_* can be explained as a dependence of e on particle momentum, as suggested by Wiberg and Smith (1985).

5.4 Experiments on saltation of sand

5.4.1 Experimental study

Experimental setup

The experiments were conducted in a rectangular open channel 18.6 m long, 0.297 m wide, and 0.280 m high, which has an observation window located a distance of about 12 m downstream of the entrance. A fixed bed of sand particles which have an approximately uniform size of 0.53 mm was formed inside the flume by glueing the particles to the channel bottom. The channel slope was set to a value of about 0.0009.

A high-speed video system, Kodak Ektapro TR Motion Analyzer, was used to record particle motion. The solid state sensor of this system has a pixel array structure of 240 columns and 192 rows. Blocks of 16 rows are read simultaneously by means of 16 channels, which gives the system the capability to record up to 1000 frames per second in full frame mode, or up to 6000 frames per second in split screen mode.

A strobe light with a flash-duration of 20 microseconds was synchronized with the high-speed video system to provide whole-field illumination. This type of illumination was preferred to a laser

sheet, mainly because the extremely short pulse of the strobe light helped to reduce image blur due to particle motion. Also, since the light sensitivity of the high-speed video camera is rather poor it was found that the quality of the images obtained with the strobe light illumination was better than those obtained using an available, relatively low power, laser.

The video images acquired with the high-speed video system were downloaded from special high-speed Kodak tapes onto standard VHS tapes, from where were digitized into a personal computer using a frame grabber. The images were analyzed using the National Institute of Health's *Image* public domain software. A schematic view of the experimental setup is shown in Fig. 5.12.

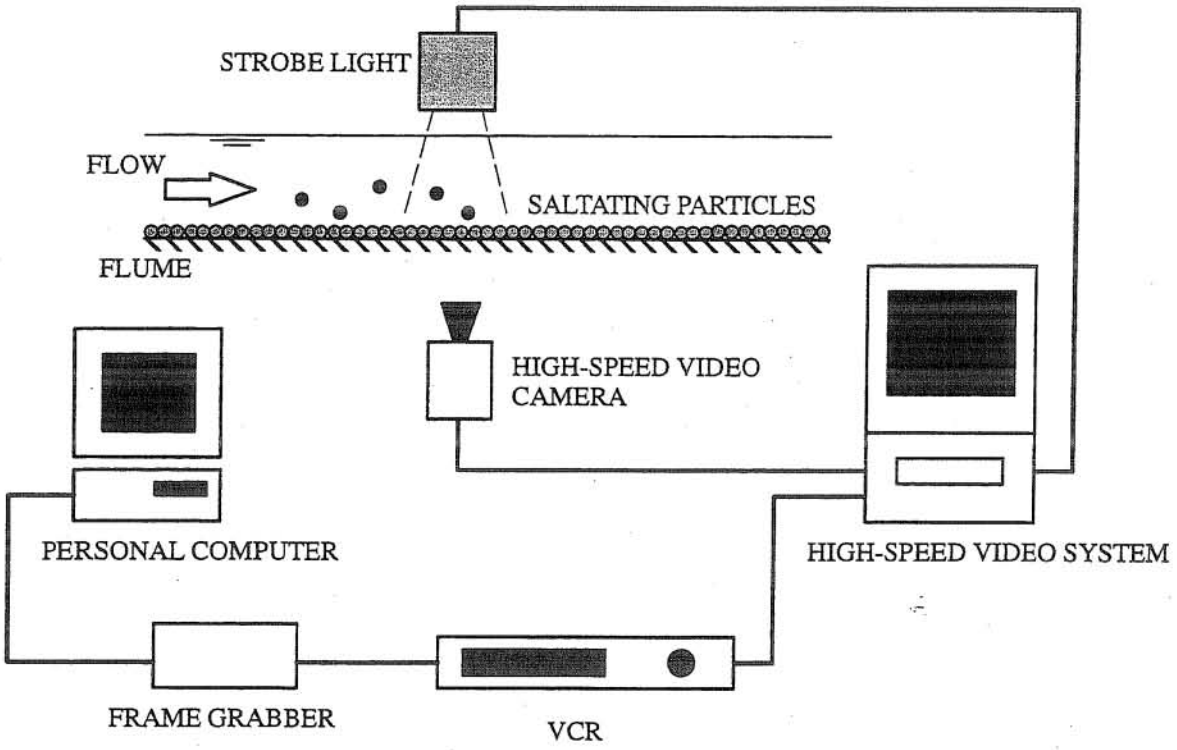

Fig. 5.12 Schematic view of experimental set–up.

Experimental method

The experiments were carried out under uniform flow conditions. Particles were fed externally to the flow at a distance sufficiently far upstream from the observation window as to allow particle saltation motion to reach steady conditions before going into the field of view of the camera. Particle motion was recorded from the side, through the observation window, and in some cases also from the top, using the high-speed video system set at a recording rate of 250 frames per second (fps).

In the case of side views, typical dimensions of the flow field registered by the camera were about 1.3 to 1.5 cm in the streamwise direction by about 1.1 to 1.3 cm in the vertical. This corresponded to flow fields of about 19 by 16 particle diameters to about 22 by 18 particle diameters.

These dimensions were found adequate to spatially resolve particle trajectories during saltation, corresponding roughly to 2 to 3 particle jump lengths.

Likewise, the recording rate of 250 fps was found to provide an adequate temporal resolution of the particle saltation trajectories. It is important to note that a recording rate of 250 fps is about 8.3 times faster than that of regular video. From this point of view, the information obtained from the use of the high-speed video system is unique and could not be obtained by using standard video

Experimental conditions

Flow depths used in both series of experiments covered a range from about 28 mm to about 50 mm. Flow conditions corresponded to values of the Reynolds number (defined as $Re = Uh/\nu$, where U denotes flow mean velocity) in the range from about 7800 to about 21500, and to values of the Froude number of about 0.5 to 0.6, which corresponded to subcritical flows. Values of u_* were in the range from about 0.021 m/s to about 0.032 m/s. Two different series of experiments were conducted using natural sand particles having a mean value of d_p of about 0.53 mm: Series S1, where particle motion was recorded from the side, and Series S2, where particle motion was recorded from the top. The particles had a submerged specific density, R, of about 1.65 and a value of R_p associated with the nominal mean values of d_p of about 50. A summary of the experimental conditions in Series S1 and S2, including values of the dimensionless parameter h/d_p, is presented in Table 5.2.

Table 5.2 Experimental conditions saltation of sand

Exp	h (m)	u_* (m/s)	h/d_p	Fr	Re
S11	0.0285	0.0207	53.8	0.515	7750
S12	0.0347	0.0240	65.5	0.541	10955
S13	0.0398	0.0266	75.1	0.561	13941
S14	0.0430	0.0282	81.1	0.572	15971
S15	0.0463	0.0299	87.4	0.583	18188
S16	0.0509	0.0321	96.0	0.598	21484
S21	0.0290	0.0210	54.7	0.517	7991
S22	0.0338	0.0235	63.8	0.538	10460
S23	0.0378	0.0256	71.3	0.553	12733

5.4.2 Method of analysis

The video recordings of particle saltation were analyzed in order to determine characteristics of the saltation trajectories and particle collisions with the bed. Selected frames of the video recordings were digitized into a personal computer. Images were analyzed in order to obtain the position of individual particles in successive frames. This was done by visually tracking the particles in each frame. Usually only one saltating particle appeared in each frame, which made the manual

tracking much faster and efficient than the use of an automatic tracking algorithm, which would involve manipulating and processing a large number of images with only a few pixels of relevant information in each. The size of each saltating particle was also measured from the digitized images.

Additionally, the video recordings were analyzed to determine the angular velocity of the saltating particles. This was done by estimating the number of revolutions described by the particles during each jump from the frame by frame analysis of the saltation motion. The mean angular velocity of each particle analyzed was obtained by dividing the number of revolutions by the duration of the saltation.

Since in the present experiments the bed was fixed, the number of particles moving through the field of view was controlled by the external feeding. As already commented, generally only one particle was moving through the field of view of the video camera at a time. A minimum of about 100 individual saltating particles were tracked for each experimental condition, with at least one to two complete saltation jumps for each particle. This was found to generate records long enough to obtain representative mean values and standard deviations of the variables of interest.

5.4.3 Experiments of Series S1

5.4.3.1 Experimental results

Statistics of saltation trajectories

Typical examples of saltation events are shown in Fig. 5.13 for different experimental conditions, where the position of the particles is given in dimensionless coordinates (x_p, y_p), which have been made dimensionless with d_p (Fig. 5.1). The jumps shown therein are typically about 8 to 12 particle diameters in length, with maximum heights of about 1.3 to 1.8 particle diameters, and have durations of about 0.036 to 0.048 s. In most cases the transition from one jump to the next is clearly of the collision-rebound type.

Scatter plots of the measured values of dimensionless saltation heights and lengths in experiments of Series S1 are shown in Figs. 5.14 and 5.15, respectively, plotted as functions of τ_*. It must be recalled that for each saltation event registered, the corresponding particle diameter was also measured, and even though the sand used in the present experiments was fairly uniform, some variation of particle size was indeed observed. Hence, although the shear velocity of the flow remained constant in each experiment, the value of τ_* varied for each particle, since it is a function of the particle diameter, which explains the range of values of τ_* obtained for each experimental condition as seen in Figs. 5.14 and 5.15.

For each experiment of Series S1 the mean value and standard deviation of τ_* was computed, together with its associated mean values and standard deviations of dimensionless saltation height and length. These are plotted in Figs. 5.16 and 5.17. Therein symbols denote mean values, while

vertical lines represent a total length of two standard deviations of the corresponding variable, and horizontal lines represent a total length of two standard deviations of τ_*.

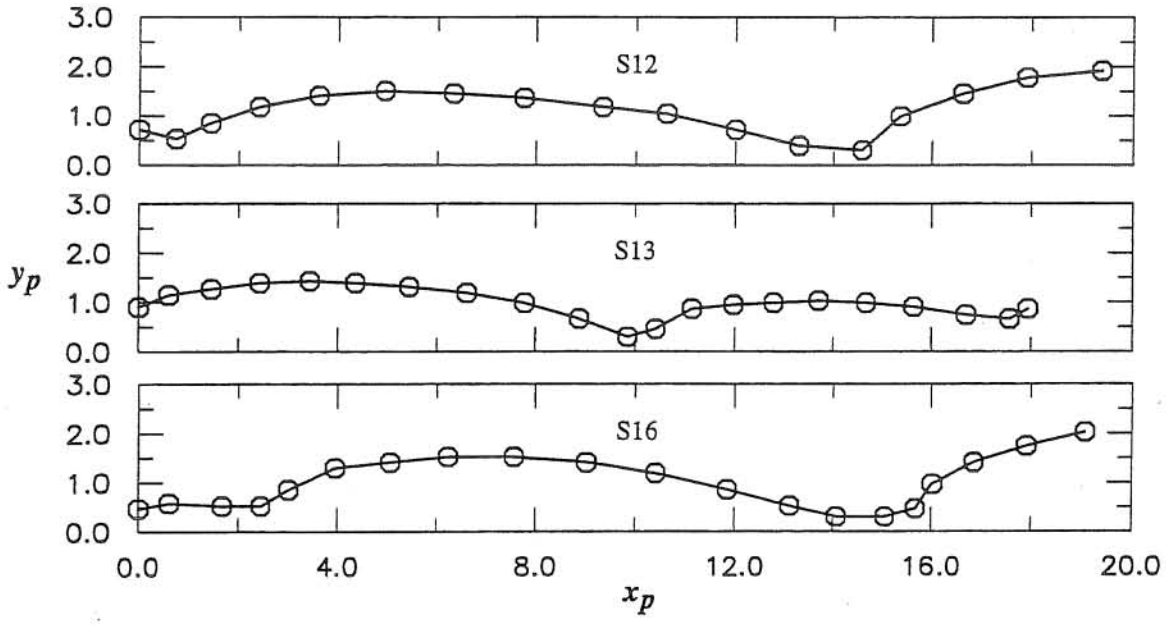

Fig. 5.13 Examples of typical dimensionless saltation trajectories. Symbols correspond to measurements taken 0.004 s apart. Experiments of Series S1.

Mean values and standard deviations of the dimensionless mean streamwise particle velocity during the saltation events shown in Figs. 5.14 and 5.15, computed as explained in Section 5.3.3, are plotted as a function of the mean value of τ_* for each experiment of Series S1 in Fig. 5.18. Therein symbols denote mean values, while vertical lines represent a total length of two standard deviations of u_s, and horizontal lines represent a total length of two standard deviations of τ_*.

In order to characterize the bed normal component of the particle velocity during saltation, maximum values of this variable, made dimensionless with u_*, during upward and downward phases of the observed trajectories are plotted in Fig. 5.19, as functions of corresponding dimensionless values (in terms of particle diameters) of the elevations at which those velocities occur, for three experiments of Series S1. A frequency analysis of the maximum dimensionless upward and downward particle velocities shown in Fig. 5.19 is presented in Fig. 5.20.

Statistics of particle collision with the bed

From the analysis of recorded events of particle collision with the bed, particle velocity changes and incidence and takeoff angles at collision can be obtained. Associated values of the dynamic friction coefficient, μ_d, were estimated from the evaluation of the mean particle streamwise velocity change at collision, Δu_s, and the mean values of λ_s and u_s shown in Figs. 5.17 and 5.18, using (5.3). Mean values and standard deviations of this variable are plotted in Fig. 5.21

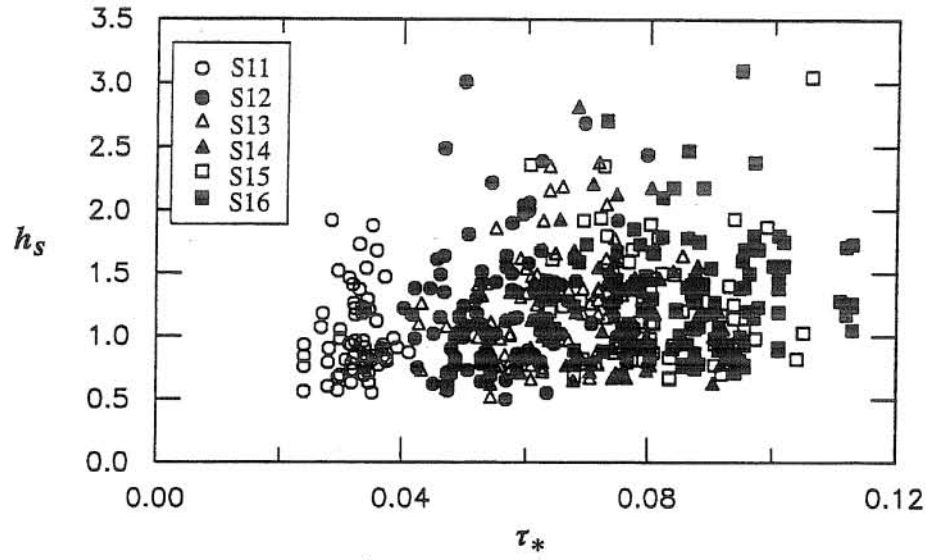

Fig. 5.14 Dimensionless heights of individual saltation events. Experiments of Series S1.

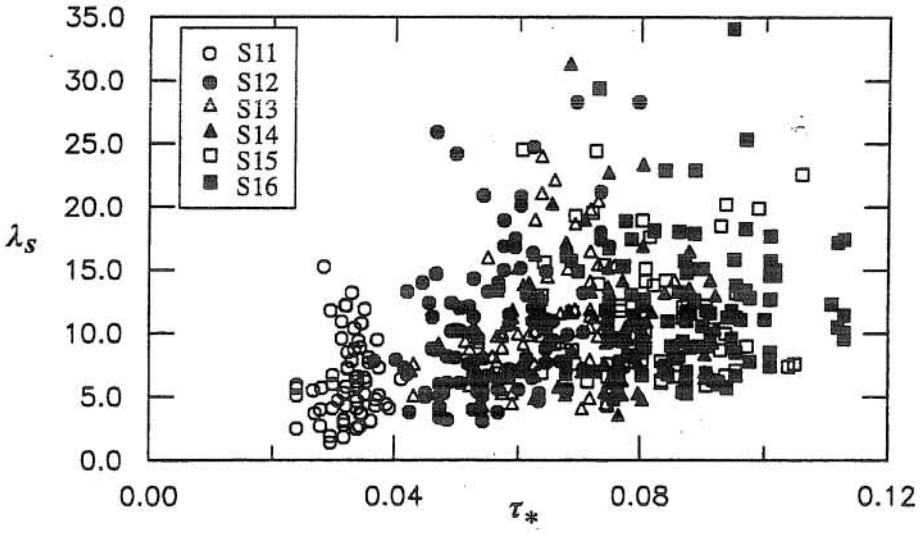

Fig. 5.15 Dimensionless lengths of individual saltation events. Experiments of Series S1.

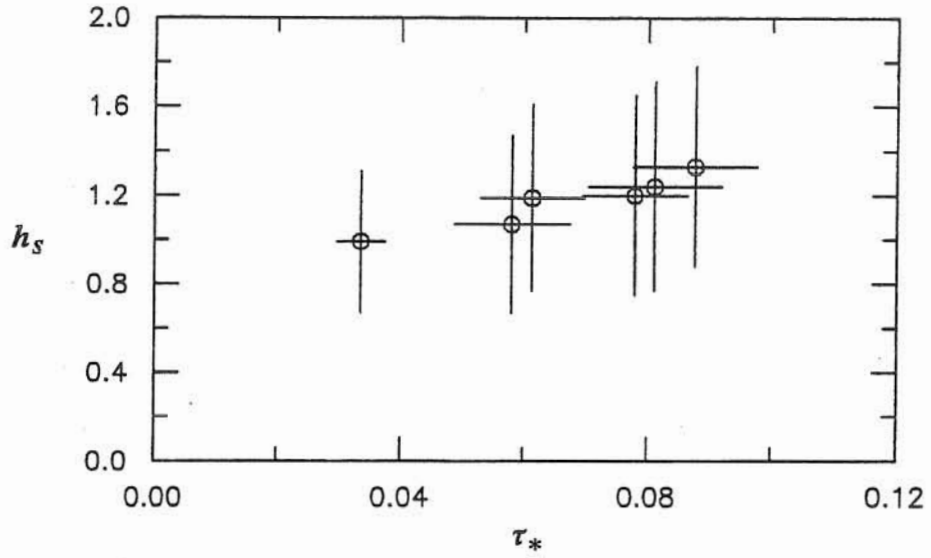

Fig. 5.16 Dimensionless saltation height. Symbols represent mean values, vertical lines represent a total length of two standard deviations of the saltation height, and horizontal lines represent a total length of two standard deviations of the dimensionless bed shear stress. Experiments of Series S1.

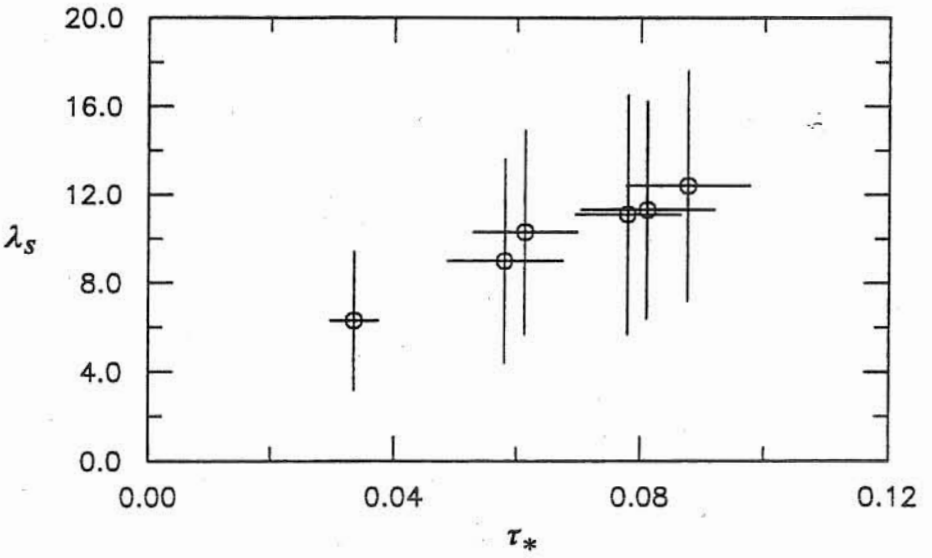

Fig. 5.17 Dimensionless saltation length. Symbols represent mean values, vertical lines represent a total length of two standard deviations of the saltation length, and horizontal lines represent a total length of two standard deviations of the dimensionless bed shear stress. Experiments of Series S1.

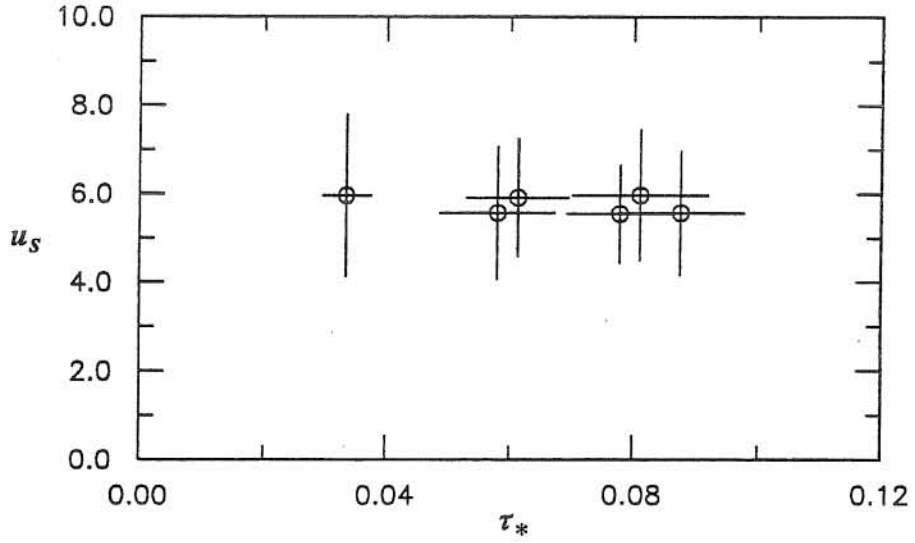

Fig. 5.18 Dimensionless streamwise saltation velocity. Symbols represent mean values, vertical lines represent a total length of two standard deviations of the saltation velocity, and horizontal lines represent a total length of two standard deviations of the dimensionless bed shear stress. Experiments of Series S1.

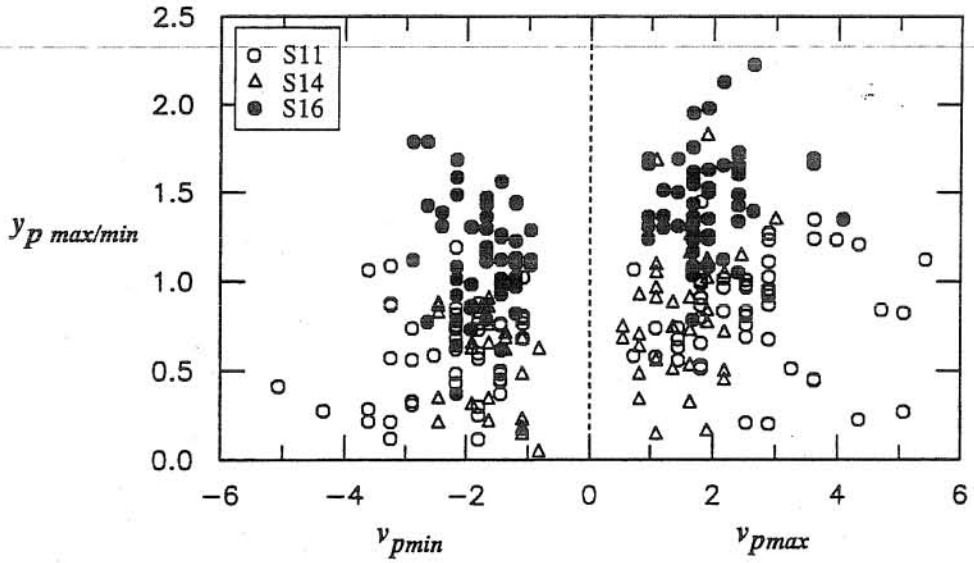

Fig. 5.19 Dimensionless maximum upward and downward particle saltation velocities and corresponding dimensionless vertical location. Experiments of Series S1.

as functions of the mean values of τ_* in each experiment of Series S1. Since values of μ_d were not measured directly, associated values of the standard deviation were estimated from the standard deviations of λ_s, u_s, and Δu_s, using (5.3). This appear to overestimate the standard deviation of μ_d. In fact, mean values of μ_d minus one standard deviation in Fig. 5.21 appear to be negative, which has no physical meaning.

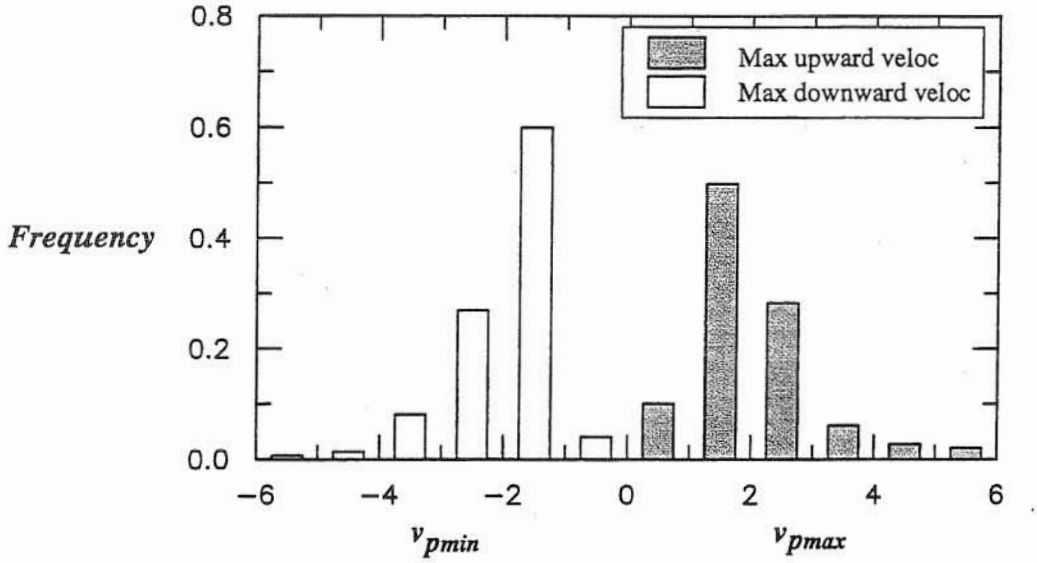

Fig. 5.20 Frequency distribution of dimensionless maximum upward and downward particle saltation velocities. Experiments of Series S1.

Values of Δu_s were determined using three particle positions: the one closest to the instant of collision available from the recorded images, and those observed one frame immediately before and after. Given the recording rate of 250 fps, the values of Δu_s estimated in the experiments of Series S1 are much more accurate than those in the experiments with gravel, obtained with a recording rate of only 30 fps, because of the better temporal resolution of the instant of collision obtained in the former case.

Angles of incidence, θ_{in}, and takeoff, θ_{out}, at collision, measured with respect to a line parallel to the channel bottom, were evaluated through the estimation of normal and streamwise particle velocities just before and after the collision with the bed particles. Individual values of these angles estimated for the experiments of Series S1 are plotted in Fig. 5.22. Therein, the set of angles θ_{out} with corresponding zero values of θ_{in}, is associated to events in which the initiation of saltation was observed.

Mean values and standard deviations of incidence and takeoff angles at collision shown in Fig. 5.22 are plotted in Fig. 5.23 as a function of corresponding mean values of τ_*. In Fig. 5.24, mean values and standard deviations of the takeoff angles corresponding to initiation of saltation events

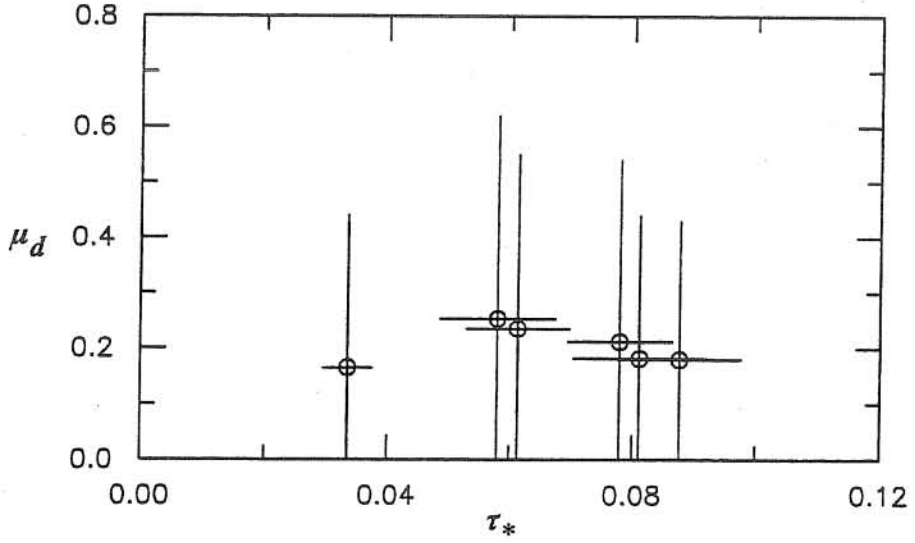

Fig. 5.21 Dynamic friction coefficient. Symbols represent mean values, vertical lines represent a total length of two standard deviations of the dynamic friction coefficient, and horizontal lines represent a total length of two standard deviations of the dimensionless bed shear stress. Experiments of Series S1.

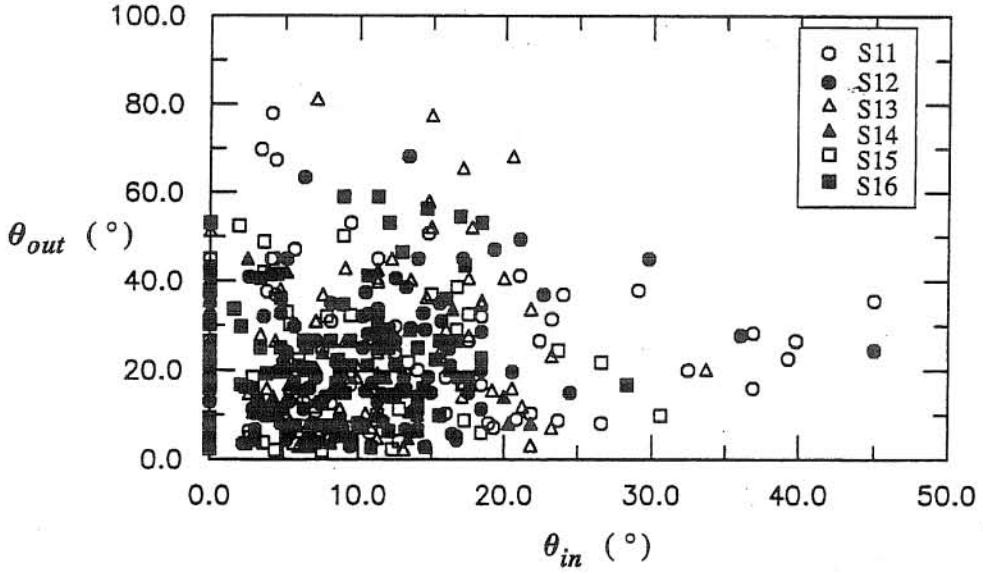

Fig. 5.22 Incidence and takeoff angles at collision. Experiments of Series S1.

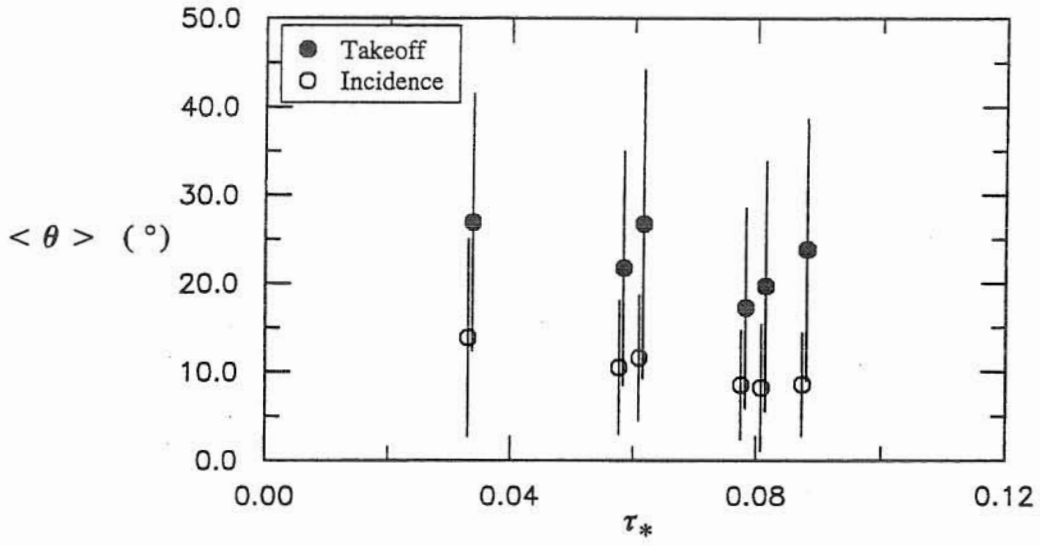

Fig. 5.23 Incidence and takeoff angles at collision. Symbols represent mean values, vertical lines represent a total length of two standard deviations. Experiments of Series S1.

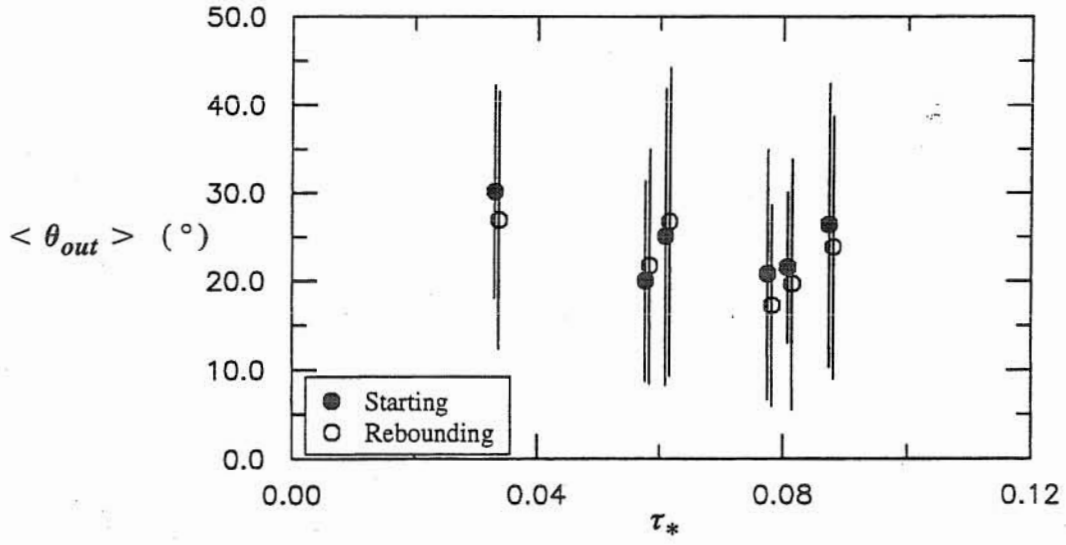

Fig. 5.24 Takeoff angles for the situations: starting a saltation sequence, and rebounding after collision with the bed. Symbols represent mean values, vertical lines represent a total length of two standard deviations. Experiments of Series S1.

are plotted as a function of corresponding mean values of τ_*, together with the mean values and standard deviations of the takeoff angles shown in Fig. 5.23, for comparison purposes.

Statistics of particle rotation

From the analysis of particle rotation, the particle mean angular velocity during saltation, Ω, expressed in Hz, was estimated for each jump, and the dimensionless particle angular velocity, S, defined as:

$$S = \Omega \, d_p/u_* \tag{5.14}$$

was computed. Mean values and standard deviations of this variable estimated for different experimental conditions are plotted in Fig. 5.25 as a function of τ_*.

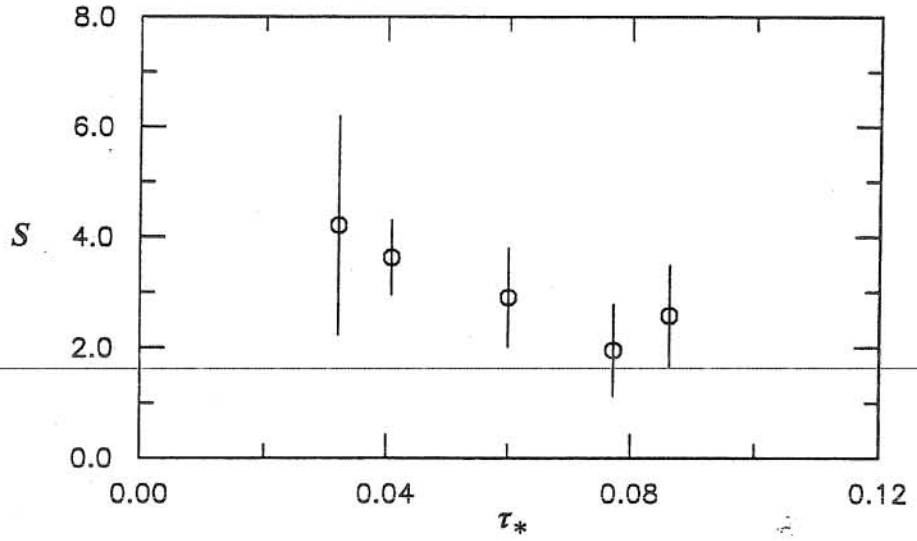

Fig. 5.25 Dimensionless particle angular velocity during saltation. Symbols represent mean values, vertical lines represent a total length of two standard deviations. Experiments of Series S1.

The observations of particle rotation seem to indicate that the particle angular velocity is controlled mainly by the process of collision with the bed and therefore appears to be a random variable. It was observed that particle angular velocity tends to be somewhat larger right after impact and then it tends to decrease during the rest of the jump, probably due to viscous effects. As a consequence of the importance of the collision on Ω, the shape of the particle was observed to play a major role on the resulting angular velocity, such that elongated shapes colliding with the bed at the proper orientation seem to result in higher particle angular velocities than more spherical shapes.

5.4.3.2 Analysis of experimental results

Statistics of saltation trajectories

Results shown in Figs. 5.16 and 5.17 indicate that mean values of h_s are in the range 1.0 to 1.3, while mean values of λ_s are in the range 6 to 12. Both variables increase with τ_*. Corresponding

standard deviations are about 30 to 40% of the mean values for h_s, and about 40 to 50% of the mean values for λ_s. Results shown in Fig. 5.18 indicate that mean values of u_s are fairly constant, equal to about 5.8, and seem to be independent of τ_*. Corresponding standard deviations are about 20 to 30% of the mean values.

Experimental results for h_s and λ_s of Series S1 shown in Figs. 5.16 and 5.17 are plotted in Figs. 5.26 and 5.27 as functions of the ratio τ_*/τ_{*c}, together with those corresponding to gravel saltation (Series G1 and G2) shown in Fig. 5.3, and the experimental results of Abbott and Francis (1977) and Lee and Hsu (1994), for comparison purposes. Similarly, experimental results for u_s of Series S1 shown in Fig. 5.18 are plotted in Fig. 5.28 as a function of the ratio τ_*/τ_{*c}, together with those corresponding to gravel saltation (Series G1 and G2) shown in Fig. 5.4, the experimental results of Francis (1973), Fernandez-Luque and van Beek (1976), and Lee and Hsu (1994), and the theoretical relationship of Ashida and Michiue (1972), for comparison purposes.

Using the ratio τ_*/τ_{*c} as independent variable instead of τ_* allows a better comparison of data with extremely different values of R_p, such as those corresponding to the experiments with gravel of Section 5.3 and with fine sand of Series S1. The range of values of R_p for each data set plotted in Figs. 5.26 to 5.28 is specified in the respective legends.

As seen in Fig. 5.26, mean values of h_s in the experiments of Series S1 agree well with corresponding data by Abbott and Francis (1977) and the gravel experiments of Series G2, R_p = 21900, showing a similar tendency to grow moderately with the ratio τ_*/τ_{*c}. On the other hand, they are much lower than the mean values of h_s corresponding to the gravel experiments of Series G1, R_p = 7400, which are somewhat closer to the rather high values of h_s measured by Lee and Hsu (1994). Since the unusually high values of h_s observed in the gravel experiments corresponding to R_p = 7400 were explained as a possible effect of the high Froude number of the flow in such experiments, it is apparent that the values of h_s observed by Lee and Hsu (1994) for the saltation of sand at low values of Fr are extremely high, and show a tendency to grow with τ_*/τ_{*c} at a much higher rate than that defined by Abbott and Francis', Series S1, and gravel data sets.

From Fig. 5.27, it is apparent that the mean values of λ_s in the experiments of Series S1 are somewhat larger than corresponding gravel and Abbott and Francis' data sets, although they exhibit a similar tendency to grow with τ_*/τ_{*c}. Again, Lee and Hsu's data seem to be much higher than the rest of the data plotted in Fig. 5.27, and have a tendency to grow with τ_*/τ_{*c} at a much higher rate than that shown by Abbott and Francis' or present results.

The values of the standard deviations of λ_s observed in the experiments with sand of Series S1, of about 40 to 50% with respect to corresponding mean values, appear to be somewhat larger than the equivalent values of about 30 to 40% observed in the experiments with gravel of Series G1

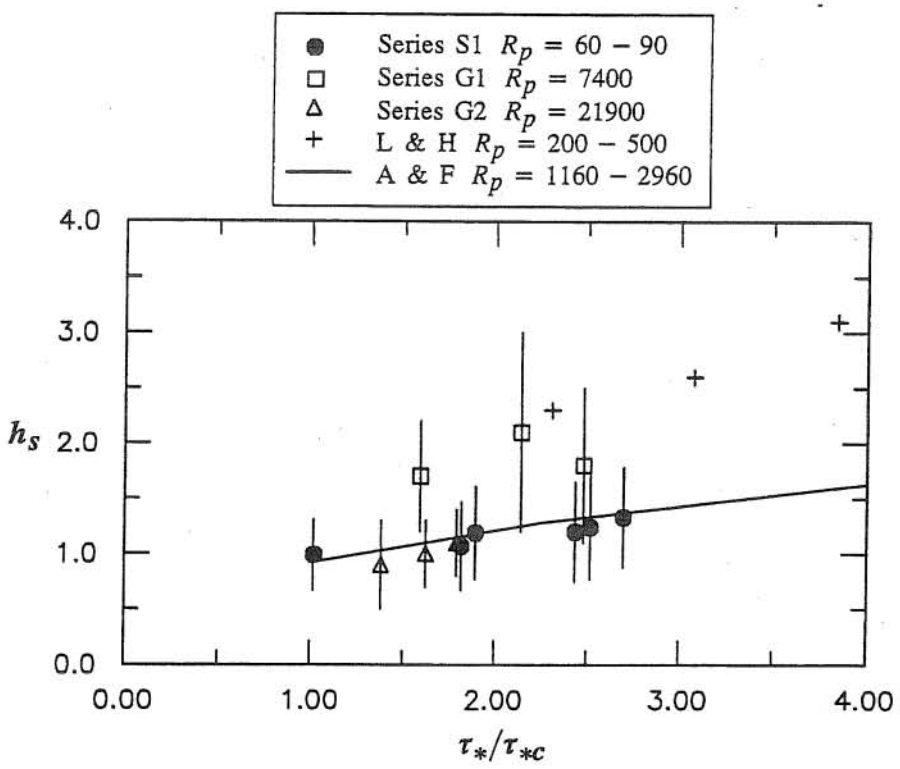

Fig. 5.26 Dimensionless saltation height. Symbols represent mean values, vertical lines represent a total length of two standard deviations. In the legend, L & H denotes Lee and Hsu (1994), and A & B denotes Abbott and Francis (1977).

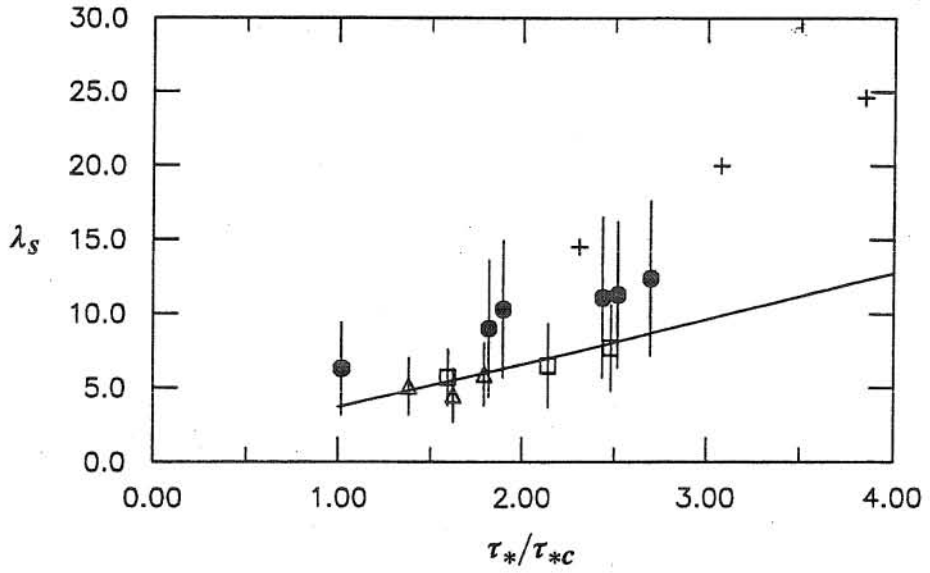

Fig. 5.27 Dimensionless saltation length. Symbols represent mean values, vertical lines represent a total length of two standard deviations. Legend as in Fig. 5.26.

and G2, although the values 30 to 40% observed in Series S1 for h_s agree well with those of the latter experiments. In the case of gravel saltation, the randomness exhibited by the variables characterizing such process was regarded mainly as an effect of the randomness of the process of particle collision with the bed, since it was apparent that the turbulence of the flow did not influence the motion of the large gravel particles. The above result, however may be indicative of a slightly larger effect of the turbulence of the flow on the motion of the fine sand particles of Series S1 than in the case of the coarse gravel particles analyzed in Section 5.3, which appears to affect more strongly the saltation lengths.

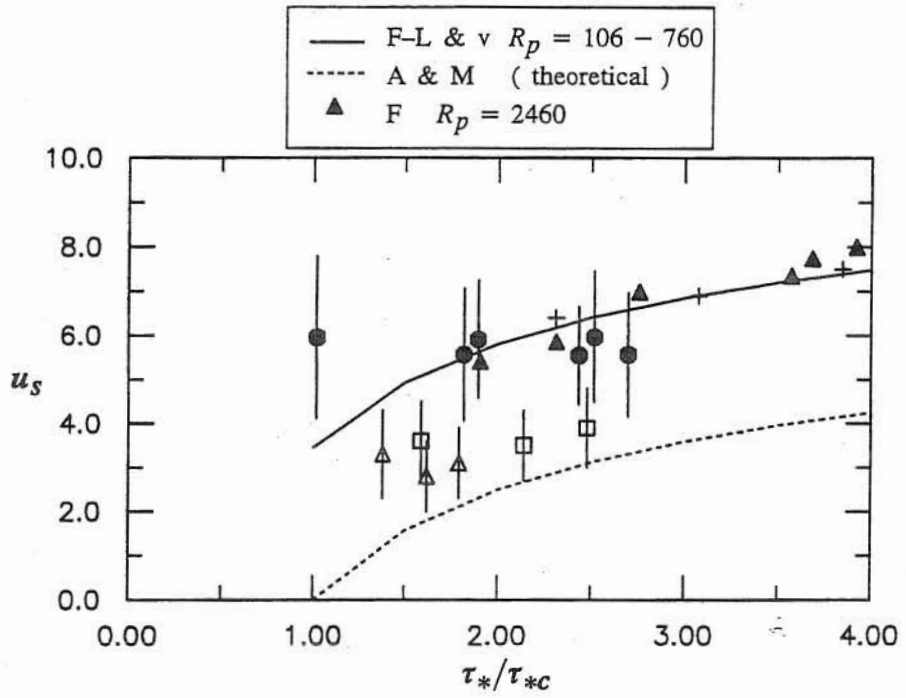

Fig. 5.28 Dimensionless saltation streamwise velocity. Symbols represent mean values, vertical lines represent a total length of two standard deviations. In the legend, F-L & v denotes Fernandez-Luque and van Beek (1976), A & M denotes Ashida and Michiue (1972), and F denotes Francis (1973). All other symbols are as in Figs. 5.26 and 5.27.

Mean values of u_s in experiments of Series S1 appear to be about 1.5 to 2.0 times as large as corresponding values in the gravel experiments (Fig. 5.28), although associated standard deviations are of similar magnitude relative to the mean values in both series of experiments. On the other hand mean values of u_s in experiments of Series S1 appear to be well described by Fernandez-Luque and van Beek's curve for values of τ_*/τ_{*c} larger than about 2. In such range a good agreement with the experimental results of Francis and Lee and Hsu is also apparent. However, it seems from the comparison shown in Fig. 5.28, that the mean values of u_s in Series S1 for values of τ_*/τ_{*c} close to unity are much higher than expected. Indeed, a value $\tau_*/\tau_{*c} = 1$ implies threshold conditions for

particle motion, and therefore a low, if not zero, particle velocity. However it is clear from the results shown in Figs. 5.26 to 5.28 that saltation occur for values τ_*/τ_{*c} of about 1, which indicates that the estimation of τ_{*c} using Shields would not be suitable for a particle lying over a bed of similar particles. As discussed in Section 5.3.4, a reduction of τ_{*c} in such situation can be expected, which would explain the high observed values of u_s at low values of τ_*/τ_{*c} with τ_{*c} estimated using Shields.

Evaluation of the grain Froude number for the experiments of Series S1 gives values of F_g^2 in the range 0.31 to 0.43, with a mean value of about 0.36, which is very close to the value of 0.33 obtained for the experiments with gravel of Series G1 and G2. These values are also similar to those estimated by Leeder (1979) for Abbott and Francis' (1977) experiments. According to Leeder, values of F_g much lower than unity imply that upward forces other than those arising from particle collision with the bed must drive the particle motion during saltation.

The characterization of the bed normal component of the particle velocity during saltation in the experiments of Series S1 shown in Figs. 5.19 and 5.20 indicates that maximum dimensionless values of this variable in the upward phase of the trajectory are in the range 0.5 to 5.5, with a mean value in the range 1.0 to 2.0. These values are similar, although of opposite sign, to those observed in the downward phase of the trajectory. From the frequency analysis presented in Fig. 5.20, there appears to be a slight tendency for the maximum bed normal particle velocities to be somewhat larger in magnitude in the upward phase than in the downward phase of the trajectory. Interestingly, although the sand particles of Series S1 were not entrained into suspension by the flow, as discussed in Chapter 7, the bed normal component of the particle velocity during the upward phase of the saltation is of the same order of magnitude as that measured during the entrainment of particles into suspension by flow ejection events as discussed in Chapter 8.

It must be pointed out however that the turbulence of the flow seems to play a much less important role on the motion of particles in the saltation mode than during ejection-into-suspension events. In fact, saltation trajectories such as those shown in Fig. 5.13 rarely exhibit variations that could be caused by turbulent fluctuations of the flow velocity. Particle motion during saltation appears to be controlled mainly by streamwise momentum transfer from the mean flow to the particle, and the process of particle collision with the bed that redistributes part of the streamwise particle momentum into vertical momentum, which maintains the saltation as a self sustained process.

Further analysis of the characteristics of saltation of sand is presented in Chapter 6, where the results of a numerical simulation of particle saltation is reported. The results of the numerical

simulation is used to explain some of the features of the observed saltation trajectories of sand particles and the differences with respect to the saltation of coarser particles.

Statistics of particle collision with the bed

Estimated values of the dynamic friction coefficient for the experiments of Series S1 shown in Fig. 5.21 appear to be fairly independent of τ_*, with a mean value of about 0.25. A comparison of these results with those obtained in the experiments with gravel of Series G1 and G2, and those by Francis (1973) and Abbott and Francis (1977) is presented in Fig. 5.29, where μ_d is plotted as a function of the ratio τ_*/τ_{*c}. As seen therein the value of μ_d for the fine sand of Series S1 is very close to the value of about 0.3 obtained in the experiments with gravel, much lower than the value 0.8 predicted numerically by Sekine and Kikkawa (1992) and in relatively good agreement with the value 0.32 obtained experimentally by Bagnold (1956) for smooth spheres. Besides, the value of μ_d obtained in Series S1 and in the gravel experiments are somewhat smaller than the values of about 0.4 obtained by Francis and Abbott and Francis (Fig. 5.29), which are also smaller than the value of 0.63 (equal to the static friction coefficient, *tan* ϕ, of natural sediment) predicted by Bagnold (1973), as discussed in Section 5.3.4.

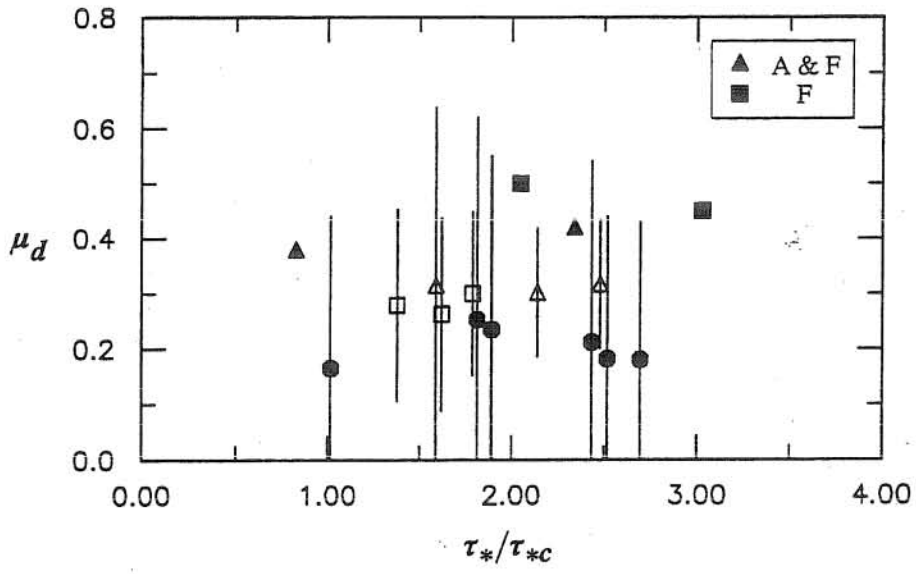

Fig. 5.29 Dynamic friction coefficient. Symbols represent mean values, vertical lines represent a total length of two standard deviations. In the legend, A & F denotes Abbott and Francis (1977), and F denotes Francis (1973). All other symbols are as in Figs. 5.25 to 5.27.

According to Abbott and Francis (1977) their values of μ_d are smaller than that predicted by Bagnold (1973) as consequence of a bias introduced by the inability to accurately determine particle velocities just before and after the collision with the bed from the experimental observations. This explanation seems plausible given the rate of 40 Hz used by these researchers to acquire images of

particle motion. However, the high-speed video system used to analyzed particle motion in Series S1 allowed a recording rate about 6 times faster, which would improve the resolution of the moment of collision substantially. Accordingly, the estimation of μ_d in Series S1 must be considered much more accurate than in all other experimental studies revised herein, and therefore this suggests that the value of μ_d would be actually lower than $tan\ \phi$, in agreement with Bagnold's earlier ideas and all experimental data available.

The analysis of the collision with the bed shows that incidence angles are in the range 0° to 50°, while takeoff angles spread out in the range 0° to 80° (Fig. 5.22). These ranges are very similar to those observed in the experiments with gravel of Series G1 and G2 (Fig. 5.6). Fig. 5.23 shows that mean values of both, θ_{in} and θ_{out} tend to decrease as τ_* increases, with trends that are almost parallel to each other. On the other hand, corresponding standard deviations are about 60 to 80% of the mean values, similar for both incidence and takeoff angles. A comparison of the results shown in Fig. 5.23 with those obtained in the gravel experiments is presented in Fig. 5.30, where mean values of incidence and takeoff angles are plotted as functions of the ratio τ_*/τ_{*c}. As seen therein, mean values of both incidence and takeoff angles in the gravel experiments are larger than corresponding values in the fine sand experiments of Series S1 for values of τ_*/τ_{*c} lower than about 2.5. Both incidence and takeoff angles are seen to decrease with increasing τ_*/τ_{*c} (with parallel tendencies) in both series of experiments, although the data corresponding to the gravel experiments define a slope that is about three times larger than that of the fine sand experiments.

The initiation of saltation occurred generally through a transient rolling motion during which the saltating particle rolls over a bed particle, which allows for the conversion of streamwise momentum into vertical momentum. It seems possible that turbulent bursting events related to both flow ejections and sweeps may have some influence on the initiation of saltation. In fact, flow ejections would directly transfer vertical momentum to the particle, while sweeps would increase the particle streamwise momentum which could be converted into vertical momentum through the rolling motion discussed previously. Mean values and standard deviations of the takeoff angles during the initiation of saltation for the experiments of Series S1 were plotted in Fig. 5.24. As seen therein, they do not differ much from the takeoff angles after collision with the bed. Mean values of the takeoff angles in both situations are in the range 20° to 30° and tend to decrease with τ_*. Corresponding standard deviations are about 60 to 80% of the mean values.

The high temporal resolution provided by the high-speed video system used in the experiments of Series S1 allows for much more detailed observations of the collision process than those obtained with standard video. According to the present observations, most of the interactions between the saltating fine sand particles and the bed were of the collision-rebound type. An example of this type

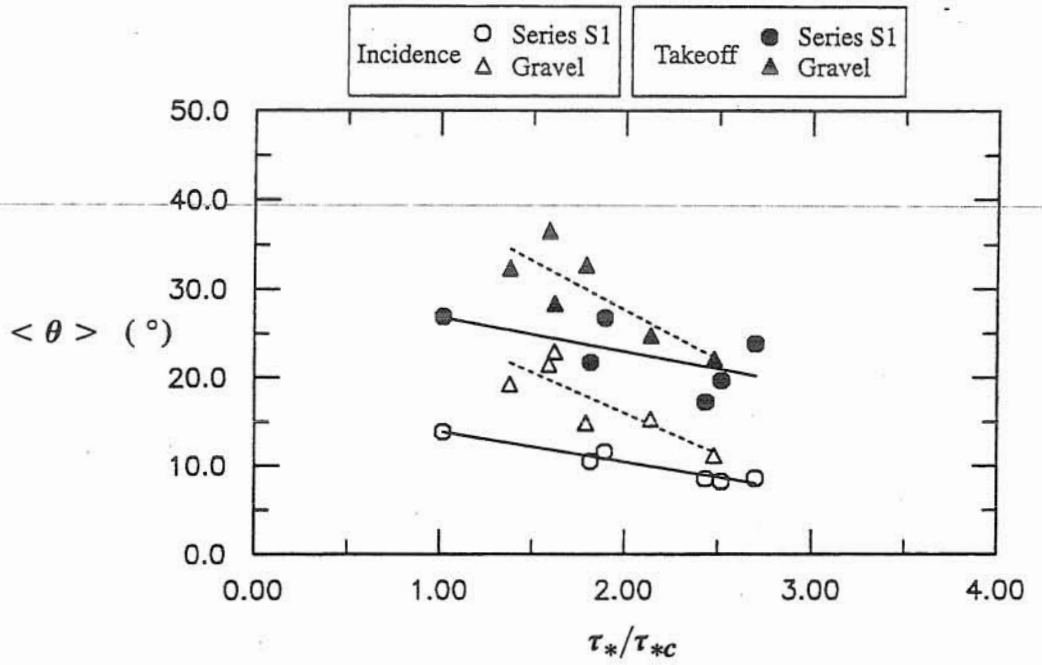

Fig. 5.30 Mean incidence and takeoff angles at collision. Lines represent linear relationships fitted to the respective sets of data. Solid lines correspond to experiments of Series S1, dashed lines correspond to experiments of Series G1 and G2.

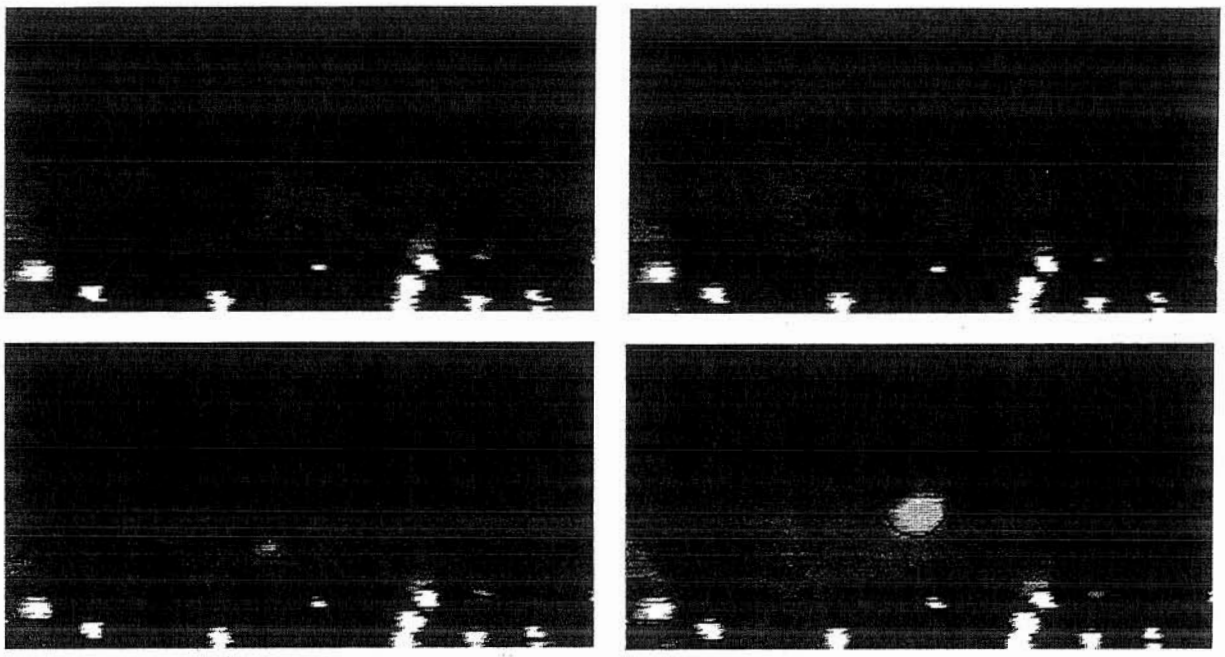

Fig. 5.31 Sequence of images of a collision-rebound event. Field of view is 7.4 mm by 3.8 mm, time interval between images is 0.004 s. Experiments of Series S1, d_p = 0.9 mm, R_p = 108.6, τ_*/τ_{*c} = 1.2.

of interaction is presented in Fig. 5.31, which shows a sequence of images taken 0.004 s apart of a saltating particle moving downward, colliding with a bed particle, and rebounding upward to continue the saltation motion. This is concrete proof that collision-rebound is possible, and argues against statements by Gordon et al. (1972) and Abbott and Francis (1977) denying such possibility.

Determination of the splash function

Following the same procedure explained in Section 5.3.4, the velocity coefficients e and f were estimated for the saltation of fine sand using the results for the collision with the bed of Series S1. From (5.10) and (5.11), e and f are functions of incidence and takeoff angles and particle velocities at collision, and the bed angle θ_b (Fig. 5.9). Unfortunately, the angle θ_b is rather difficult to measure. In fact, although enough images of the moment of collision acquired in the present study are sufficiently clear as to try to measure the angle θ_b, it seems that this angle depends on the surface landscape of the colliding particles, which is impossible to resolve from the images available. Because of this, the same stochastic model described in Section 5.3.4, based on a description of saltating and bed particles as spheres, was used herein to estimate θ_b as the expected value shown in Fig. 5.10b.

The resulting values of e and f are plotted in Fig. 5.32 as functions of τ_*. Values of f are fairly constant, independent of τ_*, with a mean value of about 0.89, whereas values of e are in the range 0 to 0.4, and show a clear tendency to decrease as τ_* increases. A comparison of these results with those of the gravel experiments of Series G1 and G2 is shown in Fig. 5.33, where the values of e and f are plotted as functions of the ratio τ_*/τ_{*c}. As seen in this figure, the values of f corresponding to the fine sand experiments tend to be somewhat larger than those corresponding to the gravel experiments, although in both cases f appears to be independent of τ_*/τ_{*c}. This seems to imply that the collision of fine sand is associated with slightly less friction than the collision of gravel particles, which is in agreement with the fact that the dynamic friction coefficient, μ_d, is slightly smaller in the former case than in the latter (Fig. 5.29). On the other hand the values of e in both fine sand and gravel experiments suggest a unique tendency to decrease with τ_*/τ_{*c}. In fact the following linear relationship can be fitted to all the e data:

$$e = 0.75 - 0.25\ \tau_*/\tau_{*c} \tag{5.15}$$

which is very similar to (5.13) obtained from the gravel data only, and predicts vanishing values of e for values of τ_*/τ_{*c} larger than 3.

The results shown in Fig. 5.33 indicate that only about 70% to 90% of the tangential component of particle velocity is conserved at collision, which contradicts the argument of Gordon et al. (1972) who affirm that all such component would be conserved. The latter would imply no

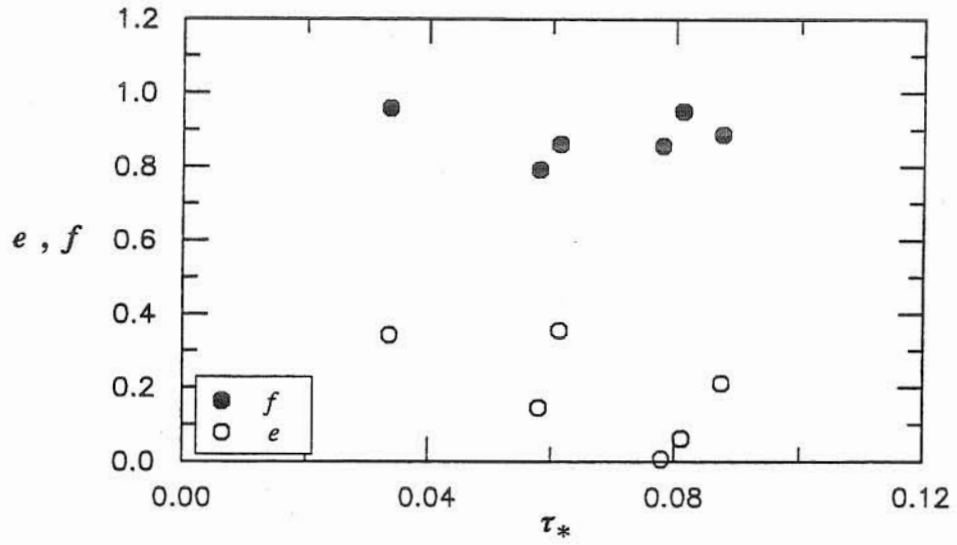

Fig. 5.32 Values of the tangential and normal velocity coefficients. Experiments of Series S1.

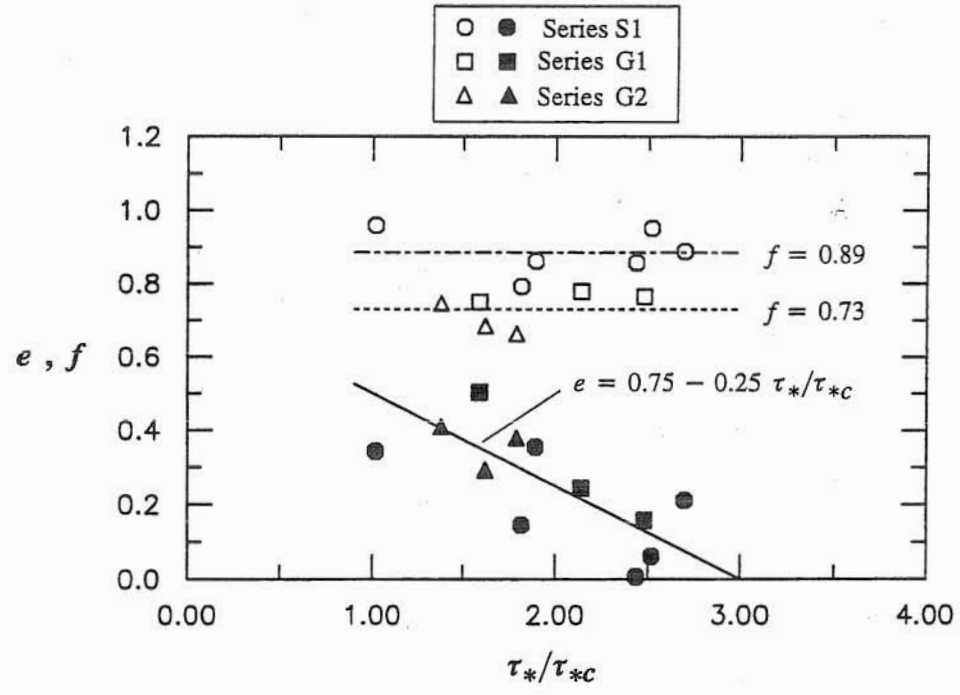

Fig. 5.33 Values of the tangential and normal velocity coefficients. Experiments with gravel of Series G1 and G2 and with fine sand of Series S1.

friction which does not make sense physically. With respect to the normal component of the particle velocity the results shown in Fig. 5.33 indicate that generally less than 40 % of the downward velocity is converted into upward velocity, and that eventually all this component is lost at impact, for values of τ_*/τ_{*c} larger than about 3.

Statistics of particle rotation

As seen in Fig. 5.25 the dimensionless mean particle angular velocity during saltation, S, have values in the range from about 2 to 4, with a tendency to decrease as τ_* increases. This tendency seems to come mainly for the variation of u_* with τ_*, since the data for the dimensional particle angular velocity Ω indicates that this variable is fairly constant, independent of τ_*, having values of about 95 to 105 Hz (about 15 to 17 rev/sec). The standard deviations of S are in the range of about 20 to 50% of the mean values.

In Fig. 5.34 the values of S shown in Fig. 5.25 have been plotted as a function of τ_*/τ_{*c}. A linear relationship can be fitted to the experimental data, such that:

$$S = 5.11 - 1.13\ \tau_*/\tau_{*c} \tag{5.16}$$

which has also been plotted in Fig. 5.34, and allows to estimate the particle angular velocity during saltation given a value of the ratio τ_*/τ_{*c}.

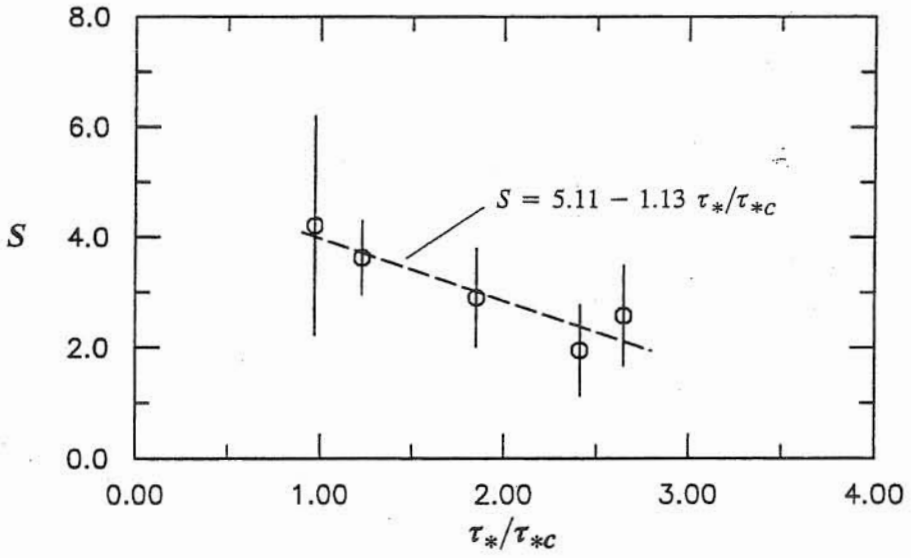

Fig. 5.34 Dimensionless particle angular velocity during saltation. Symbols represent mean values, vertical lines represent a total length of two standard deviations, dashed line represents a linear relationship fitted to the mean values. Experiments of Series S1.

As expected, the mean values of Ω for the saltation of sand in water measured in the experiments of Series S1 are much lower than those reported for wind saltation, because of the reduced fluid viscosity in the latter case. In fact, White and Schulz (1977) presented some limited

empirical evidence which indicates that in the case of wind saltation, Ω would take values of about 100 to 500 rev/sec, while Chepil (1945) suggested values of Ω as high as 1000 rev/sec in such case.

On the other hand, according to Lee and Hsu (1994), Hui and Hu (1991) reported values of Ω of about 40 rev/sec for saltation in water, which appear to be about 2.5 higher than the values of this variable observed herein. Unfortunately Hui and Hu's report is in Chinese, and Lee and Hsu do not give details about the experimental conditions or the methods used to measure the spin rate of the particles.

Lee and Hsu (1994) conclude that in order to match the numerical results of a model for sediment saltation in water with their observations of particle trajectories in such situation, they needed to include the extra lift given by the Magnus force estimated using Rubinow and Keller's (1961) equation, with values of Ω of about 60 to 70 rev/sec. The present results of Series S1 indicate that these values of Ω are rather high. This can be explained by noting that in general, Lee and Hsu's saltation heights and lengths are much larger than those corresponding to all other empirical evidence available (Figs. 5.26 and 5.27). It is also possible that some error in the estimation of the Magnus force in the case of saltation of natural sediment in water using Rubinow and Keller's (1961) equation might occur, since this equation was originally derived for the case of spheres at vanishingly small values of the particle Reynolds number.

5.4.4 Experiments of Series S2

5.4.4.1 Experimental results

Resting time and particle re-entrainment

From the plan view recordings of particle motion performed during experiments of Series S2, observations regarding particle resting time, and the characteristics of the initiation of particle motion from rest can be easily obtained. Unfortunately, because the field of view required to resolve individual particles with the high-speed video system was of rather small dimensions, other interesting variables characterizing particle motion, such as the number of jumps a particle experiences before coming to rest, could not be measured.

The resting time, T_r, is defined as the time elapsed between the moment a given particle comes to a stop and the moment it resumes motion. In dimensionless terms, this variable is expressed as:

$$t_r = T_r \, u_*/d_p \tag{5.17}$$

Mean values and standard deviations of t_r computed from estimations of this variable extracted from the analysis of the video recordings is presented in Fig. 5.35 as a function of τ_*. It is important to note therein that the maximum value of τ_* for which t_r was measured is about 0.06, which corresponds to about 2/3 of the maximum values of this variable in the experiments of Series

S1. This is because at large values of τ_* (or equivalently at large values of the Reynolds number of the flow) free surface oscillations induced too much blur in the plan view video observations, which affected the quality of the images.

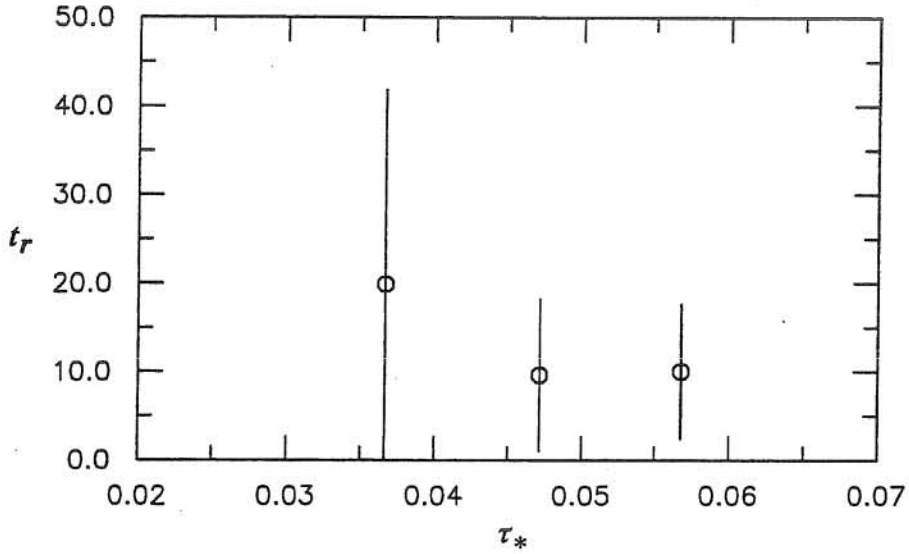

Fig. 5.35 Dimensionless particle resting time. Symbols represent mean values, vertical lines represent a total length of two standard deviations.

From the video observations, two different situations for the initiation of particle motion from the rest could be identified. The first situation corresponds to cases in which the particle resumed its motion apparently driven by the turbulence of the flow alone. In the second situation, the particle resumed its motion due to interactions with other particles. Table 5.3 shows the relative frequency of occurrence of each of these situations, in terms of the ratio between the number of occurrences of a particular type of entrainment event and the total number of entrainment events observed.

Table 5.3 Frequency of occurrence of different type of re-entrainment events

Exp	τ_*	% Case a)	% Case b)
S21	0.037	92	8
S22	0.047	60	40
S23	0.057	64	36

Case a) Re-entrainment due to turbulence effects
Case b) Re-entrainment due to particle-particle interactions

Particles forming the bed of the experimental channel were fixed to the bottom. On top of such bed, the externally fed, loose particles moved intermittently through the system. Those particles were observed to come to rest when they got trapped in some kind of hole or obstacle in the local topography of their surroundings. While at rest, the particles remained more or less exposed to the flow depending on the local configuration of the bed where they were located. In those

re-entrainment events which were classified as turbulence driven in Table 5.3, no other moving particles were observed in the neighborhood of the particle at the moment of entrainment, such that it is apparent that some large magnitude flow velocity fluctuation, perhaps related to sweep or ejection events, induced the particle motion. In those cases in which the initiation of motion was induced by the interaction with other particles, such interaction was usually in the form of a moving particle touching the entrained particle while the former was either saltating or rolling over the latter, or passing it by the side. Although it is difficult to tell from the analysis of the video recordings, it is apparent that the interactions almost always involved some kind of contact between the particles, although this contact was not in the form of a violent collision.

Characterization of transverse particle motion

Trajectories of moving particles in the x-z plane were obtained by tracking individual particles along successive video frames recorded in the experiments of Series S2. A few examples of the typical trajectories observed are shown in Fig. 5.36, where x_p and z_p denote coordinates of particle centroid in the streamwise and transverse directions, respectively, made dimensionless with d_p.

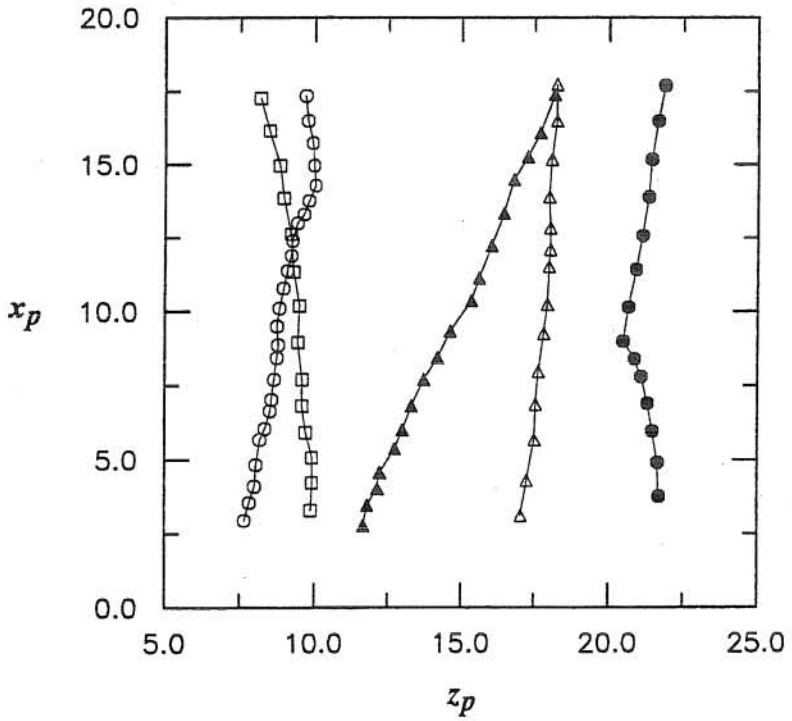

Fig. 5.36 Examples of typical dimensionless particle trajectories in the x-z plane. Symbols correspond to measurements taken 0.004 s apart. Experiment S23.

By observing the particle motion from the top, it is difficult to tell whether the particle is moving in the saltation or rolling mode, nevertheless such differentiation can be made in some cases by analyzing the trajectories of the particles. In general, symbols that appear to be more spaced correspond most likely to saltating particles (which move faster through the field of view of the

camera), while symbols that tend to overlap most likely correspond to rolling particles (which are typically associated with lower velocities).

In some cases an abrupt change of direction of the particle trajectory was observed, which was usually caused by a rather tangential collision with a bed particle. In such an event, part of the streamwise component of particle momentum is transferred into its transverse component which causes the particle to move diagonally with respect to the streamwise direction. In some other cases, the particle trajectory was observed to curve or display some relatively mild change of direction while the particle was apparently saltating. In such situations it is apparent that the particle was being driven by cross-flows associated with turbulent velocity fluctuations.

Statistics of particle streamwise velocity

From the analysis of plan view recordings of particle motion in the experiments of Series S2, the streamwise mean particle velocity, U_p, was measured by tracking individual particles along successive video frames. This variable was made dimensionless using u_* such that:

$$u_p = U_p/u_* \tag{5.18}$$

Herein u_p is distinguished from the mean dimensionless streamwise saltation velocity defined previously, u_s, because in the measurement of the former saltation and rolling events were both included indistinctly in the analysis.

Mean values and standard deviations of u_p estimated from the analysis of the plan view images are presented in Fig. 5.37. Therein, mean values and standard deviations of u_s measured from the side views recordings shown previously in Fig. 5.21 are also plotted for comparison purposes

5.4.4.2 Analysis of experimental results

Resting time and particle re-entrainment

As shown in Fig. 5.35, mean values of the dimensionless resting time, t_r, are in the range 10 to 20, which correspond to dimensional values of this variable in the range of about 0.3 to 0.7 sec. The mean values of t_r appear to decrease as τ_* increases. Corresponding standard deviations of t_r are about 80% to 112% of the mean values, which implies a large variability in the values of the resting time, and they tend to be larger at lower values of τ_*.

As already discussed, the resuming of particle motion appears to be controlled either by the turbulence of the flow or by particle-particle interactions. In the first case it is apparent that bursting events, being them sweeps or ejections (see Chapter 3 for definitions), would be most responsible for setting particles into motion, mainly because they are associated with large velocity fluctuations responsible for the production of most of the turbulent kinetic energy of the flow (Robinson, 1991). Indeed, some field measurements of sediment transport by tidal currents suggest that bedload

movement of sea-bed gravel is caused principally by bursting activity, with sweep-type events being more effective than outwards ejections in transporting sediment (Heathershaw and Thorne, 1985). Since the frequency and intensity of sweep and ejection events tend to increase with u_* (see Chapter 3), then it is expected that as u_* increases (τ_* increases) the particle resting time would tend to decrease, in agreement with the present observations. On the other hand, as τ_* increases so does the number of particles moving per unit time per unit bed area (i.e. the bedload), which obviously increases the number of re-entrainment events due to particle-particle interactions so reducing the resting time, also in agreement with the results of Fig. 5.35.

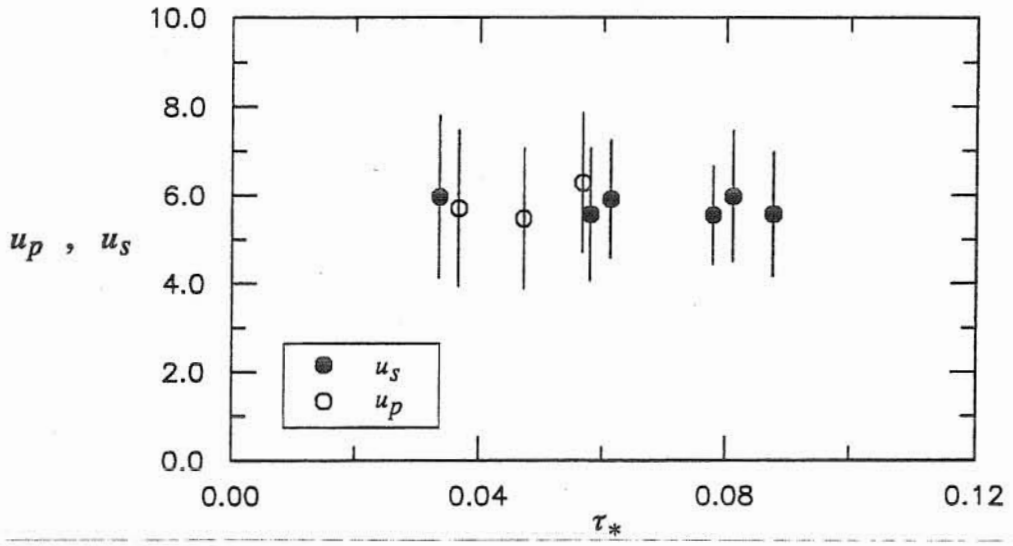

Fig. 5.37 Dimensionless particle streamwise velocity measured form plan view video recordings, u_p. Comparison with dimensionless streamwise saltation velocity, u_s. Symbols represent mean values, vertical lines represent a total length of two standard deviations. Experiments of Series S2.

The results shown in Table 5.3 indicate that while at low values of τ_* most of the re-entrainment events are caused by turbulence effects, as τ_* increases the effect of particle-particle interactions tend to become more important. This is expected since as τ_* increases the bedload increases and so does the probability of occurrence of particle-particle interactions, which would enhance the relative importance of the latter in the number of re-entrainment events occurring in the system. It is important to recall, however, that since the amount of particles moving at a given time in any particular region of the bed is controlled in the present experimental setup mainly by the external feeding (i.e. it does not result from an internal equilibrium of the system), the particular values of the frequency of occurrence of one or another mechanism for particle re-entrainment shown in Table 5.3 have only qualitative significance, and should not be considered as characteristic of an equilibrium situation.

Characterization of transverse particle motion

As seen in Fig. 5.36, particle trajectories in the x-z plane show some deviation from the streamwise direction, with angles that appear to range from positive to negative values with zero mean. The estimated cumulative probability distribution of the absolute value of the angles of deviation, α_d, from the streamwise direction of the particle trajectories analyzed in Series S2 is shown in Fig. 5.38. This distribution appears to be independent of τ_*, so the result plotted in Fig. 5.38 corresponds to the cumulative probability computed over all the trajectories analyzed independently of their τ_* value.

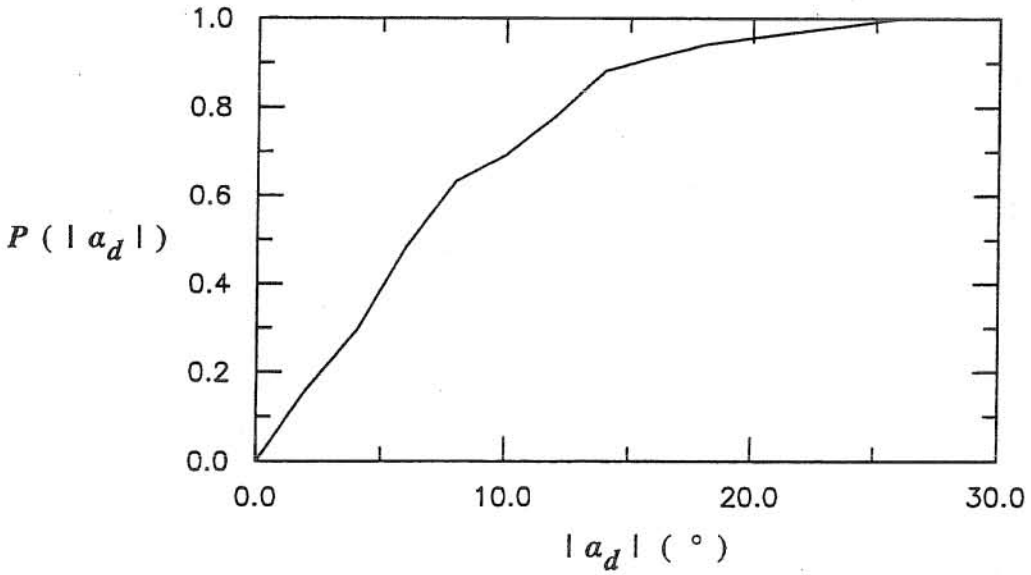

Fig. 38 Cumulative probability distribution function of the absolute value of the deviation angle, α_d, of the particle trajectories with respect to the streamwise direction. Experiments of Series S2.

From Fig. 5.38, it seems that 90% of the deviation angles are lower than about 15°. Similarly, 50% of those angles appear to be lower than about 6°. The mean and standard deviations of the absolute value of α_d are plotted in Fig. 5.39 as a function of τ_*. As seen therein, the mean of the absolute values of the deviation angle appears to be independent of τ_*, as discussed previously, and equal to about 7.5°. Corresponding standard deviations are about 70% to 80% of the mean values.

As already pointed out, the deviation of the particle trajectories from the streamwise direction seems to be caused by two mechanisms, the first is associated with the initial condition imparted by a collision with a bed particle, while the second would be related to cross-flow turbulent events. Although in some of the trajectories analyzed it seems possible to distinguish which one of these processes is taking place, most of the times this is not the case, and eventually both processes could be operating at the same time. Because of this no distinction of the processes was made in the analysis of the deviation angles presented in Figs. 5.38 and 5.39.

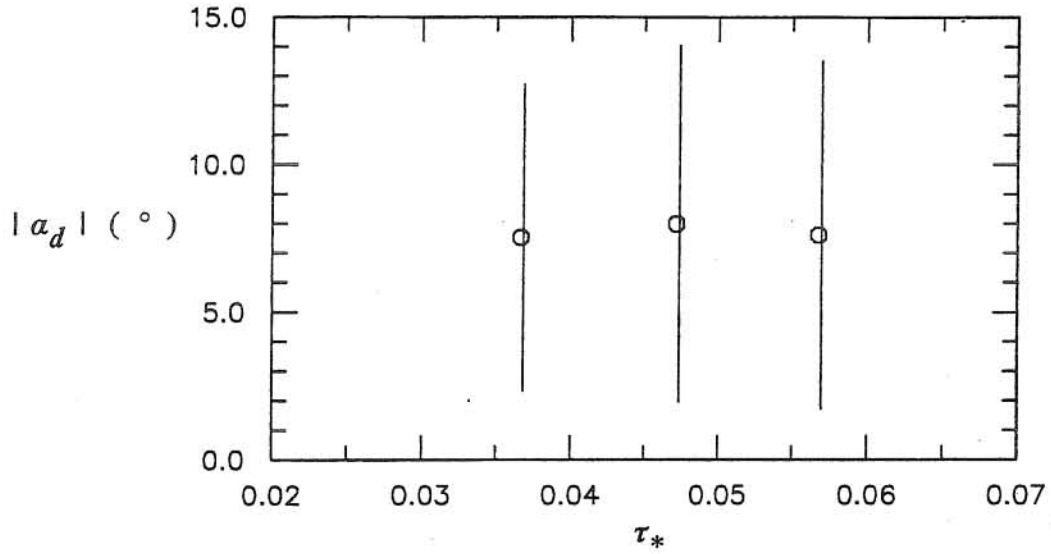

Fig. 5.39 Absolute value of the deviation angle, a_d, of the particle trajectories with respect to the streamwise direction. Symbols represent mean values, vertical lines represent a total length of two standard deviations. Experiments of Series S2.

In any case it seems that, statistically, particle trajectories do not deviate significantly from the streamwise direction. For example, considering a typical deviation angle of about 7.5°, and a dimensionless saltation length, λ_s, of about 10, then the total transverse displacement of the particle in one saltation event is slightly larger than about one particle diameter. From a conceptual point of view this result has importance in that it seems that each individual saltation event could be modelled basically as a two-dimensional process without incurring in important errors. This conclusion somehow validates the two-dimensional analysis of particle saltation presented in Chapter 6.

On the other hand, given the stochastic nature of the deviation of the saltation trajectory from the streamwise direction, it is apparent that several repetitions of the saltation process would lead to a transverse dispersion process for the bedload, in which the variance of the particle transverse position increases in time. The phenomenon of transverse dispersion of bedload particles may have importance in some fluvial processes, such as the development of stable channel cross-section (e.g., Ikeda et al., 1988), or the formation of longitudinal streaks which are typically observed in wide erodible-bed channels (e.g., Colombini, 1993).

Statistics of particle streamwise velocity

From Fig. 5.37 it is apparent that mean values of u_p are relatively constant, independent of τ_*, with values of about 6, and that corresponding standard deviations are about 30% of the mean values. As seen therein, mean values and standard deviations of u_p do not seem to differ much from mean values and standard deviations of u_s, although there is some tendency for the mean values of the

former to be slightly smaller than those of the latter, particularly for values of τ_* lower than about 0.05.

As already discussed, in the estimation of u_p no distinction was made of the mode of particle motion (rolling or saltation). Since in general it is apparent that the particles move faster in the saltation mode, it is expected for u_p to be somewhat smaller than u_s, maybe more so than observed in Fig. 5.37. Nevertheless, it is possible that in the digitization process the sampling of rolling particles may have been biased toward particles that were moving relatively faster, since their displacement through the field of view of the camera is more evident and easier to track from the frame by frame analysis of the video recordings. Since particle motion in the rolling mode tend to be less frequent than in the saltation mode, especially as τ_* increases, and to occur mainly as transient motion in between saltation events, then the weight of their associated velocity in the estimation of the mean values of u_p would have been relatively low compared to that of the saltation mode, which would explain the similarities observed in Fig. 5.37 between u_p and u_s.

5.4.5 Conclusions

High-speed video has proved to be an extremely useful tool to study bedload transport of fine sand particles. Characteristic time and length scales of the saltation of sediment in this size range are such that only high rates of image acquisition, such as those given by this equipment, can provide the amount of information needed to resolve details of the Lagrangian properties of particle motion. The results obtained with this technique yield unprecedented data and new insights on the saltation phenomenon of fine natural sand.

Mean values of h_s measured in the experiments of Series S1 are in the range 1.0 to 1.3, while corresponding mean values of λ_s are in the range 6 to 12. Both of these variables increase with τ_*/τ_{*c} for values of this parameter in the range 1 to 3. Mean values of u_s appear to be rather constant, independent of τ_*/τ_{*c}, and equal to about 5.8. Standard deviations of h_s are about 30 to 40% of the mean values, those of λ_s are about 40 to 50% of the mean values, and those of u_s about 20 to 30% of the mean values.

Mean values of h_s corresponding to the experiments with fine sand of Series S1 are similar to those reported by Abbott and Francis (1977), corresponding to relatively coarse particles, and also similar to those corresponding to the gravel experiments of previous section (except those of Series G1, which appear to exceed Abbott and Francis' and Series G2 data). On the other hand, mean values of h_s reported by Lee and Hsu (1994) for fine sand appear to be much larger than all corresponding data discussed above. Values of the standard deviation of h_s measured in the experiments with fine sand of Series S1 are also similar to those corresponding to the gravel experiments of Series G1 and G2.

Mean values of λ_s in the fine sand experiments tend to be somewhat larger than those corresponding to the gravel experiments of Series G1 and G2, and also than those of Abbott and Francis (1977). Again, Lee and Hsu's (1994) data seem to be much higher than all other data revised. Values of the standard deviation of λ_s corresponding to the experiments with fine sand are also somewhat larger than those measured in the gravel experiments. This may be a consequence of the turbulence of the flow which would introduce an extra variability in the saltation process, and which would be more important for smaller particle sizes. Also, this effect seems to influence more the variability of the lengths than that of the heights of the saltation trajectories.

Mean values of u_s corresponding to the experiments with sand tend to be about 1.5 to 2 times as large as those in the gravel experiments, although standard deviations are of similar magnitude in both cases. For values of τ_*/τ_{*c} larger than about 2, mean values of u_s for fine sand agree well with those given by Fernandez-Luque and van Beek's (1976) curve and also with the experimental data by Lee and Hsu (1994). For lower values of τ_*/τ_{*c} mean values of u_s for fine sand tend to be somewhat larger than Fernandez-Luque and van Beek's curve.

Experimental values of F_g^2 in the experiments with fine sand of Series S1 are in the range 0.31 to 0.44, very similar to that measured in the experiments with gravel of Series G1 and G2, which indicates that upward forces other than those arising from particle collision with the bed must drive particle motion during saltation.

Mean values of the maximum dimensionless particle vertical velocity in the upward phase of the saltation trajectories of fine sand are in the range 1 to 2, and they are similar but of opposite sign to those observed in the downward phase of the saltation trajectories.

Estimated values of μ_d for the saltation of fine sand appear to be independent of τ_* with a mean value of about 0.25. This value is close to the value 0.3 obtained for the saltation of gravel, and somewhat smaller than the value 0.4 obtained by Francis (1973) and Abbott and Francis (1977). All of these estimations of μ_d, however, are lower than the value $tan\ \phi = 0.63$ predicted by Bagnold (1973). The high temporal resolution of the present measurements yields a good accuracy to the estimation of μ_d in the experiments of Series S1, which suggests that the values of this variable would be actually lower than $tan\ \phi$, in agreement with all experimental data available.

The analysis of particle collision with the bed in the experiments with fine sand show that incidence angles at collision are in the range 0° to 50°, while takeoff angles spread out in the range 0° to 80°. These ranges are very similar to those observed in the experiments with gravel. Mean values of both, θ_{in} and θ_{out} tend to decrease as τ_* increases, with trends that are almost parallel to each other, similarly as for the gravel experiments. Standard deviations of these variables are about 60 to 80% of the mean values.

The high temporal resolution provided by the high-speed video system yielded concrete proof that the collision-rebound type of interaction between saltating and bed particles is possible, and argues against statements by Gordon et al. (1972) and Abbott and Francis (1977) denying this possibility. The present observations indicate that most of the interactions between saltating fine sand particles and the bed were of this type.

Values of the friction coefficient f in the fine sand experiments are independent of τ_* and have a mean value of about 0.89, whereas values of the restitution coefficient e are in the range 0 to 0.4, and show a clear tendency to decrease as τ_* increases. Values of f for fine sand appear to be slightly larger than those obtained in the gravel experiments, which suggests that the collision in the former case is associated with less friction than in the latter, and which is in agreement with the fact that μ_d is also slightly smaller in the case of fine sand than in the case of gravel.

Mean values of the dimensionless particle angular velocity, S, measured in the experiments of Series S1 are in the range 2 to 4, with a tendency to decrease as τ_* increases. Corresponding standard deviations are about 20 to 50% of the mean values. The present observations indicate that this variable is controlled mainly by the process of particle collision with the bed, and that it tends to be somewhat larger right after impact. Also, the shape of the particle seems to play an important role on the resulting angular velocity.

Mean values of the dimensionless resting time, t_r, observed in the experiments of Series S2 are in the range 10 to 20, with a tendency to decrease as τ_* increases. Corresponding standard deviations are about 80 to 112% of the mean values. Resuming of particle motion from the rest appears to be controlled either by the turbulence of the flow or by particle-particle interactions. At low values of τ_* most of the re-entrainment events are apparently driven by turbulence. As τ_* increases so does the number of saltating particles per unit bed area per unit time, which implies an increasing importance of the particle-particle interactions in the re-entrainment process.

The deviation of particle trajectories from the streamwise direction in the experiments of Series S2 seems to be controlled either by the collisions with the bed or by cross-flows associated with the turbulence of the flow. The present observations suggest that 90% of the deviation angles are lower than about 15°, and that 50% of those angles appear to be lower than 6°. These results imply that during individual jumps particles do not deviate significantly from the streamwise direction, which indicates that this process could be modelled as two-dimensional without incurring in important errors.

Mean values of u_p measured in the experiments of Series S2 are relatively constant, independent of τ_*, with values of about 6. Corresponding values of the standard deviations are about 30% of the mean values. These results do not seem to differ much from those corresponding to u_s

measured in the experiments of Series S1, although there is some tendency for the mean values of u_p to be slightly lower than those of u_s for low values of τ_*.

5.5 References

Abbott, J. E., and Francis, J. R. D. (1977). "Saltation and suspension trajectories of solid grains in a water stream". *Philos. Trans., Royal Soc. of London.* A, 284, pp 225–254.

Anderson, R. S., and Haff, P. K. (1988). "Simulation of eolian saltation". *Science*, 241, pp 820–823.

Ashida, K., and Michiue, M. (1972). "Study on hydraulic resistance and bedload transport rate in alluvial streams". *Proc. Japan Soc. Civ. Engrg.*, 206, pp 59–69.

Ayala, L., and Valenzuela, R. (1993). "Elemental motion of coarse uniform particles and its relation with sediment transport". *Pub. CRH 93–77–I of the Water Resour. Center, Dep. of Civil Engrg, Univ. of Chile*. Santiago, Chile. (In Spanish).

Ayala, L., López A., and Valenzuela, R. (1992). "Elemental particle motion and sediment transport". *Proc. XV I.A.H.R. Latin American Congress of Hydraulics,* Colombia. (In Spanish).

Ayala, L., López A., and Campos, J. (1990). "Incipient particle motion in large–scale–roughness flows". *Pub. CRH 90–64–I of the Water Resour. Center, Dep. of Civil Engrg, Univ. of Chile.* Santiago, Chile. (In Spanish).

Bagnold, R. A. (1956). "The flow of cohesionless grains in fluids". *Philos. Trans., Royal Soc. of London.* A, 249, pp 235–297.

Bagnold, R. A. (1973). "The nature of saltation and of 'bed–load' transport in water". *Proc. R. Soc. of London*. A, 332, pp 473–504.

Bridge, J. S., and Bennett, S. J. (1992). "A model for the entrainment and transport of sediment grains of mixed sizes, shapes, and densities". *Water Resour. Res.*, 28 (2), pp 337–363.

Bridge, J. S., and Dominic, D. F. (1984). "Bed load grain velocities and sediment transport rates". *Water Resour. Res.*, 20 (4), pp 476–490.

Chepil, W. S. (1945). "Dynamics of wind erosion I. Nature of movement of soil by wind.". *Soil Sci.* 60, pp 305-320.

Colombini, M. (199?). "Turbulence-driven secondary flows and formation of sand ridges". *J. Fluid Mech.*, vol 254, pp 701-719.

Drake, T. G., Shreve, R. L., Dietrich, W. E., Whiting, P. J., and Leopold, L. B. (1988). "Bedload transport of fine gravel observed by motion–picture photography". *J. Fluid Mech.*, vol. 192, pp 193–217.

Engelund, F., and Fredsøe, J. (1976). "A sediment transport model for straight alluvial channels". *Nordic Hydrol.*, 7, pp 293–306.

Fernandez–Luque, R., and Van Beek, R. (1976). "Erosion and transport of bed sediment". *J. Hydr. Res.*, 14(2), 127–144.

Francis, J. R. D. (1973). "Experiments on the motion of solitary grains along the bed of a water stream". *Proc. R. Soc. of London*. A, 332, pp 443–471.

García, M., and Niño, Y. (1992). "Lagrangian description of bedload transport by saltating particles". *Proc. VI I.A.H.R. Int. Symp. on Stochastic Hydraulics*, Taipei, Taiwan, pp 259–266.

Gilbert, G. K. (1914). "The transportation of debris by running water". *Prof. Paper 86, US Geological Survey*, Reston, Va.

Gordon, R., Carmichael J. B., and Isackson, F. J. (1972). "Saltation of plastic balls in a 'one–dimensional' flume". *Water Resources Res.*, 8 (2), pp 444–459.

Heathershaw, A. D., and Thorne, P. D. (1985). "Sea-bed noises reveal role of turbulent bursting phenomenon in sediment transport by tidal currents". *Nature*, vol 316, pp 339–342.

Hui, Y., and Hu, E. (1991). "Saltation characteristics of particle motions in water". *Shuili Xuebao*, No 12, pp 59-64 (in Chinese).

Ikeda, S., Parker, G., and Kimura, Y. (1988). "Stable width and depth of self-formed straight gravel rivers with heterogeneous bed materials". *Water Resour. Res.*, 24 (5), pp 713-722.

Lee, H., and Hsu, I. (1994). "Investigation of saltating particle motions". *J. Hydr. Engrg.*, ASCE, 120 (7), pp 831–845.

Leeder, M. R. (1979). "Bedload dynamics: Grain impacts, momentum transfer and derivation of a grain Froude number". *Earth Surface Processes*, vol 4, pp 291–295.

Meland, N., and Norman, J. O. (1969). "Transport velocities of individual size fractions in heterogeneous bedload". *Geographiska Annaler* 51, A, 3, pp 127–144.

Rickenmann, D. (1990). "Bedload transport capacity of slurry flows at steep slopes". *Versuchsanstalt für Wasserbau, Hydrologie und Glaziologie der Eidgenössischen Technischen Hochschule Zürich*, Mitteilungen 103.

Robinson, S. K. (1991). "Coherent motions in the turbulent boundary layer". *Annu. Rev. Fluid Mech.*, 23, pp 601–639.

Rubinow, S. and Keller, J. (1961). "The transverse force on a spinning sphere moving in a viscous fluid". *J. Fluid Mech.*, vol 11, pp 447-459.

Sekine, M., and Kikkawa, H. (1992). "Mechanics of saltating grains. II". *J. Hydr. Engrg.*, ASCE, 118 (4), pp 536–558.

Tsujimoto, T., and Nakagawa, H. (1983). "Stochastic study on successive saltation by flowing water". *Proc. 2nd Int. Symp. on River Sedimentation*, Beijing, China. pp 187–201.

White, B. R. and Schulz, J. C. (1977). "Magnus effect in saltation". *J. Fluid Mech.*, vol. 81, part 3, pp 497-512.

Wiberg, P. L., and Smith, J. D. (1985). "A theoretical model for saltating grains in water". *J. Geophysical Res.*, 90 (C4), pp 7341–7354.

6. MODELLING SALTATION

6.1 Introduction

The main motivation for studying particle saltation in water flows is that kinematic and geometric characteristics of saltation can be used in developing models of bedload transport (Yalin, 1958). Saltation is the dominant mode of bedload transport, with rolling and sliding occurring to a lesser extent, mainly near the threshold of entrainment and in between individual saltation events (Bridge and Dominic, 1984). A typical approach in developing bedload equations has been the use of semi-empirical relationships for the mean velocity of saltating particles and other parameters characterizing saltation (Ashida and Michiue, 1972; Bagnold, 1973; Engelund and Fredsøe, 1976; Bridge and Dominic, 1984; Bridge and Bennett, 1992). It was not until recently that sediment transport rates have been evaluated by using numerical models for particle saltation in water (Wiberg and Smith, 1989; Sekine and Kikkawa, 1992; Sekine and Parker, 1992; García and Niño, 1992).

The numerical description of trajectories followed by saltating particles in water has been attempted by several researchers (e.g., Tsuchiya, 1969; Reizes, 1978; Hayashi and Ozaki, 1980; Murphy and Hooshiari, 1982; Van Rijn, 1984; Wiberg and Smith, 1985; Sekine and Kikkawa, 1992). Basically, all such models consist of a Lagrangian equation governing particle motion, which is coupled with assumptions regarding the boundary conditions for the integration of saltating particle trajectories. It is crucial to evaluate those boundary conditions adequately, particularly taking into account the stochastic nature of the particle collision with the bed, which only Wiberg and Smith (1985) and Sekine and Kikkawa (1992) consider explicitly.

The objective of this chapter is to develop a numerical model for the estimation of the variables describing gravel saltation. The aforementioned models for particle saltation are improved by introducing new data on the stochastic process of particle collision with the bed reported in Chapter 5, as well as a better equation for particle motion. The analysis covers saltation phenomena at different scales of particle sizes, ranging from gravel to fine sand. Different models of bedload transport based on saltation characteristics that can be estimated using the saltation model are analyzed.

6.2 Lagrangian equation for particle motion in an unbounded fluid

One of the most recent and complete forms of the governing equation for the motion of a small spherical particle in an unbounded fluid, within the Stokes drag range, is that presented by Mei et al. (1991), based on the equation proposed earlier by Maxey and Riley (1983). The ith–component of this equation can be written as:

$$\varrho_s \frac{du_p{}^*{}_i}{dt^*} = (\varrho_s - \varrho) g_i - \frac{18\,\mu}{d_p^2} (u_p{}^*{}_i - u_f{}^*{}_i - \frac{1}{24} d_p^2 \nabla^2 u_f{}^*{}_i) +$$

$$+ \frac{9}{d_p} \sqrt{\frac{\varrho\,\mu}{\pi}} \int_0^{t^*} \frac{d}{d\tau} (u_f{}^*{}_i - u_p{}^*{}_i + \frac{1}{24} d_p^2 \nabla^2 u_f{}^*{}_i) \frac{d\tau}{\sqrt{t^* - \tau}} +$$

$$+ \varrho\, C_m \frac{d}{dt^*} (u_f{}^*{}_i - u_p{}^*{}_i + \frac{1}{40} d_p^2 \nabla^2 u_f{}^*{}_i) + \varrho \frac{Du_f{}^*{}_i}{Dt^*} \qquad (6.1)$$

where ϱ_s and ϱ denote particle and fluid densities respectively, C_m denotes added mass coefficient, g_i denotes the component of gravitational acceleration in the ith direction, μ denotes fluid dynamic viscosity, d_p denotes particle diameter, t^* denotes time, τ denotes a dummy variable for integration, and $u_p{}^*{}_i$ and $u_f{}^*{}_i$ denote instantaneous particle and fluid velocity components in the ith direction, respectively. In (6.1), the terms of the right hand side correspond to the following forces per unit volume: submerged gravitational force, Stokes drag, Basset history force, and forces due to added mass and fluid acceleration, respectively, and the flow velocity total derivatives correspond to:

$$\frac{du_f{}^*{}_i}{dt^*} = \frac{\partial u_f{}^*{}_i}{\partial t^*} + u_p{}^*{}_j \frac{\partial u_f{}^*{}_i}{\partial x^*{}_j} \quad , \quad \frac{Du_f{}^*{}_i}{Dt^*} = \frac{\partial u_f{}^*{}_i}{\partial t^*} + u_f{}^*{}_j \frac{\partial u_f{}^*{}_i}{\partial x^*{}_j} \qquad (6.2a, b)$$

where the summation convention for the subindexes, commonly used in tensor notation, applies. Terms showing $\nabla^2 u_f{}^*{}_i$ in (6.1) are normally small as compared with the other terms, and thus they are neglected in the subsequent analysis (Mei et al., 1991).

Since equation (6.1) considers linear (viscous) drag, it is only valid when the particle Reynolds number ($Re = | \boldsymbol{u}_p{}^* - \boldsymbol{u}_f{}^* | \, d_p \, / \nu$, where the bold face represents velocity vectors, and ν denotes fluid kinematic viscosity) is much smaller than unity (Hinze, 1971; Lumley, 1978). In order to extend the governing equation to the nonlinear drag regime, the drag force term in (6.1) can be rewritten in terms of a drag coefficient, C_D, as:

$$-\frac{3}{4} \frac{C_D}{d_p} \varrho \, | \boldsymbol{u}_p{}^* - \boldsymbol{u}_f{}^* | \, (u_p{}^*{}_i - u_f{}^*{}_i) \qquad (6.3)$$

The main problem with (6.3) is that the behavior of C_D in an unsteady particle motion is not known (Yen, 1992), and the only alternative available is to approximate the value of this coefficient by the steady free-falling single sphere drag coefficient. Herein we use the following approximation for C_D as a function of Re, proposed by Yen (1992):

$$C_D = \frac{24}{Re} (1 + 0.15 \sqrt{Re} + 0.017\, Re) - \frac{0.208}{1 + 10^4\, Re^{-0.5}} \qquad (6.4)$$

The Basset term in (6.1) is a type of history term which indicates that the resistance to motion at any given time, due to the unsteadiness of the flow is, in part, a function of the resistance at a

previous time (Brush et al., 1964). As pointed out by Mei (1990), a difficulty in the application of (6.1) to the non-Stokesian drag range is that the behavior of the Basset term is also not known in that range. However, Mei's numerical analysis seems to indicate that the memory of the classical expression for the Basset force is too long, and that the initial transient does not decay fast enough at large times. Mei concludes that the integrand in the Basset force term must decay much faster than $(t^* - \tau)^{-1/2}$ at large times, which was confirmed by Lawrence and Mei (1995), who found that a decay $(t^* - \tau)^{-2}$ would most likely prevail at large times.

Another source of uncertainty in (6.1) is the added mass coefficient. Theoretically, a solid sphere immersed in a potential flow of an inviscid fluid has a value $C_m = 0.5$. This value is commonly used to model the motion of particles in a viscous fluid (Rizk and Elghobashi, 1985; Elghobashi and Truesdell, 1992). However, according to Yen (1992), experimental evidence has shown that the value of C_m for a sphere is greater than 0.5. This appears to contradict the numerical analysis by Mei (1990), which indicates that the force due to the added mass on a sphere at finite Reynolds number would be the same as that given by potential flow theory.

6.3 Equation for sediment particle saltation in a turbulent boundary layer

In order to apply the equation for particle motion to the case of sediment saltation in water flows, it is necessary to consider that the particle Reynolds number is relatively high and that the flow is not unbounded, but corresponds to a boundary layer flow over a rough bed. Furthermore, an equation for the mean particle motion, averaged over turbulence, is sought.

Consider the situation illustrated in Fig. 6.1, where a particle is saltating along a bed formed by similar particles, and inclined to an angle θ with respect to the horizontal. The coordinates in the normal and streamwise directions are denoted by y^* and x^*, respectively, the particle instantaneous velocity components in those directions are denoted by v_p^* and u_p^*, respectively, and the fluid instantaneous velocity components in the same directions are denoted by v_f^* and u_f^*, respectively. Assuming that the instantaneous velocity components consist of a mean and a fluctuation, we can write:

$$u_f^* = \overline{u}_f + u'_f \quad , \quad v_f^* = v'_f \quad , \quad u_p^* = \overline{u}_p + u'_p \quad , \quad v_p^* = \overline{v}_p + v'_p \qquad (6.5a\text{–}d)$$

where overbars represent mean values computed over ensembles of many realizations of the particle saltation, and primes represent fluctuations with respect to the mean. In (6.5), it has also been assumed that the flow has a zero mean velocity in the y^* direction, as it would be the case if the flow is uniform and the boundary layer is completely developed. In such a case: $\overline{u}_f = \overline{u}_f (y^*)$.

Replacing (6.3) and (6.4) in (6.1), ensemble averaging the components of this equation in the y^* and x^* directions over many realizations of the saltation experiments and neglecting terms of

order higher than $O(\ <u'_{ki}\ u'_{lj}>\ /|\overline{u}_R|^2\ )$, where the subindexes k and l indicate whether the velocity corresponds to the particle or to the flow, the subindexes i and j indicate whether the velocity corresponds to the streamwise or vertical component, the angular brackets represent ensemble average, and $\overline{u}_R$ denotes particle slip velocity, such that $|\overline{u}_R|^2 = (\ \overline{u}_p - \overline{u}_f\ )^2 + \overline{v}_p^2$, then the following system of equations is obtained:

$$(\ \varrho_s + C_m\ \varrho\ )\ \frac{d\overline{u}_p}{dt^*} = -\frac{3}{4}\ \frac{C_D}{d_p}\ \varrho\ |\overline{u}_R|\ (\ \overline{u}_p - \overline{u}_f\ ) + \varrho\ C_m\ \overline{v}_p\ \frac{\partial \overline{u}_f}{\partial y^*} + (\ \varrho_s - \varrho\ )\ g\ \sin\theta + \\ + \frac{9}{d_p}\ \sqrt{\frac{\varrho\ \mu}{\pi}}\ \int_0^{t^*} \frac{d}{d\tau}(\ \overline{u}_f - \overline{u}_p\ )\ \frac{d\tau}{\sqrt{t^* - \tau}} \qquad (6.6a)$$

$$(\ \varrho_s + C_m\ \varrho\ )\ \frac{d\overline{v}_p}{dt^*} = -\frac{3}{4}\ \frac{C_D}{d_p}\ \varrho\ |\overline{u}_R|\ \overline{v}_p + (\ \varrho - \varrho_s\ )\ g\ \cos\theta - \\ - \frac{9}{d_p}\ \sqrt{\frac{\varrho\ \mu}{\pi}}\ \int_0^{t^*} \frac{d\overline{v}_p}{d\tau}\ \frac{d\tau}{\sqrt{t^* - \tau}} \qquad (6.6b)$$

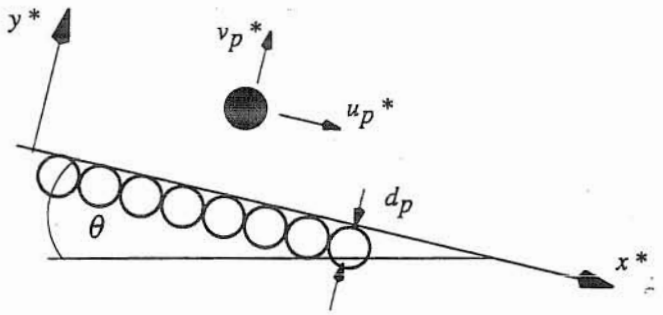

Fig. 6.1 Definition sketch for saltating particle.

It is important to notice that neglecting second order terms in (6.6) implies neglecting turbulence effects on the saltation process. Although this may not introduce large errors in the case of saltation of large size particles which due to their large inertia tend not to respond to high frequency fluctuations of the flow velocity, it seems that the opposite may be true in the case of smaller particles. Keeping higher order terms in (6.6) requires introducing closures for the auto- and cross-correlations of particle and fluid velocity, which would over-complicate the present model. As it is shown later in this chapter, this does not appear to have a major impact on the simulations of particle saltation as compared with the experimental observations reported in Chapter 5. A detailed analysis of turbulent effects on particle saltation is presented in Chapter 9.

As the mean flow velocity gradient in the y^* direction can be large in the region close to the bed, and since the particle sizes considered in the present analysis are also large, a lift force in the y^* direction, such as that used by Wiberg and Smith (1985), must be taken into account. Following

Wiberg and Smith, the lift force term to be added to the right hand side of (6:6b) can be estimated as:

$$\frac{3}{4}\frac{C_L}{d_p}\,\varrho\,(\,|\overline{u}_R|_T^2 - |\overline{u}_R|_B^2\,) \tag{6.7}$$

where the subindexes T and B denote particle top and bottom, respectively, so:

$$|\overline{u}_R|_T^2 = (\,\overline{u}_p\,(\,y_p{}^*\,) - \overline{u}_f\,(\,y_p{}^* + \frac{d_p}{2}\,)\,)^2 + \overline{v}_p^2\,(\,y_p{}^*\,) \tag{6.8a}$$

$$|\overline{u}_R|_B^2 = (\,\overline{u}_p\,(\,y_p{}^*\,) - \overline{u}_f\,(\,y_p{}^* - \frac{d_p}{2}\,)\,)^2 + \overline{v}_p^2\,(\,y_p{}^*\,) \tag{6.8b}$$

and $y_p{}^*$ denotes the y^* coordinate of the centroid of the saltating particle. Much less is known about the lift coefficient, C_L, than about the drag coefficient, C_D. Based on the measurements of lift and drag forces on immobile hemispheres near a boundary made by Chepil (1958), Wiberg and Smith (1985) proposed a mean value $C_L = 0.2$, which is used herein.

An alternative way for estimating the lift force term is that proposed by Patnaik et al. (1994), who measured the lift force acting on fixed spheres immersed in a wind tunnel flow. Following their definition of the lift coefficient C_L, the lift force term to be added to the right hand side of (6.6b) can be estimated as:

$$\frac{3}{4}\frac{C_L}{d_p}\,\varrho\,|\overline{u}_R|^2 \tag{6.9}$$

Patnaik et al.'s (1994) results indicate that C_L decreases with increasing values of Re and the ratio $d_p/y_p{}^*$, with values of C_L in the range 0.15 to 0.40 for values of $d_p/y_p{}^*$ in the range 0.2 to 0.5. Unfortunately, Patnaik et al. present only a few experimental points in the range of values of $d_p/y_p{}^*$ larger than 0.5, which as discussed in Chapter 5 correspond to the range of values of this parameter associated with particle saltation, and furthermore those results show large scatter. Based on this, it seems that (6.7) may give a more reliable estimation of the lift force term to be used in (6.6) than (6.9).

Eventually, the rotation of the saltating particle can introduce another force in the y^* direction, known as Magnus force. In order to evaluate this force the following term, proposed by White and Schulz (1977), and derived originally by Rubinow and Keller (1961) for spheres at vanishingly small values of Re, is added to the right hand side of (6.6b):

$$\frac{3}{4}\,\varrho\,|\overline{u}_R|\,(\,\Omega - \frac{1}{2}\frac{\partial \overline{u}_f}{\partial y^*}\,) \tag{6.10}$$

where Ω denotes particle angular velocity. The main shortcoming of (6.10) is that Ω is an external variable that must be estimated a priori. From the observations made in the experiments reported

in Chapter 5, it is apparent that the particle angular velocity is controlled mainly by the particle collision with the bed, which makes this variable highly random, and thus difficult to estimate.

Introducing lift and Magnus terms, (6.8) and (6.10), in (6.6) and making the resulting equation dimensionless by introducing the scaling:

$$(x^* , y^*) = d_p (x , y) \quad , \quad (\overline{u}_p , \overline{v}_p) = u_* (u_p , v_p) \qquad (6.11a, b)$$

$$t^* = (d_p / u_*) t \quad , \quad \overline{u}_f = u_* u_f \qquad (6.11c, d)$$

with u_* denoting fluid shear velocity, the following equations are obtained:

$$\frac{du_p}{dt} = -\frac{3}{4} \alpha C_D |u_R| (u_p - u_f) + \alpha C_m \frac{du_f}{dy} v_p + \frac{\alpha \sin\theta}{\tau_*} + $$

$$+ 9 \frac{\alpha}{\sqrt{R_p}\, \tau_*^{1/4}} \frac{1}{\sqrt{\pi}} \int_0^t \frac{d}{d\tau} (u_f - u_p) \frac{d\tau}{\sqrt{t-\tau}} \qquad (6.12a)$$

$$\frac{dv_p}{dt} = -\frac{3}{4} \alpha C_D |u_R| v_p + \frac{3}{4} \alpha C_L (|u_R|_T^2 - |u_R|_B^2) - \frac{\alpha \cos\theta}{\tau_*} -$$

$$- 9 \frac{\alpha}{\sqrt{R_p}\, \tau_*^{1/4}} \frac{1}{\sqrt{\pi}} \int_0^t \frac{d}{d\tau} (v_p) \frac{d\tau}{\sqrt{t-\tau}} + \frac{3}{4} \alpha |u_R| (S - \frac{1}{2} \frac{du_f}{dy}) \qquad (6.12b)$$

Dimensionless parameters appearing in (6.12) are defined as:

$$\alpha = (1 + R + C_m)^{-1} \quad , \quad R = (\varrho_s / \varrho - 1) \quad , \quad R_p = \sqrt{R\, g\, d_p^{\,3}} / \nu \qquad (6.13a–c)$$

$$\tau_* = \frac{u_*^2}{g\, R\, d_p} \quad , \quad S = \frac{\Omega\, d_p}{u_*} \qquad (6.13d, e)$$

Equation (6.12) is complemented with the Lagrangian equations for the particle trajectory:

$$u_p = \frac{dx_p}{dt} \quad , \quad v_p = \frac{dy_p}{dt} \qquad (6.14a, b)$$

where x_p and y_p denote dimensionless coordinates of the particle centroid, made dimensionless with d_p as in (6.11a).

In (6.12) and (6.14) the local mean flow velocity, u_f, must be specified. Herein the semi-logarithmic law for the mean velocity profile in turbulent open channel flows is used, which can be written in dimensionless form as:

$$u_f = \frac{1}{\kappa} \ln (y) + B \qquad (6.15)$$

where κ denotes von Karman's constant taken to be equal to 0.4, the roughness height, k_s, has been taken to be equal to the particle diameter, and the coefficient B is equal to 8.5 for fully rough flows, and is a function of $k_{s+} = u_* \, k_s/\nu$ for transitionally rough flows (see Chapter 3).

Given proper initial conditions, the system formed by (6.12) and (6.14) is easily solved numerically using a fourth order Runge-Kutta scheme. However since this is a system of integro-differential equations, some attention must be given to the treatment of the integral (Basset) term in them. Following Brush et al. (1964), the Basset term corresponding to the direction i can be written in general form as:

$$BI_i (t) = K \int_0^t \frac{d}{d\tau} (u_{s_i}) \frac{d\tau}{\sqrt{t-\tau}} \tag{6.16}$$

where $K = (9 \, \alpha)/(\sqrt{R_p} \; \tau_*^{1/4} \sqrt{\pi})$, and u_{s_i} denotes the ith component of the particle slip velocity. However (6.16) can be rewritten as:

$$BI_i (t) = K (\int_0^{t-\delta t} \frac{d}{d\tau} (u_{s_i}) \frac{d\tau}{\sqrt{t-\tau}} + \int_{t-\delta t}^{t} \frac{d}{d\tau} (u_{s_i}) \frac{d\tau}{\sqrt{t-\tau}}) \tag{6.17}$$

and assuming δt is very small so the derivative $du_{s_i}/d\tau$ can be considered approximately constant in the interval $t - \delta t < \tau < t$, then (6.17) simplifies to:

$$BI_i (t) = BI_i (t - \delta t) + 2 \, K \sqrt{\delta t} \; \frac{d}{dt} (u_{s_i}) \tag{6.18}$$

Replacing (6.18) in (6.12) and using the definitions (6.2), then the new system of governing equations for the saltating particle velocities are:

$$\frac{du_p}{dt} (1 + 2 \, K \sqrt{\delta t}) = -\frac{3}{4} \, \alpha \, C_D \, |u_R| \, (u_p - u_f) + (\alpha \, C_m + 2 \, K \sqrt{\delta t}) \frac{du_f}{dy} \, v_p + + \frac{\alpha \, \sin \theta}{\tau_*} + BI_u (t - \delta t) \tag{6.19a}$$

$$\frac{dv_p}{dt} (1 + 2 \, K \sqrt{\delta t}) = -\frac{3}{4} \, \alpha \, C_D \, |u_R| \, v_p + \frac{3}{4} \, \alpha \, C_L \, (|u_R|_T^2 - |u_R|_B^2) - \frac{\alpha \, \cos \theta}{\tau_*} + + BI_v (t - \delta t) + \frac{3}{4} \, \alpha \, |u_R| \, (S - \frac{1}{2} \frac{du_f}{dy}) \tag{6.19b}$$

where:

$$BI_u (t - \delta t) = K \int_0^{t-\delta t} (\frac{du_f}{dy} \, v_p - \frac{du_p}{d\tau}) \frac{d\tau}{\sqrt{t-\tau}} \tag{6.20a}$$

$$BI_V\ (\ t - \delta t\ ) = -\ K \int_0^{t-\delta t} \frac{dv_p}{d\tau}\ \frac{d\tau}{\sqrt{t-\tau}} \qquad (6.20b)$$

The numerical evaluation of (6.20) was made herein by using Simpson's quadrature, and a value of δt equal to the time interval used in the Runge-Kutta scheme.

6.4 Stochastic simulation of particle saltation

In order to solve the system of equations for particle saltation formed by (6.14) and (6.19), initial conditions are required for particle position and velocity. In the case of successive hops of the particle, those initial conditions are controlled by the particle collision with the bed. Grain-grain collisions during saltation were not observed in the experimental study reported in Chapter 5, probably due to the relatively low bedload concentrations of those experiments. Consequently, they are not taken into account in the present analysis.

Particle velocities immediately after the collision are estimated from particle velocities immediately before the collision, by introducing coefficients of restitution, e, and friction, f, which reduce the incident particle velocity components in the normal and tangential directions with respect to the surface of contact at the bed, respectively. For the situation shown in Fig. 6.2, the angle of contact corresponds to $\theta_{in} + \theta_b$, where the bed angle, θ_b, is clearly a random variable, even in the idealized situation of a bed formed by uniformly packed spheres.

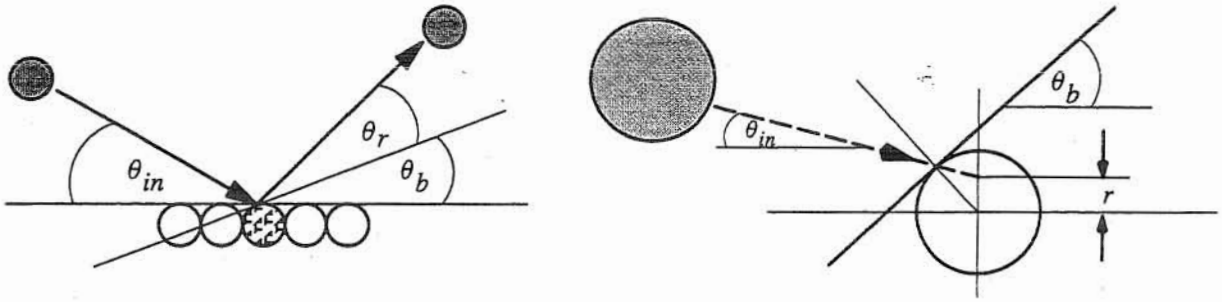

Fig. 6.2 Definition diagram for particle collision with the bed.

In order to make a stochastic evaluation of θ_b, we follow the method proposed in Chapter 5, which assumes a bed formed by uniformly packed spheres. With reference to Fig. 6.2, θ_b can take values in the range (–30°, 30°). Mapping this range of angles onto a set of values r along a vertical line passing through the center of the bed particle, then geometrical transformations allow to determine the values θ_b associated with given values of θ_{in} and r. The stochastic estimation of θ_b is obtained by using a random number generator to produce values of r with uniform probability density, for given values of the incidence angle θ_{in}. Prescribing a uniform probability density for r is equivalent to assuming that the bed particle has a uniform probability of being located anywhere

in the bed. Values of θ_{in} can be obtained deterministically from the trajectory of the saltating particle previous to the current collision with the bed.

Based on the analysis of experimental results presented in Chapter 5, a constant value of the friction coefficient f is used in the numerical simulation, as well as a linear relationship for the variation of the restitution coefficient, e, with τ_*, which can be expressed as:

$$e = \begin{cases} A - B\,\tau_* & 0 < \tau_* < A/B \\ 0 & \tau_* > A/B \end{cases} \tag{6.21}$$

According to the experimental results presented in Chapter 5 f is about 0.73, while A and B take the values 0.84 and 4.84, respectively, for the saltation of gravel. For the saltation of fine sand, f is about 0.89, while A and B take the values 0.75 and $0.25/\tau_{*c}$, respectively, where τ_{*c} denotes the critical dimensionless bed shear stress for particle motion estimated from Shields curve.

Four hundred successive hops of a saltating gravel particle were simulated for different values of governing dimensionless parameters with the aim of estimating statistics of parameters characterizing gravel saltation. This was done by solving the equations for gravel saltation numerically, using a fourth order Runge-Kutta scheme, coupled with the model of particle collision with the bed explained above. The particle is initially released at a distance of 2 particle diameters from the bed, with zero velocity. The first 20 hops are discarded when computing statistics of saltation, in order to get results that are independent of the arbitrary initial condition.

6.5 Modelling gravel saltation

6.5.1 Analysis of the equation for particle saltation

In order to contrast the results of this model with empirical evidence, as well as to analyze the importance of different terms in the equation of motion, we used initial conditions estimated from measurements of the trajectories of individual saltations obtained in the experiments reported in Chapter 5. These initial conditions consist of values of normal and streamwise components of particle velocity at the beginning of a saltation. Examples of the results obtained are presented in Figs. 6.3 and 6.4, where the following values have been used in the computations: $C_m = 0.5$, $C_L = 0.2$, and C_D is estimated from (6.4). Also, since natural gravel particles are considered, a value $R = 1.65$ is utilized throughout.

One sampled trajectory of a saltating gravel particle is plotted in Fig. 6.3. In the same figure, associated computed trajectories are also shown to illustrate the effect of different terms in the equations of motion. The importance of the lift force is evident, which indicates that the inclusion of this term is essential for the adequate modelling of observed trajectories. This conclusion is in agreement with discussions by Leeder (1979a), Bridge and Bennett (1992), and that of Chapter 5

regarding the value of the grain Froude number, F_g, which would indicate that upwards forces arising from particle collisions with the bed, are insufficient to maintain observed trajectories of saltating particles. From Fig. 6.3, it is also apparent that the Basset force has a negligible effect in the rising part of the particle trajectory, although in the falling part its cumulative effect is to slightly increase the saltation length. Some local influence of the turbulence over the saltation can be observed in Fig. 6.3, however the computed mean particle trajectory seems to reproduce the observed one satisfactorily.

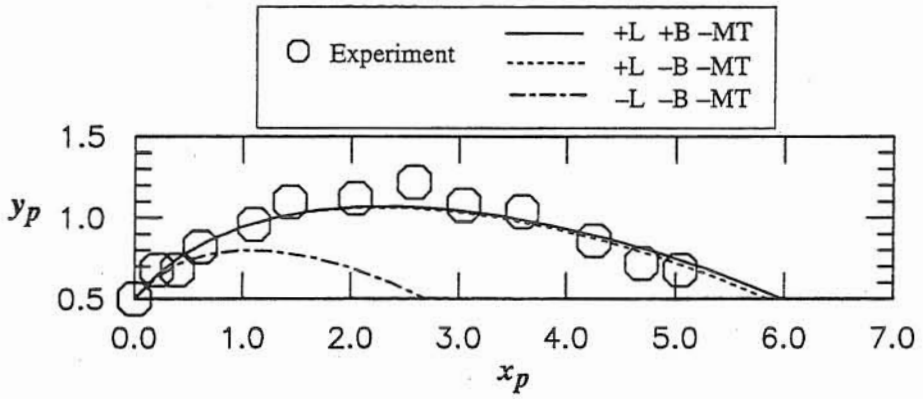

Fig. 6.3 Comparison between simulated dimensionless saltation trajectories and experimental observations reported in Chapter 5. Experimental conditions correspond to: $\tau_* = 0.104$, $R_p = 21900$, $tan\ \theta = 0.07$. In the legend, L denotes lift term, B denotes Basset term, and MT denotes Magnus term, and the symbols + and – indicate that the respective term is included or neglected in the simulation, respectively.

The results of the numerical simulations shown in Fig. 6.3 do not take into account the Magnus term due to particle rotation. Nevertheless, particle rotation does not seem to be always negligible, as is shown in Fig. 6.4. Therein, another sampled particle trajectory is plotted, together with the corresponding results of the numerical model for the cases: i) neglecting Magnus term, and ii) considering Magnus term, using a value $S = 2.0$, which produces a good fit to the observed trajectory. Apparently, the extra lift needed in this case in order to better reproduce the observed trajectory could be explained by the Magnus term. The value of S used corresponds to a particle angular velocity $\Omega = 14.0\ s^{-1}$ (2.2 rev/sec), which compares relatively well with the value $\Omega = 20.9\ s^{-1}$ (3.3 rev/sec) estimated from the video analysis of the experimental trajectory, given the uncertainty associated with the Magnus term (6.10).

The above analyses demonstrate that the modelling of lift forces, including Magnus force, acting upon saltating particles is essential to an adequate simulation of the saltation trajectories. Even though a more comprehensive comparison between experimental and numerical trajectories, of which the results presented in Figs. 6.3 and 6.4 are examples, leads to the conclusion that given

appropriate initial conditions, the equations for gravel saltation proposed herein perform satisfactorily, the uncertainties associated with the lift coefficient, C_L, and with the Magnus term (6.10), would indicate that more research is necessary to further the present understanding of fluid lift on particles.

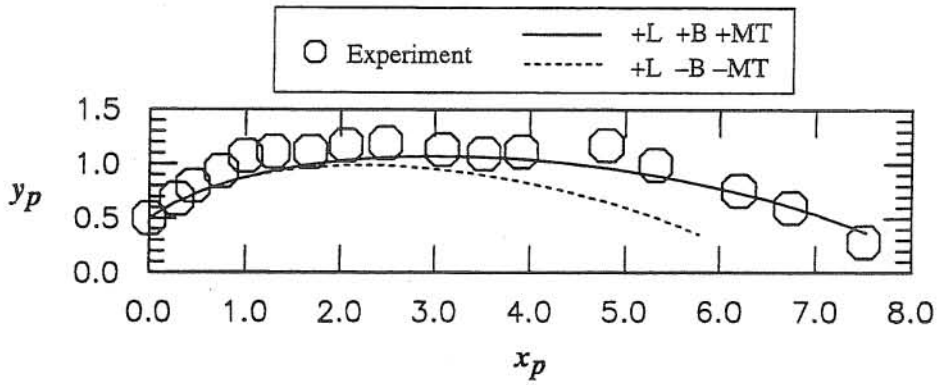

Fig. 6.4 Comparison between simulated dimensionless saltation trajectories and experimental observations reported in Chapter 5. Experimental conditions correspond to: $\tau_* = 0.094$, $R_p = 21900$, $tan\ \theta = 0.05$. In the legend, L denotes lift term, B denotes Basset term, and MT denotes Magnus term, and the symbols + and – indicate that the respective term is included or neglected in the simulation, respectively. In the simulation with +MT a value of $S = 2$ was used.

6.5.2 Statistics of gravel saltation

Gravel saltation was simulated stochastically following the procedure outlined in Section 6.4. Given the impossibility of estimating particle rotation a priori, the Magnus term is neglected in the equation for particle saltation. A succession of simulated saltations of a gravel particle is shown in Fig. 6.5 as an example of the results obtained.

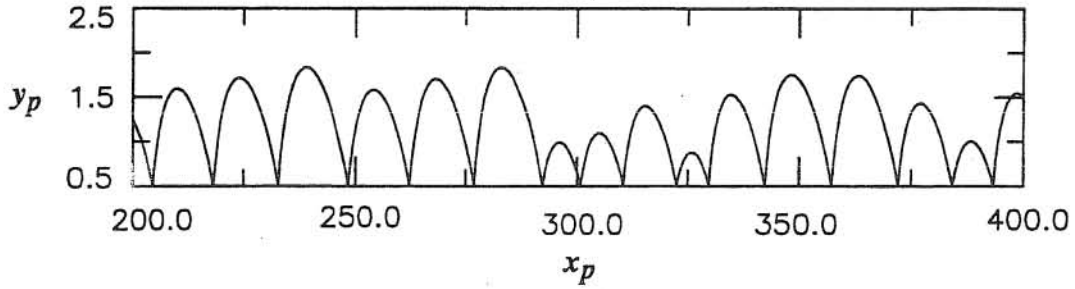

Fig. 6.5 Simulated succession of saltations, $\tau_* = 0.15$, $R_p = 7400$, $tan\ \theta = 0.05$.

Let $\lambda_s{*}$, $t_s{*}$, $h_s{*}$, and $u_s{*}$ denote length, duration, height, and mean streamwise particle velocity of individual saltations, where $u_s{*}$ is computed as:

$$u_s{*} = \frac{1}{t_s{*}} \int_0^{t_s{*}} \overline{u}_p\ (\ t{*}\ )\ dt{*} \qquad (6.22)$$

Ensemble averaging over the four hundred realizations of the saltation process allows calculation of mean values and standard deviations of the dimensionless variables λ_s, h_s, and u_s, which are defined as:

$$\lambda_s = \frac{\lambda_s{}^*}{d_p} \quad , \quad h_s = \frac{h_s{}^*}{d_p} \quad , \quad u_s = \frac{u_s{}^*}{u_*} \qquad (6.23a\text{–}c)$$

These variables are functions of the dimensionless parameters R, τ_*, R_p, and θ as suggested by the system of dimensionless governing equations (6.19).

The resulting mean values and standard deviations of λ_s, h_s, and u_s are plotted in Figs. 6.6 to 6.8 as functions of τ_*, for the values of R_p of 1000 and 25000. This range of values of R_p covers the values 7400 and 21900 used in the experiments reported in Chapter 5. Those experimental results are also plotted in Figs. 6.6 to 6.8, for comparison purposes. In the computations, the values $R = 1.65$, $C_m = 0.5$, and $C_L = 0.2$ were used, and the values of C_D were estimated from (6.4). Also, the value $tan\ \theta = 0.05$ was selected in order to compare with the experimental results, where $tan\ \theta$ was in the range 0.03 to 0.07.

The dynamic friction coefficient, μ_d, estimated as (see Chapter 5):

$$\mu_d = (R + 1)\ \tau_* \ (\Delta u_s\ u_s) \ / \ \lambda_s \qquad (6.24)$$

is plotted in Fig. 6.9, together with the experimental values of this variable obtained in Chapter 5. In (6.18), Δu_s denotes the dimensionless ensemble averaged particle velocity change before and after the collision with the bed, made dimensionless with u_*.

6.5.3 Analysis of numerical simulation

The results presented in Figs. 6.6 to 6.9, suggest that R_p does not have an important effect in the geometric and kinematic characteristics of gravel saltation, since no large differences are obtained in the results of the simulation for a variation of R_p in the range 1000 to 25000, which corresponds to particle with diameters ranging from 4 to 34 mm. Because of this, there is no need to do simulations at the exact experimental values of R_p to compare with the results of Chapter 5.

The simulated mean values of saltation length shown in Fig. 6.6, agree well with the experimental results of Chapter 5. Given the comparison presented therein, we conclude that the simulated values of λ_s also agree well with the experimental results of Abbott and Francis (1977). The simulated standard deviations of λ_s are on the order of 50% of the mean values, which is slightly larger than the experimental values of 30% to 40% reported in Chapter 5.

Although the simulated mean values and standard deviations of saltation height shown in Fig. 6.7 agree relatively well with the experimental results of Chapter 5 for $R_p = 21900$, they do not agree

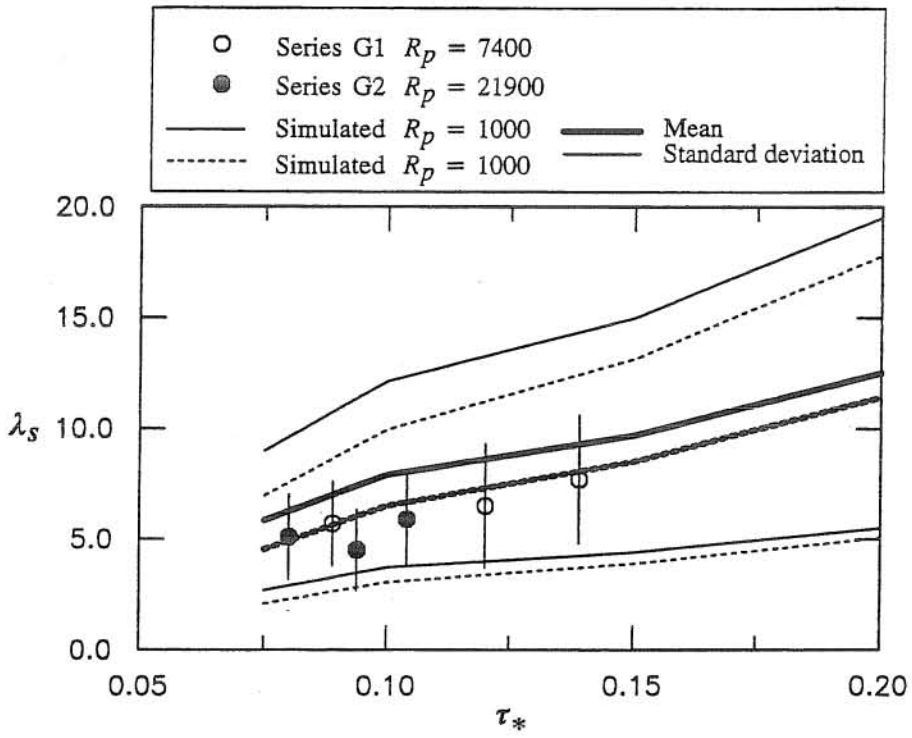

Fig. 6.6 Comparison between simulated dimensionless saltation lengths and experimental results of Series G1 and G2 of Chapter 5. Thicker lines correspond to mean values and thinner lines correspond to mean values plus and minus one standard deviation. Symbols correspond to experimental mean values and vertical lines represent a total length of two standard deviations.

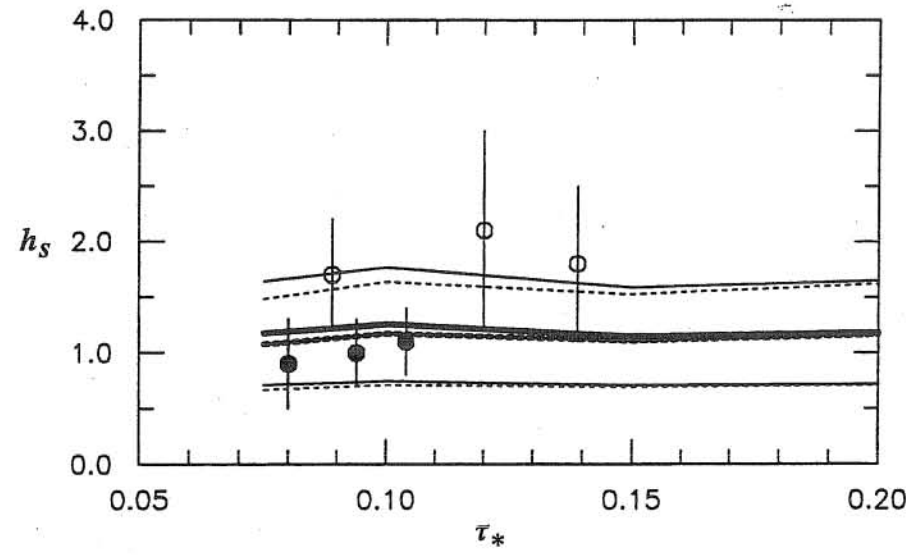

Fig. 6.7 Comparison between simulated dimensionless saltation heights and experimental results of Series G1 and G2 of Chapter 5. Legend as in Fig. 6.6.

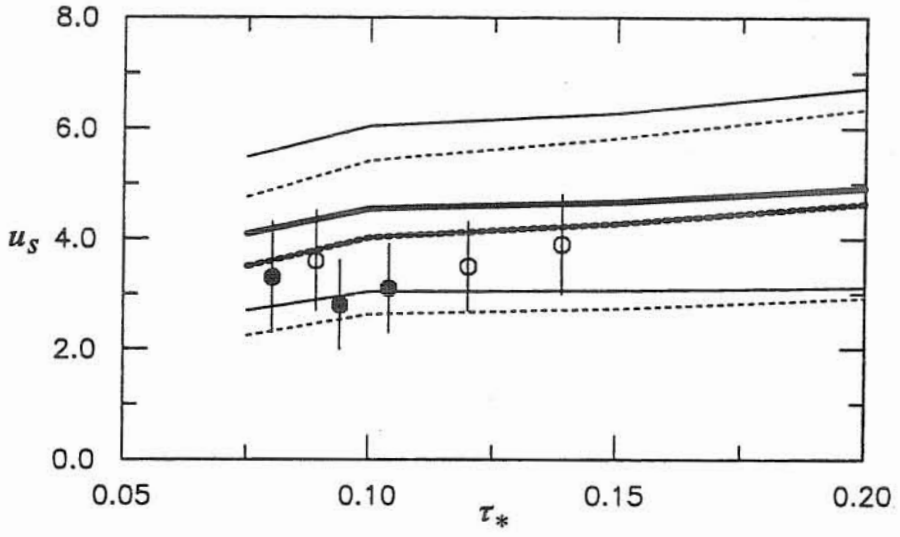

Fig. 6.8 Comparison between simulated dimensionless streamwise saltation velocity and experimental results of Series G1 and G2 of Chapter 5. Legend as in Fig. 6.6.

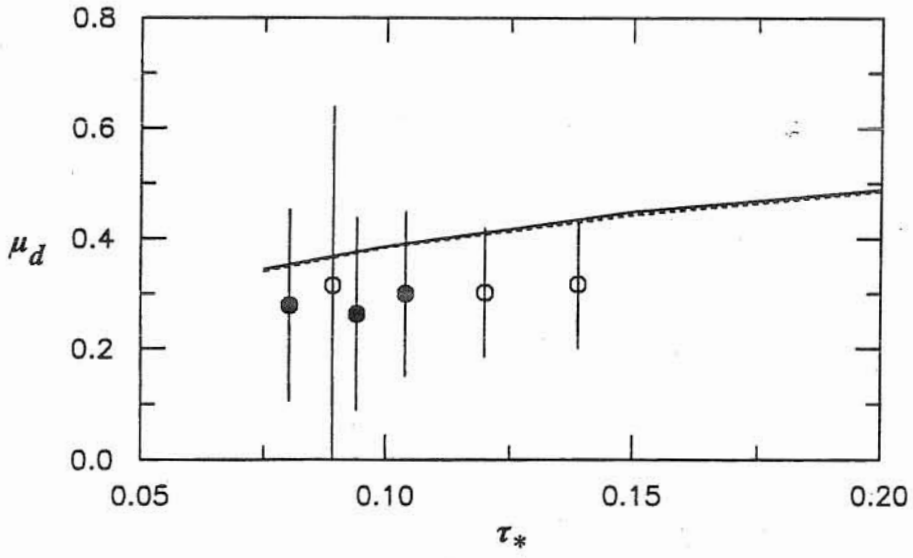

Fig. 6.9 Comparison between simulated dimensionless streamwise saltation velocity and experimental results of Series G1 and G2 of Chapter 5. Legend as in Fig. 6.6.

with those observations corresponding to R_p = 7400, which tend to be underestimated by the numerical results.

The simulated mean values of saltation streamwise velocity shown in Fig. 6.8 tend to overestimate the experimental results of Chapter 5, particularly those corresponding to $R_p = 21900$, with differences of the order of 20%. The simulated standard deviations of u_s are of the order of 35% of the mean values, which is slightly larger than the experimental values of about 30% reported in Chapter 5.

One way to explain the poor prediction of h_s for the particles corresponding to $R_p = 7400$ (d_p = 15 mm) is that they may be more prone to rotate after collisions with the bed than particles of larger or smaller size ranges. This would enhance saltation height due to Magnus lift (which was neglected in the simulations) as well as the corresponding standard deviation, the latter probably due to the randomness of the particle angular velocity after the collision with the bed. For some reason this enhanced saltation height does not appear to affect the corresponding saltation length and mean streamwise velocity appreciably. Although the above explanation seems plausible, it is also possible that lift forces (other than Magnus lift, and possibly also those associated with surface waves as discussed in Chapter 5) are not being adequately described in the present formulation. Clearly, more research on fluid lift is necessary to improve the results given by the present model.

Another aspect of the present formulation that may be improved is the model for the particle collision with the bed. In fact, the values of the friction and restitution coefficients at collision have an important incidence on the characteristics of the subsequent saltations. Although the experimental coefficients e and f determined in Chapter 5 were used, the estimation of those coefficients still involved some modelling, which may be improved with more detailed observations of the particle collision with the bed. The stochastic model for particle collision with the bed also affects the standard deviations of saltation variables. The fact that experimental standard deviations of such variables are generally overestimated by the present simulations may call for an improvement on that model, in order to reduce the range of takeoff angles.

The numerical simulation of the dynamic friction coefficient tend to slightly overestimate the experimental values reported in Chapter 5, giving values of μ_d in the range 0.35 to 0.50, for values of τ_* lower than 0.2 (Fig. 6.9). These values of μ_d also compare favorably with those of Francis (1973) and Abbott and Francis (1977) (see Chapter 5). According to Bagnold (1973), the value of μ_d should be very close to the static friction coefficient, $tan\ \phi$, which for natural sediment takes a value of about 0.63. The fact that the numerical values of μ_d given by the present model are lower than 0.63, and closer to experimental evaluations of this parameter suggests that Bagnold's (1973)

assumption may be incorrect, and that experimental values of μ_d are not prone to underestimation, as argued by Abbott and Francis (1977).

6.5.4 Conclusions

The model for gravel saltation developed herein, performs satisfactorily when compared with individual saltation events obtained from experimental measurements of particle trajectories. In particular, it is found that lift forces must be included for the adequate modelling of observed trajectories, which indicate that upward forces arising from the particle collisions with the bed are insufficient to maintain such trajectories.

Computed statistics of gravel saltation generally agree well with experimental observations. In particular, the numerical results compare well with the experimental mean values of saltation length and height of Chapter 5, however they tend to underestimate those experimental values of the saltation height corresponding to R_p = 7400. The numerical results slightly overestimate experimental mean values of the streamwise saltation velocity of Chapter 5, and also the values of the standard deviations of saltation length, height and streamwise particle velocity obtained in those experiments.

An improvement of the results of the numerical simulations may require further empirical evidence on lift forces acting during saltation, as well as on the particle collision with the bed.

The values of the dynamic friction coefficient predicted by the model are in the range 0.35 to 0.5 for values of τ_* lower than 0.2, which is in agreement with experimental observations. The latter would imply that experimental values of μ_d are not prone to underestimation, as argued by Abbott and Francis (1977).

6.6 Modelling saltation of sand

6.6.1 Analysis of the equation for particle saltation

An analysis of the equation of particle saltation similar to that presented in 4.1, is carried out herein, where the numerical results of the model equations for particle motion are compared with the experimental observations of fine sand particle saltation reported in Chapter 5. This comparison is done by giving the model initial conditions estimated from measured saltation trajectories. These initial conditions consist of values of normal and streamwise components of particle velocity at the beginning of a saltation. Examples of the results obtained are presented in Fig. 6.10, where the following values have been used in the computations: $C_m = 0.5$, $C_L = 0.2$, and C_D is estimated from (6.4). A value $R = 1.65$, valid for natural sediment, was used throughout.

As seen in Fig. 6.10, the model performs generally very well, reproducing the shape as well as the height and length of the saltation events satisfactorily. As with the case of gravel saltation,

the results shown in Fig. 6.10 indicate that the lift force plays an essential role on the particle motion. On the other hand, it is interesting that in the case of sand the Basset term appears to have much more importance than in the case of the saltation of gravel for which its effect was practically negligible. It seems that the Basset force tends to increase the length of the trajectories of sand particles notoriously.

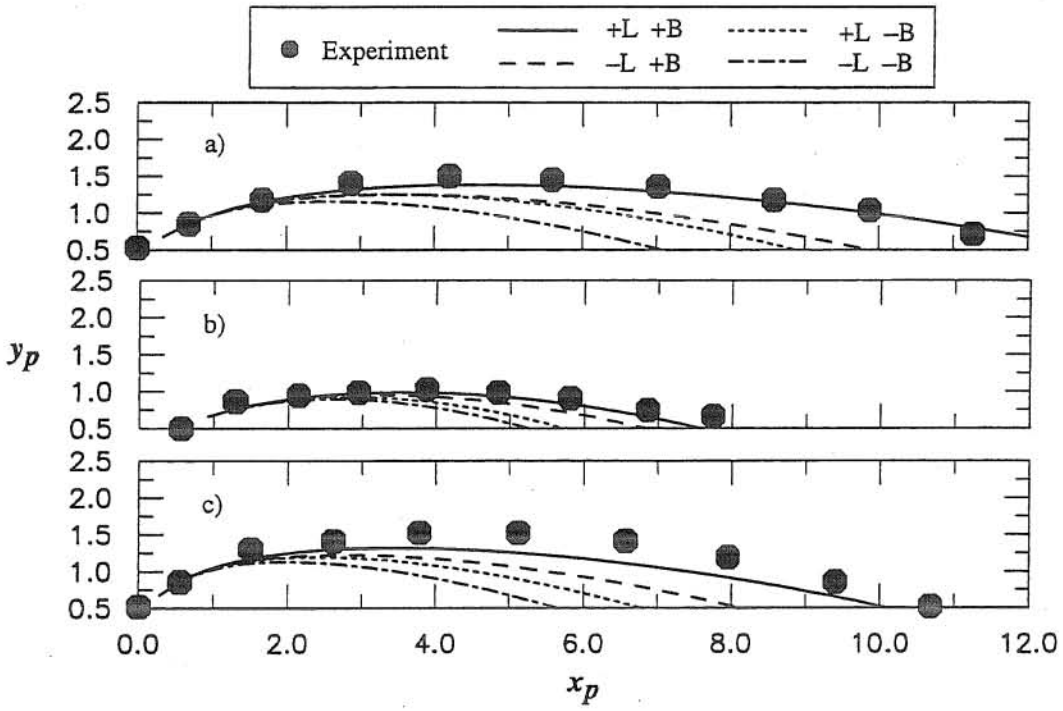

Fig. 6.10 Comparison between simulated dimensionless saltation trajectories and experimental observations reported in Chapter 5. Experimental conditions correspond to: a) τ_*= 0.067, R_p = 53; b) τ_*= 0.056, R_p = 88; c) τ_*= 0.095, R_p = 70. In the legend, L denotes lift term, and B denotes Basset term, and the symbols + and – indicate that the respective term is included or neglected in the simulation, respectively.

This effect of the Basset force is illustrated also in Fig. 6.11, where simulated trajectories of particles having values of R_p of 50, 500, and 5000 (corresponding to sediment particle sizes of about 0.5 mm, 2.5 mm, and 11.6 mm, respectively) are plotted, keeping all the other control dimensionless parameters constant, including the dimensionless initial conditions for particle saltation. In the computations, the values τ_*= 0.10, $tan\ \theta$ = 0.001, and the initial particle velocities: u_p = 3.5, v_p = 1.8, have been used. Clearly, Fig. 6.11 shows increasing importance of the Basset force on the length of the saltation trajectory as R_p decreases. From this figure it is apparent that when the Basset term is neglected, the length of the simulated saltation does not change much with R_p in the range 50 to 5000, however when the Basset term is included in the simulation, the length of the saltation corresponding to R_p = 50 seems to be about 60% longer than that corresponding to R_p = 5000,

keeping all other parameters constant. On the other hand, the results shown in Fig. 6.11 also indicate that the height of the jumps appear to be independent of R_p when the Basset term is included in the simulation, and that it seems that this term tends to increase somewhat the saltation height, although, again, its effect is higher for smaller values of R_p.

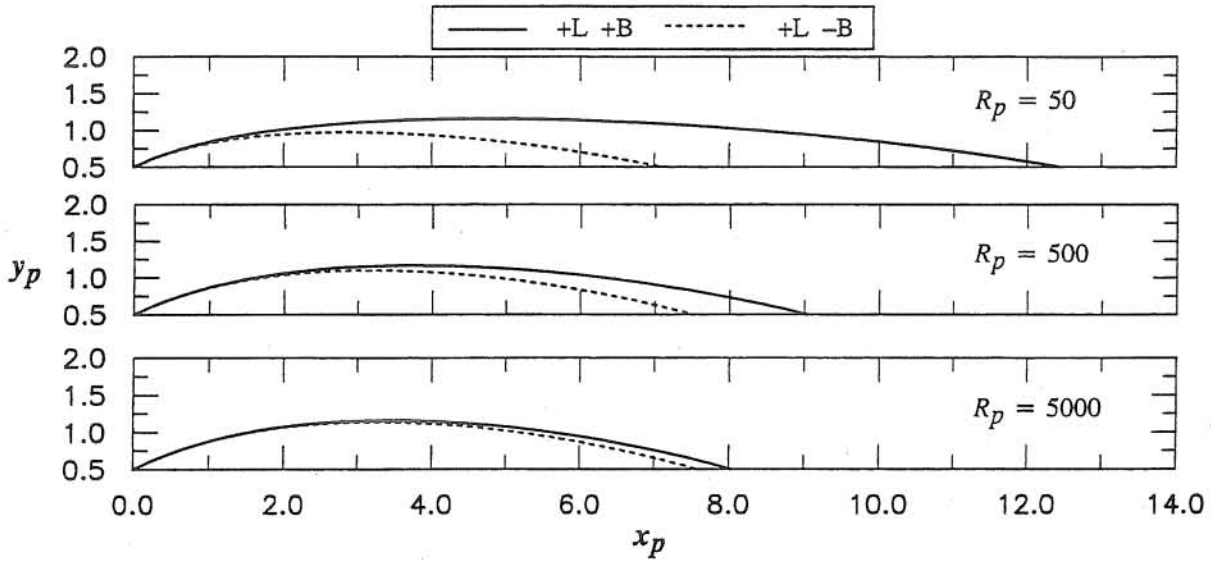

Fig. 6.11 Effect of Basset term on particle saltation as a function of R_p, for the values of this parameter: 50, 500, 5000. All other control parameters are held constant with values: τ_*= 0.10, R = 1.65, $tan\ \theta$ = 0.001. Initial conditions are x_p = 0, y_p = 0.5, u_p = 3.5, v_p = 1.8. In the legend, L denotes lift term, and B denotes Basset term, and the symbols + and – indicate that the respective term is included or neglected in the simulation, respectively.

In order to analyze the effect of particle rotation on saltation trajectories, a few simulations of particle saltation including the Magnus force term in the equations for particle motion, for the same conditions as those corresponding to the results shown in Fig. 6.10, are presented in Fig. 6.12. Therein the value of the dimensionless particle angular velocity, S, was estimated in each case using the experimental results for the mean value of this variable as a function of τ_*/τ_{*c} obtained in Chapter 5. In Fig. 6.12, corresponding experimental results are also plotted, together with the results obtained by neglecting the Magnus term. All the numerical results shown therein, correspond to computations that include lift and Basset force terms.

The results shown in Fig. 6.12 indicate that the Magnus term increases the lift acting on the particle such that the saltation height and length tend to be somewhat larger than those obtained by neglecting the effect of particle rotation. In general, those results show that the computations including the Magnus term tend to overestimate the observed saltation length, particularly in cases a) and c) by a rather large amount. This may imply that estimating the Magnus force term using (6.10), which was originally derived for the case of vanishingly small values of the particle Reynolds

number, Re, is not accurate in the case of particle saltation at larger values of Re. Nevertheless, since the effect of the turbulence of the flow has been neglected in the computations shown in Fig. 6.12, it is possible that the effect of both the particle rotation and the turbulence cancel each other, such that the simulations that neglect both effects agree fairly well with experimental observations. In fact, the analysis of turbulence effects on particle saltation presented in Chapter 9, based on a random walk model of particle motion, seems to indicate that the turbulence of the flow tends to reduce the height and length of the computed saltation trajectories.

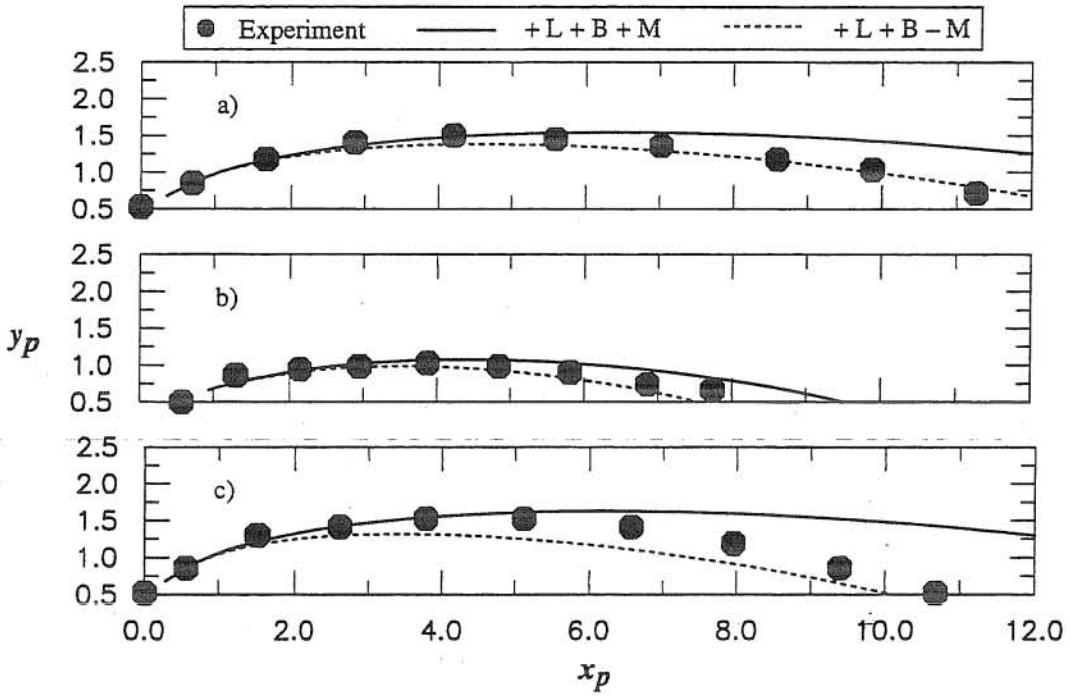

Fig. 6.12 Effect of Magnus term on particle saltation, comparison with experimental observations reported in Chapter 5. Experimental conditions correspond to: a) $\tau_* = 0.067$, $R_p = 53$, $S = 2.8$; b) $\tau_* = 0.056$, $R_p = 88$, $S = 3.2$; c) $\tau_* = 0.095$, $R_p = 70$, $S = 1.8$. In the legend, L denotes lift term, B denotes Basset term, and M denotes Magnus term, and the symbols + and – indicate that the respective term is included or neglected in the simulation, respectively.

A comprehensive comparison between experimental and numerical trajectories of sand saltation, of which the results presented in Fig. 6.10 are examples, demonstrates that given appropriate initial conditions and neglecting the Magnus term, the equations for particle saltation proposed herein perform satisfactorily. It is acknowledged, however, that such equations are only approximate, in that they neglect rotation and turbulence effects, and also because of the uncertainties regarding the added mass, drag, and lift coefficients and Basset term.

6.6.2 Statistics of saltation of sand: analysis of numerical simulation

The saltation of sand was simulated stochastically following the procedure outlined in Section 6.4. Mean values and standard deviations of λ_s, h_s, u_s, and μ_d, defined as in (6.22) to (6.24), were computed from the numerical results for different values of the ratio τ_*/τ_{*c}, and for the value $R_p =$ 73, representative of the range of values of this parameter in the experiments with sand of Series S1, Chapter 5. In the computations, the values $tan\ \theta = 0.001$, $R = 1.65$, $C_m = 0.5$, and $C_L = 0.2$ were used, and the values of C_D were estimated from (6.4).

Results using the experimentally calibrated model for velocity coefficients at collision

The restitution coefficient e given by (6.21), with values $A = 0.75$ and $B = 0.25/\tau_{*c}$ (which imply a minimum value of e equal to 0), together with the value of the friction coefficient $f = 0.89$, were used to model the process of particle collision with the bed. These values were calibrated using the experimental results of Series S1, as discussed in Chapter 5. The results of the numerical simulation of saltation of sand are presented in Figs. 6.13 to 6.16 as functions of the ratio τ_*/τ_{*c}. In those figures, the experimental results of Series S1, Chapter 5, are also plotted for comparison purposes.

As seen in Fig. 6.13, experimental mean values and standard deviations of the dimensionless saltation height appear to be well predicted by the numerical simulation, although there is a tendency for the simulated values to underestimate the experimental mean values of h_s for values of τ_*/τ_{*c} larger than about 2.5. The same good prediction of the model is observed in Fig. 6.14 for the mean values and standard deviations of the dimensionless saltation length. Again the numerical simulation tends to underestimate the observed mean values of λ_s for values of τ_*/τ_{*c} larger than about 2.5. The simulated values of the dimensionless saltation streamwise velocity, on the other hand, overestimate somewhat the observed values of both the mean and standard deviation of u_s (Fig. 6.15). Nevertheless, the numerical simulation predicts correctly the value of u_s observed at τ_*/τ_{*c} of about 1, which appeared to be rather high when compared with other experimental results (see Chapter 5, Section 5.4.3). Finally, from Fig. 6.16, the numerically estimated values of the dynamic friction coefficient seem to agree fairly well with the experimental estimations of μ_d, defining values of about 0.2 to 0.25 for this variable much lower than the value of 0.63 proposed by Bagnold (1973).

Overall, the results shown in Figs. 6.13 to 6.16 show a good agreement with the experimental observations, however there is a tendency for the simulated mean values of λ_s, h_s, and u_s to decrease in the range $2 < \tau_*/\tau_{*c} < 3$ which does not seem to be correct when compared with the experimental trends. For values $\tau_*/\tau_{*c} > 3$, simulated mean values of λ_s, h_s, and u_s seem to increase monotonically with τ_*/τ_{*c}, in agreement with the experimental observations. It is apparent that the anomalous

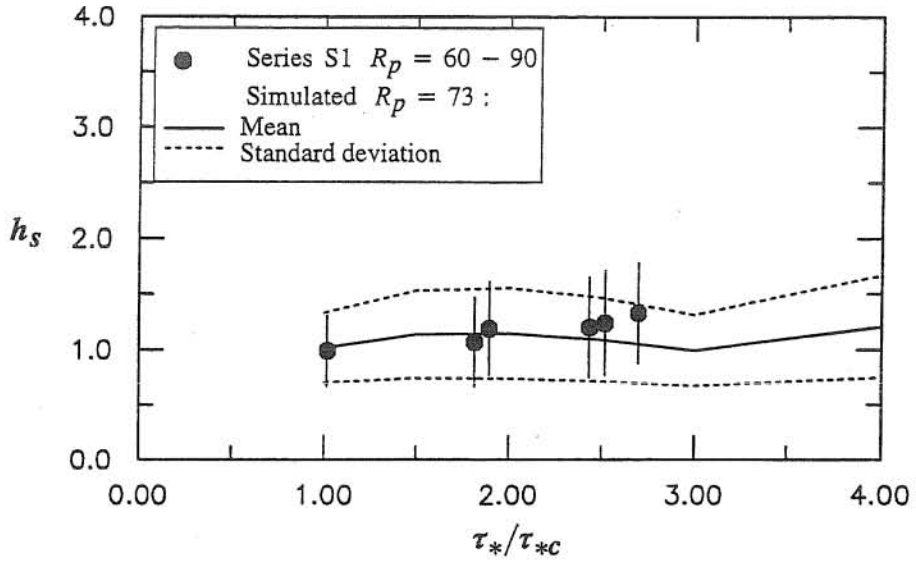

Fig. 6.13 Comparison between simulated (e_{min} = 0.0) dimensionless saltation height and experimental results of Series S1, Chapter 5. Symbols represent mean experimental values and vertical lines represent a total length of two corresponding standard deviations. Solid lines represent simulated values and dashed lines correspond to mean values plus and minus one standard deviation.

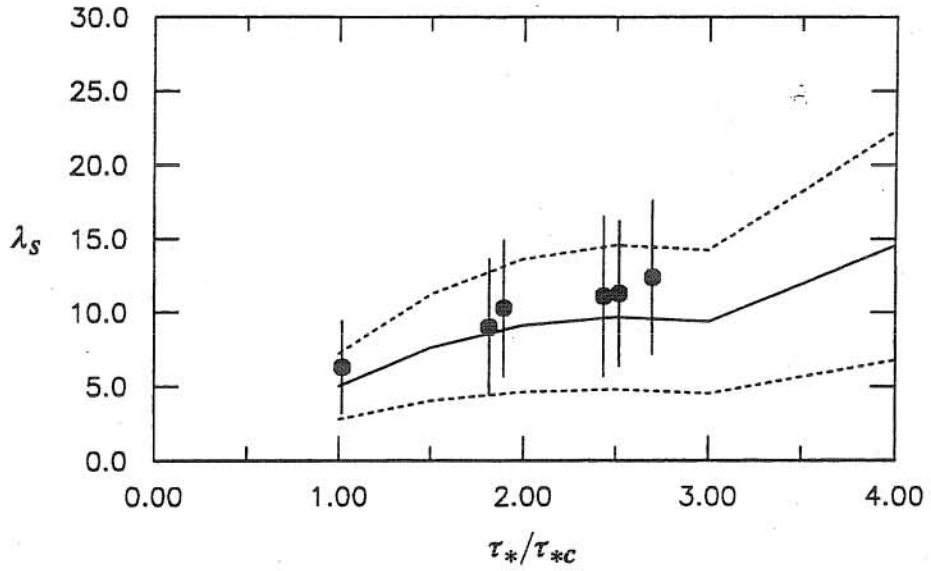

Fig. 6.14 Comparison between simulated (e_{min} = 0.0) dimensionless saltation length and experimental results of Series S1, Chapter 5. Legend as in Fig. 6.13.

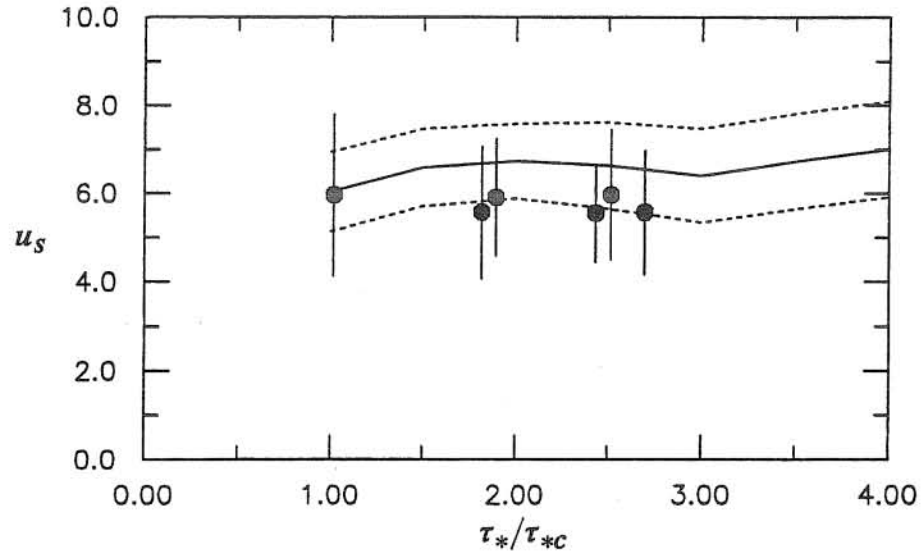

Fig. 6.15 Comparison between simulated (e_{min} = 0.0) dimensionless saltation streamwise velocity and experimental results of Series S1, Chapter 5. Legend as in Fig. 6.13.

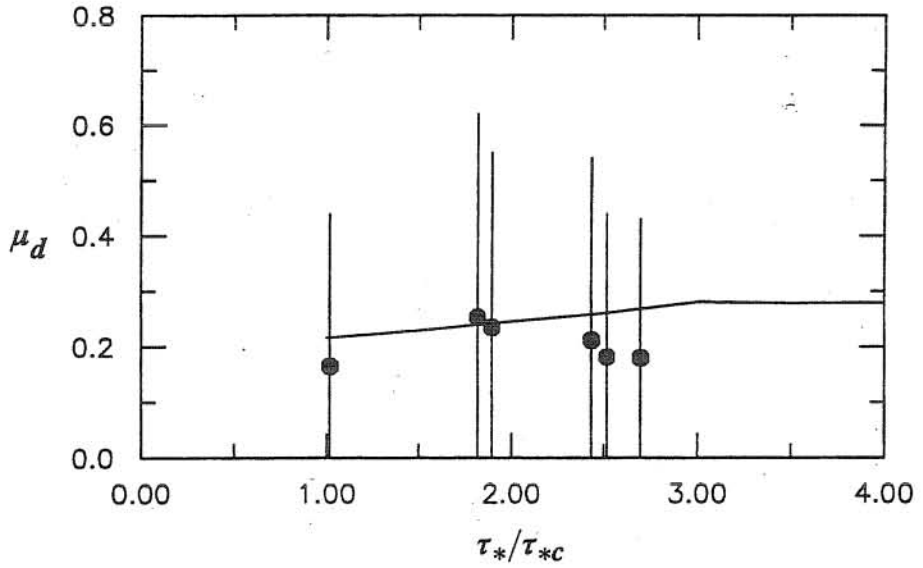

Fig. 6.16 Comparison between simulated (e_{min} = 0.0) dynamic friction coefficient and experimental results of Series S1, Chapter 5. Legend as in Fig. 6.13.

behavior of the numerical results in the range $2 < \tau_*/\tau_{*c} < 3$ is caused by the variation of the restitution coefficient, e, which according to (6.21) drops to zero in that range.

Results using a modified model for velocity coefficients at collision

A simple way to improve the numerical results presented in Figs. 6.13 to 6.16 is to impose a minimum value of e of about 0.2 to the model given by (6.21). The modified model for e with this restriction is given by:

$$e = \begin{cases} 0.75 - 0.25\ \tau_*/\tau_{*c} & 0 < \tau_*/\tau_{*c} < 2.2 \\ 0.2 & \tau_*/\tau_{*c} > 2.2 \end{cases} \tag{6.25}$$

with τ_{*c} given by Shields curve.

The results of the numerical simulation of saltation of sand using (6.25), and the same value of $f = 0.89$ as before, are presented in Figs. 6.17 to 6.20 as functions of the ratio τ_*/τ_{*c}. In those figures, the experimental results of Series S1, Chapter 5, and those of Francis (1973), Abbott and Francis (1977), Fernandez-Luque and van Beek (1976), and Lee and Hsu (1994), are also plotted for comparison purposes.

As seen in Fig. 6.17, a very good agreement between the simulated mean values and standard deviations of h_s and those of Series S1 is obtained with the slightly modified model for e. A very good agreement is also apparent between the simulated mean values of h_s and corresponding observations by Abbott and Francis (1977). On the other hand, the model tends to underestimate the experimental values of h_s of Lee and Hsu (1994), which nevertheless appear to be extremely high compared to all other experimental data available.

From Fig. 6.18 it is clear that the slight modification of the model for e also improves the simulated results for the dimensionless saltation length. Again, the numerical model reproduce mean values and standard deviations of λ_s observed in the experiments with sand of Series S1 very well. On the other hand, the simulated mean values of λ_s seem to be larger than corresponding values observed by Abbott and Francis (1977). It is important to note however that Abbott and Francis' experiments correspond to rather coarse particles, which are closer in size to the gravel particles analyzed in Section 6.5. These results, together with the experimental observations of Series S1, suggest that the dimensionless saltation length would increase with decreasing values of R_p. The explanation for this would be in the fact that the Basset force tends to increase the dimensionless length of the jumps as R_p decreases, as shown previously in Fig. 6.11. From the same figure it seems that this does not appear to affect the dimensionless saltation height which is in agreement with the results shown in Fig. 6.17, as discussed above. Fig. 6.18 also shows that the simulated mean values

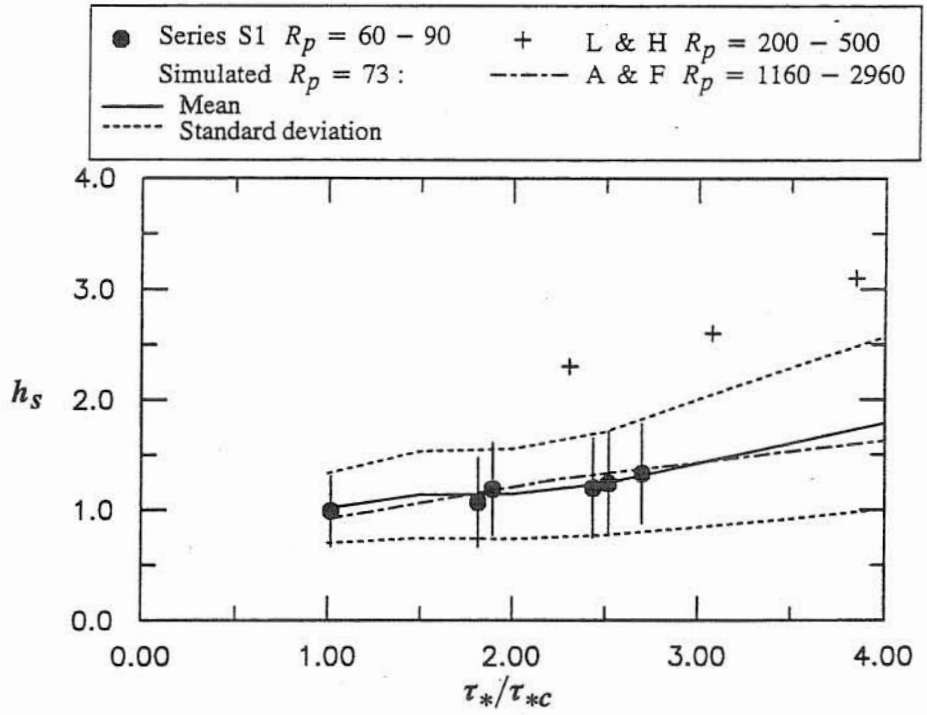

Fig. 6.17 Comparison between simulated (e_{min} = 0.2) dimensionless saltation height and experimental results of Series S1, Chapter 5. Symbols represent mean experimental values and vertical lines represent a total length of two corresponding standard deviations. Solid lines represent simulated values and dashed lines correspond to mean values plus and minus one standard deviation. In the legend, L & H denotes Lee and Hsu (1994), and A & B denotes Abbott and Francis (1977).

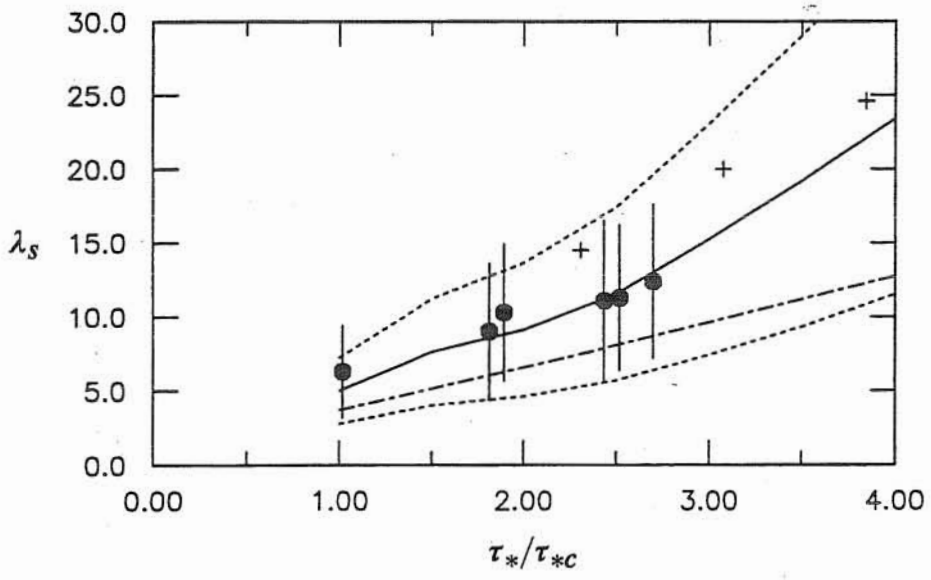

Fig. 6.18 Comparison between simulated (e_{min} = 0.2) dimensionless saltation length and experimental results of Series S1, Chapter 5. Legend as in Fig. 6.17.

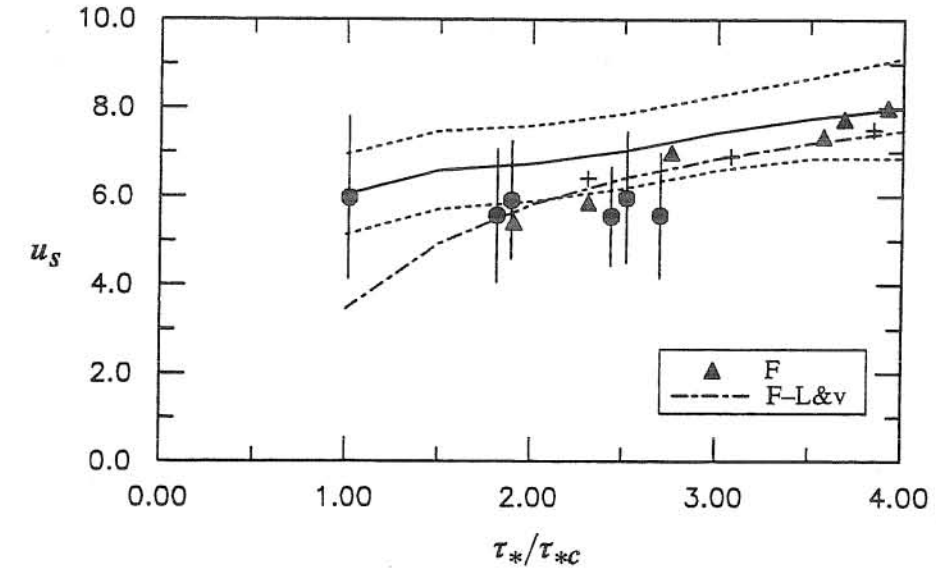

Fig. 6.19 Comparison between simulated (e_{min} = 0.2) dimensionless saltation streamwise velocity and experimental results of Series S1, Chapter 5. In the legend, F denotes Francis (1973) and F-L & v denotes Fernandez-Luque and van Beek (1976). All other symbols are as in Fig. 6.17.

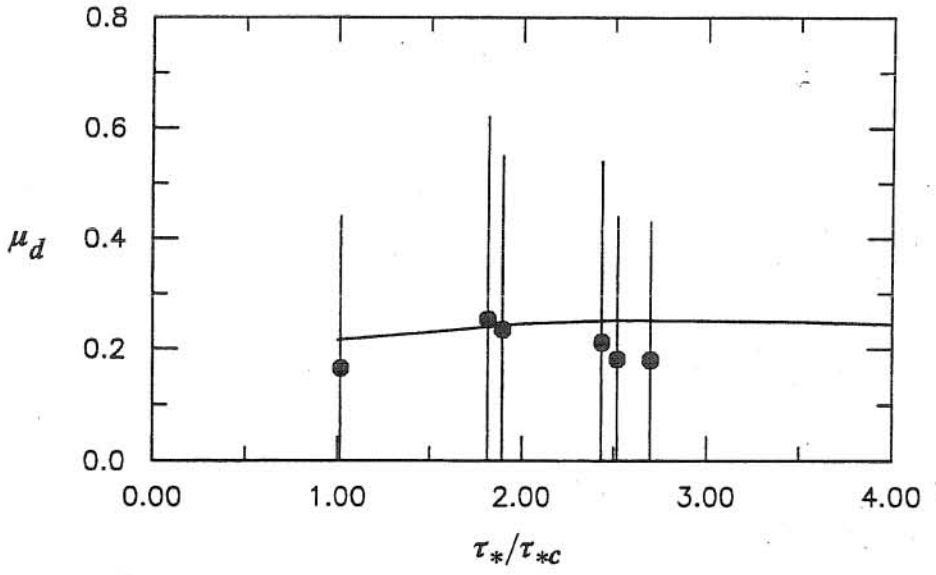

Fig. 6.20 Comparison between simulated (e_{min} = 0.2) dynamic friction coefficient and experimental results of Series S1, Chapter 5. Legend as in Fig. 6.17.

of λ_s tend to get somewhat closer to the values observed by Lee and Hsu (1994) for values of τ_*/τ_{*c} larger than about 3.5.

As with the previous model for e, simulated mean values and standard deviations of the dimensionless saltation streamwise velocity using (6.25) seem to overestimate somewhat corresponding values observed in Series S1 (Fig. 6.19). Nonetheless, the numerical results reproduce very well the apparently high mean value of u_s observed at τ_*/τ_{*c} of about 1. As seen in Fig. 6.19, the numerical results also agree well with the experimental observations by Francis (1973), Fernandez-Luque and van Beek (1976) and Lee and Hsu (1994). A more thorough analysis of the saltation streamwise velocity predicted by the numerical model is presented in next section.

The simulated values of μ_d shown in Fig. 6.20 seem to agree fairly well with the experimental estimations of this variable. Apparently, the numerical estimation of μ_d does not appear to be too sensitive to the modification of the model for e.

Finally, although the particular values of e used in the model seem to modify somewhat the magnitude of the mean values of λ_s, h_s, and u_s, they do not appear to change the slope of the curves at large values of τ_*/τ_{*c}.

Comparison with simulation of gravel saltation

A comparison between the experimental results of gravel and sand reported in Chapter 5 and the numerical results obtained with the model for particle saltation developed herein are presented in Figs. 6.21 to 6.24. The results of the simulation of the saltation of sand correspond to those presented in Figs. 6.17 to 6.20, for the values $R_p = 73$ (representative of the range of values of this variable in the experiments of Series S1), $f = 0.89$ and e given by (6.25). The results of the simulation of saltation of gravel correspond to the values $R_p = 15000$ (representative of the range of values of this variable in the gravel experiments of Chapter 5), $f = 0.73$ and e given by (6.21) with $A = 0.84$ and $B = 4.84$.

As seen in Fig. 6.21 simulated values of h_s for saltation of sand and gravel practically coincide for values of τ_*/τ_{*c} in the range 1.0 to 2.5. This is also true for the experimental observations of h_s except for the gravel points corresponding to $R_p = 7400$, which as was discussed in Section 6.5 are much larger than those corresponding to $R_p = 21900$. The differences between the simulated values of h_s for gravel and sand observed in Fig. 6.21 for values of τ_*/τ_{*c} larger than 2.5 seem to be caused by the particular values of e in that range, which in the former case drops to zero, and in the latter case remains constant at 0.2. It seems valid to recommend a minimum value of $e = 0.2$ for the saltation of gravel also, which would avoid the rather awkward behavior of the simulated values of h_s for gravel saltation in the range $2 < \tau_*/\tau_{*c} < 3$. Nevertheless, as already discussed, it is apparent

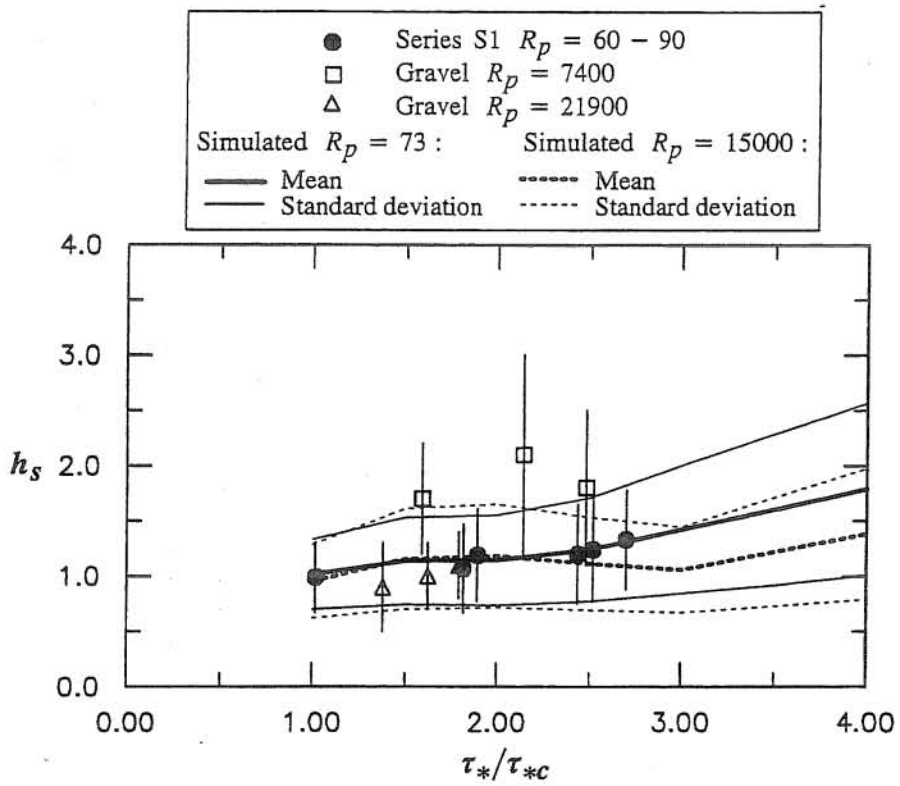

Fig. 6.21 Comparison between simulated dimensionless saltation height and experimental results of saltation of sand and gravel, Chapter 5. Symbols represent mean experimental values and vertical lines represent a total length of two corresponding standard deviations.

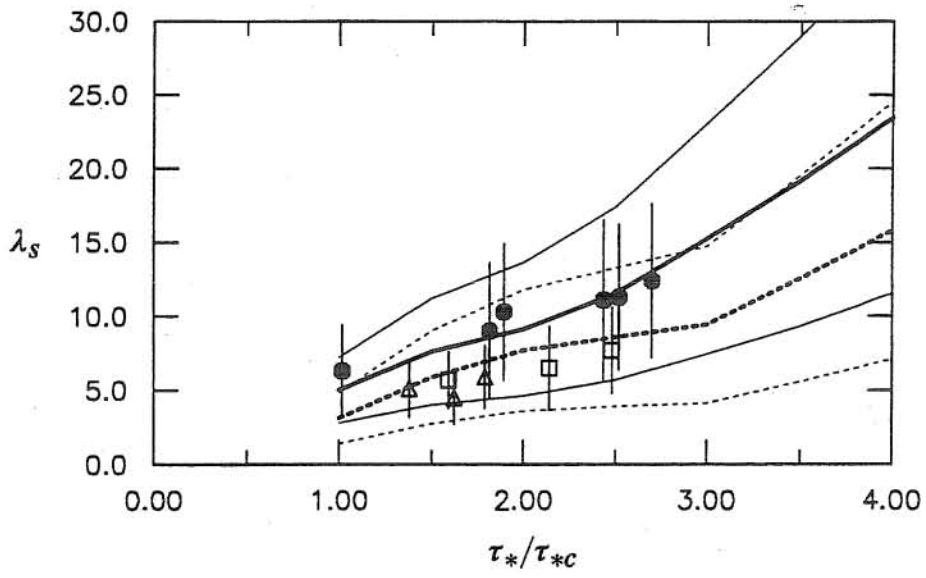

Fig. 6.22 Comparison between simulated dimensionless saltation length and experimental results of saltation of sand and gravel, Chapter 5. Legend as in Fig. 6.21.

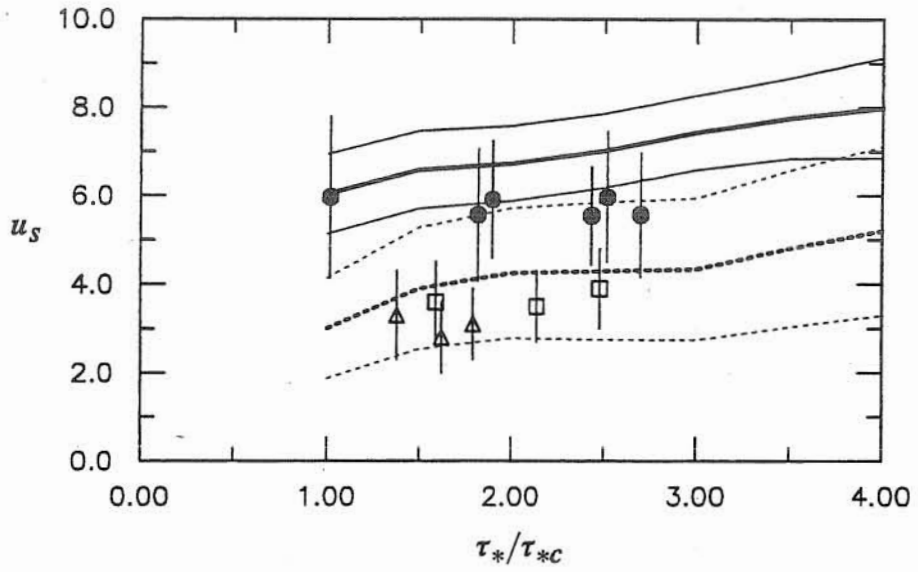

Fig. 6.23 Comparison between simulated dimensionless saltation streamwise velocity and experimental results of saltation of sand and gravel, Chapter 5. Legend as in Fig. 6.21.

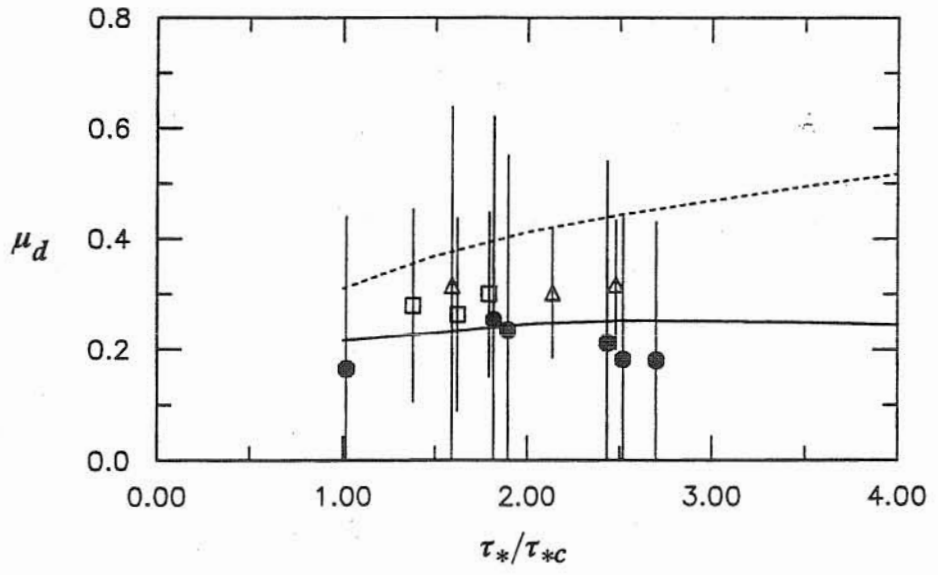

Fig. 6.24 Comparison between simulated dynamic friction coefficient and experimental results of saltation of sand, Chapter 5. Legend as in Fig. 6.21.

that the slope of the curve h_s as a function of τ_*/τ_{*c} for gravel is identical to that of sand in the range $\tau_*/\tau_{*c} > 3$, which suggest that this behavior is independent of the particular values of e and f selected in the simulation.

From Fig. 6.22 it seems that simulated values of λ_s for saltation of gravel are somewhat smaller than corresponding values for saltation of sand, and this is supported by the experimental data shown therein. As it was already discussed, this would be the effect of the Basset force which tends to increase the dimensionless saltation length as R_p decreases. Again, it seems that the slope of the curve λ_s as a function of τ_*/τ_{*c} for gravel is identical to that of sand in the range $\tau_*/\tau_{*c} > 3$, which suggest that this behavior is independent of the particular values of e and f selected in the simulation.

The results of the numerical simulations of u_s shown in Fig. 6.23 indicate that the simulated values of this variable for the case of gravel saltation are much smaller than those corresponding to the saltation of sand, which is supported by the experimental results shown in that figure. In both cases, however the simulated values of u_s tend to overestimate corresponding observed values, although this is more evident in the case of saltation of sand. The curves given by the simulated values of us as a function of τ_*/τ_{*c} for the saltation of both sand and gravel define trends that are approximately parallel to each other.

The values of μ_d estimated from the numerical simulations indicate that the values of this variable are somewhat greater in the case of saltation of gravel than in the case of saltation of sand, which is again supported by experimental data (Fig. 6.24). It is apparent that the simulated values of μ_d in the case of saltation of sand are much closer to corresponding observed values than in the case of saltation of gravel, in which the simulated values tend to overestimate slightly the observed values of μ_d. In any case, simulated and observed values of μ_d seem to be much smaller than the value 0.63 predicted by Bagnold (1973). Further discussion of this particular result is presented in next section.

6.6.3 Conclusions

The model for saltation of sand developed herein, performs satisfactorily when compared with individual saltation events obtained from experimental measurements of particle trajectories. In particular it was found that, as in the case of the saltation of gravel, lift forces must be included for the adequate modelling of observed trajectories, which indicate that upward forces arising from the particle collisions with the bed are insufficient to maintain such trajectories. It was also found that the Basset force plays a much important role in the saltation of sand than in the case of saltation of gravel. In fact, it was found that the dimensionless saltation length increases substantially as R_p decreases, which is due almost solely to the effect of the Basset force.

Computed statistics of saltation of sand agree very well with experimental observations, particularly after imposing a minimum value of the restitution coefficient, $e_{min} = 0.2$, instead of the value $e_{min} = 0$ estimated originally from the experimental observations of the collision process reported in Chapter 5. The slight modification of the model for the coefficient e proposed herein affects mainly the shape of the simulated curves for h_s, λ_s, and u_s as functions of τ_*/τ_{*c} in the range $2 < \tau_*/\tau_{*c} < 3$, nevertheless the trends defined by these curves in the range $\tau_*/\tau_{*c} > 3$ appears to be independent of the value of e in that range.

Simulated mean values and standard deviations of h_s and λ_s agree very well with corresponding observations of saltation of sand reported in Chapter 5. Simulated mean values of h_s also agree well with experimental results by Abbott and Francis (1977) and with the values corresponding to the saltation of gravel which implies that the dimensionless saltation height appears to be independent of particle size. Simulated mean values of λ_s for the saltation of sand tend to be slightly larger than those corresponding to the saltation of gravel, and this is supported by experimental observations reported in Chapter 5 and also by Abbott and Francis (1977), which implies that the dimensionless saltation length appears to decrease as the particle size increase.

Simulated mean values and standard deviations of u_s tend to overestimate somewhat observed values corresponding to the saltation of sand. However, simulated mean values of u_s at values of τ_*/τ_{*c} close to unity reproduce fairly well the rather high observed values of this variable in the experiments reported in Chapter 5, in that range of values of τ_*/τ_{*c}, as compared with similar results by Fernandez-Luque and van Beek (1973). In the range τ_*/τ_{*c} larger than about 2.5, on the other hand simulated values of u_s are in much better agreement with results by these researchers and also agree well with observations by Francis (1973) and Lee and Hsu (1994).

The values of the dynamic friction coefficient predicted by the model are about 0.25 to 0.30 which is in agreement with experimental observations. These values are slightly lower than the values simulated for the saltation of gravel, which is supported by the experimental observations. These values are much lower than the value 0.63 proposed by Bagnold (1973) for μ_d, and would indicate that the experimental evaluations of this coefficients are not prone to underestimation as suggested previously by Abbott and Francis (1977). Further discussion of this result is presented in the next section.

6.7 Application to bedload modelling

6.7.1 Theoretical considerations

The results of the numerical simulations of particle saltation can be used to analyze bedload transport in open channel flows. The situation of equilibrium sediment transport is considered, and it is assumed that the bedload transport occur in a thin, constant stress layer. Following the

theoretical derivations of Bridge and Dominic (1984) (see also, Engelund and Fredsøe, 1976; Leeder, 1979b; Bridge, 1981; Bridge and Bennett, 1992), the bedload transport rate i_b (in terms of submerged weight per unit width) can be expressed as:

$$i_b = W_b \, u_b^* \tag{6.26}$$

where W_b denotes the submerged weight of the bedload layer per unit bed area, and u_b^* denotes the mean velocity of the bedload grains.

Invoking the definition of the dynamic friction coefficient, μ_d, as the ratio between the shear stress exerted by the bedload grains over the bed and the submerged weight of the bedload layer, then W_b can be expressed as:

$$W_b = \tau_g / \mu_d \tag{6.27}$$

where τ_g denotes the grain shear stress, defined as the force per unit area exerted by the moving grains on the bed.

In order to evaluate τ_g it is necessary to consider a force balance over the bedload layer. On top of the bedload layer, the fluid exerts a force per unit are given by the shear stress of the flow τ_0, which can be considered approximately equal to the bed shear stress: $\tau_0 = \varrho \, u_*^2$. At the bottom of the bed load layer the total force is given by the force exerted by the fluid, in the form of a residual shear stress at the bed, τ_b, and that exerted by the bed as a reaction to the grain shear stress τ_g. Also considering the weight of the bedload layer and the slope of the channel given by $tan\ \theta$, the force balance implies:

$$\tau_0 + W_b \, sin\ \theta = \tau_g + \tau_b \tag{6.28}$$

According to Bagnold (1956), the residual shear stress at the bed, τ_b, at equilibrium conditions for bedload transport corresponds to the critical shear stress for the initiation of particle motion, τ_c. The argument is as follows. Within the bedload layer and due to the presence of moving particles, the fluid shear stress decreases toward the bed, from the value τ_0 on top of the bedload layer to the value τ_b at the bed. The amount of shear stress reduction increases with the concentration of particles within the bedload layer. Given a value of τ_b larger than τ_c, more and more particles are entrained into motion, however this produces a drop on the value of τ_b. If equilibrium conditions for bedload transport prevail, then a maximum concentration of particles in the bedload layer is attained, such that the flow shear stress at the bed drops to τ_c and no more particles can be entrained into motion. In this situation: $\tau_b = \tau_c$. Hence, from (6.28) and assuming that the slope of the channel is small:

$$\tau_g = \tau_0 - \tau_c \tag{6.29}$$

Replacing (6.29) and (6.27) in (6.26), i_b can be written as:

$$i_b = \frac{1}{\mu_d} (\tau_0 - \tau_c) u_b^* \tag{6.30}$$

and expressing i_b in terms of the Einstein's form for the dimensionless volumetric bedload transport rate given by $q^* = i_b / \sqrt{\varrho^2 (R g d_p)^3}$, then (6.30) can be rewritten as:

$$q^* = \frac{1}{\mu_d} \tau_*^{1/2} (\tau_* - \tau_{*c}) u_b \tag{6.31}$$

where u_b denotes the mean velocity of the bedload grains made dimensionless with u_*.

By identifying the values of u_b with the mean dimensionless streamwise saltation velocity, u_s, and the dynamic friction coefficient, μ_d, defined as in (6.27) with the value estimated as in (6.24), then results of the numerical simulation of particle saltation can be used to evaluate (6.31).

6.7.2 Bedload transport of gravel

By using simulated values of u_s and μ_d for the saltation of gravel presented in Section 6.5, and assuming that τ_{*c} is given by Shields curve, q^* can be evaluated from (6.31) for different values of τ_* and R_p. The results obtained are plotted in Fig. 6.25, together with the values estimated from bedload formulae of Meyer–Peter and Muller (1948), given by:

$$q^* = 8 (\tau_* - \tau_{*c})^{3/2} \tag{6.32}$$

where τ_{*c} is approximated as equal to 0.047, and Engelund and Fredsøe (1976), given by:

$$q^* = 18.74 (\tau_* - \tau_{*c}) (\tau_*^{1/2} - \tau_{*c}^{1/2}) \tag{6.33}$$

where τ_{*c} is approximated as equal to 0.05.

Also plotted in Fig. 6.25 are the values corresponding to the experimental measurements of gravel transport made by Meyer–Peter et al. (1934) (d_p = 28.6 mm), and Ayala and Valenzuela (1993) (d_p = 15 ; 31 mm), the latter corresponding to the gravel saltation experiments analyzed in Chapter 5. The results given by (6.31), using the present numerical simulation for gravel saltation, compare favorably with the bedload formulae mentioned above. Nevertheless, all bedload formulae including the numerical results, tend to overestimate the experimental values of q^* associated with gravel transport.

The fact that (6.31) overestimates the transport of coarse material seems to indicate that either the estimation of the ratio u_s/μ_d or the value of τ_{*c} are inadequate, or the hypotheses used in its derivation are not valid under such conditions. However, we found that the simulated values of

u_s/μ_d, which are in the range 9.5 to 12.0, agree very well with the values obtained from the gravel experiments reported in Chapter 5. Furthermore, experimental evidence (Ayala et al., 1990) indicates that the experimental points of Ayala and Valenzuela (1993) in Fig. 6.25 correspond to a value of τ_{*c} of about 0.05, which is slightly smaller than the value of about 0.06 predicted by Shields' curve for the same particles. Using a value of τ_{*c} in (6.31) which is smaller than that predicted by Shields' curve would cause this equation to overestimate even more the experimental points.

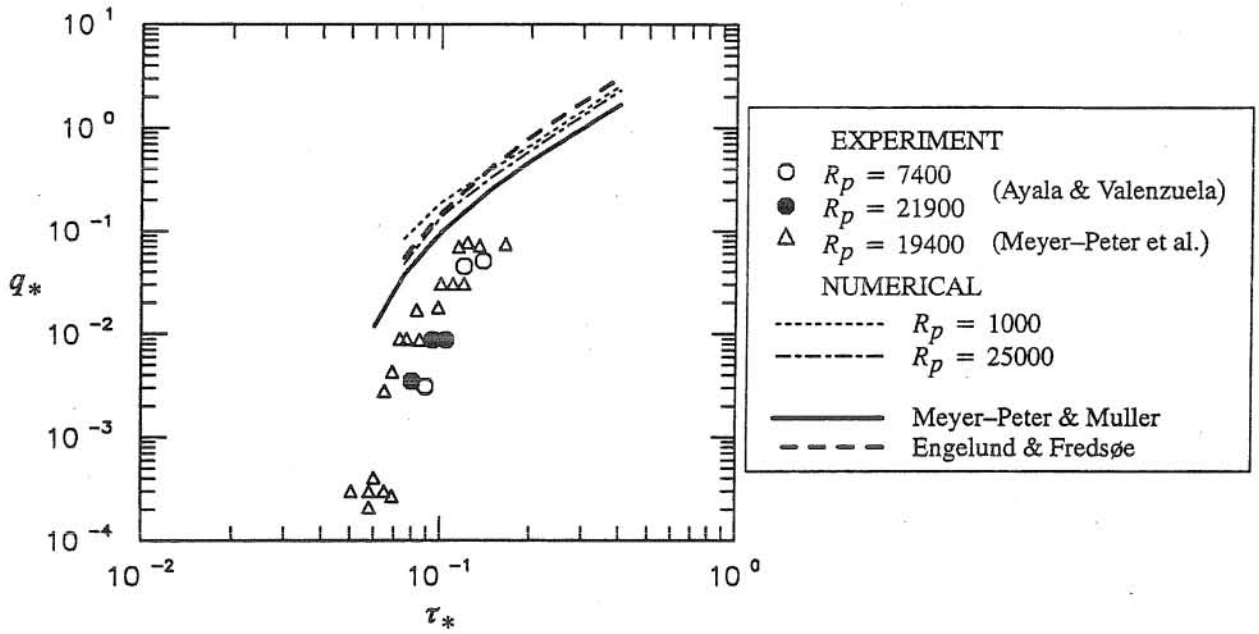

Fig. 6.25 Dimensionless bedload transport rates predicted by (6.31) and the bedload formulae of Meyer-Peter and Muller (1948) and Engelund and Fredsøe (1976). Comparison with measurements of gravel transport by Ayala and Valenzuela (1993) and Meyer-Peter et al. (1934).

Considering that typical saltation heights are of the order of two particle diameters, and that gravel sizes are of the order of a few centimeters, it is clear that the thickness of the bedload layer associated with the transport of gravel is relatively large when compared to the flow depth (generally the transport of gravel is associated with low flow depth to particle size ratios). At the same time, the concentrations associated with the bedload transport of such coarse particles are relatively low. Therefore, the conditions invoked for the development of a Bagnoldean formulation such as (6.31) do not seem to apply to the case of bedload transport of coarse sediment. An alternative analysis to estimate transport rates of coarse sediment by saltating particles would be to follow an Einstenian formulation (e.g., Einstein, 1950), in which saltation characteristics are used but there is no need to asses the shear stress exerted on the bed by the particles (Parker, 1991). Further analysis of the Bagnoldean formulation is presented next for the case of bedload transport of sand.

6.7.3 Bedload transport of sand

Analogously as in the previous section, values of $q*$ can be estimated from (6.31) by using simulated values of u_s and μ_d for the saltation of sand presented in Section 6.6. However, instead of simply replacing the numerical values of these variables in (6.31) it is instructive to further analyze the numerical results for u_s and μ_d.

Simulated values of u_s for values of R_p in the range 75 to 200, representative of the experimental conditions for the bedload transport of sand in the experiments reported in Chapter 5 and by Fernandez-Luque and van Beek (1976), are plotted in Fig. 6.26 as a function of $(\tau_*)^{-1/2}$. As observed therein, the numerical results tend, as τ_* increases, to define straight lines of variable slope. Based on this, the following general form for the dimensionless streamwise saltation velocity can be proposed:

$$u_s = a - b \, (\tau_*)^{-1/2} \tag{6.34}$$

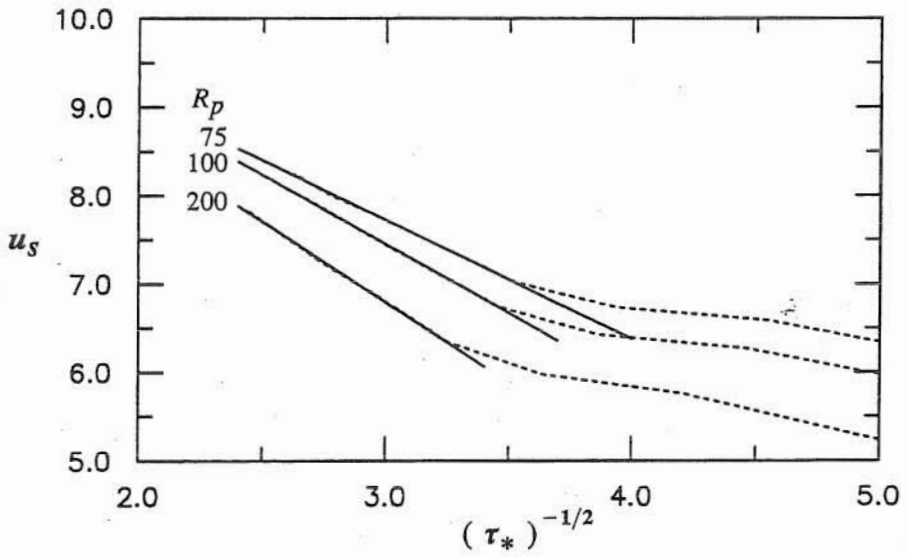

Fig. 6.26 Simulated dimensionless streamwise saltation velocity.

Table 6.1 shows values of a and b as functions of R_p fitted to the numerical results shown in Fig. 6.26. As seen therein the value of a is fairly constant in the range $75 < R_p < 200$, equal to about 12.0 with a variation of about 2%. On the other hand the value of b seems to vary relatively more than a in the same range of values of R_p, with a mean value of about 1.6.

It is easy to see that (6.34) can be rewritten as:

$$u_s = a \, (\, 1 - b' \, (\, \tau_* / \tau_{*c} \,)^{-1/2} \,) \tag{6.35}$$

where $b' = b/(a \sqrt{\tau_{*c}})$. Values of b' are also shown in Table 6.1, where values of τ_{*c} were estimated using Shields curve. As seen therein values of b' in the range $75 < R_p < 200$ are in average about 0.7.

Table 6.1 Values of constants in equation for dimensionless streamwise saltation velocity

R_p	a	b	b'
75	11.8	1.4	0.6
100	12.1	1.6	0.7
200	12.3	1.8	0.8

Interestingly, the form of (6.35) is identical to that of relationships for u_s proposed analytically and experimentally by different researchers (e.g., Ashida and Michiue, 1972; Fernandez-Luque and van Beek, 1976; Bridge and Dominic, 1984; Bridge and Bennett, 1992). Most of the models for u_s consider $b' = 1$, however experimentally Fernandez-Luque and van Beek (1976) found a value $b' = 0.7$, which is similar to the mean value of b' in the range $75 < R_p < 200$ obtained herein from the numerical simulation of saltation of sand as shown in Table 6.1. In general according to Bridge and Dominic (1984), different researchers have proposed values of a in the range 8.5 to 14.3. Fernandez-Luque and van Beek propose a value of $a = 11.5$, which is also similar to the values of this parameter shown in Table 6.1.

Simulated values of μ_d for the same values of R_p used in the analysis of the results for u_s ($75 < R_p < 200$) are plotted in Fig. 6.27 as functions of R_p and τ_*/τ_{*c}. As seen in that figure, the values of μ_d tend to increase slightly with R_p in the range considered. They also increase with τ_*/τ_{*c}, however their change with this parameter is rather small for values of τ_*/τ_{*c} larger than about 2. From the results shown in Fig. 6.27 it seems sufficient approximation to consider a constant value of μ_d of about 0.28, valid for values of R_p in the range 75 to 200 and for values of τ_*/τ_{*c} larger than about 2. It is noteworthy that this value of μ_d is in agreement with the experimental observations reported in Chapter 5, as it has already been discussed.

Replacing (6.35) in (6.31), q^* can be expressed as:

$$q^* = \frac{a}{\mu_d} (\tau_* - \tau_{*c}) (\tau_*^{1/2} - b' \tau_{*c}^{1/2}) \qquad (6.36)$$

where according to the above discussion, a, b', and μ_d can be approximated as constants, independent of R_p. It is important to mention that the form of (6.36) is identical to that of Engelund and Fredsøe (1976). The asymptotic behavior of (6.36) at large values of τ_* is : $q^* \propto \tau_*^{3/2}$, which is in agreement with most of the bedload formulae available in the literature (compare for instance

with Meyer-Peter and Muller equation (6.32)). Replacing the values $a = 12$, $b' = 0.7$, and $\mu_d = 0.28$, the following equation is obtained:

$$q^* = 43.0\ (\ \tau_* - \tau_{*c}\ )\ (\ \tau_*^{1/2} - 0.7\ \tau_{*c}^{1/2}\ ) \tag{6.37}$$

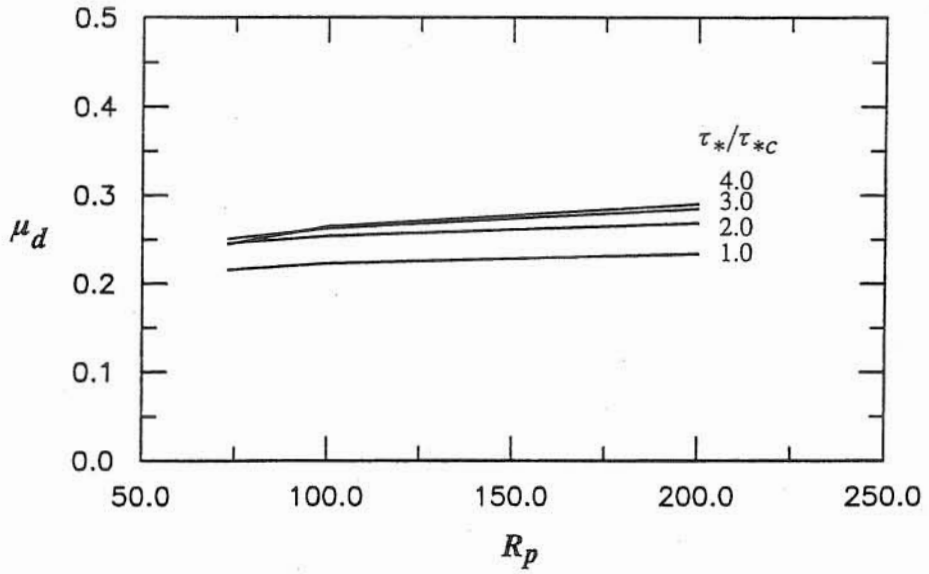

Fig. 6.27 Simulated dynamic friction coefficient.

This equation is compared with those of Meyer-Peter and Muller and Engelund and Fredsøe, (6.32) and (6.33) respectively, in Fig. 6.28. Therein the values of q^* are plotted as a function of $\tau_* - \tau_{*c}$. Since (6.37) depends on τ_{*c}, parametric curves with values of this parameter in the range 0.02 to 0.05, typical for sediment particles in the sand size range, are plotted in Fig. 6.28. As seen in this figure, the values of q^* given by (6.37) are not too sensitive to variations of τ_{*c} in the range considered. As $\tau_* - \tau_{*c}$ increases the curves for q^* tend to collapse in one, which appears to have a constant slope of 3/2 in the log-log plot, and is parallel to those given by equations (6.32) and (6.33). Nevertheless, it is also apparent that (6.37) overestimate notoriously the values of q^* predicted by those equations. In fact, the coefficient $a/\mu_d = 43$ in (6.37) is about 2.3 times larger than the corresponding coefficient appearing in Engelund and Fredsøe's equation (6.33).

Since the expression (6.35) for u_s with the values of $a = 12$, and $b' = 0.7$ is very close to that of Fernandez-Luque and van Beek (1976), and in general agrees satisfactorily with other experimental observations including those reported in Chapter 5, it must be concluded that the dynamic friction coefficient μ_d estimated from the numerical simulation of particle saltation using (6.24) seems to be about 2.3 times smaller than expected. Nonetheless, the simulated values of this parameter reproduce very well experimental observations of this parameter as it was discussed in previous sections. To elucidate this paradox it is necessary to pay some attention to the different

definitions of the dynamic friction coefficient used so far, and the form of estimating this variable from the experimental observations.

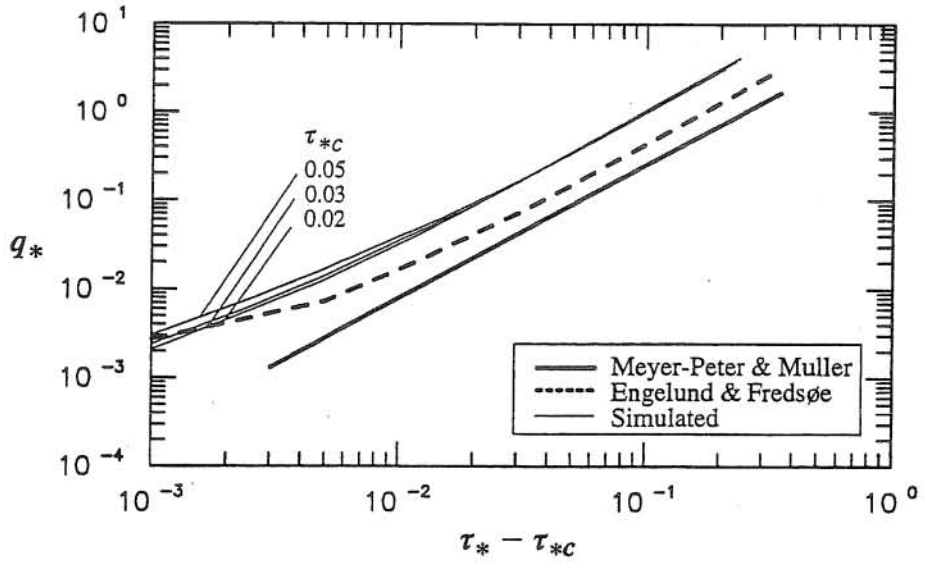

Fig. 6.28 Simulated dimensionless bedload transport rates. Comparison with formulae by Meyer-Peter and Muller (1948) and Engelund and Fredsøe (1976).

As indicated in (6.27), the definition of μ_d used in the derivation of the bedload equation (6.31) considers the dynamic friction coefficient as the ratio between the shear stress exerted by the bedload grains over the bed and the submerged weight of the bedload layer per unit area. Furthermore, the grain shear stress is assumed to equal, by force balance considerations, the reduction of the shear stress of the fluid at the bed due to the presence of the saltating grains. On the other hand the expression (6.24) corresponds to a Lagrangian estimation of μ_d, given by the ratio between the local streamwise force exerted over the bed by a saltating particle through successive collisions, and the submerged weight of the particle. The derivation of (6.24) is as follows (Abbott and Francis, 1977).

Considering a particle in continuous saltation, then its velocity just before an impact with the bed, $u_p * |_{in}$, is larger than that just after the impact, $u_p * |_{out}$, which implies the existence of a retarding force exerted by the bed over the saltating grain during the collision. In a steady saltation motion, the mean retarding force exerted by the bed must equal the mean forwarding thrust exerted by the fluid during the saltating trajectory through drag. The mean forwarding thrust can be estimated from the streamwise acceleration of the grain from a streamwise velocity $u_p * |_{out}$ just after an impact with the bed to the streamwise velocity $u_p * |_{in}$ right before the following collision with the bed. The time during which this acceleration takes place corresponds to the duration of the saltation, which is given by:

$$t_s * = \lambda_s * / u_s * \tag{6.38}$$

The particle mean streamwise momentum change per unit time during the saltation event, which is equivalent to the fluid thrust, is given by:

$$F_f = \varrho_s \, V_p \, (\, u_p{}^* \, |_{in} - u_p{}^* \, |_{out} \,) \, u_s{}^* / \lambda_s{}^* \tag{6.39}$$

where V_p denotes the particle volume. Calling: $(\, u_p{}^* \, |_{in} - u_p{}^* \, |_{out} \,) = \Delta u_p{}^*$, then the Lagrangian dynamic friction coefficient, μ_{dL}, can be written as:

$$\mu_{dL} = F_f / W_g = (\, \varrho_s \, \Delta u_p{}^* \, u_s{}^* \,) / (\, (\, \varrho_s - \varrho \,) \, g \, \lambda_s{}^* \,) \tag{6.40}$$

where $W_g = (\, \varrho_s - \varrho \,) \, g \, V_p$, denotes the particle submerged weight. Introducing dimensionless parameters already defined:

$$\mu_{dL} = (\, R + 1 \,) \, \tau_* \, \Delta u_p \, u_s \, / \, \lambda_s \tag{6.41}$$

equation which is identical to the one previously presented in (6.24), and which was the one used to estimate the experimental and numerical values of the dynamic friction coefficient presented in previous sections.

According to the previous derivation, μ_{dL} corresponds to the dynamic friction coefficient associated with the continuous saltation of one particle. It is easy to see that if n particles per unit bed area are saltating, then the total force exerted by the bed over the particles would be n times F_f, and the total immersed weight of the particles would be n times W_g, thus the dynamic friction coefficient of the group of particles is exactly equal to μ_{dL}.

The latter implies that the total force per unit bed area, i.e. the shear stress, exerted by the bed over the saltating particles increases linearly with the number of particles. However, from (6.28) the effective shear stress exerted by the bed over the saltating grains is given by the reduction of the fluid shear stress due to the presence of particles, which most likely is a nonlinear function of the number of particles in the bedload layer, since it involves nonlinear interactions between fluid and solid phases including turbulence modification by the presence of the sediment. This indicates that both concepts, the Lagrangian dynamic friction coefficient, μ_{dL}, and the dynamic friction coefficient, μ_d, used in the bedload equation (6.31) do not necessarily coincide. In fact, the latter involves somehow a continuum assumption for the bedload layer, different from the Lagrangian approach of the former, which may be valid only under conditions of relatively high concentration of particles in the bedload layer.

The previous analysis seems to justify the observed differences between the Lagrangian estimation of the dynamic friction coefficient by (6.24) or (6.41) and the value of this coefficient required to fit typical bedload formulas, which according to Bagnold (1973) should be close to the value of the static friction coefficient, $\tan \phi$, which for natural sediment is about 0.63. Interestingly,

the ratio between $tan\ \phi = 0.63$ and the numerically estimated value of $\mu_{dL} = 0.28$ gives a value of 2.3, which is equal to the factor by which the numerically derived bedload equation (6.37) overestimate the values of q^* with respect to those given by Engelund and Fredsøe's equation (6.33).

The above analysis would also explain why the experimental estimations of μ_{dL} have always been found to be lower than the value of $tan\ \phi$ predicted by Bagnold for μ_d. Accordingly, such differences would not be a bias derived from experimental inaccuracies in the temporal resolution of the moment of collision as it has been argued in the past (e.g., Abbott and Francis, 1977). The latter was also demonstrated by the experimental results reported in Chapter 5, which showed similar differences between μ_{dL} and $tan\ \phi$, although a high-speed video system helped improving the temporal resolution of the moment of collision substantially.

6.7.4 Discussion

The above results regarding the modelling of bedload transport of gravel as well as of sand seem to indicate a few problems with the Bagnoldean formulation. In the first place, it assumes the bedload layer as continuum, which may be valid only under conditions of relatively high concentration of particles, and relatively small particle size. Second, it assumes that the entrainment of particles into saltation is somehow proportional to the excess bed shear stress over the critical value τ_{*c}, such that in equilibrium bedload transport no particles are entrained into saltation and only those particles already forming part of the bedload layer are kept in motion. This, which implies a reduction of fluid shear stress at the bed to the critical value τ_{*c} due to the presence of the bedload layer, seems to be a simplification of a much more complicated process where a constant exchange of particles between the bed and the bedload layer takes place. Third, the resulting model for bedload transport appears to be very dependent on the value of τ_{*c}, which is difficult to estimate because it does not necessarily correspond to the value associated to the threshold of particle motion. In fact, Lavelle and Mofjeld (1987) have criticized the existence of the concept of threshold of particle motion and proposed the formulation of transport models that do not rely on such a concept. For instance, Parker's (1990) model for bedload transport of gravel, which does not need the estimation of τ_{*c}, represents a step in that direction.

An alternative approach to estimate bedload transport is to follow an Einstenian formulation (e.g., Einstein, 1950), as discussed previously for the case of gravel transport, in which characteristics of the saltation motion are used but there is no need to asses the shear stress exerted on the bed by the particles (Parker, 1991). For example, referring to Fig. 6.29, it is easy to see that the total volume of particles crossing the window W per unit time, per unit width, q_b, is given by:

$$q_b = E_s\ \lambda_s^* \tag{6.42}$$

where E_s denotes the volume of particles entrained into saltation per unit time, per unit bed area, and $\lambda_s *$ denotes, as before, the dimensioned saltation length. The entrainment rate E_s is given by the volume rate per unit bed area of particles that impact the bed and continue their saltation, E_{sc}, as well as by that of particles that are resting on the bed and are re-entrained, E_{sr}, such that:

$$E_s = E_{sc} + E_{sr} \tag{6.43}$$

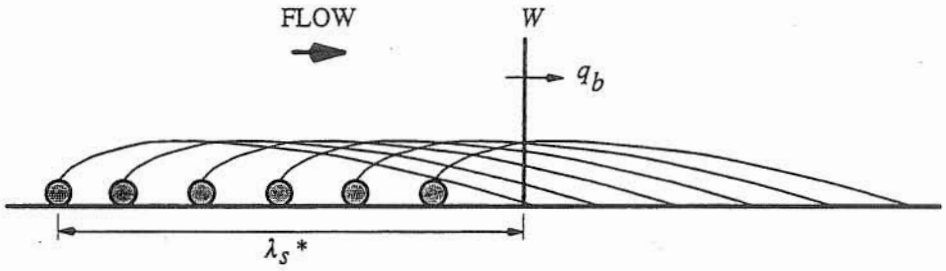

Fig. 6.29 Schematic view of particle saltation for determination of bedload rate

However, it is apparent that E_{sc} and E_{sr} are related. In fact, any saltating particle begins its trajectory of successive hops from rest. After a number of saltation and collision with the bed sequences, the particle would come to rest again. In the average, particles would displace a distance equal to, say, $m\,\lambda_s *$, where m denotes the average number of hops experienced by the saltating particles between rest periods. Now, a bed area having a total length equal to $\lambda_s *$ and a width comparable to the particle diameter is considered. If it is assumed that in the average particles are re-entrained from rest with a frequency f_r, then it can be expected that the total number of particles leaving the bed area considered per unit time, q_n, is given by:

$$q_n = m\, f_r \tag{6.44}$$

which includes $(m - 1)$ particles that collide with the bed and continue their motion, as well as the one particle that leaves the bed from rest each $1/f_r$ seconds. Under equilibrium conditions the frequency f_r must correspond to the inverse of the resting time of the particle, $t_r *$, defined as the average time elapsed between the moment a given particle comes to a stop and the moment it resumes its motion (see Chapter 5). From (6.44), E_s can be estimated as:

$$E_s = \frac{V_p\, m}{t_r *\, \lambda_s *\, d_p} \tag{6.45}$$

where V_p denotes the particle volume. Replacing (6.45) in (6.42), and converting q_b into the dimensionless volumetric bedload transport rate, q_*, the following expression is obtained:

$$q_* = \frac{\pi}{6} \sqrt{\tau_*}\, \frac{m}{t_r} \tag{6.46}$$

where t_r denotes the dimensionless particle resting time defined as: $t_r = t_r *\, u_* / d_p$.

The above formulation follows a very similar approach to that of Einstein (1950). It is based on the physics of the bedload motion as observed in the experiments of Chapter 5, it does not rely on the continuum hypothesis for the bedload layer as does the Bagnoldean formulation, and it does not make use of the concept of a critical bed shear stress. As discussed in Chapter 5, the dimensionless particle resting time would tend to decrease as τ_* increases, which according to (6.45) would increase q_*. Similarly it is expected that as τ_* increases m also increases since the transport capacity of the flow increases, which also would increase q_* as given by (6.45).

Two mechanisms were identified in Chapter 5 to determine particle re-entrainment into saltation (and thus t_r), namely turbulence effects, and also particle-particle interactions. Turbulence effects would be related to the occurrence of high intensity flow velocity fluctuations, possibly those related to bursting events, which would be most responsible for inducing particle motion. In this respect it seems that the exposition of the particle relative to the flow (given by the local topography of the bed where the particle lies) would play an important role in the efficiency of the turbulent events to re-entrain the particle. Empirical evidence presented in Chapters 3 and 4 indicates that as τ_* increases so does the intensity of bursting events, which would have the effect of reducing t_r. On the other hand, the probability of occurrence of particle-particle interactions clearly increases with the number of particles present in the bed at given location and time. Of course, such number increases with τ_* because the bedload rate increases with this variable, which implies that the number of particle-particle interactions increases with τ_*, which would also have the effect of reducing t_r.

Modelling bedload transport based on (6.46) would require modelling t_r as well as m. This would call for the modelling of near bed particle-turbulence as well as particle-particle interactions. A possible approach to the problem would be to introduce stochastic models for the turbulence characteristics of the bursting events assumed to be responsible for particle re-entrainment, and also for the local bed configuration where the above interactions occur.

6.7.5 Conclusions

A model to estimate sediment bedload transport has been developed, which is based in a Bagnoldean formulation. The model makes use of the characteristics of particle saltation which were estimated using the stochastic model presented and discussed in previous sections.

The model predictions of gravel bedload transport compare favorably with the bedload formulae of Meyer-Peter and Muller (1948) and Engelund and Fredsøe (1976). Nevertheless, all bedload formulae including the numerical results, tend to overestimate the experimental values of Meyer-Peter et al. (1934) and Ayala and Valenzuela (1993). It seems that a Bagnoldean formulation may not be applicable to the modelling of bedload transport of coarse material.

The application of the bedload model to the case of sand, using the numerically simulated characteristics of particle saltation, yields an equation which is identical in structure to that of typical bedload formulae, in particular to that by Engelund and Fredsøe (1976). Nevertheless it was found that the bedload rates predicted by such formula are about 2.3 times larger than those given by Engelund and Fredsøe's, which appears to be a consequence of the underestimation of the dynamic friction coefficient, μ_d, by the same amount.

The analysis of the Lagrangian dynamic friction coefficient, μ_{dL}, which is the value estimated from the saltation model, indicates that this variable would differ from the concept of dynamic friction coefficient used in the derivation of the bedload model. The latter seems to be given by $tan\ \phi$ = 0.63, in agreement with Bagnold (1973), whereas the values of μ_{dL} would be in the range 0.25 to 0.4, in agreement with the values observed in the experiments of Chapter 5 as well as those of Francis (1973) and Abbott and Francis (1977), and also with the numerical simulations of particle saltation presented in previous sections.

The results regarding the modelling of bedload transport of gravel as well as of sand seem to indicate that a major problem with the Bagnoldean formulation is related to the continuum assumption for the bedload layer, which would be valid only for very high particle concentrations and small particle diameters. Also this formulation appears to be very dependent on the value of τ_{*c}, which in general is difficult to estimate because it does not necessarily correspond to the value associated with the threshold of particle motion.

An alternative bedload equation based on an Einstenian formulation has been derived which appear to depend on the dimensionless resting time and the average number of jumps experienced by the saltating particle between rest periods. This approach does not rely on the continuum hypothesis for the bedload layer, and does not make use of the concept of a critical bed shear stress. A possible way to evaluate the characteristics of saltation required by the model would be to introduce stochastic models for the turbulence characteristics of the bursting events assumed to be responsible for the particle re-entrainment, and also for the local bed configuration where particle-turbulence and particle-particle interactions occur.

6.8 References

Abbott, J. E., and Francis, J. R. D. (1977). "Saltation and suspension trajectories of solid grains in a water stream". *Philos. Trans., Royal Soc. of London.* A, 284, pp 225-254.

Ashida, K., and Michiue, M. (1972). "Study on hydraulic resistance and bedload transport rate in alluvial streams". *Proc. Japan Soc. Civ. Engrg.*, 206, pp 59-69.

Ayala, L., and Valenzuela, R. (1993). "Elemental motion of coarse uniform particles and its relation with sediment transport". *Pub. CRH 93-77-I of the Water Resour. Center, Dep. of Civil Engrg., Univ. of Chile*. Santiago, Chile. (In Spanish).

Ayala, L., López A., and Campos, J. (1990). "Incipient particle motion in large-scale-roughness flows". *Pub. CRH 90-64-I of the Water Resour. Center, Dep. of Civil Engrg, Univ. of Chile*. Santiago, Chile. (In Spanish).

Bagnold, R. A. (1973). "The nature of saltation and of 'bed-load' transport in water". *Proc. R. Soc. of London*. A, 332, pp 473-504.

Bagnold, R. A. (1956). "The flow of cohesionless grains in fluids". *Philosophical trans., R. Soc. of London*. A, 249, pp 235-297.

Bridge, J. S., and Bennett, S. J. (1992). "A model for the entrainment and transport of sediment grains of mixed sizes, shapes, and densities". *Water Resour. Res.*, 28 (2), pp 337-363.

Bridge, J. S., and Dominic, D. F. (1984). "Bed load grain velocities and sediment transport rates". *Water Resour. Res.*, 20 (4), pp 476-490.

Bridge, J. S. (1981). "A discussion of Bagnold's (1956) bedload transport theory in relation to recent developments in bedload modelling". *Earth Surf. Proc. and Landforms*, vol 6, pp 187-190.

Brush, L. M., Ho, H. W., and Yen, B. C. (1964). "Accelerated motion of a sphere in a viscous fluid". *J. Hydraulic Div.*, ASCE, 90 (HY1), pp 149-160.

Chepil, W. S. (1958). "Use of evenly spaced hemispheres to evaluate aerodynamic forces on soil surfaces". *Eos. Trans.* AGU, 39 (3), pp 397-404.

Elghobashi, S., and Truesdell, G. C. (1992). "Direct simulation of particle dispersion in a decaying isotropic turbulence". *J. Fluid Mech.*, vol 242, pp 665-700.

Einstein, H., A. (1950). "The bedload function for sediment transportation in open channel flow". *U. S. Dept. Agric., Tech. Bull.* No 1026.

Engelund, F., and Fredsøe, J. (1976). "A sediment transport model for straight alluvial channels". *Nordic Hydrol.*, 7, pp 293-306.

Fernandez–Luque, R., and Van Beek, R. (1976). "Erosion and transport of bed sediment". *J. Hydr. Res.*, 14(2), 127–144.

Francis, J. R. D. (1973). "Experiments on the motion of solitary grains along the bed of a water stream". *Proc. R. Soc. of London*. A, 332, pp 443-471.

García, M., and Niño, Y. (1992). "Lagrangian description of bedload transport by saltating particles". *Proc. VI I.A.H.R. Int. Symp. on Stochastic Hydraulics*, Taipei, Taiwan, pp 259-266.

Hinze, J. O. (1971). "Turbulent fluid and particle interaction". *Progress in Heat and Mass Transfer.*, vol 6, pp 433-452.

Hayashi, T., and Ozaki, S. (1980). "On the unit step length of saltation of sediment particles in the bed-load layer". *Third Int. Symp. on Stochastic Hydraulics,* Tokyo, Japan.

Lavelle, J. W., and Mofjeld, H. O. (1987). "Do critical stresses for incipient motion and erosion really exist?". *J. Hydr. Engrg.*, vol 113, No 3, pp 370-385.

Lawrence, C. J., and Mei, R. (1995). "Long-time behaviour of the drag on a body in impulsive motion". *J. Fluid Mech.*, vol 283, pp 307-327.

Lee, H., and Hsu, I. (1994). "Investigation of salttaing particle motions". *J. Hydr. Engrg.*, ASCE, 120 (7), pp 831–845.

Leeder, M. R. (1979a). "Bedload dynamics: Grain impacts, momentum transfer and derivation of a grain Froude number". *Earth Surface Processes*, vol 4, pp 291-295.

Leeder, M. R. (1979b). "Bedload dynamics: Grain-grain interactions in water flows". *Earth Surface Processes*, vol 4, pp 229-240.

Lumley, J. L. (1978). "Two-phase and non-Newtonian flows". *Turbulence*, P. Bradshaw, ed., Chap. 7. Topics in applied physics, vol. 12, Springer-Verlag.

Maxey, M. R., and Riley, J. J. (1983). "Equation of motion for a small rigid sphere in a nonuniform flow". *Phys. Fluids*, 26 (4), pp 883-889.

Mei, R., Adrian, R. J., and Hanratty, T. J. (1991). "Particle dispersion in isotropic turbulence under Stokes drag and Basset force with gravitational settling". *J. Fluid Mech.*, vol 225, pp 481-495.

Mei, R. (1990). "Particle dispersion in isotropic turbulence and unsteady particle dynamics at finite Reynolds number". *Ph.D. Thesis, University of Illinois at Urbana-Champaign*. Urbana, Illinois.

Meyer-Peter, E., and Muller, R. (1948). "Formulas for bedload transport". *Proceedings*, 2nd Congress IAHR, Stockholm.

Meyer-Peter, E., Favre, H., and Einstein A. (1934). "Neuere versuchsresultate über den geschiebetrieb". *Schweizerische Bauzeitung*, 103 (13).

Murphy, P. J. and Hooshiari, H. (1982). "Saltation in water dynamics". *J. Hydraulic Div.*, ASCE, 108 (HY11), pp 1251-1267.

Parker, G. (1991). "Some random notes on grain sorting". *Proceedings of the International Grain Sorting Seminar*, Ascona, Switzerland. pp 19-76.

Parker, G. (1990). "Surface-based bedload transport relation for gravel bed rivers". *J. Hydr. Res.*, vol 28, No 4, pp 417-436.

Patnaik, P. C., Vittal, N., and Pande, P. K. (1994). "Lift coefficient of a stationary sphere in gradient flow". *J. Hydr. Res.*, vol 32, No 3, pp 471-480.

Reizes, J. A. (1978). "Numerical study of continuous saltation". *J. Hydraulic Div.*, ASCE, 104 (HY9), pp 1303-1321.

Rizk, M. A. and Elghobashi, S. E. (1985). "The motion of a spherical particle suspended in a turbulent flow near a plane wall". *Phys. Fluids* 28 (3), pp 806-817.

Rubinow, S. and Keller, J. (1961). "The transverse force on a spinning sphere moving in a viscous fluid". *J. Fluid Mech.*, vol 11, pp 447-459.

Sekine, M., and Kikkawa, H. (1992). "Mechanics of saltating grains. II". *J. Hydr. Engrg.*, ASCE, 118 (4), pp 536-558.

Sekine, M., and Parker, G. (1992). "Bed-load transport on transverse slope. I". *J. Hydr. Engrg.*, ASCE, 118 (4), pp 513-535.

Tsuchiya, Y. (1969). "On the mechanics of saltation of a spherical sand particle in a turbulent stream". *Proc. 13th Cong. IAHR*,2, pp 191-198.

Van Rijn, L. C. (1984). "Sediment transport, Part I: Bed load transport". *J. Hydr. Engrg.*, ASCE, 110 (10), pp 1431-1456.

White, B. R. and Schulz, J. C. (1977). "Magnus effect in saltation". *J. Fluid Mech.*, vol. 81, part 3, pp 497-512.

Wiberg, P. L., and Smith, J. D. (1989). "Model for calculating bedload transport of sediment". *J. Hydr. Engrg.*, ASCE, 115 (1), pp 101-123.

Wiberg, P. L., and Smith, J. D. (1985). "A theoretical model for saltating grains in water". *J. Geophysical Res.*, 90 (C4), pp 7341-7354.

Yalin, S. (1958). "Sur la mécanique du mouvement des matériaux solides". *La Houille Blanche*. No. 6, pp 607-618.

Yen, B. C. (1992). "Sediment fall velocity in oscillating flow". *Water Resources and Environ. Engrg. Res.* Report No. 11. Dept. of Civil Engrg. University of Virginia.

7. THRESHOLD FOR PARTICLE ENTRAINMENT INTO SUSPENSION

7.1 Introduction

The concept of a threshold bed shear stress for the initiation of motion of a sediment particle lying in a bed of similar particles has long occupied a central position in sediment transport theory (e.g., DuBoys, 1879; Shields, 1936). Nevertheless, Lavelle and Mofjeld (1987) criticized such concept and proposed, based on empirical evidence such as that by Grass (1971), an alternative statistical view of particle movement on the bed, such that turbulent fluctuations of instantaneous bottom shear stress and the range of potential for motion afforded by a bed with particles with random exposures to the flow make it possible for particles to move at all values of the turbulent shear stress, even very low ones. From this point of view, the definition of a threshold condition for the initiation of motion appears to have only statistical significance.

A similar argument can be applied to the definition of the threshold conditions for the entrainment of particles into suspension. However, as in the case of the threshold conditions for particle motion, the definition of a limit for particle entrainment into suspension can have practical significance, for example in the latter case, in distinguishing regimes of sediment transport such as bedload and suspended load. It has been argued that the morphological behavior of natural streams is highly influenced by the prevalent type of sediment transport regime, and furthermore longitudinal changes in such behavior seem to be triggered by rather abrupt changes in the sediment transport regime of certain fractions of the material carried by the flow (Paola et al., 1992; Parker, 1992). From this point of view the onset of particles into suspension appears as a bifurcation of the flow-sediment system which seems to be worth of being analyzed, not only because of its purely practical significance, but also from a more mechanistic perspective, to discern the physical processes operating in such bifurcation.

Different criteria and theories have been developed to define a threshold condition for particle entrainment into suspension. In all of these, the turbulence of the flow is assumed to have a major influence on the phenomenon. Indeed, the problem of particle entrainment into suspension has been related to turbulence-particle interactions taking place in the near bed regions of the flow (e.g., Sutherland, 1967; Grass, 1974; Sumer and Oguz, 1978; Yung et al., 1988; Rashidi et al., 1990). According to these studies, particles are lifted from the bed and entrained into suspension under the action of coherent flow structures related to the turbulent bursting process.

Bagnold (1966) proposed one of the first criteria to estimate the threshold condition for particle entrainment. This was based on the assumption that particles remain in suspension as long as the turbulent eddies have dominant vertical velocity components, which would scale with the flow

shear velocity, u_*, that exceed the particle settling velocity, v_s. Accordingly, the critical value of the flow shear velocity for the initiation of suspension would satisfy the condition: $u_*/v_s = 1$.

Previously, Engelund (1965a, b) proposed two different criteria to estimate the threshold conditions for the initiation of suspension, which unfortunately do not seem to be based on the right assumptions. In his short note of 1965a, Engelund estimated the conditions for the initiation of suspension from a stability analysis of a turbulent diffusion equation for the equilibrium sediment concentration in an open channel flow. This analysis, which requires an arguable nonlinear correction of the particle settling velocity due to sediment concentration to work, is based on the questionable assumption that an unstable concentration profile would define the conditions for which the suspension can no longer be sustained. Engelund's rather crude stability analysis leads to the condition: $u_*/v_s = 0.25$, however a more formal solution of his stability problem shows that this condition seems to be erroneous (see Appendix A).

In his paper of 1965b, Engelund estimated the conditions for the initiation of suspension from an analysis of the turbulent energy balance in the near wall region of an open channel flow. In this analysis the fraction of turbulent energy used to keep sediment particles in suspension is taken into account in the turbulent energy balance equation. After linearizing the problem, Engelund obtains the following necessary condition for the fraction of turbulent energy used to keep sediment particles in suspension not to be negative: $u_*/v_s > 0.85$, which he argues corresponds to the physical limit for which the suspension of particles is possible. From a physical point of view, however, the presence of suspended sediment can affect positively or negatively the energy balance. That is, it has been shown that small particles tend to extract turbulent energy from the flow mainly through friction, however larger particles can increase the turbulent energy of the flow mainly by creating eddies as a result of the presence of wakes (Parker and Coleman, 1986; Hetsroni, 1989; Yuan and Michaelides, 1992). A revision of Engelund's analysis, however, indicates that the equation of turbulent kinetic energy used by him can only predict a reduction of such energy due to the presence of sediment, and that his result appears to be a consequence of the linearization and mathematical manipulation of the original nonlinear equation which does not reflect any physical response of the system under consideration (see Appendix B).

More recently, van Rijn (1984) conducted a series of experiments to determine the limit conditions for the initiation of suspension. Although he did not give any details about the experiments, it seems that they correspond to observations of particle entrainment from a mobile bed formed by similar particles. Van Rijn presents his results in the form of a range of limit conditions for which turbulent bursts of sediment particles are lifted from the bed into suspension. The analysis of these results together with the condition proposed by Bagnold (1966) is presented below.

Herein some experimental results regarding the limit conditions for particle entrainment into suspension are presented. The entrainment of particles lying over a smooth boundary as well as over a rough bed is investigated, including in the latter case the phenomenon of hiding associated with the motion of particles of smaller size than that of the roughness elements of the bed.

7.2 Dimensional analysis

Consider a fully turbulent open channel flow with a bed formed by granular material of small size compared to the flow depth. A typical dimensionless relationship characterizing the limit conditions for the entrainment of bed particles into motion can be written as (Raudkivi, 1990):

$$f_1 (Re_{p*} , \tau_*) = 0 \qquad (7.1)$$

where $Re_{p*} = u_* d_p/\nu$ denotes a particle Reynolds number, with u_* denoting the flow shear velocity, d_p denoting the mean diameter of the entrained particle, and ν denoting the kinematic viscosity of the fluid, and $\tau_* = u_*^2/(g R d_p)$ denotes a dimensionless bed shear stress (i.e. Shields stress), with g denoting gravitational acceleration, and $R = (\varrho_s - \varrho)/\varrho$ denoting the submerged specific density, where ϱ_s denotes the density of the entrained particle and ϱ denotes the density of the fluid.

It can be argued that (7.1) can also be used to represent a dimensionless relationship characterizing the limit of entrainment into suspension of particles lying over the granular bed of the open channel flow. In fact, u_* besides being related to the bed shear stress is also a measure of the turbulence intensity of the flow in the near bed region, therefore τ_* can be interpreted as a measure of the ratio of turbulent to gravitational forces acting over the particle. The larger the values of τ_*, the stronger the turbulent activity of the flow is in the near wall region, and therefore the more effective the flow would be to entrain particles from the bed. On the other hand, Re_{p*} can be interpreted as a measure of the viscous forces acting over the particle, however it is also a measure of how immersed the particle is within the viscous sublayer. The smaller the value of Re_{p*} the more immersed it is, and therefore the less effective the turbulence of the flow would be in lifting particles away from the bed.

For the particular case in which the size of the entrained particle is different from the size of the particles forming the roughness elements of the bed, d_b, an extra parameter must be included in a relationship like (7.1), namely, the ratio d_p/d_b which quantifies effects like hiding, when this ratio is lower than 1.0, and over–exposure, when this ratio is larger than 1.0. The hiding effect is related to the shielding provided by the larger bed particles, which decreases the probability that a particular turbulent event would lift a smaller particle into suspension. The over–exposure effect

occurs when a big particle is surrounded by smaller ones, so that relatively, the turbulence can be more effective in lifting it than if the particle were surrounded by particles of the same size.

It is easy to see that a relationship alternative to (7.1) is the following:

$$f_2 (R_p , \tau_*) = 0 \tag{7.2}$$

where the parameter Re_{p*} has been replaced by the parameter $R_p = \sqrt{R\, g\, d_p^3}\ /\nu$, which is a kind of dimensionless particle diameter that depends on the properties of the particle and the fluid, but it is independent of flow parameters. Equations (7.1) and (7.2) are related by the transformation:

$$Re_{p*} = R_p \sqrt{\tau_*} \tag{7.3}$$

In fact, van Rijn (1984) uses a parameter space equivalent to (7.2) to plot his experimental results on the limit of particle entrainment into suspension, although he utilizes a dimensionless parameter D_* instead of R_p, such that: $D_* = R_p^{2/3}$.

Another alternative dimensionless relationship for the limit of entrainment can be written as:

$$f_3 (R_p , u_*/v_s) = 0 \tag{7.4}$$

where v_s denotes the particle settling velocity. Since this variable is a measure of the particle size, the ratio u_*/v_s is equivalent to τ_*, and can be interpreted as some kind of ratio between turbulent activity (measured by u_*) and forces that oppose particle motion (measured by v_s), such as gravitational and viscous forces acting over the particle. In fact, Bagnold's (1966) criterion for particle entrainment into suspension is expressed in terms of a relationship equivalent to (7.4).

7.3 Experiments

7.3.1 Experimental setup

The experiments were conducted in a rectangular open channel 18.6 m long, and 0.297 m wide, which has an observation window located a distance of about 12 m downstream of the entrance. A high–speed video system, Kodak Ektapro TR Motion Analyzer, was used to record particle motion. A strobe light was synchronized with the high–speed video system, which helped to reduce image blur due to particle motion. A schematic view of the experimental setup is shown in Fig. 7.1.

7.3.2 Experimental method

The experiments were carried out under uniform flow conditions. Particles were fed externally to the flow at a distance sufficiently far upstream from the observation window as to allow particle motion to reach steady conditions before going into the field of view of the camera. Particle

motion was recorded from the side, through the observation window, using the high–speed video system set at a recording rate of 250 frames per second.

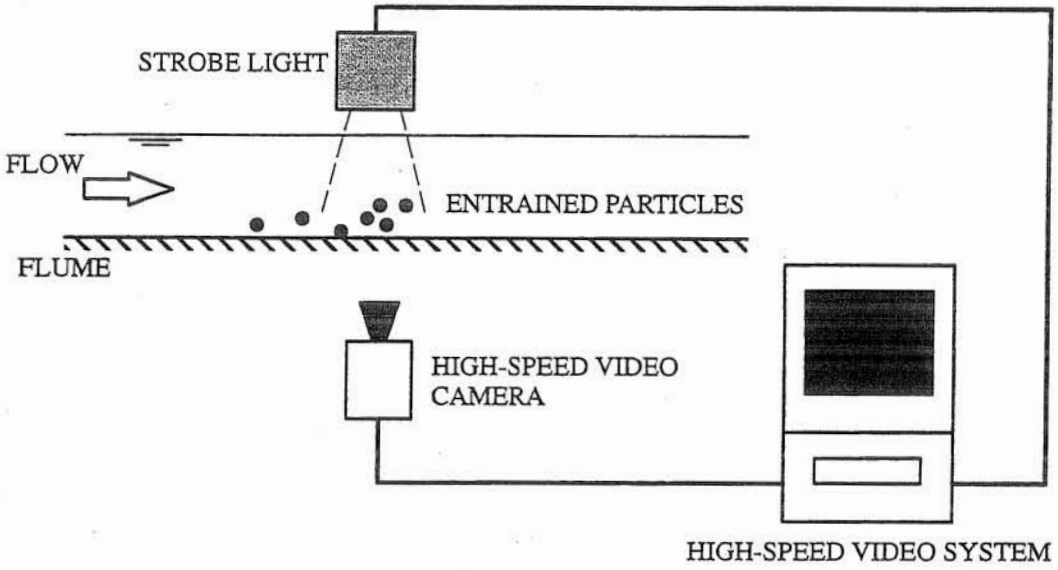

Fig. 7.1 Schematic view of experimental set–up.

Different particle sizes were analyzed. For each size, the experimental conditions were initially set so that the particles would move close to the channel bottom, as bedload only. After recording a few minutes of particle motion, the flow rate was increased so as to increase the flow depth and thus the bed shear stress. The video recording of particle motion was then repeated only after reaching uniform flow conditions. This procedure was continued until conditions of generalized particle transport in suspension were obtained.

7.3.3 Experimental conditions

Two different series of experiments (S and T) were conducted corresponding to two different surface roughness. The first series of experiments (Series S) corresponded to a channel with smooth walls. The second series (Series T) corresponded to a channel with bottom roughness in the transitionally rough regime. The bottom roughness in this case was created by glueing sand particles with a mean size of about 0.53 mm to the originally smooth surface of the channel bottom.

Flow depths used in both series of experiments covered a range from about 25 mm to about 60 mm. Flow conditions corresponded to values of the Reynolds number (defined as $Re = Uh/\nu$, where U denotes flow mean velocity, and h denotes flow depth) in the range from about 5000 to about 30000, and to values of the Froude number (defined as $Fr = U/\sqrt{gh}$) of about 0.5 to 0.6, which corresponded to subcritical flows. Values of the flow shear velocity, u_*, were in the range from about 0.015 m/s to about 0.040 m/s.

Five different particles were used in the experiments of both series S and T, namely, glass beads with mean diameter, d_p, of 38 and 94 μm, and natural sand particles with d_p values of 112, 224, and 530 μm, respectively. All the particles had a submerged specific density, R, of about 1.65. Corresponding values of the dimensionless parameter R_p were in the range from 0.9 to 50. For the present range of values of particle diameter and shear velocity, resulting values of the dimensionless shear stress, τ_*, were in the range from about 0.03 to about 2, while the values of the particle Reynolds number, $Re_{p\,*}$, ranged from 0.7 to 20. The latter indicates that in some of the experiments of Series S, the particles had sizes smaller than the corresponding thickness of the viscous sublayer. In the experiments of Series T, where the size of the particles transported by the flow, d_p, was different from the size of the particles forming the roughness elements of the bed, d_b, the ratio d_p/d_b had values in the range from 0.07 to 1.0. A summary of the characteristics of the particles used in the present experimental study is shown in Table 7.1, including associated values of the settling velocity estimated using:

$$v_s = \sqrt{\frac{4}{3}\frac{R\,g\,d_p}{c_D}} \tag{7.5}$$

which is valid for spherical particles, and where c_D denotes the drag coefficient estimated from (Yen, 1992):

$$c_D = \frac{24}{Re_p}\left(1 + 0.15\,Re_p^{1/2} + 0.017\,Re_p\right) - \frac{0.208}{1 + 10^4\,Re_p^{-0.5}} \tag{7.6}$$

with $Re_p = v_s\,d_p/\nu$.

Table 7.1 Properties of the particles used in the experimental study

d_p (μm)	v_s (cm/s)	R_p	d_p/d_b
38	0.13	0.9	0.072
94	0.70	3.7	0.177
112	0.96	4.8	0.211
224	3.00	13.5	0.423
530	8.91	49.1	1.000

7.4 Results

The video recordings of particle motion were analyzed to define the regime of sediment transport prevalent in each particular experiment. In general, the onset of particle entrainment into suspension was more or less abrupt. For low values of the bed shear stress the particles moved in contact with the bed. In the case of smooth flows, the particles moved along the bed only in the rolling and sliding modes. In the case of the transitionally rough flows the particles moved mainly

in the saltation mode, except for those with small ratios d_p/d_b which moved within the interstices of the much bigger roughness elements of the bed. As the shear stress was increased, progressively more frequent events occurred during which particles were suddenly entrained into the outer regions of the wall layer and remained in suspension for distances generally longer than 100 particle diameters. During these events the particles clearly responded to large velocity fluctuations of the flow. Therefore, there appears to be a threshold level of the bed shear stress such that for lower values of this variable the particles do not seem to respond to turbulent ejections in the near bed region, while for values of the shear stress larger than the threshold the particles do seem to respond to such events.

According to the previous discussion, a value of the threshold shear stress for particle entrainment was defined for each particle size used in the present experiments, in terms of whether or not the particles responded to the turbulence, and in particular to ejection events, as observed in the video recordings. Of course the definition of the precise threshold level has only statistical significance, in the sense that in reality there is a transition range of increasing values of the shear stress in which the frequency of the entrainment events, and the number of particles entrained by those events, increases from a negligible value to a large value. Nevertheless, this range results in practice to be rather narrow, such that a more precise definition of the threshold does not seem to be necessary.

The results obtained from the analysis described above are presented in Figs. 7.2 and 7.3, corresponding to the experiments of series S and T, respectively, plotted in the parameter space (Re_{p*} , τ_*) describing the experimental conditions. Therein clear symbols denote experiments where no (significant) particle entrainment was observed, filled symbols denote experiments where (significant) particle entrainment was observed, and dashed lines correspond to the estimated threshold limit for particle entrainment.

7.5 Analysis

As seen in Figs. 7.2 and 7.3, no particles of the larger size (d_p = 530 μm) were entrained for the present experimental range of shear stress. In the case of smooth flows such particles just moved along the bed in the sliding and rolling modes, while in the case of transitionally rough flows they moved in the saltation mode, with increasingly higher and longer jumps for increasing values of the bed shear stress, without responding sensibly to the turbulence of the flow.

It is interesting to note that in Fig. 7.2 those symbols corresponding to values of Re_{p*} lower than about 5 are associated with particle sizes smaller than the thickness of the viscous sublayer of the flow (recall that this thickness corresponds approximately to a value $y_+ = y\, u_*/\nu = 5$). It is apparent from Fig. 7.2 that particles totally immersed in the viscous sublayer are indeed entrained

into suspension, which contradicts previous observations by Sumer and Oguz (1978), and Yung et al. (1988). It is also apparent from that figure that as the particle size decreases, progressively higher values of the dimensionless shear stress are required for entrainment. This is rather obvious, since the turbulence intensities of the flow surrounding the particle, which are responsible for lifting the particle into suspension, become relatively less strong as the particle becomes more and more immersed in the viscous sublayer. This effect is shown in Fig. 7.4, where the dimensionless rms (root-mean-square) values of the streamwise and vertical components of the flow velocity fluctuations, $u_{rms+} = u_{rms}/u_*$ and $v_{rms+} = v_{rms}/u_*$ respectively, corresponding to an open channel flow, are plotted as a function of y_+. The curve for u_{rms+} shown in Fig. 7.4 represents a best fit of a model proposed by Nezu and Nakagawa (1993) to turbulence measurements made in the present flows (Chapter 3), and corresponds to a representative value of the Reynolds number $Re_* = u_*h/\nu$ = 800. The curve for v_{rms+} shown in Fig. 7.4 corresponds to a model by Nakagawa and Nezu (1981). As seen in Fig. 7.4, a strong damping of the turbulence intensities for values of y_+ lower than about 10 is apparent. This effect would explain the conclusions of Sumer and Oguz, and Yung et al., in the sense that the values of the shear stress in their flows were probably not large enough as to induce the entrainment of the particles totally immersed in the viscous sublayer.

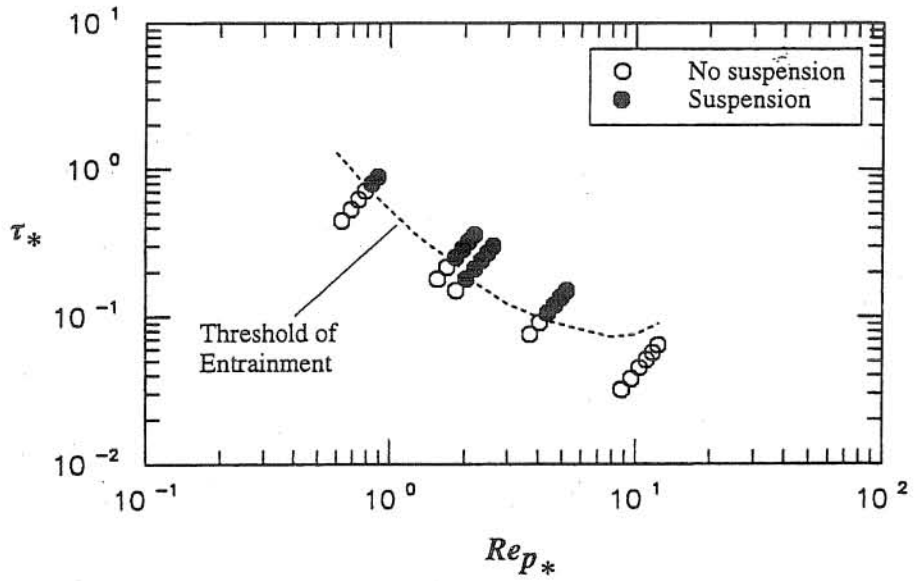

Fig. 7.2 Threshold of entrainment. Experimental results Series S.

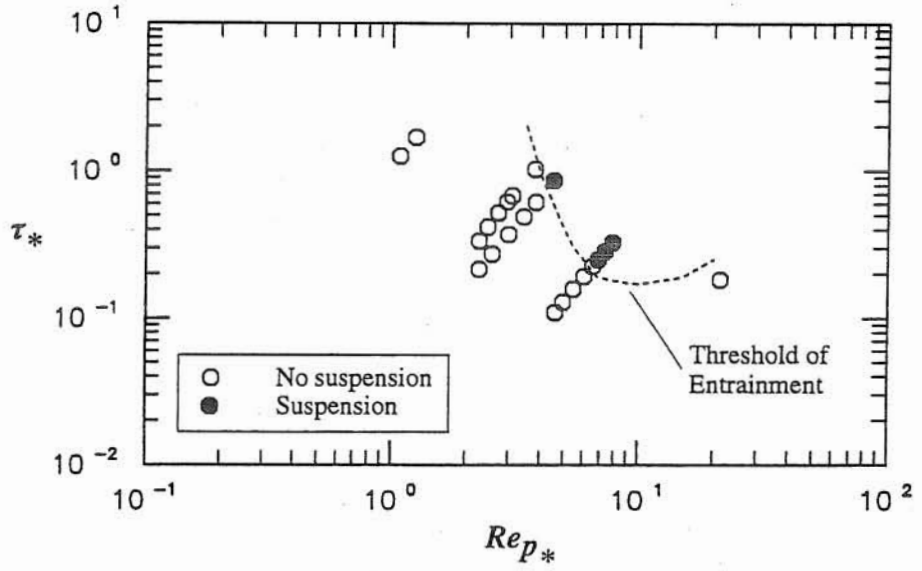

Fig. 7.3 Threshold of entrainment. Experimental results Series T.

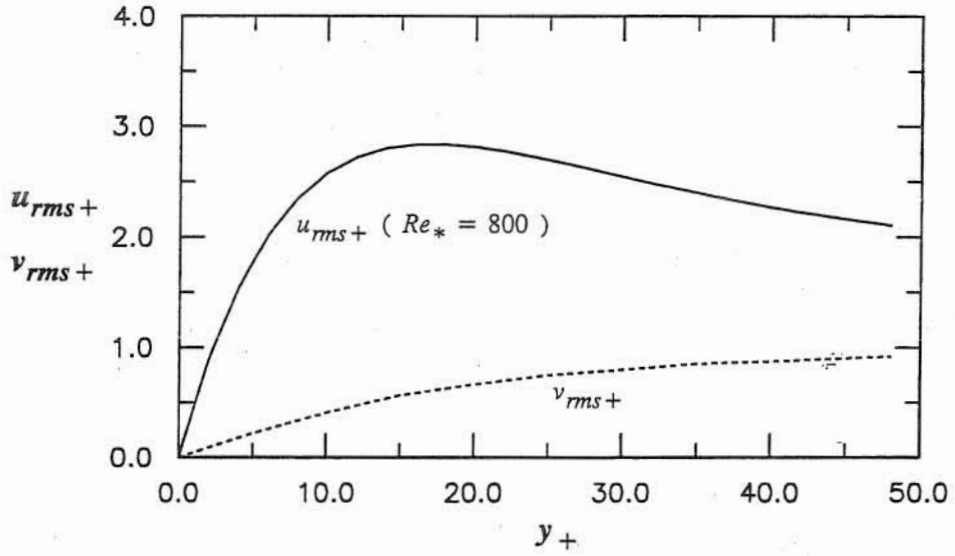

Fig. 7.4 Turbulent intensities in an open channel flow.

A comparison of the present experimental values of the threshold of entrainment in smooth flows with the experimental results of van Rijn (1984) and also with the theoretical relationship by Bagnold (1966) is presented in Fig. 7.5, in the parameter space (R_p , τ_*). Although van Rijn does not give any details about his experiments it is assumed that his results correspond to particles entrained from a mobile bed formed by similar particles, and not from a smooth bed like in the results of Series S herein. In Fig. 7.5, the classical curve of Shields for the limit of particle motion is also plotted as a reference, as given by the equation proposed by Brownlie (1981):

$$\tau_{*c} = 0.22\ R_p^{-0.6} + 0.06\ \exp\ (\ -\ 17.77\ R_p^{-0.6}\ ) \qquad (7.7)$$

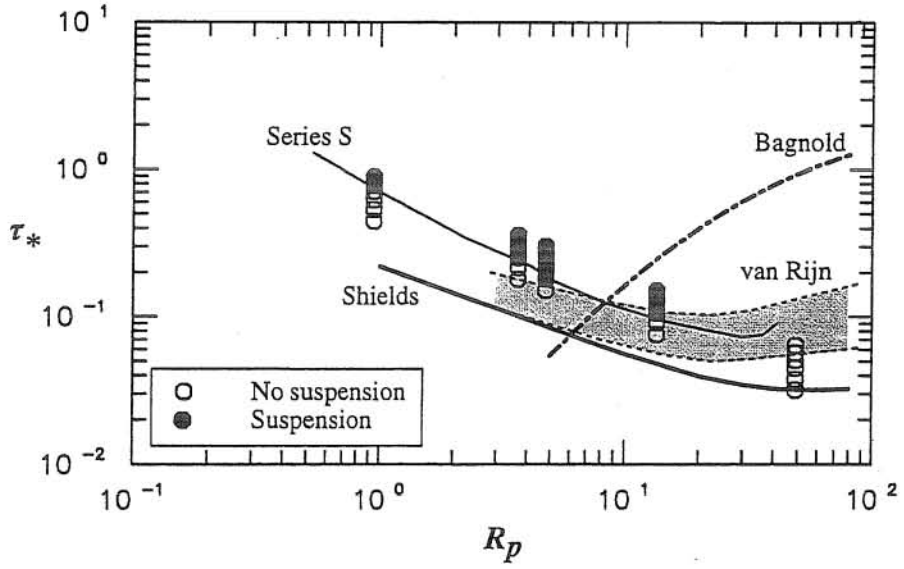

Fig. 7.5 Comparison with threshold of entrainment criteria by Bagnold (1966) and van Rijn (1984). Experimental results Series S.

As already mentioned, Bagnold's (1966) criterion for the initiation of suspension is given by the relationship: $u_*/v_s = 1$, which in terms of the dimensionless shear stress τ_*, can be expressed also as:

$$\tau_* = \frac{u_*^2}{R\ g\ d_p} = \frac{v_s^2}{R\ g\ d_p} \tag{7.8}$$

where v_s is estimated using (7.5).

According to van Rijn, Bagnold's criterion would define an upper limit at which a concentration profile of suspended sediment starts to develop, while his limit of entrainment defines an intermediate stage at which locally turbulent bursts of sediment particles are lifted from the bed into suspension. In this sense van Rijn's criterion for defining the limit of entrainment is equivalent to the one used herein. As seen in Fig. 7.5 the range proposed by van Rijn for the limit of entrainment agrees fairly well with the threshold curve proposed herein for values of R_p larger than about 8. For lower values of this parameter, however, van Rijn's range tends to underestimate the present limit values of τ_* for which particles were entrained into suspension. On the other hand, although Bagnold's criterion indeed overestimates the limit of entrainment proposed herein for values of R_p larger than about 10, his limit of entrainment at lower values of R_p defines threshold values of τ_* that are too low compared to the present observations. This is no so unexpected because Bagnold assumes that vertical velocity fluctuations of the flow, which must balance the settling velocity for the particle to be suspended, are of the order of u_*. This is true only at distances from the bed that are within the wall layer but at the same time outside of the viscous sublayer. Inside the viscous

sublayer the vertical velocity fluctuations are damped rather strongly as the bed is approached (Fig. 7.4). Because of this, Bagnold's criterion is not meant to be applicable to the physical situation prevailing at values of Re_{p*} lower than about 5, or equivalently at values of R_p lower than about 10.

The experimental limit of suspension shown in Fig. 7.2 can also be expressed in terms of the ratio u_*/v_s, since any given pair (Re_{p*} , τ_*) can be transformed into a pair (R_p , u_*/v_s) by using (7.3) together with (7.5). This was done in Fig. 7.6, where the experimental limit for the initiation of suspension proposed by van Rijn (1984):

$$u_*/v_s = \begin{cases} 4.0\, R_p^{-2/3} & 1 \le R_p \le 32 \\ 0.4 & R_p \ge 32 \end{cases} \tag{7.9}$$

was also plotted together with Bagnold's (1966) criterion. It is important to recall that the present results correspond to particle entrainment from a smooth bed, while van Rijn's apparently correspond to particle entrainment from a bed formed by similar particles.

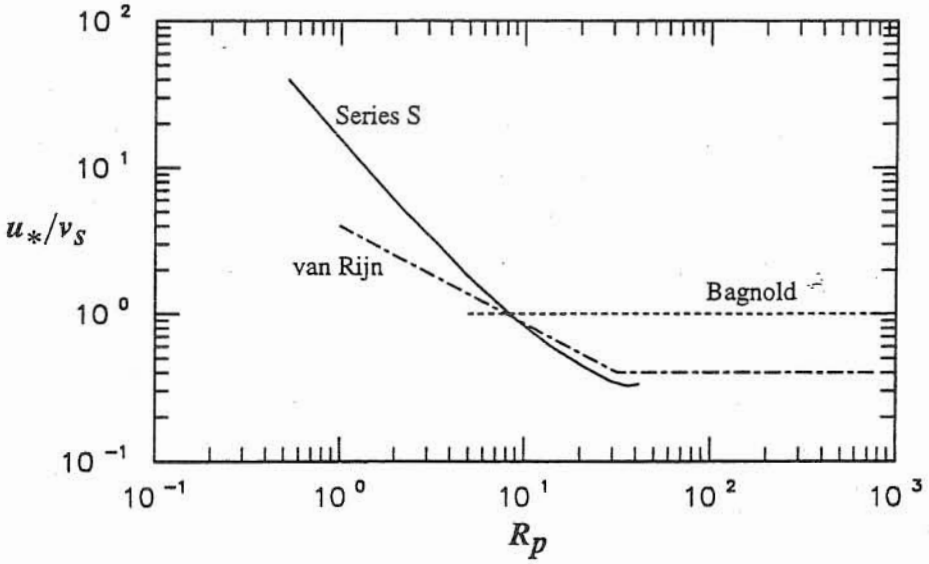

Fig. 7.6 Comparison with threshold of entrainment criteria by Bagnold (1966) and van Rijn (1984). Experimental results Series S.

As seen in Fig. 7.6, the present threshold curve for the initiation of suspension expressed in terms of u_*/v_s is in a relatively good agreement with (7.9) for values of R_p in the range from about 10 to about 50, although there is a tendency for the present results to locate below van Rijn's in that range. Unfortunately, such agreement can not be checked at larger values of R_p since the present range of flow conditions does not allow to obtain entrainment of particles in such size range. At values of R_p lower than about 10, (7.9) underestimates the threshold of entrainment observed herein.

On the other hand, as already discussed, Bagnold's criterion ,which is assumed to be valid for values of R_p larger than about 10, tends to overestimate (7.9) and also the present results by a maximum factor of about 2.5 to 3.0.

From Fig. 7.3 it is seen that no particles of sizes smaller than 112 μm were entrained in the experiments with the transitionally rough flows for the present range of shear stresses. In those cases the particles were small enough as to move within the interstices of the bed roughness elements from where they could not be taken away by the turbulence of the flow. In other words the bed roughness elements seem to contribute to a hiding effect that precludes the particle entrainment by locally affecting the turbulence structure of the flow.

In Fig. 7.7, both the results of series S and T, already presented in Figs. 7.2 and 7.3, are plotted together for comparison purposes. It is clear from this figure that the threshold curve defining conditions for the initiation of suspension in Series T displaced toward higher values of τ_* as compared to that corresponding to Series S. This implies that as the bed roughness increased (from smooth to transitionally rough), higher values of the dimensionless shear stress were required to entrain particles of the same size, which appears to be related to the hiding effect discussed in the previous paragraph.

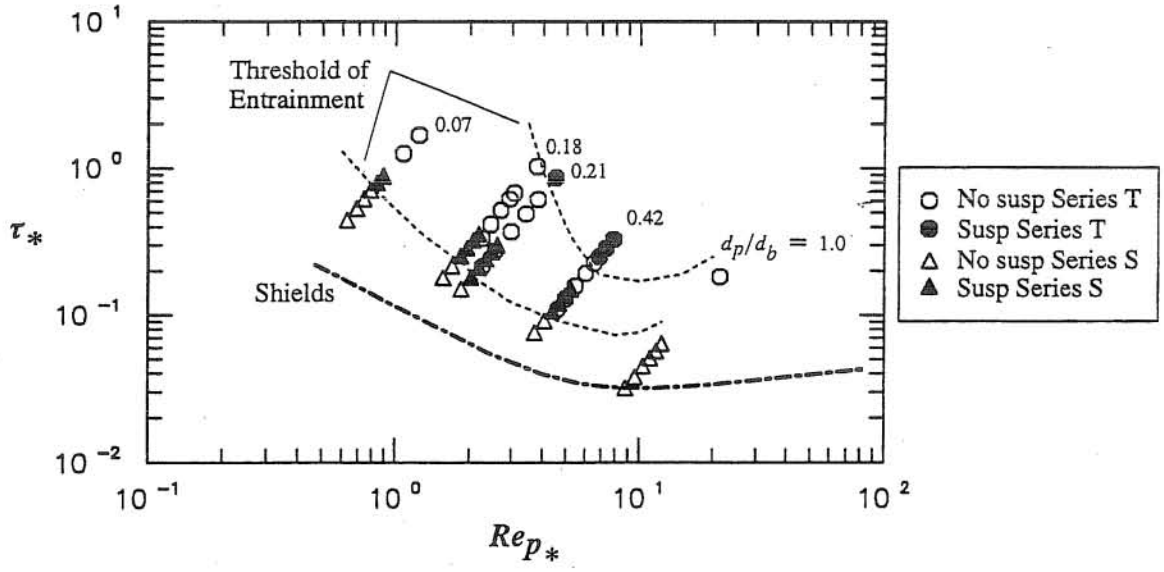

Fig. 7.7 Threshold of entrainment. Experimental results Series S and T.

In Figs. 7.2, 7.3, and 7.7, experimental points corresponding to the same particle diameter, that is to the same value of R_p, define straight lines given by the relationship (7.3). This lines in Figs. 7.3 and 7.7 also correspond to the same values of the ratio d_p/d_b. From Fig. 7.7, it is apparent that as the ratio d_p/d_b becomes smaller, progressively higher values of τ_* are needed to entrain a given particle, compared to those needed to entrain the same particle from a smooth bed.

To analyze this hiding effect, the ratio between the threshold value of τ_* corresponding to a particle of size d_p entrained from a bed of roughness d_b and the threshold value of τ_* corresponding to a particle of the same size d_p entrained from a smooth bed, τ_{*r}/τ_{*s}, is plotted in Fig. 7.8 as a function of the ratio d_p/d_b. This is done by working directly with the threshold curves and not with the individual experimental points. As observed in Fig. 7.8, for values of d_p/d_b larger than about 0.5, the ratio τ_{*r}/τ_{*s} has an almost constant value of about 2.0. For values of d_p/d_b lower than about 0.5, the ratio τ_{*r}/τ_{*s} tends to increase as the ratio d_p/d_b decreases. A power law can be adjusted to the data such that the following relationship is obtained:

$$\tau_{*r}/\tau_{*s} = 1.1\ (\ d_p/d_b\ )^{-0.82} \qquad d_p/d_b < 0.5 \tag{7.10}$$

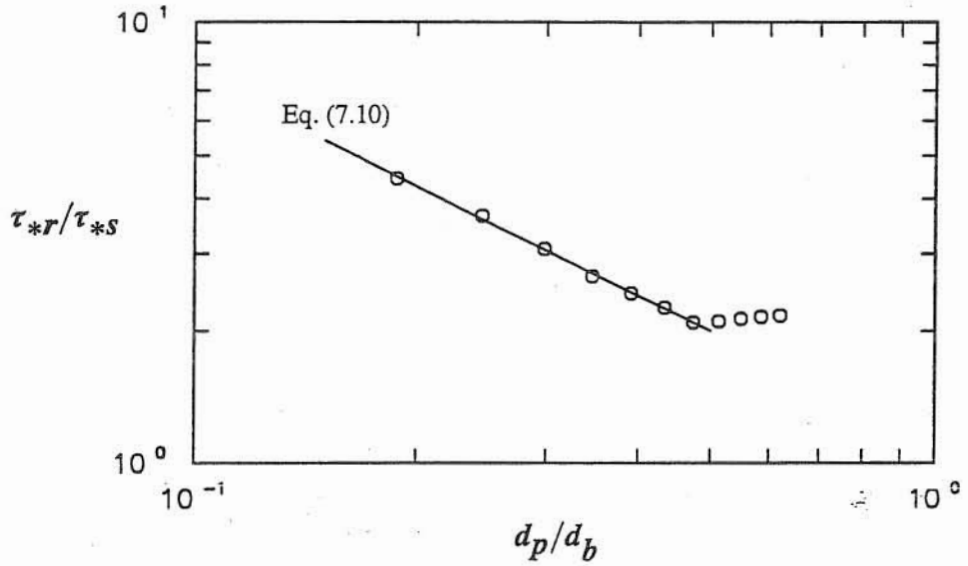

Fig. 7.8 Increase in the threshold dimensionless shear stress due to hiding effect. Experiments Series T.

Remarkably, (7.10) resembles an equivalent equation proposed by Parker (1990) to estimate the effect of hiding in the limit conditions for the initiation of particle motion. This equation can be written in the form:

$$\tau_{*i}/\tau_{*b} = (\ d_i/d_b\ )^{-\beta} \tag{7.11}$$

where τ_{*i} denotes the threshold value of τ_* for the initiation of motion of a particle of size d_i lying on a surface layer formed by particles of size d_b, which have associated a threshold value of τ_* for the initiation of motion equal to τ_{*b}. A theoretical evaluation of the exponent β, based on the concept of equal mobility, gives a value equal to 1 (Parker et al., 1982), however field evaluations of this parameter give values in the range from about 0.65 to about 0.9 (Parker, 1990). The resemblance

between (7.10) and (7.11) seems to indicate that the same physical principle is operating in the hiding effect for both cases, the initiation of motion and the initiation of suspension, namely, the modification of the structure of the turbulent flow surrounding the entrained particle by the shielding action of the coarser particles in the bed.

This turbulence modification by the action of the roughness elements appears to be related not only to a direct blockage of turbulent events by the roughness elements so as to preclude the lift of smaller particles, but also to a less local phenomenon as is discussed in the following. Consider the variable S_i, denoting the fractional contribution of the Reynolds stress due to events of quadrant i with respect to the total Reynolds shear stress, such that:

$$S_i = < u'v' >_i / \overline{u'v'} \tag{7.12}$$

where $< u'v' >_i$ denotes the conditional average of Reynolds shear stress due to events of quadrant i, $\overline{u'v'}$ denotes the total Reynolds shear stress, and u' and v' denote the streamwise and vertical components of the flow velocity fluctuations, respectively. The main contributors to $\overline{u'v'}$ are events of quadrant $i=2$, corresponding to values $u'<0$, $v'>0$, which are usually called ejections, and events of quadrant $i=4$, corresponding to values $u'>0$, $v'<0$, which are usually called sweeps. Clearly, events of quadrant 2 are most relevant to the entrainment of particles into suspension since they are associated with positive values of v'. Experimental observations indicate that in smooths flows values of S_2 are generally larger than values of S_4 all along the vertical of the flow (Nakagawa and Nezu, 1977; Raupach, 1981; Raupach et al., 1991), that is, ejections events contribute more than sweep events to the total Reynolds stress of the flow, although there is some evidence that within the viscous sublayer this tendency would reverse, that is, sweeps would become more important than ejections (Wallace et al., 1972). The latter argument would indicate that the progressively higher shear stress needed to entrain particles more and more immersed within the viscous sublayer is not only due to a drop in the turbulent intensities (as shown in Fig. 7.4), but also due to a change in the structure of the turbulence within this region, such that therein flow ejections become less important than sweeps. On the other hand, Raupach et al. (1991) conclude that in the case of rough flows, the difference S_4-S_2 changes sign from negative to positive as the bed is approached. That is, very near the bed, sweeps become more important than ejections, which implies a reduction in the ability of the flow to entrain particles into suspension. This change on the structure of the turbulence near the bed added to other local factors such as direct blockage of flow ejections by bed roughness elements, would be part of the basic physical processes related to the hiding effect discussed above.

Experimental results on the turbulence structure of the present flows (Chapter 3) agree fairly well with those discussed previously. The analysis of those results also included the use of the VITA algorithm (Blackwelder and Kaplan, 1976) to detect highly energetic ejection and sweep events in

streamwise velocity time series measured in the present experiments using a hot-film probe. Such events would be associated with the bursting process, and because of their strength they would be most responsible for particle entrainment. Some interesting conclusions derived from the analysis are that the frequency of bursting events tend to increase with u_*, and also, that the frequency of ejection events in smooth flows is larger than that of the rough flows at the same value of the bed shear stress, all of which would contribute to an increase in the values of u_* required to entrain particles into suspension from a rough bed with respect to those required in the smooth bed case.

It is interesting to note that the results shown in Fig. 7.8 suggest that in the limit $d_p/d_b \rightarrow 1$, the ratio τ_{*r}/τ_{*s} has a value of about 2.0. This means that a particle moving on a smooth bed is more prone to be entrained than the same particle moving on a bed formed by identical particles. This is related to the over-exposure effect mentioned previously, which also appears to be related to modifications in the structure of the turbulence by the presence of bed roughness elements as was discussed above.

This over-exposure effect claims for a re-assessment of the analysis of the results obtained in Series S. Although it is not clear from his paper, van Rijn's (1984) experiments correspond most probably to the entrainment of particles from a mobile bed formed by similar particles. According to the results shown in Fig. 7.8, the threshold values of τ_* for initiation of suspension corresponding to a situation like van Rijn's should be on the order of about twice those corresponding to Series S. Similarly, in terms of threshold values of the ratio u_*/v_s, the results corresponding to a situation like van Rijn's should be on the order of about $\sqrt{2}$ times those corresponding to Series S.

In order to compare the present results with van Rijn's under the same conditions of particle entrainment from a bed formed by similar particles, the present threshold values of the ratio u_*/v_s are corrected, multiplying them by a factor of $\sqrt{2}$. The results obtained are plotted in Fig. 7.9, together with the limit of suspension proposed by van Rijn and given by (7.9). From this figure it appears that in the range of values of R_p from about 10 to about 50, the corrected limit values of u_*/v_s tend to locate slightly above those of van Rijn, although defining similar tendencies. For values of R_p lower than about 10, the corrected limit values of u_*/v_s are much larger than those of van Rijn, and define a completely different tendency. Based on the corrected results presented in Fig. 7.9, and using van Rijn's results to extrapolate the observed tendencies toward higher values of R_p, the following threshold condition for the initiation of suspension is proposed, which conserves the slopes of the limit u_*/v_s curve given by (7.9) in the range of values of R_p larger than about 10, and which improves the performance of (7.9) in the range of values of R_p lower than about 10 according to the present experimental results:

$$u_*/v_s = \begin{cases} 22.0\ R_p^{-4/3} & R_p \le 11 \\ 4.5\ R_p^{-2/3} & 11 \le R_p \le 32 \\ 0.45 & R_p \ge 32 \end{cases} \qquad (7.13)$$

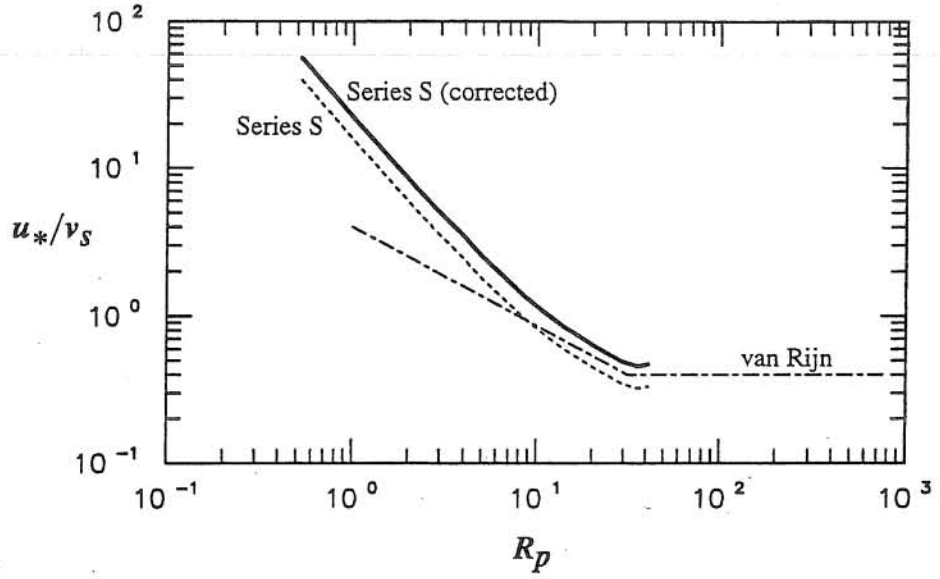

Fig. 7.9 Corrected threshold condition for entrainment. Experiments Series S.

Equation (7.13) is plotted in Fig. 7.10 together with (7.9) and the corrected limit values of u_*/v_s. It is interesting to note that the limit $R_p = 11$ for which the change of slope from –4/3 to –2/3 occurs, and which is associated with a value $u_*/v_s = 0.9$, corresponds to a value of Re_{p*} of about 5. That is, particles immersed within the viscous sublayer (values of Re_{p*} lower than about 5) seem to behave differently than those protruding over the viscous sublayer, such that they require exponentially higher turbulent intensities to get entrained into suspension. On the other hand the second change of slope from –2/3 to 0 occurs at a value $R_p = 32$, which is associated with a value $u_*/v_s = 0.45$, and which corresponds to a value of Re_{p*} of about 10. Although such particles are still immersed within the wall layer, they are considerably larger than the thickness of the viscous sublayer.

7.6 Conclusions

High-speed video recordings of particle motion were analyzed to determine limit conditions for the initiation of entrainment into suspension. A threshold level of the bed shear stress appears to exist such that for values of this variable lower than the threshold particles do not seem to respond to turbulent flow ejections in the near bed region, while for values of the shear stress larger than the threshold turbulent bursts of sediment particles are lifted from the bed into the outer regions of the

wall layer, which remain in suspension for distances generally longer than about 100 particle diameters.

Bagnold's (1966) criterion seems to define an upper limit for the bed shear stress at which a concentration profile of suspended sediment starts to develop, therefore is different from the criterion for the initiation of entrainment used herein. Furthermore Bagnold's criterion does not appear to apply for values of Re_{p_*} lower than about 5, or equivalently for values of R_p lower than about 10.

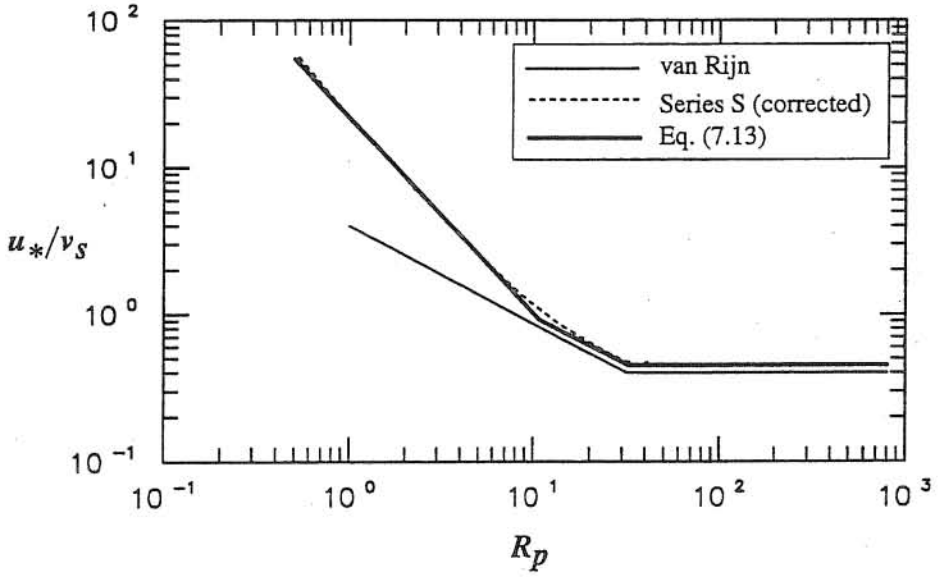

Fig. 7.10 Proposed threshold condition for particle entrainment into suspension.

Van Rijn's (1984) criterion for the threshold of entrainment is equivalent to that utilized herein. It is assumed that his experiments correspond to particle entrainment from a mobile bed formed by similar particles. A comparison between van Rijn's limit of entrainment given by (7.9) and the present results corresponding to the entrainment from a smooth bed, indicates that the limit values of u_*/v_s observed herein are in a relatively good agreement with those predicted by (7.9) in the range of R_p larger than about 10, although there is a tendency for the present results to locate below van Rijn's in that range. At values of R_p lower than about 10, (7.9) underestimates the threshold of entrainment observed herein.

The present observations indicate that particles totally immersed within the viscous sublayer can be entrained into suspension by the flow, which contradicts previous experimental results. Nevertheless, as the particle size decreases, progressively higher values of the bed shear stress are needed for entrainment, which seems to be a consequence of the rather abrupt drop of turbulent intensities within the viscous sublayer as the bed is approached, and also to a change in the turbulence

structure within this region, such that therein flow ejections would become less important than sweeps as contributors to the Reynolds shear stress.

In the experiments of Series T, where particles moved on a bed formed by particles of larger size equivalent to 530 μm, no particles of sizes smaller than 112 μm were entrained into suspension. In those cases the particles were small enough as to move within the interstices of the bed roughness elements from where they could not be lifted by the turbulence of the flow. The roughness elements appear to induce a hiding effect that tends to preclude particle entrainment by locally affecting the turbulence structure of the flow. This hiding effect seems to be dependent on the ratio d_p/d_b, such that as this ratio becomes smaller, progressively higher values of τ_* are needed to entrain the particles, compared to those needed to entrain the same particles from a smooth bed.

The hiding effect was measured by the ratio τ_{*r}/τ_{*s}, which indicates how much larger the dimensionless bed shear stress should be to entrain a particle with a given ratio d_p/d_b with respect to that needed to entrain the same particle from the smooth bed. For values of d_p/d_b larger than about 0.5, the ratio τ_{*r}/τ_{*s} has an almost constant value of about 2. For lower values of d_p/d_b, the ratio τ_{*r}/τ_{*s} follows the power law (7.10), such that it tends to increase exponentially as the ratio d_p/d_b decreases. The power law (7.10) is similar to an equivalent equation for estimating the effect of hiding in the limit conditions for the initiation of particle motion.

The hiding effect appears to be related not only with a direct blockage of flow ejection events by the roughness elements of the bed so as to preclude the lift of smaller particles, but also to a less local phenomenon involving the modification of the turbulent structure of the flow in the bed region. In fact, experimental evidence indicates that near the bed, as the size of the roughness increases, ejections become less important than sweeps as contributors to the Reynolds shear stress. Also, an increase in the roughness of the bed seems to reduce the frequency of highly energetic ejections, those related to the bursting phenomenon and which would be most effective in entraining particles into suspension, which would contribute to an increase in the values of bed shear stress needed to entrain particles into suspension as the roughness of the bed increases.

In the limit $d_p/d_b \rightarrow 1$, the ratio τ_{*r}/τ_{*s} has a value of about 2. This is an over–exposure effect which indicates that a particle moving on a smooth bed is more prone to be entrained than the same particle moving on bed formed by similar particles. The experimental values of u_*/v_s corresponding to the limit of entrainment obtained in the experiments of Series S (entrainment from the smooth bed) were corrected by multiplying them by the factor $\sqrt{2}$. The results obtained agree sufficiently well with (7.9) in the range of R_p larger than about 10, however for lower values of R_p the corrected limit values of u_*/v_s are much larger than those predicted by (7.9) and define a completely different tendency. These results allowed for a revision of (7.9), such that a new criterion for the suspension

limit is proposed in (7.13). It is interesting to note that values of R_p lower than about 10, for which the main change in tendency with respect to (7.9) occurs, correspond to particles of sizes smaller than the thickness of the viscous sublayer.

7.7 References

Bagnold, R. A. (1966). "An approach to the sediment transport problem for general physics". *Geological Survey Professional Paper* 422-I, Washington, D. C.

Blackwelder, R. F., and Kaplan, R. E. (1976). "On the wall structure of the turbulent boundary layer". *J. Fluid Mech.*, vol 76, pp 89-112.

Brownlie, W. R. (1981). "Prediction of flow depth and sediment discharge in open channels, Report No KH-R-43A, *Keck Laboratory*, California Institute of Technology.

DuBoys, P. (1879). "Le Rhone et les rivieres a lit affouillable". *Annales des Ponts at Chaussees*, Series 5, vol 18, pp 141-195.

Engelund, F. (1965a). "A criterion for the occurrence of suspended load". *La Houille Blanche*, No 8, pp 802.

Engelund, F. (1965b). "Turbulent energy and suspended load". *Progress Report No 10.* Coastal Engrg. Lab., Hydr. Lab., Tech. University of Denmark. pp 2-9.

Grass, A. J. (1974). "Transport of fine sand on a flat bed: turbulence and suspension mechanics". *Euromech* 48. Inst Hydrodynamic and Hydraulic Engrg., Tech. Univ. Denmark, pp 33-34.

Grass, A. J. (1971). "Structural features of turbulent flow over smooth and rough boundaries". *J. Fluid Mech.*, vol 50, pp 233–255.

Hetsroni, G. (1989). "Particles–turbulence interaction". *Int. J. Multiphase Flow*, vol 15, No 5, pp 735-746.

Lavelle, J. W., and Mofjeld, H. O. (1987). "Do critical stresses for incipient motion and erosion really exist?". *J. Hydr. Engrg.*, vol 113, No 3, pp 370-385.

Nakagawa, H., and Nezu, I. (1981). "Structure of space-time correlations of bursting phenomena in an open-channel flow". *J. Fluid Mech.*, vol 104, pp 1-43.

Nakagawa, H., and Nezu, I. (1977). "Prediction of the contributions to the Reynolds stress from bursting events in open-channel flows". *J. Fluid Mech.*, vol 80, pp 99-128.

Nezu, I., and Nakagawa, H. (1993). "Turbulence in open-channel flows". *IAHR Monograph.* A. A. Balkema, Rotterdam.

Paola, C., Parker, G., Seal R., Sinha, S. K., Southard, J. B., Wilcock, P. (1992). "Downstream fining by selective deposition in a laboratory flume". Science, vol 258, Dec. 11.

Parker, G. (1992). "Some random notes on grain sorting". *Proc. Int. Grain Sorting Seminar.* Ascona, Switzerland, pp 19-76.

Parker, G. (1990). "Surface-based bedload transport relation for gravel bed rivers". *J. Hydr. Res.*, vol 28, No 4, pp 417-436.

Parker, G., and Coleman, N. L. (1986). "Simple model of sediment-laden flows". *J. Hydr. Engrg.*, ASCE, 112 (5), pp 356-375.

Parker, G., Klingeman, P. C., and McLean, D. G. (1982). "Bedload and size distribution in paved gravel bed streams". *J. Hydr. Div., ASCE*, vol 108, No HY4, pp 544-571.

Rashidi, M., Hetsroni, G., and Banerjee, S. (1990). "Particle-turbulence interaction in a boundary layer". *Int. J. Multiphase Flow*, vol 16, No 6, 935-949.

Raudkivi, A. J. (1990). "Loose boundary hydraulics". *Pergamon Press.*

Raupach, M. R., Antonia, R. A., and Rajagopalan, S. (1991). "Rough-wall turbulent boundary layers". *Appl. Mech. Rev.*, vol 44, no 1.

Raupach, M. R. (1981). "Conditional statistics of Reynolds stress in rough-wall and smooth-wall turbulent boundary layers". *J. Fluid Mech.*, vol 108, pp 363-382.

Shields, A. (1936). "Anwendung der Ähnlichkeitsmechanik und der turbulenzforschung auf die geschiebebewegung". *Mitteilungen der preussischen versuchsanstalt für wasswerbau und schiffbau*, No 26, Berlin, Germany.

Sumer, B. M., and Oguz, B. (1978). "Particle motions near the bottom in turbulent flow in an open channel". *J. Fluid Mech.*, vol 86, pp 109-127.

Sutherland, A. J. (1967). "Proposed mechanism for sediment entrainment by turbulent flows". *J. Geophysical Res.*, vol 72, No 24, pp 191-198.

van Rijn, L. C. (1984). "Sediment transport, Part II: suspended load transport". *J. Hydr. Engrg.*, vol 110, No 11, pp 1613-1641.

Wallace, J. M., Eckelmann, H., and Brodkey, R. S. (1972). "The wall region in turbulent shear flow". *J. Fluid Mech.*, vol 54, pp 39-48.

Yen, B. C. (1992). "Sediment fall velocity in oscillating flow". *Water Resour. and Environ. Engrg. Res.* Report No 11. Dept. of Civil Engrg. Univ. of Virginia.

Yuan, Z., and Michaelides, E. E. (1992). "Turbulence modulation in particulate flows–a theoretical approach". *Int. J. Multiphase Flow*, vol 18, No 5, pp 779-785.

Yung, B. P. K., Merry, H., and Bott, T. R. (1988). "The role of turbulent bursts in particle re-entrainment in aqueous systems". *Chemical Engrg. Science*, vol 44, No 4, pp 873-882.

8. EXPERIMENTS ON PARTICLE-TURBULENCE INTERACTIONS IN THE NEAR WALL REGION OF A TURBULENT OPEN CHANNEL FLOW

8.1 Introduction

One of the most important engineering applications of the theory of turbulence arises from the fact that it plays an essential role in transport phenomena. Either momentum, mass or heat transfer mechanisms are strongly related to turbulent process. Turbulent diffusion of contaminants and heat transfer mechanisms have been investigated intensively, however the mechanics of sediment transport has yet to be thoroughly related to knowledge of turbulent processes. Instead, the transport of sediment has been traditionally described by empirical or semiempirical formulations, usually having limited general validity. Progress in the understanding of the physics underlying sediment transport mechanisms is related to parallel improvements in the knowledge of turbulence dynamics in open channel flows. In particular, since the interaction between flow and natural sediment occurs mainly in the vicinity of the bed, detailed knowledge of the processes that govern the turbulence structure near the wall appears to be essential to advance a mechanistic approach to sediment transport phenomena.

It is currently well known that the streamwise velocity field in the near wall region of a channel flow is organized into alternating narrow streaks of high- and low-speed fluid, which are quite persistent in time. Related to this spatial structure are intermittent, quasi-periodic events, consisting of outward ejections of low-speed fluid from the wall and inrushes of high-speed fluid toward the wall. Such near wall events, which constitute phenomena related to the so called turbulent bursting, are most responsible for the production and maintenance of turbulence in wall boundary layers (Robinson, 1991).

Sutherland (1967) was probably one of the first in speculating that a mechanism to entrain sediment grains into suspension would correspond to the interaction between turbulent vortices and particles in the near bed region of the flow. Although the details of such interaction as conceptualized by Sutherland are not totally correct in the light of the present knowledge of the structure of the turbulence in the wall region of boundary layer flows, his hypothesis delineates the basic mechanics of such phenomenon which has been verified more recently by a number of experimental studies.

Several studies have been conducted to investigate the implication of the bursting phenomenon on the mechanics of particle transport in the near wall region of boundary layers. Indeed, different experimental techniques have been applied to visualize the flow field in such region with the aim of inferring the mechanism by which particles are entrained into suspension and also, in some cases, to analyze the modulation of the turbulence due to the presence of particles (Grass, 1974; Sumer and Oguz, 1978; Sumer and Deigaard, 1981; Ashida and Fujita, 1986; Yung

et al., 1988; Rashidi et al., 1990). However, most of these studies have used almost neutrally buoyant particles of rather large sizes, which may exhibit different behavior than much heavier albeit smaller natural sand particles. In fact, although these studies have conclusively related the particle entrainment into suspension with bursting ejection events, most of them seem to indicate that such events would not be effective in entraining particles of sizes smaller than the thickness of the viscous sublayer into suspension, which contradicts experimental evidence showing that sand particles with such small sizes are indeed entrained into suspension by the flow (van Rijn, 1984).

From the cited studies only that by Grass (1974) utilized natural sediment, unfortunately his rather brief report does not provide enough details about the experiments neither presents sufficient or conclusive data. In summary, to date no precise description of the particle-turbulence interactions responsible for the transport of sediment in the wall region of an open channel flow seems to exist, which is due in part to a lack of sufficient data that provide the information and spatial-temporal resolution needed to analyze kinematic and dynamic characteristics of sediment particle motion.

Herein some experimental results regarding particle-turbulence interactions in the near wall region of a turbulent open channel flow are presented, including particle interactions with wall streaks and the phenomenon of particle entrainment into suspension. The motion of particles lying over a smooth boundary as well as over a rough bed is investigated using both particle-flow visualization and particle tracking techniques.

8.2 Experiments

8.2.1 Experimental setup

The experiments were conducted in a rectangular open channel 18.6 m long, 0.297 m wide, and 0.280 m high, with an observation window located at a distance of about 12 m downstream of the entrance. The channel slope was set to a value of about 0.0009.

A high-speed video system, Kodak Ektapro TR Motion Analyzer, was used to record particle motion. The solid state sensor of this system has a pixel array structure of 240 columns and 192 rows. Blocks of 16 rows are read simultaneously by means of 16 channels, which gives the system the capability to record up to 1000 frames per second in full frame mode, or up to 6000 frames per second in split screen mode.

A strobe light with a flash-duration of 20 microseconds was synchronized with the high-speed video system to provide whole-field illumination. This type of illumination was preferred to a laser sheet, mainly because the extremely short pulse of the strobe light helped to reduce image blur due to particle motion. Also, since the light sensitivity of the high-speed video camera is rather poor it was found that the quality of the images obtained with the strobe light illumination was better than those obtained using an available, relatively low power, laser.

The video images acquired with the high-speed video system were downloaded from special high-speed Kodak tapes onto standard VHS tapes, and then digitized into a personal computer using a frame grabber. The images were analyzed using the National Institute of Health's *Image* public domain software. A schematic view of the experimental setup is shown in Fig. 8.1.

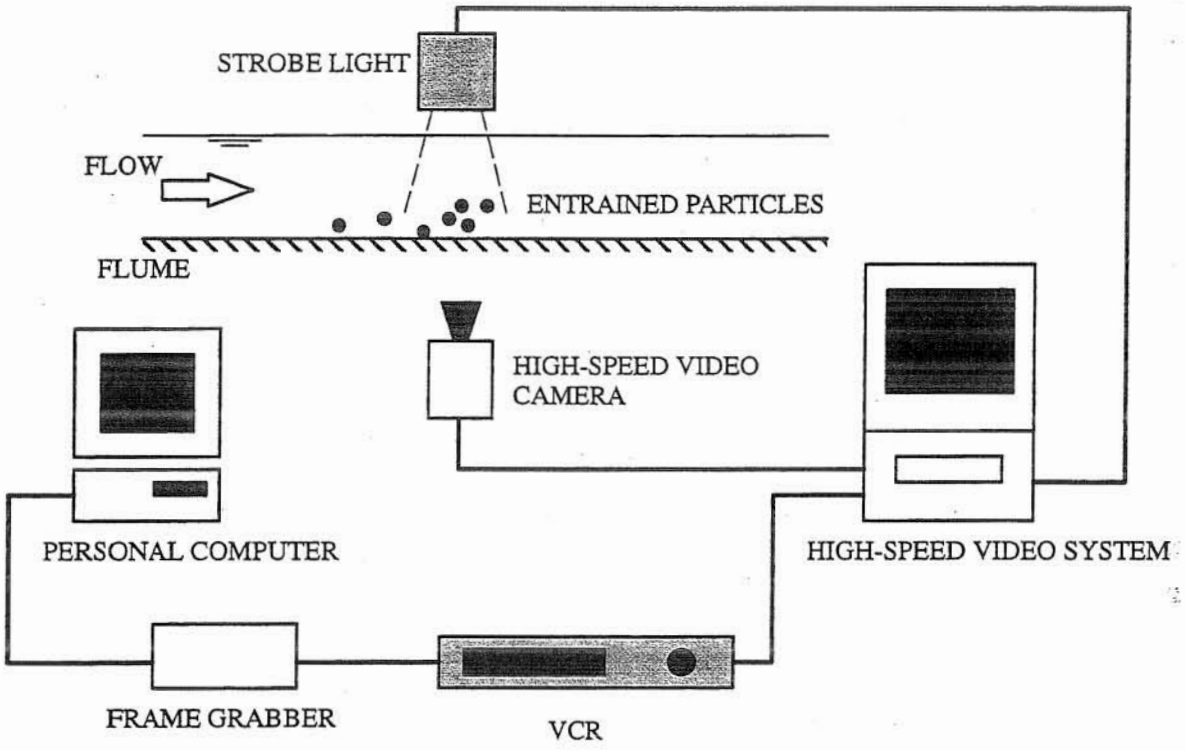

Fig. 8.1 Schematic view of experimental set–up.

8.2.2 Experimental method

The experiments were carried out under uniform flow conditions. Particles were fed externally to the flow at a distance sufficiently far upstream from the observation window as to allow particle motion to reach steady conditions before going into the field of view of the camera. Particle motion was recorded from the side, through the observation window, and in some cases also from the top, using the high-speed video system set at a recording rate of 250 frames per second (fps).

In the case of side views, typical dimensions of the flow field registered by the camera were about 1 to 2 cm in the streamwise direction by about 0.8 to 1.5 cm in the vertical direction. This corresponded to flow fields of about 200 by 150 wall units to about 550 by 400 wall units, where wall units denote the length scale: ν/u_*, with ν denoting kinematic viscosity and u_* denoting the flow shear velocity. These dimensions were found adequate to spatially resolve particle trajectories during entrainment.

Likewise, the recording rate of 250 fps was found to provide an adequate temporal resolution of the particle trajectories. It is important to note that a recording rate of 250 fps is about 8.3 times faster than that of regular video. From this point of view, the information obtained from the use of the high-speed video system is unique and could not be obtained by using standard video. In fact, if a typical particle velocity of 15 cm/s is considered, and a field of view of about 1 cm long is used to record particle motion, then standard video with a recording rate of 30 fps would most probably get just 1 image of the particle within the field of view, which is insufficient to resolve the particle trajectory. On the other hand a recording rate of 250 fps would provide most probably 15 images of the particle within the field of view, which is sufficient to resolve the particle trajectory.

A number of experiments were carried out in which a solution of white clay in water was injected through an orifice in the channel bottom to act as a marker for flow structures developing at the wall. The tracer discharge was controlled as to minimize disturbance of the flow, and to allow the tracer to displace attached to the bed before flow ejections lifted filaments away from the channel bottom. This technique allows to visualize the interaction between particles and flow ejections, however it does not provide information about the flow structure in the region above the ejection, nor is it efficient in marking sweep events.

8.2.3 Experimental conditions

Two different series of experiments (S and T) were conducted corresponding to two different surface roughness. The first series of experiments (Series S) corresponded to a channel with smooth walls. The second series (Series T) corresponded to a channel with bottom roughness in the transitionally rough regime. The bottom roughness in this case was created by glueing sand particles with a mean size of about 0.53 mm to the originally smooth surface of the channel bottom.

Flow depths used in both series of experiments covered a range from about 25 mm to about 60 mm. Flow conditions corresponded to values of the Reynolds number (defined as $Re = Uh/\nu$, where U denotes flow mean velocity, and h denotes flow depth) in the range from about 5000 to about 30000, and to values of the Froude number (defined as $Fr = U/\sqrt{gh}$, where g denotes gravitational acceleration) of about 0.5 to 0.6, which corresponded to subcritical flows. Values of the flow shear velocity, u_*, were in the range from 0.015 m/s to about 0.040 m/s.

Five different particles were used in the experiments of both series S and T, namely, glass beads with mean diameter, d_p, of 38 and 94 μm, and natural sand particles with d_p values of 112, 224, and 530 μm, respectively. All the particles had a submerged specific density, $R = (\varrho_s - \varrho)/\varrho$, where ϱ_s denotes the particle density, and ϱ denotes the fluid density, of about 1.65. Corresponding values of the dimensionless parameter $R_p = \sqrt{g\ R\ d_p^3}\ /\nu$ were in the range from 0.9 to 50. For the present range of values of particle diameter and shear velocity, resulting values of the dimensionless shear

stress, $\tau_* = u_*^2/(g R d_p)$, were in the range from about 0.03 to about 2.0, while the values of the particle Reynolds number, $Re_{p*} = u_* d_p/\nu$, were in the range from about 0.7 to about 20.0. The latter indicates that in some of the experiments of Series S the particles had sizes smaller than the corresponding thickness of the viscous sublayer. In the experiments of Series T, where the size of the particles transported by the flow, d_p, was different from the size of the particles forming the roughness elements of the bed, d_b, the ratio d_p/d_b had values in the range from 0.07 to 1.0.

8.3 Method of analysis

The video recordings of particle entrainment and particle-flow interactions were analyzed in order to elucidate the physical mechanisms involved in such phenomena. Selected frames of the video recordings were digitized into a personal computer. Images were analyzed in order to obtain the position of particles in successive frames. This was done manually in most of the cases, although an automatic particle tracking algorithm (Dill, 1994; Hassan et al., 1992) was used in some cases.

The manual digitization of particle trajectories in cases where only one or two particles were moving simultaneously proved to be much faster than the use of the particle tracking algorithm because of the large number of frames to be manipulated and processed in the latter case. On the other hand, the particle tracking algorithm was far more efficient than the manual tracking in analyzing only a few frames with a large number of particles in it.

From the digitized particle trajectories, kinematic and dynamic characteristics of particle motion during entrainment into suspension could be obtained. This information complemented the visualizations of flow-particle interactions and helped to develop a conceptual model of the mechanics of particle entrainment into suspension.

In what follows x, y, and z denote coordinates in the streamwise, vertical and transverse directions, respectively. Also, wall units denote characteristics scales formed using u_* and ν as variables, such that for example ν/u_* represents a length scale, u_* represents a velocity scale, and ν/u_*^2 represents a time scale. Variables with the subindex +, have been made dimensionless with wall units.

8.4 Particle motion in the plane x - z

8.4.1 Experiments of Series S: smooth flows. Particles immersed within the viscous sublayer

Flow visualizations of particles moving along the channel bottom in experiments of Series S, corresponding to smooth flows, showed that particles immersed within the viscous sublayer tend to be sorted in the spanwise direction, such that they accumulate along low-speed streaks of the flow. This is a well recognized phenomenon observed among others, by Grass (1971), Schmid (1985), Yung et al. (1989), and Rashidi et al. (1990). Examples of the typical situation observed from plan

views of the flow is shown in Figs. 8.2 and 8.3, with different degrees of image magnification, which correspond to the experimental conditions Re = 12400, d_p = 224 μm, Re_{p*} = 4.5, and Re = 9000, d_p = 94 μm, Re_{p*} = 1.7, respectively. Therein, lighter zones are regions where particles accumulate, marking elongated strips corresponding to low-speed streaks, while darker zones are regions with a much lower concentration of particles, which correspond to high-speed streaks.

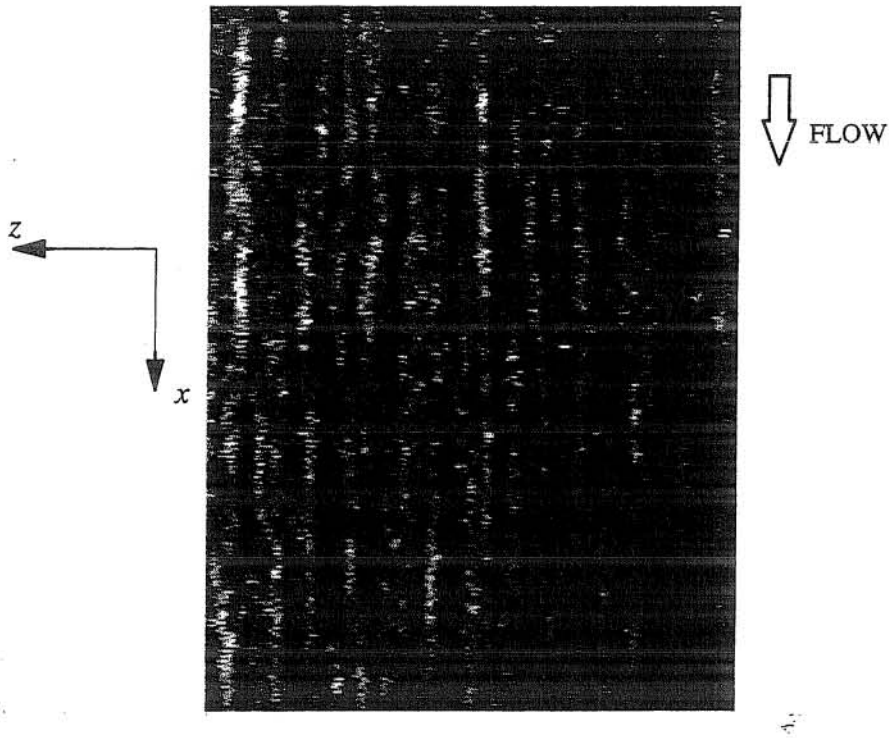

Fig. 8.2 Sand particles moving along low-speed streaks. Field of view is about 1500 by 2000 wall units. Experimental conditions correspond to Re = 12400, d_p = 224 μm, Re_{p*} = 4.5.

The low-speed streaks marked by the particles moving along the bed appear to have lengths on the order of about 1000 to 2000 wall units, and a typical transverse spacing of about 100 wall units. Average measured values of the dimensionless transverse spacing of the streaks, λ_+, observed in the present experiments are plotted in Fig. 8.4 as a function of Re. As seen therein, the present results do not depart much from the value λ_+ = 100 for the range of values of Re covered herein, which is accepted as universal for the spacing of streaks in the viscous sublayer in turbulent boundary layers (Robinson, 1991). This seems to indicate that the presence of particles in the viscous sublayer has a negligible effect on the spacing of the streaks, which is in complete agreement with the results of Rashidi et al. (1990) (see also Hetsroni, 1991). These researchers varied the loading of particles in the wall region of a channel flow and observed the effect of the presence of the particles over the streaks marked by hydrogen bubbles, concluding that although the presence of the particles seems

to influence the frequency of wall ejections, it has a negligible effect on the streaks appearance and their spacing.

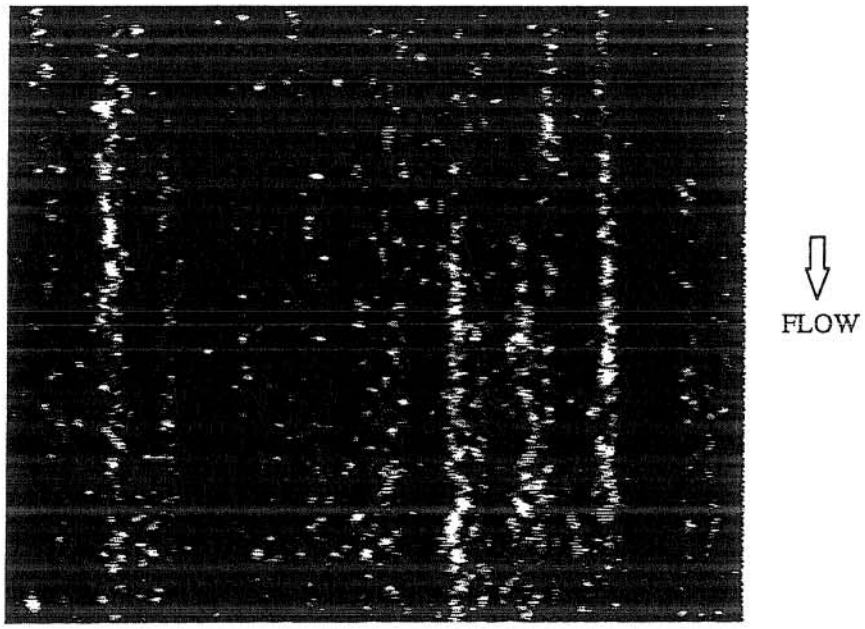

Fig. 8.3 Glass beads moving along low-speed streaks. Field of view is about 900 by 1000 wall units. Experimental conditions correspond to Re = 9000, d_p = 94 μm, Re_{p*} = 1.7.

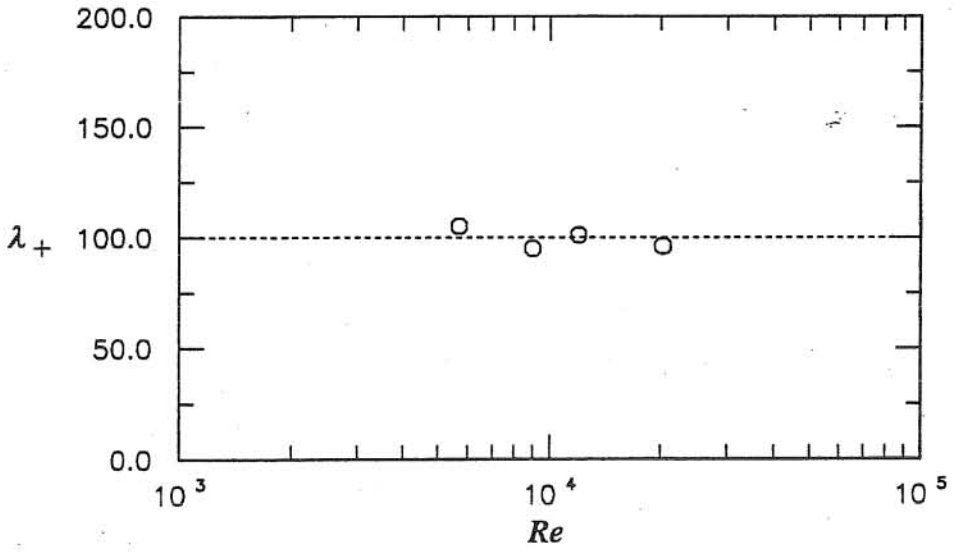

Fig. 8.4 Streaks spacing as a function of the Reynolds number. Experiments of Series S.

Rashidi et al. (1990) concluded that the presence of particles in the wall layer tends to increase the frequency of occurrence of wall ejections for particles of sizes somewhat larger than the thickness of the viscous sublayer (values of Re_{p*} larger than about 5 to 10), and to decrease such frequency for smaller particles. In the case of large particles Rashidi et al. conclude that the increase

in the frequency of wall ejections would indicate that the particles have a destabilizing effect on the coherent structures of the flow in the wall layer. Analogously, it can be concluded that particles totally immersed in the viscous sublayer would have a stabilizing effect manifested in the reduction of the frequency of ejections. Indeed, the present observations seem to indicate that such particles do have a stabilizing effect on the turbulence structure of the viscous sublayer, in that the streaks marked by them are very persistent in time and do not exhibit the strong wavering and lateral oscillations observed in flow visualizations without particles (e.g., Kline et al., 1967). In fact, according to Blackwelder (1988) the persistence of the streaks in flows without particles would be in average about 480 wall time units with some streaks persisting up to 2500 wall time units. The streaks observed herein had persistences roughly 2 to 3 times longer. It can be speculated that the stabilizing effect of the small particles would be related to the extra dissipation of energy associated with friction between fluid and particles, while the destabilizing effect of larger particles would be associated with the presence of wakes and direct interaction of the particles with flow structures. For instance Hetsroni (1991) explains the increase in the frequency of wall ejections observed in the experiments of Rashidi et al. (1990) in the presence of particles protruding over the viscous sublayer as a consequence of the direct interaction between vortex filaments and particles, such that the former would get attached to the moving particle instead of to the bottom wall, which would create a premature detachment of the vortex structure from the wall, and thus a premature ejection.

Some measurements were made of the trajectories and velocities of particles moving along low- and high-speed streaks. In general, particles completely immersed within the viscous sublayer moving along low-speed streaks have streamwise velocities on the order of 60% to 70% of the mean flow velocity, estimated using the law of the wall $u_+ = y_+$, at an elevation equal to the particle radius. Identical particles moving along high-speed streaks have streamwise velocities on the order of about 1.5 to 2.0 times the mean flow velocity at an elevation equal to the particle radius, although in this case there is much more variability of the particle velocity than in the former. This is illustrated in Fig. 8.5, where the behavior of 8 different particles tracked in one of the experiments of Series S for the conditions $Re = 9000$, $d_p = 94$ μm, $Re_{p*} = 1.7$, has been plotted in the phase space $(z_+, u_p/u_{fp})$, where u_p denotes the instantaneous streamwise particle velocity, and u_{fp} denotes the mean velocity of the flow at an elevation equal to the particle radius, such that 4 of them move along a low-speed streak and the other 4 move along a high-speed streak. As seen therein, those particles moving along the low-speed streak have values of u_p/u_{fp} generally lower than unity, with an average of about 0.7, and a standard deviation of about 0.3. On the other hand, those particles moving along high-speed streaks have values of u_p/u_{fp} as high as 3.5, although the average is about 1.5 with a standard deviation of about 0.8. Clearly the particle velocity along the high-speed streak exhibits

much more variability in time, which would be a consequence of higher turbulent intensities prevailing in those regions of the viscous sublayer.

The present observations indicate that particles are picked up from low-speed streaks, lifted away from the wall by some kind of ejection events, and deposited back to the bed along the high-speed streaks. This is in complete agreement with observations by Sumer and Oguz (1978), Sumer and Deigaard (1981), and Rashidi et al. (1990) on the entrainment into suspension of almost neutrally buoyant particles. Once the particles get deposited along the high-speed streaks, they tend to be displaced toward the low-speed streaks by the action of transverse flows related to longitudinal vorticity. This is illustrated in Fig. 8.6, where a velocity map of particles moving immersed within the viscous sublayer is plotted in the plane (x_+, z_+), for the experimental conditions $Re = 9000$, $d_p = 224$ μm, $Re_{p*} = 4.0$. As seen therein, within the low-speed streaks the velocity vectors point mainly in the streamwise direction and are of small magnitude. On the contrary, the largest velocity vectors occur along the margins of the high-speed streaks and they point in the direction of the low-speed regions, which indicates that those particles are being displaced toward the latter. This coincides with observations on the formation of streaks using fine sand made by Grass (1971). According to Grass, the fast transverse displacement of particles from the margins of the high-speed streaks toward the low-speed streaks would be indicative of the existence of strong inrushes of high momentum fluid toward the wall.

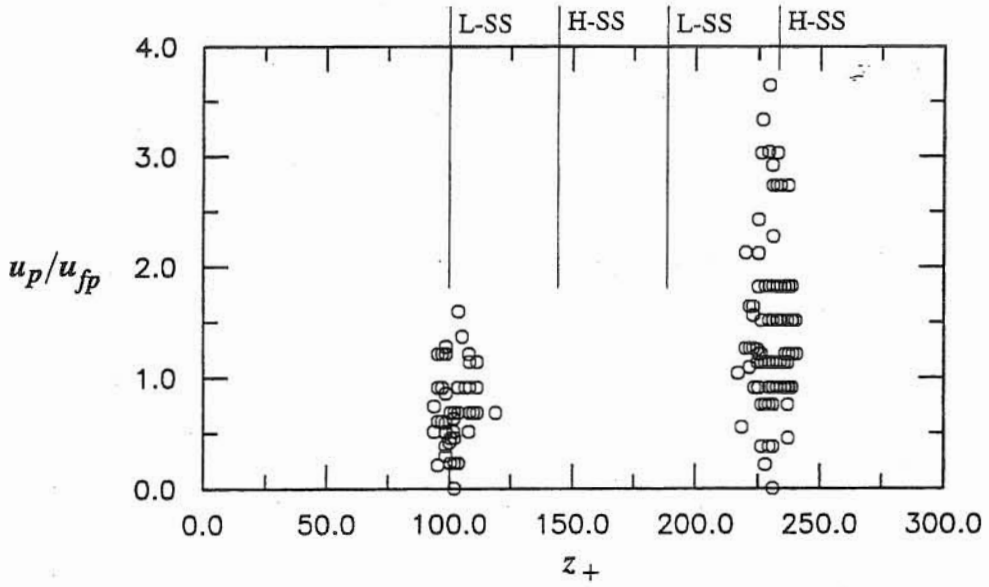

Fig. 8.5 Instantaneous streamwise particle velocities along wall streaks. Experiments of Series S, $Re = 9000$, $d_p = 94$ μm, $Re_{p*} = 1.7$. In the legend H-SS denotes high-speed streak, and L-SS denotes low-speed streak.

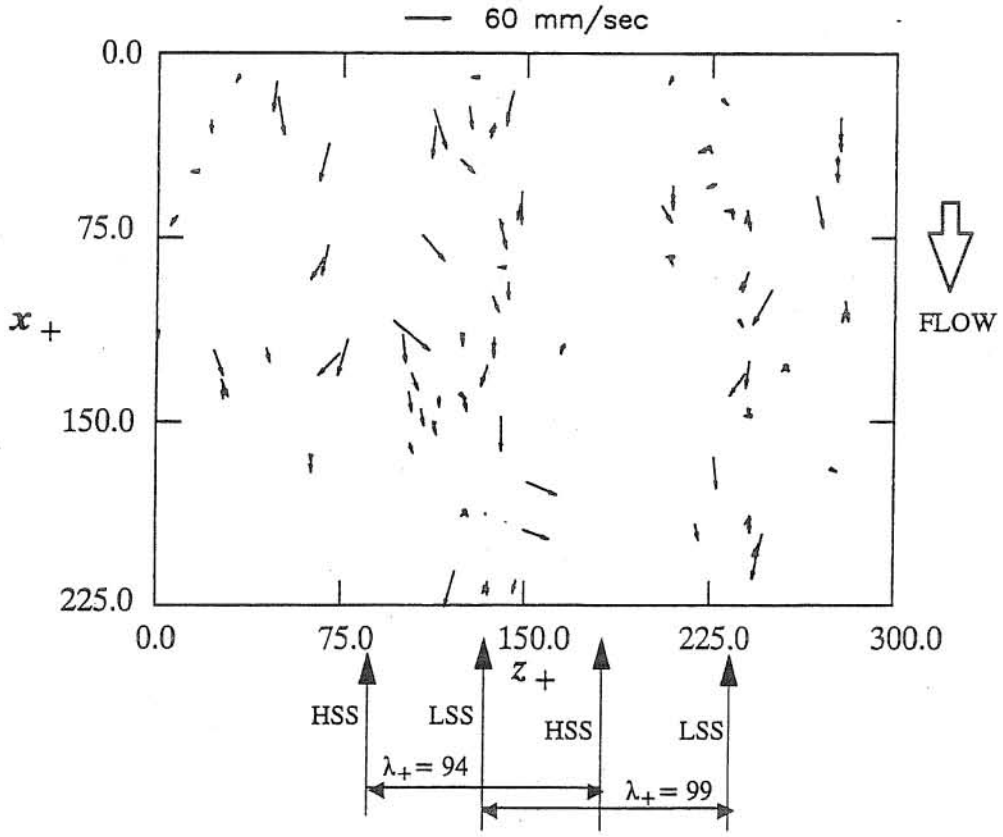

Fig. 8.6 Velocity map of particles moving along wall streaks. Experiments of Series S, Re = 9000, d_p = 224 μm, Re_{p*} = 4.0. HSS: High-speed streak, LSS: Low-speed streak.

8.4.2 Experiments of Series S: smooth flows. Particles protruding over the viscous sublayer

An interesting result of the present observations is that particles of sizes larger than the thickness of the viscous sublayer do not tend to be sorted along the wall streaks, that is they do not tend to accumulate along the low-speed streaks, although groups of particles located in certain regions along the bottom wall do seem to exhibit sudden accelerations, apparently as a consequence of the occurrence of inrush events associated with the existence of high-speed streaks. This is illustrated in Fig. 8.7, where a plan view of particles of size d_p = 530 μm, with a corresponding value Re_{p*} = 10 (equivalent to a size of about twice the thickness of the viscous sublayer), moving along the smooth bed in one experiment of Series S corresponding to Re = 9000, is shown. Such image was acquired using regular, fixed illumination, and a relatively low recording speed of 60 fps, which implies that faster particles tend to appear as short streaks. It is clear from that image that the particles tend to distribute randomly along the bed, without grouping along the wall streaks, however there are groups of particles that seem to be moving much faster than the others.

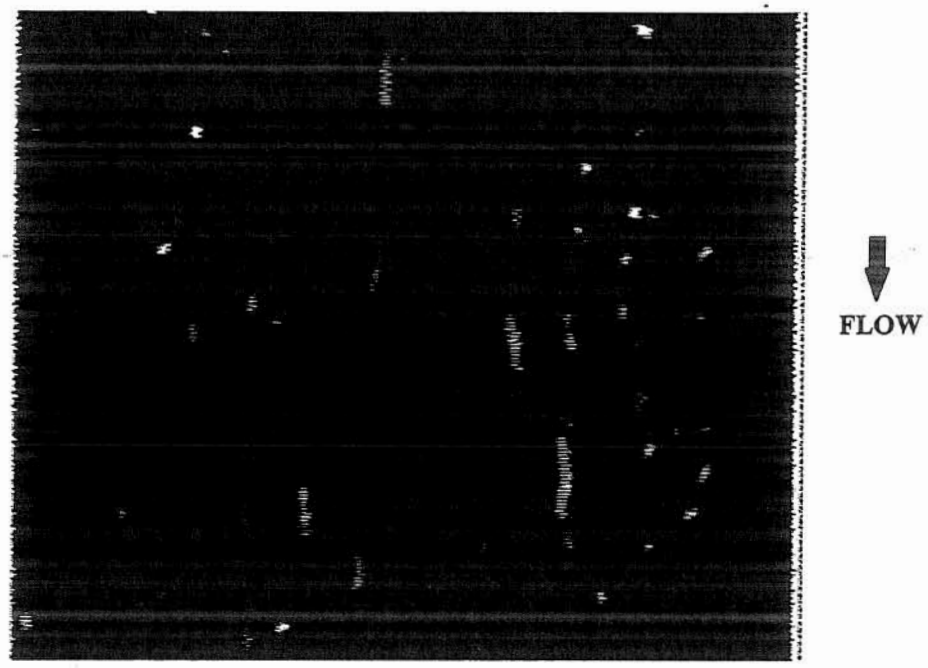

Fig. 8.7 Particles larger than the viscous sublayer moving along the smooth wall of Series S. Field of view is about 345 by 410 wall units. Experimental conditions correspond to $Re = 9000$, $d_p = 530$ μm, $Re_{p*} = 10$.

The above observation seems to indicate that the formation of wall streaks is a phenomenon related to the structure of the turbulence within the viscous sublayer, that is, it appears to be confined within elevations lower than about 5 wall units from the bottom wall, such that it is not effective in inducing the grouping of particles protruding somewhat over the viscous sublayer, although it is apparent that it can still influence their velocity. This is in agreement with Kline et al.'s (1967) flow visualizations using hydrogen bubbles, which indicate that the streaks tend to become less noticeable and eventually to vanish at distances from the bed larger than about 5 wall units.

It is necessary to mention, however, that direct numerical simulations of wall-bounded turbulent flows show the existence of streaks at values of y_+ as large as about 10 (Moin and Kim, 1982; Moin and Spalart, 1989). According to the flow visualizations of Smith and Schwartz (1983), low-speed streaks appear as well organized and very persistent structures only for values of y_+ up to about 5. At higher values of y_+ the low-speed regions are still recognizable, although they exhibit strong but intermittent outward motion combined with spanwise rotation, which make flow patterns more irregular as they evolve in time. Smith and Schwartz conclude that the most energetic and regular rotational behavior occurs in a region corresponding to values of y_+ lower than about 25, and that this rotational behavior suggest the presence of counter-rotating, streamwise vortices which would be related low-speed streak formation.

From the above discussion it is apparent that the formation of low-speed streaks is related to the presence of counter-rotating, streamwise vortices, extending distances up to about 25 wall units from the channel bottom. It seems plausible that cross flows resulting from the streamwise structures would be more persistent and well organized within the viscous sublayer, which may explain why they are more effective in pushing particles with their centroid located well within the viscous sublayer toward the low-speed regions, rather than larger particles protruding over the sublayer. Also, it must be considered that larger particles have more inertia than smaller ones and therefore they are less responsive to flow velocity fluctuations such as those associated with the cross flows.

Pedinotti et al. (1992) performed a direct numerical simulation of particle behavior in the wall region of a turbulent channel flow. They found that particles with very low specific density, $R=0.03$, tend to be grouped along low-speed streaks, however the degree of sorting appears to depend on the particle dimensionless time constant (a measure of the particle inertia), defined as: $t_{p+} = (\varrho_s \, d_p^2 \, u_*^2)/(18 \, \nu \, \varrho)$, such that maximum sorting is obtained for values of t_{p+} of about 3. For smaller values of t_{p+}, the particles tend to get distributed uniformly along the bed, and the same happens for larger values of t_{p+}. Pedinotti et al. point out that the sorting mechanism would be due to the presence of a rotation motion in the high-speed regions which pushes the particles out of them. They speculate that this mechanism would be effective on grouping particles along the viscous sublayer as long as their time constant is small enough as to follow the streak motion, but not so small as to be sensitive to high-frequency fluctuations, which would tend to distribute the particles uniformly.

In the present experiments particle grouping along low-speed streaks was observed for values of t_{p+} in the range from about 0.05 to about 4. On other hand, the particles shown in Fig. 8.7 which do not tend to group along the wall streaks have values of t_{p+} larger than 10. These results are only in partial agreement with the numerical simulations of Pedinotti et al., since according to their results sorting would be much less conspicuous than observed herein for values of t_{p+} lower than say 1. Nevertheless, the present results agree, at least qualitatively, with them in that particles with large time constants do not tend to group along wall-streaks.

8.4.3 Experiments of Series T: transitionally rough flows

Observations of the video recordings made in the experiments of Series T, corresponding to transitionally rough flows, indicate that in this situation the formation of streaks is much less evident than in the case of smooth flows. In fact, it seems that the roughness elements, with sizes of about 10 wall units, totally disrupt the structure of the viscous sublayer as compared with the smooth bed situation. Particles with sizes smaller than about 1/5 of the size of the roughness elements were

observed to move within the interstices of the latter, and therefore their path-was imposed mainly by the random distribution of bed obstacles. Larger particles were observed to move over the roughness elements, at distances well above 5 wall units from the bottom wall, and did not show any tendency to group together along preferential lines.

The above observations seem to be in total agreement with those by Sumer and Deigaard (1981). According to them, in the case of a smooth wall, inrushes of high-speed fluid hit the bottom and spread out sideways; the lateral flows of fluid along the neighboring sides of two such adjacent high-speed zones of fluid run together, merge each other and are retarded which in turn gives rise to a low-speed wall streak. In the case of a rough wall, the lateral flows of fluid along the neighboring sides of two adjacent high-speed zones are likely to be retarded by form drag of the roughness elements, which cause the fluid to be trapped between the protrusions, leading to longitudinal localization of the low-momentum fluid and thus causing the disappearance of the smooth-boundary wall streaks. Indeed, Grass (1971) reported that the long twisting streamwise vortices, very apparent close to the smooth boundary during inrush-ejection cycles, were much less evident in the transitional and rough boundary flows in his tests, which would imply that low-speed wall streaks cease to exist in the case of rough wall.

Nevertheless, new experimental evidence presented by Grass et al. (1991) seems to indicate that wall streaks would continue to exist in the transitionally rough and rough flow regimes, although their characteristics would tend to change as the bed roughness is increased. In general, Grass et al. point out that the spacing of the streaks tends to increase with the bed roughness, while their streamwise coherence is substantially reduced. On the other hand, it is also apparent that the effect of the wall streaks is felt only in a region adjacent to the roughness elements, which has a rather reduced vertical extension.

Although the wall streaks seem to persist in transitionally rough flows like those of Series T according to the previous discussion, it is also apparent that those streaks do not have the strong coherence, persistence, and vertical extension observed in the case of smooth flows. This would imply that they are not strong enough as to induce sediment particles to sort along them, which is in agreement with the present observations. As it was already mentioned, those particles that were large enough as to move over the roughness elements in the present experiments did not show any tendency to sort along preferential lines. Depending on flow conditions they were observed either saltating along the bed or being entrained into suspension by the turbulence of the flow as discussed in the next section.

8.4.4 Discussion

The evidence presented so far allows to draw a few general conclusions with respect to the motion of particles in the x-z plane along the bottom wall of a turbulent channel flow and their

interaction with wall streaks. In the first place the wall streaks in a smooth flow appear to be related to the presence of counter-rotating streamwise vortices. These would extend about 1000 to 2000 wall units in the streamwise direction, and about 15 to 25 wall units from the bottom in the vertical direction, although they appear to lose their coherence outside the viscous sublayer. The spanwise dimension of the longitudinal vortices would be lower than about 50 wall units so the total spanwise extension of the counter-rotating pair would be about 100 wall units, which corresponds to the spacing between low-speed streaks. These vortices would create a "pumping" effect which produces ejections of low-momentum fluid away from the wall on one side of the vortex core, and inrushes of high-momentum fluid toward the wall on the other (Robinson, 1990). The inrushes of high-momentum fluid would impinge against the wall and create strong cross flows toward the low-speed regions. These cross flows would be most responsible for pushing particles toward and accumulating them along the low-speed regions (Fig. 8.8). Since the cross flows are stronger and more coherent close to the bed they would be most effective in pushing particles totally immersed within the viscous sublayer, rather than particles protruding over it, such that the latter do not seem to accumulate along wall streaks.

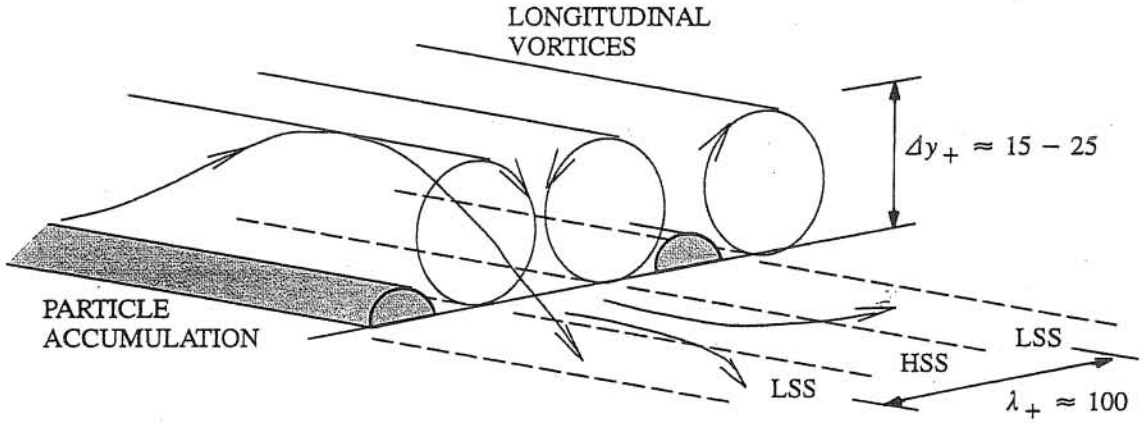

Fig. 8.8 Conceptual model of streak formation. HSS: High-speed streak, LSS: Low-speed streak.

Groups of 3 to 5 counter-rotating pairs of streamwise vortices seem to emerge and collapse quasi-periodically in time, and to distribute rather randomly along the bed (Fig. 8.9). The persistence of the structures in the absence of particles seems to be in the average about 500 wall time units, and seems to increase about 2 to 3 times in the presence of particles. This appears to indicate that the particles have a stabilizing effect on the structures of the flow, however it seems that this would be true for small particles only (smaller than say the thickness of the viscous sublayer), such that larger particles would have a destabilizing effect over such structures. The spacing of the streaks, on the other hand does not seem to be affected by the presence of particles.

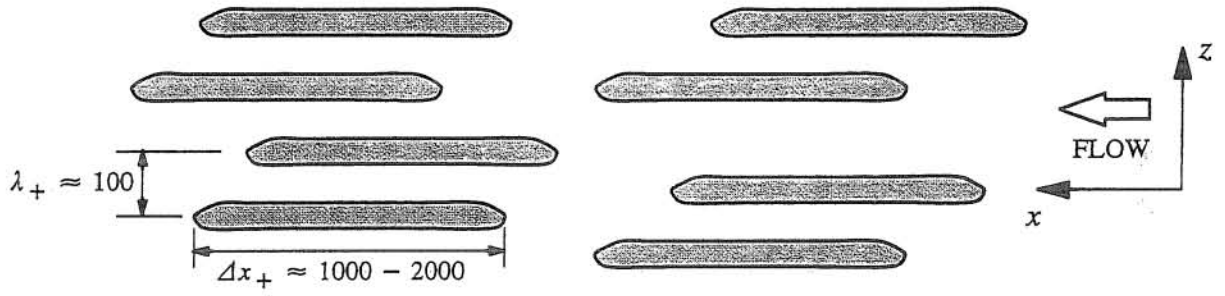

Fig. 8.9 Low-speed streaks, zones of particle accumulation. After Hetsroni (1991).

In the case of a rough boundary, the roughness elements seem to disrupt the structure of the viscous sublayer, and although the wall streaks would persist in these conditions, they would lose coherence, persistence and spatial extension. This, however, does not seem to affect the mechanism that generates ejections of low-speed fluid away from the wall, and inrushes of high-speed fluid toward the wall. Cross flows resulting from inrushes are likely to be retarded by form drag of the roughness elements, which would cause the fluid to be trapped between the protrusions, leading to longitudinal localization of low-momentum fluid. Particles of small size compared to the roughness elements (with sizes of about 1/5 of those of the roughness elements) appear to move within the interstices of the latter, and therefore their path was controlled mainly by the random distribution of bed protrusions. Larger particles seem to move over the roughness elements and do not tend to accumulate along specific regions of the flow.

8.5 Particle motion in the plane x - y

8.5.1 Experiments of Series S: smooth flows

Results from visualizations of flow and particle motion

Visualizations of particle motion in the near bed region of the smooth flows of Series S showed that particles tend to be picked up from low-speed streaks, lifted away from the wall by some kind of ejection mechanism, and deposited back to the bed along the high-speed streaks, from where they tend to be displaced toward the low-speed streaks by the action of cross flows related to longitudinal vorticity.

A typical sequence of images of the first stages of particle entrainment into suspension is shown in Fig. 8.10. The experimental conditions correspond to $Re = 22500$, $d_p = 112$ μm, $Re_{p*} = 2.6$, and the time interval between images is 0.004 s. The sequence shows a group of 4 or 5 particles being picked up from the bed, lifted to an elevation of about 50 wall units, and displaced downstream a distance of about 125 wall units, in a total time interval of about 15 wall time units. It is interesting to note that the particles tend to group along a line with an inclination angle of about 15° to the bed.

As to the mechanism that causes the ejection of the particles away from the bed, there exists enough consensus, based primarily on experimental evidence, that it would be related to interactions

between the particles and intermittent events associated with the phenomenon of turbulent bursting, during which low-momentum fluid is ejected toward the outer regions of the wall layer (Grass, 1974; Sumer and Oguz, 1978; Sumer and Deigaard, 1981; Ashida and Fujita, 1986; Yung et al., 1989; Rashidi et al., 1990). The same conclusion is reached by Pedinotti et al. (1992) whose direct numerical simulations of particle-turbulence interactions in the near wall region of a channel flow have shown that particles are lifted from the bed by the action of upflows caused by quasi-streamwise vortices which detach low-speed fluid from the wall.

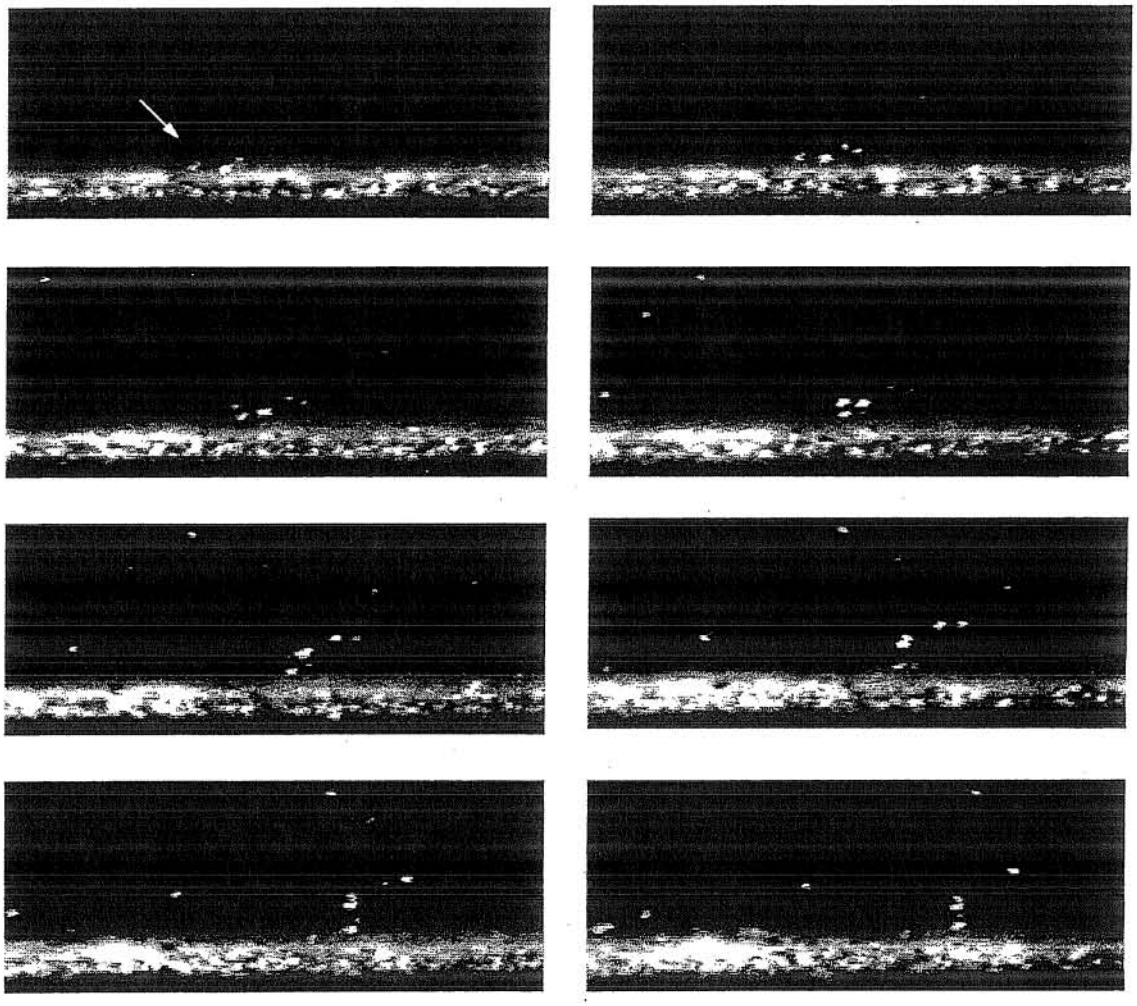

Fig. 8.10 Sequence of images of first stages of particle entrainment. Experiments of Series S, Re = 22500, d_p = 112 μm, Re_{p_*} = 2.6. Field of view of each image is about 336 by 133 wall units, and the time interval between images is 0.004 s.

As discussed in Chapter 4, the results of flow visualizations carried out in the present investigation have shown that low-speed streaks tend to be lifted-up as a consequence of quasi-periodic ejections of low-momentum fluid away from the channel bottom, and to evolve into some kind of flow coherent structure. The most frequently observed coherent structures correspond

to inclined, thin shear layers of concentrated spanwise vorticity, similar to those revealed by the analysis of data bases generated through Direct Numerical Simulations, DNS (e.g., Jimenez et al., 1988; Guezennec et al., 1989), and those observed experimentally using Particle Image Velocimetry, PIV (e.g., Liu et al., 1991; Urushihara et al., 1993). The shear layers observed herein have a shape which appears to be invariant with the Reynolds number when plotted in wall units. These structures seem to maintain their identity for as long as 60 to 80 wall time units, to extend vertically a distance of about 100 wall units with a mean inclination angle to the bed of about 14°, and to have convection velocities of about 10 wall units and frequencies of occurrence of about 0.003 wall units. Typically, at distances of about 100 to 200 wall units downstream from the structure a negative peak of the streamwise velocity fluctuations was measured, which appears to travel with the structure, and which would be correlated with positive vertical velocities of the flow in what would be an ejection event of low-momentum fluid away from the wall.

The present results seem to indicate that the shear layers described above interact with particles lying over the bed, such that the flow ejection occurring downstream of the structure would induce the lift-up of particles away from the bed. This is illustrated in Fig. 8.11, where a sequence of images of an inclined shear layer being convected and stretched in the streamwise direction is shown, together with a sand particle which is being lifted-up from the bed at a distance of about 115 wall units downstream of the structure, apparently responding to an ejection event taking place in such region. The experimental conditions correspond to Re = 15000, d_p = 224 μm, Re_{p_*} = 4.5, and the time interval between images is 0.008 s.

Once the particles are lifted-up from the bed they tend to lag somewhat the fluid ejection. That is, it is apparent that particle streamwise velocities during ejections are somewhat smaller than the convection velocity of the shear layers. This means that, as time goes by, shear layers and ejected particles tend to get closer together and to have a more direct interaction, as is illustrated in Fig. 8.12, where different images show different degrees of interaction between particles and shear layers. As seen therein particles tend to get closer to the structures and eventually to get trapped in their core. In some some cases it was observed that particles lined-up along the shear layer and followed its path as the structure was stretched toward the outer regions of the wall layer. In some other cases the particles lost correlation with the shear layer and were observed to lag behind it until it was either deposited back to the bed, or taken-up by a new developing flow ejection.

To illustrate the above point, Fig. 8.13 shows a conceptualization of the relative motion of an ejected particle with respect to the shear layer. That is, it schematizes the particle motion as seen from a system of reference moving with the convection velocity of the flow structure. In that figure, the relative flow velocity field around the shear layer is also sketched, based on the experimental measurements using PIV by Urushihara et al. (1993). According to those observations, there

appears to be a relative stagnation point located over the shear layer which corresponds to a saddle point of the relative velocity vector field. The zone downstream from the structure corresponds to a low-velocity region where the relative flow field is in the upstream direction toward the shear layer. The zone upstream from the structure corresponds to a high-velocity region where the relative flow is in the downstream direction, also toward the shear layer. Along the shear layer, the relative velocity vectors are in the direction of the inclined structure and have a larger magnitude upstream from the structure than downstream from it, so the shear layer represents a zone of concentrated transverse vorticity. The initial ejection of the particle would take place at a distance of about 100 to 200 wall units downstream from the structure. The relative motion of the particle would be in the upstream direction toward the shear layer. Eventually, the particle would get trapped in the core of the structure and move along it as the shear layer is stretched, or the particle would lose correlation with the structure, lagging behind, until it is either deposited or kept in suspension by other ejection events.

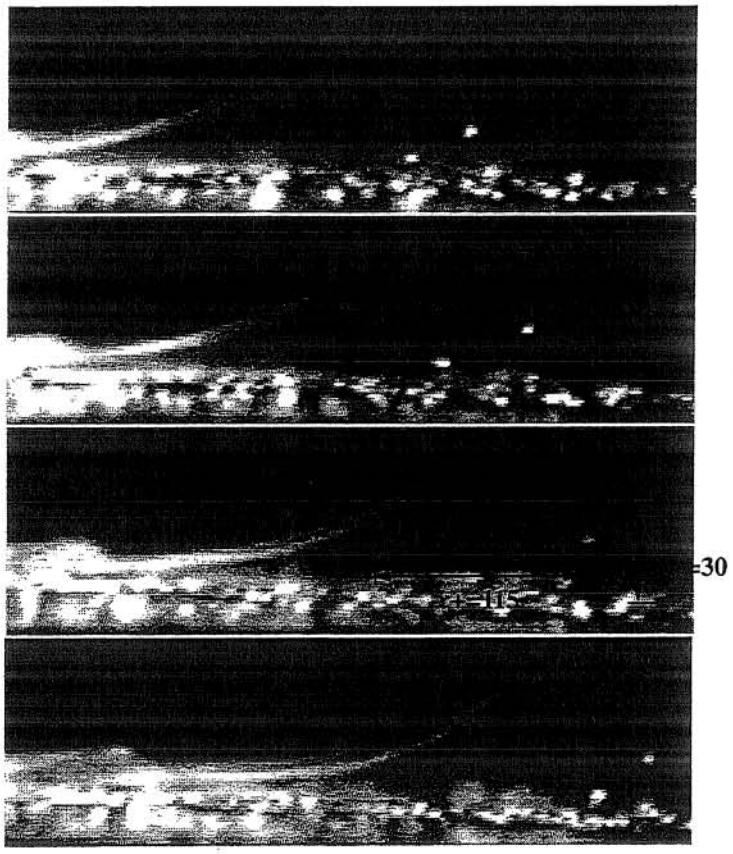

Fig. 8.11 Sequence of images of particle-shear layer interaction. Experiments of Series S, Re = 15000, d_p = 224 μm, Re_{p*} = 4.5. Field of view of each image is about 375 by 114 wall units, and the time interval between images is 0.008 s. The shear layer is marked using a solution of white clay in water injected through the bottom of the channel.

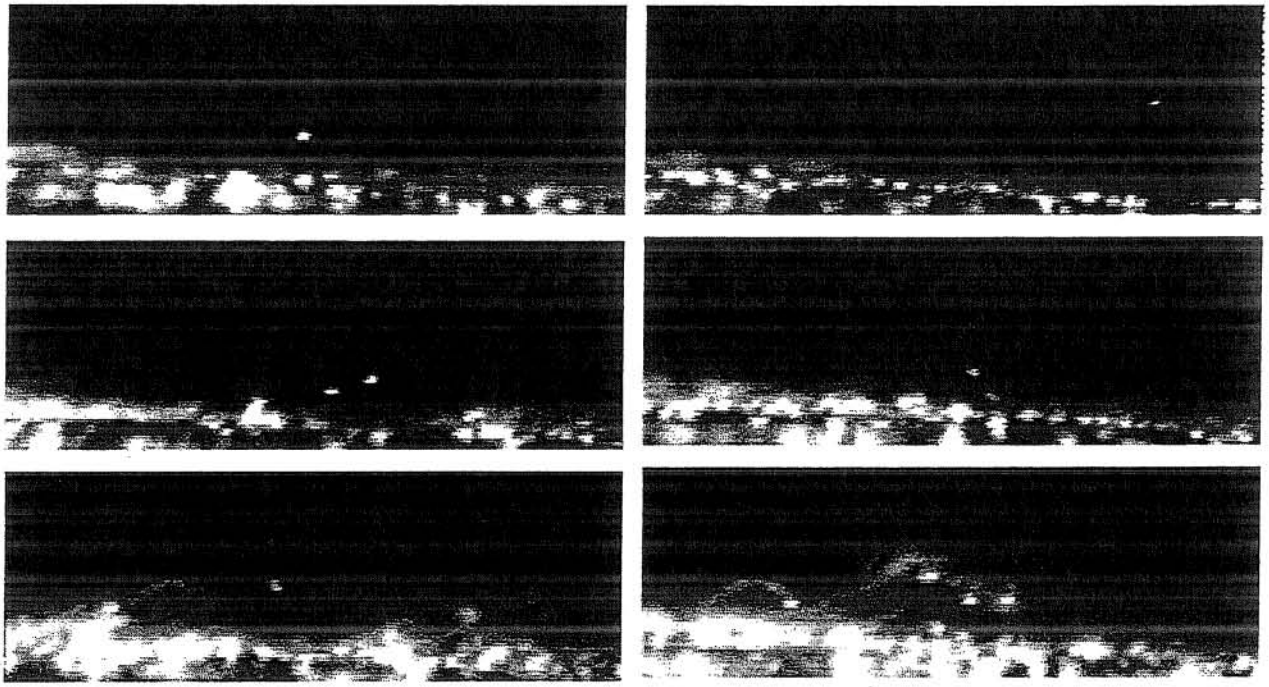

Fig. 8.12 Different degrees of particle-shear layer interaction. Experiments of Series S, Re = 15750, d_p = 224 μm, Re_{p*} = 4.7. Field of view of each image is about 307 by 105 wall units.

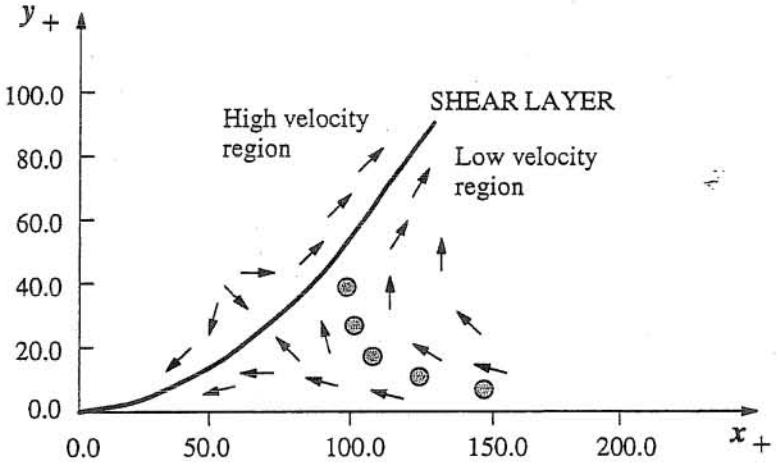

Fig. 8.13 Schematic view of particle motion as seen from a system of reference moving with the shear layer. Circles represent different relative positions of the particle as it is ejected away from the bed. Arrows sketch the relative flow velocity field surrounding the shear layer as measured by Ushihara et al. (1993).

It is important to point out that the observed flow ejection events were not always effective in entraining the heavy particles tested herein into suspension. In fact, according to the analysis of the threshold conditions for particle entrainment into suspension presented in Chapter 7, it was found that as the particle size gets smaller than the thickness of the viscous sublayer, progressively higher

values of the bed shear stress are required to entrain the particle into suspension. This suggests that the intensity of the ejection events gets weaker as the bottom wall is approached. Indeed, according to Bark (1975), values of the Reynolds stress, $\overline{u'v'}$, during flow ejection events would have the following dependence on y_+:

$$-\overline{u'v'}/u_*^2 = c_1\, y_+^3\, \exp\,(-c_2\, y_+^2) \qquad (8.1)$$

where the constants c_1 and c_2 can be obtained by adjusting (8.1) to the measurements by Kim et al. (1971), which gives the values: 1.87×10^{-3} and 4.42×10^{-3}, respectively. The results predicted by (8.1) are plotted in Fig. 8.14 together with the experimental values measured by Kim et al. As seen therein the maximum value of the shear stress seems to occur outside the viscous sublayer, at a distance from the bed slightly less than 20 wall units. Inside the viscous sublayer, the intensity of the shear stress due to the flow ejection seems to decrease sharply toward the bed.

With respect to the previous discussion, it is necessary to mention that Sumer and Oguz (1978), and Yung et al. (1989), studying the entrainment into suspension of particles with very small submerged specific density concluded that flow ejection events have a negligible effect in entraining particles totally immersed within the viscous sublayer. The present results seem to contradict this conclusion, as is evident from the visualizations shown in Figs. 8.10 to 8.12, all corresponding to heavy particles of sizes smaller than the thickness of the viscous sublayer, which appears to indicate that bed shear stresses in Sumer and Oguz's, and Yung et al.'s experiments were not sufficiently high as to cause the entrainment of such particles.

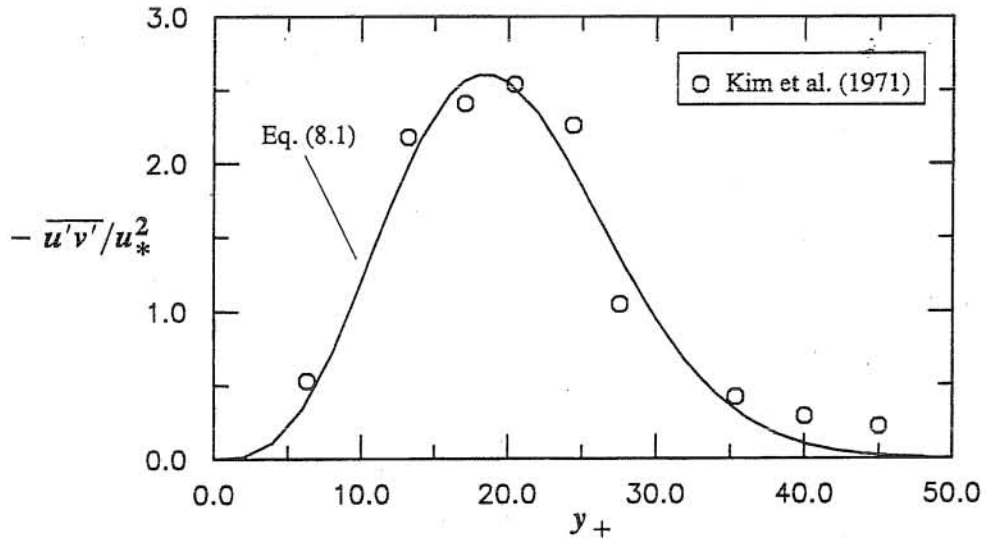

Fig. 8.14 Values of the dimensionless Reynolds stress during a bursting ejection event, as predicted by (8.1). Comparison with the experimental data of Kim et al. (1971).

On the other hand, Sumer and Oguz (1978) concluded that ejection events associated with turbulent bursting would be most effective in lifting-up almost neutrally buoyant particles (with

values of R of about 0.003 to 0.008) protruding over the viscous sublayer. This is in agreement with the above discussion in that the intensity of the ejection event appears to be higher outside the viscous sublayer (see Fig. 8.14). The present results, however, showed that sand particles of sizes larger than the thickness of the viscous sublayer were not entrained into suspension, at least for the range of values of the bed shear stress tested herein, which would indicate that such particles are too heavy to be picked up by such flow ejection events.

Particle trajectories

An analysis of particle trajectories during ejections showed different typical paths followed by them. Some examples are presented in Figs. 8.15 to 8.18. As already discussed, particles appear to be entrained by flow ejection events occurring downstream of convected shear layers. Typical angles of ejection of the particles were observed to be in the range from about 10° to about 20°, which is in good agreement with the values reported by Yung et al. (1989).

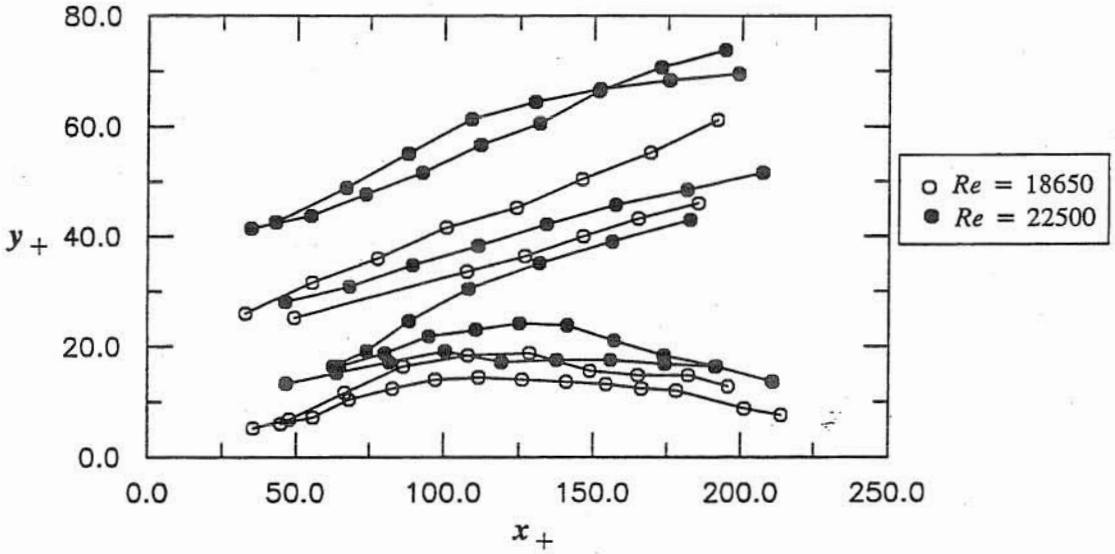

Fig. 8.15 Typical trajectories of entrained particles. Experiments of Series S, d_p = 224 μm, Re = 18650 and 22500, and values of Re_{p*} of about 5.

A few trajectories of entrained particles are shown in Fig. 8.15, for the experimental conditions d_p = 224 μm, Re = 18650 and 22500, and values of Re_{p*} of about 5. As seen therein, some particles are clearly ejected toward the outer regions of the wall layer (values of $y_+ \approx 100$), with an angle of inclination of about 12°, similar to those typical of the shear layers observed in the present experiments. On the contrary, some other particles reach maximum elevations corresponding to values of y_+ lower than about 30, after which they tend to fall back toward the bed. From these descriptions it is apparent that the interaction between flow ejections and particles is not always effective in lifting them up to the outer regions of the wall layer. Indeed, although the first group of particles appear to have been trapped in the core of the stretched shear layers and carried along

them toward such regions, the second group of particles seem to have fallen from the flow structure in a phenomenon called crossing-trajectories effect (Wells and Stock, 1983; Zhuang et al., 1989), thus losing correlation with the fluid motion before the structure loses its identity.

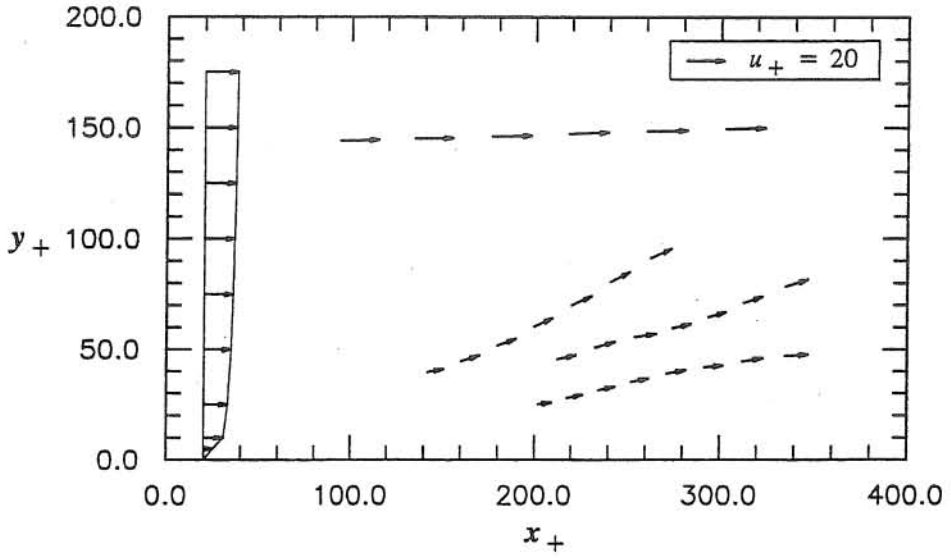

Fig. 8.16 Velocity map of suspended particles in one ejection event. Each sequence of arrows correspond to a different particle. The time interval between arrows of the same sequence corresponds to about 2 wall time units (0.004 s). The velocity profile on the left corresponds to the logarithmic mean velocity profile for smooth flows. Experiments of Series S, d_p = 112 μm, Re = 20145, Re_{p*} = 2.6.

The latter phenomenon was also observed by Sumer and Deigaard (1981). They carried out experiments with almost neutrally buoyant particles with values of R of about 0.003 to 0.008, and also with slightly heavier particles with values of R of about 0.03, concluding that while the lighter particles follow the flow ejections closely, the heavier ones tend to fall from the flow ejections back to the channel bottom due to the crossing-trajectories effect. In the present experiments, where the particles were much heavier (values of R of about 1.65), both types of behavior were observed for similar particles, which seems to indicate that the type of path taken by the particle depends on the intensity of the flow ejection event (those events are stochastic in nature, and therefore exhibit variable intensities) and also on the degree of interaction between particle and shear layer reached by the ejected particle, such that more intense events and a high degree of interaction, with the particle trapped in the core of the shear layer, would be associated with particles ejected toward the outer regions of the wall layer, while weaker flow ejection events and a low degree of particle-shear layer interaction would produce a premature particle falling from the structure. This argument leads to a slight modification of the conceptual model for the ejections of particles proposed by Sumer and Deigaard (1981), as is shown in Fig. 8.19.

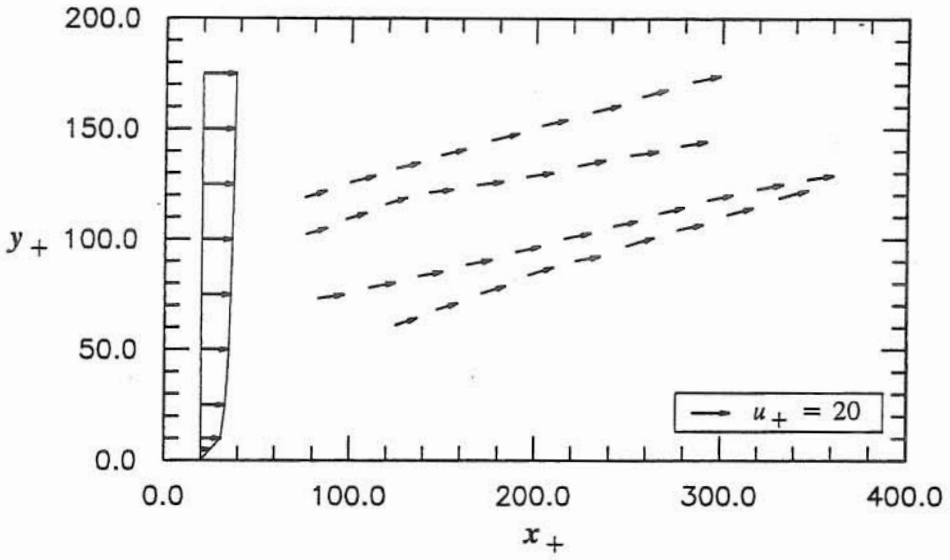

Fig. 8.17 Velocity map of suspended particles in one ejection event. Experimental conditions and details as in Fig. 8.16.

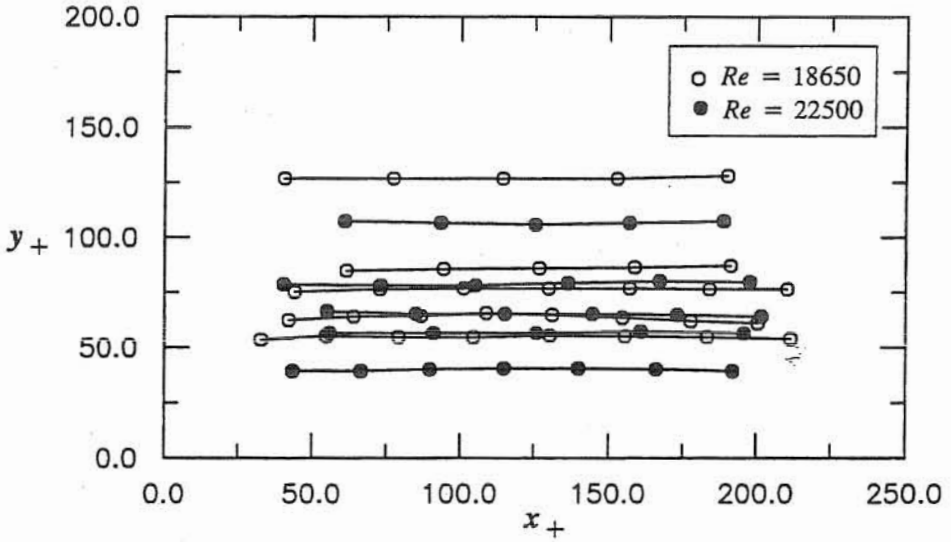

Fig. 8.18 Typical trajectories of suspended particles. Experimental conditions as in Fig. 8.15.

With respect to the above point, it was found that the ratio between the number of ejected particles observed to reach the outer region of the wall layer and the total number of ejected particles tends to increase with the dimensionless bed shear stress, τ_*, as shown in Fig. 8.20. Therein the experimental points correspond to a value of $d_p = 224$ μm, values of Re in the range from 10760 to 22500, and values of Re_{p*} in the range from 4.3 to 5.2, which is relatively narrow and defines particles sizes of the order of the thickness of the viscous sublayer, thus giving them about the same degree of relative exposure to the flow. The results in Fig. 8.20 seem to indicate that, in the average, the intensity of flow ejection events tends to increase with the bed shear stress, which is in agreement with the results of a VITA analysis of streamwise velocity fluctuations measured near the bed in the

present experiments (Chapter 3), which showed that the magnitude of the conditionally averaged velocity fluctuations during ejection events seems to be proportional to u_*. It is also apparent from Fig. 8.20 that as the values of τ_* get smaller than about 0.12 a sharp decrease in the effectiveness of flow ejections to lift particles to the outer regions of the wall layer takes place.

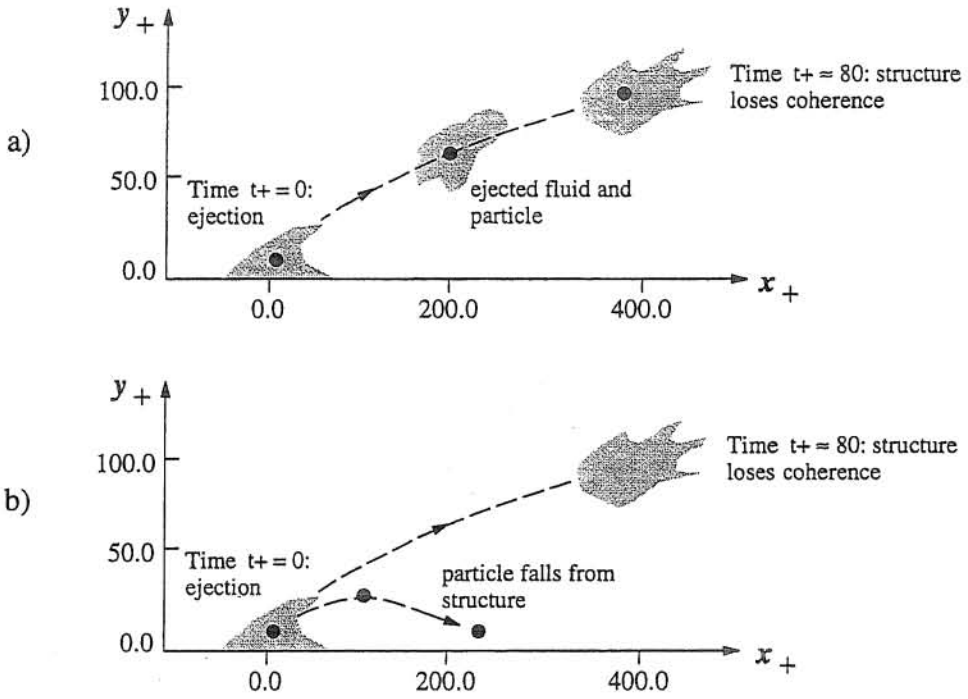

Fig. 8.19 Schematic view of particle-flow ejection interactions. a) Case of intense flow ejection event, high degree of particle-shear layer interaction: particle is trapped in the core of the shear layer and ejected to the outer regions of the wall layer until the flow structure loses coherence. b) Case of weak flow ejection event, low degree of particle-shear layer interaction: particle falls from the structure due to the crossing-trajectories effect. Adapted from Sumer and Deigaard (1981).

Velocity maps of particles being entrained in two particular ejection events corresponding to the experimental conditions $d_p = 112$ μm, $Re = 20145$, $Re_{p*} = 2.6$, are shown in Figs. 8.16 and 8.17. Therein the sequence of arrows show particle trajectories and the evolution in time of their velocity vector. The time interval between arrows of the same sequence corresponds to 0.004 s. In those figures, the logarithmic mean velocity profile for smooth flows, given by (Clauser, 1956; see also Chapter 3):

$$u_+ = \frac{1}{\varkappa} Ln\,(\,y_+\,) + 4.9 \qquad (8.2)$$

where $\varkappa$ denotes von Karman's constant taken as equal to 0.4, is also plotted as a reference. As seen in Fig. 8.16, particle trajectories during entrainment are very similar to those shown in Fig. 8.15. In this case, two of the three particles being entrained seem to be heading toward the outer regions

of the wall layer, while it seems that the third one will not reach heights larger than about 50 wall units. Clearly, the horizontal components of the measured particle velocities during entrainment are considerably lower than the local mean flow velocity predicted by the logarithmic law for smooth flows, which seems to indicate that the streamwise component of the flow velocity fluctuations, u', in the ejection event responsible for the entrainment of the particles has a negative sign. This, added to the obvious fact that the vertical component of such velocity fluctuations, v', is positive during entrainment, shows that the flow ejection event responsible for the entrainment of particles in Fig. 8.16 is an event of quadrant 2 ($u' < 0$, $v' > 0$) and thus an important contributor to the Reynolds stress $\overline{u'v'}$, which is in agreement with the results of Kim et al. (1971) shown in Fig. 8.14. It is also apparent from Fig. 8.16 that the magnitude of the particle velocity tends to increase as the particle is lifted-up away from the channel bottom, which is a consequence of the momentum transfer from the flow to the particle, which gets accelerated as it is being dragged by fluid of increasing momentum.

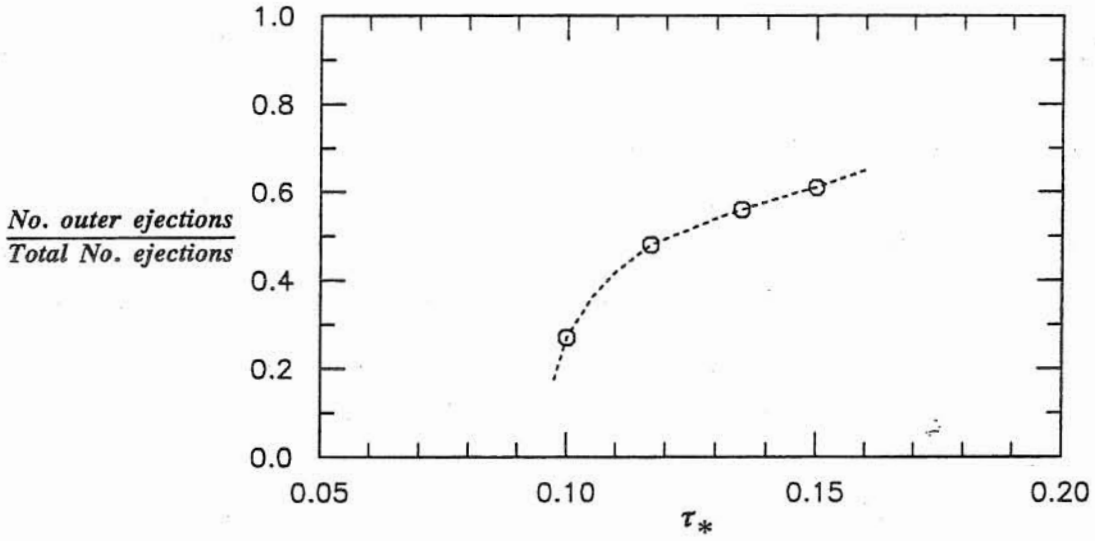

Fig. 8.20 Ratio between number of particles ejected to the outer regions of the wall layer and total number of ejected particles as a function of the dimensionless bed shear stress. Experiments of Series S, $d_p = 224$ μm, Re in the range from 10760 to 22500, Re_{p*} in the range from 4.3 to 5.2.

A similar situation is observed in Fig. 8.17. Therein, four particles are being lifted-up toward values of y_+ of about 150 to 200, which is indicative of a very strong flow ejection event. The inclination angle of the trajectories is about 13°, similar to that of the trajectories shown in Figs. 8.15 and 8.16, and also of the shear layers as already discussed. In this case, the streamwise component of the particle velocity is also somewhat smaller than the local flow mean velocity given by the logarithmic velocity profile for smooth flows, which again shows that the ejection event responsible for the entrainment of the particles of Fig. 8.17 is an event of quadrant 2, with high values of the Reynolds stress $\overline{u'v'}$.

An interesting feature of the situation shown in Fig. 8.16 is that there is a fourth particle, which does not seem to be part of the ejection event involving the other three particles, and which appears to be moving almost horizontally at a height of about 150 wall units, with a velocity close to that of the local mean flow velocity. Such particle must have been lifted to the outer region of the wall layer by a previous ejection event, and was kept in suspension by the turbulence of the outer flow. Fig. 8.18 shows a few examples of this situation, where particle trajectories corresponding to the same experimental conditions as those of Fig. 8.15 are plotted. As seen therein particles that have been ejected away from the channel bottom can be kept in suspension with trajectories almost parallel to the mean flow velocity for quite long distances, and at elevations as close to the bed as about 40 wall units.

These results seem to indicate that once the particles escape from the lower regions of the wall layer, the turbulence activity prevailing at elevations higher than about 40 wall units somehow induce them to remain suspended for rather long distances before they get deposited back to the bed. Indeed, Browand and Plocher (1985) analyzing the entrainment of relatively light particles by the action of turbulent spots in an otherwise laminar flow concluded that there is a difference between entrainment (the actual lift-up of bed material) and what might be called "suspendability", which they define as the propensity of particles to remain suspended in a turbulent flow, such that some of the particles they tested, which were never observed to be lifted from the bed by turbulent spots, remained suspended with no difficulty when they were injected in the spots above the wall.

According to their observations of trajectories of almost neutrally buoyant particles, Sumer and Oguz (1978) and Sumer and Deigaard (1981) concluded that the mechanism that keeps particles in suspension would be also related to flow ejections events. They point out that after the particles are lifted-up to the outer regions of the flow by the action of the bursting flow ejections, they tend to fall back to the wall. On the way to the wall the particles are expected to meet fresh lifting fluid due to the next burst from further upstream which will rise them up again, or else, in the case where the particles reach the bottom, they would be entrained again by a new flow ejection event. This was also observed by Browand and Plocher (1985) and in the present experiments. In fact, in many cases particles that were lifted-up through their interaction with a shear layer and were lagging that particular structure due to a loss of correlation with it were observed to interact with new developing structures which forced the particles to stay suspended.

It must be pointed out that such mechanism of particle suspension is plausible within the wall layer, however the flow ejection events that would be responsible for such mechanism do not extend to the outer flow regions. Therein, different flow coherent structures are suspected to occur, such as the typical eddies (distorted vortex ring-like configurations) and large scale motions proposed by Falco (1991), which it can be argued, would interact with particles raised to such outer regions by

the wall ejection events and keep the particles in suspension, defining in the average the process of turbulent diffusion typical of sediment transport in suspension. A typical criterion applied to estimate the conditions required to keep particles in suspension is that of Bagnold (1966), according to which a particle would remain suspended as long as its settling velocity is of lower magnitude than upward turbulent velocity fluctuations of the flow, a measure of which would be given by the standard deviation of the vertical velocity fluctuations. It has been argued that a further condition required to keep the particle suspended is the asymmetry of the vertical velocity fluctuation time series, such that large positive velocity fluctuations must be more frequent than high negative ones. That is, the skewness of the vertical velocity fluctuations time series must be positive (Bagnold, 1966; Wei and Willmarth, 1991), which would assure a net upward momentum flux to counteract the effect of gravity on the particle motion. Yen (1992) on the other hand points out that the fall velocity of a particle in an asymmetric oscillating flow is different from that in still water, such that for certain conditions of frequency, amplitude, and skewness, levitation and hovering against gravitation would be possible. Although, there is sufficient evidence that the skewness of the vertical flow velocity fluctuations is indeed positive in wall bounded turbulent flows, at least outside of the viscous sublayer (Nakagawa and Nezu, 1977; Raupach, 1981), Wei and Willmarth's (1991) experimental results show negative values of such skewness in the range $10 < y_+ < 30$. As it is show herein, however, this, if true, does not appear to affect the upward transport of sediment from the bed toward the outer regions of the wall layer by bursting ejection events.

Particle velocities

Local instantaneous values of the streamwise and vertical components of the particle ejection velocity expressed in wall units, u_{p+} and v_{p+}, respectively, are plotted in Figs. 8.21 and 8.22, respectively, as a function of the local value of y_+ where they were measured. Therein each data point corresponds to a different ejected particle, and the values of y_+ correspond to the closest position to the bed available for each case. Experimental conditions are $d_p = 224$ μm, values of Re in the range from 10760 to 22500, and values of Re_{p*} in the range from 4.3 to 5.2. In Fig. 8.21, the local mean flow velocity, u_+, given by the law of the wall, $u_+ = y_+$, and the logarithmic velocity profile (8.2), is also plotted as a reference, together with the lines defined by $u_+ \pm u_{rms+}$, where u_{rms+} denotes the dimensionless standard deviation of the streamwise flow velocity fluctuations, which was estimated using a best fit of a model proposed by Nezu and Nakagawa (1993) to turbulence measurements made in the present flows, given by:

$$u_{rms+} = 2.00 \exp\left(-1.08 \frac{y_+}{Re_*}\right)\left(1 - \exp\left(-\frac{y_+}{11.6}\right)\right) + 0.34\, y_+ \exp\left(-\frac{y_+}{11.6}\right) \qquad (8.3)$$

where $Re_* = u_* h/\nu$. A value of $Re_* = 900$ was used, which is representative of the range of values of this parameter corresponding to the experimental data shown in Figs. 8.21 and 8.22. In Fig. 8.22,

the vertical distribution of the dimensionless standard deviation of the vertical component of the flow velocity fluctuations, v_{rms+}, which was estimated using the model proposed by Nakagawa and Nezu (1981), is also plotted as a reference.

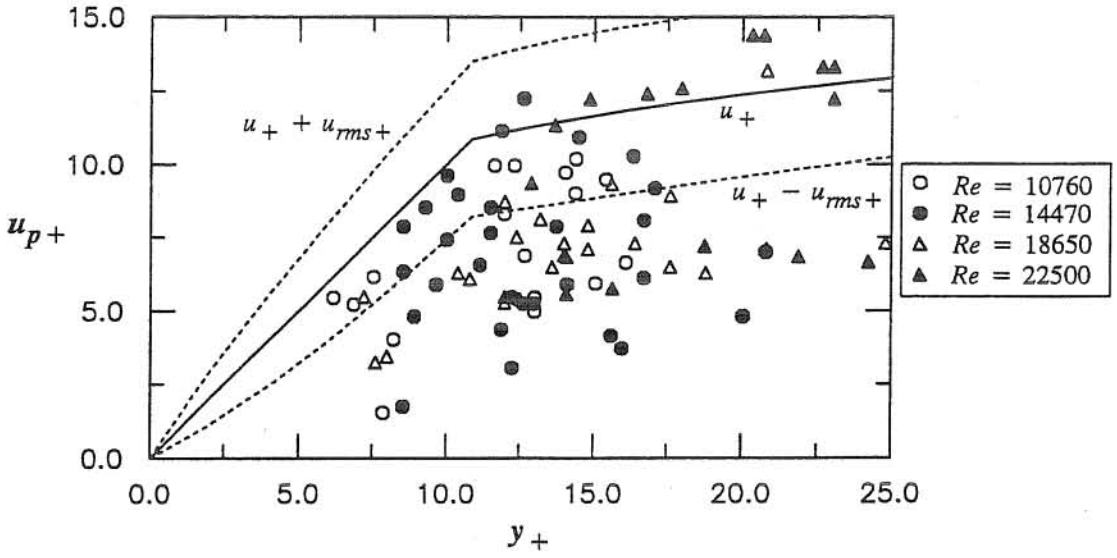

Fig. 8.21 Dimensionless local instantaneous values of the streamwise component of particle ejection velocity. Experiments of Series S, $d_p = 224$ μm, Re in the range from 10760 to 22500, Re_{p*} in the range from 4.3 to 5.2.

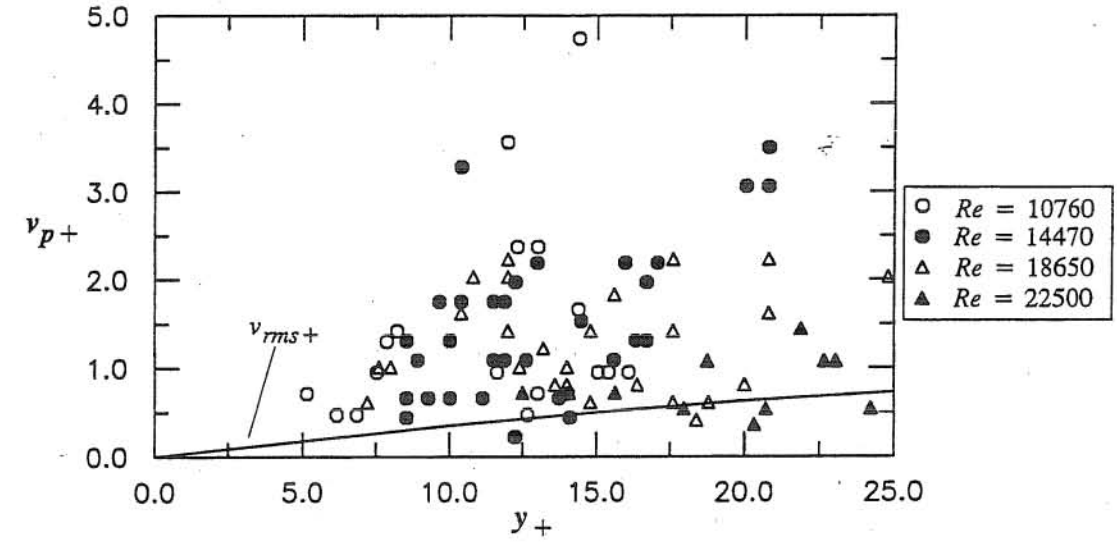

Fig. 8.22 Dimensionless local instantaneous values of the vertical component of particle ejection velocity. Experimental conditions as in Fig. 8.21.

As seen in Fig. 8.21, all but a couple of the experimental points have a streamwise ejection velocity smaller than or about equal to the theoretically estimated mean flow velocity, u_+. Furthermore, over about 70 % of the experimental points have a streamwise ejection velocity smaller than the theoretically estimated values of the mean flow velocity minus one standard

deviation, $u_+ - u_{rms+}$. On the other hand, from Fig. 8.22 it is clear that the observed values of the vertical component of the particle ejection velocity are in general much larger than the local values of the standard deviation of the vertical component of the flow velocity fluctuations, with extreme values of v_{p+} close to about 5. The results presented in Figs. 8.21 and 8.22 suggest that the turbulent bursting events responsible for ejecting particles away from the wall would be extreme events of quadrant 2 ($u' < 0$, $v' > 0$) with large values of the flow velocity fluctuations, which is in agreement with the overall discussion about the mechanism for particle entrainment into suspension presented so far.

From the upward trajectories of ejected particles observed in the present experiments, vertical distributions of ensemble averaged values of the streamwise and vertical components of particle ejection velocity, $\bar{u}_{p+}$ and $\bar{v}_{p+}$, respectively, were computed together with corresponding standard deviations. This was done by dividing the y_+ coordinate in intervals of dimension Δy_+, and ensemble averaging all the velocity data points (for all the experimental conditions available) contained in each of those intervals. A value $\Delta y_+ = 20$ was used to be consistent with Sumer and Oguz's (1978) analogous analysis. The results obtained are presented in Figs. 8.23 and 8.24. In Fig. 8.23 the results for $\bar{u}_{p+}$ and corresponding standard deviations are plotted as a function of y_+ in the range $0 < y_+ < 150$, together with the mean flow velocity profile given by the law of the wall and the logarithmic profile given by (8.2), and the lines defined by $u_+ \pm u_{rms+}$ as in Fig. 8.21. In Fig. 8.24 the results for $\bar{v}_{p+}$ and corresponding standard deviations are plotted as a function of y_+ in the range $0 < y_+ < 150$, together with the values of v_{rms+} given by the model of Nakagawa and Nezu (1981), and the experimental data by Brodkey et al. (1974), Grass (1974), Sumer and Oguz (1978), and Sumer and Deigaard (1981).

The data by Brodkey et al. (1974) correspond to estimations made by Sumer and Oguz (1978) of conditionally averaged values of the vertical component of flow velocity during events of quadrant 2 ($u' < 0$, $v' > 0$), obtained from the conditional probability density distributions of such velocity presented by Brodkey et al. in their Fig. 11. It is important to point out that these data do not correspond to bursting events, that is, they do not correspond to particular events of high turbulent intensity but, instead, to all the events of quadrant 2 regardless of their intensity. The data by Grass (1974) correspond to average vertical ejection velocities of sand particles with values d_p = 150 μm and $Re_{p\,*}$ = 4.4, resulting from the turbulence activity in a boundary layer flow created by towing a flat plate through still water. The data by Sumer and Oguz (1978) and Sumer and Deigaard (1981) correspond to ensemble averaged vertical components of the velocity of ejected particles in an open channel flow. The particles used by them had rather small values of the

submerged specific density, with values of R in the range from 0.003 to 0.03, and values of Re_{p*} in the range from about 30 to about 50.

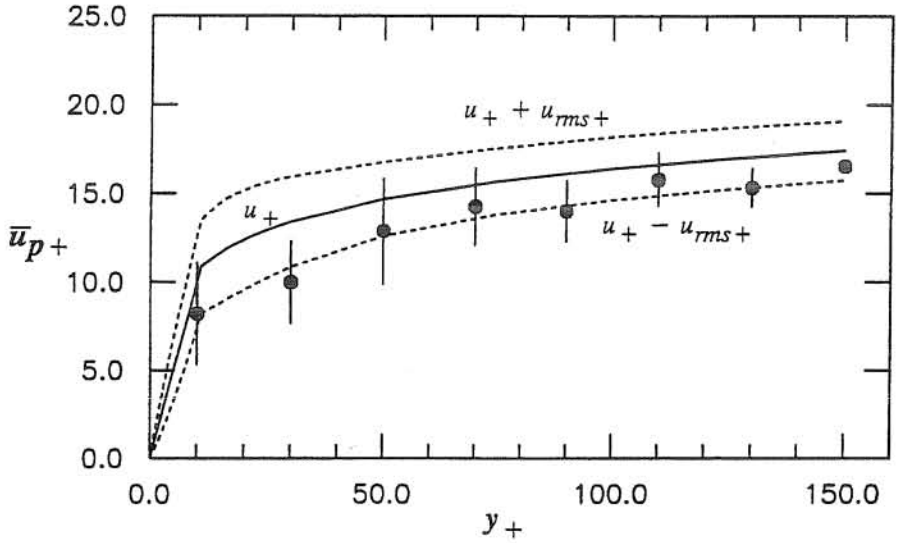

Fig. 8.23 Dimensionless ensemble averaged values of the streamwise component of particle ejection velocity. Experiments of Series S, $d_p = 224$ μm, Re in the range from 10760 to 22500, Re_{p*} in the range from 4.3 to 5.2. Symbols denote mean values and vertical lines represent a total length of two standard deviations.

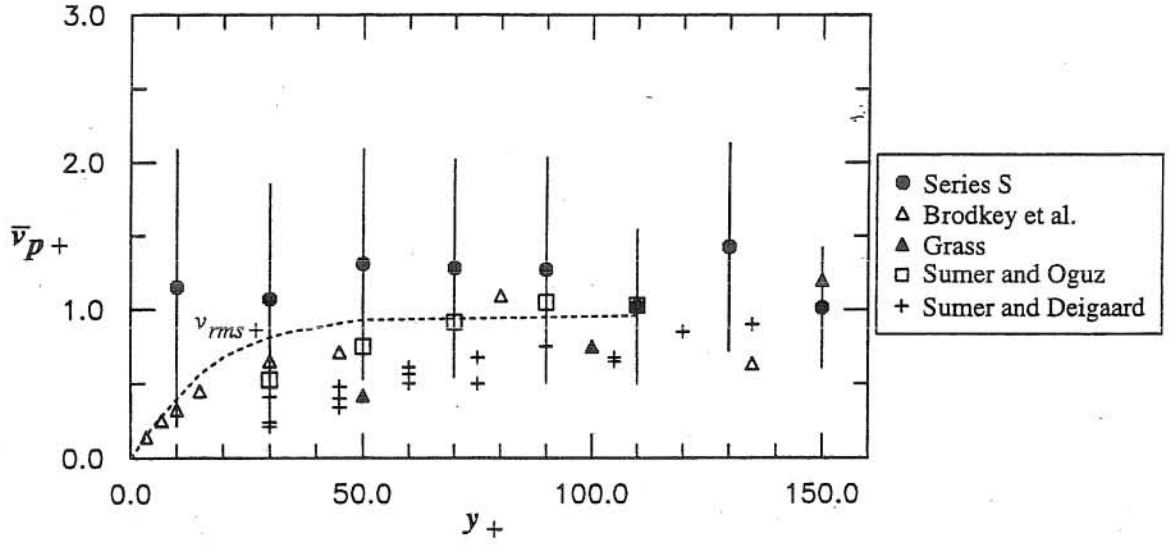

Fig. 8.24 Dimensionless ensemble averaged values of the vertical component of particle ejection velocity. Experimental conditions as in Fig. 8.23. Symbols denote mean values and vertical lines represent a total length of two standard deviations.

As seen in Fig. 8.23 the values of $\overline{u}_{p+}$ computed from the present data are generally smaller than the local mean flow velocity, and appear to be well described by the curve given by $u_+ - u_{rms+}$.

Also there is a tendency for $\bar{u}_{p+}$ to get closer to u_+ for values of y_+ larger than 100. Although it can be expected that the particles would tend to lag somewhat the flow ejection, these results seem to indicate that the particles are ejected from the bed by events of quadrant 2, with rather high negative values of u', which would be of larger magnitude than the corresponding standard deviation. As the particles are lifted to the outer regions of the wall layer they tend to accelerate such that their streamwise velocity gets closer to u_+, which appears to be a consequence of the acceleration of the flow ejection driving the particles due to momentum transfer from the mean flow as it intrudes into regions of high momentum fluid. It is interesting to note also that the standard deviation of the particle velocity tends to decrease as y_+ increases, and to be of rather small magnitude in the regions outside of the wall layer. This is expected since as pointed out, the flow ejection driving the particles tend to lose coherence as it reaches the outer regions of the wall layer, such that its velocity tends to get close to the mean flow velocity, u_+, with a characteristic standard deviation equal to u_{rms+}, which tends to decrease with y_+ as shown in Fig. 8.23. It is also expected for the values of the standard deviation of the particle velocity to be smaller than the values of u_{rms+}, since due to inertial effects the particles tend to filter out high frequency motions of the driving fluid, thus decreasing the total turbulent energy of the particle motion with respect to that of the flow (Hinze, 1971).

As seen in Fig. 8.24, the values of $\bar{v}_{p+}$ computed from the present data tend to be almost constant and equal to about 1.0 to 1.3, with values of the corresponding standard deviation of about 0.5 to 0.9, for values of y_+ in the range from 0 to 150. The values of $\bar{v}_{p+}$ tend to be much larger than the theoretical values of v_{rms+} close to the bed, however they tend to get closer to the latter as the outer regions of the wall layer are approached. This again seems to prove the argument that particle ejections are caused by rather strong flow events of quadrant 2, with typical vertical velocity fluctuations much larger than the corresponding values of the standard deviation. It is also apparent from Fig. 8.24 that the values of $\bar{v}_{p+}$ computed from the present data tend to be much larger than the other experimental data presented therein, specially close to the bed, although such differences seem to decrease substantially as the outer regions of the wall layer are approached.

It is important to note that the data by Brodkey et al. (1974) agree fairly well with the theoretical values of v_{rms+}. Nevertheless, it would be expected for those data points to locate slightly above the values of the standard deviation of the vertical flow velocity fluctuations, for as already explained, they correspond to conditionally averaged values of such fluctuations during events of quadrant 2. Since the vertical flow velocity fluctuations appear to be positively skewed (Nakagawa and Nezu, 1977; Raupach, 1981) high values of positive fluctuations are more frequent than negative ones, which would imply that conditionally averaged values of positive vertical flow velocity fluctuations are of somewhat larger magnitude than the corresponding standard deviation. In any

case, it is clear from Fig. 8.24 that the data by Brodkey et al. do not correspond to bursting events, and therefore it is expected for the present values of $\bar{v}_{p+}$, which have been related to particularly strong flow ejection events, to be larger than the conditionally averaged vertical velocities corresponding to events of quadrant 2 measured by Brodkey et al., in agreement with the results shown in Fig. 8.24.

Curiously enough, the particle vertical ejection velocities measured by Grass (1974), Sumer and Oguz (1978), and Sumer and Deigaard (1981), tend to be much smaller than the theoretical values of v_{rms+} close to the bed, which somehow contradicts the above discussion. Of the experimental data plotted in Fig. 8.24, those of Grass correspond to experimental conditions very close to those of the present experiments, unfortunately this author does not provide much detail about his experiments neither about how the average particle ejection velocities were computed. On the other hand, the experimental data of Sumer and Oguz and Sumer and Deigaard correspond to particles much larger although lighter than those used in the present study. The ratio between the particle settling velocity, v_s, and the shear velocity in their experiments was in the range 0.4 to 2.0, very similar to the present range of 1.3 to 1.6, however the dimensionless time constant, t_{p+}, of their particles was of the order of 100, while that of the present particles is in the range from 2.7 to 4.0. Since t_{p+} is a measure of the inertia of the particles, it is clear that Sumer and Oguz's and Sumer and Deigaard's particles would respond much slower to sudden accelerations of the flow than the present particles. In terms of the response to flow ejection events, it can be expected for particles with high values of t_{p+} to have ejection velocities of lower magnitude than that associated with the flow ejections, and to accelerate slowly to match the flow velocity as they are lifted away from the bed. On the other hand particles with low values of t_{p+} would have ejection velocities of magnitude similar to that associated with the flow ejections and would tend to follow the turbulence of the flow rather closely. This would explain the generally low values of the ejection velocities exhibited by Sumer and Oguz's and Sumer and Deigaard's particles in the wall region, as compared to the v_{rms+} values and also to the present experimental results.

From the same upward trajectories of ejected particles analyzed to obtain the velocity data presented in Figs. 8.23 and 8.24, a correlation between the streamwise and vertical components of the particle ejection velocity was estimated as follows. For each instantaneous particle velocity measured, the dimensionless streamwise and vertical components, u_{p+} and v_{p+}, were computed. The dimensionless particle relative velocity with respect to the mean flow was estimated as $u'_{p+} = u_{p+} - u_+$, $v'_{p+} = v_{p+}$, where u_+ was estimated using the law of the wall and the logarithmic profile (8.2), and the product $(u'_{p+}v_{p+})$ was computed. Finally, using the same discretization of the vertical coordinate y_+ as previously, with a value $\Delta y_+ = 20$, the ensemble

average $< u'_{p+} v_{p+} >$ was computed as a function of y_+. The results obtained are shown in Fig. 8.25, plotted together with the experimental data for the Reynolds stress during flow ejection events, $\overline{u'v'}_+$, of Kim et al. (1971) shown in Fig. 8.14, and the fitted curve (8.1).

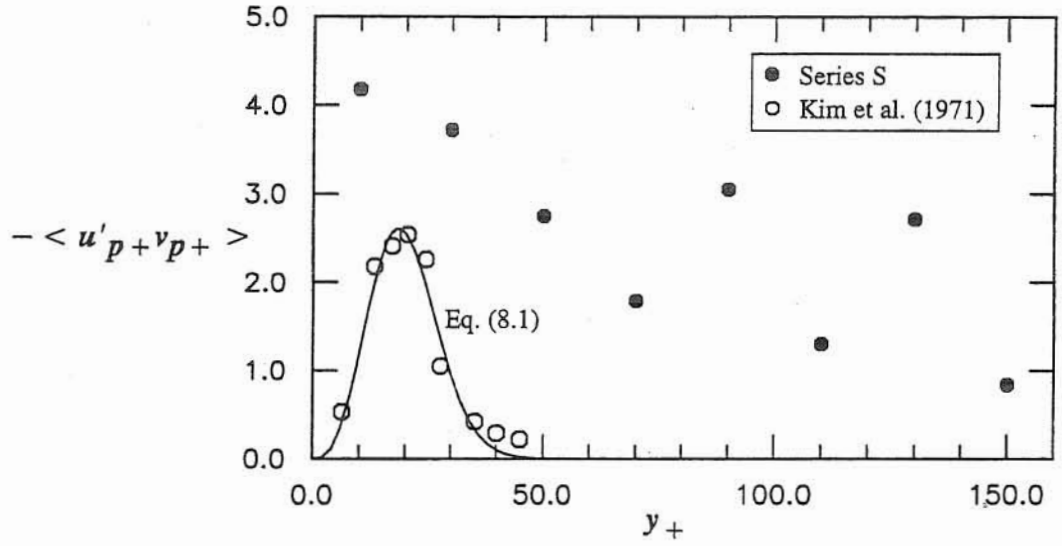

Fig. 8.25 Dimensionless correlation between streamwise and vertical components of particle ejection velocity relative to the mean flow velocity. Experiments of Series S, d_p = 224 μm, Re in the range from 10760 to 22500, Re_{p*} in the range from 4.3 to 5.2.

As seen in Fig. 8.25, the correlation $< u'_{p+} v_{p+} >$ attains a minimum of about –4.0 close to the wall and then tend to increase toward zero as the outer region of the flow is approached, although the data show large scattering. Clearly the absolute values of $< u'_{p+} v_{p+} >$ during particle ejections are much larger than the absolute values of the Reynolds stress during flow ejection events as measured by Kim et al., which appear to have a maximum of about 3.0 at a distance of about 20 wall units form the bed, and to vanish for values of y_+ larger than 50. There appear to be two issues here. The first is that it is expected for the particles to have a non zero relative velocity with respect to the driving fluid, which makes the product $(u'_{p+} v_{p+})$ different from the instantaneous Reynolds stress $(u'v')_+$. The second, and perhaps more important issue, is the fact that not every flow ejection event causes the entrainment of particles into suspension, and it can be expected that only the most energetic events would cause such entrainment. Therefore, particles seem to filter out flow ejections having low absolute values of the Reynolds stress, such that the absolute values of the ensemble average $< u'_{p+} v_{p+} >$ would be biased toward values of large magnitude.

The present discussion has concentrated so far in the analysis of particle velocities as they move upward driven by flow ejections, however it is also interesting to analyze particle velocities in their downward path as they fall back to the bed. The results of such analysis are presented in Figs. 8.26 and 8.27. Therein vertical distributions of ensemble averaged values of the streamwise

and vertical components of particle velocity during downward paths, $\overline{u}_{p+}$ and $\overline{v}_{p+}$, respectively, are plotted together with corresponding standard deviations. In Fig. 8.27, the mean streamwise flow velocity profile given by the law of the wall and the logarithmic law (8.2), and the lines defined by $u_+ \pm u_{rms+}$, with u_{rms+} given by (8.3), are also plotted. In Fig. 8.28, the vertical distribution of v_{rms+} given by the model of Nakagawa and Nezu (1981), the experimental data of Brodkey et al. (1974), and Sumer and Deigaard (1981), and lines corresponding to the average dimensionless settling velocity, v_{s+}, of the particles used in the present study and in Sumer and Deigaard's are also plotted for comparison purposes.

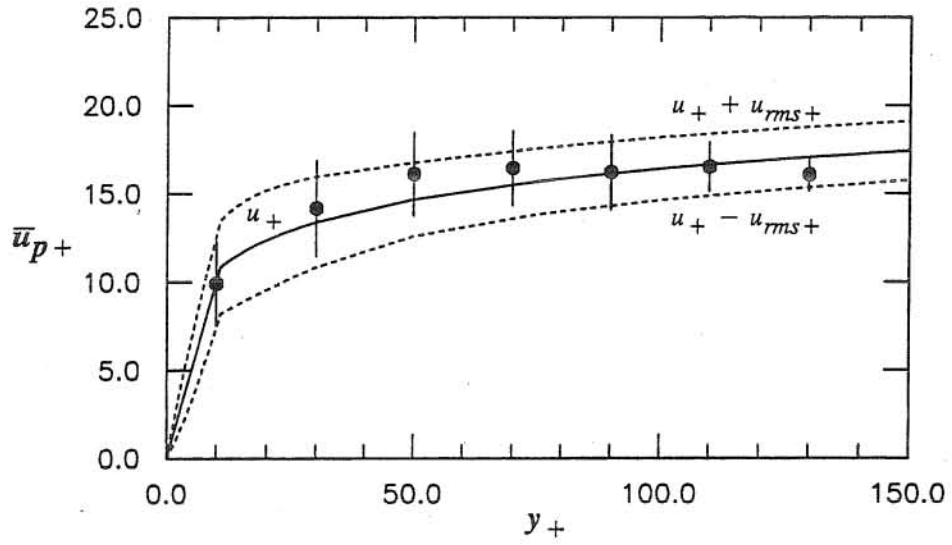

Fig. 8.26 Dimensionless ensemble averaged values of the streamwise component of particle downward velocity. Experiments of Series S, d_p = 224 μm, Re in the range from 10760 to 22500, Re_{p*} in the range from 4.3 to 5.2. Symbols denote mean values and vertical lines represent a total length of two standard deviations.

The data by Brodkey et al. (1974) correspond to estimations made by Sumer and Deigaard (1981) of conditionally averaged values of the vertical component of flow velocity during events of quadrant 4 ($u' > 0$, $v' < 0$), obtained from the conditional probability density distributions of such velocity presented by Brodkey et al. in their Fig. 11. It is important to point out that these data do not correspond to bursting events, that is, they do not correspond to particular events of high turbulent intensity but, instead, to all the events of quadrant 4 regardless of their intensity. The data by Sumer and Deigaard (1981) correspond to ensemble averaged vertical components of particle velocity during downward trajectories, for the same experimental conditions as those shown in Fig. 8.24.

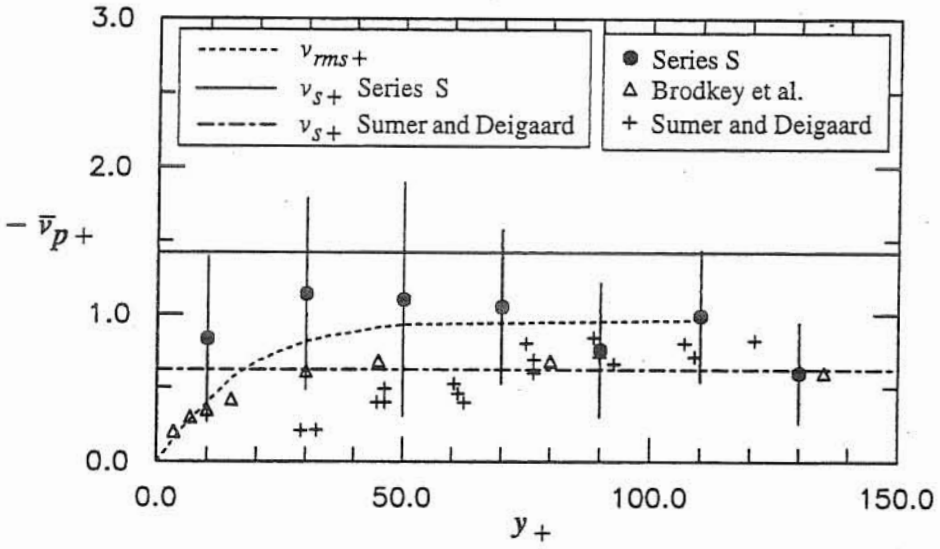

Fig. 8.27 Dimensionless ensemble averaged values of the vertical component of particle downward velocity. Experimental conditions as in Fig. 8.26. Symbols denote mean values and vertical lines represent a total length of two standard deviations.

As seen in Fig. 8.26 the values of $\overline{u}_{p+}$ computed from the downward trajectories are generally very similar to the values of the theoretical local mean flow velocity, u_+, although they tend to be slightly larger than this variable in the range of values of y_+ from about 40 to about 70. This is a clear difference with respect to the observed behavior of the values of $\overline{u}_{p+}$ during ejections which tend to be much smaller than u_+, and is in good agreement with observations by Sumer and Deigaard (1981) who reported larger values of streamwise particle velocities during downward trajectories than during ejections. The corresponding standard deviations of $\overline{u}_{p+}$ for downward trajectories tend to decrease as y_+ increases and to be of smaller magnitude than the values of u_{rms+} of the flow outside of the wall layer, similarly to what was observed for ejection trajectories.

Fig. 8.27 shows that the absolute values of $\overline{v}_{p+}$ for the downward trajectories are somewhat larger than the local values of v_{rms+} for values of y_+ lower than about 70, and that they tend to be about equal or smaller than such values as the outer region of the wall layer is approached. From Fig. 8.27 is also apparent that the absolute values of $\overline{v}_{p+}$ during downward trajectories are in general only about 60% of the value corresponding to the dimensionless settling velocity of the particles.

In Fig. 8.27 it is also seen that the vertical velocity data by Brodkey et al. (1974) for flow events of quadrant 4 are similar to v_{rms+} for values of y_+ lower than about 20, and tend to be smaller in absolute value than v_{rms+} for larger values of y_+, which would indicate that the vertical velocity fluctuations have a positive skewness, in agreement with experimental results discussed previously (Nakagawa and Nezu, 1977; Raupach, 1981).

It has been argued that relatively light particles would be deposited back to the bed by the action of downward inrushes of high-speed fluid, or sweep events (Cleaver and Yates, 1976). Sweep events correspond to highly energetic events of quadrant 4 which would induce streamwise particle velocities at least larger than the local mean flow velocity, and vertical particle velocities at least larger than the corresponding settling velocity. It seems from the present observations that the particles are only rarely being deposited by the action of sweep events, and rather they appear in the average to be falling back toward the bed with velocities smaller than the settling velocity as they lose correlation with the turbulent structures that lifted them from the bed and kept them suspended for some time. In fact, the present particle velocity data during downward trajectories seem to show that only a few extreme events have values of u_{p+} larger than $u_+ + u_{rms+}$, and absolute values of v_{p+} larger than v_{s+}. This seems to be supported also by Sumer and Deigaard's (1981) $\bar{v}_{p+}$ data for downward trajectories, which show that the absolute values of $\bar{v}_{p+}$ tend to be smaller than the corresponding values of v_{s+} in the range of y_+ lower than about 70, although similar to such value for larger values of y_+.

It is interesting to note that the latter conclusion is in agreement with the analytical results obtained by Yen (1992) in the sense that it is apparent that the fall velocity of particles immersed in a turbulent flow is reduced with respect to the corresponding settling velocity in still water, which would be a consequence of a positive skewness of the vertical component of the flow velocity fluctuations.

8.5.2 Experiments of Series T: transitionally rough flows

Results from visualizations of flow and particle motion

Visualizations of particle motion in the near wall region of the transitionally rough flows of Series T showed that sand particles tend to be lifted away from the bed by the same ejection mechanism discussed in the previous section for smooth flows, which is in complete agreement with the experimental results for rough flows of Sumer and Deigaard (1981) and Ashida and Fujita (1986).

In fact as described in Chapter 4, shear layers of characteristics similar to those observed in the smooth flows of Series S were also commonly observed in the transitionally rough flows of Series T. These structures seem to maintain their identity for as long as about 60 to 80 wall time units, to extend vertically a distance of about 100 wall units with a mean inclination angle to the bed of about 14°, and to have convection velocities of about 6.5 wall units and frequencies of occurrence of about 0.001 wall units. It is interesting to note that the convection velocity of the structures in the transitionally rough flows tend to be smaller than that observed in the smooth flows, which would indicate that the roughness elements of the bed tend to retard the motion of the shear layers. Also, the frequency of occurrence of the shear layers in the transitionally rough flows tend to be about 1/3

of that observed in the smooth flows, which would indicate that the roughness elements have a stabilizing effect on the mechanism that generates the flow ejections. Rashidi et al. (1990) found that the presence of particles of sizes smaller than the thickness of the viscous sublayer in the near wall region has the effect of reducing the frequency of observed flow ejections, while larger particles produce the opposite effect. It seems plausible that the relatively small roughness elements of the present transitionally rough flows have a similar effect to that of small loose particles in the near bed region as observed by Rashidi et al.

As already mentioned, the present observations seem to indicate that the mechanism of interaction between particles and shear layers that results in the lifting-up of particles from the bed is the same for smooth and transitionally rough flows. Fig. 8.28 shows a few examples of particle-shear layer interactions observed in one the experiments of Series T, corresponding to the experimental conditions: $Re =$ 18840, $d_p = 224$ μm, $Re_{p*} = 6.8$. As seen therein the particles tend to be ejected from the bed at a distance of about 100 to 200 wall units downstream from the shear layer, after which they appear to interact more directly with the structure, and in some cases to get trapped in the core of it and lifted-up to the outer regions of the wall layer.

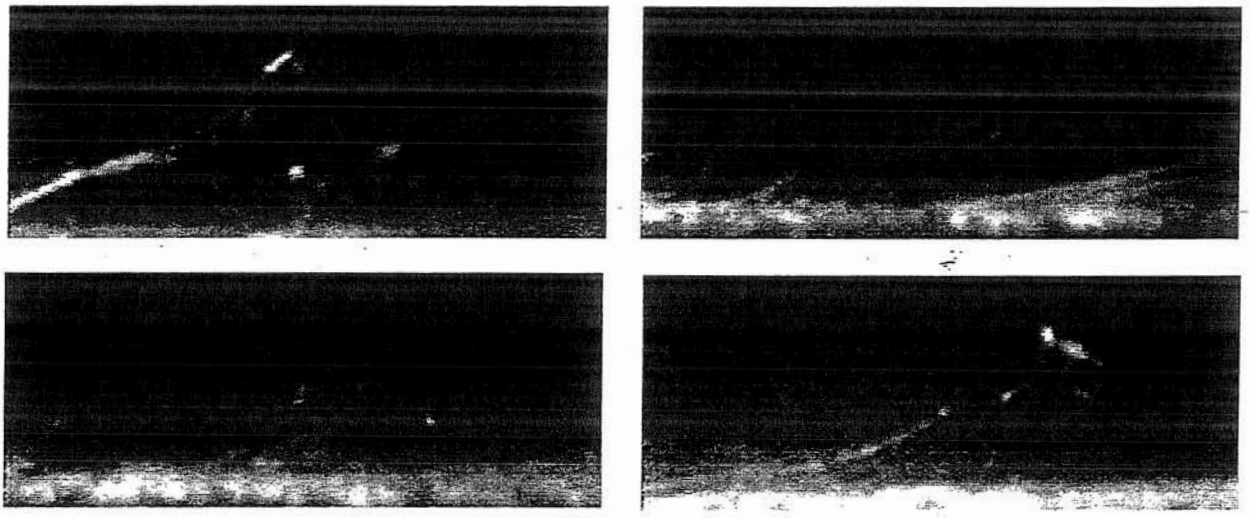

Fig. 8.28 Particle-shear layer interactions. Experiments of Series T, $Re =$ 18840, $d_p = 224$ μm, $Re_{p*} = 6.8$. Field of view of each image is about 380 by 150 wall units.

It must be pointed out, however, that since the particles used in the present experimental study had in general sizes smaller than the roughness elements of the bed, a hiding effect was observed which tends to prevent particles from being entrained into suspension by flow ejections. Indeed, as found from the analysis of conditions for the initiation of suspension in Chapter 7, as the bed roughness increases (say from smooth to transitionally rough), higher values of the dimensionless bed shear stress τ_* are required to entrain particles of the same size. This hiding effect seems to be

dependent on the ratio d_p/d_b, such that as this ratio becomes smaller progressively higher values of τ_* are needed to entrain the particles into suspension, which appears to be related not only with a direct blockage of flow ejections by the roughness elements of the bed so as to preclude the lift of smaller particles, but also to a less local phenomenon involving the modification of the turbulent structure of the flow in the near bed region. In fact, experimental evidence indicates that near the bed, as the roughness increases, events of quadrant 2 become less important than events of quadrant 4 as contributors to the Reynolds shear stress (Raupach et al., 1991), which implies a reduction in the ability of the flow to entrain particles into suspension.

Particle trajectories

Just as the mechanism of particle entrainment into suspension appears to be common to smooth and rough beds, also the trajectories of entrained particles in the transitionally rough flows of Series T seem to be very similar to those observed in the smooth flows of Series S. The particles appear to be picked up from the bed by flow ejection events, with typical angles of ejection in the range from 10° to about 20°, which is the same as that observed in the experiments of Series S.

A few trajectories of entrained particles are shown in Fig. 8.29 for the experimental conditions $d_p = 224$ μm, $Re = 18840$ and 21480, and values of Re_{p*} of about 7. As seen therein, some particles are ejected toward the outer regions of the wall layer with an angle of inclination of about 14°, similar to those typical of the shear layers observed in the present experiments. On the contrary, some other particles seem to be unable to reach elevations over about 50 wall units from the bed. This latter behavior, which corresponds to the crossing–trajectories effect discussed previously, is also totally analogous to that observed for the smooth flows.

An apparent difference in the behavior of the entrained particles in the transitionally rough flows with respect to those observed in the smooth flows is that in the average the former tend to reach higher elevations than the latter. In fact, it seems that in the case of transitionally rough flows relatively more particles are able to reach the outer regions of the wall layer than in the case of smooth flows. This is shown in Fig. 8.30, where the ratio between the number of ejected particles observed to reach the outer region of the wall layer and the total number of ejected particles is plotted as a function of the dimensionless bed shear stress, τ_*, for the experiments of Series T corresponding to a value of $d_p = 224$ μm, values of Re in the range from 16360 to 25240, and values of Re_{p*} in the range from 6.4 to 7.7. In the same figure equivalent results for the experiments of Series S presented previously in Fig. 8.20 are also plotted for comparison purposes.

As seen in Fig. 8.30, it is apparent that for values of τ_* lower than about 0.22 no particles are ejected to the outer region of the wall layer in the transitionally rough flows, in opposition to what was observed in the case of smooth flows for which particles were still ejected to such regions in

that range of values of τ_*. This is related to the hiding effect discussed previously, and described in detail in Chapter 7. For values of τ_* larger than about 0.28 the ratio between the number of outer ejections and the total number of ejections for the transitionally rough flows is larger than 0.8, and it can be speculated that it seems to tend asymptotically to a curve extrapolated from the results corresponding to the smooth flows in the range of values of τ_* lower than 0.15.

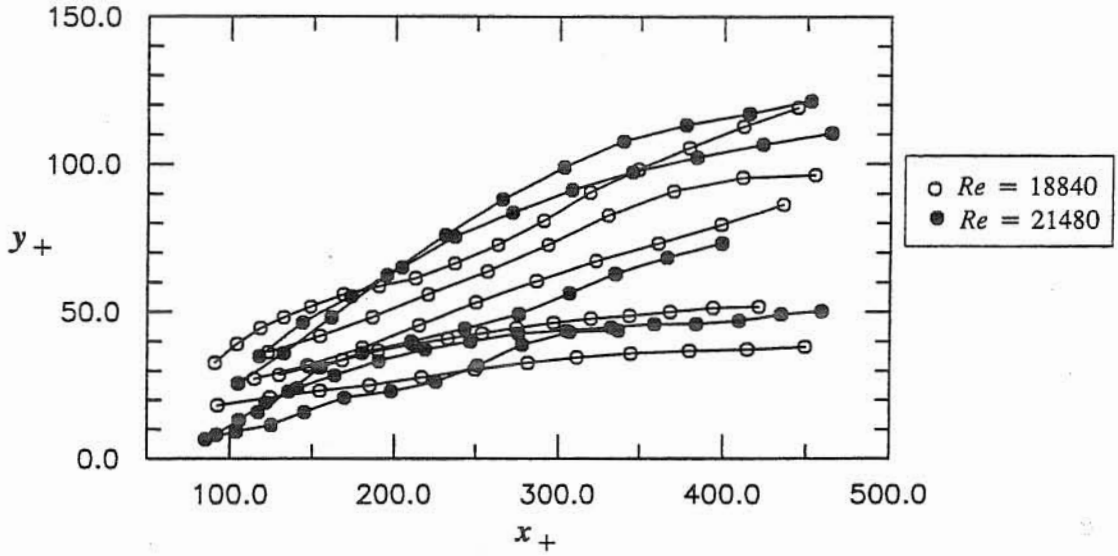

Fig. 8.29 Typical trajectories of entrained particles. Experiments of Series T, d_p = 224 μm, Re = 18840 and 21480, and values of Re_{p*} of about 7.

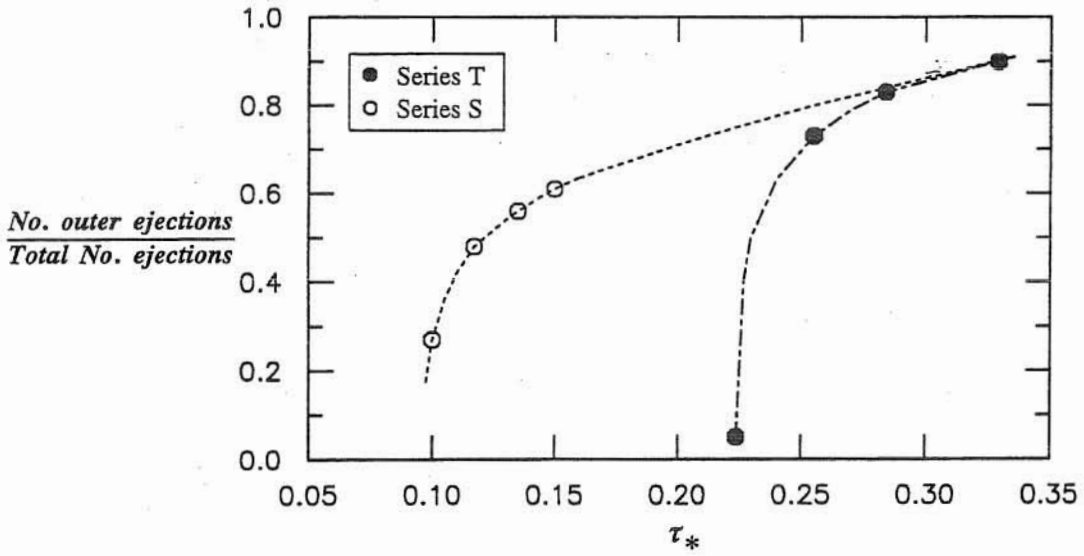

Fig. 8.30 Ratio between number of particles ejected to the outer regions of the wall layer and total number of ejected particles as a function of the dimensionless bed shear stress. Experiments of Series T correspond to d_p = 224 μm, Re in the range from 16360 to 25240, Re_{p*} in the range from 6.4 to 7.7. Experiments of Series S correspond to same conditions as those of Fig. 8.20.

The results shown in Fig. 8.30 clearly demonstrate that, in the average, less particles were able to reach the outer regions of the wall layer in the case of the smooth flows of Series S than in the case of the transitionally rough flows of Series T, simply because the intensity of the flow ejection events responsible for the entrainment of particles (which seems to be positively correlated with τ_*) in the former case was lower than in the latter.

Particle velocities

Local instantaneous values of the streamwise and vertical components of the particle ejection velocity expressed in wall units, u_{p+} and v_{p+}, respectively, corresponding to experiments of Series T are plotted in Figs. 8.31 and 8.32, respectively, as a function of the local value of y_+ where they were measured. Therein each data point corresponds to a different ejected particle, and the values of y_+ correspond to the closest position to the bed available for each case. Experimental conditions are: $d_p = 224$ μm, Re in the range from 18840 to 25240, and values of Re_{p_*} in the range from 6.8 to 7.7. In Fig. 8.31, the local mean flow velocity given by the logarithmic velocity profile valid for transitionally rough flows (Schlichting, 1968):

$$u_+ = \frac{1}{\kappa} Ln \left(\frac{y_+}{k_{s+}} \right) + B \tag{8.4}$$

where k_{s+} corresponds to the bed roughness size made dimensionless with wall units and B is a parameter which is a function of k_{s+}, is also plotted as a reference, together with the lines defined by $u_+ \pm u_{rms+}$, where u_{rms+} was estimated using the relation (8.3) valid for smooth flows. A value $k_{s+} = 32.3$ was used in (8.4) together with its associated value $B = 9.1$, while a value $Re_* = 1665$ was used in (8.3), which are representative of the range of values of these parameters corresponding to the experimental data shown in Figs. 8.31 and 8.32. In Fig. 8.32, the vertical distribution of the dimensionless standard deviation of the vertical component of the flow velocity fluctuations, v_{rms+}, which was estimated using the model proposed by Nakagawa and Nezu (1981) for smooth flows, is also plotted as a reference.

As seen in Fig. 8.31, over 90% of the experimental points have a streamwise ejection velocity lower or about equal than the theoretically estimated local mean flow velocity, u_+. Furthermore, over 60% of the experimental points have a streamwise ejection velocity lower or about equal than the theoretically estimated values of the mean flow velocity minus one standard deviation, $u_+ - u_{rms+}$. These observations are in total agreement with those corresponding to the smooth flows.

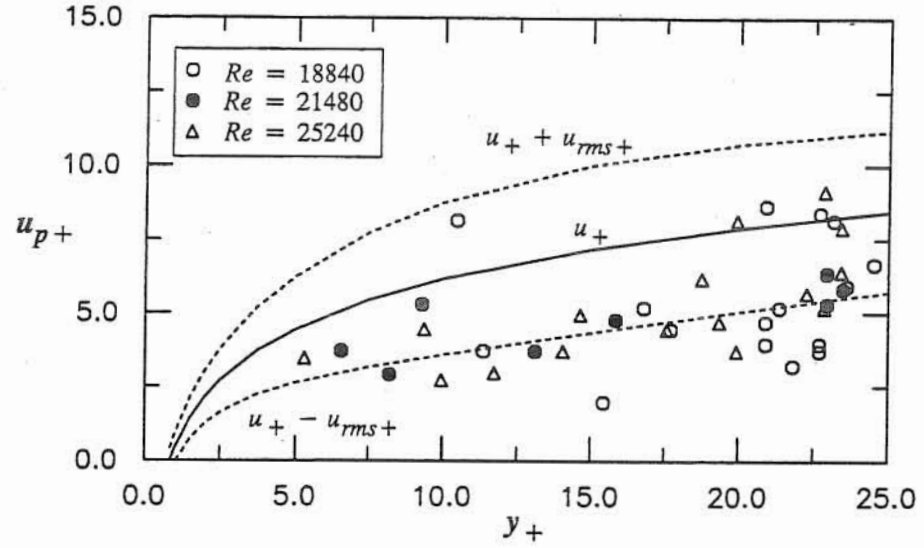

Fig. 8.31 Dimensionless local instantaneous values of the streamwise component of particle ejection velocity. Experiments of Series T, $d_p = 224$ μm, Re in the range from 18840 to 25240, Re_{p*} in the range from 6.8 to 7.7.

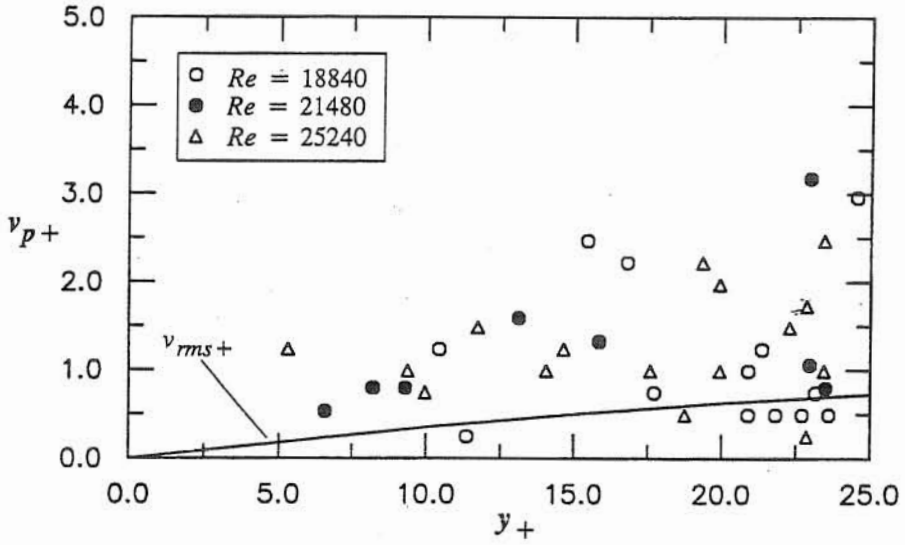

Fig. 8.32 Dimensionless local instantaneous values of the vertical component of particle ejection velocity. Experimental conditions as in Fig. 8.31.

On the other hand, from Fig. 8.32 it is clear that the observed values of the vertical component of the particle ejection velocity are in general much larger than the local values of v_{rms+}, with extreme values of v_{p+} on the order of about 3. Again, these observations agree totally with those corresponding to the smooth flows.

The results shown in Figs. 8.31 and 8.32 appear to imply no sensible differences neither in the behavior nor in the magnitude of the particle ejection velocity between the transitionally rough and smooth flow cases. The experimental evidence in both such cases appears to suggest that extreme

flow events of quadrant 2 with large values of the velocity fluctuations would be most responsible for the entrainment of particles into suspension from the bed.

From the upward trajectories of ejected particles observed in the experiments of Series T, vertical distributions of ensemble averaged values of the streamwise and vertical components of particle ejection velocity, $\overline{u}_{p+}$ and $\overline{v}_{p+}$, respectively, were computed together with corresponding standard deviations. This was done by discretizing the y_+ coordinate in the same way as it was done previously for the results shown in Figs. 8.23 and 8.24. The results obtained are presented in Figs. 8.33 and 8.34. In Fig. 8.33 the results for $\overline{u}_{p+}$ and corresponding standard deviations are plotted as a function of y_+ in the range $0 < y_+ < 150$, together with the distribution of u_+ given by (8.4) and the lines defined by $u_+ \pm u_{rms+}$, similarly as in Fig. 8.31. In Fig. 8.34, the results for $\overline{v}_{p+}$ and corresponding standard deviations are plotted as a function of y_+ also in the range $0 < y_+ < 150$, together with the distribution of v_{rms+} for smooth flows, similarly as in Fig. 8.32, the data of Grass (1971), the data of Sumer and Deigaard (1981) corresponding to rough flows, and the results obtained in Series S and presented in Fig. 8.24, for comparison purposes.

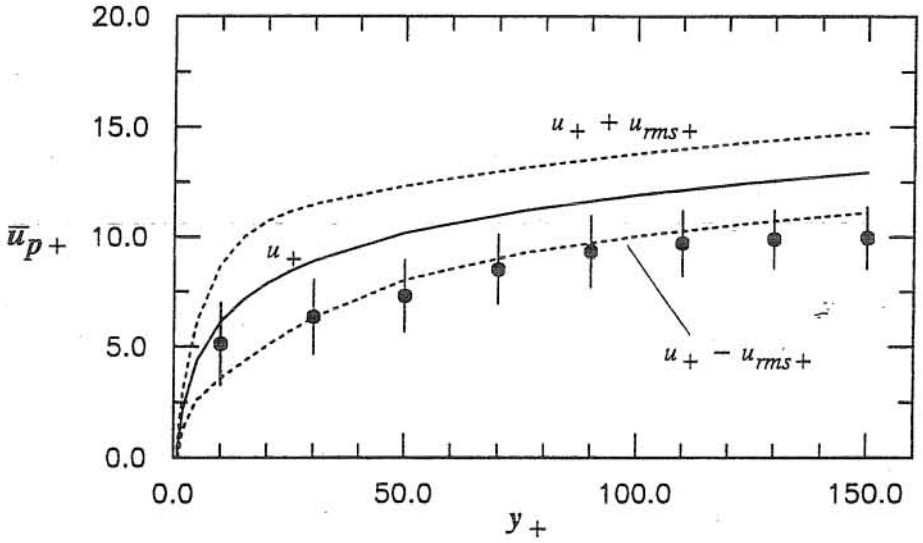

Fig. 8.33 Dimensionless ensemble averaged values of the streamwise component of particle ejection velocity. Experiments of Series T, $d_p = 224$ μm, Re in the range from 18840 to 25240, Re_{p*} in the range from 6.8 to 7.7. Symbols denote mean values and vertical lines represent a total length of two standard deviations.

As seen in Fig. 8.33, the values of $\overline{u}_{p+}$ computed from the data of Series T are generally smaller than the theoretical local mean flow velocity, and appear to be well described by the curve given by $u_+ - u_{rms+}$, which implies a behavior completely analogous to that observed in the smooth flows experiments. Nevertheless, there is a tendency for the closest point to the bed to have a velocity somewhat larger than $u_+ - u_{rms+}$, which can be explained by pointing out that the values

of u_{rms+} plotted in Fig. 8.33 are those corresponding to smooth flows, which are known to be larger than those associated with rough flows close to the bottom wall, although both of them become similar as y_+ increases over about 60 (Nezu and Nakagawa, 1993). From Fig. 8.33 is also apparent that standard deviations corresponding to the values of $\overline{u}_{p+}$ tend to decrease as y_+ increase, similarly as u_{rms+}, and to be of smaller magnitude than the values of this variable, which is expected because of particle inertial effects as it was discussed previously. This behavior of the standard deviation of $\overline{u}_{p+}$ is also analogous to that observed in the case of smooth flows.

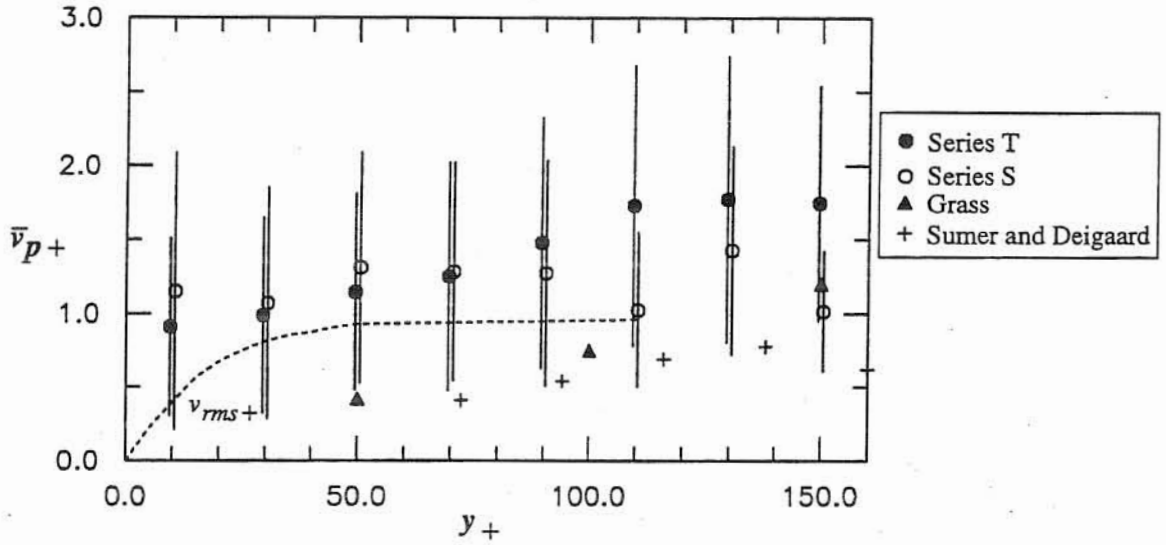

Fig. 8.34 Dimensionless ensemble averaged values of the vertical component of particle ejection velocity. Experimental conditions as in Fig. 8.33. Symbols denote mean values and vertical lines represent a total length of two standard deviations.

In Fig. 8.34, the values of $\overline{v}_{p+}$ computed from the data of Series T show some tendency to increase as y_+ increases, from values close to about 1.0 near the bottom wall to values close to about 2.0 in the regions outside of the wall layer, with corresponding values of the standard deviation of about 0.5 to 0.9. As in the smooth flow case, the values of $\overline{v}_{p+}$ seem to be always larger than the theoretically estimated values of v_{rms+}, at least in the range $0 < y_+ < 150$. As seen in Fig. 8.34, the $\overline{v}_{p+}$ values are very similar to those estimated in the smooth flow case except for values of y_+ larger than about 100, for which the values of $\overline{v}_{p+}$ of Series T tend to be larger than those of Series S. This behavior seems to suggest that the flow ejections in a rough bed would be more intense than those in a smooth flow, which is in agreement with the observations of Sumer and Deigaard (1981) who also reported somewhat larger particle vertical ejection velocities in the case of rough flows than in the case of smooth flows. Grass (1971) concluded from his observations that although the flow ejection mechanism would be much the same over a rough bed as over a smooth surface, flow entrainment tends to be much more violent in the rough bottom case. Nevertheless, as pointed out

by Sumer and Deigaard (1981), this enhanced intensity does not appear to influence much the behavior of particles entrained from the rough bed, which does not seem to differ appreciably from that corresponding to the smooth surface case.

From Fig. 8.34, it is also apparent that the values of $\bar{v}_{p+}$ computed from the data of Series T tend to be much larger than the experimental values of this variable reported by Grass (1974) and Sumer and Deigaard (1981), the latter corresponding to their experiments over a rough bed. It is also apparent that their estimated values of $\bar{v}_{p+}$ are smaller than the values of v_{rms+}, which somehow contradicts the notion of having particularly strong events of quadrant 2 driving the particle ejections from the bed. As indicated previously, there is no sufficient information available about Grass's experiments as to try to explain the apparent differences with the present observations, however the differences between the present experimental results and those of Sumer and Deigaard can be again explained in terms of the different values of the dimensionless particle time constant, t_{p+}, in both cases. In fact, the values of t_{p+} in Sumer and Deigaard's rough bed experiments were about 240, much larger than those in the present experiments of Series T, which were only about 7 to 9. Since t_{p+} is a measure of the inertia of the particles, it is clear that Sumer and Deigaard's particles would respond much slower to sudden accelerations of the flow, such as those associated with flow ejection events, than those of Series T, which would imply smaller vertical ejection velocities in the former case than in the latter. This conclusion is analogous to that given to explain equivalent differences observed in the case of smooth flows.

8.6 Conclusions

The experimental results presented and analyzed herein provide new and unique data on the qualitative and quantitative aspects of sediment particle entrainment into suspension. These experimental results differ from others in that heavy although small natural sand particles are observed to interact with the turbulence of the flow, as opposed to the light (almost neutrally buoyant), large-size particles that have been used in previous studies. Also, the present investigation concentrates solely on the processes occurring in the wall layer of open channel flows, as opposed to other studies that analyze almost the whole flow field, thus having a better spatial resolution of particle motion during the initial stages of particle entrainment. Furthermore, the high-speed video system used herein provided enough temporal resolution to adequately resolve such motion.

The evidence presented herein seems to indicate that wall streaks in a smooth channel flow would be related to the presence of counter-rotating quasi-streamwise vortices. These would extend about 1000 to 2000 wall units in the streamwise direction, and about 15 to 25 wall units in the vertical direction, persist in the average for about 500 wall time units and have a transverse wavelength of about 100 wall units. Groups of 3 to 5 counter-rotating pairs of such vortices seem to emerge and

collapse quasi-periodically in time, and to distribute rather randomly along the bottom wall. These vortices appear to induce particle sorting along low-speed streaks when the particles are of sizes about equal or smaller than the thickness of the viscous sublayer. Larger particles do not tend to accumulate along wall streaks, however they appear to respond to the near bed flow velocity streaky pattern by moving faster when they are located in high-speed regions. The presence of particles of sizes about equal to or smaller than the thickness of the viscous sublayer does not seem to affect the wavelength of the wall streaks, however it seems to stabilize somehow these flow structures, such that they appear to have durations about 2 to 3 times longer than those observed in the absence of particles.

In the case of a rough boundary, the roughness elements seem to disrupt the structure of the viscous sublayer, and although the wall streaks persist in these conditions, they would lose coherence, persistence, and spatial extension. Particles of sizes smaller than about 1/5 of the size of the roughness elements move within the interstices of them without sorting along any preferential paths. Larger particles move over the roughness elements, however they do not seem to respond to the sorting effect of the rather weak wall streaks, such that they do not accumulate along specific regions of the bed in this situation either.

Low-momentum fluid seems to be lifted-up from the bed as a consequence of quasi-periodic ejection events and to evolve into some kind of coherent structure. This mechanism appears to be common to the flow over both smooth and rough surfaces. The most frequently observed coherent structures correspond to shear layers of concentrated spanwise vorticity, which have a typical inclination angle to the bed of about 14°. These structures extend vertically a distance of about 100 wall units and have convection velocities of about 10 wall units in the case of smooth flows, and about 6.5 wall units in the case of transitionally rough flows. The frequency of occurrence of the shear layers is about 0.003 wall units in the case of smooth flows and about 0.001 wall units in the case of transitionally rough flows. Apparently, an intense flow ejection (event of quadrant 2) occurs downstream from the shear layer, at a distance of about 100 to 200 wall units.

Particles seem to be picked up from the bed by flow ejection events occurring downstream of the shear layers. Particle ejection angles are in the range 10 to 20°, very similar to the angle of inclination of the shear layers. After the particles are lifted from the bed their relative motion is toward the shear layer so they eventually interact more directly with the flow structures. Different types of interaction seem to occur. When particles get trapped in the core of the shear layers they are raised toward the outer regions of the wall layer as the flow structure is stretched out into such regions. After the shear layers lose coherence the particles tend to fall back to the bed, although in some cases they appear to be maintained in suspension for rather long period of times by some other coherent motions developing in the outer region of the wall layer. In their path back to the wall the

particles can either be deposited or picked up by a new developing ejection event and returned to the outer regions of the wall layer. A second type of interaction occurs when the particle tends to lag the flow ejection such that it eventually falls from the structure back to the bed, without reaching elevations higher than about 50 wall units, defining the so called crossing-trajectories effect, in which particles lose correlation with the flow structure before it loses its coherence.

The number of particles reaching the outer regions of the wall layer seems to increase with the dimensionless bed shear stress, τ_*, which would indicate that also the intensity of the flow ejections responsible for the particle entrainment into suspension increases with this variable. In the case of transitionally rough flows, a hiding effect was observed, which tend to preclude particles from being entrained into suspension at values of τ_* for which such entrainment was observed in the case of smooth flows. This hiding effect seems to be associated with a direct obstruction of the flow ejection by the roughness elements as well as with a less local effect related to a change in the structure of the turbulence of the flow in the near bed region with respect to that in the smooth flows.

The measured instantaneous particle velocities during ejections in both smooth and transitionally rough flows show that their streamwise component tends to be much lower than the local mean flow velocity, while their vertical component tends to be rather intense, much larger than the local standard deviation of the vertical flow velocity fluctuations, which would indicate that such particles are responding to rather extreme flow events of quadrant 2. In the case of smooth flows, dimensionless ensemble averaged values of the streamwise component of particle velocity during ejections appear to be well described by a theoretical line given by the local mean flow velocity minus one standard deviation of the flow streamwise velocity fluctuations, $u_+ - u_{rms+}$. On the other hand, dimensionless ensemble averaged values of the vertical component of the particle velocity during ejections tend to be approximately constant in the range $0 < y_+ < 150$, with values of about 1.0 to 1.5 wall units. These values appear to be much larger than v_{rms+} close to the bed, however they tend to be more similar to this variable in the outer region of the wall layer. The values of this velocity seem to be also much larger than other experimental results, however the differences could be explained in terms of the dimensionless particle time constant, t_{p+}, which appears to be much smaller in the present experiments indicating a much faster response of the present particles to sudden accelerations of the flow.

In the case of the transitionally rough flows, the values of the dimensionless ensemble averaged streamwise component of the particle velocity during ejections, as in the case of smooth flows, appear to be well described by a line given by: $u_+ - u_{rms+}$. The dimensionless ensemble averaged values of the vertical component of the particle velocity during ejections appear also to be very similar to those observed in the smooth flows, however they tend to be larger than them for values of y_+ larger than about 100, reaching values of about 2.0 wall units in such region. This seems

to indicate that flow ejections in the transitionally rough flows would be more intense than those in the smooth flows, which is in agreement with other observations. Nevertheless, these enhanced ejections do not seem to affect substantially the characteristics of the particle ejections as compared to those observed in the smooth flows, which also is in agreement with previous experimental results.

The analysis of the particle velocity during downward trajectories shows that the dimensionless values of the ensemble averaged streamwise component of the particle velocity tend to be about the same magnitude as the local mean flow velocity, while corresponding values of the dimensionless ensemble averaged vertical component of the particle velocity tend to be somewhat smaller in absolute value than the particle dimensionless settling velocity, although larger than v_{rms+}. These results suggest that particles would be only rarely deposited by the action of sweep events, and rather they appear to be falling back toward the bed as they lose correlation with the turbulent structures that lifted them from the bed and kept them suspended for some time. It is also apparent from these results that the fall velocity of a particle immersed in a turbulent flow would be somewhat smaller than its settling velocity in still water, which is in agreement with analytical results by others.

8.7 References

Ashida, K., and Fujita, M. (1986). "Stochastic model for particle suspension in open channels". *J. of Hydroscience and Hydr. Engrg.*, vol 4, No 2, pp 21-46.

Bagnold, R. A. (1966). "An approach to the sediment transport problem for general physics". *Geological Survey Professional Paper* 422-I, Washington, D. C.

Bark, F. (1975). "On the wave structure of the wall region of a turbulent boundary layer". *J. Fluid Mech.*, vol 70, part 2, pp 229-250.

Blackwelder, R. F. (1988). "Coherent structures associated with turbulent transport". *Transport phenomena in Turbulent flows: Theory, experiments, and numerical simulation.* Hirata, M. and Kasagi, N., editors. pp 69-88

Brodkey, R. S., Wallace, J. M., and Eckelmann, H. (1974). "Some properties of truncated turbulent signals in bounded shear flows". *J. Fluid Mech.*, vol 63, pp 209-224.

Browand, F. K., and Plocher, D. A. (1985). "Image processing for sediment transport". Proc., 21st Congress I.A.H.R., Melbourne, Australia. pp 8-14.

Clauser, F. H. (1956). "The turbulent boundary layer". *Adv. Applied Mech.*, Vol. 4, pp 1–31.

Cleaver, J. W., and Yates, B. (1976). "The effect of re-entrainment on particle deposition". *Chemical Engrg. Science.*, vol 31, pp 147–151.

Dill, A. J. (1994). "Video-based particle tracking velocimetry technique for measuring flow velocity in porous media". *Masters Thesis*. Dept. Civil Engrg., Univ. of Illinois at Urbana-Champaign, Illinois.

Falco, R. E. (1991). "A coherent structure model of the turbulent boundary layer and its ability to predict Reynolds number dependence". *Phil. Trans. R. Soc. Lond.* A, vol 336, pp 103-129.

Grass, A. J., Stuart, R. J., and Mansour-Tehrani, M. (1991). "Vortical structures and coherent motion in turbulent flow over smooth and rough boundaries". *Phil. Trans. R. Soc. Lond.* A, vol 336, pp 35-65.

Grass, A. J. (1974). "Transport of fine sand on a flat bed: turbulence and suspension mechanics". *Euromech* 48. Inst. Hydrodynamic and Hydraulic Engrg., Tech. Univ. Denmark, pp 33-34.

Grass, A. J. (1971). "Structural features of turbulent flow over smooth and rough boundaries". *J. Fluid Mech.*, vol 50, pp 233–255.

Guezennec, Y. G., Piomelli, U., and Kim, J. (1989). "On the shape and dynamics of wall structures in turbulent channel flow". *Phys. of Fluids* A 1 (4), pp 764-766.

Hassan, Y. A., Blanchat, T. K., Seeley, C. H., and Canaan, R. E. (1992). "Simultaneous velocity measurements of both components of a two-phase flow using Particle Image Velocimetry". *Int. J. Multiphase Flow*, vol 18, No 3, pp 371-395.

Hetsroni, G. (1991). "The effect of particles on the turbulence in a boundary layer". *Two Phase Flow*, Chap. 8. M. Rocco, Ed. Butterworth.

Hinze, J. O. (1971). "Turbulent fluid and particle interaction". *Progress Heat Mass Transfer*, 6, pp 433-452.

Jimenez, J., Moin, P., Moser, R., and Keefe, L. (1988). "Ejection mechanisms in the sublayer of a turbulent channel". *Phys. of Fluids*, 31, pp 1311-1313.

Kim, H. T., Kline, S. J., and Reynolds, W. C. (1971). "The production of turbulence near a smooth wall in a turbulent boundary layer". *J. Fluid Mech.*, vol 50, part 1, pp 133-160.

Kline, S. J., Reynolds, W. C., Schraub, F. A., and Runstadler, P. W. (1967). "The structure of turbulent boundary layers". *J. Fluid Mech.*, 30, pp 741-773.

Liu, Z., Landreth, C. C., Adrian, R. J., and Hanratty, T. J. (1991). "Measurements in turbulent channel flow by high resolution Particle Image Velocimetry". *Experiments in Fluids*, 10, pp 301-312.

Moin, P., and Spalart, P. R. (1989). "Contributions of numerical simulation data bases to the physics, modelling, and measurement of turbulence". *Advances in Turbulence*. George, W. K., and Arndt, R., editors. pp 11-38.

Moin, P., and Kim, J. (1982). "Numerical investigation of turbulent channel flow". *J. Fluid Mech.*, vol 118, pp 341-377.

Nakagawa, H., and Nezu, I. (1981). "Structure of space-time correlations of bursting phenomena in an open-channel flow". *J. Fluid Mech.*, vol 104, pp 1-43.

Nakagawa, H., and Nezu, I. (1977). "Prediction of the contributions to the Reynolds stress from bursting events in open-channel flows". *J. Fluid Mech.*, vol 80, pp 99-128.

Nezu, I., and Nakagawa, H. (1993). "Turbulence in open-channel flows". *IAHR Monograph.* A. A. Balkema, Rotterdam.

Pedinotti, S., Mariotti, G. and Banerjee, S. (1992). "Direct numerical simulation of particle behavior in the wall region of turbulent flows in horizontal channels". *Int J. Multiphase Flow*, vol 18, No 6, pp 927-941.

Rashidi, M., Hetsroni, G., and Banerjee, S. (1990). "Particle-turbulence interaction in a boundary layer". *Int. J. Multiphase Flow*, vol 16, No 6, pp 935-949.

Raupach, M. R., Antonia, R. A., and Rajagopalan, S. (1991). "Rough-wall turbulent boundary layers". *Appl. Mech. Rev.*, vol 44, no 1.

Raupach, M. R. (1981). "Conditional statistics of Reynolds stress in rough-wall and smooth-wall turbulent boundary layers". *J. Fluid Mech.*, vol 108, pp 363-382.

Robinson, S. K. (1991). "Coherent motions in the turbulent boundary layer". *Annu. Rev. Fluid Mech.*, 23, pp 601-639.

Robinson, S. K. (1990). "Kinematics of turbulent boundary layer structure". *Ph.D. dissertation.* Standford Univ., Stanford, California.

Schlichting, H. (1968). "Boundary-layer theory". *McGraw-Hill Book Company.*

Schmid, A. (1985). "Wandnahe turbulente bewegungsabläufe und ihre bedeutung für die riffelbildung". *Institute für Hydromechanik und Wasserwirtschaft*, ETH, Zürich. R 22-85.

Smith, C. R., and Schwartz, S. P. (1983). "Observation of streamwise rotation in the near wall region of a turbulent boundary layer". *Phys. of Fluids*, 26 (3), pp 641-652.

Sumer, B. M., and Deigaard, R. (1981). "Particle motions near the bottom in turbulent flow in an open channel. Part 2". *J. Fluid Mech.*, vol 109, pp 311-337.

Sumer, B. M., and Oguz, B. (1978). "Particle motions near the bottom in turbulent flow in an open channel". *J. Fluid Mech.*, vol 86, pp 109-127.

Sutherland, A. J. (1967). "Proposed mechanism for sediment entrainment by turbulent flows". *J. Geophysical Res.*, vol 72, No 24, pp 191-198.

Urushihara, T., Meinhart, C. D., and Adrian, R. J. (1993). "Investigation of the logarithmic layer in pipe flow using Particle Image Velocimetry". *Near-wall turbulent flows*. R. M. C. So, C. G. Speziale and B. E. Launder (Eds.). Elsevier Science Publishers B. V.

van Rijn, L. C. (1984). "Sediment transport, Part II: suspended load transport". *J. Hydr. Engrg.*, vol 110, No 11, pp 1613-1641.

Wei, T., and Willmarth, W. (1991). "Examination of v–velocity fluctuations in a turbulent channel flow in the context of sediment transport". *J. Fluid Mech.*, vol 233, pp 241-252.

Wells, M. R., and Stock, D. E. (1983). "The effects of crossing trajectories on the dispersion of particles in a turbulent flow". *J. Fluid Mech.*, vol 136, pp 31-62.

Yen, B. C. (1992). "Sediment fall velocity in oscillating flow". *Water Resour. and Environ. Engrg. Res.* Report No 11. Dept. of Civil Engrg. Univ. of Virginia.

Yung, B. P. K., Merry, H., and Bott, T. R. (1988). "The role of turbulent bursts in particle re-entrainment in aqueous systems". *Chemical Engrg. Science*, vol 44, No 4, pp 873-882.

Zhuang, Y., Wilson, J. D., and Lozowski, E. P. (1989). "A trajectory-simulation model for heavy particle motion in turbulent flow". *J. Fluids Engrg.*, vol 111, pp 492-494.

9. MODELING PARTICLE-TURBULENCE INTERACTIONS

9.1 Heuristic model for particle entrainment into suspension

9.1.1 Introduction

Observations of particle entrainment into suspension reported in Chapter 8 indicate that the mechanism that causes such phenomenon is related to interactions between particles and coherent structures of the flow. The experimental evidence suggests that flow ejection events occurring in the wall region of open channel flows are most responsible for lifting sediment particles away from the wall. It has been argued that the particle entrainment is induced by the flow ejections mainly via drag and lift forces exerted by the upward moving fluid over particles lying over the bed.

Herein a heuristic model for the flow coherent structures in the near wall region of a turbulent, hydraulically smooth boundary layer, based on ideas by Landahl (1984, 1990), is used. The proposed flow field interacts with sediment particles lying over the smooth bed. This interaction is induced by the forcing introduced by the flow field on the particle motion. The particle motion is modelled by means of a system of governing equations proposed by Mei (1990), similar to that used in Chapter 6 to model particle saltation.

The heuristic model for particle entrainment proposed herein is applied to analyze some of the characteristics of the particle motion during entrainment, and also to asses the threshold conditions for particle entrainment into suspension.

9.1.2 Modelling flow coherent structures

Evidence presented in Chapter 8 regarding the existence of wall streaks and the sediment particle sorting induced by this flow pattern suggests that these phenomena are related to the presence of quasi-streamwise vortices which have a transverse wavelength of about 100 wall units, a length of about 1000 wall units, and are very persistent in time. The observations reported in Chapter 8 indicate that sediment particles are seen to be picked up from low-speed streaks by rather energetic flow ejections events, and deposited along high-speed streaks.

Robinson (1990) proposed a conceptual model for the quasi-periodic sequence of flow ejections and inrushes (or sweeps) associated with turbulent bursting, based on the existence of convected quasi-streamwise rolls. The streamwise vorticity associated with such structures would induce ejections at one side of the vortex core and inrushes at the opposite side, which Robinson calls "pumping" effect of the rolls.

Landahl (1984, 1990) analyzed the dynamics of coherent structures in the wall region of a turbulent boundary layer, which according to him correspond basically to large three-dimensional eddies that are flat, i.e., that have large horizontal dimensions compared to their vertical extent. He

proposed a simplified theoretical model in which nonlinear activity is assumed to be intermittent and to act locally in space and during a very short initial time so as to set up the initial conditions for the subsequent linear and inviscid evolution of the resulting three-dimensional disturbance. The nonlinear activity would be associated to a local inflectional instability caused by streamwise stretching of the mean shear. As a result of Landahl's analysis for the initial eddy, he proposed a base solution consisting in streamwise vortices, which have a longitudinal and transverse structure corresponding to a modified Gaussian "hat". The vertical structure of the vortices is based on that obtained from measurements of the Reynolds stress during flow ejections reported by Kim et al. (1971) and agrees with a similar analysis by Bark (1975).

Although the method proposed by Landahl (1990) allows to compute the evolution of the initial disturbance, this is not done herein. In fact, since the objective of this section is simply to propose a heuristic model for the process of particle entrainment into suspension, a very simplified model for the flow field would suffice. Accordingly, it is assumed herein that the coherent structures responsible for the entrainment of particles into suspension are given by the initial eddies proposed by Landahl (1990). Hence, the transverse flow field associated with the streamwise vortices is specified through a streamfunction which satisfies no-slip conditions at the bottom wall. Assuming that the streamwise velocity fluctuations can be neglected as a first order approximation when compared to the mean flow velocity, then the streamwise flow field can be specified by the uniform mean flow velocity, which is invariant in the longitudinal and transverse directions. The three-dimensional flow field so defined readily satisfies continuity.

Following Landahl (1990), the dimensionless streamfunction, Ψ, for the transverse flow field is given by:

$$\Psi = -\frac{1}{2}\, C\, l_{3+}\, y_+^3\, E \tag{9.1.1a}$$

$$E = \exp\left(-\left(x_+/l_{1+} \right)^2 - \left(y_+/l_{2+} \right)^2 - \left(z_+/l_{3+} \right)^2 \right) \tag{9.1.1b}$$

where x_+, y_+, and z_+, denote coordinates in the streamwise, vertical, and transverse directions, respectively, made dimensionless with wall units (that is using as length scale the value ν/u_* with u_* denoting the flow shear velocity and ν denoting the kinematic viscosity), l_{1+}, l_{2+}, and l_{3+}, denote length scales in the longitudinal, vertical, and transverse directions, respectively, also made dimensionless with wall units, and C denotes a parameter characterizing the intensity of the transverse flow field. The vertical and transverse flow velocities, v_{f+} and w_{f+}, made dimensionless with u_*, respectively, are given by:

$$v_{f+} = -\frac{\partial \Psi}{\partial z_+} \qquad , \qquad w_{f+} = \frac{\partial \Psi}{\partial y_+} \tag{9.1.2a, b}$$

The streamwise flow velocity, u_{f+}, made dimensionless with u_*, for smooth fully turbulent open channel flow within the viscous sublayer ($y_+ < 5$) is given by the law of the wall:

$$u_{f+} = y_+ \tag{9.1.3a}$$

and outside of the viscous sublayer by the logarithmic law (Clauser, 1956):

$$u_{f+} = \frac{1}{\varkappa} \, Ln \, (\, y_+ \,) + B \tag{9.1.3b}$$

where $\varkappa = 0.4$ denotes the von Karman constant, and B is a constant with a value of 4.9.

From (9.1.1) and (9.1.2) it is easy to see that:

$$v_{f+} = - \, C \, y_+^3 \, z_+ \, E \tag{9.1.4a}$$

$$w_{f+} = - \, C \, l_{3+}^3 \, y_+^2 \, (\, 3/2 - (\, y_+ / l_{2+} \,)^2 \,) \, E \tag{9.1.4b}$$

From (9.1.4), it can be shown that the vertical flow velocity component, v_{f+}, is maximum at:

$$y_+|_{vf+max} = \sqrt{3/2} \; l_{2+} \qquad , \qquad z_+|_{vf+max} = - \sqrt{1/2} \; l_{3+} \tag{9.1.5a, b}$$

Landahl (1990) proposes the values $l_{1+} = 100$, $l_{2+} = 15$, $l_{3+} = 30$, which gives dimensions and dynamics characteristics of the streamwise vortices similar to those obtained numerically by Alfredsson et al. (1988). Also the vertical extension and structure of the flow field obtained is in reasonable agreement with the measurements by Kim et al. (1971).

Table 9.1.1 shows different values of the maximum vertical flow velocity, v_{f+max}, for different values of the parameter C, and the values $l_{1+} = 100$, $l_{2+} = 15$, $l_{3+} = 30$. In the present analysis a value of $C = 1 \times 10^{-4}$ will be used throughout. As seen in Table 9.1.1, this value of C corresponds to a value v_{f+max} of about 1.78, which is about 78% larger than the typical standard deviation of the vertical velocity fluctuations in open channel flows at locations y_+ larger than about 30 (Nezu and Nakagawa, 1993). Nevertheless, it is possible that this value of v_{f+max} is smaller than that corresponding to typical vertical flow velocities during intense flow ejections events such as those responsible for the entrainment of sediment particles as discussed in Chapter 8. As reported therein, some of the measured vertical components of particle ejection velocities showed values as large as 3 to 4 wall units, although the corresponding mean values were in the range of about 1.5 to 2. From this point of view, it seems that a value $v_{f+max} = 1.78$ would be representative of conditions prevailing during ejections of average intensity.

Fig. 9.1.1 shows a vector plot of the transverse flow velocity field obtained using the values $C = 1 \times 10^{-4}$, $l_{1+} = 100$, $l_{2+} = 15$, $l_{3+} = 30$, evaluated at $x_+ = 0$. A three-dimensional rendering of

the transverse velocity field is shown in Fig. 9.1.2, which shows the Gaussian decay of the coherent structure in the streamwise direction. The dimensionless vertical flow velocity variation in the transverse plane, y_+- z_+, evaluated at x_+= 0, is presented in Fig. 9.1.3. The vertical structure of the dimensionless vertical flow velocity and its variation in the x_+ direction, evaluated at $z_+|_{vf+max}$ = –21.2 resulting from (9.1.5) for the value l_{3+}= 30, is plotted in Fig. 9.1.4.

Table 9.1.1 Values of the maximum dimensionless flow velocity as a function of C

C	v_{f+max}
0.5×10^{-4}	0.89
1.0×10^{-4}	1.78
2.0×10^{-4}	3.56
3.0×10^{-4}	5.34

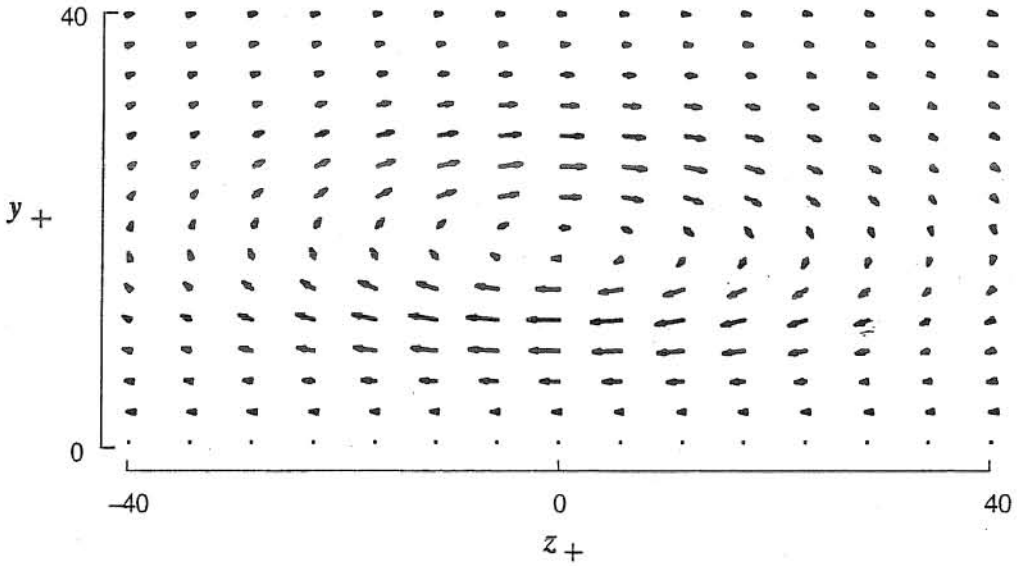

Fig. 9.1.1 Transverse flow velocity field at x_+= 0. $C = 1 \times 10^{-4}$, $l_{1+} = 100$, $l_{2+} = 15$, $l_{3+} = 30$.

9.1.3 Modelling particle motion

To model particle motion, the system of governing equations proposed by Mei (1990) is used, adapted as in Chapter 6 for the analysis of particle saltation but extended to the three-dimensional situation analyzed herein. Including nonlinear drag and the lift force term proposed by Wiberg and Smith (1985) as in Chapter 6, then the system of governing equations can be written in dimensionless terms, using wall units to scale them, as:

$$\frac{du_{p+}}{dt_+} = -\frac{3}{4}\,\alpha\,\frac{C_D}{Re_{p_*}}\,|u_R|_+\,(\,u_{p+}-u_{f+}\,)+\frac{\alpha\,\sin\theta}{\tau_*\,Re_{p_*}}+\alpha\,C_m\,\frac{du_{f+}}{dy_+}\,v_{p+}+$$

$$+\,\alpha\,\frac{du_{f+}}{dy_+}\,v_{f+}+9\,\frac{\alpha}{Re_{p_*}}\,\frac{1}{\sqrt{\pi}}\int_0^{t_+}\frac{d}{d\tau}(\,u_{f+}-u_{p+}\,)\,\frac{d\tau}{\sqrt{t_+-\tau}} \qquad (9.1.6a)$$

$$\frac{dv_{p+}}{dt_+} = -\frac{3}{4}\,\alpha\,\frac{C_D}{Re_{p_*}}\,|u_R|_+\,(\,v_{p+}-v_{f+}\,)+\frac{3}{4}\,\alpha\,\frac{C_L}{Re_{p_*}}\,(\,|u_R|^2_{T+}-|u_R|^2_{B+}\,)-\frac{\alpha\,\cos\theta}{\tau_*\,Re_{p_*}}+$$

$$+\,\alpha\,C_m\,\frac{dv_{f+}}{dt_+}+\alpha\,\frac{Dv_{f+}}{Dt_+}+9\,\frac{\alpha}{Re_{p_*}}\,\frac{1}{\sqrt{\pi}}\int_0^{t_+}\frac{d}{d\tau}(\,v_{f+}-v_{p_+}\,)\,\frac{d\tau}{\sqrt{t-\tau}} \qquad (9.1.6b)$$

$$\frac{dw_{p+}}{dt_+} = -\frac{3}{4}\,\alpha\,\frac{C_D}{Re_{p_*}}\,|u_R|_+\,(\,w_{p+}-w_{f+}\,)+\alpha\,C_m\,\frac{dw_{f+}}{dt_+}+\alpha\,\frac{Dw_{f+}}{Dt_+}+$$

$$+\,9\,\frac{\alpha}{Re_{p_*}}\,\frac{1}{\sqrt{\pi}}\int_0^{t_+}\frac{d}{d\tau}(\,w_{f+}-w_{p_+}\,)\,\frac{d\tau}{\sqrt{t-\tau}} \qquad (9.1.6c)$$

where u_{p+}, v_{p+}, and w_{p+} denote the particle streamwise, vertical, and transverse velocity components, respectively, made dimensionless with u_*, and $|u_R|_+$ denotes the magnitude of the particle relative velocity, also made dimensionless with u_*, given by:

$$|u_R|_+ = (\,(\,u_{p+}-u_{f+}\,)^2+(\,v_{p+}-v_{f+}\,)^2+(\,w_{p+}-w_{f+}\,)^2\,)^{1/2} \qquad (9.1.7)$$

Similarly, $|u_R|_{T+}$ and $|u_R|_{B+}$ denote the magnitude of the dimensionless particle relative velocity evaluated on top and bottom of the particle, respectively. Also, in (9.1.6) t_+ denotes time made dimensionless with ν/u_*^2, τ denotes a dummy variable for integration, $\sin\theta$ denotes the channel slope, C_m denotes the added mass coefficient assumed to be equal to 0.5, C_L denotes the lift coefficient used by Wiberg and Smith (1985) taken to be equal to 0.2, and C_D denotes the drag coefficient estimated using the following approximation proposed by Yen (1992):

$$C_D = \frac{24}{Re}\,(\,1+0.15\,\sqrt{Re}\,+0.017\,Re\,)-\frac{0.208}{1+10^4\,Re^{-0.5}} \qquad (9.1.8)$$

where $Re = |u_R|\,d_p\,/\nu$, with $|u_R|$ denoting the dimensional magnitude of the particle relative velocity and d_p denoting the particle diameter. The rest of the dimensionless parameters appearing in (9.1.6) are defined as:

$$\alpha = (\,1+R+C_m\,)^{-1}\quad,\qquad R = (\,\varrho_s\,/\varrho-1\,) \qquad (9.1.9a, b)$$

$$\tau_* = u_*^2/(\,g\,R\,d_p\,)\quad,\qquad Re_{p_*} = u_*\,d_p/\nu \qquad (9.1.9c, d)$$

where ϱ denotes fluid density, ϱ_s denotes particle density, and g denotes gravitational acceleration.

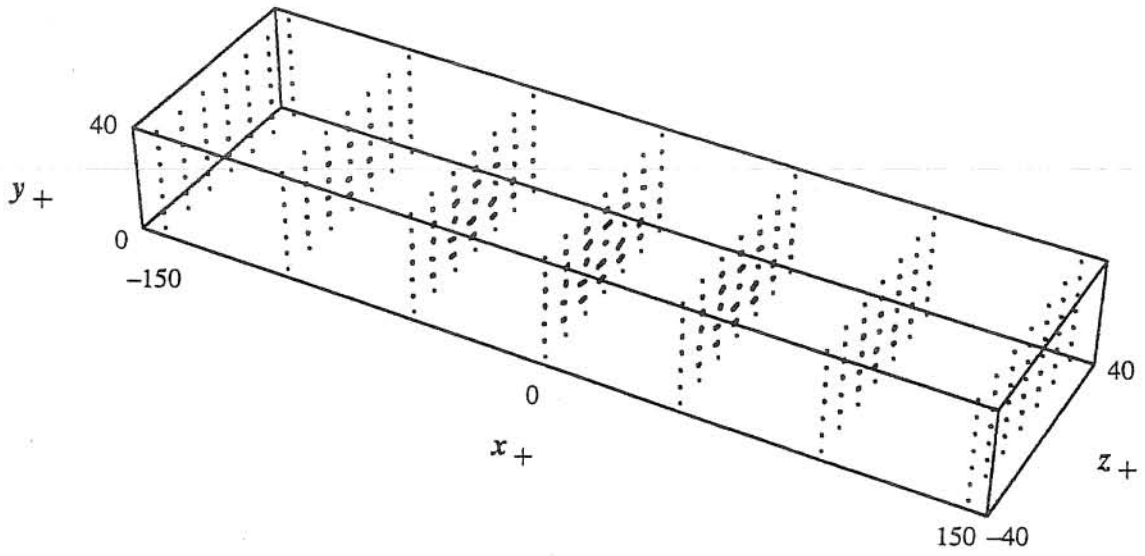

Fig. 9.1.2 3-D rendering of transverse flow velocity field. $C = 1 \times 10^{-4}$, $l_{1+} = 100$, $l_{2+} = 15$, $l_{3+} = 30$.

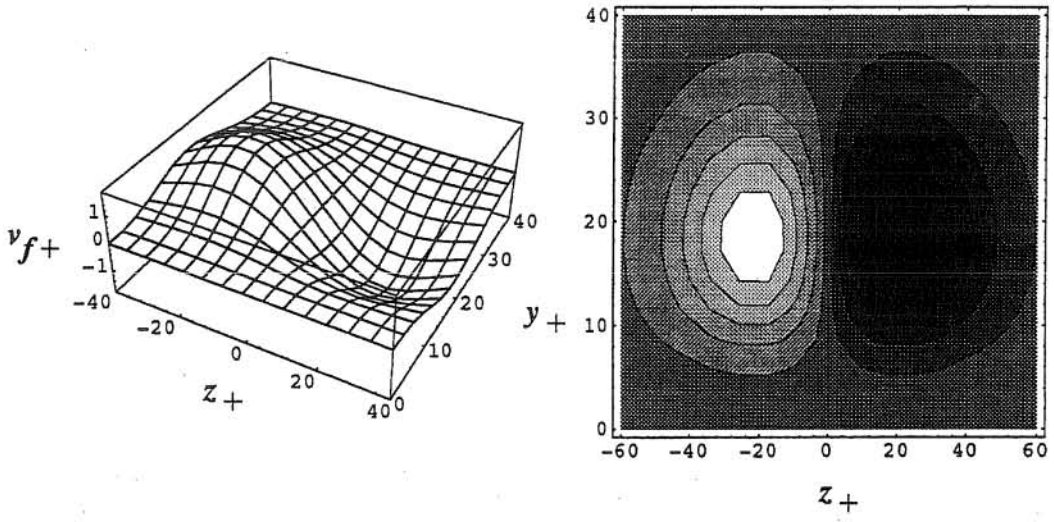

Fig. 9.1.3 Dimensionless vertical flow velocity field, v_{f+}, in the transverse plane, y_+- z_+, at x_+= 0. Shading represents the magnitude of the velocity: black is negative, white is positive. $C = 1 \times 10^{-4}$, $l_{1+} = 100$, $l_{2+} = 15$, $l_{3+} = 30$.

In (9.1.6), the fluid acceleration terms are estimated as (Mei, 1990):

$$\frac{du_{f+}}{dt_+} = v_{p+}\frac{du_{f+}}{dy_+} \tag{9.1.10a}$$

$$\frac{dv_{f+}}{dt_+} = u_{p+}\frac{\partial v_{f+}}{\partial x_+} + v_{p+}\frac{\partial v_{f+}}{\partial y_+} + w_{p+}\frac{\partial v_{f+}}{\partial z_+} \tag{9.1.10b}$$

$$\frac{Dv_{f+}}{Dt_+} = u_{f+}\frac{\partial v_{f+}}{\partial x_+} + v_{p+}\frac{\partial v_{f+}}{\partial y_+} + w_{p+}\frac{\partial v_{f+}}{\partial z_+} \tag{9.1.10c}$$

$$\frac{dw_{f+}}{dt_+} = u_{p+}\frac{\partial w_{f+}}{\partial x_+} + v_{p+}\frac{\partial w_{f+}}{\partial y_+} + w_{p+}\frac{\partial w_{f+}}{\partial z_+} \tag{9.1.10d}$$

$$\frac{Dw_{f+}}{Dt_+} = u_{f+}\frac{\partial w_{f+}}{\partial x_+} + v_{p+}\frac{\partial w_{f+}}{\partial y_+} + w_{p+}\frac{\partial w_{f+}}{\partial z_+} \tag{9.1.10e}$$

The system of equations (9.1.6) for the particle velocities is complemented with the Lagrangian equations for the particle trajectory:

$$\frac{dx_{p+}}{dt_+} = u_{p+} \quad , \quad \frac{dy_{p+}}{dt_+} = v_{p+} \quad , \quad \frac{dz_{p+}}{dt_+} = w_{p+} \tag{9.1.11a–c}$$

where x_{p+}, y_{p+}, and z_{p+} denote dimensionless coordinates of the particle centroid.

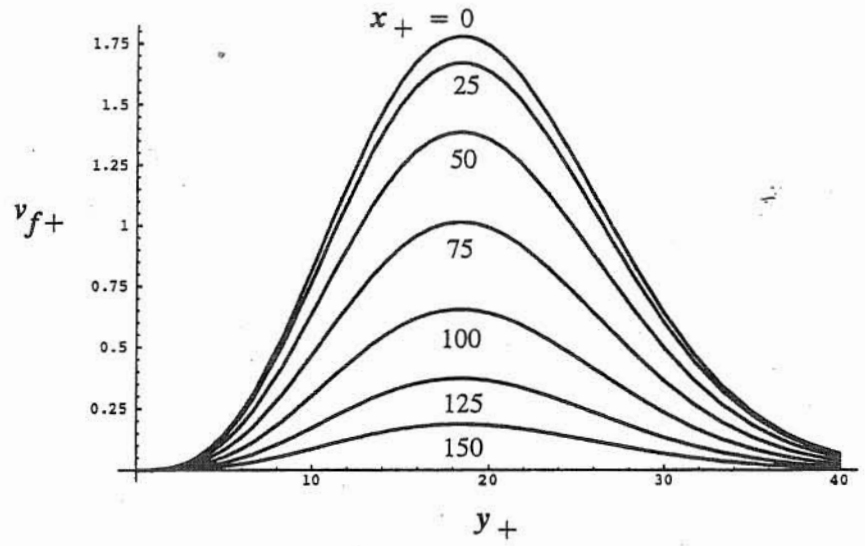

Fig. 9.1.4 Dimensionless vertical flow velocity, v_{f+}, as a function of y_+ and x_+, evaluated at $z_+|_{vf+max} = -21.2$. $C = 1 \times 10^{-4}$, $l_{1+} = 100$, $l_{2+} = 15$, $l_{3+} = 30$.

The validity of the system of governing equations (9.1.6) in the case of sediment transport in open channel flows has been discussed in Chapter 6, particularly, with respect to the issues concerning the added mass, drag, and lift coefficients, and the Basset term. It is assumed herein that this system of equations is a good enough approximation, which might yield as good an estimation

of the particle motion in the present situation as in the case of particle saltation analyzed in Chapter 6.

Flow velocity components in (9.1.6) to (9.1.11) are evaluated using (9.1.3) and (9.1.4), which act as a forcing for the particle motion. The initial conditions for integrating (9.1.6) and (9.1.11) are specified as follows. It is assumed that initially the particle is lying at rest on the channel bottom located in a low-speed streak when it is picked up by the coherent flow structure. In this situation, the particle centroid is assumed to be located at:

$$x_{p+}(0) = 0 \quad , \quad y_{p+}(0) = Re_{p_*}/2 \quad , \quad z_{p+}(0) = -20 \tag{9.1.12a}$$

where the vertical location corresponds to a distance equal to $d_p/2$ over the channel bottom and the transverse location corresponds approximately to the point where the vertical flow velocity component is maximum according to (9.1.5), and the particle velocity is assumed to be zero, such that:

$$u_{p+}(0) = 0 \quad , \quad v_{p+}(0) = 0 \quad , \quad w_{p+}(0) = 0 \tag{9.1.12b}$$

The system of equations (9.1.6) to (9.1.11) subject to the forcing of the flow field given by (9.1.3) and (9.1.4), and the initial conditions (9.1.12), is solved numerically using a fourth-order Runge-Kutta scheme, similarly as in Chapter 6. Also, the treatment of the Basset integral in (9.1.6) is identical to that explained in detail in Chapter 6.

9.1.4 Threshold conditions for particle entrainment into suspension

The model proposed herein can be used to investigate the threshold conditions for the entrainment of particles into suspension. As discussed in Chapter 7, experimental observations reported therein indicate the existence of a threshold value for the bed shear stress which controls the onset of particle entrainment into suspension. For low values of the bed shear stress, particles of a given size were observed to move in contact with the bed, which in the case of smooth boundary occurs in the rolling and sliding modes only. For increasing values of the bed shear stress, progressively more frequent events were observed during which particles are suddenly entrained into the outer regions of the wall layer and remain in suspension for distances generally longer than 100 particle diameters. During these events particles clearly respond to large velocity fluctuations of the flow. Therefore, for values of the bed shear stress lower than the threshold particles do not seem to respond to turbulent ejections in the near bed region, while for values of the bed shear stress larger than the threshold particles do seem to respond to such events.

Of course the definition of the precise threshold level has only statistical significance, in the sense that in reality there is a transition range of increasing values of the shear stress in which the frequency of the entrainment events, and the number of particles entrained by those events, increases from a negligible value to a large value. Nevertheless, as concluded in Chapter 7, this range results

in practice to be rather narrow, such that a more precise definition of the threshold does not seem to be necessary.

As to what exactly is considered an entrainment-into-suspension event, the most common criterion used is related to the length of the trajectory described by the lifted particle. For instance, van Rijn's (1984) criterion corresponds to particles ejected from the bed having lengths of the trajectory from the point of entrainment to the point of deposition, or distrainment, at the bed exceeding 100 particle diameters. This clearly differentiates ejection events from saltation events, for which the length of the jumps is generally smaller than about 25 particle diameters (see Chapter 5), however the particular value 100 is totally arbitrary.

In the case of a particle lying on the channel bottom, entrainment would occur as long as the net upward force induced on the particle by the fluid exceeds the submerged weight of the particle. Nevertheless, this criterion is clearly less demanding that the one involving the length of the trajectory of the entrained particle.

The experimental results reported in Chapter 7 indicate that the range of values of the bed shear stress comprising the limit situation for which the particle starts responding to the turbulence and that for which the length of the trajectories of the entrained particles exceeds values of the order of 100 particle diameters is rather narrow. Accordingly, in order to be able to compare the results of the present heuristic model for entrainment with those obtained from the experimental study of Chapter 7, the criterion involving the length of the particle trajectory is used.

As deduced from (9.1.6), the dimensionless control parameters for particle motion are R, τ_*, Re_{p_*}, and θ. Considering the case of entrainment of natural sediment, the value of R can be estimated as equal to 1.65. Also, for simplicity, the slope of the channel can be considered sufficiently small so that $sin\ \theta \approx 0$, and $cos\ \theta \approx 1$. Hence, in this situation, the threshold conditions for the onset of particle entrainment into suspension are defined in the parameter space (Re_{p_*}, τ_*) in complete agreement with the analysis of Chapter 7.

For values of the particle Reynolds number, Re_{p_*}, in the range 2 to 20, similar to that of the experiments of Chapter 7, values of the dimensionless bed shear stress, τ_*, were iterated in order for the numerical solution of the heuristic model for particle entrainment presented in previous sections to yield values of the ratio λ/d_p, where λ denotes the length of the particle trajectory, equal to 50 and 100.

Results obtained for the values of τ_* associated with the ratios $\lambda/d_p = 50$ and 100, are plotted Fig. 9.1.5 as a function of Re_{p_*}, for the situation in which the lift term is neglected in the equations governing particle motion. Neglecting lift forces in the equation of motion means that the only

upward forces acting on the particle correspond to the drag exerted by the ejected fluid. The results shown in Fig. 9.1.5 indicate that for sufficiently high values of the dimensionless bed shear stress the drag exerted by the upflow associated with the coherent structure is sufficient to overcome the submerged weight of the particle and lift it up away from the bed. As the particle moves in the downstream direction the effect of the upflow decays and the particle falls back to the bed by the effect of gravity. The length of the particle trajectory increases as τ_* increases.

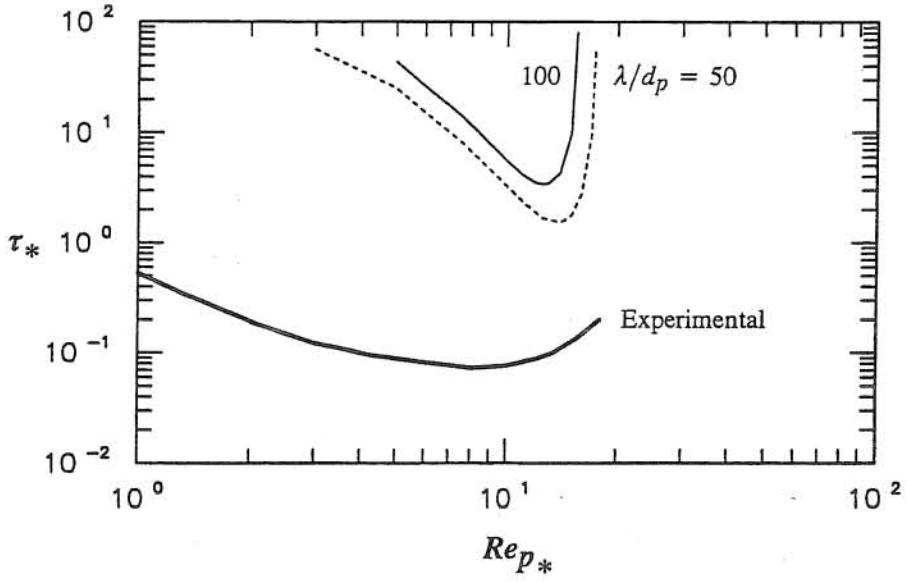

Fig. 9.1.5 Threshold conditions for particle entrainment into suspension. Theoretical curves correspond to computations with no lift.

Interestingly the basic shape of the theoretical curves for the limit of entrainment (expressed as a constant value for the ratio λ/d_p) is similar to that obtained experimentally. As the particle gets smaller compared to the vertical extension of the coherent structure, that is as Re_{p_*} decreases, increasingly higher values of τ_* are required to lift-up the particle from the bed. This is because the intensity of the vertical flow velocity associated with the coherent structure decays exponentially as the bottom wall is approached. On the other hand, as the particle gets larger compared to the vertical dimensions of the coherent structure, that is as Re_{p_*} increases, there is a dimensionless limit size for which the weight of the particle can not be exceeded by the upward drag exerted by the flow, and therefore no entrainment into suspension is predicted by the model to occur for values of Re_{p_*} larger than about 20. A minimum of the theoretical threshold curves is obtained for values of Re_{p_*} of about 12, which is in reasonably good agreement with the experimental observations.

Although the basic features of the experimental threshold of entrainment are well reproduced by the present heuristic model, it is also apparent that the theoretical threshold curves strongly overestimate the observed one. A better agreement with the experimental curve is obtained when

lift forces are considered in the numerical computations. The results obtained in this situation are presented in Fig. 9.1.6.

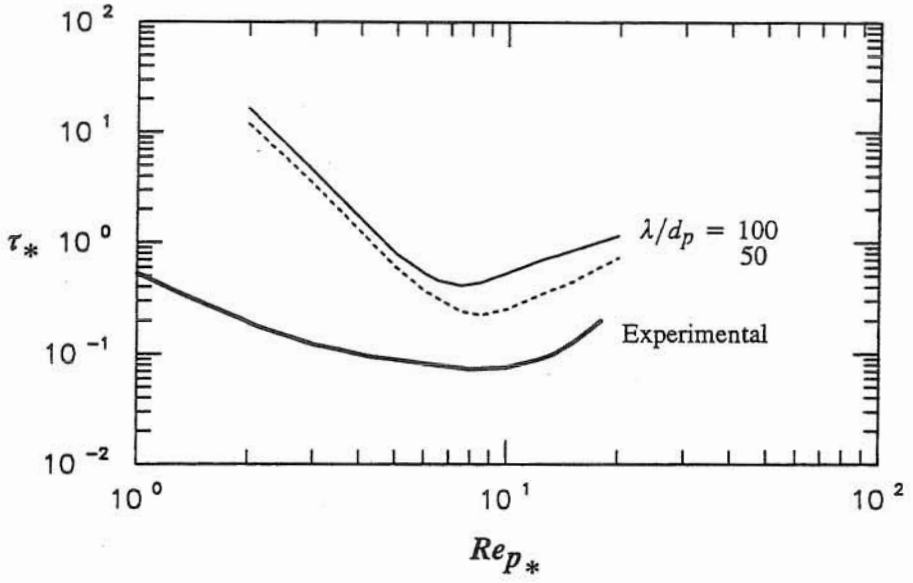

Fig. 9.1.6 Threshold conditions for particle entrainment into suspension. Theoretical curves correspond to computations with lift force included.

The effect of the lift force is to lower the value of the theoretical threshold shear stress. The theoretical threshold curves including lift shown in Fig. 9.1.6 are much closer in shape and magnitude to the corresponding experimental curve than the curves with no lift shown in Fig. 9.1.5. The minimum of the threshold shear stress occurs now for a value of Re_{p_*} of about 7 to 9, in good agreement with the experimental results. Nevertheless, the theoretical curves still overestimate notoriously the experimental values of the threshold bed shear stress. Also, the slope of the theoretical curves in the region Re_{p_*} lower than about 5 is much steeper than that of the experimental one, which somehow seems to imply that the decay of the intensity of the upflow associated with the model coherent structure as the bottom wall is approached is stronger than expected.

On the other hand, it is apparent from Fig. 9.1.6 that the theoretical curves for $\lambda/d_p = 50$ and 100 are very close together specially in the region Re_{p_*} lower than about 5. This indicates that the model predicts a rather abrupt onset of the particle entrainment into suspension, which appears to resemble the experimental observations very well.

It is important to recall that the lift force term used in the equations for particle motion requires the use of a lift coefficient, C_L, of which not much is known. As discussed in Chapter 6, Wiberg and Smith (1985) proposed the use of a constant value 0.2 for the case of particle saltation, based on experimental results by Chepil (1958). Although Patnaik et al. (1994) suggest that C_L is a function of the Reynolds number of the particle, Re, and the ratio d_p/y_p*, where y_p* denotes the

elevation of the particle centroid over the channel bottom, the use of a constant value of $C_L = 0.2$ appears to yield satisfactory results for the simulation of particle saltation (see Chapter 6). Nevertheless, it must be recognized that the validity of the use of this value of C_L in the case of a particle initially lying on the bottom surface is totally uncertain.

It is necessary to point out that the most important aspect of the present heuristic model for particle entrainment into suspension corresponds to the characteristics of the flow coherent structure which forces the particle motion. With respect to this, the intensity of the vertical upflow and its distribution in the vertical appear to be most relevant for the phenomenon of particle entrainment. In fact, the rate of decay of the vertical flow velocity as y_+ goes to zero seems to control the slope of the theoretical threshold curve in the range Re_{p_*} lower than about 5. On the other hand, the vertical extension of the coherent structure and the magnitude of the vertical flow velocity would control the heights reached by the entrained particles. Since particles that are ejected to higher elevations are accelerated to larger streamwise velocities due to momentum transfer from the mean flow, they can jump longer distances, which therefore would decrease the nominal values of τ_* required to having values of $\lambda/d_p = 50$ or 100. Further analysis of these issues is presented in the next section.

So far, the model flow coherent structure has been considered to be at rest with respect to the channel bottom. In this situation, the flow ejection appears to decay rather fast in the streamwise direction, which implies that the particle is subjected to vertical drag only during a brief initial transient. As discussed previously, Robinson (1990) suggests that the quasi-streamwise vortices corresponding to the coherent structures responsible for flow ejection events displace in the downstream direction with an almost constant convection velocity. Evidence presented in Chapter 4 shows that coherent structures in the wall layer of an open channel flow with smooth boundaries displace downstream with a constant dimensionless convection velocity $u_{c+} = 10$ (made dimensionless with u_*). By introducing the following transformation:

$$x'_+ = x_+ - u_{c+}\, t_+ \tag{9.1.13}$$

in the equations (9.1.3) and (9.1.4) for the velocity field associated with the coherent structure, then the threshold conditions for particle entrainment into suspension corresponding to the case of a convected coherent structure can be sought for, similarly as it was done for the results shown in Figs. 9.1.5 and 6. The new results obtained using $u_{c+} = 10$ and including the lift term are shown in Fig. 9.1.7.

As seen therein, the theoretical threshold curves in the range Re_{p_*} lower than about 5 do not differ sensibly from those obtained for $u_{c+} = 0$, shown in Fig. 9.1.6. In the range of Re_{p_*} from 5 to about 10, the theoretical threshold curves get much closer to the experimental one than those of

Fig. 9.1.6, and predict threshold values for τ_* that coincide fairly well with the experimental observations. Nevertheless, in the range of Re_{p_*} from about 10 to about 15 the solution of the model appears to be double valued. For values of Re_{p_*} larger than about 15 the solution for the threshold τ_* appears to be single valued again, with values that tend to overestimate somehow the experimental results.

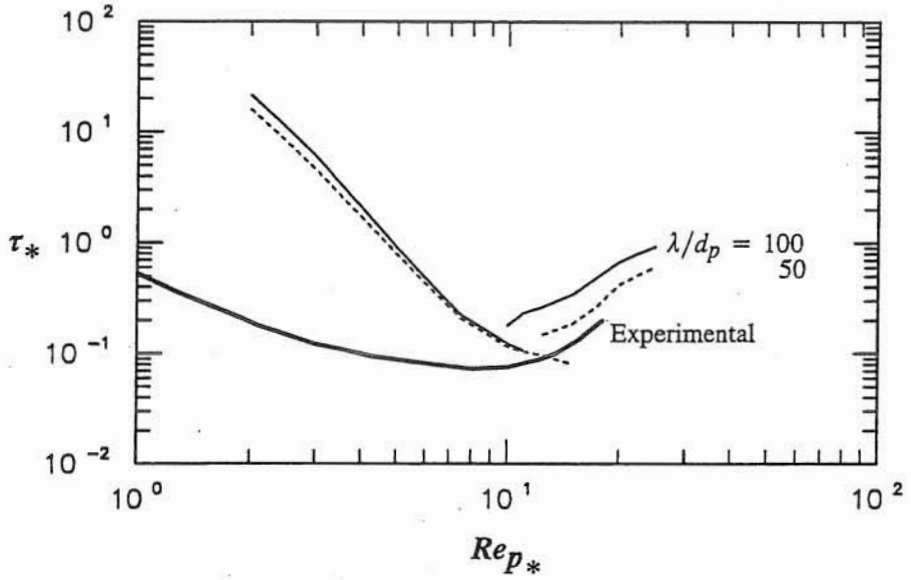

Fig. 9.1.7 Threshold conditions for particle entrainment into suspension. Theoretical curves correspond to computations with lift force included, and assuming the flow coherent structure is moving with a constant convective velocity $u_{c+}= 10$.

The fact that the theoretical threshold curves with values of $u_{c+}= 0$ and 10 do not differ too much in the range Re_{p_*} lower than about 5 seems to indicate that in the present model the entrainment in this range is controlled mainly by the lift force and less importantly by the flow ejection. In the range $Re_{p_*} > 5$, however, the convected flow structure appears to be more efficient in increasing the length of the entrained particle trajectories than the one at rest. This would be a consequence of the occurrence of a reduced relative motion between the coherent structure and entrained particle in the former case with respect to the latter, which implies that in the case of the convected flow structure the particle is subjected to the drag induced by the upflows for a longer period of time, which results in longer particle trajectories.

The "double-valuedness" of the solution in the range of Re_{p_*} from about 10 to about 15 seems to be a mathematical result of the present model, which might not resemble any physical response of the real system analyzed. In this sense it is necessary to recall that the present model is only heuristic in nature, and therefore intended only to reproduce the general features of the phenomenon of particle entrainment into suspension.

As already discussed, an improvement in the predictions of the present model for particle entrainment into suspension would require a revision of the characteristics and structure of the streamwise vortices characterizing the flow field during particle ejections. To further analyze the results of the present model, the characteristics of the particle trajectories during entrainment are discussed next

9.1.5 Characteristics of particle motion during entrainment

To illustrate the characteristics of the particle motion during entrainment predicted by the present model two examples are presented. The first considers the case of the coherent structure at rest with respect to the channel bottom, and the second the case of convected coherent structure. For brevity, only the results corresponding to the following set conditions are reported, although they are fairly representative of the overall behavior of the present model: Case i) $Re_{p_*}= 10$, $\tau_*= 0.6$, $u_{c+}= 0$, Case ii) $Re_{p_*}= 10$, $\tau_*= 0.25$, $u_{c+}= 10$. These conditions give values of λ/d_p on the order of 100.

Results of the particle trajectory corresponding to Case i) are shown in Figs. 9.1.8 and 9.1.9. As seen therein the length of the jump described by the particle is of the order of 1000 wall units. The ejection angle measured with respect to the channel bottom is about 12°, which is in good agreement with the experimental observations reported in Chapter 8. The particle initially picked up at $z_+ = -20$ is deposited at a value z_+ of about 10. This can be interpreted as the particle being picked up from one side of the streamwise vortex (a low-speed wall streak), and deposited at the other side of the vortex core (along the contiguous high-speed streak). The maximum elevation reached by the particle is about 30 wall units. This is a rather low elevation compared to those typically reached by entrained particles, which according to the observations reported in Chapter 8 can be of the order of the wall layer thickness, about 80 to 100 wall units. As shown in Fig. 9.1.4, the vertical extent of the upflow associated with the model coherent structure is not higher than about 40 wall units, therefore the particles entrained by such structure can not reach elevations higher than that. This seems to be basically the reason for the rather poor predictions of the threshold bed shear stress given by the present heuristic model. Particles that are lifted to higher elevations can be accelerated to higher streamwise velocities and therefore can describe longer trajectories for the same value of the bed shear stress, which given the criterion for the limit of particle entrainment used herein would lower the theoretical limit for the onset of particle entrainment into suspension, thus yielding a better agreement with the experimental observations reported in Chapter 7.

Some experimental evidence showing that the vertical extension of the model coherent structure used herein is rather low is presented in Fig. 9.1.10. Such figure, presented previously in Chapter 8, shows the vertical distribution of the conditional cross-correlation of the particle

velocities during ejections from the channel bottom, $< u'_{p+} v_{p+} >$ as a function of y_+, where the angular brackets represent conditional ensemble average during ejection, u'_{p+} denotes the particle dimensionless velocity component in the streamwise direction relative to the local mean flow velocity, and v_{p+} denotes the dimensionless particle velocity component in the vertical direction. In Fig. 9.1.10 the experimental results reported by Kim et al. (1971) of the conditional values of the Reynolds stress, $\overline{u'v'}$, during flow ejections are also plotted for comparison purposes, together with the curve fitted by Bark et al. (1975) to Kim et al.'s experimental results which is given by:

$$- \overline{u'v'}/u_*^2 = c_1 \, y_+^3 \, \exp \, (\, - c_2 \, y_+^2 \,) \tag{9.1.14}$$

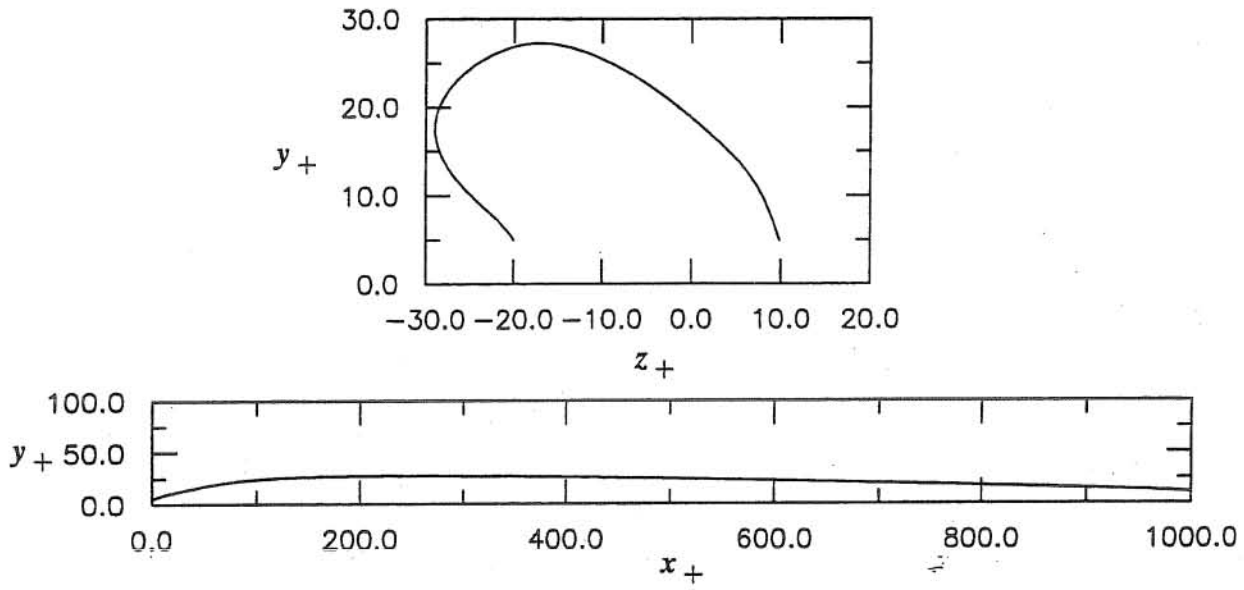

Fig. 9.1.8 Dimensionless entrained particle trajectory. $Re_{p_*} = 10$, $\tau_* = 0.6$, $u_{c+} = 0$.

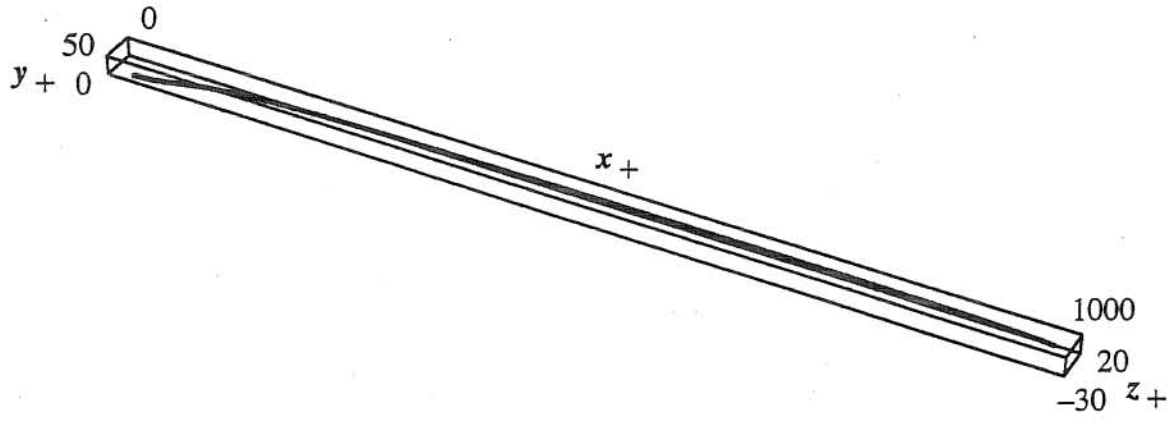

Fig. 9.1.9 Dimensionless entrained particle trajectory. $Re_{p_*} = 10$, $\tau_* = 0.6$, $u_{c+} = 0$.

As already mentioned, the vertical structure of the model streamwise vortices used herein is based on the observations of Kim et al. Clearly the results shown in Fig. 9.1.10 indicate that the particle velocities during entrainment reported in Chapter 8 exhibit coherence that extends to elevations much higher than those corresponding to Kim et al.'s results, and goes all the way up to the outer regions of the wall layer.

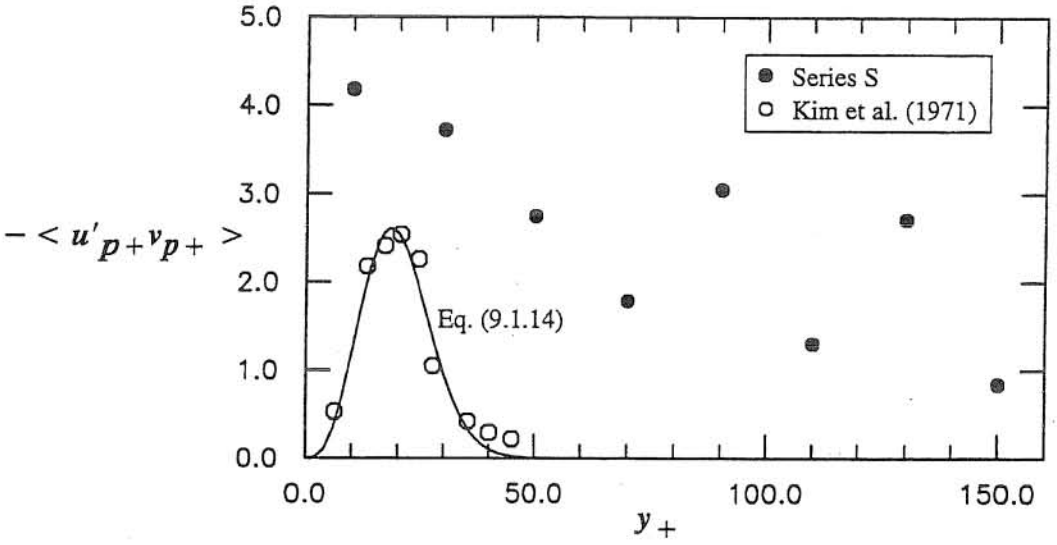

Fig. 9.1.10 Dimensionless conditional correlation between streamwise and vertical components of particle ejection velocity relative to the mean flow velocity. Experiments of Series S, Chapter 8. Comparison with conditional Reynolds stress during flow ejections measured by Kim et al. (1971).

Results of the particle trajectory corresponding to Case ii) are shown in Fig. 9.1.11. As in Fig. 9.1.8, the length of the jump described by the particle is of the order of 1000 wall units. Again, the ejection angle is about 12°, similar to that of Case i) and in good agreement with the experimental observations of Chapter 8. The particle initially picked up at $z_+ = -20$ is deposited at a value z_+ of about 50, which gives a total lateral displacement of the particle of about twice that of Case i). Clearly this is a result of a more complete interaction between the convected coherent structure and the particle than in the case of non-convected structure, which occurs due to the reduced relative motion between particle and flow structure. The maximum elevation reached by the particle in Case ii) is about 40 wall units, slightly higher than that observed in Case i), which would also be a consequence of the enhanced interaction between flow and particle in the former case. Nevertheless this elevation is still too low compared to the experimental observations as it has been already discussed.

Finally, it can be said that the presence of the cross-flow associated with the streamwise vortices seems to be able to induce particle sorting in the transverse direction, such that they would accumulate along the upflow zone of the vortices, a low-speed wall streak, in agreement with

observations reported in Chapter 8. In this way particles deposited along the high-speed streaks are rapidly displaced toward the low-speed streaks from where they are picked up by the flow ejections.

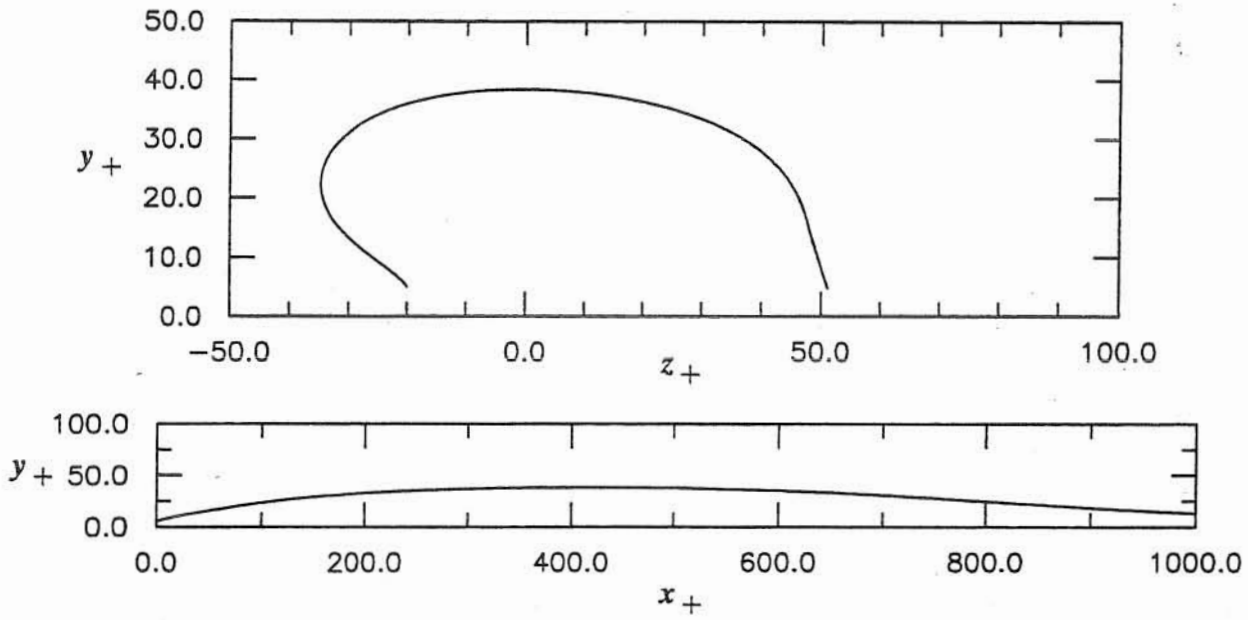

Fig. 9.1.11 Dimensionless entrained particle trajectory. $Re_{p_*} = 10$, $\tau_* = 0.25$, $u_{c+} = 10$.

9.1.6 Conclusions

A heuristic model for particle entrainment into suspension has been developed based on the interaction between particles lying on the smooth surface of an open channel flow and near-wall flow coherent structures. Flow coherent structures responsible for particle entrainment, assumed to consist on streamwise vortices, were characterized by a very simplistic model which, nevertheless, captures the essential features of typically observed flow structures in the near wall region of turbulent boundary layers.

The model for particle entrainment into suspension was applied to analyze the threshold conditions for the onset of particle entrainment. The results obtained neglecting lift forces reproduce satisfactorily the basic shape of the experimental curve for the threshold dimensionless bed shear stress, τ_*, as a function of the particle Reynolds number, Re_{p_*}, reported in Chapter 7. Theoretical and experimental curves have a minimum for values of Re_{p_*} of about 10. In the Range Re_{p_*} lower than about 10, the threshold value of τ_* tend to increase as Re_{p_*} decreases, which seems to be a consequence of the decay of the intensity of the upflows associated with the flow coherent structure as the bottom wall is approached. In the range Re_{p_*} larger than about 10, the threshold value of τ_* tend to increase as Re_{p_*} increases, which would result from the fact that as Re_{p_*} gets larger so does the particle weight relative to the intensity of the upflow.

Although the shape of the threshold curve predicted by the model with no lift is in agreement with experimental observations, the threshold values of τ_* seem to be strongly overpredicted by the model when compared with the experimental results. Including lift force in the equations for particle motion seems to improve substantially the model results in terms of shape of the threshold curve and also its magnitude, however the theoretical values of the threshold τ_* appears to be still overpredicted by the model. A final element included in the model corresponds to allowing the streamwise vortices to displace in the streamwise direction with a constant convection velocity. This decreases the relative motion between the structure and the particle thus increasing the degree of interaction between them which results on a reduction of the theoretical threshold values of τ_* in the range of values of Re_{p_*} around 10. Although these results match the experimental observations very well, the solution of the model appears to be double valued in the vicinity of this region, which does not appear to make physical sense.

The reasons for the overprediction of the threshold conditions for particle entrainment into suspension appear to be in the fact that the vertical flow velocity associated with the model coherent structure seems to decay too fast in the vertical, such that the total height of the structure seems to be lower than about 40 wall units. Experimental evidence suggest that such height should be on the order of 100 wall units.

The maximum height of particle jumps induced by the model flow coherent structure are generally lower than 40 wall units, which appears to be also a consequence of the reduced vertical extent of the model streamwise vortices. A bigger extent in the vertical of the upflows that cause particle entrainment would increase the elevations reached by the entrained particles, which would increase the length of the induced jumps for a constant value of the bed shear stress, thus reducing the threshold value of this variable for the onset of particle entrainment into suspension.

The simulated trajectories of entrained particles agree well, at least qualitatively, with those measured experimentally. Ejections angles have values of about 12° with respect to the channel bottom. Particles picked up in the upflow zone of the streamwise vortices (which would correspond to a low-speed wall streak) are deposited on the other side of the vortex core (which would correspond to a contiguous high-speed streak). The presence of the transverse flow induced by the streamwise vortices also would explain the accumulation of particles along low-speed streaks of the wall typically observed experimentally.

9.1.7 References

Alfredsson, P. H., Johansson, A. V., and Kim, J. (1988). "Turbulence production near walls, the role of flow structures with spanwise asymmetry". *Proc. 2nd Summer Prog. Center for Turb. Res.* NASA Ames/Standford University.

Bark, F. (1975). "On the wave structure of the wall region of a turbulent boundary layer". *J. Fluid Mech.*, vol 70, part 2, pp 229-250.

Chepil, W. S. (1958). "The use of evenly spaced hemispheres to evaluate aerodynamic forces on a soil surface". *Eos. Trans. AGU*, 39 (3), pp 397-404.

Clauser, F. H. (1956). "The turbulent boundary layer". *Adv. Applied Mech.*, vol. 4, pp 1–31.

Kim, H. T., Kline, S. J., and Reynolds, W. C. (1971). "The production of turbulence near a smooth wall in a turbulent boundary layer". *J. Fluid Mech.*, vol 50, part 1, pp 133-160.

Landahl, M. T. (1990). "On sublayer streaks". *J. Fluid Mech.*, vol 212, pp 593-614.

Landahl, M. T. (1984). "On the dynamics of large eddies in the wall region of a turbulent boundary layer". In *Turbulence and Chaotic Phenomena in Fluids*. T. Tatsumi (ed). Elsevier. pp 467-473.

Mei, R. (1990). "Particle dispersion in isotropic turbulence and unsteady particle dynamics at finite Reynolds number". *Ph.D. Thesis*, University of Illinois at Urbana-Champaign.

Nezu, I., and Nakagawa, H. (1993). "Turbulence in open-channel flows". *IAHR Monograph.* A. A. Balkema, Rotterdam.

Patnaik, P. C., Vittal, N., and Pande, P. K. (1994). "Lift coefficient of a stationary sphere in gradient flow". *J. Hydr. Res.*, vol 32, No 3, pp 471-480.

Robinson, S. K. (1990). "Kinematics of turbulent boundary layer structure". *Ph.D. dissertation.* Standford Univ., Stanford, California.

van Rijn, L. C. (1984). "Sediment transport, Part II: suspended load transport". *J. Hydr. Engrg.*, vol 110, No 11, pp 1613-1641.

Wiberg, P. L., and Smith, J. D. (1985). "A theoretical model for saltating grains in water". *J. Geophysical Res.*, 90 (C4), pp 7341–7354.

Yen, B. C. (1992). "Sediment fall velocity in oscillating flow". *Water Resour. and Environ. Engrg. Res.* Report No 11. Dept. of Civil Engrg. Univ. of Virginia.

9.2 Effect of turbulence on particle saltation: ensemble averaged approach

9.2.1 Introduction

The analysis of particle saltation presented in Chapter 6 was based on the use of an equation for particle motion which was ensemble averaged over the turbulence. Nevertheless, therein only zero-order terms were retained in the resulting equation, and all the terms involving velocity fluctuations were neglected. Hence, the equation for mean particle motion used in Chapter 6 actually does not account for turbulence effects on the characteristics of saltation. It must be pointed out that this is also true of all the other existing models for particle saltation cited in Chapters 5 and 6 (e.g.,

Tsuchiya, 1969; Reizes, 1978; Hayashi and Ozaki, 1980; Murphy and Hooshiari, 1982; van Rijn, 1984; Wiberg and Smith, 1985).

The analysis of Chapter 6, indicates that first order terms involving velocity fluctuations in the ensemble averaged equation governing particle motion are of order $V'^2/\ |u_R|^2$, where the variance V'^2 is a measure of the intensity of the velocity fluctuations (being they those of the flow or the particle), and $|u_R|$ denotes the magnitude of the particle relative velocity with respect to that of the fluid. Clearly first order terms are negligible only if the particle relative velocity is sufficiently large, which occurs when the inertia of the particle is large, that is for large size particles. In this sense, it was argued that neglecting turbulence effects would induce larger errors in the case of relatively small particles, which tend to follow the flow velocity more closely than larger particles, and such errors would decrease as the particle size increases. Nevertheless, no attempt was made in Chapter 6 to asses the range of particle sizes for which turbulence effects would be negligible, or to quantify turbulence effects on the saltation of particles of smaller size.

Herein, a more formal ensemble averaging of the equations for particle saltation than that of Chapter 6 is presented. First order terms are retained, and some attempt to close the resulting equations is made by including some simple modelling of terms involving auto- and cross-correlations of flow and particle velocities.

9.2.2 Equations for particle motion

The present analysis is based on the instantaneous equation for particle motion proposed by Mei (1990) (see also Maxey and Riley, 1983) which has been already discussed in Chapter 6, and applied to the case of particle saltation. In such case, including nonlinear drag, the ith-component of this equation can be written as:

$$\varrho_s \frac{du_p{}^*{}_i}{dt^*} = (\varrho_s - \varrho)\, g_i - \frac{3}{4} \frac{C_D}{d_p} \varrho \, | u_p{}^* - u_f{}^* | \, (u_p{}^*{}_i - u_f{}^*{}_i) +$$

$$+ \frac{9}{d_p} \sqrt{\frac{\varrho\, \mu}{\pi}} \int_0^{t^*} \frac{d}{d\tau} (u_f{}^*{}_i - u_p{}^*{}_i) \frac{d\tau}{\sqrt{t^* - \tau}} +$$

$$+ \varrho\, C_m \frac{d}{dt^*} (u_f{}^*{}_i - u_p{}^*{}_i) + \varrho \frac{Du_f{}^*{}_i}{Dt^*} \qquad (9.2.1)$$

where ϱ_s and ϱ denote particle and fluid densities, respectively, C_m denotes the added mass coefficient, C_D denotes the drag coefficient, g_i denotes the component of gravitational acceleration in the ith direction, μ denotes the fluid dynamic viscosity, d_p denotes the particle diameter, t^* denotes time, τ denotes a dummy variable for integration, and $u_p{}^*{}_i$ and $u_f{}^*{}_i$ denote instantaneous particle and fluid velocity components in the ith direction, respectively. In (9.2.1), the flow velocity total derivatives correspond to:

$$\frac{du_f{}^*{}_i}{dt^*} = \frac{\partial u_f{}^*{}_i}{\partial t^*} + u_p{}^*{}_j \frac{\partial u_f{}^*{}_i}{\partial x^*{}_j} \quad , \quad \frac{Du_f{}^*{}_i}{Dt^*} = \frac{\partial u_f{}^*{}_i}{\partial t^*} + u_f{}^*{}_j \frac{\partial u_f{}^*{}_i}{\partial x^*{}_j} \qquad (9.2.2a, b)$$

where the summation convention for the subindexes applies.

For a particle that saltates in an uniform turbulent open channel flow along a bed formed by similar particles and inclined to an angle θ with respect to the horizontal, the coordinates in the normal and streamwise directions are denoted by y^* and x^*, respectively, the particle instantaneous velocity components in those directions are denoted by $v_p{}^*$ and $u_p{}^*$, respectively, and the fluid instantaneous velocity components in the same directions are denoted by $v_f{}^*$ and $u_f{}^*$, respectively.

In order to obtain an equation for the mean particle motion, averaged over the turbulence, the following experiment is considered. It is assumed that the initial conditions for particle saltation (in terms of initial location and velocity components of the saltating particle) can be controlled, such that in a series of repeated saltation events particles are released into a turbulent open channel flow with the same initial conditions. Because of the turbulence of the flow, particle trajectories and velocities vary from one experiment to the other. Ensemble averages of the particle position and velocity components can be computed over all the realizations of the saltation experiment as a function of time.

Accordingly, the instantaneous Lagrangian particle and flow velocity components during a saltation experiment at a given time t^* can be decomposed into a mean and a fluctuation, such that:

$$u_f{}^* = \overline{u}_f + u'_f \quad , \quad v_f{}^* = \overline{v}_f + v'_f \quad , \quad u_p{}^* = \overline{u}_p + u'_p \quad , \quad v_p{}^* = \overline{v}_p + v'_p \qquad (9.2.3a\text{–}d)$$

where overbars represent mean values computed over ensembles of many realizations of the particle saltation, and primes represent fluctuations with respect to the mean.

It is assumed next that at any time t^*, the variation of the particle vertical location among all the realizations of the saltation experiment is rather low. In such circumstances, the Lagrangian ensemble averaged mean flow velocity at time t^* can be approximated by the Eulerian local mean velocity at the position $y^* = \overline{y}^*\ (\ t^*\ )$, corresponding to the ensemble averaged vertical location of the particle at time t^*. Since the flow under consideration is uniform, then the mean flow velocity has only a streamwise component which is a function of $\overline{y}^*$ only, so:

$$\overline{u}_f = \overline{u}_f\ (\ \overline{y}^*\ ) \quad , \quad \overline{v}_f = 0 \qquad (9.2.4a, b)$$

Replacing (9.2.3) and (9.2.4) in (9.2.1), ensemble averaging the components of this equation in the y^* and x^* directions over many realizations of the saltation experiments and neglecting terms of order higher than $O(\ <u'_{ki}\ u'_{lj}>\ /|\overline{u}_R|^2\ )$, where the subindexes k and l indicate whether the velocity corresponds to the particle or to the flow, the subindexes i and j indicate whether the

velocity corresponds to the streamwise or vertical component, the angular brackets represent ensemble average, and $\overline{u}_R$ denotes particle slip velocity, such that:

$$|\overline{u}_R|^2 = (\overline{u}_p - \overline{u}_f)^2 + \overline{v}_p^2 \tag{9.2.5}$$

then the following system of equations is obtained:

$$\begin{aligned}(\varrho_s + C_m \varrho) \frac{d\overline{u}_p}{dt^*} = & -\frac{3}{4} \frac{C_D}{d_p} \varrho \, |\overline{u}_R| \, ((1 + \frac{(\overline{u'^2_p} - 2\,\overline{u'_p\,u'_f} + \overline{u'^2_f})}{|\overline{u}_R|^2}) (\overline{u}_p - \overline{u}_f) + \\ & + \frac{(\overline{u'_p\,v'_p} - \overline{u'_f\,v'_p} - \overline{u'_p\,v'_f} + \overline{u'_f\,v'_f})}{|\overline{u}_R|^2} \overline{v}_p) + \varrho \, C_m (\frac{\partial \overline{u}_f}{\partial y^*} \overline{v}_p + \\ & + \overline{u'_p \frac{\partial u'_f}{\partial x^*}} + \overline{v'_p \frac{\partial u'_f}{\partial y^*}}) + \varrho \frac{\partial \overline{u'_f\,v'_f}}{\partial y^*} + (\varrho_s - \varrho) \, g \, \sin\theta \\ & + \frac{9}{d_p} \sqrt{\frac{\varrho\,\mu}{\pi}} \int_0^{t^*} \frac{d}{d\tau} (\overline{u}_f - \overline{u}_p) \frac{d\tau}{\sqrt{t^* - \tau}}\end{aligned} \tag{9.2.6a}$$

$$\begin{aligned}(\varrho_s + C_m \varrho) \frac{d\overline{v}_p}{dt^*} = & -\frac{3}{4} \frac{C_D}{d_p} \varrho \, |\overline{u}_R| \, ((1 + \frac{(\overline{v'^2_p} - 2\,\overline{v'_p\,v'_f} + \overline{v'^2_f})}{|\overline{u}_R|^2}) \overline{v}_p + \\ & + \frac{(\overline{u'_p\,v'_p} - \overline{u'_f\,v'_p} - \overline{u'_p\,v'_f} + \overline{u'_f\,v'_f})}{|\overline{u}_R|^2} (\overline{u}_p - \overline{u}_f)) + \\ & + \varrho \, C_m \overline{(u'_p \frac{\partial v'_f}{\partial x^*} + v'_p \frac{\partial u'_f}{\partial y^*})} + \varrho \frac{\partial \overline{v'^2_f}}{\partial y^*} - (\varrho_s - \varrho) \, g \, \cos\theta - \\ & - \frac{9}{d_p} \sqrt{\frac{\varrho\,\mu}{\pi}} \int_0^{t^*} \frac{d\overline{v}_p}{d\tau} \frac{d\tau}{\sqrt{t^* - \tau}}\end{aligned} \tag{9.2.6b}$$

Clearly, averaging over the turbulence brings in the well known closure problem of estimating second order moments of the fluctuating velocity components. In this case, because of the interactions between particle and turbulence, there are 10 second order moments to evaluate, namely, 3 involving self interactions of the fluid velocity components: $\overline{u'^2_f}$, $\overline{u'_f\,v'_f}$, $\overline{v'^2_f}$, 3 involving self interactions of the particle velocity components: $\overline{u'^2_p}$, $\overline{u'_p\,v'_p}$, $\overline{v'^2_p}$, and 4 involving cross interactions between fluid and particle velocity components: $\overline{u'_p\,u'_f}$, $\overline{u'_p\,v'_f}$, $\overline{v'_p\,u'_f}$, $\overline{v'_p\,v'_f}$. Besides, because of terms corresponding to fluid accelerations, 4 extra cross correlation terms between particle velocities and fluid velocity derivatives appear in (9.2.6). It is assumed that these cross correlations are of rather small magnitude compared to the other terms in the equations of motion and therefore they are neglected in the subsequent analysis.

Invoking the same hypothesis as before that the variation of the particle vertical position at a given time t^* among all the realizations of the saltation experiment is relatively low, then the Lagrangian statistics of the flow velocity components can be approximated by the Eulerian local statistics of the flow velocity components at the position $y^* = \bar{y}^*\ (\ t^*\ )$, which can be estimated from experimental evidence (e.g., Nezu and Nakagawa, 1993). However, other 7 terms involving the auto- and cross-correlations of particle velocity components and the cross-correlations between particle and flow velocity still need to be estimated.

The simplest way to estimate such terms is to relate them to the known Eulerian statistics of the flow velocity components. For instance, because of particle inertia effects, it can be expected that $\overline{u'^2_f}$ is of larger magnitude than $\overline{u'^2_p}$, and it is not totally unplausible that a relationship exists between these two variables such that: $\overline{u'^2_p} = a_{up}\ \overline{u'^2_p}$, where a_{up} is a coefficient that would be generally lower than 1. Based on this approach, the following set of relationships can be proposed:

$$\overline{u'^2_p} = a_{up}\ \overline{u'^2_f} \quad , \quad \overline{v'^2_p} = a_{vp}\ \overline{v'^2_f} \quad , \quad \overline{u'_p\ v'_p} = a_{uvp}\ \overline{u'_f\ v'_f} \qquad (9.2.7a\text{-}c)$$

$$\overline{u'_p\ u'_f} = a_{upf}\ \overline{u'^2_f} \quad , \quad \overline{v'_p\ v'_f} = a_{vpf}\ \overline{v'^2_f} \qquad (9.2.7d, e)$$

$$\overline{u'_p\ v'_f} = a_{uvpf}\ \overline{u'_f\ v'_f} \quad , \quad \overline{v'_p\ u'_f} = a_{vupf}\ \overline{u'_f\ v'_f} \qquad (9.2.7f, g)$$

where the a-coefficients would be generally lower than 1.

Grouping the a-coefficients according to how they appear in (9.2.6), the following coefficients are defined:

$$a_1 = 1 + a_{up} - 2\ a_{upf} \quad , \quad a_2 = 1 + a_{uvp} - a_{uvpf} - a_{vupf} \qquad (9.2.8a, b)$$

$$a_3 = 1 + a_{vp} - 2\ a_{vpf} \qquad (9.2.8c)$$

Since it is expected that the a-coefficients would take values in the range 0 to 1, then the coefficients a_1, a_2, and a_3 would take values in the range –1 to 2. Nevertheless, most probably they would not take values too close to –1 or 2, since that would require extremely high values of the correlations involving cross interactions between particle and fluid velocity components and too low values of the correlations involving self interactions between particle velocity components, or vice versa. It can also be speculated that the coefficients a_1, a_2, and a_3 would all take similar values, possibly in the range 0 to 1.

It is apparent that the values of the a-coefficients defined in (9.2.7) would be functions of the inertia of the particle, such that big or heavy particles would not tend to follow flow velocity fluctuations and therefore in such cases the a-coefficients would tend to 0, and on the other hand, small light particles that follow most of the flow velocity fluctuations spectrum, would tend to have

values of the α-coefficients close to 1. Because of the combinations of the α-coefficients in the definitions (9.2.8) for α_1, α_2, and α_3, particles with large inertia would tend to have values for these parameters close to 1, while for particles with small inertia they would take values more close to 0.

It is important to point out that because of the nonlinearity of the drag term appearing in (9.2.1), the anisotropy and heterogeneity of the open channel flow field, and also due to the intrinsic unsteadiness of the particle motion during saltation events, a Fourier analysis of the equation governing particle velocity (such as those carried out by Tchen, 1947; Hinze, 1959; Reeks, 1977; Pismen and Nir, 1978; Rizk and Elgobashi, 1985; Mei et al., 1991, and others) is not possible. Such an analysis typically yields a relationship between the particle power spectrum and the Lagrangian power spectrum of the flow velocity. Usually, the independence approximation proposed by Corrsin (1959) is invoked to relate the Lagrangian statistics of flow velocity with the corresponding Eulerian statistics, which are easier to measure (see also Weinstock, 1976). The latter is a much formal procedure than the rather crude approximation introduced in (9.2.6) to relate Lagrangian and Eulerian statistics of flow velocity, however because of the reasons mentioned above it is not applicable to the present situation.

By introducing (9.2.7) and (9.2.8) in (9.2.6) the following system of equations is obtained:

$$\frac{du_p}{dt} = -\frac{3}{4}\,\alpha\,C_D\,|u_R|\,\left(\left(1+\alpha_1\frac{u'^2}{|u_R|^2}\right)(u_p-u_f)+\alpha_2\frac{u'v'}{|u_R|^2}\,v_p\right)+\alpha\,C_m\frac{du_f}{dy}\,v_p+$$

$$+\alpha\,\frac{du'v'}{dy}+\frac{\alpha\,\sin\theta}{\tau_*}+9\,\frac{\alpha}{\sqrt{R_p}\,\tau_*^{1/4}}\,\frac{1}{\sqrt{\pi}}\int_0^t\frac{d}{d\tau}(u_f-u_p)\,\frac{d\tau}{\sqrt{t-\tau}} \qquad (9.2.9a)$$

$$\frac{dv_p}{dt} = -\frac{3}{4}\,\alpha\,C_D\,|u_R|\,\left(\left(1+\alpha_3\frac{v'^2}{|u_R|^2}\right)v_p+\alpha_2\frac{u'v'}{|u_R|^2}\,(u_p-u_f)\right)+\alpha\,\frac{dv'^2}{dy}-$$

$$-\frac{\alpha\,\cos\theta}{\tau_*}-9\,\frac{\alpha}{\sqrt{R_p}\,\tau_*^{1/4}}\,\frac{1}{\sqrt{\pi}}\int_0^t\frac{d}{d\tau}(v_p)\,\frac{d\tau}{\sqrt{t-\tau}} \qquad (9.2.9b)$$

which has been made dimensionless using the following scaling:

$$(x^*,\,y^*)=d_p\,(x,\,y) \quad , \quad (\overline{u}_p,\,\overline{v}_p)=u_*\,(u_p,\,v_p) \qquad (9.2.10a,\,b)$$

$$t^*=(d_p/u_*)\,t \quad , \quad \overline{u}_f=u_*\,u_f \qquad (9.2.10c,\,d)$$

Dimensionless parameters appearing in (9.2.9) are defined as:

$$\alpha=(1+R+C_m)^{-1} \quad , \quad R=(\varrho_s/\varrho-1) \qquad (9.2.11a,\,b)$$

$$\tau_*=\frac{u_*^2}{g\,R\,d_p} \quad , \quad R_p=\sqrt{R\,g\,d_p^{\,3}}/\nu \qquad (9.2.11c,\,d)$$

and the dimensionless correlations of flow velocity components are defined as:

$$u'^2 = \overline{u'^2}/u_*^2 \quad , \quad v'^2 = \overline{v'^2}/u_*^2 \quad , \quad u'v' = \overline{u'\,v'}/u_*^2 \qquad (9.2.12a, b)$$

Finally, (9.2.9) is complemented with the Lagrangian equations for the particle trajectory:

$$u_p = \frac{dx_p}{dt} \quad , \quad v_p = \frac{dy_p}{dt} \qquad (9.2.13a, b)$$

where x_p and x_p denote dimensionless coordinates defining the ensemble averaged position of the particle centroid, made dimensionless as in (9.2.10).

9.2.3 Modelling flow velocity statistics in open channel flow

As already pointed out, it is assumed herein that the Lagrangian statistics of flow velocity components at time t can be approximated by the corresponding Eulerian statistics at the location $y = y_p\ (\ t\ )$. This is based in the hypothesis that there is not much variation in the particle vertical position at time t among all the realizations of the saltation experiment.

The Eulerian dimensionless streamwise mean flow velocity, u_f, in turbulent open channel flow is estimated using the semi-logarithmic law given by:

$$u_f = \frac{1}{\varkappa}\ \ln\ (\ y\ ) + B \qquad (9.2.14)$$

where $\varkappa$ denotes von Karman's constant taken to be equal to 0.4, the roughness height, k_s, has been taken to be equal to the particle diameter, and the coefficient B is equal to 8.5 for fully rough flows, and is a function of $k_{s+} = u_*\ k_s/\nu$, where ν denotes the fluid kinematic viscosity, for transitionally rough flows (see Chapter 3).

Nezu and Nakagawa (1993) propose empirical and semi-empirical relations to estimate second order moments of the flow velocity fluctuations, u'^2, v'^2, and $u'v'$, in open channel flows, which are given in general as a function of the dimensionless variables $y' = y*/h$, where h denotes the flow depth, and $y_+ = y*\ u_*/\nu$, which corresponds to the vertical coordinate made dimensionless with wall units, that is with the length scale ν/u_*.

By force balance considerations, the following relation can be written for a sufficiently wide open channel flow:

$$u_*^2 = g\ sin\ \theta\ h \qquad (9.2.15)$$

which can be used to relate the dimensionless coordinates y' and y, such that:

$$y' = y\ \frac{sin\ \theta}{R\ \tau_*} \qquad (9.2.16)$$

On the other hand, it is easy to see that the dimensionless coordinates y_+ and y are related by:

$$y_+ = y\, R_p \sqrt{\tau_*} \tag{9.2.17}$$

Based on (9.2.16) and (9.2.17), and following Nezu and Nakagawa (1993), the dimensionless second order moments of the flow velocity fluctuations can be estimated as:

$$\sqrt{u'^2} = 2.30 \exp\left(- y \frac{\sin\theta}{R\,\tau_*} \right) \tag{9.2.18a}$$

$$\sqrt{v'^2} = 1.27 \exp\left(- y \frac{\sin\theta}{R\,\tau_*} \right) \tag{9.2.18b}$$

$$u'v' = -\left(\left(1 - y \frac{\sin\theta}{R\,\tau_*} \right) - \frac{1}{\varkappa\, y\, R_p \sqrt{\tau_*}} \right) \tag{9.2.18c}$$

It is necessary to point out that the relationships (9.2.17) are valid for smooth flows at values y_+ larger than about 20, however according to Nezu and Nakagawa (1993) those same relationships are valid for transitionally rough flows at locations y_+ somewhat larger than about k_{s+}, which implies that the roughness of the channel bottom has a rather localized effect on the structure of the turbulence in open channel flows. This was verified in Chapter 3, particularly for equation (9.2.18a), using hot-film measurements of streamwise flow velocity fluctuations. Hence, sufficiently away from the channel bottom the vertical structure of the turbulence appears to be independent of the surface roughness of the channel (see also Raupach, 1981; Raupach et al., 1991). According to this discussion, it is apparent that the relationships (9.2.18) can be applied to the present model of saltation as long as the particles have their centroid located at an elevation higher than about $y_+ =$ 20. This imposes a lower limit to the dimensionless size of the particle of about 40 wall units, that is, the particle Reynolds number defined as:

$$Re_{p_*} = d_p\, u_*/\nu = R_p \sqrt{\tau_*} \tag{9.2.19}$$

should be larger than about 40.

9.2.4 Effect of turbulence on particle saltation

In order to analyze the effect of turbulence on particle saltation, a few simulations using the model outlined in previous sections are run for given initial conditions and different values of the coefficients α_1, α_2, and α_3. This is done by solving (9.2.9) and (9.2.13) numerically using a fourth-order Runge-Kutta scheme as in Chapter 6. Also, the treatment of the Basset integral in (9.2.9) is identical to that explained in detail in Chapter 6.

As in Chapter 6, the following values are used in the simulations: $C_m = 0.5$, $R = 1.65$ (natural sediment), and C_D is approximated by the relationship proposed by Yen (1992) for free-falling spheres:

$$C_D = \frac{24}{Re} \left(1 + 0.15 \sqrt{Re} + 0.017\, Re \right) - \frac{0.208}{1 + 10^4\, Re^{-0.5}} \qquad (9.2.20)$$

where $Re = |\overline{u}_R|\, d_p / \nu$.

Results obtained from the simulation of particle saltation are presented in Fig. 9.2.1, for the initial conditions $x_p(0) = 0$, $y_p(0) = 0.5$, $u_p(0) = 3.5$, $v_p(0) = 1.8$, and the values of the parameters $R_p = 50$, 500, and 5000, $\tau_* = 0.1$, and $\tan\theta = 0.001$. The initial position corresponds to a particle lying on the bed, while the initial velocities correspond to values typically observed in the experimental study of saltation reported in Chapter 5. The takeoff angle resulting from the initial particle velocity has a value of about 27°, which also corresponds to a value typically observed for this variable as reported in Chapter 5. In Fig. 9.2.1, the particle trajectory computed by neglecting all terms involving velocity fluctuations in (9.2.9) (as done previously in Chapter 6) is plotted together with the trajectories resulting form the computations made for the conditions $a_1 = a_2 = a_3 = -0.5$, 1.0, and 1.5. The results for the condition $a_1 = a_2 = a_3 = 0$ were not plotted therein because they are very close to those obtained by neglecting all turbulence effects in (9.2.9) (these two sets of results are not identical though, because of the existence of terms involving flow velocity fluctuations that do not vanish when the coefficients a_1, a_2, and a_3 all go to zero).

In Fig. 9.2.2 results similar to those plotted in Fig. 9.2.1 are shown. Therein, all conditions and parameters are the same to those used for the results shown in Fig. 9.2.1 except that the value $R_p = 50$ was held constant throughout and τ_* took the values 0.05, 0.1, and 0.15.

As seen in Figs. 9.2.1 and 9.2.2, the results obtained for different values of $a_1 = a_2 = a_3$ indicate, as expected, that the effect of turbulence on particle saltation is larger as R_p decreases (the particle size decreases) or τ_* (a measure of the turbulence intensity relative to the particle size) increases. Apparently, the turbulence of the flow has a negligible effect on the mean particle trajectory for values of R_p larger than 500. It seems that, in general, values of $a_1 = a_2 = a_3 = -0.5$ tend to increase the height and length of the saltation trajectory with respect to that obtained by neglecting turbulence effects, while values $a_1 = a_2 = a_3 = 1.0$ and 1.5 tend to decrease the height of the jumps, and this effect is larger as the values of $a_1 = a_2 = a_3$ increase. In the cases of $a_1 = a_2 = a_3 = 1.0$ and 1.5 not much difference is observed in the length of the saltations.

It is interesting to note that in the case of the solution obtained for the values $R_p = 50$, $\tau_* = 0.15$, and $a_1 = a_2 = a_3 = 1.5$, the final part of the particle trajectory appears to bend outwards and to become almost horizontal, defining a trend that appears to be totally different to that of all other trajectories computed. An analysis of the numerical results reveals that what is happening in this particular case is that the particle slip velocity in the final part of the trajectory is getting too small, which implies that the particle is trying to follow the flow velocity. Since the system of ensemble averaged

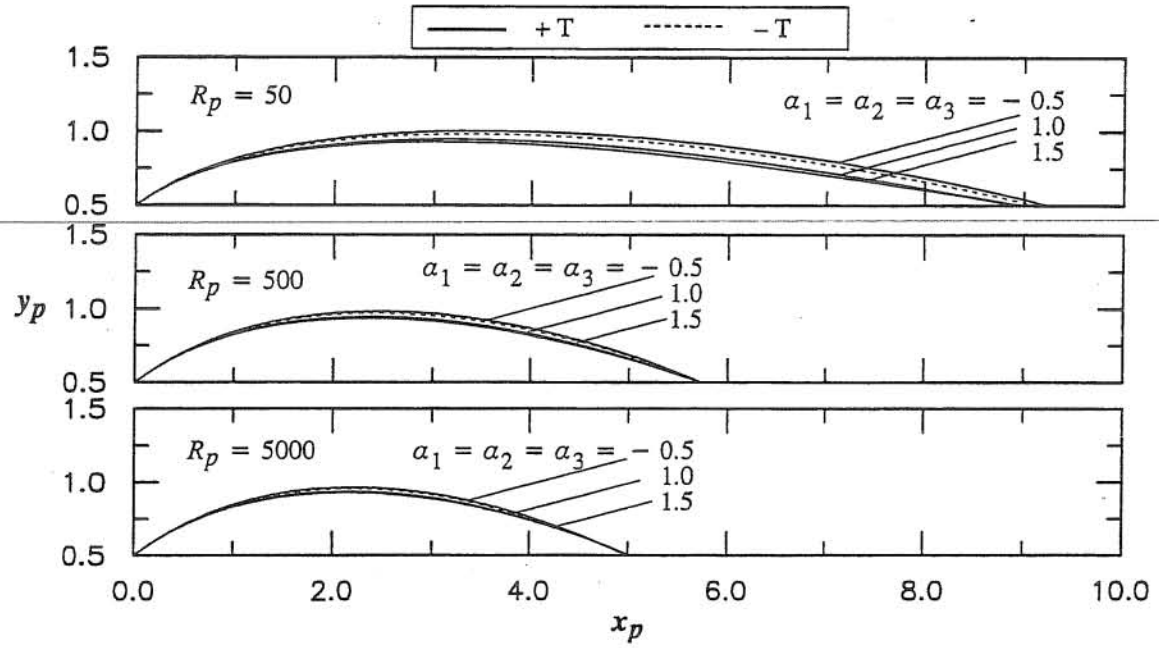

Fig. 9.2.1 Effect of turbulence on particle saltation, for different values of the coefficients $a_1 = a_2 = a_3$, as a function of R_p, for the values of this parameter: 50, 500, 5000. All other control parameters are held constant with values: $\tau_* = 0.10$, $R = 1.65$, $\tan\theta = 0.001$. Initial conditions are $x_p = 0$, $y_p = 0.5$, $u_p = 3.5$, $v_p = 1.8$. In the legend, T denotes turbulence terms in the equation for particle motion, and the symbols + and – indicate that those terms are included or neglected in the simulation, respectively.

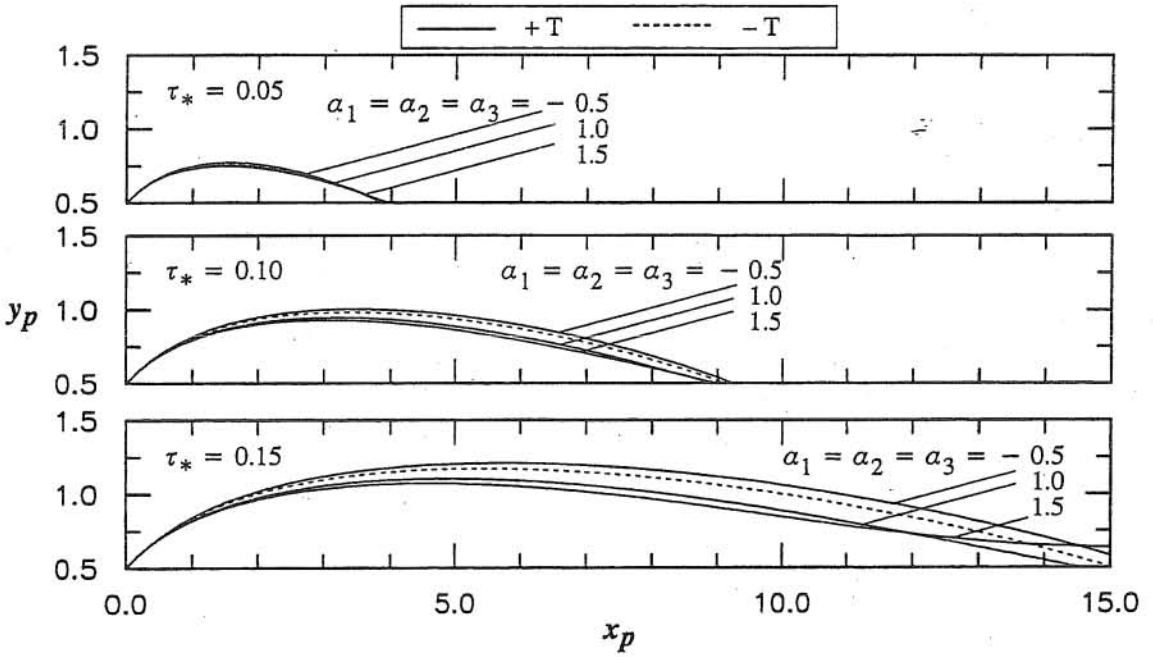

Fig. 9.2.2 Effect of turbulence on particle saltation, for different values of the coefficients $a_1 = a_2 = a_3$, as a function of τ_*, for the values of this parameter: 0.05, 0.10, 0.15. All other control parameters are held constant with values: $R_p = 50$, $R = 1.65$, $\tan\theta = 0.001$. Initial conditions and all other symbols are the same as in Fig. 9.2.1.

equations (9.2.9) is accurate to order $O(\ < u'_{ki}\ u'_{lj} > /|\overline{u}_R|^2\ )$, the expansions involved in its derivations clearly break down for sufficiently small values of $|u_R|$. Therefore, it seems that if the values of the coefficients a_1, a_2, and a_3 all happen to be similar and too high (say closer to about 1.5), then the present analysis may be not valid for too high values of τ_*, and too low values of R_p.

Results for different values of the parameters a_1, a_2, and a_3 in the range 0 to 2 are presented in Fig. 9.2.3 for the same initial conditions used for the results shown in Figs. 9.2.1 and 9.2.2, and the values $R_p = 50$, $\tau_* = 0.1$. These results indicate that due to turbulence effects, and depending on the values of a_1, a_2, and a_3, the saltation length can be reduced as much as 13%, or increased as much as 11% with respect to that obtained by neglecting turbulence effects. On the other hand, the effect of turbulence seems to slightly reduce the saltation height with respect to that obtained by neglecting turbulence in all cases shown in Fig. 9.2.3. In fact, the reductions in saltation height observed in such figure were in general smaller than 6%.

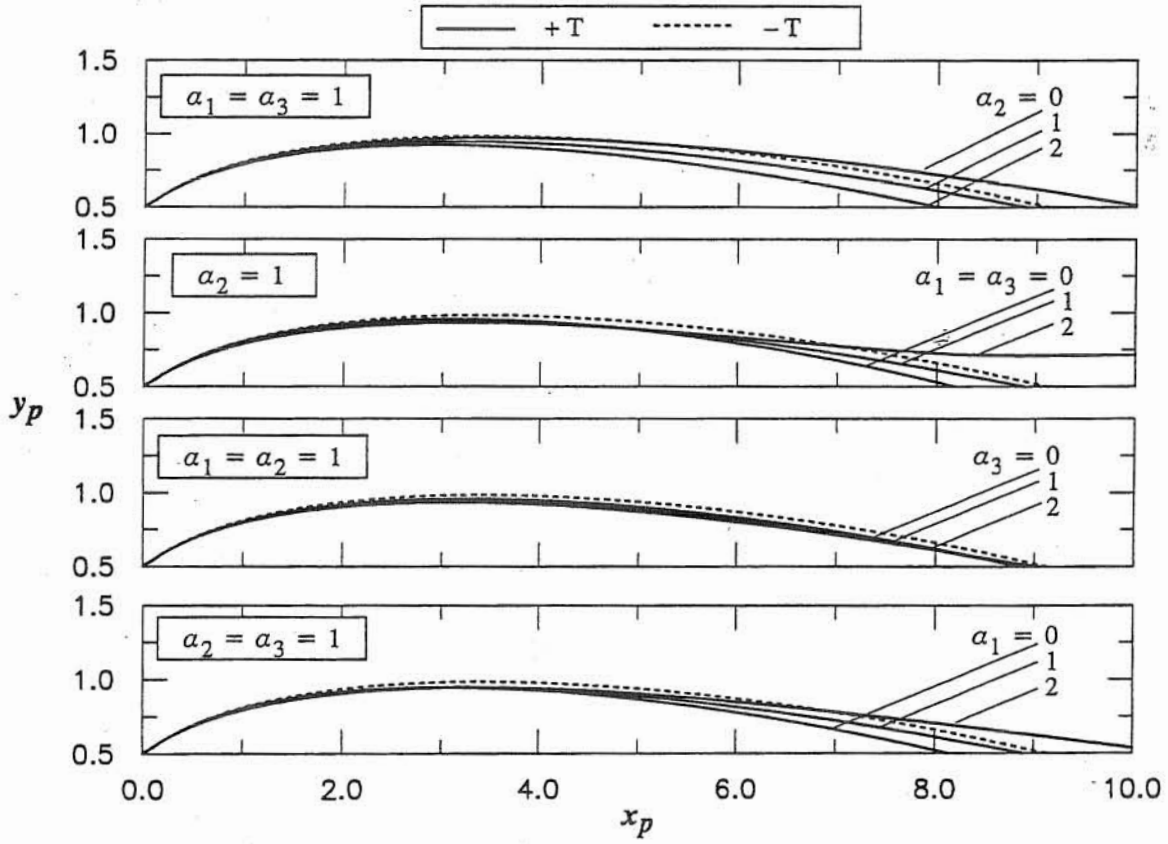

Fig. 9.2.3 Effect of turbulence on particle saltation, for different values of the coefficients a_1, a_2, a_3. All other control parameters are held constant with values: $R_p = 50$, $\tau_* = 0.10$, $R = 1.65$, $\tan\theta = 0.001$. Initial conditions and all other symbols are the same as in Fig. 9.2.1.

It is also observed in Fig. 9.2.3 that for the values $a_1 = a_3 = 2$, $a_2 = 1$, the final part of the simulated particle trajectory becomes almost horizontal which is due to a drop in the particle slip velocity as discussed previously. In such case the approximations used in deriving (9.2.9) break down, which renders that particular solution invalid.

From the results shown in Figs. 9.2.1 to 9.2.3 it is clear that for values of R_p lower than about 500 and values of τ_* larger than about 0.05, the turbulence of the flow can affect the characteristics of particle saltation. Of course, since values of the coefficients a_1, a_2, and a_3 are unknown, and so is their dependence on the parameters governing particle saltation and even their behavior during the saltation events (so far they have been assumed to be constants), no more precise conclusions can be derived from the present analysis. Besides, it is apparent that approximations involved in deriving (9.2.9) break down for certain conditions and parameters governing the saltation motion, which occurs when the particle slip velocity becomes relatively small.

Since turbulence effects are most important for small particles, which generally have relatively small slip velocities, and given the uncertainties regarding the a-coefficients, it seems that the present approach does not lead too far in the analysis of turbulence effects on particle saltation. In the next section, an alternative analysis based on a random walk model for particle motion is proposed which allows to improve the present results and conclusions.

9.2.5 Conclusions

An equation for the mean particle motion, averaged over the turbulence, during saltation events was derived which is accurate to order $O(< u'_{ki}\, u'_{lj} > / |\overline{u}_R|^2)$. This equation requires the estimation of auto- and cross-correlations between particle and flow fluctuation velocity components. Such correlations are evaluated by introducing coefficients that relate statistics of particle velocity with those of the flow. Lagrangian statistics of the flow velocity are approximated with corresponding Eulerian statistics evaluated at the location given by mean particle trajectory.

Saltation trajectories were simulated by numerically solving the governing equations for particle motion. The results obtained indicate that the turbulence of the flow does seem to affect the characteristics of saltation trajectories, in particular for values of R_p lower than about 500 and values of τ_* larger than about 0.05. For different values of the coefficients a_1, a_2, and a_3 within the range of physical relevance of these parameters, it was found that due to turbulence effects the saltation length can be reduced as much as 13%, or increased as much as 11% with respect to that obtained by neglecting turbulence effects. Similarly, the effect of turbulence seems to reduce as much as 6% the saltation height with respect to that obtained by neglecting turbulence.

It was found that for relatively low values of R_p and certain values of a_1, a_2, and a_3, the particle tends to accelerate in the final part of the saltation trajectory so that its slip velocity gets small enough

as to render the approximations involved in the derivation of the ensemble averaged equations for particle motion inaccurate. In those cases the model for particle saltation predicts trajectories that are almost horizontal.

Turbulence effects are most important for small particles, which generally have relatively small slip velocities. For this reason, it is expected that the ensemble averaged equations for particle motion proposed herein are not very accurate in such case. Also, given the uncertainties regarding evaluation of the coefficients α_1, α_2, and α_3, it seems that the present approach does not lead too far in the analysis of turbulence effects on particle saltation.

9.2.6 References

Corrsin, S. (1959). "Progress report on some turbulent diffusion research". *Advances in Geophysics* 6, pp 161-164.

Hayashi, T., and Ozaki, S. (1980). "On the unit step length of saltation of sediment particles in the bed-load layer". *Third International Symposium on Stochastic Hydraulics*, IAHR. Tokyo, Japan.

Hinze, O (1975). "Turbulence". McGraw-Hill.

Maxey, M. R., and Riley, J. J. (1983). "Equation of motion for a small rigid sphere in a nonuniform flow". *Phys. Fluids*, 26 (4), pp 883-889.

Mei, R., Adrian, R. J., and Hanratty, T. J. (1991). "Particle dispersion in isotropic turbulence under Stokes drag and Basset force with gravitational settling". *J. Fluid Mech.*, vol 225, pp 481-495.

Mei, R. (1990). "Particle dispersion in isotropic turbulence and unsteady particle dynamics at finite Reynolds number". *Ph.D. Thesis*, University of Illinois at Urbana-Champaign.

Murphy, P. J., and Hooshiari, H. (1982). "Saltation in water dynamics". *J. Hydraul. Div.*, ASCE, 108 (HY11), pp 1251-1267.

Nezu, I., and Nakagawa, H. (1993). "Turbulence in open-channel flows". *IAHR Monograph.* A. A. Balkema, Rotterdam.

Pismen L. M., and Nir, A. (1978). "On the motion of suspended particles in stationary homogeneous turbulence". *J. Fluid Mech.*, vol 84, part 1, pp 193-206.

Raupach, M. R., Antonia, R. A., and Rajagopalan, S. (1991). "Rough-wall turbulent boundary layers". *Appl. Mech. Rev.*, vol 44, no 1.

Raupach, M. R. (1981). "Conditional statistics of Reynolds stress in rough-wall and smooth-wall turbulent boundary layers". *J. Fluid Mech.*, vol 108, pp 363-382.

Reeks, M. W. (1977). "On the dispersion of small particles suspended in an isotropic turbulent fluid". *J. Fluid Mech.*, vol 83, part 3, pp 529-546.

Reizes, J. A. (1978). "Numerical study of continuous saltation". *J. Hydr. Div.*, ASCE, 104 (HY9), pp 1303-1321.

Rizk, M. A., and Elgobashi, S. E. (1985). "The motion of a spherical particle suspended in a turbulent flow near a plane wall". *Phys. Fluids* 28 (3), pp 806-817.

Tchen, C. M. (1947). "Mean value and correlations problems connected with the motion of small particles suspended in a turbulent fluid". *Ph.D. Thesis*, Delft.

Tsuchiya, Y. (1969). "On the mechanics of saltation of a spherical sand particle in a turbulent stream". 13th IAHR Congress. Kyoto, Japan.

van Rijn, L. C. (1984). "Sediment transport, Part II: suspended load transport". *J. Hydr. Engrg.*, vol 110, No 11, pp 1613-1641.

Weinstock, J. (1976). "Lagrangian-Eulerian relation and the independence approximation". *Phys. Fluids* 9 (11), pp 1702-1711.

Wiberg, P. L., and Smith, J. D. (1985). "A theoretical model for saltating grains in water". *J. Geophysical Res.*, 90 (C4), pp 7341–7354.

Yen, B. C. (1992). "Sediment fall velocity in oscillating flow". *Water Resour. and Environ. Engrg. Res.* Report No 11. Dept. of Civil Engrg. Univ. of Virginia.

9.3 Effect of turbulence on particle saltation: random walk model

9.3.1 Introduction

The analysis of particle saltation presented in Chapter 6 did not take into account turbulent effects on this phenomenon. Therein an equation for particle motion averaged over the turbulence was derived but only zero-order terms were retained and all terms involving velocity fluctuations were neglected. The analysis of previous section intended to include the effect of turbulence on the equation for the mean particle motion by retaining first-order terms, that is, auto- and cross-correlations between fluid and particle velocities. Such analysis revealed that turbulence affects the characteristics of the mean saltation trajectory, particularly for particles of relatively small size. Nonetheless, it was found that for too small particles the first order terms, which are inversely proportional to the particle slip velocity, blow up as this velocity becomes smaller, and therefore the equation governing particle motion cease to be valid in those circumstances. Furthermore, the analysis requires the evaluation of cross correlations between particle and fluid velocities that are difficult to estimate, which renders this approach uncertain.

Herein a different approach to analyze turbulent effects on particle saltation is developed. This is based on the use of a random walk model to simulate two-dimensional turbulent flow fields forcing the instantaneous equations governing particle motion. Particle trajectories are simulated

by taking into account the crossing-trajectories effect (i.e. the loss of correlation between the particle velocity and that of the turbulent eddy initially driving the particle motion, which occurs before the eddy loses coherence, due to gravity effects) following the methodology proposed by Zhuang et al. (1989). This approach allows to perform numerical experiments in which a large number of particles are released into an open channel flow field with identical initial conditions, in order to generate an ensemble of realizations of particle saltation. Statistics of the characteristics of the saltation trajectories are computed over all the realizations of this process, which are used to evaluate the effect of turbulence on particle saltation.

9.3.2 Trajectory simulation model for heavy particle motion in turbulent flow

In the case of a heavy particle moving in a turbulent flow field, the particle motion is driven by the fluid velocity as well as by gravity. According to Zhuang et al. (1989), because the heavy particle tends to slip through the flow field, the driving fluid velocity undergoes abrupt, random changes as the particle encounters new eddies. Between these changes, while the particle passes through a given eddy, the driving fluid velocity remains correlated along the particle path. Eventually, the particle loses temporal as well as spatial correlation with the eddy that was originally driving its motion and a new eddy is encountered with an abrupt change in the flow velocity field surrounding the particle. This process, in which the particle "falls" from the eddy before it loses coherence, has been called crossing-trajectories effect (see also Lumley, 1978; Wells and Stock, 1983).

Zhuang et al. (1989) propose a methodology to compute heavy particle trajectories taking into account the crossing-trajectories effect. They apply their method to the simulation of dispersion of heavy particles in grid turbulence, with values of the ratio of particle to fluid density exceeding 1000. Herein their methodology is adapted to the case of sediment particle saltation in turbulent open channel flow, mainly by introducing a more complete equation for particle motion and by taking into account the particular characteristics of the turbulent flow under consideration.

The basic idea behind Zhuang et al.'s methodology is explained next. It is assumed that initially, at time t_0 *, a particle and the fluid parcel that is driving its motion (for simplicity called an "eddy") coincide at position P_0 (see Fig. 9.3.1). At time t_1 *, the particle moved to position P_{p1} (slipping downwards due to the effect of gravity in the example shown in Fig. 9.3.1), while the eddy moved to position P_{f1}. As time goes by, particle and eddy move in their own paths, however the fluid velocity driving the particle motion (that of the fluid parcel surrounding the particle at each time) remains correlated with that of the eddy. This is true as long as the separation between the particle and the eddy does not exceed a length scale, L *, characterizing the size of the eddy. In the example shown in Fig. 9.3.1, this occurs at time t_3 *, when the particle is at position P_{p3}, the eddy

is at position P_{f3}, and the distance R^* between particle and eddy is larger than L^*. It is assumed that at this moment the particle encounters a new eddy, with a new velocity field that is not correlated with that of the previous eddy. In this situation the positions of particle and eddy coincide again, and the process outlined above repeats itself.

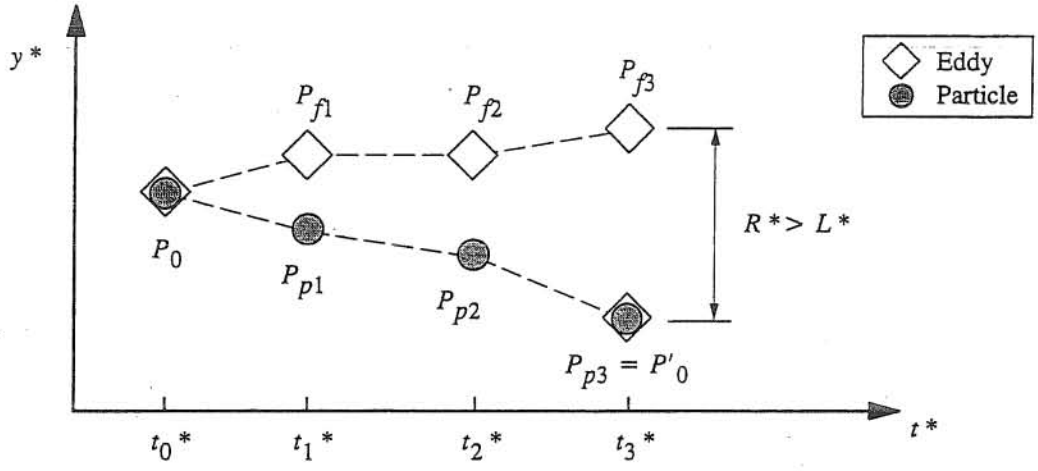

Fig. 9.3.1 Schematic view of particle and eddy trajectories. For clarity, motion is shown only in the vertical direction, y^*. In the example shown, the particle is slipping downwards with respect to the initial eddy. At time t_0^* particle encounters an eddy, at time t_3^* particle loses correlation with the eddy and encounters a new one.

Assuming two-dimensional open channel flow, the Lagrangian equations governing the motion of fluid parcels, are given by:

$$u_f = \frac{dx_f}{dt} \quad , \quad v_f = \frac{dy_f}{dt} \tag{9.3.1a, b}$$

which have been made dimensionless using the following scaling,

$$(x_f^* , y_f^*) = d_p (x_f , y_f) \quad , \quad (u_f^* , v_f^*) = u_* (u_f , v_f) \tag{9.3.2a, b}$$

where x_f and y_f denote dimensionless streamwise and vertical coordinates of the fluid parcel, respectively, u_f and v_f denote dimensionless instantaneous streamwise and vertical flow velocity components, respectively, u_* denotes the flow shear velocity, and d_p denotes the size of the heavy particle.

The instantaneous dimensionless flow velocity components can be decomposed into a local Eulerian mean and a fluctuation such that:

$$u_f = \overline{u}_f + u'_f \quad , \quad v_f = \overline{v}_f + v'_f \tag{9.3.3a, b}$$

where the overbar indicates the mean and the prime indicates the fluctuation. In uniform open channel flow it can be assumed that: $\overline{u}_f = \overline{u}_f (y)$, where y denotes the vertical coordinate made dimensionless with d_p, and $\overline{v}_f = 0$.

To determine the trajectory of the initial eddy, (9.3.1) and (9.3.3) are used, which requires the knowledge of time series of the streamwise and vertical velocity fluctuations. These are generated synthetically using Markov chains. Following Zhuang et al. (1989) and Legg and Raupach (1982) the dimensionless flow velocity fluctuation components associated with the motion of the initial eddy, u'_f and v'_f, are generated using:

$$u'_f{}^{(k)} = \sqrt{\overline{u'^2_f}}\; q_{fu}{}^{(k)} \qquad , \qquad v'_f{}^{(k)} = \sqrt{\overline{v'^2_f}}\; q_{fv}{}^{(k)} \qquad \text{(9.3.4a, b)}$$

where the superindex k denotes the time level in the Markov chain, $\overline{u'^2_f}$ and $\overline{v'^2_f}$ denote the Lagrangian variance of the dimensionless streamwise and vertical components of the flow velocity fluctuations, respectively, and the variables q_{fu} and q_{fv} are given by:

$$q_{fu}{}^{(k+1)} = a_{fu}\, q_{fu}{}^{(k)} + \mu_{fu}{}^{(k+1)} \qquad , \qquad q_{fv}{}^{(k+1)} = a_{fv}\, q_{fv}{}^{(k)} + \mu_{fv}{}^{(k+1)} + F \qquad \text{(9.3.5a, b)}$$

with:

$$a_{fu} = \exp (- \Delta t / T_{Lu}) \qquad , \qquad a_{fv} = \exp (- \Delta t / T_{Lv}) \qquad \text{(9.3.6a, b)}$$

$$\mu_{fu}{}^{(k)} = \sqrt{1 - a^2_{fu}}\; r_u{}^{(k)} \qquad , \qquad \mu_{fv}{}^{(k)} = \sqrt{1 - a^2_{fv}}\; r_v{}^{(k)} \qquad \text{(9.3.7a, b)}$$

where Δt denotes the dimensionless time step used in the Markov chain, T_{Lu} and T_{Lv} denote the dimensionless Lagrangian integral time scale for the flow streamwise and vertical velocity components, respectively, r_u and r_v denote Gaussian random numbers having zero mean and unit variance which are assumed to be independent of each other, and F denotes a correction term that takes into account the effect of the vertical gradient in the variance of the Eulerian vertical velocity of the open channel flow under consideration. Terms involving time have been made dimensionless with the time scale d_p/u_*.

According to Legg and Raupach (1982), the vertical gradient in the variance of the Eulerian vertical velocity induces a mean vertical pressure gradient which affects the motion of fluid parcels generating a mean vertical drift velocity on them. Legg and Raupach indicate that a correction term F should be included in the Markov chain to account for this effect. Not doing so, results in the random walk simulation predicting the accumulation of fluid particles in regions of low turbulence intensity (Wilson et al., 1983). Different correction terms have been proposed. Among them, Legg and Raupach's (1982) is given by:

$$F = (1 - a_{fv}) T_{Lv} \frac{1}{(\overline{v'^2_{fE}})^{1/2}} \frac{d\overline{v'^2_{fE}}}{dy} \tag{9.3.8}$$

where $\overline{v'^2_{fE}}$ denotes the Eulerian variance of the flow dimensionless vertical velocity component, Wilson et al. (1983) proposes:

$$F = (1 - a_{fv}) T_{Lv} \frac{d(\overline{v'^2_{fE}})^{1/2}}{dy} \tag{9.3.9}$$

and similarly, Ley and Thomson (1983) give:

$$F = \Delta t \frac{1}{(\overline{v'^2_{fE}})^{1/2}} \frac{d\overline{v'^2_{fE}}}{dy} \tag{9.3.10}$$

One way to measure the effectivity of the proposed forms for the correction term F, is to analyze the vertical concentration distribution of fluid particles predicted by the random walk model. At any time, such distribution should be uniform. Not including F results in the model predicting a higher concentration of fluid particles in the regions of the flow with low values of $\overline{v'^2_{fE}}$. The most efficient correction term F corresponds to that which makes the vertical concentration distribution of fluid particles most uniform. This analysis is done herein and is presented in next sections.

To determine the solid particle trajectory, Lagrangian equations governing particle motion are used. Following Mei (1990) and including nonlinear drag, the instantaneous dimensionless particle velocity components are given by (see discussion of this equation in Chapter 6, and also in Section 9.2 this chapter):

$$\frac{du_p}{dt} = \frac{a \ sin \ \theta}{\tau_*} - \frac{3}{4} a \ C_D \ |u_R| \ (u_p - u_{fp}) + a \ C_m \frac{du_{fp}}{dt} + a \frac{Du_{fp}}{Dt} + $$

$$+ 9 \frac{a}{\sqrt{R_p} \ \tau_*^{1/4}} \frac{1}{\sqrt{\pi}} \int_0^t \frac{d}{d\tau} (u_{fp} - u_p) \frac{d\tau}{\sqrt{t - \tau}} \tag{9.3.11a}$$

$$\frac{dv_p}{dt} = - \frac{a \ cos \ \theta}{\tau_*} - \frac{3}{4} a \ C_D \ |u_R| \ (v_p - v_{fp}) + a \ C_m \frac{dv_{fp}}{dt} + a \frac{Dv_{fp}}{Dt} + $$

$$+ 9 \frac{a}{\sqrt{R_p} \ \tau_*^{1/4}} \frac{1}{\sqrt{\pi}} \int_0^t \frac{d}{d\tau} (v_{fp} - v_p) \frac{d\tau}{\sqrt{t - \tau}} \tag{9.3.11b}$$

where u_p and v_p denote dimensionless instantaneous streamwise and vertical particle velocity components, respectively, which have been made dimensionless with u_*, $sin \ \theta$ denotes the slope of the channel, $|u_R|$ denotes the magnitude of the dimensionless slip velocity, which is given by:

$$|u_R|^2 = (u_p - u_{fp})^2 + (v_p - v_{fp})^2 \qquad (9.3.12)$$

u_{fp} and v_{fp} denote dimensionless instantaneous streamwise and vertical components of the flow velocity driving the particle, respectively, C_m denotes the added mass coefficient, and C_D denotes the drag coefficient. Dimensionless parameters appearing in (9.3.11) are defined as:

$$\alpha = (1 + R + C_m)^{-1} \quad , \quad R = (\varrho_s / \varrho - 1) \qquad (9.3.13a, b)$$

$$\tau_* = \frac{u_*^2}{g\, R\, d_p} \quad , \quad R_p = \sqrt{R\, g\, d_p^{\,3}}\, /\nu \qquad (9.3.13c, d)$$

where ϱ_s and ϱ denote the density of the particle and the fluid respectively, g denotes gravitational acceleration, and ν denotes fluid kinematic viscosity.

In (9.3.11), the flow dimensionless velocity total derivatives correspond to:

$$\frac{du_{fp}}{dt} = \frac{\partial u_{fp}}{\partial t} + u_p \frac{\partial u_{fp}}{\partial x} + v_p \frac{\partial u_{fp}}{\partial y} \quad , \quad \frac{Du_{fp}}{Dt} = \frac{\partial u_{fp}}{\partial t} + u_{fp} \frac{\partial u_{fp}}{\partial x} + v_{fp} \frac{\partial u_{fp}}{\partial y} \qquad (9.3.14a, b)$$

$$\frac{dv_{fp}}{dt} = \frac{\partial v_{fp}}{\partial t} + u_p \frac{\partial v_{fp}}{\partial x} + v_p \frac{\partial v_{fp}}{\partial y} \quad , \quad \frac{Dv_{fp}}{Dt} = \frac{\partial v_{fp}}{\partial t} + u_{fp} \frac{\partial v_{fp}}{\partial x} + v_{fp} \frac{\partial v_{fp}}{\partial y} \qquad (9.3.14c, d)$$

The particle trajectory is given by the Lagrangian dimensionless equations:

$$u_p = \frac{dx_p}{dt} \quad , \quad v_p = \frac{dy_p}{dt} \qquad (9.3.15a, b)$$

where x_p and y_p denote the dimensionless streamwise and vertical coordinates of particle centroid, made dimensionless with d_p.

To determine the trajectory of the particle, (9.3.11) and (9.3.15) must be integrated, which requires the knowledge of time series of the streamwise and vertical components of the flow velocity driving particle motion. According to the previous discussion, this velocity is equivalent to that of the initial eddy (Fig. 9.3.1) as long as the particle is still within the radius of action of the eddy, however, due to the particle relative motion with respect to the eddy there is a partial loss of correlation which implies that the velocity of the eddy is not identical to that of the parcel of fluid surrounding the particle, although they are still correlated.

The velocity components of the fluid parcel surrounding the particle can be decomposed into a local Eulerian mean and a fluctuation, similarly as done for the velocity components of the initial eddy:

$$u_{fp} = \overline{u}_{fp} + u'_{fp} \quad , \quad v_{fp} = \overline{v}_{fp} + v'_{fp} \qquad (9.3.16a, b)$$

where again the overbar indicates the mean and the prime indicates the fluctuation. In uniform open channel flow it can be assumed that: $\overline{u}_{fp} = \overline{u}_f (y_p)$ and $\overline{v}_{fp} = 0$.

Following Zhuang et al. (1989), the dimensionless flow velocity fluctuation components associated with the parcel of fluid surrounding the particle, u'_{fp} and v'_{fp}, are generated using the Markov chain:

$$u'_{fp}{}^{(k)} = \sqrt{\overline{u'^2_{fp}}}\; q_{pu}{}^{(k)} \quad , \quad v'_{fp}{}^{(k)} = \sqrt{\overline{v'^2_{fp}}}\; q_{pv}{}^{(k)} \qquad (9.3.17a, b)$$

where $\overline{u'^2_{fp}}$ and $\overline{v'^2_{fp}}$ denote the Lagrangian variance of the dimensionless streamwise and vertical components of the flow velocity fluctuations associated with the fluid parcel surrounding the particle, respectively, and the variables q_{pu} and q_{pv} are given by:

$$q_{pu}{}^{(k+1)} = \alpha_{pu}\; q_{pu}{}^{(k)} + \mu_{pu}{}^{(k+1)} \quad , \quad q_{pv}{}^{(k+1)} = \alpha_{pv}\; q_{pv}{}^{(k)} + \mu_{pv}{}^{(k+1)} + F \qquad (9.3.18a, b)$$

with:

$$\alpha_{pu} = \exp\,(\, -\Delta t/T_{Lu} - |\Delta x|/L_{gu}\,) \quad , \quad \alpha_{pv} = \exp\,(\, -\Delta t/T_{Lv} - |\Delta y|/L_{gv}\,) \qquad (9.3.19a, b)$$

$$\mu_{pu}{}^{(k)} = \sqrt{1-\alpha^2_{pu}}\; r_u{}^{(k)} \quad , \quad \mu_{pv}{}^{(k)} = \sqrt{1-\alpha^2_{pv}}\; r_v{}^{(k)} \qquad (9.3.20a, b)$$

where $|\Delta x|$ and $|\Delta y|$ correspond to the absolute value of the particle dimensionless displacement in the streamwise and vertical directions, respectively, with respect to the position it had in the previous time step, and L_{gu} and L_{gv} denote the Lagrangian integral length scale for the flow streamwise and vertical velocity components, respectively. It is important to note that in (9.3.20), the Gaussian random numbers r_u and r_v are identical to those used in (9.3.7) for the Markov chain corresponding to the velocity time series of the initial eddy. Also, the correction term F in (9.3.18) is identical to that appearing in (9.3.5). This implies that the velocity time series for the initial eddy and the parcel of fluid surrounding the particle only differ due to the partial loss of correlation associated with the particle displacement.

According to Zhuang et al. (1989) the time step used in the simulation must be specified as:

$$\Delta t = 0.1\; Min\,(\,\tau_p\;,\; T_{Lu}\;,\; T_{Lv}\,) \qquad (9.3.21)$$

where τ_p denotes the dimensionless particle time constant, which is a measure of the inertia of the particle and is given by:

$$\tau_p = \frac{(\,R+1\,)}{18}\; R_p\; \sqrt{\tau_*} \qquad (9.3.22)$$

As stated previously, it is assumed herein that whenever the total separation between the initial eddy and the particle, $R*$, exceeds the length scale characterizing the size of the eddy, $L*$, then the velocity of the fluid parcel surrounding the particle abruptly loses all correlation with that of the initial eddy (Fig. 9.3.1). In this situation, the values of the flow velocity fluctuations are reset so that:

$$q_{fu}^{(k+1)} = q_{pu}^{(k+1)} = r_u^{(k+1)} \quad , \quad q_{fv}^{(k+1)} = q_{pv}^{(k+1)} = r_v^{(k+1)} \qquad (9.3.23a, b)$$

and the position of the eddy is also reset so that now it again coincides with that of the particle. Zhuang et al. (1989) propose the use of the following relationship to estimate the dimensionless size of the eddy, $L = L^*/d_p$:

$$L = c\, Lg \qquad (9.3.24)$$

where L_g denotes the dimensionless Lagrangian integral length scale of the flow velocity fluctuations, and c is a constant, which Zhuang et al. estimate as equal to 1.5 based on the comparison of their simulations of heavy particle dispersion with the experimental observations by Snyder and Lumley (1971).

Since the open channel flow under consideration is inhomogeneous, it is necessary to define the variables:

$$R_u = |x_f - x_p| \quad , \quad R_v = |y_f - y_p| \qquad (9.3.25)$$

which denote the dimensionless separation between the eddy and the particle in the streamwise and vertical directions, respectively. It is assumed that the particle loses total correlation with the eddy whenever one of the following conditions is satisfied:

$$R_u > c\, L_{gu} \quad , \quad R_v > c\, L_{gv} \qquad (9.3.26)$$

By introducing (9.3.16) in (9.3.14), the accelerations of the fluid parcel surrounding the particle can be rewritten as:

$$\frac{du_{fp}}{dt} = v_p \frac{d\bar{u}_{fp}}{dy} + \frac{du'_{fp}}{dt} \quad , \quad \frac{Du_{fp}}{Dt} = v'_{fp} \frac{d\bar{u}_{fp}}{dy} + \frac{Du'_{fp}}{Dt} \qquad (9.3.27a, b)$$

$$\frac{dv_{fp}}{dt} = \frac{dv'_{fp}}{dt} \quad , \quad \frac{Dv_{fp}}{Dt} = \frac{Dv'_{fp}}{Dt} \qquad (9.3.27c, d)$$

Because of the difficulty of modelling the Lagrangian accelerations associated with the velocity fluctuations, and as a first approximation to the problem, terms involving the total derivatives of the flow velocity fluctuations in (9.3.27) are neglected in the present analysis.

9.3.3 Modelling Lagrangian statistics of flow velocity

The random walk model described in the previous section requires the evaluation of a series of variables involving Lagrangian statistics of flow velocity, such as variances and integral time and length scales of the velocity fluctuations. In general these statistics are difficult to measure or to evaluate and therefore it is necessary to introduce some assumptions and approximations for their estimation.

From (9.3.3) and (9.3.16) the flow velocity fluctuations can be expressed as:

$$u'_f = u_f - \overline{u}_f(y_f) \quad , \quad v'_f = v_f \qquad (9.3.28a, b)$$

$$u'_{fp} = u_{fp} - \overline{u}_f(y_p) \quad , \quad v'_{fp} = v_{fp} \qquad (9.3.28c, d)$$

where as indicated previously, $\overline{u}_f(y)$ denotes the Eulerian dimensionless mean flow velocity.

According to Legg (1983), u'_f and u'_{fp} defined as in (9.3.28) are not true Lagrangian fluctuations. However, although their mean value does not necessarily vanish, it is expected to be small compared to the value of the corresponding variance. Legg proposes using Corrsin's (1959) hypothesis, stating that after sufficiently long migration times fluid particles may be considered to have velocities that are unbiased samples of the turbulent velocities at their positions in an Eulerian reference frame. Thus, the following approximations are introduced (see also Wilson et al., 1981):

$$\overline{u'^2_f} = \overline{u'^2_{fp}} = \overline{u'^2_{fE}}(y) \quad , \quad \overline{v'^2_f} = \overline{v'^2_{fp}} = \overline{v'^2_{fE}}(y) \qquad (9.3.29a, b)$$

where $\overline{u'^2_{fE}}$ and $\overline{v'^2_{fE}}$ denote the Eulerian variance of the flow dimensionless velocity components in the streamwise and vertical directions, respectively.

Herein, $\overline{u'^2_{fE}}$ and $\overline{v'^2_{fE}}$ are estimated using Nezu and Nakagawa's (1993) semiempirical relations valid for open channel flow. These relationships are expressed as functions of the dimensionless vertical coordinate defined as: $y' = y^* / h$, where h denotes the flow depth. Another dimensionless variable relevant to this analysis is: $y_+ = y^* u_* / \nu$, which corresponds to the vertical coordinate made dimensionless with wall units, that is with the length scale ν / u_*.

By force balance considerations, the following relation can be written for a sufficiently wide open channel flow:

$$u_*^2 = g \sin\theta \, h \qquad (9.3.30)$$

which can be used to relate the dimensionless coordinates y' and y, such that:

$$y' = y \frac{\sin\theta}{R \tau_*} \qquad (9.3.31)$$

On the other hand, it is easy to see that the dimensionless coordinates y_+ and y are related by:

$$y_+ = y R_p \sqrt{\tau_*} \qquad (9.3.32)$$

Based on (9.3.31), and following Nezu and Nakagawa (1993), $\overline{u'^2_{fE}}$ and $\overline{v'^2_{fE}}$ can be estimated as:

$$\sqrt{\overline{u'^2_{fE}}} = 2.30 \exp\left(- y \frac{\sin\theta}{R\,\tau_*} \right) \qquad (9.3.33a)$$

$$\sqrt{\overline{v'^2_{fE}}} = 1.27 \exp\left(- y \frac{\sin\theta}{R\,\tau_*} \right) \qquad (9.3.33b)$$

It is necessary to point out that the relationships (9.3.32) are valid for smooth flows at values y_+ larger than about 20, however according to Nezu and Nakagawa (1993) those same relationships are valid for transitionally rough flows at locations y_+ somewhat larger than about k_{s+}, which implies that the roughness of the channel bottom has a rather localized effect on the structure of the turbulence in open channel flows. This was verified in Chapter 3, particularly for equation (9.3.33a), using hot-film measurements of streamwise flow velocity fluctuations. Hence, sufficiently away from the channel bottom the vertical structure of the turbulence appears to be independent of the surface roughness of the channel (see also Raupach, 1981; Raupach et al., 1991). According to this discussion, it is apparent that the relationships (9.3.33) can be applied to the present model of saltation as long as the particles have their centroid located at an elevation higher than about $y_+ =$ 20. This imposes a lower limit to the dimensionless size of the particle of about 40 wall units, that is, the particle Reynolds number defined as:

$$Re_{p_*} = d_p\, u_*/\nu = R_p \sqrt{\tau_*} \qquad (9.3.34)$$

should be larger than about 40.

The Eulerian dimensionless streamwise mean flow velocity, $\overline{u}_f$, in turbulent open channel flow is estimated using the semi-logarithmic law given by:

$$\overline{u}_f = \frac{1}{\varkappa} \ln (y) + B \qquad (9.3.35)$$

where $\varkappa$ denotes von Karman's constant taken to be equal to 0.4, the roughness height, k_s, has been taken to be equal to the particle diameter, and the coefficient B is equal to 8.5 for fully rough flows, and is a function of $k_{s+} = u_*\, k_s/\nu$, where ν denotes the fluid kinematic viscosity, for transitionally rough flows (see Chapter 3).

Wilson et al. (1981) invokes Batchelor's (1957) hypothesis of Lagrangian similarity to approximate Lagrangian values of length, time and velocity scales by their corresponding Eulerian values, which according to them, seems to be a useful procedure that has been validated experimentally. Based on this, the dimensionless Lagrangian integral length scale of the flow velocity fluctuations is estimated by its Eulerian counterpart. That is, it is assumed that:

$$L_{gu} = L_{uE}(y) \quad , \quad L_{gv} = L_{vE}(y) \qquad (9.3.36a, b)$$

where L_{uE} and L_{vE} denote the Eulerian integral length scale of the streamwise and vertical components of the flow velocity fluctuations, respectively, which are estimated using the relationsships proposed by Nezu and Nakagawa (1993), such that:

$$L_{uE} = \begin{cases} \left(\frac{R\,\tau_*}{\sin\theta}\, y \right)^{1/2} & y < 0.6\,\frac{R\,\tau_*}{\sin\theta} \\ 0.775\,\frac{R\,\tau_*}{\sin\theta} & y > 0.6\,\frac{R\,\tau_*}{\sin\theta} \end{cases} \qquad (9.3.37a)$$

$$L_{vE} = \varkappa\ y\ \frac{1 - y\,\sin\theta/(R\,\tau_*)}{\left(\overline{v'^2_{fE}}\right)^{1/2}} \qquad (9.3.37b)$$

The validity of (9.3.37a) in the case of transitionally rough open channel flow was checked in Chapter 3 using hot-film measurements of streamwise flow velocity fluctuations. According to Nezu and Nakagawa (1993) (9.3.37a) is also valid for fully rough flows, however in those cases there is a tendency for L_{uE} to be somewhat smaller than the value predicted by this equation in the region closer to the channel bottom.

Following Wilson et al. (1981), the Lagrangian time scale of the flow velocity fluctuations is approximated by its Eulerian counterpart, i.e.:

$$T_{Lu} = T_{uE}(y) \quad , \quad T_{Lv} = T_{vE}(y) \qquad (9.3.38a, b)$$

where T_{uE} and T_{vE} denote Eulerian integral time scale of the streamwise and vertical components of the flow velocity fluctuations, respectively, which according to Raupach et al. (1991) can be estimated from L_{uE} and L_{vE} by invoking Taylor's frozen turbulence hypothesis. Thus,

$$T_{uE} = L_{uE} / \overline{u}_f \quad , \quad T_{vE} = L_{vE} / \overline{u}_f \qquad (9.3.39a, b)$$

with L_{uE} and L_{vE} given by (9.3.37) and $\overline{u}_f$ given by (9.3.35).

9.3.4 Modelling fluid particle dispersion in open channel flow

In order to check the validity of the assumptions and approximations introduced in the formulation of the random walk model for particle motion presented in previous sections, a simple analysis of fluid particle dispersion in turbulent open channel flow predicted by the model is carried out next. This analysis also aims at selecting the most appropriate correction term F of those given by equations (9.3.8) to (9.3.10). In the simulations, the governing equations for fluid particle motion, (9.3.1), are solved numerically using a fourth-order Runge-Kutta scheme.

A numerical experiment is conducted, in which a line source of tracers (marked fluid particles) is released at $t = 0$, $x = 0$, uniformly distributed in the vertical. Because of turbulent dispersion, the initial line of tracers spreads out in the streamwise direction, such that the variance of tracer positions

in x within the resulting cloud of tracers grows as a function of time. This is a result mainly of vertical turbulent diffusion and the non-uniformity of the mean velocity profile in the vertical (Taylor, 1954).

Fig. 9.3.2 shows as an example, the results of a simulation of fluid particle dispersion for the condition $R\tau_*/sin\ \theta = h/d_p = 165$ (although the dispersion of fluid elements does not depend on d_p, the coordinates x and y are made dimensionless with this parameter so it is necessary to specify the ratio h/d_p). In the simulation, 300 tracers were tracked as a function of time using the random walk model described in previous sections. The results plotted in Fig. 9.3.2 correspond to the times $t =$ 150, 450, and 800. Therein, four different expressions for the correction term F have been used, namely, a) $F = 0$, b) F given by (9.3.8), c) F given by (9.3.9) and d) F given by (9.3.10).

As seen in Fig. 9.3.2 the model predicts a growth of the streamwise dispersion of the cloud of tracer particles as time increases. However, in case a) ($F = 0$) there is a clear tendency for the fluid particles to gather in the region close to the free surface, where the turbulence intensity is lowest. It is also apparent that in case b) (F given by Legg and Raupach's correction (9.3.8)) the tendency is the opposite: the particles tend to accumulate near the bottom of the channel, which appears to be the result of an over-compensation of the mean drift velocity effect discussed previously. Cases c) and d) (F given by Wilson et al.'s correction (9.3.9) and by Ley and Thomson's correction (9.3.10), respectively) appear to have a more uniform particle distribution in the vertical, although it is apparent that in case d) there is still some tendency for the particles to gather near the free surface.

The non-uniformity of the tracer vertical distribution can be more easily analyzed by computing the probability density function of the vertical position of the tracers predicted by the model. A perfect correction would produce a uniform probability density. The results obtained for the same cases shown in Fig. 9.3.2 are presented in Fig. 9.3.3. Clearly those results show that the best correction appears to be that given by Wilson et al. (1983) corresponding to equation (9.3.9), which yields the most nearly uniform vertical distribution of tracers of those analyzed herein.

Another result obtained from the simulation corresponds to the dispersion coefficient associated with the long-time behavior of the turbulent dispersion process, ε_t. According to Taylor's analysis (see Fisher et al., 1979), after some start-up time the variance of a spreading cloud of tracers in stationary, uniform turbulent motion grows linearly with time, such that the dispersion coefficient is given by:

$$\varepsilon_t = \frac{1}{2}\frac{\overline{dx_f^{*\prime 2}}}{dt^*} = constant \qquad (9.3.40)$$

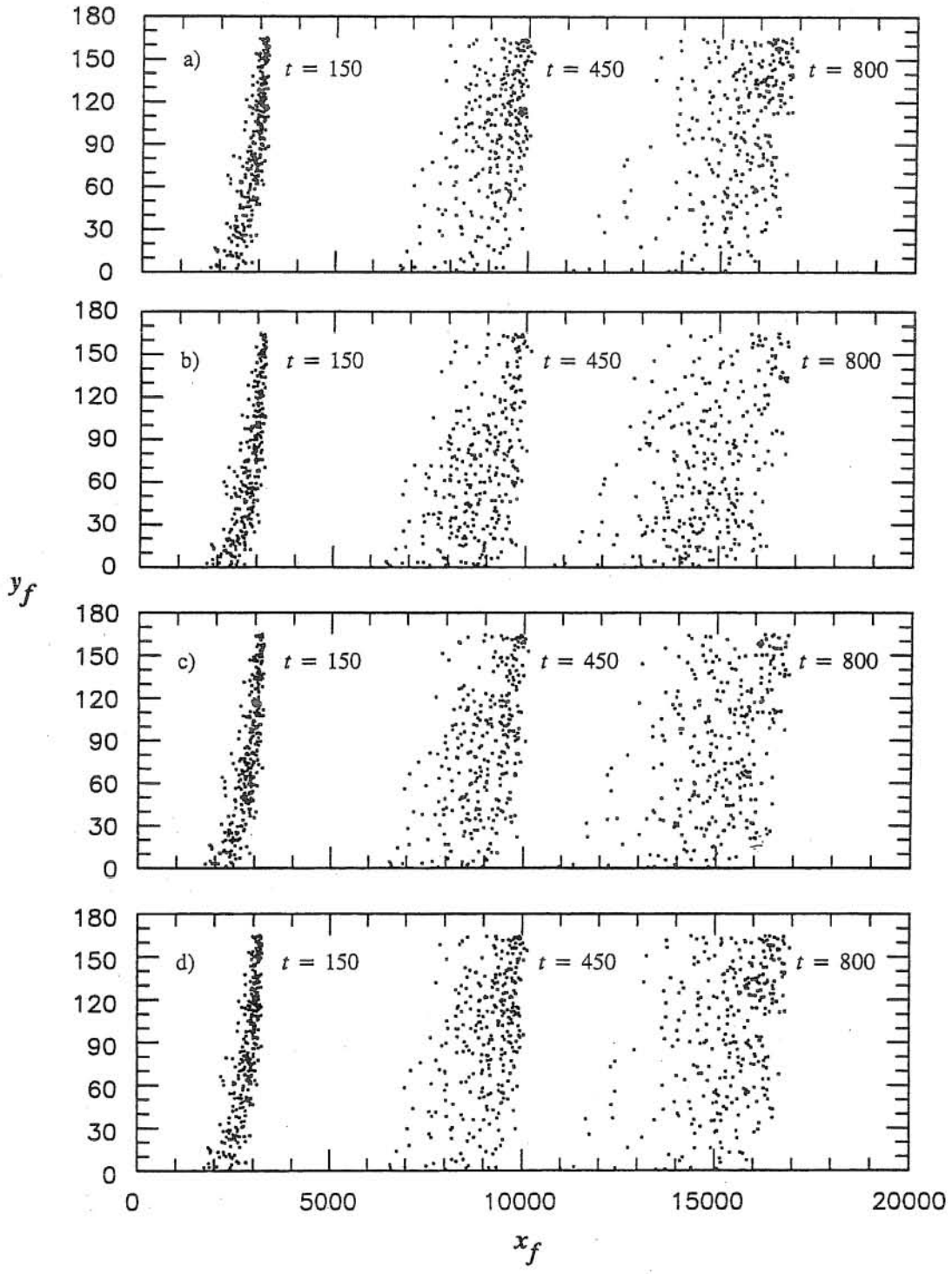

Fig. 9.3.2 Simulation of fluid particles dispersion as a function of time with random walk model. a) No correction term: $F = 0$, b) Correction term by Legg and Raupach (9.3.8), c) Correction term by Wilson et al. (9.3.9), d) Correction term by Ley and Thomson (9.3.10). Conditions correspond to $R\ \tau_*/sin\ \theta = 165$.

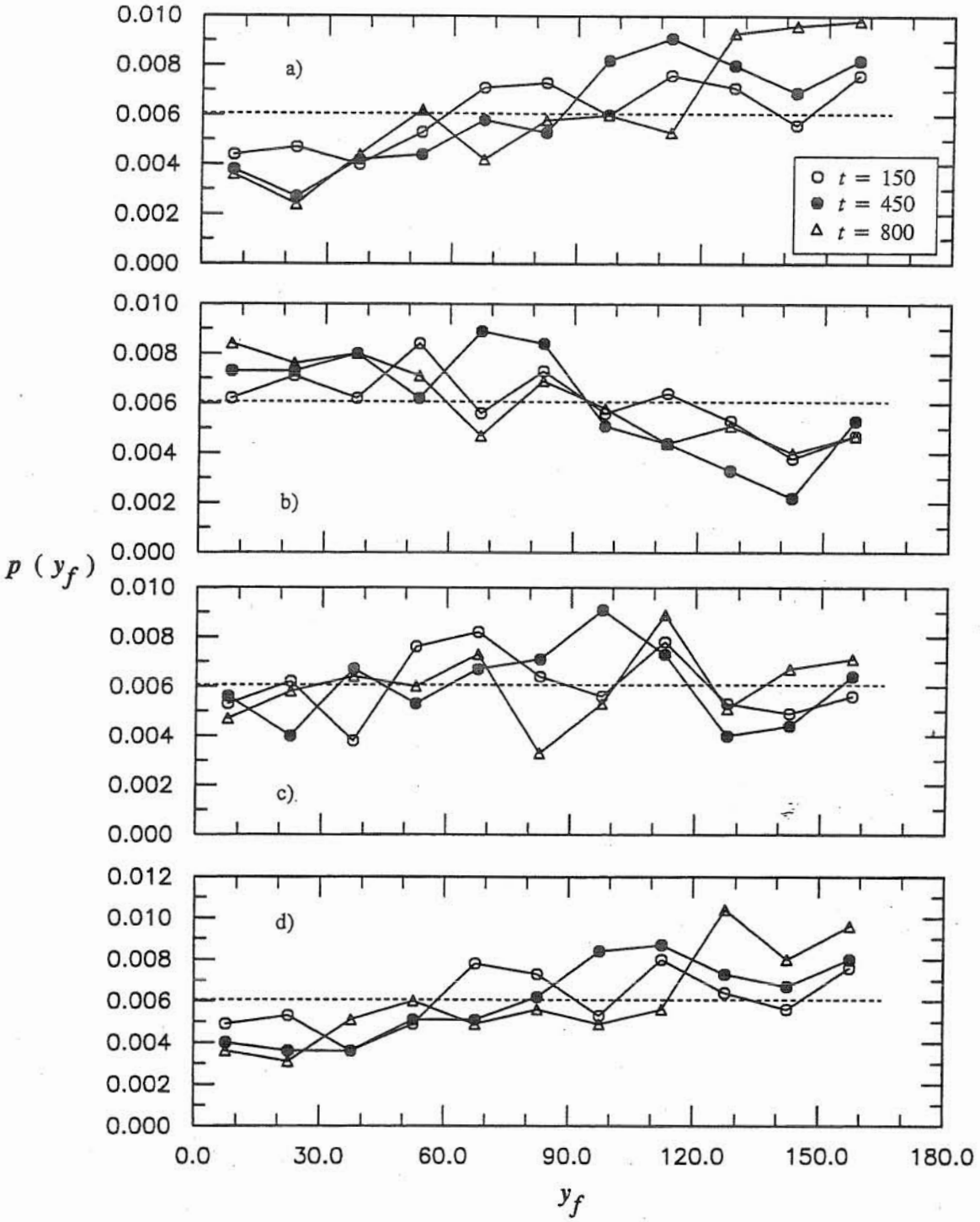

Fig. 9.3.3 Probability density function of the tracer distribution in the vertical predicted by the random walk model for the results shown in Fig. 9.3.2. a) No correction term: $F = 0$, b) Correction term by Legg and Raupach (9.3.8), c) Correction term by Wilson et al. (9.3.9), d) Correction term by Ley and Thomson (9.3.10).

where $\overline{x_f^{*\prime 2}}$ denotes the variance of the (dimensioned) x-positions of the tracers in the cloud at time t^*.

The present random walk model does predict the long-time linear growth of the variance $\overline{x_f^{*\prime 2}}$ with time. As an example, Table 9.3.1 shows the results obtained for the dimensionless dispersion coefficient, $\varepsilon_t/(\, u_* h\,)$, computed using (9.3.40) by fitting a linear relationship to the simulated values of the variance as a function of time at large times, corresponding to the same results presented in Figs. 9.3.2 and 9.3.3. In the same table, the prediction given by Elder (1959) for open channel flow:

$$\varepsilon_t/(\, u_* h\,) = 5.9 \tag{9.3.41}$$

is also shown for comparison purposes.

Table 9.3.1 Values of $\varepsilon_t/(\, u_* h\,)$ given by the random walk model

Case a)	Case b)	Case c)	Case d)	Eq. (9.3.41)
5.1	7.1	6.2	5.7	5.9

Case a) no correction term: $F = 0$, Case b) correction term by Legg and Raupach (9.3.8),
Case c) correction term by Wilson et al. (9.3.9), Case d) correction term by Ley and Thomson (9.3.10).

As seen in Table 9.3.1, the values of $\varepsilon_t/(\, u_* h\,)$ obtained in each case of those shown in Figs. 9.3.2 and 9.3.3 are generally close to that predicted by (9.3.41). The best results appear to be those corresponding to the use of the correction term F given by Wilson et al. (1983) (9.3.9), and Ley and Thomson (1983) (9.3.10), which yield values of $\varepsilon_t/(\, u_* h\,)$ that differ less than about 5% with respect to that given by (9.3.41). Interestingly, those same corrections were observed to give the most uniform vertical distribution of tracers as discussed previously.

The examples presented herein seem to indicate that the random walk model developed in previous sections predicts reasonably well the dispersion of fluid tracers in an open channel flow. This implies that the assumptions introduced in the derivation of the model, particularly those related with the estimation of Lagrangian statistics of flow velocity components, seem to be useful in terms of the overall results given by the model. In what follows, the correction term F given by Wilson et al. (1983), (9.3.9), is adopted because it yields the most uniform vertical distribution of dispersed tracers with a good estimation of the dispersion coefficient.

9.3.5 Modelling particle saltation

To analyze the effect of turbulence on the characteristics of particle saltation, the random walk model for simulating heavy particle trajectories in open channel flow developed in previous sections is used. This is done by performing a numerical experiment in which a large number of particles

are released from the bed of the channel with identical initial conditions. Due to the randomness of the velocity field simulated by the model, the trajectories of individual saltating particles differ. By computing ensemble averages over all the realizations of the saltation process, mean values and standard deviations of variables such as saltation length and height can be estimated.

The simulations are carried out by solving equations (9.3.1), governing the motion of the eddy (Fig. 9.3.1), and equations (9.3.11), governing the motion of the solid particle, simultaneously. This is done numerically using a fourth-order Runge-Kutta scheme. The treatment of the Basset term in (9.3.11) is essentially identical to that explained in detail in Chapter 6.

As in Chapter 6, the following values are used in the simulations: $C_m = 0.5$, $R = 1.65$ (natural sediment), and C_D is approximated by the relationship proposed by Yen (1992) for free-falling spheres:

$$C_D = \frac{24}{Re} \left(1 + 0.15 \sqrt{Re} + 0.017\, Re \right) - \frac{0.208}{1 + 10^4\, Re^{-0.5}} \qquad (9.3.42)$$

where $Re = |u_R{}^*|\, d_p / \nu$, with $|u_R{}^*| = |u_R|\, u_*$ denoting the dimensional particle slip velocity.

In order to illustrate how the crossing-trajectories effect is simulated by the model, Fig. 9.3.4 shows an example of a single realization of a sediment particle falling in turbulent open channel flow. Initially the particle is released at the location $x_p\,(0) = 0$, $y_p\,(0) = 5$, with no vertical velocity, and with a streamwise velocity equal to the local mean flow velocity. The results shown in Fig. 9.3.4 correspond to the conditions: $R_p = 50$, $\tau_* = 0.1$, $\tan\theta = 0.001$. Therein, the trajectories of both the eddy and the particle are plotted together.

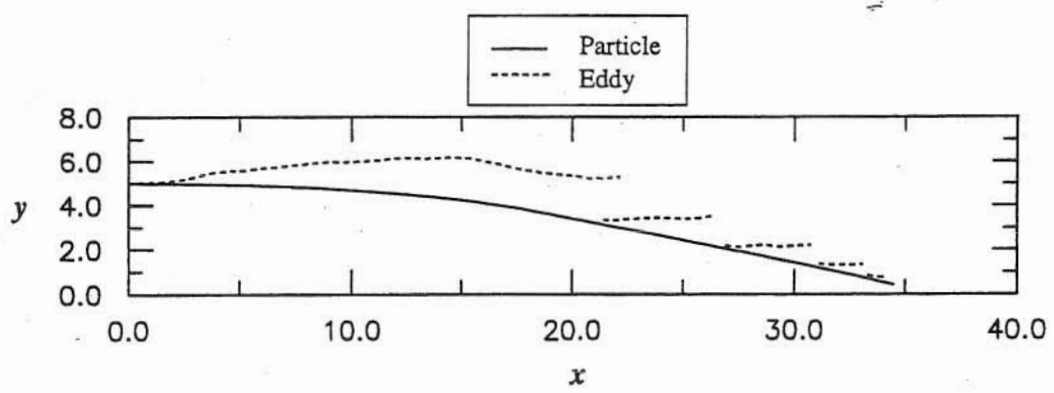

Fig. 9.3.4 Cross-trajectories effect simulated with the random walk model. Initial conditions are $x_p = 0$, $y_p = 5$, $u_p = \overline{u}_f\,(5) = 13.5$, $v_p = 0$. Values of governing parameters are $R_p = 50$, $\tau_* = 0.1$, $\tan\theta = 0.001$.

From Fig. 9.3.4 it is clear that the heavy sediment particle is slipping downwards through the turbulent flow field due to the effect of gravity. Initially the position of particle and eddy coincides. As time increases particle and eddy get separated, however the flow field of the eddy and that of the

fluid parcel surrounding the particle remain correlated until the distance between them exceeds one of the characteristic length scales of the eddy (in the case shown in Fig. 9.3.4 it corresponds to the vertical length scale, $c\ L_{gv}$). At this point the particle abruptly loses all correlation with the eddy and encounters a new one. The process is repeated until the particle is deposited on the channel bottom.

Examples showing the effect of turbulence on particle saltation are presented in Fig. 9.3.5. Therein 20 different realizations of the saltation process are shown for each of the values of the parameter R_p = 50, 500, and 5000. All other parameters are held constant with values: $\tau_* = 0.1$, $\tan\theta = 0.001$. Initial conditions are also held constant with values $x_p\ (0) = 0$, $y_p\ (0) = 0.5$, $u_p\ (0) = 3.5$, $v_p\ (0) = 1.8$. The initial position corresponds to a particle lying on the bed, while the initial velocities correspond to values typically observed in the experimental study of saltation reported in Chapter 6. The takeoff angle resulting from the initial particle velocity has a value of about 27°, which also corresponds to a value typically observed for this variable as reported in Chapter 6.

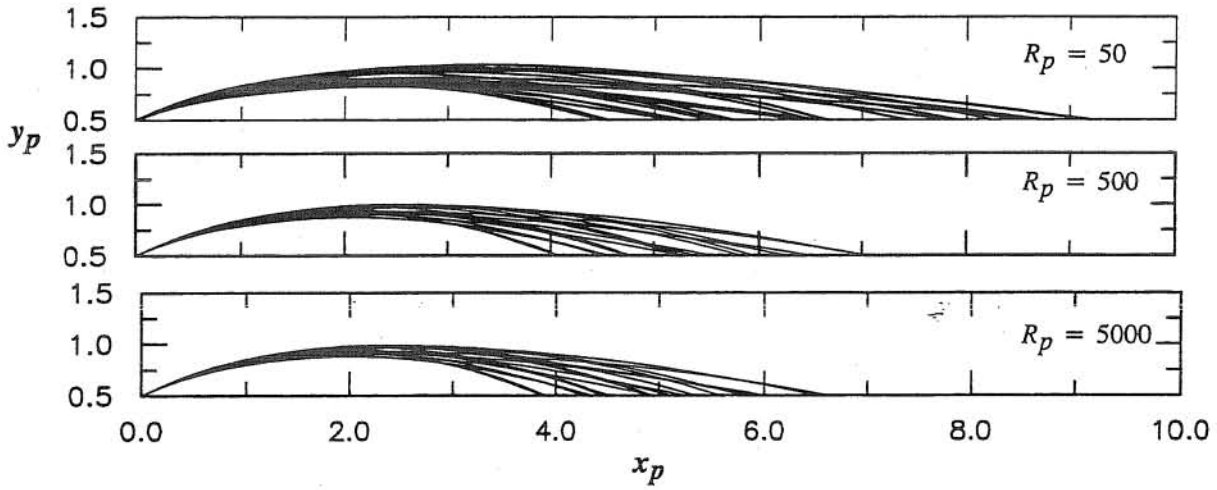

Fig. 9.3.5 Effect of turbulence on saltation trajectories. Simulations of the random walk model for the values R_p = 50, 500, and 5000. All other parameters are held constant with values: $\tau_* = 0.1$, $\tan\theta = 0.001$. Initial conditions are $x_p = 0$, $y_p = 0.5$, $u_p = 3.5$, $v_p = 1.8$.

As seen in Fig. 9.3.5, the turbulence tends to spread out the saltation trajectories, such that the saltation lengths appear to vary in a relatively wide range. The shape of the trajectories is rather similar in all cases, and does not exhibit high frequency fluctuations. Apparently, the lengths of the saltations have much more variability than corresponding heights. It is also apparent that the variability of the saltation length tends to decrease as R_p increases, i.e. as the particle size increases. This would be a consequence of increasing particle inertia, which tends to dump the particle response to the turbulence.

Figs. 9.3.6 to 9.3.9 present ensemble averaged values (over 150 realizations of the saltation process) of the dimensionless saltation length, λ_s, and height, h_s, simulated with the random walk model for the same initial conditions as those corresponding to the results presented in Fig. 9.3.5, plotted as a function of τ_*, and for the values of the parameter $R_p = 50$ and 500. In those figures, mean values and standard deviations of λ_s and h_s are plotted together with the results of a simulation of particle saltation that considers only the existence of mean flow, and neglects all fluctuating components of the flow velocity, as done previously in Chapter 6.

The results in Figs. 9.3.6 and 9.3.8 indicate that the turbulence of the flow tends to decrease the mean value of λ_s with respect to the value computed neglecting turbulence, and this effect seems to be enhanced as τ_* increases, and lessened as R_p increases. A similar behavior is observed in Figs. 9.3.7 and 9.3.9 for the mean value of h_s. Since τ_* can be considered as a measure of the intensity of the Reynolds stress relative to the particle weight, it is expected that any turbulence effect would be enhanced as this parameter increases. On the other hand, as R_p increases, i.e. as the particle size increases, particle inertia also increases, which tends to dump the particle response to the turbulence.

In order to analyze the effect of R_p over the reduction of saltation length and height due to turbulence effects, mean values of λ_s and h_s predicted by the random walk model are plotted as functions of R_p in Figs. 9.3.10 and 9.3.11, for the values of $\tau_* = 0.1$ and 0.2. In those figures corresponding values of the dimensionless saltation length and height computed neglecting turbulence effects are also plotted for comparison purposes.

Fig. 9.3.10 shows that as R_p increases the values of λ_s computed neglecting turbulence approach asymptotically the mean values of λ_s predicted by the random walk model. At values of $R_p = 50$, neglecting turbulence leads to overestimate the mean values of the dimensionless saltation length in about 40% for values of $\tau_* = 0.1$, and about 60% for values of $\tau_* = 0.2$. At values of $R_p = 200$ these values have been reduced to about 5% and 15%, respectively. At values of R_p larger than about 2000, the turbulence does not appear to influence the mean values of λ_s.

A similar behavior is observed in Fig. 9.3.11 for the mean dimensionless saltation heights. However, neglecting turbulence leads to much less important overestimation of the mean values of h_s than in the case of λ_s. In fact, at values of $R_p = 50$, such overestimation amounts to about 8% for values of $\tau_* = 0.1$, and about 15% for values of $\tau_* = 0.2$. At values of R_p larger than 200 these values are less than about 3% for values of $\tau_* = 0.1$, and about 10% for values of $\tau_* = 0.2$.

The results shown in Figs. 9.3.10 and 9.3.11 seem to indicate that for values of R_p larger than say 500, turbulence effects can be neglected in modelling mean trajectories of sediment particle saltation without incurring in important errors. In terms of the particle size this limit corresponds to about 2.5 mm.

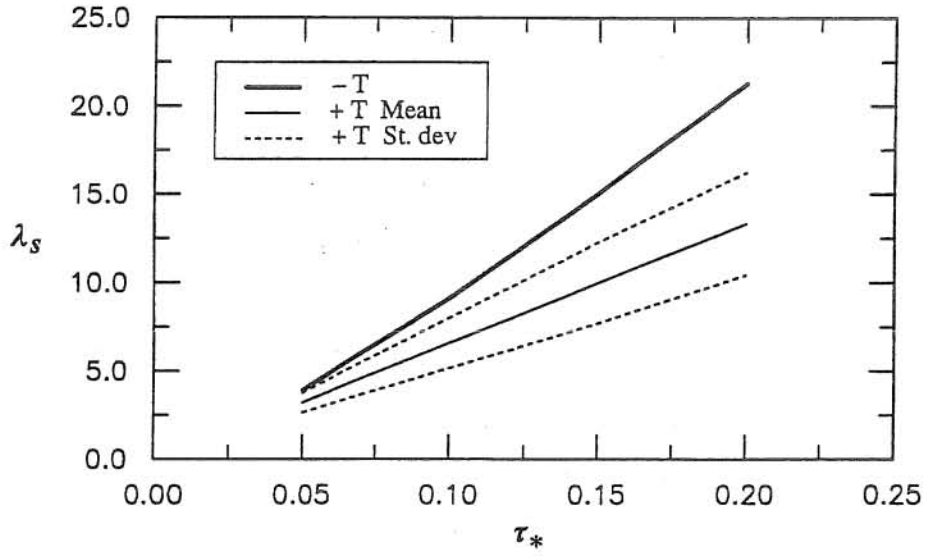

Fig. 9.3.6 Effect of turbulence on saltation length for the value $R_p = 50$. In the legend, – T denotes computations which do not include turbulence, + T denotes computations carried on with the random walk model. Dashed lines correspond to the mean plus and minus one standard deviation.

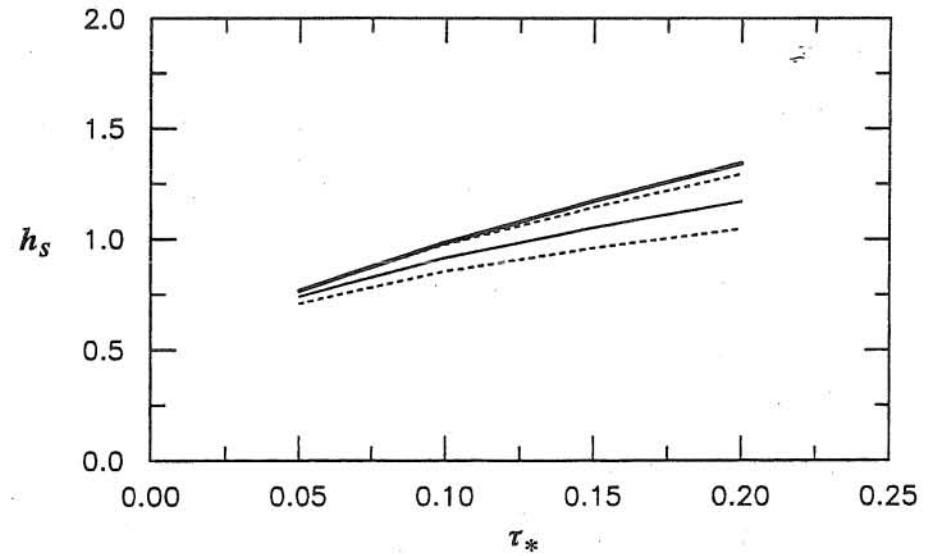

Fig. 9.3.7 Effect of turbulence on saltation height for the value $R_p = 50$. Legend as in Fig. 9.3.6.

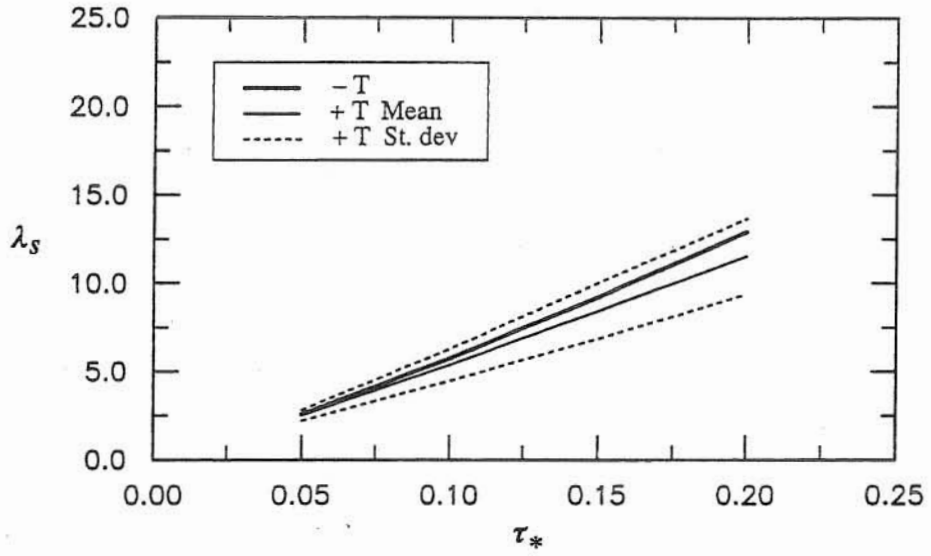

Fig. 9.3.8 Effect of turbulence on saltation length for the value $R_p = 500$. In the legend, – T denotes computations which do not include turbulence, + T denotes computations carried on with the random walk model. Dashed lines correspond to the mean plus and minus one standard deviation.

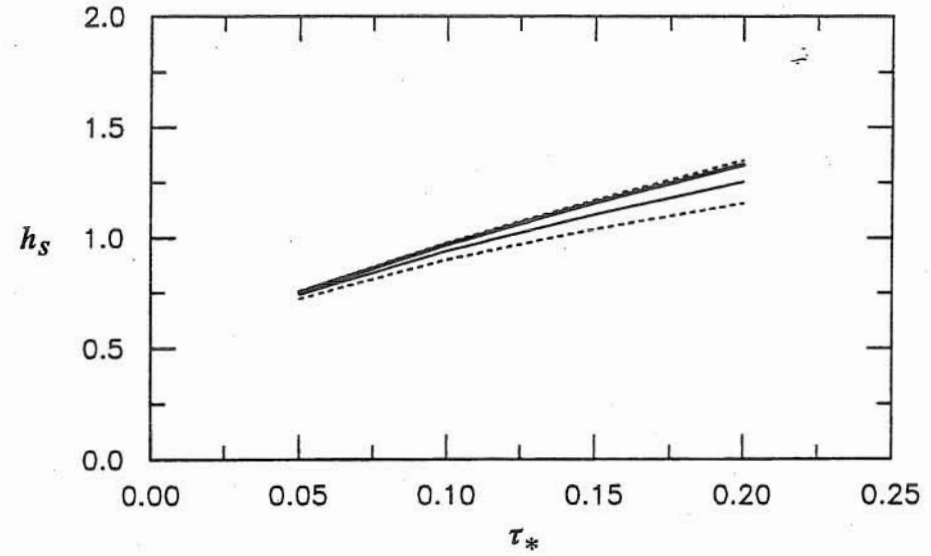

Fig. 9.3.9 Effect of turbulence on saltation height for the value $R_p = 500$. Legend as in Fig. 9.3.8.

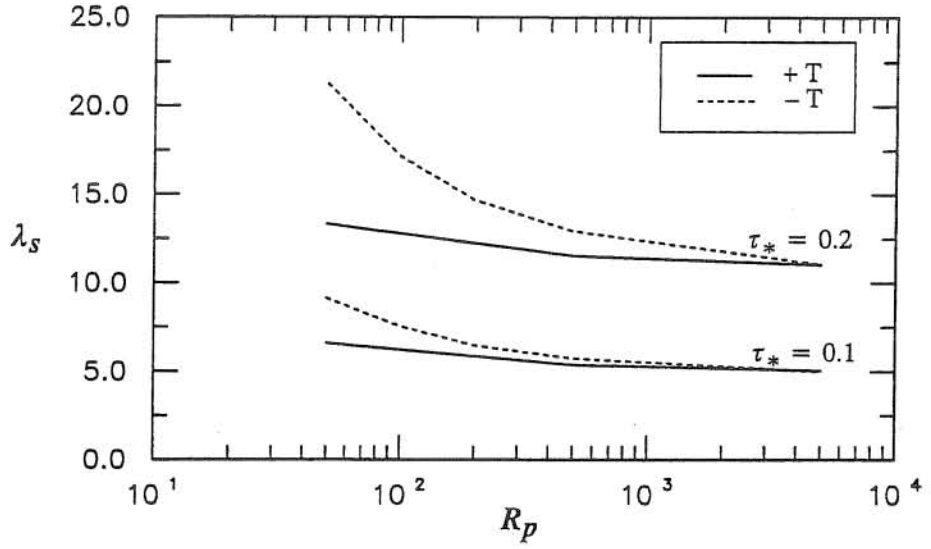

Fig. 9.3.10 Effect of turbulence on mean saltation length as a function of R_p and τ_* . In the legend, – T denotes computations which do not include turbulence, and + T denotes computations carried on with the random walk model.

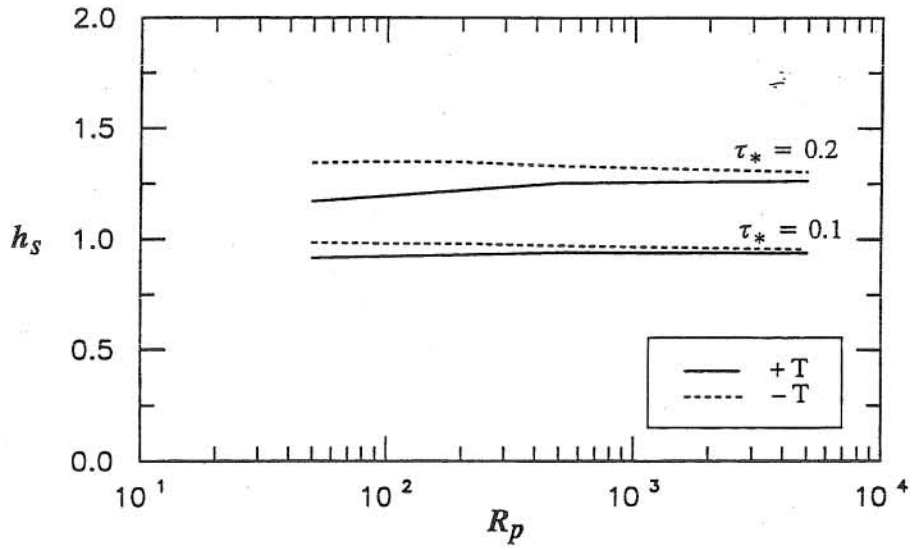

Fig. 9.3.11 Effect of turbulence on mean saltation height as a function of R_p and τ_*. Legend as in Fig. 9.3.10.

Although the effects of turbulence on the mean particle trajectory tend to become negligible as the particle size increases, it is apparent that the standard deviations of saltation length and height do not vanish even at values of R_p as high as 5000. This is illustrated in Figs. 9.3.12 and 9.3.13 where the coefficients of variation $\sigma_{\lambda_s} / < \lambda_s >$ and $\sigma_{h_s} / < h_s >$, where σ denotes standard deviation and angular brackets denote mean values, predicted by the random walk model are plotted as a function of τ_* for the values of R_p = 50, 500, and 5000.

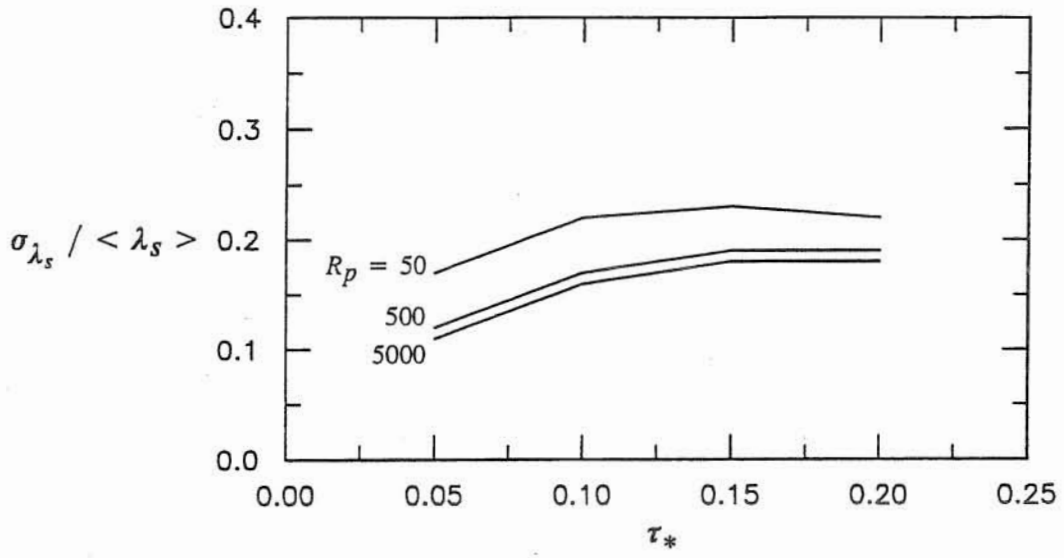

Fig. 9.3.12 Coefficient of variation of saltation length as a function of τ_* and R_p. Results of the random walk model.

As seen in Fig. 9.3.12 values of the standard deviations of λ_s predicted by the random walk model are about 10% to 20% of corresponding mean values, for values of R_p and τ_* in the range shown therein. In general there is a tendency for $\sigma_{\lambda_s} / < \lambda_s >$ to decrease with increasing R_p, however this variation tends to become negligible as R_p increases. That is, for given values of τ_* and as R_p increases, it seems that $\sigma_{\lambda_s} / < \lambda_s >$ decreases asymptotically towards a constant value which appears to be different from zero.

From Fig. 9.3.13 it appears that the behavior of $\sigma_{h_s} / < h_s >$ is very similar to that of $\sigma_{\lambda_s} / < \lambda_s >$, although the former tend to have much lower values that the latter. In fact, values of the standard deviations of h_s predicted by the random walk model seem to be generally less than 10% of corresponding mean values, for values of R_p and τ_* in the range shown therein, and to have values as low as less than about 2.5% for low values of τ_* and values of R_p larger than 500.

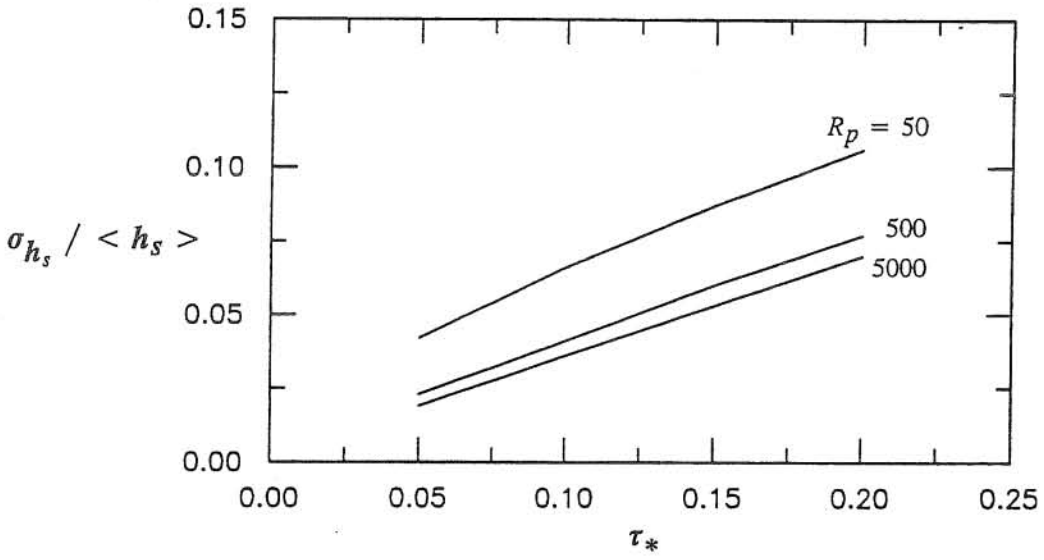

Fig. 9.3.13 Coefficient of variation of saltation height as a function of τ_* and R_p. Results of the random walk model.

9.3.6 Discussion

The above analysis has important implications regarding the results of the model of particle saltation presented in Chapter 6. Those results, which were obtained by neglecting turbulence effects in the equation governing the mean particle motion, showed a very good agreement with experimental observations reported in Chapter 5. It is necessary to recall that such results were obtained by neglecting also particle rotation, which as discussed in Chapter 6 tends to increase the length and height of the saltation trajectories. Since the turbulence of the flow seems to induce the opposite effect on the characteristics of the saltation, this suggests that particle rotation and turbulence effects tend to cancel each other, such that neglecting both of them in the simulation of particle saltation would result in a reasonable estimation of the mean particle trajectory.

With respect to the standard deviations of the saltation length and height observed experimentally in Chapter 5, the results obtained herein seem to indicate that they would not be a result of the stochasticity induced by the process of particle collision the bed alone, as suggested in previous chapters, but also of the turbulence of the flow. Although the latter seems to have more relevance at low values of R_p, its effect does not appear to vanish even at values of R_p as large as 5000. The values of the coefficients of variation, $\sigma_{\lambda_s} / < \lambda_s >$ and $\sigma_{h_s} / < h_s >$, measured experimentally are nevertheless much larger than those induced by the turbulence of the flow, as deduced from the present analysis, which somehow implies that the process of particle collision with the bed introduces a more important random element in the phenomenon of particle saltation than the turbulence of the flow, independently of the particle size.

The model of particle saltation developed in Chapter 6 reduced all the stochastic element of the saltation process to the randomness associated with the particle collision with the bed. Nonetheless, resulting values of the simulated standard deviations of saltation length and height obtained therein agree reasonably well with those observed experimentally, as reported in Chapter 5. This seems to imply that the rather high variability in the characteristics of the saltation trajectories induced by the process of particle collision with the bed somehow overshadows the extra variability given by the turbulence of the flow.

Finally, to close this discussion it can be pointed out that the application of the random walk model developed herein is not limited to the phenomenon of particle saltation. Indeed, with rather limited effort the model could be adapted to simulate transport of suspended sediment in a turbulent open channel flow. For instance the present model could be applied to analyze concentration distributions of suspended particles in different equilibrium and non-equilibrium situations, ranging from the estimation of suspended sediment concentration profiles in uniform open channel flow (e.g., Rouse, 1937), to the analysis of development of concentration profiles of suspended sediment over a loose sand bed downstream of a non-erodible surface (e.g., Celik and Rodi, 1988), and fine sediment trapping in a bed formed by coarser sediment (e.g., Einstein, 1968), to mention only a few.

In order to implement those applications some attention has to be paid to the following aspects. In the first place, the random walk model developed herein considers that the probability density function of both streamwise and vertical components of the flow velocity fluctuations are well described by a Gaussian distribution. Although this appears to be reasonably true for the streamwise component of the velocity fluctuations (see Nezu, 1977), it does not seem to be accurate in the case of the vertical component of the velocity. Such component appears to be positively skewed in wall bounded turbulent flows, at least outside of the viscous sublayer (Nakagawa and Nezu, 1977; Raupach, 1981), which has important implications regarding the transport of suspended sediment (Bagnold, 1966; Wei and Willmarth, 1991).

A second aspect of primary importance regarding the application of a random walk model to analyze the transport of suspended sediment in an open channel flow, is related to the need of modelling the process of particle entrainment into suspension from the channel bed. In the literature this has been approached from an Eulerian point of view, and some empirical relationships exist to estimate the volume rate of sediment particle entrainment into suspension per unit bed area under equilibrium conditions (e.g., García and Parker, 1991). From a Lagrangian point of view modelling particle entrainment into suspension would require establishing ejection velocities of entrained particles, as well as the frequency of particle ejection events and some measure of the effectivity of those events, for example in terms of an average number of particles ejected per event. Empirical information that could be used to develop such a model has been reported in Chapters 4 and 8.

9.3.7 Conclusions

A random walk model has been developed to simulate trajectories of heavy sediment particles in turbulent open channel flow, which takes into account the cross-trajectories effect. This model has been used to analyze the effect of the turbulence of the flow on the characteristics of particle saltation.

The model was used to analyze the problem of dispersion of fluid tracers in turbulent open channel flow. This analysis showed that the correction term F proposed by Wilson et al. (1983) gives a reasonably uniform vertical distribution of tracers. The dispersion coefficient predicted by the model is in good agreement with previous analytical results. This is taken as a confirmation of the validity of the approximations involved in the formulation of the model.

The application of the random walk model to the analysis of particle saltation indicates that due to turbulence effects, mean values of the saltation length and height predicted by the model tend to be lower than those predicted by the model presented in Chapter 6 which neglected turbulence. This reduction of the mean values of saltation length and height was observed to be enhanced as τ_* increases, and lessened as R_p increases. Also, the reduction in the saltation length seems to be more important than that in the saltation height. In general, the results obtained with the random walk model show that turbulence effects can be neglected in modelling mean trajectories of sediment particle saltation without incurring in important errors for values of R_p larger than about 500, which corresponds to a particle size of about 2.5 mm.

Although the effects of turbulence on the mean particle trajectory tend to become negligible as the particle size increases, the results of the simulations of particle saltation indicate that the standard deviations of saltation length and height do not vanish even at large values of R_p. The standard deviations predicted by the model for the saltation length have values that are about 10% to 20% those of the corresponding mean value for the conditions analyzed herein, while those values are generally less than 10% in the case of the saltation height.

The results of the simulations of particle saltation with the random walk model suggest that the effects of the turbulence of the flow and particle rotation on the mean saltation trajectories tend to cancel each other, such that the model of particle saltation developed in Chapter 6, which neglected both effects, performs satisfactorily when compared with the experimental results reported in Chapter 5.

On the other hand, such model, which introduces an stochastic element in the saltation phenomenon only through the model of particle collision with the bed, generates standard deviations of the saltation length and height that compare reasonably well with the observed ones reported in Chapter 6. This seems to imply that the rather high variability in the characteristics of the saltation

trajectories induced by the process of particle collision with the bed somehow overshadows the extra variability given by the turbulence of the flow.

9.3.8 References

Bagnold, R. A. (1966). "An approach to the sediment transport problem for general physics". *Geological Survey Professional Paper* 422-I, Washington, D. C.

Batchelor, G. K. (1957). "Diffusion in free turbulent shear flows". *J. Fluid Mech.*, vol 3, pp 67-80.

Celik, I, and Rodi, W. (1988). "Modelling suspended sediment transport in non-equilibrium situations". *J. Hydr. Engrg.*, ASCE, 114 (10), pp 1157-1191.

Corrsin, S. (1959). "Progress report on some turbulent diffusion research". *Advances in Geophysics* 6, pp 161-164.

Einstein, H. A. (1968). "Deposition of suspended particles in a gravel bed". *J. Hydr. DIv.*, ASCE, vol 94, pp 1197-1205.

Elder, J. W. (1959). "The dispersion of marked fluid in turbulent shear flow". *J. Fluid Mech.*, vol 5, pp 544-560.

Fisher, H. B., List, E. J., Koh, R. C., Imberger, J., and Brooks, N. H. (1979). "Mixing in inland and coastal waters". *Academic Press.*

García, M. and Parker, G. (1991). "Entrainment of bed sediment into suspension". *J. Hydr. Engrg.*, ASCE, vol 117, No 4, pp 414-435.

Legg, B. J. (1983). "Turbulent dispersion from an elevated line source: Markov chain simulations of concentration and flux profiles". *Quart. J. R. Met. Soc.*, 109, pp 645-660.

Legg, B. J., and Raupach, M. R. (1982). "Markov-chain simulation of particle dispersion in inhomogeneous flows: the mean drift velocity induced by a gradient in Eulerian velocity variance". *B. Layer Meteor.*, 24, pp 3-13.

Ley, A., and Thomson, D. J. (1983). "A random walk model of dispersion in the diabatic surface layer". *Quart. J. R. Met. Soc.*, 109, pp 847-880.

Lumley, J. L. (1978). "Two-phase and non-Newtonian flows". *Turbulence*, P. Bradshaw, ed., Chap. 7. Topics in applied physics, vol. 12, Springer-Verlag.

Mei, R. (1990). "Particle dispersion in isotropic turbulence and unsteady particle dynamics at finite Reynolds number". *Ph.D. Thesis, University of Illinois at Urbana-Champaign.* Urbana, Illinois.

Nakagawa, H., and Nezu, I. (1977). "Prediction of the contributions to the Reynolds stress from bursting events in open-channel flows". *J. Fluid Mech.*, vol 80, pp 99-128.

Nezu, I., and Nakagawa, H. (1993). "Turbulence in open-channel flows". *IAHR Monograph.* A. A. Balkema, Rotterdam.

Nezu, I. (1977). "Turbulent structure in open-channel flows". *Translation of Doctoral dissertation in Japanese*. Kyoto University, Kyoto, Japan.

Raupach, M. R., Antonia, R. A., and Rajagopalan, S. (1991). "Rough-wall turbulent boundary layers". *Appl. Mech. Rev.*, vol 44, no 1.

Raupach, M. R. (1981). "Conditional statistics of Reynolds stress in rough-wall and smooth-wall turbulent boundary layers". *J. Fluid Mech.*, 108, pp 363-382.

Rouse, H. (1937). "Modern conceptions of the mechanics of turbulence". *Trans. ASCE*, vol 102, pp 463-543.

Snyder, W. H., and Lumley, J. L. (1971). "Some measurements of particle velocity autocorrelation functions in a turbulent flow". *J. Fluid Mech.*, vol 48, part 1, pp 41-71.

Taylor, G. I. (1954). "The dispersion of matter in turbulent flow through a pipe". *Proc. R. Soc. London Ser. A*, 223, pp 446-468.

Wei, T., and Willmarth, W. (1991). "Examination of v–velocity fluctuations in a turbulent channel flow in the context of sediment transport". *J. Fluid Mech.*, vol 233, pp 241-252.

Wells, M. R., and Stock, D. E. (1983). "The effect of crossing trajectories on the dispersion of particles in a turbulent flow". *J. Fluid Mech.*, vol 136, pp 31–62.

Wilson, J. D., Legg, B. J., and Thomson, D. J. (1983). "Calculation of particle trajectories in the presence of a gradient in turbulent-velocity variance". *B. Layer Meteor.*, 27, pp 163-169.

Wilson, J. D., Thurtell, G. W., and Kidd, G. E. (1981). "Numerical simulation of particle trajectories in inhomogeneous turbulence, I: systems with constant turbulent velocity scale". *B. Layer Meteor.*, 21, pp 295-313.

Yen, B. C. (1992). "Sediment fall velocity in oscillating flow". *Water Resour. and Environ. Engrg. Res.* Report No 11. Dept. of Civil Engrg. Univ. of Virginia.

Zhuang, Y., Wilson, J. D., and Lozowski, E. P. (1989). "A trajectory-simulation model for heavy particle motion in turbulent flow". *J. Fluids Engrg.* Vol 111, pp 492–494.

10. CLOSURE REMARKS

A few general conclusions regarding the research reported in previous chapters are presented next. Some recommendations for future research, including issues that can be addressed by directly applying the experimental and analytical methods used herein and a few others which would require the development or application of new techniques, are presented as well.

General conclusions

The high-speed video system utilized in the experimental studies of Chapters 5, 7 and 8 proved to be a very useful tool to analyze motion of sediment particles with sizes in the range 40 to 700 μm. The use of a recording rate of 250 fps was sufficiently high in most cases to resolve the details of particle trajectories. Another successful application of this system was reported in Chapter 4, where flow visualizations were recorded synchronous with hot-film velocity measurements. The recording rate of 500 fps used therein allowed to keep a direct correspondence between images and velocity data, which were acquired at a rate of 500 Hz, satisfying at the same time Nyquist criteria given maximum frequencies of the velocity fluctuations of about 200 Hz. The relatively low spatial resolution and rather poor sensitivity to light of the high-speed video camera, however, makes its application to simultaneous tracking of particles and flow tracers rather unfeasible.

The experiments on saltation in water flows of Chapter 5 provide new insights as well as unprecedented data on this phenomenon. In particular, it seems that no previous experimental studies on saltation have covered particle sizes in the range of fine sand, as done herein, mainly because of difficulties regarding the small time and length scales typical of particle motion in this range of particle sizes. The characterization of the process of particle collision with the bed resulting from the observations reported in Chapter 5 appears also to provide new information on this phenomenon. Indeed, video images have shown that the collision-rebound type of interaction between saltating particles and the bed is the predominant one in particle saltation in water flows, which contradicts previous arguments stating the physical impossibility of such type of interaction.

The stochastic model for particle saltation of Chapter 6 appears to be a useful tool to simulate statistics of particle saltation. Indeed, results of those simulations compare very well with the experimental data reported in Chapter 5. The results of the saltation model, however, seem to be very dependent on the model for particle collision with the bed, which was somehow calibrated with results of the experimental study in Chapter 5. It must be pointed out also, that the model for particle saltation does not describe the entire cycle of particle motion, which goes from the moment at which the particle initiates the saltation from rest, through successive saltation-collision sequences, to the final distrainment of the particle. It seems that incorporating re-entrainment and distrainment processes in the model for particle saltation would overcomplicate it without affecting

significatively its predictive capabilities. On the other hand, incorporating such processes in the model would have advantages which are discussed later in this chapter.

The Bagnoldean formulation for developing bedload models discussed in Chapter 6, seems to depend heavily on the concept of a continuum bedload layer. However, such hypothesis may be valid only in the case of rather high particle concentration and relatively small particle diameter. For instance, the concept of a bedload layer breaks down in the case of saltation of gravel particles, which is typically associated with low flow depth to particle size ratios, and for which the thickness of the bedload layer is comparable to the total flow depth. Also, the Bagnoldean formulation requires the estimation of a threshold bed shear stress associated with a vanishing net entrainment of particles from the bed to the bedload layer. Such a threshold is rather difficult to estimate since it does not necessarily correspond to the concept of limit conditions for particle entrainment into motion. An alternative formulation for bedload models also discussed in Chapter 6 follows an Einsteinian approach, which is still based on the physics of particle saltation but does not invoke the existence of a continuum bedload layer or a threshold bed shear stress.

The experiments on the threshold conditions for particle entrainment into suspension of Chapter 7 provide new data on this phenomenon, particularly extending the range of particle sizes of previous investigations toward smaller values in the range 40 to 200 μm. Also, results of hiding effects in the case of particle entrainment into suspension from a coarser bed, which have great influence on the threshold conditions for particle entrainment, have apparently not been previously reported. Nonetheless, this phenomenon seems to be very similar to that observed in the case of bedload motion of sediment mixtures.

The experimental technique used in Chapter 4 to characterize coherent structures in the near bed region of an open channel flow, which combines simultaneous flow visualization and hot-film anemometry, seems to yield valuable information that contributes to advance the present understanding of the structure of wall bounded turbulence, particularly in the case of open channel flow which appears to be typically less studied than other flow configurations in turbulence research.

As discussed in Chapter 8, shear layers typically observed in the near wall region of the open channel flow analyzed interact with sediment particles lying in the channel bottom, which eventually results in the particles being entrained into suspension. Although there has been some speculation that this process would not be effective in entraining particles totally immersed in the viscous sublayer, the results presented in Chapter 8 demonstrate the opposite. Measurements of particle velocity during entrainment of fine sand with sizes in the range of about 200 μm reported in that chapter also offers new information on this phenomenon, mainly because the characteristics of the particles analyzed therein differ from those of previous similar studies. Previous research has

concentrated in the case of much larger particles of very small submerged specific density, which however have larger inertia and thus a much slower response to the turbulence of the flow.

In Chapter 9, a heuristic model characterizing the flow field associated with near bed coherent structures has been used to analyze the problem of particle entrainment into suspension. Although the results obtained are of more qualitative than quantitative value, this effort appears to be a first attempt to introduce concepts derived from observations of the interaction between particles and coherent structures into an analytical model for particle entrainment into suspension.

Apparently no previous attempts have been made to asses the effects of turbulence on the characteristics of particle saltation. The random walk model developed in Chapter 9 gives the possibility of studying such effects by analyzing statistics of the saltation trajectories, which are computed over many realizations of the saltation process under the influence of the turbulence of the flow. It seems also, that the formulation of a random walk model for sediment particle motion in turbulent open channel flow, which incorporates modelling of the crossing-trajectories effect, represents in itself a contribution to the analytical study of sediment transport.

Based on the improved understanding of the processes of particle saltation in water and particle entrainment into suspension obtained from the present research, it seems appropriate to revise Bagnold's (1973) definition of saltation, which has been already given in Chapters 2 and 5. Bagnold described saltation as the unsuspended transport of particles over a granular bed by a fluid flow, in the form of consecutive hops, and in which no upward impulses are imparted to the particles other than those attributable to successive contacts between them and the bed. As already pointed out, this definition is not totally correct because there is now enough evidence, both experimental and theoretical, that hydrodynamic lift forces play a fundamental role on the saltation process. Moreover, it is also apparent that the turbulence of the flow influences the saltation motion, which implies that turbulent upward and downward impulses are indeed exerted over the saltating particle during its motion. Accordingly, saltation could be better described as the unsuspended transport of particles over a granular bed by a fluid flow, in the form of consecutive hops that nonetheless keep the particles within the near bed region, which is governed mainly by the action of hydrodynamic forces that carry the particles through the flow, the downward pull of gravity, and the particles collision with the bed which transfers their streamwise momentum into upward momentum thus sustaining the saltation motion. This process is fundamentally different from particle transport in suspension, in that the latter is governed mainly by the turbulence of the flow, through convective and diffusive processes, in which particle motion is not confined to the near bed region but rather extends to the whole water column, and in which particle collision with the bed plays no significant role in sustaining particle motion.

Recommendations for future research

The characterization of the turbulence and related coherent structures of the open channel flow under consideration was made in the present investigation based on measurements of the streamwise flow velocity component only. A natural improvement in the description of the turbulent flow field would be to measure at least two components of the velocity field, in the streamwise and bed normal directions. The use of either a two-component LDV system or PIV, therefore, appears to be a necessity to accomplish such improvement.

From the point of view of the experimental study of particle-turbulence interactions, an improvement over the methodology employed in the present research would be to attempt the simultaneous measurement of particle and fluid velocities, which would call for the use of either a PDV (phase Doppler velocimetry) system or PIV applied to the case of two-phase flow. The latter would have the advantage of providing an instantaneous picture of the flow field as well as the velocity and position of solid particles, however it lacks the capability of resolving particle trajectories. A way of obtaining particle trajectories together with the flow field would be to apply PIV principles to analyze video images instead of still photographs. Nevertheless, given the time and length scales of particle motion measured in the present research, it seems that the recording rate given by standard video would be insufficient to resolve particle motion. On the other hand, as already discussed, it is apparent that the high-speed video system used in the present research has rather poor spatial resolution and light sensitivity, which would make its use to perform the PIV analyses mentioned above difficult. Undoubtedly, this problem requires the development of special experimental techniques.

Improving the description of the turbulent structure of the flow, including the characteristics of flow coherent structures, and also that of particle-turbulence interactions might improve also the understanding of the physical processes involved in the transport of sediment, particularly in relation to the mechanism governing particle entrainment into suspension. This would also help developing physically sound analytical models for such processes. For instance, a better description of the coherent structure of the streamwise vortices introduced in the formulation of the heuristic model for particle entrainment into suspension presented in Chapter 10 may improve the predictions of such model as discussed therein. Improving the heuristic model itself would require for example to incorporate a stochastic element for the characteristics of flow coherent structures.

An alternative method to study particle-turbulence interactions in the near bed region of the flow is to use flow fields generated using DNS to force the equations governing particle motion. Although a few attempts in this direction have already been made, the studies have concentrated on the case of smooth fixed wall. The application of this methodology to the case of a boundary formed by loose particles appears to be difficult given the present possibilities of DNS.

The present research has concentrated on analyzing particle transport processes taking place in the near bed region of the flow, however a complete understanding of the transport of sediment in open channel flow would require to study particle motion throughout the whole flow field. An interesting aspect to investigate would be for example the role of coherent structures in the outer region of the flow in transporting sediment particles within such region, and how these transport processes interact with those taking place near the wall.

With respect to research related to saltation phenomena, it is apparent that the model for particle saltation developed herein can be applied to situations different from the canonical case of straight, one dimensional, uniform, and steady open channel flow. Of course modelling saltation in non-canonical cases requires introducing models for the flow field in such cases, which may involve important research efforts.

For example, the saltation model could be extended to consider particle motion in the transverse direction, which would require also to modify the present model for the process of particle collision with the bed to account for the possibility of occurrence of non-zero values of the transverse particle velocity component after impact with the bed. Accounting for three-dimensional saltation would help simulating the process of transverse dispersion of bedload particles, which has importance regarding the formation of stable channels with loose boundaries and also on the emergence of longitudinal bedforms called ridges or longitudinal streaks. Similarly, the model could be applied to simulate particle saltation in channel bends or transversely inclined beds. This would help analyzing the issue of transverse bedload transport, which is important regarding modelling sediment transport in meandering channels as well as over three-dimensional bedforms such as alternate bars. Modelling particle saltation on top of bedforms of the dune type would also be an interesting extension of the present model, which has importance regarding the evolution of these sedimentary waves and also the estimation of bedload transport in this situation.

Modelling sediment transport of non-uniform sediment has importance specially in the study of coarse bed alluvial channels. Studying the saltation of mixtures would require experimental research to elucidate the physics involved in many aspects of this phenomenon, such as the formation of a coarser surface layer (armoring), the existence of hiding effects, and others. Modelling particle saltation of mixtures would imply incorporating those aspects to the simulation, which may call for the description of the entire cycle of particle motion, starting from the moment of particle re-entrainment, through successive saltation-collision sequences, to final distrainment of the particle when it gets trapped in the local topography of the bed. This could be approached by introducing stochastic models for different processes involved, such as the effect of bursting events and particle placement (or its relative exposition to the flow) in the case of particle re-entrainment, the effect of the local topography of the bed at the point of collision, and others.

Applications of the random walk model developed herein are not limited to the phenomenon of particle saltation. Indeed, such model could be applied to analyze sediment transport in a number of equilibrium and non-equilibrium situations, ranging from the estimation of suspended sediment concentration profiles in uniform open channel flow, to the analysis of development of concentration profiles of suspended sediment over a mobile bed downstream of a non-erodible surface, and fine sediment trapping in a bed formed by coarser sediment, to mention only a few. Implementing those applications would require to account for a non-Gaussian, skewed probability density distribution for the vertical component of the flow velocity fluctuations, which has great importance in the transport of suspended particles as discussed in Chapter 9, as well as to incorporate in the model the process of particle entrainment into suspension from the channel bed.

With regards to the Lagrangian equations for particle motion that have been used throughout the present investigation, basic research in a few related aspects seems to be necessary. For example, not much is known about the behavior of drag and lift coefficients for unsteady particle motion in turbulent flow close to a solid boundary, and similar conclusions are true for Basset and Magnus forces. The use of the equations for particle motion in the present research has relied on more or less valid approximations for these aspects, however there is no definite knowledge about how good the approximations invoked really are. These are complex issues that require major research efforts involving experimental as well as theoretical studies.

APPENDIX A

Engelund's (1965) criterion for the occurrence of suspended load

The basic idea behind Engelund's analysis is the following. Consider an open channel flow, in which, initially, due to turbulence there is a small concentration distribution $c(y , t)$ of suspended sediment, where y denotes a vertical coordinate measured from the bottom of the open channel, and t denotes time. This concentration profile will grow or decay on time. If it decays, the system is not able to maintain sediment in suspension (e.g., too small turbulence intensities, too large particles, etc.). If, on the other hand it grows, then the system allows suspension. The neutral stability of the concentration profile would be, therefore, related to incipient conditions for suspension.

Engelund proposed to analyze the stability of the following equation for the temporal evolution of the concentration of suspended sediment:

$$\frac{\partial c}{\partial t} = \frac{\partial}{\partial y} \left(\varepsilon \frac{\partial c}{\partial y} + w\, c\, (1 - c)^n \right) \tag{A.1}$$

where ε denotes the eddy diffusivity of the flow, w is the settling velocity of a single particle, and the term $w\, c\, (1 - c)^n$ is a correction to account for the modification of the particle settling velocity due to the concentration c, where the exponent n is about 5 for small particles.

It is important to note that in analyzing the stability of (A.1), Engelund's initial criterion for the initiation of suspension gets necessarily reformulated, such that now, if the initial concentration profile is stable then suspension is possible, and if it is unstable then it is assumed that suspension is not possible, although this does not follow strictly from the stability analysis. Moreover, the latter correction to the particle settling velocity, which is not usually accounted for in an equation for the suspended sediment concentration like (A.1), introduces a nonlinearity in the problem which turns out to be the only element that can render the initial concentration profile unstable. Therefore, Engelund's incipient condition for suspension seems to be based solely on this rather questionable correction.

Considering the following decomposition of the concentration: $c = c_0 + c_1$, where c_0 is the temporal mean value of the concentration, and c_1 denotes a small time dependent perturbation of the mean, and replacing in (A.1), equations for the mean and the perturbation are obtained as:

$$\frac{\partial}{\partial y} \left(\varepsilon \frac{\partial c_0}{\partial y} + w\, c_0\, (1 - c_0)^n \right) = 0 \tag{A.2}$$

$$\frac{\partial c_1}{\partial t} = \frac{\partial}{\partial y} \left(\varepsilon \frac{\partial c_1}{\partial y} + w\, \beta\, c_1 \right) \tag{A.3}$$

with:

$$\beta = (1 - c_0)^n (1 - n\, c_0/(1 - c_0)) \qquad (A.4)$$

Boundary conditions for c_0 are: i) the net flux of sediment must be conserved in the vertical, and ii) at a reference height near the bed $y = y_R$, $c_0 = c_R$, where c_R is a reference near-bed concentration. Boundary conditions for c_1 are the following: i) at $y = 0$, $c_1 = 0$, and ii) at $y = H$, $c_1 = 0$.

The eddy diffusivity of the flow can be estimated using the parabolic profile (Rouse, 1937):

$$\varepsilon = \varkappa\, u_*\, y\, (1 - y/H) \qquad (A.5)$$

where $\varkappa$ denotes von Karman constant, u_* denotes the flow shear velocity, and H denotes the flow depth.

The linear problem posed by (A.3) can be solved by separation of variables, where c_1 can be written as:

$$c_1 (y , t) = \psi(y)\, \phi(t) \qquad (A.6)$$

Replacing (A.6) in (A.3) gives the following form for $\phi(t)$:

$$\phi(t) = \phi_0 \exp (- p\, t) \qquad (A.7)$$

where p denote the eigenvalues of the system, which result from a solution of the following eigenvalue problem:

$$\xi (1 - \xi) \frac{d^2\psi}{d\xi^2} + ((1 - 2\, \xi) + \frac{w}{\varkappa\, u_*}\, \beta) \frac{d\psi}{d\xi} + (p \frac{H}{\varkappa\, u_*} + \frac{w}{\varkappa\, u_*} \frac{d\beta}{d\xi})\, \psi = 0 \qquad (A.8)$$

with the boundary conditions:

$$\psi(0) = \psi(1) = 0 \qquad (A.9)$$

where $\xi = y/H$, and β is given by (A.4).

The eigenvalue problem can be rewritten in the more general form:

$$f(\xi) \frac{d^2\psi}{d\xi^2} + g(\xi) \frac{d\psi}{d\xi} + h(\xi)\, \psi = \omega\, \psi \qquad (A.10)$$

where $\psi(\xi)$ represents the eigenfunctions and ω represents the eigenvalues, such that $\omega > 0$ implies that the system is unstable, $\omega < 0$ implies that the system is stable, and $\omega = 0$ corresponds to neutral stability. From (A.8), $\omega = - (p\, H)/(\varkappa\, u_*)$.

The eigenvalue problem (A.8) does not have an analytical solution, therefore the eigenvalues must be found numerically. Nevertheless, Engelund did a rather crude analytical estimation of the eigenvalues and found the following condition associated with neutral stability:

$$u_*/w \approx 0.25 \qquad (A.11)$$

Herein (A.10) is solved numerically, introducing a discretization of the vertical coordinate ξ. The number of eigenvalues of the numerical problem is given by the number of points used in the discretization of ξ. The most important eigenvalue is the one with maximum value, $\omega_{\max}$. If $\omega_{\max} > 0$ then there is at least one mode of the solution that will grow in time, and therefore the concentration profile will become unstable.

To find the maximum eigenvalue numerically, it is necessary first to solve the problem for c_0. It is easy to see that a solution of (A.2) with ε given by (A.5) and subjected to the boundary conditions already specified, is:

$$\sum_{j=1}^{n-1} \frac{1}{j\,(1-c_R)^j}\left(\left(\frac{1-c_R}{1-c_0}\right)^j - 1\right) + \ln\left(\frac{c_0}{c_R}\,\frac{1-c_R}{1-c_0}\right) = \ln\left(\frac{\xi_R}{\xi}\,\frac{1-\xi}{1-\xi_R}\right)^Z \qquad (A.12)$$

where $Z = w/(\varkappa\, u_*)$. The expression (A.12) represents a nonlinear equation for $c_0(\xi)$, which can be solved numerically for given values of c_R, $\xi_R = y_R/H$, and Z. This implies that the eigenvalue problem (A.10), and thus the values of $\omega_{\max}$ depend on Z as well as on the reference level and reference concentration ξ_R, c_R, respectively.

The numerical problem specified above was solved assuming a value of $n = 5$, and a reference level $\xi_R = 0.01$. The results obtained for $\omega_{\max}$ are summarized in Fig. A.1, as a function of Z and c_R. As seen therein, for values of c_R lower than about 10%, $\omega_{\max}$ is always negative, and therefore the concentration profile $c_0(\xi)$ is stable, for values of Z in the range from 0 to 10. For larger values of c_R, however, $\omega_{\max}$ becomes positive for values of Z larger than about 1, which implies that the concentration profile $c_0(\xi)$ becomes unstable for such conditions.

The more formal solution of the eigenvalue problem presented herein seems to indicate that Engelund's approximate solution (A.11) is not totally valid. In the first place it fails to include the influence of c_R in the condition for neutral stability. Besides, the neutral condition (A.11) can be rewritten as: $Z = (0.25\,\varkappa)^{-1} \approx 10.0$ (where a value $\varkappa = 0.4$ was used), for which as seen in Fig. A.1 the present solution predicts a stable initial concentration profile, even for values of c_R as high as 10%. For the typical near-bed concentrations found in natural streams, which are rarely larger than about 1%, the present solution indicates that the initial concentration is always stable. Moreover, it is not clear what an unstable concentration would mean physically. For Engelund's hypothesis identifying the neutral stability with the incipient conditions for suspension to be valid, an unstable concentration profile would have to evolve to a new attractor characterized by a zero concentration profile, which is not a solution of the problem for $c_0(\xi)$ posed by (A.2). Hence, it is possible that since the conditions for which the initial concentration profile becomes unstable were found to lie

outside the physical range, it is possible that the unstable profile would evolve to an also non-physical solution for $c_0(\xi)$. All the above indicates that although Engelund's initial idea for finding the incipient conditions for suspension looks plausible, the basic equation (A.1) does not appear to model the physics required to pursue such idea.

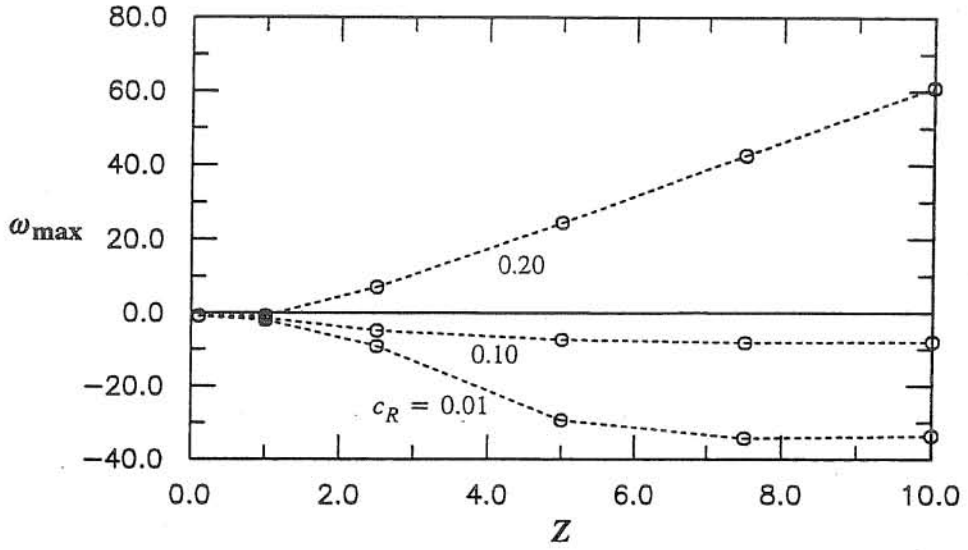

Fig. A.1 Values of the most unstable eigenvalue as a function of Z and c_R

References

Engelund, F. (1965). "A criterion for the ocurrence of suspended load". *La Houille Blanche*, No 8, pp 802.

Rouse, H. (1937). "Modern conceptions of the mechanics of turbulence". *Trans. ASCE*, vol 102, pp 463-543.

APPENDIX B

Engelund's (1965) analysis of turbulent energy and suspended load

Engelund analyzed the effect of suspended sediment on the distribution of the turbulent energy in a two-dimensional open channel flow using a one-equation model.

Consider a uniform flow of depth D in an open channel of constant slope S_0, carrying suspended load with a concentration distribution $c(y)$, where y denotes a vertical coordinate measured from the channel bottom. In this situation, the Navier-Stokes equation in the streamwise direction can be reduced to:

$$\frac{d}{dy}\left(\nu_t \frac{du}{dy} \right) = S_0 \, g \, (1 + R \, c) \tag{B.1}$$

where $u(y)$ is the vertical distribution of mean flow velocity, g denotes gravitational acceleration, R denotes the submerged specific density of the sediment, and ν_t denotes the eddy diffusivity of the flow. From force balance considerations:

$$D \, S_0 \, g = u_*^2 \tag{B.2}$$

where u_* denotes the flow shear velocity. Replacing (B.2) in (B.1), and introducing the following dimensionless parameters:

$$\eta = y/D \quad , \quad \bar{u} = u/u_* \quad , \quad \bar{\nu}_t = \nu_t/(u_* \, D) \tag{B.3}$$

the following relation is obtained:

$$\frac{d}{d\eta}\left(\bar{\nu}_t \frac{d\bar{u}}{d\eta} \right) = (1 + R \, c) \tag{B.4}$$

Neglecting the effect of the concentration c, and assuming that $d\bar{u}/d\eta = 0$ at $\eta = 1$:

$$\bar{\nu}_t \frac{d\bar{u}}{d\eta} = 1 - \eta \tag{B.5}$$

A one–equation model for the turbulent kinetic energy, K, can be written for the uniform open channel flow considered as (Rodi, 1984):

$$\frac{d}{dy}\left(\frac{\nu_t}{\sigma_k} \frac{dK}{dy} \right) + \nu_t \left(\frac{du}{dy} \right)^2 + R \, g \, \frac{\nu_t}{\sigma_t} \frac{dc}{dy} - c_D \frac{K^{3/2}}{L} = 0 \tag{B.6}$$

where σ_k and σ_t are diffusion constants for the turbulent kinetic energy and concentration of suspended sediment, respectively, L denotes a length scale characterizing the large-scale turbulent motion, and c_D is a constant of the model with a value of about 1.0. This equation can be rewritten in dimensionless form as:

$$\frac{d}{d\eta}\left(\frac{\bar{\nu}_t}{\sigma_k} \frac{d\bar{K}}{d\eta} \right) + \bar{\nu}_t \left(\frac{d\bar{u}}{d\eta} \right)^2 + \frac{R}{S_0} \frac{\bar{\nu}_t}{\sigma_t} \frac{dc}{d\eta} - c_D \frac{\bar{K}^{3/2}}{L/D} = 0 \tag{B.7}$$

where $\tilde{K} = K/u_*^2$.

The equation for the steady state concentration distribution is given by:

$$\frac{d}{dy}\left(\frac{\nu_t}{\sigma_t} \frac{dc}{dy} + w\, c \right) = 0 \tag{B.8}$$

where w denotes the particle settling velocity. Assuming that the total flux of sediment in the vertical is conserved, (B.8) can be integrated yielding:

$$\frac{\nu_t}{\sigma_t} \frac{dc}{dy} + w\, c = \text{constant} = 0 \tag{B.9}$$

therefore, in dimensionless terms:

$$\frac{\tilde{\nu}_t}{\sigma_t} \frac{dc}{d\eta} = -\tilde{w}\, c \tag{B.10}$$

where $\tilde{w} = w/u_*$.

Introducing the model relationship for the eddy diffusivity (Rodi, 1984):

$$\tilde{\nu}_t = c_\mu' \sqrt{\tilde{K}}\, L/D \tag{B.11}$$

where c_μ' is a constant of order 0.1, and replacing (B.5), (B.10), and (B.11) in (B.7), the following dimensionless equation for the turbulent kinetic energy is obtained:

$$\tilde{\nu}_t \frac{d}{d\eta}\left(\frac{\tilde{\nu}_t}{\sigma_k} \frac{d\tilde{K}}{d\eta} \right) - \frac{R}{S_0}\, \tilde{\nu}_t\, \tilde{w}\, c - c_\mu'\, c_D\, \tilde{K}^2 = -(1-\eta)^2 \tag{B.12}$$

In the absence of suspended sediment, $c = 0$, and the buoyancy term $-(R/S_0)\, \tilde{\nu}_t\, \tilde{w}\, c$, which is related to the amount of turbulent kinetic energy used to maintain the sediment in suspension, vanishes. In this situation the boundary condition for K at the channel bottom is obtained by assuming the existence of an equilibrium layer where the production of turbulent kinetic energy balances the dissipation of such energy, and where the shear stress is approximately equal to the wall shear stress (Rodi, 1984), such that:

$$\tilde{K}(\eta \approx 0) = \tilde{K}_w = \frac{1}{\sqrt{c_\mu'\, c_D}} \tag{B.13}$$

To analyze the effect of the suspended sediment on K, Engelund assumed the following decomposition:

$$\tilde{K} = \tilde{K}_0 - \tilde{K}_s \tag{B.14}$$

where $\tilde{K}_0$ denotes the turbulent kinetic energy of the flow without sediment, i.e. for $c = 0$, and $\tilde{K}_s$ represents a correction corresponding to the amount of energy spent in keeping the sediment in

suspension, which is assumed to be small, that is $\tilde{K}_s << \tilde{K}_0$, and always positive, that is there is a net reduction of the turbulent kinetic energy of the flow, with respect to the clear water situation, due to the presence of the suspended sediment.

Engelund, furthermore, assumed that the presence of the suspended sediment does not affect the length scale L. Substituting (B.14) in (B.12) and linearizing, the following equation is obtained for $\tilde{K}_s$:

$$\frac{d}{d\eta}\left(\frac{1}{2}\,\tilde{\nu}_{t0}\,\frac{\tilde{K}_s}{\tilde{K}_0}\,\frac{d\tilde{K}_0}{d\eta}\right)+\frac{d}{d\eta}\left(\tilde{\nu}_{t0}\,\frac{d\tilde{K}_s}{d\eta}\right)+\frac{R}{S_0}\,\tilde{w}\,c-2\,c_{\mu}'\,c_D\,\frac{\tilde{K}_0\,\tilde{K}_s}{\tilde{\nu}_{t0}}=0 \qquad \text{(B.15)}$$

where $\tilde{\nu}_{t0}$ denotes the dimensionless eddy diffusivity of the clear water flow. Engelund restricted the analysis to the wall layer where he assumed $\tilde{K}_0$ was approximately constant, equal to $\tilde{K}_w$ given by (B.13). Nevertheless, at the same time he assumed that $\tilde{K}_s$ varied within the wall layer. Also, Engelund assumed that in such layer:

$$\tilde{\nu}_{t0}=\varkappa\,\eta \qquad \text{(B.16)}$$

where $\varkappa$ denotes the von Karman constant.

Replacing (B.16) in (B.10), the concentration distribution within the wall layer can be expressed as:

$$c=k\,\eta^{-Z} \qquad \text{(B.17)}$$

where k is a dimensionless factor and $Z=\tilde{w}/\varkappa$.

Engelund neglected the first term of the right hand side of (B.15). Replacing (B.16) and (B.17) in (B.15), the following equation for $\tilde{K}_s$ is obtained:

$$\eta^2\,\frac{d^2\tilde{K}_s}{d\eta^2}+\eta\,\frac{d\tilde{K}_s}{d\eta}-\frac{2}{\varkappa^2}\,\frac{\tilde{K}_s}{\tilde{K}_w}+\frac{R}{S_0}\,k\,Z\,\eta^{(1-Z)}=0 \qquad \text{(B.18)}$$

Engelund did not speculate about the boundary conditions for this equation, however it is easy to see that a solution is:

$$\tilde{K}_s=a\,\eta^{(1-Z)} \qquad \text{(B.19)}$$

where a is given by:

$$a=\frac{(R/S_0)\,k\,Z}{2/(\varkappa^2\,\tilde{K}_w)-(Z-1)^2} \qquad \text{(B.20)}$$

Since it is required that $\tilde{K}_s>0$, then also $a>0$. This gives the following condition for Z:

$$1-\frac{1}{\varkappa}\sqrt{\frac{2}{\tilde{K}_w}}<Z<1+\frac{1}{\varkappa}\sqrt{\frac{2}{\tilde{K}_w}} \qquad \text{(B.21)}$$

Replacing (B.13) in (B.21), considering that $\varkappa = 0.4$, c_μ' is about 0.1, and c_D is about 1.0, then:

$$-1 < Z < 3 \tag{B.22}$$

which by definition of Z gives the following condition for $\tilde{K}_s$ not to be negative:

$$u_*/w > 0.83 \tag{B.23}$$

This condition was interpreted by Engelund as the limit for which suspension of sediment can occur. However, from (B.20) it is easy to see that for $\tilde{K}_s$ to be bounded as $\eta \rightarrow 0$ (recall that $\tilde{K}_s$ must be much smaller than $\tilde{K}_0$ for the linearized equation (B.18) to be valid) it is required that $Z > 1$, giving the following condition, which results to be more restrictive than (B.23) and thus renders such relationship invalid:

$$u_*/w > 2.5 \tag{B.24}$$

Hence, for the linearized equation (B.18) to be valid, (B.24) must be satisfied, with which $\tilde{K}_s$ would never be negative, and the condition for the limit of suspension proposed by Engelund would never apply. Nevertheless, it is necessary to point out that the validity of (B.18), and thus of its solution (B.19), is rather unclear. In fact, as already discussed, Engelund assumed, without much justification, that $\tilde{K}_0$ was constant in the wall layer and at the same time that $\tilde{K}_s$ varied with η in such region. Besides, he did not discussed about the boundary conditions for $\tilde{K}_s$.

A more formal evaluation of the effect of suspended sediment on the turbulent kinetic energy in the wall region can be made by considering the following discussion. García (1992) introduced a correction function, ϕ_K, to account for the variation of the turbulent kinetic energy near the bed in the presence of suspended sediment, $\tilde{K}_{ws}$, with respect to that in clear water flow, $\tilde{K}_w$, given by (B.13), such that:

$$\tilde{K}_{ws} = \tilde{K}_w \, \phi_K(y/L_{MO}) \tag{B.25}$$

where L_{MO} denotes the Monin–Obukov length (Turner, 1973), which is defined in terms of the rate of energy spent in maintaining the sediment in suspension, B, given in dimensionless terms by:

$$\tilde{B} = B \, D/u_*^3 = (R/S_0) \, \tilde{w} \, c \tag{B.26}$$

so:

$$L_{MO}/D = (\varkappa \, \tilde{B})^{-1} \tag{B.27}$$

In the presence of sediment it is assumed that in the equilibrium layer near the wall, the production of turbulent kinetic energy is balanced by the sum of viscous dissipation and the rate of work done against the sediment-induced density gradient. In such region, García proposed:

$$\phi_K = 1 - 0.5\ y/L_{MO} \tag{B.28}$$

which from (B.26) and (B.27) can be written as:

$$\phi_K = 1 - 0.5\ \varkappa\ \bar{B}\ \eta = 1 - 0.5\ \varkappa\ (\ R/S_0\ )\ \bar{w}\ c\ \eta \tag{B.29}$$

It is clear from (B.29) that at a given distance from the bed η, ϕ_K would always be lower or equal than 1.0, for any (physically valid) values of $\bar{w}$ or c. Therefore it can be concluded from this analysis that the effect of the suspended sediment on the turbulent kinetic energy near the wall is to reduce such energy, such that the difference would be used to maintain the sediment suspension, and that the reduction increases with the concentration and also with the ratio w/u_*.

The above conclusion appears to indicate that Engelund condition for the limit of suspension results only from mathematical manipulations and assumptions involved in his analysis and would not represent the physics of the problem.

It is necessary to add that the most important assumption invoked in deriving the buoyancy term $\bar{B}$ in the equation for the turbulent kinetic energy (B.12) is that the size, d_p, of the suspended particles is small in comparison with the Kolmogorov microscale of the turbulence η_K (Monin and Yaglom, 1971). This condition can be expressed as:

$$du_p/\eta_K < 1 \tag{B.30}$$

By definition, the Kolmogorov microscale can be written as (Tennekes and Lumley, 1972):

$$\eta_K = (\ \nu^3/\varepsilon\ )^{1/4} \tag{B.31}$$

where ε denotes the rate of energy dissipation. From Rodi (1984) the value of ε near the wall can be estimated as:

$$\varepsilon = u_*^3/(\ \varkappa\ y\ ) \tag{B.32}$$

Replacing (B.31) and (B.32) in (B.30) gives:

$$Re_{p_*} < (\ \varkappa\ y_+\ )^{1/4} \tag{B.33}$$

where $Re_{p_*} = u_*\ dp/\nu$ and $y_+ = u_*\ y/\nu$. According to Rodi (1984) (B.32) is valid in the region $30 < y_+ < 100$, therefore the right hand side of (B.33) has a value of about 2.0 to 2.5. Based on this the following relationship is proposed, for the particle size to be lower than the Kolmogorov microscale in the near wall region:

$$Re_{p_*} < 2.0 \tag{B.34}$$

As long as (B.34) is satisfied, the presence of the suspended particles have the effect of reducing the turbulent kinetic energy of the flow, mainly by using part of the turbulent energy

production in maintaining the particles in suspension, which physically corresponds to a work done against the sediment-induced density gradient.

Nevertheless there is substantial experimental evidence showing that sufficiently large suspended particles can enhance the turbulence of the flow, and thus increase the turbulent kinetic energy with respect to that of the clear water situation (Hetsroni, 1989; Tsuji, 1991; Hetsroni, 1991). Physically this occurs when the particle Reynolds number is large enough so wake shedding would increase the production of turbulent kinetic energy (Yuan and Michaelides, 1992). Hetsroni (1989) concluded that turbulent enhancement would occur for particle Reynolds numbers defined as $Re_p = u_r\, d_p/\nu$, where u_r denotes particle relative velocity, larger than about 400, for which vortex shedding from the particle wake exists. For lower values of Re_p the presence of the particles tend to reduce the turbulent kinetic energy as discussed previously. Hetsroni (1991), on the other hand, concluded that near the bed, values of Re_{p_*} larger than about 5 to 10 would increase the turbulent kinetic energy, while values of Re_{p_*} lower than about 2 would decrease such energy. This latter condition is in complete agreement with (B.34).

Based on the above discussion, it can be expected that near the wall turbulent enhancement would occur for:

$$Re_{p_*} > 7.5 \tag{B.35}$$

Conditions (B.34) and (B.35) are plotted in the parameter space $\tau_* = u_*^2/(\,R\,g\,d_p\,)$, $R_p = \sqrt{R\,g\,d_p^3}\,/\nu$ in Fig. B.1, together with Shields curve, the range of conditions for initiation of suspension proposed by van Rijn (1984), and the experimental threshold conditions for particle entrainment into suspension reported in Chapter 7. Therein is apparent that turbulence enhancement can occur for suspended sediment with values of R_p larger than about 20, at not so large values of the dimensionless shear stress τ_*. It is also clear from Fig. B.1 that the buoyancy term $\tilde{B}$ in the equation for turbulent kinetic energy is supposed to be valid only for values of R_p lower than about 10, for which the particle size is smaller than the Kolmogorov microscale. The latter conclusion has importance in applying one-equation and K-ε models to the analysis of suspended sediment.

References

Engelund, F. (1965). "Turbulent energy and suspended load". *Progress Report No 10.* Coastal Engrg. Lab., Hydr. Lab., Tech. University of Denmark. pp 2-9.

García, M. (1992). "Boundary conditions for sediment–laden flows". *Proceedings of the Hydraulic Engineering Sessions at Water Forum*, ASCE. Baltimore.

Hetsroni, G. (1991). "The effect of particles on the turbulence in a boundary layer". *Two Phase Flow*, Chap. 8. M. Rocco, Ed. Butterworth.

Hetsroni, G. (1989). "Particles-turbulence interaction". *Int. J. Multiphase Flow*, vol 15, No 5, pp 735–746.

Monin, A. S., and Yaglom, A. M. (1971). "Statistical fluid mechanics, vol. 1". *The MIT Press*, Cambridge, Massachusetts.

Rodi, W. (1984). "Turbulence models and their application in hydraulics". *State of the Art paper, IAHR*. Second Revised Edition.

Tennekes, H., and Lumley, J. L. (1972). "A first course in turbulence". *The MIT Press*, Cambridge, Massachusetts.

Tsuji, Y. (1991). "Review: Turbulence modifications in fluid-solid flows". *First Joint Conference*, ASME–JSME Fluids Engineering.

Turner, J. S. (1973). "Buoyancy effects in fluids". *Cambridge University Press*, New York.

van Rijn, L. C. (1984). "Sediment transport, Part II: suspended load transport". *J. Hydr. Engrg.*, vol 110, No 11, pp 39-48.

Yuan, Z. and Michaelides, E. E. (1992). "Turbulence modulation in particulate flows–a theoretical approach". *Int. J. Multiphase Flow*, vol 18, No 5, pp 779–785.

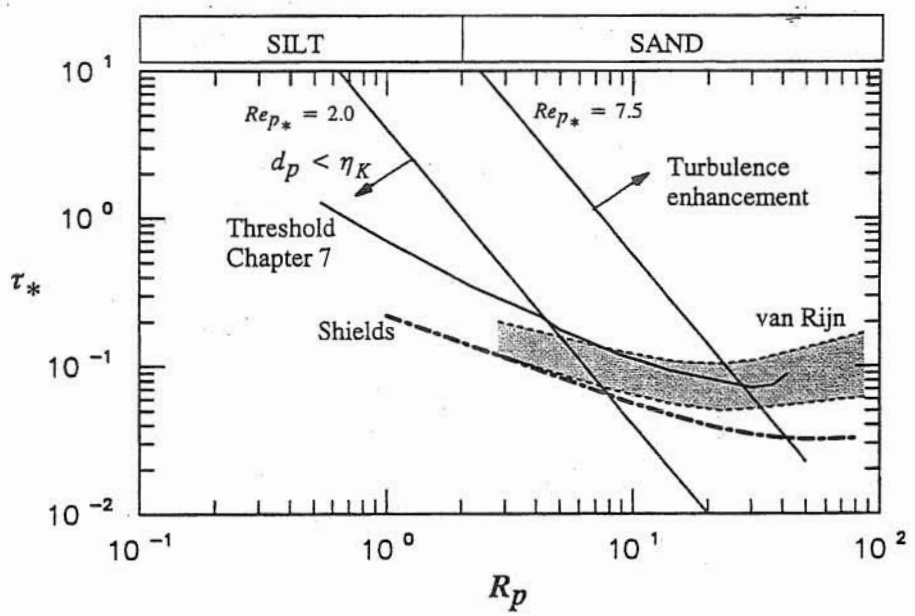

Fig. B.1 Limits for turbulence enhancement and for particle size smaller than Kolmogorov's microscale.

APPENDIX C

Tables with experimental data

Tables with experimental data corresponding to the results reported in Chapters 3, 4, 5, 7 and 8 are presented next. In the tables symbols correspond to those explained and defined in the text of the respective chapters. Likewise, the experiments have been identified with the same code as in the text of those chapters, so corresponding experimental conditions, when they have not been specified in the tables, can be obtained from the information given therein.

C.1 Chapter 3: Characterization of turbulence in open channel flow

Table C.1 Basic statistics of turbulent open channel flow

Series	Experiment	h (m)	y/h	u_{rms}/u	u_{rms}/u_*	S_u	F_u
S1	S11	0.0250	0.080	0.143	2.121	–0.450	2.976
			0.200	0.091	1.515	–0.404	3.005
			0.320	0.080	1.394	–0.465	3.101
			0.520	0.064	1.152	–0.403	2.894
			0.720	0.050	0.909	–0.433	3.167
	S12	0.0350	0.057	0.132	1.950	–0.322	2.729
			0.200	0.085	1.450	–0.275	2.885
			0.314	0.071	1.300	–0.547	3.186
			0.486	0.061	1.200	–0.656	3.364
			0.657	0.044	0.900	–0.404	3.198
S2	S21	0.0300	0.067	0.146	1.989	–0.411	3.002
			0.100	0.131	1.989	–0.419	3.048
			0.200	0.089	1.492	–0.299	2.881
			0.333	0.075	1.381	–0.423	2.906
			0.500	0.056	1.050	–0.465	3.176
			0.667	0.048	0.939	–0.664	3.537
	S22	0.0410	0.049	0.135	2.036	–0.256	2.952
			0.098	0.108	1.810	–0.177	2.829
			0.195	0.091	1.493	–0.272	2.778
			0.293	0.084	1.448	–0.284	2.712
			0.488	0.056	1.222	–0.372	3.021
			0.732	0.043	0.995	–0.452	3.193
	S23	0.0460	0.043	0.136	2.036	–0.280	2.954
			0.109	0.107	1.810	–0.128	2.762

Table C.1 (continued)

Series	Experiment	h (m)	y/h	u_{rms}/u	u_{rms}/u_*	S_u	F_u
			0.217	0.081	1.493	–0.383	2.944
			0.304	0.074	1.448	–0.277	2.638
			0.543	0.061	1.222	–0.229	2.579
			0.696	0.047	0.995	–0.425	3.283
	S24	0.0520	0.038	0.136	2.017	–0.228	2.957
			0.096	0.097	1.639	–0.152	2.842
			0.288	0.083	1.555	–0.179	2.623
			0.481	0.060	1.218	–0.336	2.772
			0.673	0.042	0.924	–0.610	3.561
T1	T11	0.0271	0.074	0.197	2.146	–0.242	2.858
			0.148	0.133	1.749	–0.293	2.780
			0.295	0.117	1.749	–0.455	3.205
			0.554	0.086	1.382	–0.458	3.017
			0.812	0.058	0.935	–0.368	3.230
	T12	0.0298	0.067	0.176	2.100	–0.385	2.952
			0.134	0.157	2.072	–0.278	2.836
			0.268	0.119	1.694	–0.200	2.764
			0.503	0.080	1.282	–0.397	3.176
			0.839	0.057	0.986	–0.483	3.051
	T13	0.0329	0.061	0.179	2.094	–0.143	2.737
			0.122	0.141	1.785	–0.132	2.976
			0.243	0.115	1.691	–0.288	2.703
			0.456	0.088	1.430	–0.539	2.862
			0.760	0.059	1.018	–0.658	4.106
T2	T21	0.0335	0.060	0.197	2.192	–0.138	2.703
			0.119	0.157	2.021	–0.181	2.822
			0.239	0.125	1.770	–0.302	2.877
			0.447	0.092	1.498	–0.593	3.162
			0.746	0.059	1.046	–0.609	3.660
	T22	0.0415	0.048	0.215	2.222	–0.080	2.641
			0.121	0.150	1.969	–0.169	2.688
			0.241	0.127	1.868	–0.133	2.691
			0.483	0.085	1.441	–0.414	2.960

Table C.1 (continued)

Series	Experiment	h (m)	y/h	u_{rms}/u	u_{rms}/u_*	S_u	F_u
			0.724	0.066	1.194	–0.139	2.894
	T23	0.0460	0.043	0.206	2.294	–0.206	2.659
			0.109	0.155	1.959	–0.062	2.650
			0.217	0.113	1.652	–0.201	2.855
			0.435	0.097	1.655	–0.504	3.032
			0.761	0.066	1.208	–0.486	3.119
	T24	0.0506	0.040	0.207	1.703	–0.004	2.712
			0.119	0.138	1.909	–0.119	2.768
			0.237	0.123	1.788	–0.152	2.843
			0.494	0.086	1.456	–0.255	2.807
			0.692	0.062	1.153	–0.459	3.260
T3	T31	0.0389	0.051	0.189	2.213	–0.004	2.745
			0.103	0.167	2.060	–0.150	2.621
			0.206	0.129	1.906	–0.236	2.789
			0.386	0.103	1.648	–0.160	2.788
			0.643	0.071	1.213	–0.465	3.274

Table C.2 Characteristic scales of turbulent open channel flow

Series	Exp.	h (m)	y/h	L_x/h	λ/h (1)	λ/h (2)	η/h	$\varepsilon\ h/u_*^3$
S1	S11	0.0250	0.080	0.320	0.139	0.092	0.0052	19.298
			0.200	0.400	0.137	0.122	0.0071	5.626
			0.320	0.560	0.154	0.150	0.0082	3.129
			0.520	0.640	0.163	0.177	0.0098	1.544
			0.720	0.680	0.178	0.205	0.0119	0.715
	S12	0.0350	0.057	0.229	0.089	0.062	0.0034	20.989
			0.200	0.457	0.105	0.102	0.0051	4.315
			0.314	0.571	0.127	0.121	0.0059	2.488
			0.486	0.714	0.145	0.140	0.0066	1.565
			0.657	0.629	0.151	0.152	0.0079	0.750
S2	S21	0.0300	0.067	0.200	0.102	0.066	0.0040	25.453
			0.100	0.267	0.109	0.076	0.0043	19.090
			0.200	0.400	0.116	0.107	0.0058	5.369

Table C.2 (continued)

Series	Exp.	h (m)	y/h	L_x/h	λ/h (1)	λ/h (2)	η/h	$\varepsilon\ h/u_*^3$
			0.333	0.467	0.145	0.120	0.0064	3.653
			0.500	0.600	0.140	0.156	0.0084	1.247
			0.667	0.600	0.160	0.165	0.0091	0.893
	S22	0.0410	0.049	0.244	0.071	0.057	0.0029	21.222
			0.098	0.268	0.078	0.065	0.0034	12.149
			0.195	0.512	0.094	0.092	0.0041	5.361
			0.293	0.634	0.117	0.104	0.0045	3.959
			0.488	0.561	0.114	0.115	0.0055	1.722
			0.732	0.610	0.128	0.135	0.0067	0.786
	S23	0.0460	0.043	0.239	0.064	0.052	0.0025	22.842
			0.109	0.435	0.076	0.074	0.0032	8.823
			0.217	0.500	0.088	0.087	0.0039	4.308
			0.304	0.652	0.102	0.101	0.0042	3.012
			0.543	0.783	0.121	0.121	0.0050	1.508
			0.696	0.783	0.125	0.134	0.0058	0.816
	S24	0.0520	0.038	0.192	0.057	0.042	0.0021	27.599
			0.096	0.308	0.063	0.059	0.0027	9.252
			0.288	0.577	0.104	0.083	0.0033	4.214
			0.481	0.827	0.111	0.113	0.0044	1.415
			0.673	0.615	0.117	0.112	0.0050	0.830
T1	T11	0.0271	0.074	0.258	0.105	0.072	0.0040	24.746
			0.148	0.443	0.130	0.104	0.0053	7.814
			0.295	0.480	0.154	0.109	0.0055	7.213
			0.554	0.664	0.179	0.144	0.0071	2.571
			0.812	0.664	0.168	0.175	0.0095	0.795
	T12	0.0298	0.067	0.235	0.099	0.065	0.0036	25.526
			0.134	0.336	0.117	0.078	0.0039	17.145
			0.268	0.470	0.127	0.102	0.0050	6.692
			0.503	0.604	0.149	0.132	0.0065	2.258
			0.839	0.671	0.175	0.159	0.0082	0.923
	T13	0.0329	0.061	0.243	0.091	0.061	0.0032	24.437
			0.122	0.243	0.090	0.066	0.0036	15.127

Table C.2 (continued)

Series	Exp.	h (m)	y/h	L_x/h	λ/h (1)	λ/h (2)	η/h	$\varepsilon\, h/u_*^3$
			0.243	0.578	0.123	0.104	0.0047	5.413
			0.456	0.730	0.151	0.127	0.0056	2.596
			0.760	0.730	0.164	0.150	0.0072	0.936
T2	T21	0.0335	0.060	0.179	0.091	0.049	0.0027	38.105
			0.119	0.298	0.090	0.065	0.0032	17.905
			0.239	0.388	0.123	0.080	0.0038	9.252
			0.447	0.716	0.151	0.118	0.0050	3.038
			0.746	0.656	0.164	0.135	0.0064	1.129
	T22	0.0415	0.048	0.193	0.074	0.041	0.0020	36.788
			0.121	0.362	0.097	0.060	0.0026	13.643
			0.241	0.540	0.121	0.071	0.0029	8.741
			0.483	0.618	0.141	0.094	0.0038	2.972
			0.724	0.695	0.155	0.107	0.0044	1.576
	T23	0.0460	0.043	0.196	0.068	0.038	0.0018	39.913
			0.109	0.304	0.081	0.052	0.0022	15.990
			0.217	0.326	0.094	0.058	0.0026	8.947
			0.435	0.782	0.142	0.090	0.0032	3.751
			0.761	0.761	0.146	0.104	0.0041	1.500
	T24	0.0506	0.040	0.138	0.044	0.034	0.0018	23.104
			0.119	0.296	0.084	0.047	0.0020	15.193
			0.237	0.514	0.098	0.064	0.0024	7.192
			0.494	0.791	0.133	0.088	0.0031	2.528
			0.692	0.830	0.141	0.102	0.0037	1.195
T3	T31	0.0389	0.051	0.206	0.088	0.046	0.0023	34.084
			0.103	0.360	0.099	0.063	0.0027	15.698
			0.206	0.540	0.128	0.080	0.0032	8.295
			0.386	0.618	0.148	0.092	0.0037	4.688
			0.643	0.695	0.158	0.113	0.0048	1.664

(1) Computed using (3.32)
(2) Computed using (3.33)

C.2 Chapter 4: Characterization of near bed coherent structures in open channel flow

Table C.3 Convective velocity of shear layers

Series	Re	u_{c+}	$\sigma_{u_{c+}}$	u_c/U	u_c/u
ES1-S	5300	9.9	2.5	0.69	0.71
	12400	10.3	1.5	0.59	0.70
	18100	10.4	3.0	0.55	0.68
ES1-T	11840	6.6	2.4	0.50	0.68
	15170	6.2	1.7	0.47	0.65
	18840	6.5	1.5	0.50	0.70

Table C.4 Vertical variation of minima of conditional ensemble averaged velocity distributions associated with shear layers

Series	y_+	$\lvert < u' >_{min} \rvert / u_{rms}$	$\lvert < u' >_{min} \rvert / u_*$
ES2	38	2.57	6.38
	52	2.00	4.50
	64	2.23	5.00
	80	1.59	2.71

C.3 Chapter 5: Experiments on saltation

Table C.5 Mean values of variables characterizing saltation

Series	Exp.	τ_*	τ_*/τ_{*c}	h_s	λ_s	u_s	μ_d
G1	G11	0.090	1.59	1.70	5.70	3.60	0.32
	G12	0.120	2.14	2.10	6.50	3.50	0.30
	G13	0.140	2.48	1.80	7.70	3.90	0.32
G2	G21	0.080	1.38	0.90	5.10	3.30	0.28
	G22	0.090	1.62	1.00	4.50	2.80	0.26
	G23	0.100	1.79	1.10	5.90	3.10	0.30
S1	S11	0.033	1.02	0.99	6.30	5.96	0.17
	S12	0.058	1.82	1.07	9.00	5.57	0.25
	S13	0.061	1.90	1.19	10.30	5.91	0.24
	S14	0.078	2.44	1.20	11.10	5.55	0.21
	S15	0.081	2.52	1.24	11.30	5.97	0.18
	S16	0.088	2.70	1.33	12.40	5.57	0.18

Table C.6 Standard deviations of variables characterizing saltation

Series	Exp.	τ_*	τ_*/τ_{*c}	σ_{h_s}	σ_{λ_s}	σ_{u_s}	σ_{μ_d}
G1	G11	0.090	1.59	0.5	1.9	0.9	0.3
	G12	0.120	2.14	0.9	2.8	0.8	0.1
	G13	0.140	2.48	0.7	2.9	0.9	0.1
G2	G21	0.080	1.38	0.4	1.9	1.0	0.2
	G22	0.090	1.62	0.3	1.8	0.8	0.2
	G23	0.100	1.79	0.3	2.1	0.8	0.2
S1	S11	0.033	1.02	0.3	3.1	1.8	0.3
	S12	0.058	1.82	0.4	4.6	1.5	0.4
	S13	0.061	1.90	0.4	4.6	1.3	0.3
	S14	0.078	2.44	0.5	5.4	1.1	0.3
	S15	0.081	2.52	0.5	4.9	1.5	0.3
	S16	0.088	2.70	0.5	5.2	1.4	0.3

Table C.7 Mean values and standard deviations of incidence and takeoff angles

Series	Exp.	τ_*	τ_*/τ_{*c}	$< \theta_{in} > (^\circ)$	$< \theta_{out} > (^\circ)$	$\sigma_{\theta_{in}} (^\circ)$	$\sigma_{\theta_{out}} (^\circ)$
G1	G11	0.090	1.59	21.5	36.6	9.3	20.1
	G12	0.120	2.14	15.3	24.8	7.5	14.8
	G13	0.140	2.48	11.2	22.1	6.0	12.0
G2	G21	0.080	1.38	19.2	32.4	8.3	17.9
	G22	0.090	1.62	22.9	28.4	11.6	18.4
	G23	0.100	1.79	14.9	32.8	8.7	16.4
S1	S11	0.033	1.02	13.9	26.9	11.2	14.6
	S12	0.058	1.82	10.5	21.7	7.5	13.2
	S13	0.061	1.90	11.6	26.8	7.1	17.4
	S14	0.078	2.44	8.5	17.3	6.1	11.3
	S15	0.081	2.52	8.2	19.7	7.2	14.1
	S16	0.088	2.70	8.6	23.8	5.8	14.8

Table C.8 Mean values and standard deviations of dimensionless particle angular velocity

Series	Exp.	τ_*	τ_*/τ_{*c}	S	σ_S
S1	S11	0.033	1.02	4.21	2.0
	S12	0.041	1.23	3.63	0.7
	S13	0.061	1.90	2.91	0.9
	S14	0.078	2.44	1.95	0.8
	S16	0.088	2.70	2.57	0.9

Table C.9 Mean values and standard deviations of dimensionless particle resting time

Series	Exp.	τ_*	τ_*/τ_{*c}	t_r	σ_{t_r}
S2	S21	0.037	1.15	19.9	22.0
	S22	0.047	1.45	9.6	8.6
	S23	0.057	1.76	10.0	7.6

Table C.10 Values of restitution and friction coefficients

Series	Exp.	τ_*	τ_*/τ_{*c}	e	f
G1	G11	0.090	1.59	0.50	0.75
	G12	0.120	2.14	0.24	0.78
	G13	0.140	2.48	0.16	0.77
G2	G21	0.080	1.38	0.41	0.75
	G22	0.090	1.62	0.29	0.68
	G23	0.100	1.79	0.38	0.66
S1	S11	0.033	1.02	0.34	0.96
	S12	0.058	1.82	0.15	0.79
	S13	0.061	1.90	0.36	0.86
	S14	0.078	2.44	0.01	0.86
	S15	0.081	2.52	0.06	0.95
	S16	0.088	2.70	0.21	0.89

C.4 Chapter 7: Threshold for particle entrainment into suspension

Table C.11 Threshold conditions for particle entrainment into suspension

Series	Exp.	R_p	Re_{p_*}	τ_*	Suspension
S1	S11	0.94	0.63	0.446	No
	S12		0.69	0.534	No
	S13		0.74	0.622	No
	S14		0.79	0.710	No
	S15		0.84	0.798	Yes
	S16		0.89	0.886	Yes
S2	S21	3.66	1.56	0.180	No
	S22		1.70	0.216	No
	S23		1.84	0.252	Yes
	S24		1.96	0.287	Yes
	S25		2.08	0.323	Yes
	S26		2.19	0.358	Yes
S3	S31	4.77	1.85	0.151	No
	S32		2.03	0.181	Yes
	S33		2.19	0.211	Yes
	S34		2.34	0.241	Yes
	S35		2.48	0.271	Yes
	S36		2.61	0.301	Yes
S4	S41	13.48	3.71	0.076	No
	S42		4.06	0.091	No
	S43		4.38	0.106	Yes
	S44		4.68	0.120	Yes
	S45		4.96	0.135	Yes
	S46		5.23	0.150	Yes
S5	S51	49.06	8.78	0.032	No
	S52		9.61	0.038	No
	S53		10.37	0.045	No
	S54		11.08	0.051	No
	S55		11.74	0.057	No
	S56		12.37	0.064	No
T1	T11	0.94	1.08	1.258	No

Table C.11 (continued)

Series	Exp.	R_p	Re_{p_*}	τ_*	Suspension
	T12		1.25	1.681	No
T2	T21	3.66	2.26	0.335	No
	T22		2.45	0.416	No
	T23		2.70	0.520	No
	T24		2.71	0.520	No
	T25		2.93	0.619	No
	T26		3.08	0.680	No
	T27		3.79	1.027	No
T3	T31	4.77	2.27	0.215	No
	T32		2.55	0.273	No
	T33		2.98	0.372	No
	T34		3.42	0.489	No
	T35		3.82	0.613	No
	T36		4.52	0.862	Yes
T4	T41	13.48	4.61	0.109	No
	T42		4.96	0.129	No
	T43		5.46	0.157	No
	T44		6.04	0.193	No
	T45		6.53	0.225	No
	T46		6.87	0.250	Yes
	T47		7.33	0.285	Yes
	T48		7.86	0.328	Yes
T5	T51	49.06	21.36	0.182	No

C.5 Chapter 8: Experiments on particle-turbulence interaction in the near wall region of a turbulent open channel flow

Table C.12 Ratio between number of outer ejections and total number of ejections

Series	τ_*	No outer ejec/total No ejec
S	0.100	0.27
	0.117	0.48
	0.135	0.56
	0.150	0.61

Table C.12 (continued)

Series	τ_*	No outer ejec/total No ejec
T	0.224	0.05
	0.255	0.73
	0.284	0.83
	0.329	0.90

Table C.13 Dimensionless local instantaneous particle ejection velocities

Series	Re	y_+	u_{p+}	v_{p+}
S	10760	8.22	4.03	1.42
		14.39	10.19	1.66
		11.98	8.30	3.56
		15.41	9.48	0.95
		11.64	9.96	0.95
		15.06	5.93	0.95
		7.53	6.16	0.95
		13.01	4.98	0.71
		12.67	6.88	0.47
		7.87	1.54	1.30
		16.09	6.64	0.95
		14.04	9.72	0.71
		12.32	9.96	2.37
		6.16	5.45	0.47
		6.85	5.22	0.47
		14.38	9.01	4.74
		13.01	5.45	2.37
	14470	9.28	8.53	0.66
		16.33	10.28	1.31
		12.62	12.25	1.09
		16.70	8.09	1.31
		10.02	7.43	1.31
		20.04	4.81	3.06
		11.88	11.15	1.09
		14.48	10.93	1.53

Table C.13 (continued)

Series	Re	$y+$	u_p+	v_p+
		12.99	5.25	2.19
		15.59	4.15	1.09
		12.25	5.47	0.22
		13.73	7.87	0.66
		11.14	6.56	0.66
		10.39	11.37	3.28
		8.54	7.87	1.31
		8.91	4.81	1.09
		10.02	9.62	0.66
		20.79	7.00	3.06
		8.54	1.75	0.66
		15.96	3.72	2.19
		11.51	8.53	1.09
		20.79	7.00	3.50
		17.07	9.18	2.19
		11.88	4.37	1.75
		12.25	3.06	1.97
		14.10	5.90	0.44
		16.70	6.12	1.97
		12.62	5.25	1.09
		8.54	6.34	0.44
		11.51	7.65	1.75
		9.65	5.90	1.75
		10.39	8.97	1.75
	18650	20.80	7.10	2.23
		24.80	7.30	2.03
		26.80	8.12	1.01
		14.80	14.81	1.42
		17.60	15.42	1.42
		18.40	15.02	0.41
		20.00	15.42	0.81
		7.20	5.48	0.61
		10.40	6.29	1.62

Table C.13 (continued)

Series	Re	$y+$	u_p+	v_p+
		12.40	7.51	1.01
		14.00	7.30	0.81
		8.00	3.45	1.01
		12.00	5.48	2.03
		13.60	6.49	0.81
		14.80	7.10	0.61
		14.80	7.91	
		16.40	7.30	0.81
		17.60	6.49	0.61
		18.80	6.29	0.61
		7.60	3.25	1.01
		12.00	5.28	2.23
		14.00	6.90	1.01
		12.00	8.72	1.42
		15.60	9.33	1.83
		10.80	6.09	2.03
		13.20	8.12	1.22
		17.60	8.93	2.23
		20.80	13.19	1.62
	22500	20.71	14.39	0.54
		23.05	13.32	1.08
		26.18	11.52	1.44
		27.35	11.34	0.54
		27.35	10.80	
		20.32	14.39	0.36
		22.66	13.32	1.08
		25.79	11.52	1.44
		27.74	11.34	0.90
		23.05	12.24	1.08
		25.01	13.14	0.90
		25.40	12.60	0.18
		26.57	12.60	0.54
		12.50	5.40	0.72

Table C.13 (continued)

Series	Re	$y+$	u_p+	v_p+
		14.07	5.58	0.72
		14.07	6.84	
		15.63	5.76	0.72
		18.76	7.20	1.08
		21.88	6.84	1.44
		24.23	6.66	0.54
		17.97	12.60	0.54
		16.80	12.42	
		14.85	12.24	
		13.68	11.34	
		12.89	9.36	
T	18840	22.72	3.95	0.49
		20.90	4.69	0.49
		22.72	3.70	0.49
		21.81	3.21	0.49
		20.90	3.95	0.49
		11.36	3.70	0.25
		20.90	8.63	0.99
		16.81	5.18	2.22
		17.72	4.44	0.74
		22.72	8.39	0.49
		23.62	5.92	0.49
		23.17	8.14	0.74
		21.35	5.18	1.23
		24.53	6.66	2.96
		10.45	8.14	1.23
		15.45	1.97	2.47
	21480	8.20	2.91	0.79
		13.12	3.70	1.59
		22.96	5.29	3.18
		25.69	6.61	2.38
		27.88	5.29	3.44
		26.78	3.70	1.32

Table C.13 (continued)

Series	Re	$y+$	u_{p+}	v_{p+}
		22.96	6.35	1.06
		15.85	4.76	1.32
		23.50	5.82	0.79
		6.56	3.70	0.53
		9.29	5.29	0.79
	25240	18.76	6.17	0.49
		19.35	4.69	2.22
		9.38	4.44	0.99
		14.66	4.93	1.23
		23.45	6.41	2.46
		11.72	2.96	1.48
		19.93	3.70	1.97
		22.86	5.18	0.25
		22.86	9.13	1.73
		19.93	8.14	0.99
		5.28	3.45	1.23
		9.97	2.715	0.74
		14.07	3.70	0.99
		22.28	5.67	1.48
		17.59	4.44	0.99
		23.45	7.89	0.99

Table C.14 Dimensionless ensemble averaged particle ejection velocities

Series	$y+$	$\overline{u}_{p+}$	$\sigma_{u_{p+}}$	$\overline{v}_{p+}$	$\sigma_{v_{p+}}$	$-<u'_{p+}v_{p+}>$
S	10.0	8.22	2.87	1.15	0.94	4.18
	30.0	9.99	2.30	1.07	0.78	3.72
	50.0	12.87	2.96	1.31	0.78	2.75
	70.0	14.26	2.17	1.28	0.74	1.79
	90.0	14.01	1.72	1.27	0.76	3.05
	110.0	15.80	1.49	1.02	0.52	1.30
	130.0	15.33	1.06	1.43	0.70	2.71
	150.0	16.54	0.20	1.01	0.41	0.84

Table C.14 (continued)

Series	y_+	$\overline{u}_{p+}$	$\sigma_{u_{p+}}$	$\overline{v}_{p+}$	$\sigma_{v_{p+}}$	$-<u'_{p+}v_{p+}>$
T	10.0	5.13	1.86	0.91	0.60	5.90
	30.0	6.35	1.69	0.99	0.66	6.44
	50.0	7.31	1.63	1.14	0.66	7.74
	70.0	8.53	1.57	1.25	0.77	7.93
	90.0	9.33	1.63	1.48	0.85	8.57
	110.0	9.71	1.48	1.73	0.95	11.71
	130.0	9.90	1.32	1.77	0.97	11.24
	150.0	9.96	1.40	1.75	0.80	11.51

Table C.15 Dimensionless ensemble averaged particle downward velocities

Series	y_+	$\overline{u}_{p+}$	$\sigma_{u_{p+}}$	$-\overline{v}_{p+}$	$\sigma_{v_{p+}}$
S	10.0	9.94	2.37	0.83	0.56
	30.0	14.17	2.70	1.14	0.65
	50.0	16.12	2.34	1.10	0.79
	70.0	16.44	2.10	1.05	0.52
	90.0	16.21	2.10	0.76	0.46
	110.0	16.51	1.39	0.99	0.45
	130.0	16.08	0.92	0.60	0.34

VITA

Yarko Niño was born April 24, 1961, in Santiago, Chile. After completing his high school studies, he entered the University of Chile, obtaining the degree of Civil Engineer in 1986. He was awarded the Chilean National Prize of Hydraulics in 1987, given every other year to the best graduate in Hydraulic Engineering of the last two generations from all Chilean Universities. Upon graduation, Yarko Niño was hired as a junior faculty member in the Civil Engineering Department of his alma mater, where he has been an instructor in several undergraduate courses, and has participated in a number of research projects and model studies at the hydraulics laboratory. In August, 1990, Mr. Niño came to the University of Illinois to complete his academic training, obtaining a Master's degree in Civil Engineering in May 1992. During his tenure at Illinois he has been a Research Assistant in the Hydrosystems Laboratory. Mr. Niño's work has resulted in several publications in scientific journals. In 1995, upon completion of this thesis, Mr. Niño will return to the University of Chile, where he is on leave of absence.